HEAT TRANSFER DIVISION
Chair, **Y. BAYAZITOGLU**
Vice Chair, **R. D. SKOCYPEC**
Past Chair, **Y. JALURIA**
Secretary, **T. TONG**
Treasurer, **R. W. DOUGLASS**
Member, **M. K. JENSEN**

Editor, **V. DHIR (2005)**

Associate Editors,
S. ACHARYA (2006)
C. AMON (2004)
N. K. ANAND (2006)
P. AYYASWAMY (2004)
K. BALL (2004)
G. CHEN (2005)
J. N. CHUNG (2005)
G. DULIKRAVICH (2004)
A. EMERY (2005)
B. FAROUK (2006)
C. P. GRIGOROPOULOS (2006)
M. JENSEN (2004)
D. B. R. KENNING (2004)
K. KIHM (2005)
H. LEE (2004)
J. H. LIENHARD V (2006)
P. M. LIGRANI (2006)
R. M. MANGLIK (2006)
V. PRASAD (2005)
S. THYNELL (2005)
S. P. VANKA (2005)

BOARD ON COMMUNICATIONS
Chair and Vice President
OZDEN OCHOA

OFFICERS OF THE ASME
President, **REGINALD VACHON**
Executive Director,
VIRGIL R. CARTER
Treasurer,
R. E. NICKELL

PUBLISHING STAFF
Managing Director, Engineering
THOMAS G. LOUGHLIN

Director, Technical Publishing
PHILIP DI VIETRO

Production Coordinator
COLIN McATEER

Production Assistant
MARISOL ANDINO

Transactions of the ASME, Journal of Heat Transfer (ISSN 0022-1481) is published bi-monthly (Feb., Apr., June, Aug., Oct., Dec.) by The American Society of Mechanical Engineers, Three Park Avenue, New York, NY 10016. Periodicals postage paid at New York, NY and additional mailing offices. POSTMASTER: Send address changes to Transactions of the ASME, Journal of Heat Transfer, c/o THE AMERICAN SOCIETY OF MECHANICAL ENGINEERS, 22 Law Drive, Box 2300, Fairfield, NJ 07007-2300. **CHANGES OF ADDRESS** must be received at Society headquarters seven weeks before they are to be effective. Please send old label and new address.

STATEMENT from By-Laws. The Society shall not be responsible for statements or opinions advanced in papers or ... printed in its publications (B7.1, Para. 3), **COPYRIGHT © 2004** by The American Society of Mechanical Engineers. For authorization to photocopy material for internal or personal use under those circumstances not falling within the fair use provisions of the Copyright Act, contact the Copyright Clearance Center (CCC), 222 Rosewood Drive, Danvers, MA 01923, tel: 978-750-8400, *www.copyright.com.* Request for special permission or bulk copying should be addressed to Reprints/Permission Department. **INDEXED** by Applied Mechanics Reviews and Engineering Information, Inc. Canadian Goods & Services Tax Registration #126148048.

Journal of Heat Transfer

Published Bimonthly by ASME

VOLUME 126 • NUMBER 3 • JUNE 2004

Conduction

Evaporation, Boiling, and Condensation

Experimental Techniques

Heat Pipes

Heat Transfer in Manufacturing

Micro/Nanoscale Heat Transfer

Natural and Mixed Convection

Porous Media

(Contents continued on inside back cover)

This journal is printed on acid-free paper, which exceeds the ANSI Z39.48-1992 specification for permanence of paper and library materials. ∞™
♲ 85% recycled content, including 10% post-consumer fibers.

Downloaded 05 Feb 2011 to 141.219.44.39. Redistribution subject to ASME license or copyright; see http://www.asme.org/terms/Terms_Use.cfm

(**Contents continued**)

Journal of Heat Transfer **Volume 126, Number 3** **JUNE 2004**

The ASME Journal of Heat Transfer is abstracted and indexed in the following:

Applied Science and Technology Index, AMR Abstracts Database, Chemical Abstracts, Chemical Engineering and Biotechnology Abstracts (Electronic equivalent of Process and Chemical Engineering), Civil Engineering Abstracts, Compendex (The electronic equivalent of Engineering Index), Corrosion Abstracts, Current Contents, E & P Health, Safety, and Environment, Ei EncompassLit, Engineered Materials Abstracts, Engineering Index, Enviroline (The electronic equivalent of Environment Abstracts), Environment Abstracts, Environmental Engineering Abstracts, Environmental Science and Pollution Management, Fluidex, Fuel and Energy Abstracts, Index to Scientific Reviews, INSPEC, International Building Services Abstracts, Mechanical & Transportation Engineering Abstracts, Mechanical Engineering Abstracts, METADEX (The electronic equivalent of Metals Abstracts and Alloys Index), Petroleum Abstracts, Process and Chemical Engineering, Referativnyi Zhurnal, Science Citation Index, SciSearch (The electronic equivalent of Science Citation Index), Theoretical Chemical Engineering

Ted D. Bennett
Department of Mechanical and Environmental Engineering,
University of California,
Santa Barbara, CA 93106

Determining Anisotropic Film Thermal Properties Through Harmonic Surface Heating With a Gaussian Laser Beam: A Theoretical Consideration

The phase of a temperature field resulting from the harmonic surface heating of a film can contain sufficient information to determine the film thermal properties. The case of a film having anisotropic properties and heated by a Gaussian laser beam is analytically analyzed. The transient part of the solution is expressed in terms of a complex temperature field to relay both amplitude and phase information. A general solution for the temperature distribution throughout the film and substrate is presented and analyzed to assess strategies for resolving multiple thermal properties of the film based on the underlying heat transfer. A sensitivity analysis is performed and two limiting cases of the solution are analyzed to resolve the in-plane conductivity, across-plane conductivity, and heat capacity of the film using surface temperature phase measurements. [DOI: 10.1115/1.1735758]

Keywords: *Analytical, Heat Transfer, Periodic, Properties, Thin Films*

1 Introduction

The temperature field resulting from modulated surface heating of a film can be interrogated for phase information, which in turn may be used to determine thermal properties of the film. Many approaches have been adopted, with the significant differences being related to the method of heating and the method of temperature detection. Analysis performed in support of these measurements usually differs in the temporal form of heating (pulsed or periodic) and the geometry of the heat diffusion path (heat dissipated from a plane, line or point being some of the limiting cases). The use of temperature phase measurements of a film heated with a modulated source is becoming a well established method for determining thermal properties of films. However, except for the simplest situations, few analytic solutions have been worked out, with the more complicated situations, such as anisotropic films, being resolved numerically. While this does not hinder the ability to fit experimental measurements, it does inhibit the insight gained from seeing the form of the solution that is realized though analytic work. The current analytic analysis shows dimensionally how the anisotropic film thermal properties dictate the phase relationship between the laser heating and the temperature field. Analysis reveals that the phase shift in temperature is a consequence of multiple thermal diffusion length scales interacting with other important length scales such as the film thickness and the beam radius. Since both the beam size and the diffusion length scale may be varied, limiting cases of the solution are analyzed with some practical relevance.

Many film property measurement techniques have been developed over the years. Flash methods measures the diffusion time across a thin film by probing the temperature rise at the back surface resulting from a heat pulse delivered to the front surface [1,2]. Many variations on this technique exist, distinguished in part by the method of heating and temperature sensing. Lasers are frequently used as the heating source, in which case the method is known as laser flash. The laser flash method has been used to investigate anisotropic films by varying the position of the temperature measurement on the back surface [3]. One disadvantage of the flash method is that access to the back surface requires thin free-standing samples. However, other methods have been developed to probe the front surface. The photo-acoustic method heats the surface of a film with a laser and probes the phase of the front surface temperature rise from the acoustic wave emitted through the air [4,5]. The mirage or optical beam-deflection method heats the surface with a laser and probes the front surface temperature rise through refractive index changes that occur in the air above the surface [6–8]. The mirage method has been applied to the study of anisotropic samples [9]. The thermal reflectance technique heats the surface with a laser and probes the surface temperature rise through reflectivity changes that occur at the wavelength of a probe beam. This technique has been used with heating and probing beams in close proximity, for lateral diffusivity measurements at micrometer scales [10].

Harmonic heating of films can also be accomplished with Joule heating. The $3-\Omega$ technique uses a lithographically patterned wire affixed to the surface of a film for both Joule heating and the temperature measurement via resistivity changes [11]. This technique has also been used to investigate the thermal properties of anisotropic films [12]. A variant of this technique uses optical thermometry to monitor the wire temperature, and variation in the wire (film) width to determine in-plane versus across-plane conductivities [13]. A major draw back to the $3-\Omega$ technique is the extensive sample preparation required, in contrast to most of the techniques using a laser as the heating source.

In the present work, theoretical analysis is performed on an anisotropic film heated by a spatially Gaussian laser beam. The purpose of this analysis is to elucidate the dependency between the phase of the temperature field and the thermophysical parameters of the problem, thereby illuminating strategies for measuring these properties. The most convenient access point to probe the temperature field is the surface. Phase information is preferred over amplitude because of the difficulty of making absolute temperature measurements (with pyrometric techniques for example). In contrast, the absolute value of phase can be directly determined using the laser as a reference.

Contributed by the Heat Transfer Division for publication in the JOURNAL OF HEAT TRANSFER. Manuscript received by the Heat Transfer Division March 11, 2003; revision received February 20, 2004. Associate Editor: C. P. Grigoropoulos.

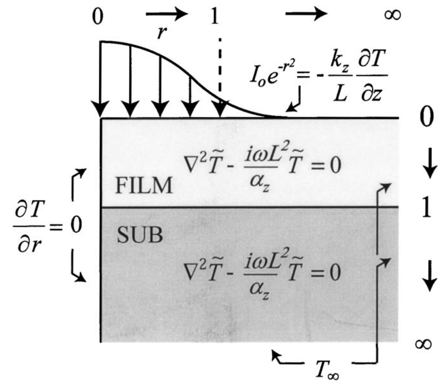

Fig. 1 Mathematical problem posed by an anisotropic film heated with a Gaussian beam. The Laplacian operator is given by: $\nabla^2 \equiv k_r/k_z(L/R)^2(\partial^2/\partial r^2 + (1/r)\partial/\partial r) + \partial^2/\partial z^2$.

The heating source and geometry are chosen for relative ease of experimental implementation and for having sufficient dimensional complexity to resolve anisotropic properties. Complexities of the actual temperature measurement needed are not addressed in this work; elsewhere, pyrometric measurements are being incorporated into a numerical solution of this problem. Here, analysis of the temperature is performed to assess theoretical strategies for resolving multiple thermal properties of the film. The film surface at the beam center is used as an interrogation point to understand the characteristics of the solution. However, the exact solution could be used to evaluate any or all parts of the domain, depending on actual interrogation requirements.

2 General Solution

The problem is illustrated in Fig. 1. The film is assumed to be spatially homogeneous with isotropic in-plane conductivity, k_r, but distinct across-plane conductivity, k_z, characteristic of films with columnar microstructures. The substrate properties are isotropic. The present solution assumes negligible thermal resistance at the interface between the film and the substrate. This is not always the case. It is assumed that the optical penetration depth at the laser wavelength is sufficiently small compared to the film thickness such that heat can be introduced as a surface flux. Since all lasers have a finite optical penetration depth, this factor will invalidate the current solution for high laser frequencies where the thermal penetration depth is comparable to the optical penetration depth.

The problem is axisymmetric with respect to the laser beam. Spatial variables in Fig. 1 are presented in dimensionless form. The radial coordinate is made dimensionless by the radius of the Gaussian beam R, such that the heat flux imposed by the laser becomes

$$\tilde{I} = \tilde{I}_o \exp(-r^2) \tag{1}$$

$\tilde{I}_o$ is the complex amplitude of the heat flux at the centerline. The axial coordinate is made dimensionless by the film thickness L, such that $z=1$ at the interface between the film and the substrate. In terms of these dimensionless spatial variables, the axisymmetric conduction equation for an anisotropic medium in cylindrical coordinates becomes

$$\rho C L^2 \frac{\partial T}{\partial t} = k_r\left(\frac{L}{R}\right)^2\left(\frac{\partial^2 T}{\partial r^2} + \frac{1}{r}\frac{\partial T}{\partial r}\right) + k_z\frac{\partial^2 T}{\partial z^2} \tag{2}$$

A solution can be derived through the superposition of steady and transient temperature fields $T(r,z,t) = \overline{T}(r,z) + T^*(r,z,t)$. For phase analysis, only the transient temperature field $T^*(r,z,t)$ must be known. Using the method of complex combination [14], the transient temperature is expressed in terms of a complex spatial variable $\tilde{T}(r,z)$ through the relation: $T^*(r,z,t) = re\{\tilde{T}(r,z)e^{i\omega t}\}$. This approach is used to determine the sustained transient solution, where the temporal form of the solution is dictated by harmonic laser heating at an angular frequency of ω. Applied to the conduction equation, the complex combination transformation gives

$$\frac{k_r}{k_z}\left(\frac{L}{R}\right)^2\left(\frac{\partial^2\tilde{T}}{\partial r^2} + \frac{1}{r}\frac{\partial\tilde{T}}{\partial r}\right) + \frac{\partial^2\tilde{T}}{\partial z^2} - \frac{i\omega L^2}{\alpha_z}\tilde{T} = 0 \tag{3}$$

Equation (3) governs the spatial variation in the complex temperature field, which provides both the amplitude $abs\{\tilde{T}\}$ and phase $\arg\{\tilde{T}\}$ of the transient temperature field. The conduction equation can be further nondimensionalized using four dimensionless length scales defined by

$$\ell \equiv \frac{\sqrt{[\alpha_z]_{\text{film}}/\omega}}{L} \quad a \equiv \sqrt{\frac{\alpha_z}{[\alpha_z]_{\text{film}}}} \quad b \equiv \frac{R}{L} \quad c \equiv \sqrt{\left(\frac{k_r}{k_z}\right)} \tag{4a–d}$$

The variable "ℓ" is a dimensionless axial thermal penetration depth relative to the film thickness L. In the substrate, the variable "a" contrasts the axial diffusion length in the substrate with that in the film. In the film $a_{\text{film}} = 1$. The variable "b" provides the beam radius relative to the film thickness. The variable "c" contrasts the length scales of radial and axial diffusion, and is a measure of diffusion anisotropy. In the substrate $c_{\text{sub}} = 1$. In terms of these dimensionless length scales the conduction equation becomes

$$\frac{\partial^2\tilde{\theta}}{\partial r^2} + \frac{1}{r}\frac{\partial\tilde{\theta}}{\partial r} + \frac{b^2}{c^2}\frac{\partial^2\tilde{\theta}}{\partial z^2} - \frac{ib^2\tilde{\theta}}{a^2c^2\ell^2} = 0 \tag{5}$$

where the complex temperature is made dimensionless by the definition

$$\tilde{\theta} \equiv \frac{\tilde{T}}{L\tilde{I}_o/[k_z]_{\text{film}}} \tag{6}$$

Although the appearance of b/c in the conduction equation suggests that b and c may be combined without loss of information, the boundary conditions considered next will demonstrate that these two variables play distinct roles in the solution.

There are six boundary conditions that must be applied to the solution. The surface has a heat flux boundary condition and the centerline is adiabatic. The heat flux and temperature at the interface between the film and the substrate must match. The domain extends to infinity in the radial and axial directions, and the complex temperature amplitude must go to zero in these limits. Mathematically, the boundary conditions for the problem at hand are given in dimensionless form as

$$\text{surface:} \quad \{[-\partial\tilde{\theta}/\partial z|_{z=0}]_{\text{film}} = \exp(-r^2) \tag{7a}$$

$$\text{interface:} \quad \begin{cases}[\tilde{\theta}(z=1)]_{\text{film}} = [\tilde{\theta}(z=1)]_{\text{sub}} \\ [-k(\partial\tilde{\theta}/\partial z)|_{z=1}]_{\text{film}} = [-k(\partial\tilde{\theta}/\partial z)|_{z=1}]_{\text{sub}}\end{cases} \tag{7b,c}$$

$$\text{substrate:} \quad \{[\tilde{\theta}(z\to\infty)]_{\text{sub}} = 0 \tag{7d}$$

$$\text{centerline:} \quad \{(\partial\tilde{\theta}/\partial r)|_{r=0} = 0 \tag{7e}$$

$$\text{periphery:} \quad \{\tilde{\theta}(r\to\infty) = 0 \tag{7f}$$

A solution is sought by the separation of variables method, starting with the usual assumption that $\tilde{\theta} = \tilde{R}(r)\tilde{Z}(z)$. The separated governing equation yields two ordinary differential equations that can be integrated and expressed in terms of a separation constant ν. The solution becomes governed by the ordinary differential equations

$$\tilde{R} = \tilde{M}J_0(\nu r) + \tilde{N}Y_0(\nu r) \tag{8a}$$

$$\tilde{Z}=\begin{cases}\tilde{A}\cosh(\tilde{\nu}z/\ell)+\tilde{B}\sinh(\tilde{\nu}z/\ell) & (z\leqslant 1)\\ \tilde{C}\exp[\hat{\nu}(z-1)/(a_{\mathrm{sub}}\ell)]+\tilde{D}\exp[\hat{\nu}(1-z)/(a_{\mathrm{sub}}\ell)] & \\ & (z>1)\end{cases}\tag{8b}$$

in which

$$\tilde{\nu}=\sqrt{i+(\nu c_{\mathrm{film}}\ell/b)^2}\quad\text{and}\quad\hat{\nu}=\sqrt{i+(\nu a_{\mathrm{sub}}\ell/b)^2}\tag{8c,d}$$

Using all the homogeneous boundary conditions imposed on the problem, the integrations constant are found to be $\tilde{A}=-\tilde{B}\tilde{F}$, $\tilde{N}=\tilde{C}=0$, $\tilde{D}=\tilde{B}[\sinh(\tilde{\nu}/\ell)-\tilde{F}\cosh(\tilde{\nu}/\ell)]$, where

$$\tilde{F}=\frac{\tilde{\nu}+\hat{\nu}\gamma\tanh(\tilde{\nu}/\ell)}{\hat{\nu}\gamma+\tilde{\nu}\tanh(\tilde{\nu}/\ell)}\tag{9}$$

and

$$\gamma=\sqrt{\frac{[k_z\rho C]_{\mathrm{sub}}}{[k_z\rho C]_{\mathrm{film}}}}\tag{10}$$

Notice that $\tilde{F}$ captures the effect of the film on the solution. Notice also that the film anisotropy factor appears without the relative beam radius "b," in contrast to their grouping in the conduction equation, Eq. (5). A finial point to observe is that a new dimensionless parameter γ has been introduced into the solution as a consequence of satisfying interface conditions between the film and substrate. The parameter γ describes the effusivity contrast between the substrate and the film.

The final inhomogeneous boundary condition cannot be imposed on either of the separate spatial functions $\tilde{R}(r)$ or $\tilde{Z}(z)$ alone. Therefore, reconstructing the temperature field gives

$$\tilde{R}(r)\tilde{Z}(z)=\ell\tilde{G}(\nu)J_0(\nu r)\tilde{\zeta}(\nu,z)\tag{11}$$

where

$$\tilde{\zeta}(\nu,z)=\frac{1}{\tilde{\nu}}\begin{cases}[\tilde{F}\cosh(\tilde{\nu}z/\ell)-\sinh(\tilde{\nu}z/\ell)] & (z\leqslant 1)\\ [\tilde{F}\cosh(\tilde{\nu}/\ell)-\sinh(\tilde{\nu}/\ell)]\exp\left(\hat{\nu}\dfrac{(1-z)}{a_{\mathrm{sub}}\ell}\right) & (z>1)\end{cases}\tag{12}$$

and $\tilde{F}$ is given by Eq. (9). The remaining integration constants have been grouped by letting $\tilde{G}(\nu)=-\tilde{B}\tilde{M}\tilde{\nu}/\ell$. Any single choice of the separation constant ν will be unsuitable for satisfying the final inhomogeneous boundary condition at the surface with the remaining integration constant. Therefore, a solution is sought by superposition of solutions using all possible separation constants ν

$$\tilde{\theta}=\int_0^\infty\tilde{R}(r)\tilde{Z}(z)\,d\nu=\ell\int_0^\infty\tilde{G}(\nu)J_0(\nu r)\tilde{\zeta}(\nu,z)\,d\nu\tag{13}$$

where suitable integration constants for each choice of ν are determined by application of the final boundary condition

$$[-\partial\tilde{\theta}/\partial z|_{z=0}]_{\mathrm{film}}=\int_0^\infty\tilde{G}(\nu)J_0(\nu r)\,d\nu=\exp(-r^2)\tag{14}$$

The remaining integration constant $\tilde{G}(\nu)$ is established from

$$\tilde{G}(\nu)=\nu\int_0^\infty rJ_0(\nu r)\exp(-r^2)\,dr=\frac{\nu}{2}\exp\left(\frac{-\nu^2}{4}\right),\tag{15}$$

and the final solution for the complex temperature field in the film and substrate is, therefore,

$$\tilde{\theta}=\frac{\ell}{2}\int_0^\infty J_0(\nu r)\tilde{\zeta}(\nu,z)\exp\left(\frac{-\nu^2}{4}\right)\nu\,d\nu\tag{16}$$

where $\tilde{\zeta}(\nu,z)$ is given by Eq. (12).

It is seen that the solution depends on five thermal parameters: (1) the thermal penetration relative to the film thickness ℓ, (2) the relative axial thermal penetration in the substrate compared to the film a_{sub}, (3) the heating beam radius relative to the film thickness b, (4) the degree of diffusion anisotropy in the film c_{film}, and (5) the effusivity contrast between the substrate and the film γ. Two parameters are variables of the measurement, the dimensionless thermal penetration depth ℓ and the dimensionless beam radius b. Note that while the thermal penetration depth ℓ is variable, it cannot be quantified without knowledge of the axial diffusivity in the film.

3 Limiting Cases of General Solution

Some limiting cases of the solution will be explored with the expectation that a reduction in the number of dependent variables can be realized with consequential simplification of analysis. Experimentally there are two variables that can be utilized toward this end, the beam size b, and the thermal penetration depth ℓ. However, some limiting cases for these variables prove to be useless for the desired measurement. The limit $b\ll\ell$, yields a solution in which the phase of the temperature at the point of heating is zero, independent of the film thermal properties. The limit $b\gg 1$ with $\ell\ll 1$ or $\ell\gg 1$ yields a solution in which the phase of the surface temperature is insensitive to the film properties. The interesting limiting cases, which will prove to be valuable, are $\ell\approx 1$ with $b\gg 1$ and $\ell\ll 1$ with $b\approx\ell$. These cases are considered next.

3.1 One-Dimensional Heating. The case in which the beam diameter becomes large compared with axial thermal penetration, $b/\ell\gg 1$, is considered. In this limit, the solution of the dimensionless temperature field becomes a function of z alone

$$\tilde{\theta}_{b/\ell\gg 1}=\frac{\ell}{\sqrt{i}}\begin{cases}[\tilde{F}_{b/\ell\gg 1}\cosh(\sqrt{i}z/\ell)-\sinh(\sqrt{i}z/\ell)] & (z\leqslant 1)\\ [\tilde{F}_{b/\ell\gg 1}\cosh(\sqrt{i}/\ell)-\sinh(\sqrt{i}/\ell)] & \\ \quad\times\exp\left(\sqrt{i}\dfrac{(1-z)}{a_{\mathrm{sub}}\ell}\right) & (z\geqslant 1)\end{cases}\tag{17a}$$

where $\tilde{F}_{b/\ell\gg 1}$ results from the limiting case of $\tilde{F}(b\rightarrow\infty)$ and is

$$\tilde{F}_{b/\ell\gg 1}=\frac{1+\gamma\tanh(\sqrt{i}/\ell)}{\gamma+\tanh(\sqrt{i}/\ell)}\tag{17b}$$

Note: $\tilde{I}_o$ in the definition of $\tilde{\theta}$ is replaced by $\tilde{I}(r)$ in this limit.

It is seen that the one-dimensional solution depends only on two thermal parameters: (1) the thermal penetration relative to the film thickness ℓ, and (2) the effusivity contrast between the substrate and the film γ. The surface temperature becomes

$$\tilde{\theta}_{b\gg 1}(0)=\frac{\ell\tilde{F}_{b/\ell\gg 1}}{\sqrt{i}}\tag{18}$$

Notice that the phase of the temperature field is as follows: $\arg\{\ell\tilde{F}_{b/\ell\gg 1}/\sqrt{i}\}=\arg\{\tilde{F}_{b/\ell\gg 1}\}-\pi/4$, where the fixed phase shift of $-\pi/4$ comes from $\arg\{1/\sqrt{i}\}$. The variability of the surface temperature phase is described by $\arg\{\tilde{F}_{b/\ell\gg 1}\}$ alone. The result for the surface temperature phase for the one-dimensional case ($b/\ell\gg 1$) is

$$\arg\{\tilde{\theta}_{b/\ell\gg 1}(0)\}=\tan^{-1}\left(\frac{2(\gamma^2-1)\sin(1/\sqrt{2}\ell)\cos(1/\sqrt{2}\ell)}{(\gamma^2+1)\sinh(\sqrt{2}/\ell)+2\gamma\cosh(\sqrt{2}/\ell)}\right)-\pi/4\tag{19}$$

It is interesting to note that if the effusivity contrast between the substrate and the film disappears, $\gamma=1$, then $\arg\{\tilde{F}_{b/\ell\gg 1}\}=0$ and the surface phase becomes fixed at $-\pi/4$.

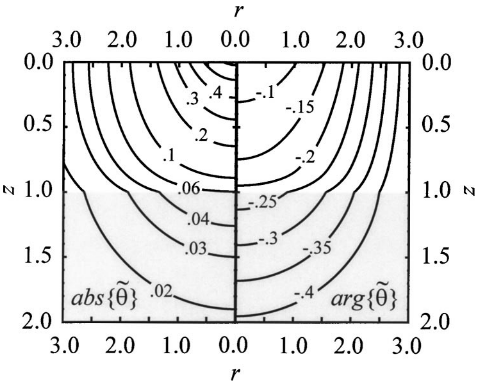

Fig. 2 Illustrative solution for the complex temperature amplitude and phase, using $\ell=2$, $b=1/2$, $\gamma=2$, $a_{\text{sub}}=2$, and $c_{\text{film}}=1/2$. The left panel shows dimensionless amplitude, while the right panel shows phase in units of radians.

3.2 Semi-Infinite Film When the thermal penetration depth is small compared with the film thickness, $\ell \ll 1$, the film appears to be semi-infinite. In this limit $\tilde{F}(\ell \to 0)=1$. Again the phase of the surface temperature is of interest. However, the phase is a function of radial position. Hence, the center of the laser beam is chosen for interrogation, where the temperature is found to be

$$\tilde{\theta}_{\ell \ll 1}(0,0)=\ell \int_0^\infty \frac{\exp(-\nu^2/4)}{2\tilde{\nu}} \nu d\nu$$

$$= \frac{\sqrt{\pi}b}{2c_{\text{film}}} \exp\left(\frac{i}{4}\left(\frac{b}{c_{\text{film}}\ell}\right)^2\right) \operatorname{erfc}\left(\frac{\sqrt{i}b}{2c_{\text{film}}\ell}\right) \qquad (20)$$

It can be seen from Eq. (20) that the phase $\arg\{\tilde{\theta}_{\ell \ll 1}(0,0)\}$ will depend on only one variable $b/(c_{\text{film}}\ell)$ formed from the beam size b, the degree of diffusion anisotropy in the film c_{film}, and the thermal penetration depth ℓ. The effect of the beam size relative to the film anisotropy b/c_{film} influences the amplitude of the temperature, but not the phase. The quantity $b/(c_{\text{film}}\ell)$ depends only on beam radius relative to the radial thermal penetration depth in the film

$$\frac{b}{c_{\text{film}}\ell} = \frac{R}{\sqrt{[\alpha_r]_{\text{film}}/\omega}} \qquad (21)$$

This result is interesting in that it demonstrates that the radial component of thermal diffusivity is the only material property important to the phase shift. Without the effusivity contrast provided by the interface between film and substrate, there is no means to determine the axial component of thermal diffusivity.

4 Discussion

Figure 2 illustrates the general solution given by Eq. (16) for $\ell=2$, $b=1/2$, $\gamma=2$, $a_{\text{sub}}=2$, and $c_{\text{film}}=1/2$. The situation describes film of lower conductivity than the substrate, where the volumetric heat capacity of both the film and the substrate are the same. The beam diameter $(2R)$ equals the film thickness for the case illustrated. Notice that the ordinate scale is expanded relative to the abscissa scale in the figure. The spatial variation in temperature amplitude and phase are shown in the left and right panels, respectively. Moving away from the heat source, the transient temperature field amplitude decays in both radial and axial directions, while the phase delay progressively increases. Crossing the interface, the isolines for temperature and phase spread further apart, as heat penetrates into the higher conductivity substrate.

There are two experimental variables over which control may be leveraged, the beam diameter b and the thermal depth ℓ. It is of interest to map the sensitivity of the temperature phase to the thermal properties of the film (as characterized by a_{sub}, c_{film}, and γ). Figure 3 shows the phase measurement sensitivity to film properties over a range of values for b and ℓ. The ratio between change in temperature phase at the interrogation point and the corresponding change in an individual film parameter defines the sensitivity of the measurement to that parameter. The temperature phase is taken at the surface and centerline of the laser beam ($r=0$, $z=0$). Since ℓ depends on film properties, it is useful to define an alternative thermal penetration parameter using the substrate properties: $\ell_{\text{sub}} \equiv a_{\text{sub}}\ell$, which is used for the abscissa in Fig. 3.

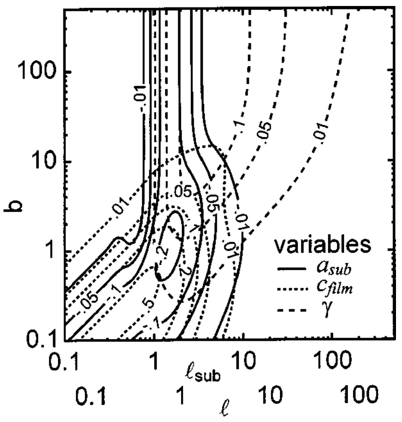

Fig. 3 Map of temperature phase sensitivity to the unknown thermal properties of the film. Sensitivity to any variable "X" is defined as $\partial\tilde{\theta}(0,0)/\partial X$. The map uses $a_{\text{sub}}=2$, $c_{\text{film}}=1/2$, and $\gamma=2$ for the nominal film parameters.

The phase measurement sensitivity to a_{sub}, which contrasts the axial diffusion length scale in the substrate with that in the film, is seen in Fig. 3 to be strongest for thermal penetration depths of the order of unity. This maximum extends broadly over a range of beam size b, indicating low sensitivity of a_{sub} to the choice of b. Sensitivity of the measurement to a_{sub} becomes small as the thermal penetration depth becomes large because of the dominance of substrate diffusion alone on heat transport. On the other hand, as the thermal penetration depth drops below unity, the sensitivity also decreases because of the diminished influence of axial diffusion in the substrate. It will be shown that for $\ell \ll 1$, the phase of temperature field at a given point becomes a function of radial diffusion alone.

The phase measurement sensitivity to c_{film}, which contrasts the length scales of radial and axial diffusion in the film, is strongest for thermal penetration depths smaller that unity and when the beam size is comparable to the thermal penetration depth. If the beam size is large compared to the thermal penetration depth, axial diffusion dominates, and the solution is insensitive to radial diffusion in the film. If the beam size is small compared with the thermal penetration depth, the phase at the heating source goes to zero, corresponding to the solution for heating at a point source.

The phase measurement sensitivity to the film-substrate effusivity contrast, γ, is seen in Fig. 3 to be strongest for large beams over a range of thermal penetration depths that are a few times greater than unity. Under this circumstance, the solution is dominated by one-dimensional heat transfer through the film.

Although the general solution contains information pertaining to all of the desired film properties, it also presents the most difficulty in resolving complimentary effects on the experimental measurement. In contrast, more clearly resolvable, but limited information, can be obtained by exploring the limiting cases. Therefore, the results found for the limiting cases of $b \to \infty$ and $\ell \ll 1$ are explored in the context of measurements that can be made to

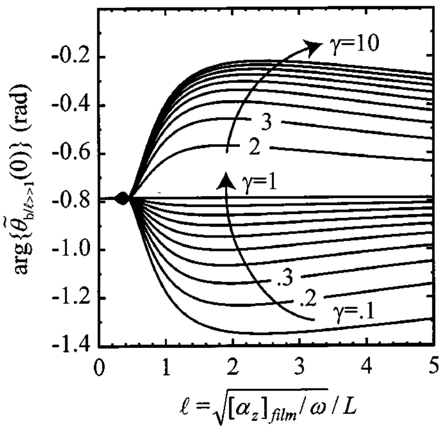

Fig. 4 Surface temperature phase for the limiting case of large beam diameter $b/\ell \gg 1$ as a function of thermal penetration depth and effusivity contrast parameter

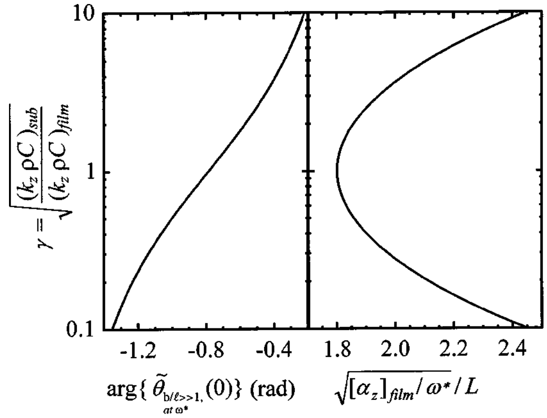

Fig. 5 Relationship between the surface temperature phase extremum (left abscissa), the effusivity contrast parameter γ (ordinate), and the corresponding thermal penetration depth (right abscissa), for the beam diameter $b/\ell \gg 1$ case. The surface temperature phase extremum corresponds to the laser frequency ω^* at which $\partial/\partial\ell\ \arg\{\tilde{\theta}_{b/\ell\gg1}(0)\}=0$.

determine the anisotropic properties of the film. It is assumed that the thermal properties of the substrate and the film thickness are known.

4.1 One-Dimensional Heating As was already observed, the phase of the surface temperature for the limiting case of $b/\ell \gg 1$ depends on two parameters: the thermal penetration relative to the film thickness ℓ and the effusivity contrast between the substrate and the film γ. The relative thermal penetration is a variable of the measurement related to the frequency of the laser modulation ω. An experiment can be constructed in which the thermal penetration is varied as the surface temperature phase is measured. Figure 4 illustrates the predicted results of such a measurement for a range of cases having different effusivity contrasts γ between 0.1 and 10. The phase shift of the surface temperature is influenced by the properties of the substrate relative to the film as quantified by γ. For $\gamma = 1$, the measured phase shift is fixed at a value of $-\pi/4$, regardless of the value of the thermal penetration depth ℓ. However, for $\gamma > 1$, the high conductivity of the substrate shortens the delay in phase of the peak surface temperature. In contrast, for $\gamma < 1$ the phase shift is further delayed by the low conductivity of the substrate. An important observation that can be made from Fig. 4 is that a unique maximum in phase shift occurs for all $\gamma > 1$ and that a unique minimum phase shift value occurs for all $\gamma < 1$. The uniqueness of the extremum phase shift value to the value of γ suggests that the effusivity contrast between the substrate and the film can be found through this measurement. Furthermore, the phase shift extremum occurs at a thermal penetration depth that depends uniquely on the value of γ. Therefore, once the effusivity γ is found, the thermal penetration depth ℓ for that case can be determined. Knowledge of both the effusivity contrast γ and thermal penetration depth ℓ is sufficient to determine the volumetric specific heat ρC and across-plane conductivity k_z of the film.

A procedure for analyzing the one-dimensional measurements is illustrated in Fig. 5. The relationship between the phase of the phase shift extremum, labeled on the left abscissa, and the effusivity contrast, labeled on the ordinate, is shown. Once the effusivity contrast is known, the thermal penetration depth is read from the right abscissa. If the substrate properties are known, the effusivity contrast value provides one relation for two unknowns: the volumetric specific heat ρC and across-plane conductivity k_z of the film. Knowledge of the laser frequency ω, corresponding to the phase shift extremum, and film thickness L makes ρC and k_z for the film the only unknowns in the expression for ℓ. Combining these two results allows for determination of both unknowns.

It should be noted that when $\gamma \gg 1$, the surface temperature becomes $\tilde{\theta}_{\substack{\gamma\gg1\\ b/\ell\gg1,}}(0) = (\ell/\sqrt{i})\tanh(\sqrt{i}/\ell)$, which is independent of γ, and therefore ρC and k_z cannot be resolved independently. Equally true, when $\gamma \ll 1$ the surface temperature becomes $\tilde{\theta}_{\substack{\gamma\ll1\\ b/\ell\gg1,}}(0) = (\ell/\sqrt{i})\coth(\sqrt{i}/\ell)$, which is also independent of γ. Finally, if $\gamma = 1$, the surface temperature becomes $\tilde{\theta}_{b/\ell\gg1}(0) = \ell/\sqrt{i}$, the phase of which is fixed and independent of γ and ℓ. Therefore, although some effusivity contrast ($\gamma \neq 1$) is required to resolve ρC and across-plane conductivity k_z of the film independently, it is apparent that too much contrast is unsatisfactory to this goal as well.

4.2 Semi-Infinite Film When the axial thermal penetration depth is sufficiently short $\ell \ll 1$, the effusivity contrast provided by the substrate is unobserved in the solution for the transient temperature field. Furthermore, the phase of the temperature field at the surface-center becomes dependent only on one variable $b/(c_{\text{film}}\ell)$, as illustrated by Eq. (20). The surface-center temperature phase is plotted in Fig. 6 as a function of $b/(c_{\text{film}}\ell)$, where $b/(c_{\text{film}}\ell) = R/\sqrt{[\alpha_r]_{\text{film}}/\omega}$ can be interpreted as the beam radius R made dimensionless by the radial thermal diffusion length. Because the extensive heat capacity of the material is responsible for the lagging temperature phase, the phase shift is observed to as-

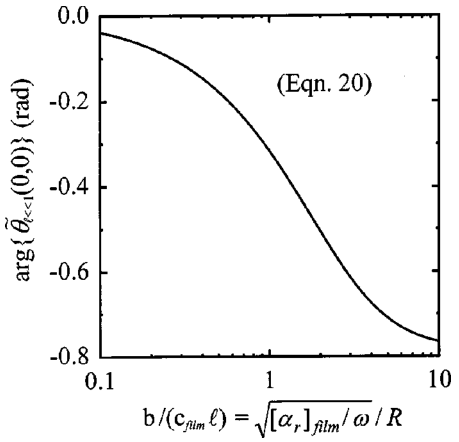

Fig. 6 The surface-center temperature phase plotted as a function of the beam diameter made dimensionless by the radial thermal diffusion length $R/\sqrt{[\alpha_r]_{\text{film}}/\omega}$ for the limiting case of small thermal penetration depth $\ell \ll 1$

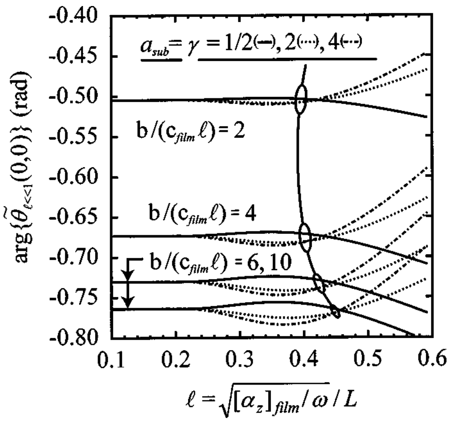

Fig. 7 Convergence of the surface-center temperature phase to the limiting case of $\ell \ll 1$ for measurements made with constant $R\sqrt{\omega}$

ymptotically approach zero as the beam size becomes small. In the other limit, as the beam size becomes large, the phase shift asymptotically approaches $-\pi/4$, as revealed by the one-dimensional solution without the influence of the effusivity contrast between the film and the substrate. Figure 6 indicates that determining the radial diffusivity of the film can be accomplished through a single measurement of the phase shift under the condition that $\ell \ll 1$. If the axial properties are measured in advance, sufficient information would be available to ensure this condition. Therefore, with knowledge of the beam radius and the heating frequency used during the measurement, the radial diffusivity can be determined from the phase shift using Fig. 6.

More generally, a measurement might be conducted without prior knowledge of the axial diffusivity of the film. In this case, an experiment can be conducted in which measurements are made as $\ell \ll 1$ while the beam size is simultaneously varied such that $R\sqrt{\omega} = \text{const}$. Under this circumstance, $b/(c_{\text{film}}\ell)$ will remain a constant and the analysis resulting in Eq. (20) dictates that the phase shift should asymptotically approach a unique value determined by $R/\sqrt{[\alpha_r]_{\text{film}}/\omega}$ according to Fig. 6. The variation in the surface-center temperature phase as $\ell \ll 1$ is shown for a number of constant values of $b/(c_{\text{film}}\ell)$ in Fig. 7. In general, the value of $b/(c_{\text{film}}\ell)$ would be unknown prior to determining the asymptotic value of the phase shift. Therefore, the cases shown are simply for illustration. The asymptotic value of phase shift is independent of the effusivity contrast, as illustrated with the simultaneous plots using $a_{\text{sub}} = \gamma = 1/2$, 2, 4. In general, $a_{\text{sub}} \neq \gamma$ and the cases illustrated in Fig. 7 using $a_{\text{sub}} = \gamma$ result only when ρC of the film and the substrate are the same. It is notable that the asymptotic value of phase shift is revealed when the thermal penetration depth is as large as 20 percent of the film thickness $\ell = 0.2$.

5 Summary

A film having anisotropic properties and heated harmonically by a modulated Gaussian shaped laser beam was analyzed. An analytic solution was presented for the temperature field in the film and underlying substrate. The general solution, Eq. (15), reveals dependency on five dimensionless parameters: the axial thermal penetration depth $\ell = \sqrt{[\alpha_z]_{\text{film}}/\omega}/L$, the relative axial thermal penetration in the substrate compared to the film $a_{\text{sub}} = \sqrt{[\alpha_z]_{\text{sub}}/[\alpha_z]_{\text{film}}}$, the heating beam size relative to the film thickness $b = R/L$, the degree of diffusion anisotropy in the film $c_{\text{film}} = \sqrt{[k_r/k_z]_{\text{film}}}$, and the effusivity contrast between the substrate and the film $\gamma = \sqrt{[k_z\rho C]_{\text{sub}}/[k_z\rho C]_{\text{film}}}$. A sensitivity study was performed on the temperature solution revealing that the phase is sensitive to a_{sub} when $\ell \approx 1$, is sensitive to c_{film} when $\ell \approx b \leq 1$, and is sensitive to γ when $\ell \approx 1$ and $b \gg 1$. Analysis of two limiting cases revealed reduced dependency on these parameters. As the beam diameter becomes large, the solution, Eq. (16), depends only on two parameters: the axial thermal penetration depth ℓ, and the effusivity contrast between the substrate and the film γ. As the axial thermal penetration depth becomes small compared with the film thickness, the solution, Eq. (20), depends only on the beam radius relative to the film anisotropy b/c_{film}, and on the beam radius relative to the radial diffusion length $b/(c_{\text{film}}\ell) = R/\sqrt{[\alpha_r]_{\text{film}}/\omega}$.

The phase of a temperature field at the surface of the film was explored as a means of determining the anisotropic thermal properties of the film. The limiting cases of the solution corresponding to a large beam diameter and a small thermal penetration depth were shown to offer a substantial simplification in analysis. It was seen that a unique phase shift extremum exists for the large beam diameter limit of the solution, from which the effusivity contrast parameter Eq. (10) and axial thermal penetration depth Eq. (4*a*) can be determined. Furthermore, it was shown that surface temperature phase at the centerline of the laser beam depends only on the beam radius relative to the radial thermal penetration in the film, Eq. (14). Using measurements from both of these two limiting cases, it was shown how the in-plane conductivity k_r, the across-plane conductivity k_z, and the volumetric specific heat ρC of the film can be determined.

Acknowledgment

This work was supported by the National Science Foundation under Grants No. CTS-9875860 and DMR-0099695.

Nomenclature

$\tilde{A},\tilde{B},\tilde{C},\tilde{D}$ = complex integration constants, Eq. (8*b*)
a = dimensionless axial diffusion length relative to substrate value, Eq. (4*b*)
b = dimensionless beam radius relative to the film thickness, Eq. (4*c*)
C = heat capacity (J/kg K)
c = dimensionless diffusion anisotropy, Eq. (4*d*)
$\tilde{F}$ = see Eq. (9)
$\tilde{G}$ = complex integration constant, Eq. (15)
$\tilde{I}$ = complex heat flux (W/m^2)
$\tilde{I}_o$ = centerline heat flux of laser (W/m^2)
i = equals $\sqrt{-1}$
J_0 = order zero Bessel function of the first kind
k = thermal conductivity (W/m K)
L = film thickness (m)
ℓ = dimensionless axial thermal penetration depth, Eq. (4*a*)
$\tilde{M}$, $\tilde{N}$ = complex integration constants, Eq. (8*a*)
r = dimensionless radial position (relative to R)
$\tilde{R}$ = complex radial temperature function, Eq. (8*a*)
R = beam radius, (m)
T = temperature (K)
$\underline{T}$ = steady temperature solution (K)
T^* = transient temperature solution (K)
$\tilde{T}$ = complex temperature, $T^* = re\{\tilde{T}e^{i\omega t}\}$, (K)
t = time (s)
z = dimensionless axial position (relative to L)
$\tilde{Z}$ = complex axial temperature function, Eq. (8*b*)

Greek Symbols

α = diffusivity, $\alpha = k/(\rho C)$, (m^2/s)
γ = substrate-film effusivity contrast, Eq. (10)
$\tilde{\nu}$ = see Eq. (8*c*)
$\hat{\nu}$ = see Eq. (8*d*)
ρ = density

$\tilde{\theta}$ = dimensionless complex temperature, Eq. (6)
ω = laser angular frequency, (rad/s)
$\tilde{\zeta}$ = see Eq. (12)

Subscripts

film = film property
r = radial component
sub = substrate property
z = axial component

References

[1] Parker, R. L., 1961, ''A Flash Method of Determining Thermal Diffusivity, Heat Capacity, and Thermal Conductivity,'' J. Appl. Phys., **32**, pp. 1679.
[2] Cowan, 1963, ''Pulse Method of Measuring Thermal Diffusivity at High Temperature,'' J. Appl. Phys., **46**, pp. 714–719.
[3] Choy, C. L., Yang, G. W., and Wong, Y. W., 1997, ''Thermal Diffusivity of Polymer Films by Pulsed Photothermal Radiometry,'' J. Polym. Sci., Part B: Polym. Phys., **35**(10), pp. 1621–1631.
[4] Rosencwaig, A., and Gersho, A., 1976, ''Theory of the Photoacoustic Effect With Solids,'' J. Appl. Phys., **47**(1), pp. 64–69.
[5] Hu, H., Wang, X., and Xu, X., 1999, ''Generalized Theory of the Photoacoustic Effect in a Multilayer Material,'' J. Appl. Phys., **86**(7), pp. 3953–3958.
[6] Boccara, A. C., Fournier, D., and Badoz, J., 1980, ''Thermo-Optical Spectroscopy: Detection by the 'Mirage Effect',' Appl. Phys. Lett., **36**(2), pp. 130–132.
[7] Aamodt, L. C., and Murphy, J. C., 1981, ''Photothermal Measurements Using a Localized Excitation Source,'' J. Appl. Phys., **52**(8), pp. 4903–5400.
[8] Kuo, P. K., Sendler, E. D., Favro, L. D., and Thomas, R. L., 1986, ''Mirage Effect Measurement of Thermal Diffusivity. II. Theory,'' Can. J. Phys., **64**(9), pp. 1168–1671.
[9] Salazar, A., Sanchez-Lavega, A., Ocariz, A., Guitonny, J., and Pandey, J. C., 1995, ''Novel Results on Thermal Diffusivity Measurements on Anisotropic Materials Using Photothermal Methods,'' Appl. Phys. Lett., **67**(5), pp. 626–628.
[10] Hartmann, J., Voigt, P., and Reichling, M., 1997, ''Measuring Local Thermal Conductivity in Polycrystalline Diamond With a High Resolution Photothermal Microscope,'' J. Appl. Phys., **81**(7), pp. 2966–2972.
[11] Cahill, D. G., 1990, ''Thermal Conductivity Measurement From 30 to 750 K: The 3 Omega Method,'' Rev. Sci. Instrum., **61**(2), pp. 802–808.
[12] Kurabayashi, K., Asheghi, M., Touzelbaev, M., and Goodson, K. E., 1999, ''Measurement of the Thermal Conductivity Anisotropy in Polyimide Films,'' J. Microelectromech. Syst., **8**(2), pp. 180.
[13] Ju, Y. S., Kurabayashi, K., and Goodson, K. E., 1999, ''Thermal Characterization of Anisotropic Thin Dielectric Films Using Harmonic Joule Heating,'' Thin Solid Films, **339**(1–2), pp. 160–164.
[14] Myers, G. E., 1998, *Analytical Methods in Conduction Heat Transfer*, 2nd ed. AMCHT Publications, Madison, WI.

Koichi Hata
e-mail: hata@iae.kyoto-u.ac.jp
Mem. ASME
Institute of Advanced Energy,
Kyoto University,
Gokasho, Uji, Kyoto 611-0011,
Japan

Masahiro Shiotsu
Dept. of Energy Science and Technology,
Kyoto University,
Gokasho, Uji, Kyoto 611-0011,
Japan

Nobuaki Noda
National Institute for Fusion Science,
322-6, Oroshi-cho, Toki, Gifu 509-5292,
Japan

Critical Heat Fluxes of Subcooled Water Flow Boiling Against Outlet Subcooling in Short Vertical Tube

The critical heat fluxes (CHFs) of subcooled water flow boiling are systematically measured for the flow velocities ($u=4.0$ to 13.3 m/s), the outlet subcoolings ($\Delta T_{\mathrm{sub,out}}=3$ to 129 K) and the outlet pressure ($P_{\mathrm{out}}=800$ kPa). The SUS304 test tubes of 3, 6, 9 and 12 mm in inner-diameter, d, and 33, 66, 99 and 133 mm in length, L, respectively for $L/d=11$ are used. The CHFs first become lower and then become higher with the increase in subcooling. The CHFs for four different inner-diameters with $L/d=11$ measured here become higher with the decrease in the diameter. CHF correlation for the latter increasing regime was given in non-dimensional form against average outlet subcoolings based on the experimental data. The correlation can describe not only the CHFs obtained in this work at the outlet pressure of 800 kPa but also the authors' published CHFs (1284 points) for the wide range of $P_{\mathrm{out}}=159$ kPa to 1 MPa, $d=6$, 9 and 12 mm, $L=49$, 99 and 149 mm, $\Delta T_{\mathrm{sub,out}}=-4$ to 140 K and $u=4.0$ to 13.3 m/s within 15% difference for 50 K $\leq \Delta T_{\mathrm{sub,out}} \leq 140$ K and within −10 to +30% for 30 K $< \Delta T_{\mathrm{sub,out}} < 50$ K.
[DOI: 10.1115/1.1725101]

Keywords: *Boiling, Experimental, Forced Convection, Heat Transfer, Turbulent*

Introduction

Highly subcooled water flow boiling is expected as the cooling system of accommodating very high heat fluxes. Understanding the critical heat fluxes (CHFs) is most important for design of cooling configurations such as plasma facing components in fusion reactor and ion beam targets. There have been many critical heat flux data on inner surface of a heated tube with forced flow of highly subcooled water. The effect of tube inner diameter on CHF was investigated experimentally by Nariai et al. [1], Celata et al. [2], Vandervolt et al. [3], and Mudawar and Bowers [4].

The critical heat fluxes (CHFs) of subcooled water flow boiling in relatively short tubes to establish the database for designing the divertor plates of a helical type fusion experimental device which is Large Helical Device (LHD) located in National Institute for Fusion Science, Japan have been studied. The CHFs for wide ranges of experimental condition have been already reported by Hata et al. [5,6] and Sato et al. [7]. Hata et al. [8] clarified the influences of the tube length on CHFs for the same inner-diameter tubes of different lengths, and expressed by the correlation based on inlet conditions such as flow velocity, inlet subcooling, and tube length-to-diameter ratio, L/d. Recently, the subcooled flow boiling critical heat fluxes (CHFs) and the heat transfer coefficients (HTCs) data for $L=49$, 99, and 149 mm with 9 mm inner diameter were applied to thermal analysis on the Flat-plate type divertor and the Mono-block type one of LHD by Sato et al. [7] and Hata et al. [8,9]. Incident CHFs for the divertor with the cooling tube diameter, *d*, of 10 mm, the plate width, *w*, ranging from 16 to 30 mm for the Flat-plate type and the carbon armor outer diameter, *D*, of 26 and 33 mm for the Mono-block type were numerically analyzed based on the measured CHFs and HTCs at the inlet pressure of 594 kPa to 1 MPa.

It can be considered that the CHFs are determined not by the inlet conditions but by the outlet ones. However, there exist few correlations that can generally describe CHFs as a function of outlet parameters. When the inlet subcooling is fixed, tube inner-diameter and length affect the outlet subcooling by the ratio L/d, and may affect CHFs not only by this variation of subcooling but also by other effects of *d* and *L*. CHF experiments for the test tubes with combinations of length and diameter to give a fixed L/d will be useful to clarify the latter effects of *d* and *L*.

The purposes of this study are threefold. First is to measure the CHFs on inner side of a tube with combinations of *d* and *L* for a fixed L/d, for wide ranges of flow velocity and outlet subcooling. Second is to clarify dominant variables on CHFs for outlet subcoolings. Third is to obtain the relation between the CHFs and the outlet subcoolings for wide ranges of conditions as a database to establish the generalized CHF correlation in non-dimensional form.

Experimental Apparatus and Method

Experimental Water Loop. The schematic diagram of experimental water loop is shown in Fig. 1. The loop is made of SUS304 stainless steel and is capable of working up to 2 MPa. The loop has four test sections whose inner diameters are 3, 6, 9, and 12 mm. Test sections were vertically oriented with water flowing upward. The circulating water was distilled and deionized with about 5 MΩ cm specific resistivity. The circulating water through the loop was heated or cooled to keep a desired inlet temperature by pre-heater or cooler. The flow velocity was measured by a mass flow meter using a vibration tube (Nitto Seiko, CLEANFLOW 63FS25, Flow range=100 and 750 Kg/min). The flow velocity was controlled by regulating the frequency of the three-phase alternating power source to the canned type circulation pump (Nikkiso Co., Ltd., Non-Seal Pump HT24B-B2, pump flow rate$=75$ m^3/h, pump head$=18$ m). The water was pressurized by nitrogen gas. The pressure at the inlet of the test tube was controlled within ±1 kPa of a desired value by using a pressure controller.

Test Section. The cross-sectional view of the test section is shown in Fig. 2. The rough inner surface was fabricated by annealing the test tubes first in the air and was then acidized. The rough inner surface test tube was used as a standard one. The tube was reinforced with the heat-shrink Teflon tube because the tube wall was too thin for high-pressure experiment. The silver-coated 5 mm thickness copper-electrode-plates to supply heating current

---

Contributed by the Heat Transfer Division for publication in the JOURNAL OF HEAT TRANSFER. Manuscript received by the Heat Transfer Division July 22, 2003; revision received January 21, 2004. Associate Editor: M. K. Jensen.

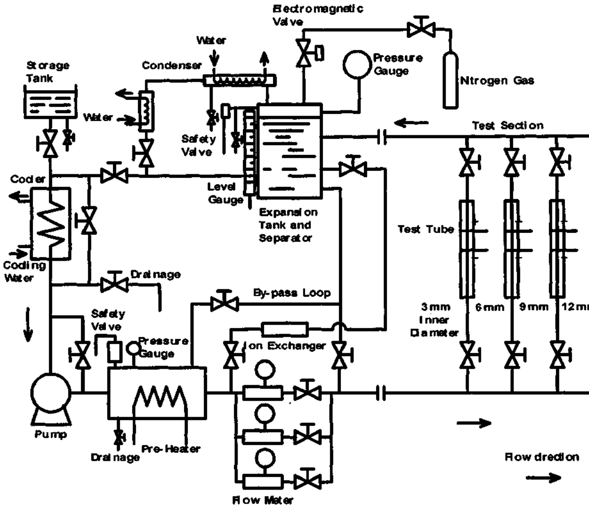

Fig. 1 Schematic diagram of experimental apparatus

were soldered on the surfaces of the both ends of the test tube. The both ends of tube were electrically isolated from the loop by Bakelite plates of 14 mm thickness. The tube was also thermally insulated from atmosphere with a Bakelite block of 120 mm wide, 80 mm deep and *L* mm high. The electrical resistance versus temperature relation for the test heater was calibrated in the flowing water before each experimental run. The test water was heated up to 423 K with the flow velocity of 10 m/s.

Method of Heating Test Tube. The tube was heated with a steadily increasing current supplied from a current source (DC 3000 A, 35 V) through the two copper electrodes shown in Fig. 3. The CHF, $q_{cr,\mathrm{sub}}$, was realized by a steadily increasing heat input to the tube. At the CHF, the tube average temperature rapidly increases. The current for the heat input to the test tube was automatically cut off when the measured average temperature increased up to the preset temperature, which was several tens of Kelvin higher than corresponding CHF surface temperature. The preset one for each experimental run was gradually increased as far as a steep temperature jump was observed on the signal. This procedure avoided the actual burnout of the tube.

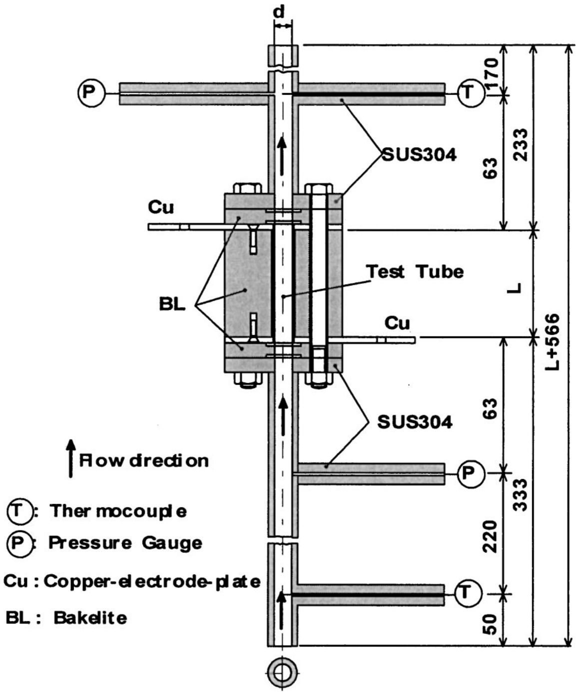

Fig. 2 Vertical cross-sectional view of the test section

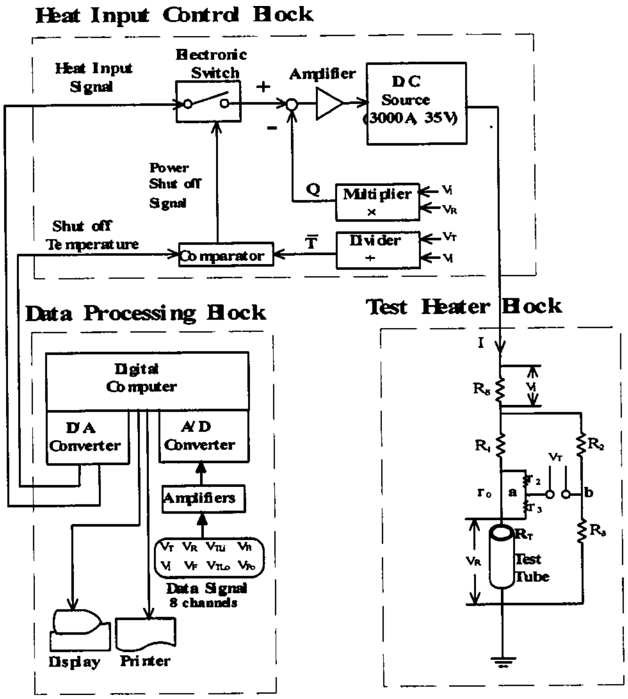

Fig. 3 Measurement and data processing system

Measurement of CHF, Temperature, and Pressure for Test Tube. The transient average temperature of the test tube was measured with resistance thermometry participating as a branch of a double bridge circuit for the temperature measurement. The output voltages from the bridge circuit together with the voltage drops across the two electrodes and across a standard resistance were amplified and then were sent via a D/A converter to a digital computer. These voltages were simultaneously sampled at a constant time interval ranging from 60 to 200 μs. The average temperature of the test tube was calculated with the aid of previously calibrated resistance-temperature relation. The heat generation rate in the test tube was calculated from the measured voltage difference between the potential taps of the test tube and the standard resistance. The surface heat flux is the difference between the heat generation rate per unit surface area and the rate of change of energy storage in the test tube obtained from the faired average temperature versus time curve.

$$q(t)=\frac{V}{S}\left(Q(t)-\rho c_p\frac{d\overline{T}}{dt}\right) \tag{1}$$

where ρ, c_p, V, and S are the density of the test heater, the specific heat of the test heater, the volume of the test heater and the inner surface area of the test heater, respectively. The inner surface temperature was also obtained by solving the heat conduction equation in the test tube under the conditions of measured average temperature and heat generation rate of the test tube. The temperature of the heater surface, T_s, can described as follows:

$$T_s=\overline{T}-\frac{qr_i}{4(r_o^2-r_i^2)^2\lambda}\left[4r_o^2\left\{r_o^2\left(\ln r_o-\frac{1}{2}\right)-r_i^2\left(\ln r_i-\frac{1}{2}\right)\right\}-(r_o^4-r_i^4)\right]-\frac{qr_i}{2(r_o^2-r_i^2)\lambda}(r_i^2-2r_o^2\ln r_i) \tag{2}$$

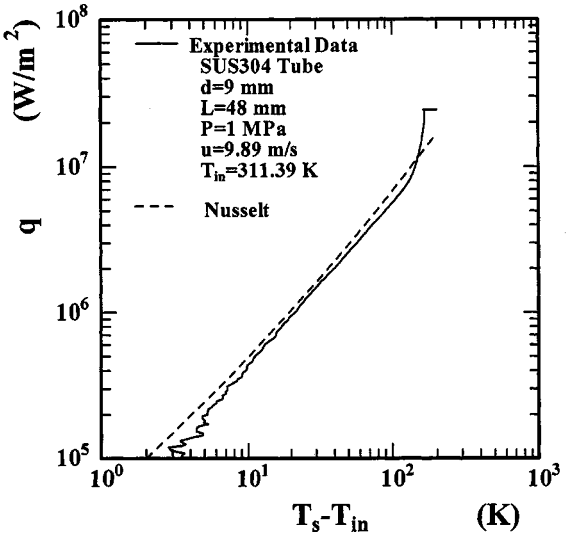

Fig. 4 Relationship between q and T_s-T_L

Figure 4 shows the heat transfer characteristics for $d=9$ mm tube. The heat flux gradually becomes higher with an increase in $(T_s-T_{\rm in})$ on the forced convection curve derived from Nusselt correlation [10] up to the point where the slope begins to increase with heat flux following the onset of nucleate boiling, and increases up to a value called CHF where the heater surface temperature rapidly jumps from the nucleate boiling heat transfer regime (N-B) to the film boiling one (F-B). Figure 5 shows a typical photograph of the test tube burned out. The dark section near the tube outlet is the trace of the vapor patch; the local temperature on the tube jumped to that of the film boiling region at the occurrence of CHF. The location of the vapor patch was almost observed near the tube outlet in this experiment. The tube wall does not clearly melted down along the circumference of the tube, because the heating current to the tube was instantaneously cut off when the measured average temperature rapidly increased up to the preset temperature lower than the actual burnout temperature of the tube. By using this burnout detector, several CHF data were obtained for a single tube without the actual burnout.

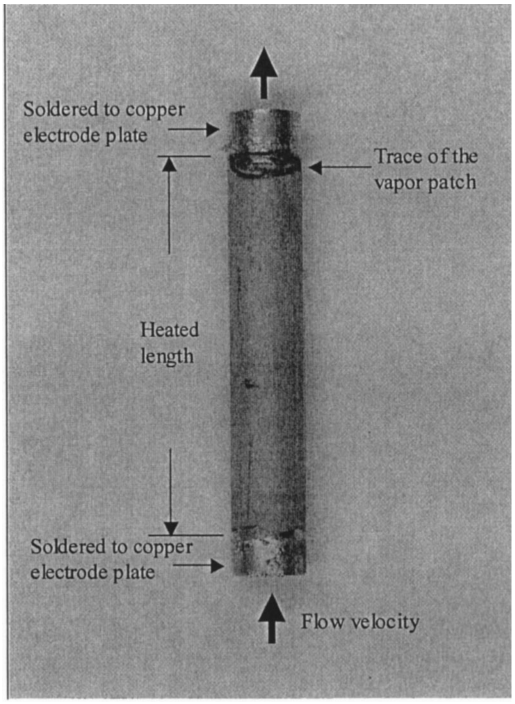

Fig. 5 Typical photograph of the test tube burned out

The inlet and outlet liquid temperatures were measured by 1 mm o.d., sheathed, K-type thermocouples which are located at the centerline of the tube at the upper and lower stream points of 283 mm and 63 mm from the tube inlet and outlet points. The inlet and outlet pressures were measured by the strain gauge transducers, which were located near the entrance of conduit at upper and lower stream points of 63 mm from the tube inlet and outlet points. The thermocouples and the transducers were installed in the conduits as shown in Fig. 2.

The inlet and outlet pressures were calculated from the pressures measured by inlet and outlet pressure transducers as follows. The pressure drop at inlet was predicted as single-phase liquid flow.

$$P_{\rm in}=P_{\rm ipt}-\{(P_{\rm ipt})_{\rm wnh}-(P_{\rm opt})_{\rm wnh}\}\times\frac{0.063}{0.126+L} \tag{3}$$

$$P_{\rm out}=P_{\rm in}-(P_{\rm in}-P_{\rm opt})\times\frac{L}{0.063+L} \tag{4}$$

Outline of these equations is shown in the appendix.

The outlet subcooling averaged over the cross sectional area is calculated by the energy balance as follows:

$$(\Delta T_{\rm sub,out})_{\rm cal}=T_{\rm sat,out}-(T_{\rm out})_{\rm cal}=T_{\rm sat,out}-\left(T_{\rm in}+\frac{4Lq_{\rm cr,sub}}{uc_{pl}\rho_l d}\right) \tag{5}$$

Thermo-physical properties were evaluated at the temperature of $\{T_{\rm in}+(T_{\rm out})_{\rm cal}\}/2$. The average outlet subcoolings calculated are compared with those measured experimentally. The calculated ones are slightly lower than the measured one in the whole experimental range and the differences become larger with an increase in the outlet subcooling and the inner diameter. We have adopted the calculated outlet subcoolings considering that the differences may be due to imperfect mixing at the measuring point. Details are shown in appendix.

Experimental errors are estimated to be ±1 K in inner tube surface temperature and ±2% in heat flux. Inlet flow velocity, inlet and outlet subcoolings, and inlet and outlet pressures were measured within the accuracy ±2%, ±1 K, and ±1 kPa, respectively.

Experimental Results and Discussion

Experimental Conditions. The initial experimental conditions such as inlet flow velocity, inlet subcooling and inlet pressure for the flow boiling CHF experiments were determined independently each other before each experimental run.

The experimental conditions were as follows:

Heater Material	304 stainless steel
Surface Condition	Rough surface (commercial one)
Inner Diameter (d)	3, 6, 9 and 12 mm
Heated Length (L)	33, 66, 99 and 133 mm
L/d	11
Wall Thickness	0.3, 0.4 and 0.5 mm
Inlet flow velocity (u)	4.0, 6.9, 9.9 and 13.3 m/s
Froude number (Fr)	134.6–6030.5
Inlet Pressure ($P_{\rm in}$)	730–880 kPa
Outlet Pressure ($P_{\rm out}$)	730–860 kPa
Inlet Subcooling ($\Delta t_{\rm sub,in}$)	12 K–140 K
Outlet Subcooling ($\Delta T_{\rm sub,out,exp}$)	3 K–129 K
Inlet Liquid Temperature	303 K–431 K
Steadily Increasing Heat Input	$Q_{0\ \exp}(t/\tau)$, τ=10, 20 and 33.3 s

Flow Boiling CHFs in Water Flowing Upward. The CHF, $q_{cr,\rm sub}$, for inner diameters, of 3, 6, 9, and 12 mm with $L/d=11$ at the outlet pressure of around 800 kPa were shown versus the average outlet subcoolings calculated, $(\Delta T_{\rm sub,out})_{\rm cal}$, with the flow

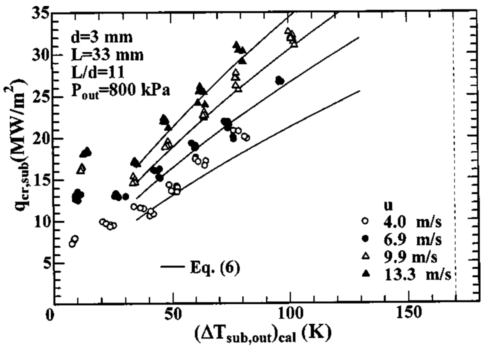

Fig. 6 $q_{cr,\mathrm{sub}}$ versus $(\Delta T_{\mathrm{sub,out}})_{\mathrm{cal}}$ for an inner diameter of 3 mm with a heated length of 33 mm at an outlet pressure of 800 kPa

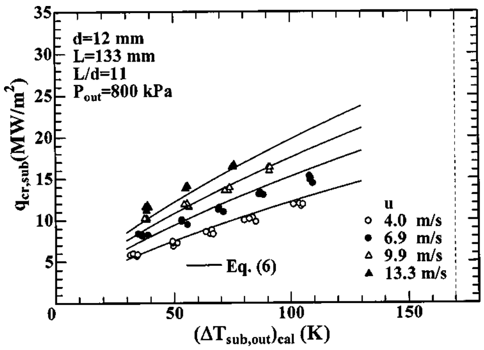

Fig. 9 $q_{cr,\mathrm{sub}}$ versus $(\Delta T_{\mathrm{sub,out}})_{\mathrm{cal}}$ for an inner diameter of 12 mm with a heated length of 133 mm at an outlet pressure of 800 kPa

velocities of 4.0, 6.9, 9.9, and 13.3 m/s in Figs. 6–9, respectively. The CHFs become higher with an increase in flow velocity at a fixed $(\Delta T_{\mathrm{sub,out}})_{\mathrm{cal}}$. These figures illustrate the trends in the variation of CHF with increasing outlet subcooling. The CHFs first decrease to the minimum CHF at the $(\Delta T_{\mathrm{sub,out}})_{\mathrm{cal}}$ of about 30 K, and then increase with an increase in $(\Delta T_{\mathrm{sub,out}})_{\mathrm{cal}}$. The increasing rate becomes lower for higher $(\Delta T_{\mathrm{sub,out}})_{\mathrm{cal}}$. It has been already found by Hata et al. [5,6] and Sato et al. [7] on CHF data for the heated length of 50 mm with the inner diameters of 6, 9, and 12 mm.

It is assumed that, in the first low subcooling range, flushing-like phenomenon due to the vapor bubbles from inner side of a small diameter tube may be occurring and inducing the increase of flow velocity through the reduction in macroscopic density of two-phase mixture. The enhancement of CHF by this mechanism will become insignificant with the increase of subcooling. It is likely that the first low subcooling range would become narrower by using a larger diameter test tube. More detailed study on the CHFs in the first low subcooling range for a vertical short tube will appear in the near future.

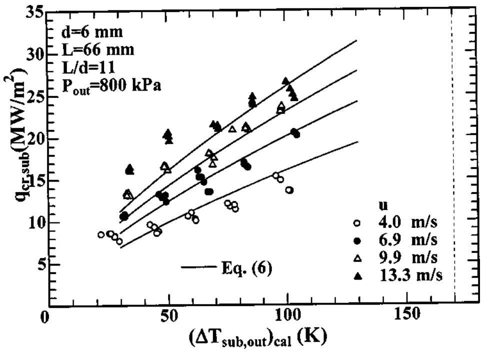

Fig. 7 $q_{cr,\mathrm{sub}}$ versus $(\Delta T_{\mathrm{sub,out}})_{\mathrm{cal}}$ for an inner diameter of 6 mm with a heated length of 66 mm at an outlet pressure of 800 kPa

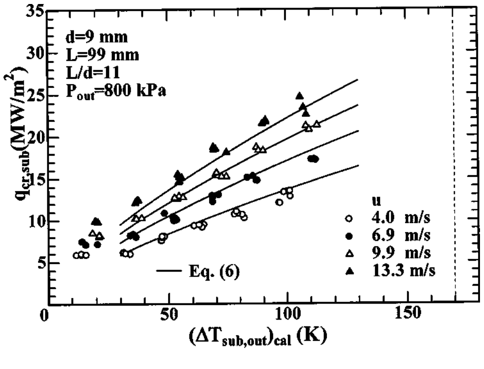

Fig. 8 $q_{cr,\mathrm{sub}}$ versus $(\Delta T_{\mathrm{sub,out}})_{\mathrm{cal}}$ for an inner diameter of 9 mm with a heated length of 99 mm at an outlet pressure of 800 kPa

Sakurai et al. [11] reported that the CHFs in the latter range could be divided into two groups: those in the lower subcooling range with relatively high increasing rate and in the higher subcooling range with lower increasing rate. They also reported that the CHFs in the lower subcooling range are higher for higher pressure but those for higher subcooling are independent of pressure. They assumed that the mechanism of CHF in the lower subcooling range would be hydrodynamic instability and that for the higher subcooling range would be heterogeneous spontaneous nucleation. In this work, only the data for $(\Delta T_{\mathrm{sub,out}})_{\mathrm{cal}} \geqslant 50$ K are used to derive the pressure independent correlation for higher subcooling referring to the paper.

Influence of Inner-Diameter, Flow Velocity, Outlet Subcooling, and *L*/*d* on CHF. Figures 10 to 11 show the influence of the inner diameter on the CHF against the outlet subcooling, $(\Delta T_{\mathrm{sub,out}})_{\mathrm{cal}}$, of 50 and 90 K, respectively. The $q_{cr,\mathrm{sub}}$ for the inner diameter of 3, 6, 9, and 12 mm were shown versus the inner diameter with the flow velocity ranging from 4.0 to 13.3 m/s. The CHFs for four different inner-diameters with $L/d = 11$ become linearly higher with the decrease in the diameter. The slope on the log-log graph kept almost constant about -0.4 with the flow velocity ranging from 4.0 to 13.3 m/s.

The effect of flow velocity on CHF against $(\Delta T_{\mathrm{sub,out}})_{\mathrm{cal}}$ of 50 and 90 K was represented versus u with the tube inner diameter as a parameter in Figs. 12 to 13, respectively. In Fig. 12, CHFs for each tube diameter are proportional to $u^{0.4}$ in the range of tube

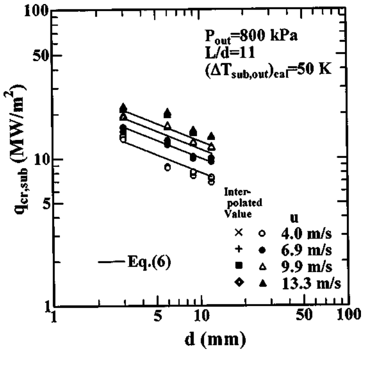

Fig. 10 $q_{cr,\mathrm{sub}}$ versus d at $(\Delta T_{\mathrm{sub,out}})_{\mathrm{cal}}$ of 50 K with the flow velocity of 4.0, 6.9, 9.9 and 13.3 m/s at P_{out} of 800 kPa

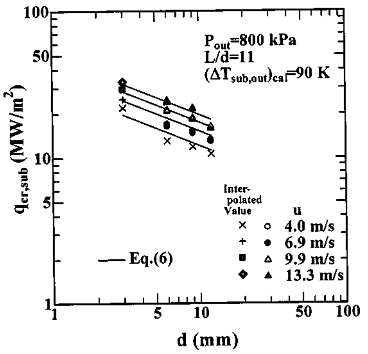

Fig. 11 $q_{cr,\mathrm{sub}}$ **versus** d **at** $(\Delta T_{\mathrm{sub,out}})_{\mathrm{cal}}$ **of 90 K with the flow velocity of 4.0, 6.9, 9.9, and 13.3 m/s at** P_{out} **of 800 kPa**

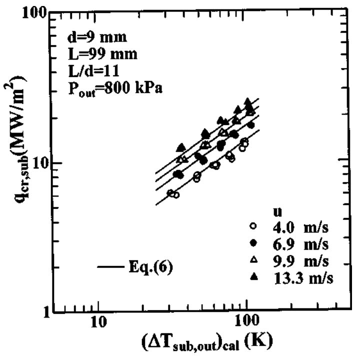

Fig. 14 $\log(q_{cr,\mathrm{sub}})$ **versus** $\log\{(\Delta T_{\mathrm{sub,out}})_{\mathrm{cal}}\}$ **for an inner diameter of 9 mm with a heated length of 99 mm at** P_{out} **of 800 kPa**

diameter from 3 to 12 mm. Increasing rate of CHFs for other $(\Delta T_{\mathrm{sub,out}})_{\mathrm{cal}}$ shows nearly the same trend of those for $(\Delta T_{\mathrm{sub,out}})_{\mathrm{cal}}=50$ K.

Figure 8 is rewritten on $\log(q_{cr,\mathrm{sub}})$ versus $\log\{(\Delta T_{\mathrm{sub,out}})_{\mathrm{cal}}\}$ graph in Fig. 14 to check the influence of $(\Delta T_{\mathrm{sub,out}})_{\mathrm{cal}}$ on CHF for flow velocity of 4.0 to 13.3 m/s. The CHFs for each flow velocity become linearly higher with an increase in $(\Delta T_{\mathrm{sub,out}})_{\mathrm{cal}}$ with a similar slope of 0.7.

Figure 15 to 16 show the influence of L/d on the CHF for inner diameters of 9 and 12 mm at $\Delta T_{\mathrm{sub,out}}$, of 90 K, respectively. The $q_{cr,\mathrm{sub}}$ for the L/d ranging from 4.08 to 16.5 were shown versus the L/d with the flow velocity as a parameter. The CHFs become linearly lower with the increase in the L/d. The slope of each curve on the log-log graph is almost constant about -0.1.

Flow Boiling CHF Correlation Against Outlet Subcooling The CHF correlation for higher subcooling range $(\Delta T_{\mathrm{sub,out}})_{\mathrm{cal}} \geqslant 30$ K is derived as follows based on the effects of inner-diameter, flow velocity, outlet subcooling and L/d clarified in this work.

$$\mathrm{Bo}=0.082\left\{\frac{d}{\sqrt{\sigma/g(\rho_l-\rho_g)}}\right\}^{-0.1}\mathrm{We}^{-0.3}\left(\frac{L}{d}\right)^{-0.1}$$

$$\times\,\mathrm{Sc}^{0.7}\quad\text{for outlet subcooling }(\Delta T_{\mathrm{sub,out}}\geqslant 30\ \mathrm{K})\tag{6}$$

Saturated thermo-physical properties were evaluated at the outlet pressure.

The curves derived from Eq. (6) at each flow velocity are shown in Figs. 6–9 for comparison. The CHF data for $(\Delta T_{\mathrm{sub,out}})_{\mathrm{cal}}\geqslant 50$ K are in good agreement with the values given by the correlation. It seems that the Eq. (6) can also be applicable

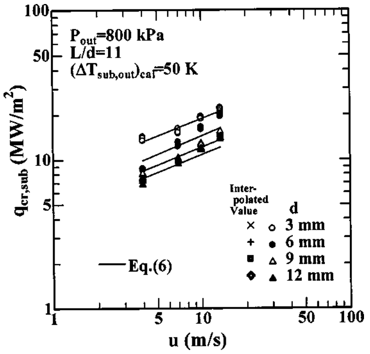

Fig. 12 $q_{cr,\mathrm{sub}}$ **versus** u **at** $(\Delta T_{\mathrm{sub,out}})_{\mathrm{cal}}$ **of 50 K with the inner diameter of 3, 6, 9, and 12 mm at** P_{out} **of 800 kPa**

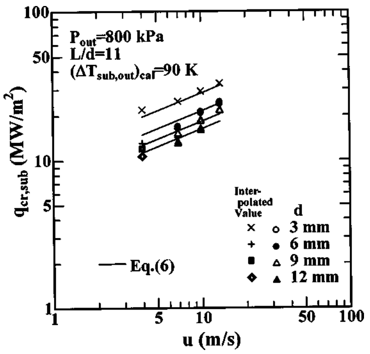

Fig. 13 $q_{cr,\mathrm{sub}}$ **versus** u **at** $(\Delta T_{\mathrm{sub,out}})_{\mathrm{cal}}$ **of 90 K with the inner diameter of 3, 6, 9, and 12 mm at** P_{out} **of 800 kPa**

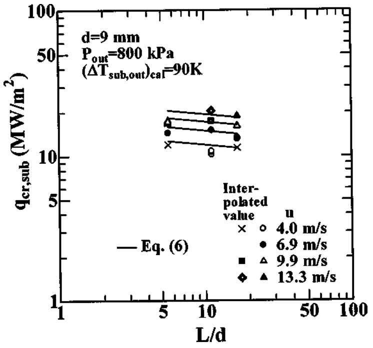

Fig. 15 $q_{cr,\mathrm{sub}}$ **versus** L/d **for an inner diameter of 9 mm at** $\Delta T_{\mathrm{sub,out}}$ **of 90 K with the flow velocity of 4.0, 6.9, 9.9, and 13.3 m/s**

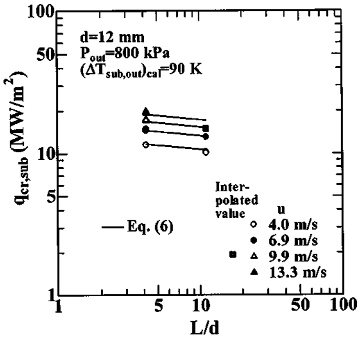

Fig. 16 $q_{cr,\mathrm{sub}}$ **versus** L/d **for an inner diameter of 12 mm at** $\Delta T_{\mathrm{sub,out}}$ **of 90 K with the flow velocity of 4.0, 6.9, 9.9, and 13.3 m/s**

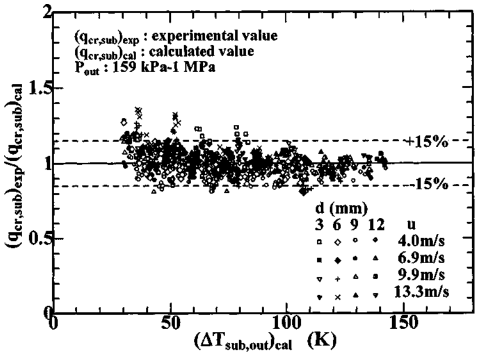

Fig. 17 Ratio of CHF data for the inner diameter of 3, 6, 9, and 12 mm to the values derived from the CHF correlation versus $(\Delta T_{sub,out})_{cal}$ at outlet pressures of 159 kPa–1 MPa

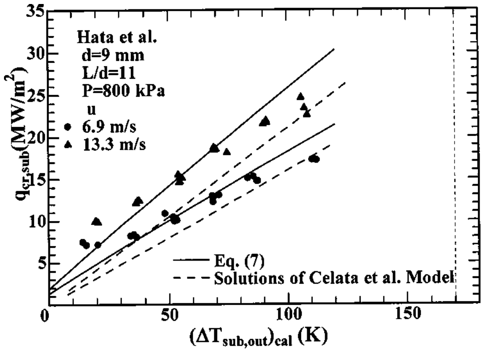

Fig. 20 Comparison of CHF data for the inner diameter of 9 mm with Eq. (7) and Solutions of Celata et al. model

to the CHFs for the subcoolings between about 30 and 50 K at this pressure, although there is a tendency to somewhat under-predict the CHFs within the range.

Equation (6) was derived based on the experimental data at the outlet pressure of 800 kPa. Besides the experimental data obtained in this work, we [5–8] have already reported the CHFs (1284 points) for the wide range of $P_{out}=159$ kPa to 1 MPa, $d=6$, 9 and 12 mm, $L=49$, 99 and 149 mm, $\Delta T_{sub,out}=-4$ to 140 K and $u=4.0$ to 13.3 m/s. To confirm the applicability of Eq. (6) to the data for wide range of pressures, the ratios of these CHF data to the corresponding values calculated by Eq. (6) are shown versus $(\Delta T_{sub,out})_{cal}$ in Fig. 17. Most of the data for $50\ \mathrm{K} \leqslant (\Delta T_{sub,out})_{cal} \leqslant 140$ K are within ±15% and those for $30\ \mathrm{K} < (\Delta T_{sub,out})_{cal} < 50$ K are within -10 to $+30\%$.

Comparison of the Measured CHFs With Other Workers' CHF Correlation. Many researchers gave CHF correlations of subcooled flow boiling including the effect of tube diameter. Tong [12] gave the flow boiling CHF correlation using the concept of boundary layer separation suggested by Kutateladze [13,14]. Tong [15] developed a phenomenological CHF correlation by combining the effects local subcooling, turbulent mixing, bubble layer shielding and two-phase flow friction on CHF. Celata et al. [16] expressed the CHF correlation modifying the Tong correlation [12]. Recently, Celata et al. [17] presented a mechanistic model for the prediction of CHF in flow boiling of subcooled water. Hall and Mudawar [18] developed the inlet and outlet conditions cor-

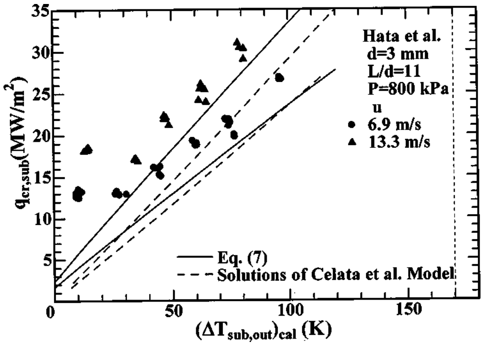

Fig. 18 Comparison of CHF data for the inner diameter of 3 mm with Eq. (7) and Solutions of Celata et al. model

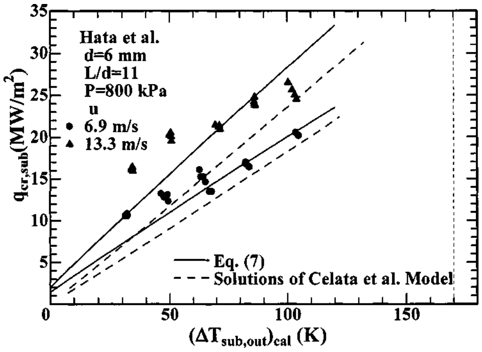

Fig. 19 Comparison of CHF data for the inner diameter of 6 mm with Eq. (7) and Solutions of Celata et al. model

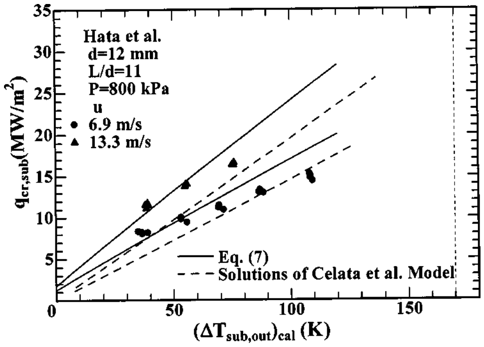

Fig. 21 Comparison of CHF data for the inner diameter of 12 mm with Eq. (7) and Solutions of Celata et al. model

Table 1 Comparison of the measured CHFs with other workers' CHF correlation

d (mm)	u (m/s)	$(\Delta T_{sub,out})_{cal}$ (K)	Eq. (7)	Solutions of Celata et al. model
3	6.9	50	−32%	−32%
		100	−14%	−16%
	13.3	50	−14%	−32%
		100	−11%	−23%
6	6.9	50	−15%	−31%
		100	0%	−5%
	13.3	50	−18%	−50%
		100	10%	−6%
9	6.9	50	0%	−19%
		100	14%	0%
	13.3	50	0%	−26%
		100	14%	−6%
12	6.9	50	0%	−19%
		100	14%	0%
	13.3	50	0%	−26%
		100	14%	−6%

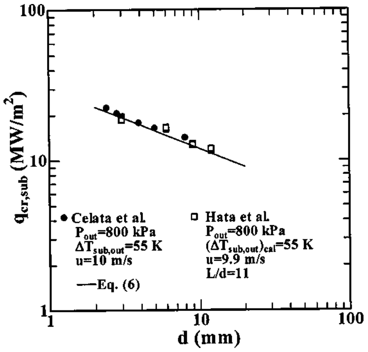

Fig. 22 Comparison of Celata et al. data and our data with the values derived from the CHF correlation

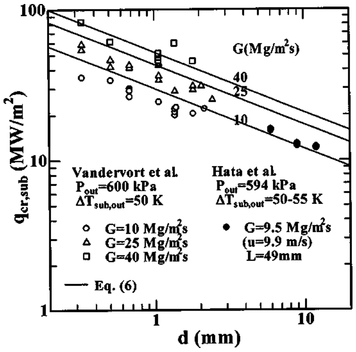

Fig. 24 Comparison of Vandervort et al. data and our data with the values derived from the CHF correlation

relations for subcooled high-CHF based on the experimental data. Hall and Mudawar correlation [18] for the outlet conditions is as follows:

$$\mathrm{Bo}=0.0332\mathrm{We}^{-0.235}\left(\frac{\rho_l}{\rho_g}\right)^{-0.681}\left[1-0.6837\left(\frac{\rho_l}{\rho_g}\right)^{0.832}\chi_{\mathrm{out}}\right] \quad (7)$$

The experimental data for $u=6.9$ and 13.3 m/s at $P_{\mathrm{out}}=800$ kPa are compared with Eq. (7) and solutions of the model by Celata et al. [17] in Figs. 18 to 21 for $d=3$, 6, 9, and 12 mm, respectively.

In case of $d=3$ mm shown in Fig. 18, the values by Eq. (7) for $u=13.3$ m/s are about 14% and 11% lower than the data at $(\Delta T_{\mathrm{sub,out}})_{\mathrm{cal}}$ of around 50 K and 100 K, and those for $u=6.9$ m/s are 32% and 14% lower at $(\Delta T_{\mathrm{sub,out}})_{\mathrm{cal}}$ of 50 K and 100 K, respectively. The solutions of Celata et al. model for $u=13.3$ m/s are 32% and 23% lower than CHF data, and those for 6.9 m/s are 32% and 16% lower at the $(\Delta T_{\mathrm{sub,out}})_{\mathrm{cal}}$ of around 50 K and 100 K, respectively.

In case of $d=6$ mm shown in Fig. 19, the values by Eq. (7) for $u=13.3$ m/s are about 18% lower than the data at $(\Delta T_{\mathrm{sub,out}})_{\mathrm{cal}}$ of 50 K and 10% higher than the data at $(\Delta T_{\mathrm{sub,out}})_{\mathrm{cal}}$ of 100 K. The values by Eq. (7) for $u=6.9$ m/s are 15% and 0% lower at $(\Delta T_{\mathrm{sub,out}})_{\mathrm{cal}}$ of 50 K and 100 K, respectively. The solutions of Celata et al. model for $u=13.3$ m/s are 50% and 6% lower than CHF data, and those for 6.9 m/s are 31% and 5% lower at the $(\Delta T_{\mathrm{sub,out}})_{\mathrm{cal}}$ of around 50 K and 100 K, respectively.

In case of $d=9$ mm shown in Fig. 20, the values by Eq. (7) for $u=13.3$ m/s and $u=6.9$ m/s are about 0% and 14% higher than the data at $(\Delta T_{\mathrm{sub,out}})_{\mathrm{cal}}$ of 50 K and 100 K, respectively. The solutions of Celata et al. model for $u=13.3$ m/s are 26% and 6% lower than CHF data, and those for 6.9 m/s are 19% and 0% lower at the $(\Delta T_{\mathrm{sub,out}})_{\mathrm{cal}}$ of around 50 K and 100 K, respectively.

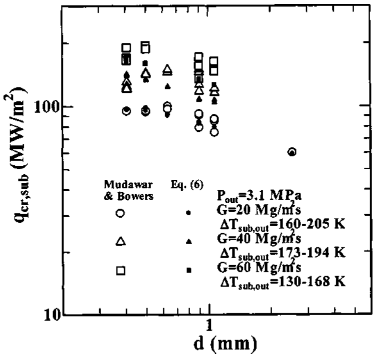

Fig. 23 Comparison of Mudawar and Bowers data and our data with the values derived from the CHF correlation

In case of $d=12$ mm shown in Fig. 21, the values by Eq. (7) for $u=13.3$ m/s are about 0% and 14%, and those for $u=6.9$ m/s are 0% and 14% higher than the data at $(\Delta T_{\mathrm{sub,out}})_{\mathrm{cal}}$ of 50 K and 100 K, respectively. The solutions of Celata et al. model for $u=13.3$ m/s are 26% and 6% lower than CHF data, and those for 6.9 m/s are 19% and 0% lower than the data at the $(\Delta T_{\mathrm{sub,out}})_{\mathrm{cal}}$ of around 50 K and 100 K, respectively.

It seems from these comparisons that the increasing rates of CHF for $(\Delta T_{\mathrm{sub,out}})_{\mathrm{cal}}$ derived from solutions of Celata et al. model and Hall and Mudawar correlation are larger than the experimental ones. However, most of our data are within ±15% of the predicted values for $50\ \mathrm{K}\leqslant(\Delta T_{\mathrm{sub,out}})_{\mathrm{cal}}\leqslant 140$ K. These comparisons are presented in Table 1 for quick reader comprehension.

Comparison of Our Correlation With Other Workers' CHF Data. Celata et al. [2] and our CHF data, for $P_{\mathrm{out}}=800$ kPa, $u=10$ m/s and $\Delta T_{\mathrm{sub,out}}=55$ K are plotted versus tube inner diameter in Fig. 22. The values derived from our correlation are also shown as a straight line in the figure for comparison. These data are in close agreement with the correlation. The trend of $d^{0.4}$ dependence for our data can also be seen for the experimental data by Celata et al.

Figure 23 shows the comparison between Mudawar and Bowers CHF data [4] for $d=0.406$–2.54 mm, $\Delta T_{\mathrm{sub,out}}=130$–205 K, $G=20$–60 Mg/m^2 s and $P_{\mathrm{out}}=3.1$ MPa and the values predicted by our correlation. The predicted values are very close to their data at $G=20$ Mg/m^2 s, however they become smaller with an increase of G. The deviations between the predicted values and their CHF data are ranging from 8.3 to 30.6% at $G=40$ and 60 Mg/m^2 s.

Figure 24 shows CHF data by Vandervort et al. [3] for $d=0.33$–2.44 mm, $\Delta T_{\mathrm{sub,out}}=50$ K, $G=10$–40 Mg/m^2 s, and $P_{\mathrm{out}}=600$ kPa versus inner diameter together with our CHF data for $u=9.9$ m/s and $P_{\mathrm{out}}=594$ kPa. The values derived from our correlation for $G=10$, 20 and 40 Mg/m^2 s are also shown in the figure. Their experimental data are within 15% of the values obtained from our correlation.

It was confirmed that the CHF correlation for the short vertical tube can be widely applicable for the inner diameters (0.33–12 mm), the outlet subcoolings (30–205 K), the flow velocities (4–60 m/s) and the outlet pressures (159 kPa–3.1 MPa).

Conclusions

The critical heat fluxes (CHFs) of subcooled water flow boiling are systematically measured for the inner-diameter ($d=3$, 6, 9, and 12 mm) with $L/d=11$, the flow velocities ($u=4.0$ to 13.3 m/s), the outlet subcoolings ($\Delta T_{\mathrm{sub,out}}=3$ to 129 K) and the outlet pressure ($P_{\mathrm{out}}=800$ kPa). Experimental results lead to the following conclusions.

1. The CHFs first decrease to the minimum CHF at the $\Delta T_{\mathrm{sub,out}}$ of about 30 K, and then increase with an increase in $\Delta T_{\mathrm{sub,out}}$. The increasing rate becomes lower for higher $\Delta T_{\mathrm{sub,out}}$.

2. The CHFs for $\Delta T_{\text{sub,out}} \geqslant 50$ K for four different inner-diameters with $L/d = 11$ become linearly higher with the decrease in the diameter. The slope on the log-log graph kept almost constant about -0.4 for the flow velocities ranging from 4.0 to 13.3 m/s.

3. The CHFs in the range of tube diameter 3 to 12 mm at a fixed outlet subcooling higher than 50 K are proportional to $u^{0.4}$ for each tube diameter.

4. The CHFs for flow velocities from 4.0 to 13.3 m/s become linearly higher with an increase in outlet subcooling with a slope of 0.7 on the log-log graph.

5. The CHF correlation in nondimensional form is derived as outlet conditions based on the experimental data for $\Delta T_{\text{sub,out}} \geqslant 30$ K.

6. The correlation can describe not only the CHFs obtained in this work at the outlet pressure of 800 kPa but also the authors' published CHFs (1284 points) for the wide range of $P_{\text{out}} = 159$ kPa to 1 MPa, $d = 6$, 9, and 12 mm, $L = 49$, 99 and 149 mm, $\Delta T_{\text{sub,out}} = -4$ to 140 K and $u = 4.0$ to 13.3 m/s within 15% difference for 50 K$\leqslant \Delta T_{\text{sub,out}} \leqslant$140 K and within -10 to $+30$% for 30 K$< \Delta T_{\text{sub,out}} <$50 K.

7. It was confirmed in comparison with other workers experimental data that the CHF correlation for the short vertical tube can be widely applicable for the inner diameters (0.33–12 mm), the outlet subcoolings (30–205 K), the flow velocities (4–60 m/s) and the outlet pressures (159 kPa −3.1 MPa).

Nomenclature

Bo = boiling number, q_{cr}/Gh_{fg}
c_p = specific heat at constant pressure, J/kg K
d = test tube inner diameter, m
D = outer diameter, m
Fr = $= u^2/gd$, Froude number
G = $= \rho_l u$, mass flux, kg/m^2 s
g = acceleration of gravity, m/s^2
h_{fg} = latent heat of vaporization, J/kg
L = heated length, m
P_{in} = pressure at inlet of heated length, kPa
P_{ipt} = pressure measured by inlet pressure transducer, kPa
P_{out} = pressure at outlet of heated length, kPa
P_{opt} = pressure measured by outlet pressure transducer, kPa
Q = heat generation rate of test heater, W/m^3
Q_0 = initial exponential heat input, W/m^2
q = heat flux, W/m^2
$q_{cr,\text{sub}}$ = critical heat flux for subcooled condition, W/m^2
r_i = test tube inner radius, m
r_o = test tube outer radius, m
Re = Reynolds number, Gd/μ_l
S = surface area of test heater
Sc = nondimensional subcooling, $c_{pl}(\Delta T_{\text{sub,out}})_{\text{cal}}/h_{fg}$
t = time, s
T_{in} = inlet liquid temperature, K
T_{out} = outlet liquid temperature, K
T_s = heater inner surface temperature, K
$(T_{\text{out}})_{\text{cal}}$ = calculated outlet liquid temperature, K
T_{sat} = saturation temperature, K
$T_{\text{sat,out}}$ = outlet saturation temperature, K
$\Delta T_{\text{sub,in}}$ = $(T_{\text{sat}} - T_{\text{in}})$, inlet liquid subcooling, K
$\Delta T_{\text{sub,out}}$ = $(T_{\text{sat}} - T_{\text{out}})$, outlet liquid subcooling, K
$(\Delta T_{\text{sub,out}})_{\text{cal}}$ = calculated outlet liquid subcooling, K
u = flow velocity, m/s
V = volume of test heater
We = Weber number, $G^2 d/\rho_l \sigma$
χ = thermal equilibrium quality
ρ = density, kg/m^3
σ = surface tension, N/m
τ = exponential period, s

Subscript

cal = calculated
exp = experimental
g = vapor
in = inlet
out = outlet
l = liquid
sat = saturated conditions
sub = subcooled conditions
wnh = with no heating

Appendix

Inlet and Outlet Pressures, P_{in} and P_{out}. Figure 25 shows the time variations in the pressures measured by the inlet and outlet pressure transducers, P_{ipt} and P_{opt}, the inlet and outlet pressures calculated by Eqs. (3) and (4), P_{in} and P_{out}, heat flux, q, and heater inner surface temperature, T_s, for $P_{\text{out}} = 735$ kPa, $(\Delta T_{\text{sub,out}})_{\text{cal}} = 91.49$ K and $u = 13.3$ m/s. The values of P_{ipt} kept almost constant in the whole experimental range as they are controlled within ±1 kPa of the desired value by the controller, although they oscillated violently near the CHF point. It is considered especially in case of the small diameter tube that the pressure drop in two-phase flow becomes larger than that in single phase due to the vapor bubble confined in the small diameter tube. However, the P_{opt} values showed almost the same ones, too. Therefore, we derived Eqs. (3) and (4) by the use of linear interpretation for the calculation of inlet and outlet pressures, P_{in} and P_{out}: the two-phase pressure drop could not be clearly observed in high subcooling range.

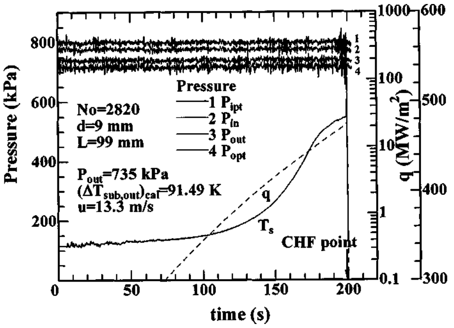

Fig. 25 Time variations in P_{ipt}, P_{opt}, P_{in}, P_{out}, q and T_s for $P_{\text{out}} = 735$ kPa, $(\Delta T_{\text{sub,out}})_{\text{cal}} = 91.49$ K and $u = 13.3$ m/s

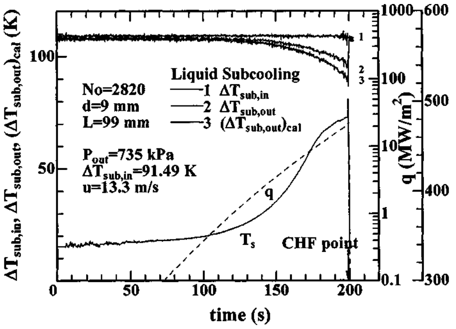

Fig. 26 Time variations in $\Delta T_{\text{sub,in}}$, $\Delta T_{\text{sub,out}}$, $(\Delta T_{\text{sub,out}})_{\text{cal}}$, q and T_s for $P_{\text{out}} = 735$ kPa, $(\Delta T_{\text{sub,out}})_{\text{cal}} = 91.49$ K and $u = 13.3$ m/s

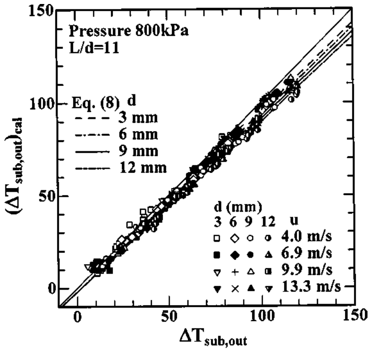

Fig. 27 Relationship between measured outlet subcooling and calculated outlet subcooling for the inner diameter of 3, 6, 9, and 12 mm with $L/d=11$

Relations Between the Measured Outlet Subcooling and the Calculated One. The outlet subcooling averaged over the cross sectional area was calculated by Eq. (5) as mentioned before. On the other hand, the outlet liquid temperature was measured by 1-mm o.d., sheathed, K-type thermocouple located at the centerline of the tube at lower stream point of 63 mm from the tube outlet. Figure 26 shows the time variations in the inlet and outlet subcoolings measured, $\Delta T_{sub,in}$ and $\Delta T_{sub,out}$, the outlet subcooling calculated by Eq. (5), $(\Delta T_{sub,out})_{cal}$, q and T_s for $P_{out}=735$ kPa, $(\Delta T_{sub,out})_{cal}=91.49$ K and $u=13.3$ m/s. The values of $\Delta T_{sub,in}$ kept almost constant in the whole experimental range, although those of $\Delta T_{sub,out}$ and $(\Delta T_{sub,out})_{cal}$ became gradually lower with an increase in the heat flux. The average outlet subcoolings calculated, $(\Delta T_{sub,out})_{cal}$, at the CHF point for the test tubes of $d=3$, 6, 9, and 12 mm are compared with those measured experimentally, $\Delta T_{sub,out}$ in Fig. 27. The $(\Delta T_{sub,out})_{cal}$ is slightly lower than the $\Delta T_{sub,out}$ in the whole experimental range and the difference becomes larger with an increase in the outlet subcooling and the inner diameter. Relation between $(\Delta T_{sub,out})_{cal}$ and $\Delta T_{sub,out}$ is almost described by the following equation:

$$(\Delta T_{sub,out})_{cal}=(-0.0055d+0.9825)\Delta T_{sub,out}-2 \tag{8}$$

This difference may be due to imperfect mixing, and may be dependent on the distance of the measuring point from the tube outlet. Therefore, we have adopted the calculated outlet subcooling as a standard parameter.

References

[1] Nariai, H., Inasaka, F., and Shimura, T., 1987, "Critical Heat Flux of Subcooled Flow Boiling in Narrow Tube," *Proceedings of the 1987 ASME-JSME Thermal Engineering Joint Conference*, **5**, Hemisphere, New York, pp. 455–462.

[2] Celata, G. P., Cumo, M., Mariani, A., Nariai, H., and Inasaka, F., 1993, "Influence of Channel Diameter on Subcooled Flow Boiling at High Heat Fluxes," Int. J. Heat Mass Transfer, **36(13)**, pp. 3407–3410.

[3] Vandervort, C. L., Bergles, A. E., and Jensen, M. K., 1994, "An Experiment Study of Critical Heat Flux in Very High Heat Flux Subcooled Boiling," Int. J. Heat Mass Transfer, **37**, Suppl. 1, pp. 161–173.

[4] Mudawar, I., and Bowers, M. B., 1999, "Ultra-high Critical Heat Flux (CHF) for Subcooled Water Flow Boiling-I: CHF Data and Parametric Effects for Small Diameter Tubes," Int. J. Heat Mass Transfer, **42**, pp. 1405–1428.

[5] Hata, K., Fukuda, K., Shiotsu, M., Sakurai, A., Noda, N., Motojima, O., and Iiyoshi, A., 1998, "Critical Heat Fluxes in Subcooled Boiling of Water Flowing Upward in a Vertical Tube for Wide Ranges of Liquid Velocity, Subcooling and Pressure," Proceedings of 6th International Conference on Nuclear Engineering, Paper No. ICONE-6362, pp. 1–16.

[6] Hata, K., Fukuda, K., Shiotsu, M., and Sakurai, A., 1999, "The Effect of Diameter on Critical Heat Flux in Vertical Heated Short Tubes of Various Inside Diameters Cooled with an Upward Flow of Subcooled Water," *Ninth International Topical Meeting on Nuclear Reactor Thermal Hydraulics*, pp. 1–20.

[7] Sato, G., Hata, K., Shiotsu, M., and Noda, N., 2000, "Critical Heat Fluxes on Short Vertical Tube Inner Surface in Water Flowing Upward (Effect of tube Inner Diameter and Application to Thermal Analysis of Divertor Plate)," *Proceedings of 8th International Conference on Nuclear Engineering*, Paper No. ICONE-8126, pp. 1–12.

[8] Hata, K., Sato, T., and Shiotsu, M., 2001, "Influence of Tube Length on Critical Heat Fluxes in Water Flowing Upward," *Proceedings of 9th International Conference on Nuclear Engineering*, Paper No. ICONE-9569, pp. 1–12.

[9] Hata, K., Tanimoto, T., Komori, H., Shiotsu, M., and Noda, N., 2003, "Thermal Analysis on Mono-Block Type Divertor Based on Subcooled Flow Boiling Critical Heat Flux Data against Inlet Subcooling in Short Vertical Tube," Proceedings of 11th International Conference on Nuclear Engineering, Paper No. ICONE11-36118, pp. 1–10.

[10] Nusselt, W., 1931, "Der Wärmeaustausch zweischen Wand und Wasser im Rohr," Forsch. Geb. Ingenieurwes., **2**, p. 309.

[11] Sakurai, A., Shiotsu, M., Hata, K., and Fukuda, K., 1999, "The Mechanisms of Flow Boiling Critical Heat Fluxes on a Vertical Cylinder and a Short Tube With Upward Flowing Highly Subcooled Water," *Ninth International Topical Meeting on Nuclear Reactor Thermal Hydraulics*, American Nuclear Society (ANS), Thermal Hydraulic Division, pp. 1–36.

[12] Tong, L. S., 1968, "Boundary-layer Analysis of the Flow Boiling Crisis," Int. J. Heat Mass Transfer, **11**, pp. 1208–1211.

[13] Kutateladze, S. S., and Leont'ev, A. I., 1966, "Some Applications of the Asymptotic Theory of the Turbulent Boundary Layer," *Proceedings of the Third International Heat Transfer Conference*, **3**, Am. Inst. Chem. Engrs., New York.

[14] Kutateladze, S. S., 1966, "The Concept of a Fluid with Disappearing Viscosity and Some Problems of the Phenomenological Theory of Turbulence near the Wall," Invited Lecture, Third International Heat Transfer Conference, Chicago, IL.

[15] Tong, L. S., 1975, "A Phenomenological Study of Critical Heat Flux," ASME Paper 75-HT-68, ASME, New York.

[16] Celata, G. P., Cumo, M., and Mariani, A., 1993, "Burnout in Highly Subcooled Water Flow Boiling in Small Diameter Tubes," Int. J. Heat Mass Transfer, **36(5)**, pp. 1269–1285.

[17] Celata, G. P., Cumo, M., Mariani, A., Simoncini, M., and Zummo, G., 1994, "Rationalization of Existing Mechanistic Models for the Prediction of Water Subcooled Flow Boiling Critical Heat," Int. J. Heat Mass Transfer, **37**, Suppl. 1, pp. 347–360.

[18] Hall, D. D., and Mudawar, I., 1999, "Ultra-high Critical Heat Flux (CHF) for Subcooled Water Flow Boiling-II: high-CHF Database and Design Equation," Int. J. Heat Mass Transfer, **42**, pp. 1429–1456.

Jean-Pierre M. Bukasa
Department of Mechanical Engineering,
Rand Afrikaans University,
PO Box 524,
Auckland Park 2006,
Johannesburg, South Africa

Leon Liebenberg
Associate Professor,
Department of Mechanical and Aeronautical Engineering,
University of Pretoria,
Pretoria 0002, South Africa

Josua P. Meyer
Member ASME (#4032447), Professor and Head,
Department of Mechanical and Aeronautical Engineering,
University of Pretoria,
Pretoria 000, South Africa
e-mail: jmeyer@up.ac.za

Heat Transfer Performance During Condensation Inside Spiralled Micro-Fin Tubes

The effect of the spiral angle on the heat transfer performance in micro-fin tube condensers has not yet been clearly established because other geometric parameters affecting the heat transfer performance were simultaneously varied in previous studies. This paper reports on the influence of the spiral angle on the heat transfer during condensation inside spiralled micro-fin tubes having all other geometric parameters constant. Tests were conducted for condensation of R-22, R-134a, and R-407C inside a smooth (9.52 mm outer diameter) and three micro-fin tubes with approximately the same diameter, having spiral angles of 10 deg, 18 deg, and 37 deg, respectively. Experimental results indicated a heat transfer augmentation with spiral angle increase. A new semi-empirical predictive correlation was developed for practical design of spiralled micro-fin tubes. The proposed new correlation predicted the majority of experimental results of the present study within a deviation zone of ±20%. [DOI: 10.1115/1.1737777]

Keywords: *Condensation, Enhancement, Finned Surfaces, Heat Transfer*

Introduction

Efforts have been deployed in recent years toward designing heat exchangers that simultaneously meet the requirements of energy saving, size reduction and subsequent cost reduction. This has led to an extensive use of heat transfer augmentation technology in order to improve heat exchangers performance. In addition, the use in the last decade of alternative refrigerants such as zeotropic mixtures, which produce heat transfer degradation during condensation, has critically contributed to the development and use of advanced enhancement techniques such as internally finned tubes in order to counterbalance the heat transfer penalty. Micro-fin tubes have emerged as one of the most efficient and commonly used internally finned tubes as they produce a favorable combination of heat transfer augmentation and small pressure penalty. Different types of micro-fin tubes have been developed and among them, spiralled micro-fin tubes have received special attention.

Schlager et al. [1] reported the condensation heat transfer coefficients and pressure drop of R-22 for three micro-fin tubes of 12.7 mm outside diameter and having three different spiral angles (15 deg, 18 deg, and 25 deg). However, their tubes had different geometric parameters such as fin height and pitch, so they could not define the effect of specific geometric factors on the performance differences of the micro-fin tubes. Yasuda et al. [2] investigated the condensation heat transfer coefficients and pressure drop for micro-fin tubes of outside diameter 9.52 mm, with different fin height, number of fins and spiral angle. They reported that the condensation heat transfer coefficient increases with groove depth and spiral angle. Chiang [3] confirmed these results for condensation of R-22. His study revealed that for equal tube diameters, the heat transfer coefficient for condensation inside an axial micro-fin tube is higher than for condensation inside an 18 deg-spiralled micro-fin tube. However, the tested tubes had different fin heights and apex angles, which both have significant effects on the condensation heat transfer coefficients. Tatsumi et al. [4] conducted two-phase heat transfer and pressure drop studies using triangular and trapezoidal fins. Even though geometric parameters such as fin height, apex angle and number of fins were varied, they observed that increases in the spiral angle resulted in increased heat transfer. According to a recent review by Cavallini et al. [5], few papers in the open literature have been concerned with condensation of R-134a and R-407C inside spiralled micro-fin tubes. Cavallini et al. corroborate that condensation heat transfer in micro-fin tubes is increased because of a combination of (i) the larger surface area (A), (ii) the thinning of the condensate film (δ) by a redistribution of the liquid due to spiraling and surface tension forces, and (iii) the presence of film disturbances caused by the presence of the fins, all of which result in an increase of the thermal capacity performance of the heat exchanger. However, little work that establishes the effect of the spiral angle on the heat transfer performance is available in the open literature. Other geometric parameters affecting the heat transfer performance such as apex angle, fin height, pitch, and thickness were also varied in the pre-mentioned research studies. And this remains a serious limitation to an optimum use of spiralled micro-fin tubes. In addition, each previous study on condensation inside spiralled micro-fin tubes resulted in its own semi-empirical predictive correlation depending on the geometric parameters and refrigerant being investigated. Therefore, the present study had two objectives: first, to experimentally investigate and establish the effect of the spiral angle on the heat transfer performance during condensation inside spiralled micro-fin tubes having all other geometric parameters constant except spiral angle; second, to develop a semi-empirical correlation that can be used to predict heat transfer coefficients of spiralled micro-fin tubes.

Experimental Apparatus

A test facility was specifically constructed to measure in-tube condensation heat transfer and pressure drop of pure refrigerants and zeotropic mixtures. The condensation of the refrigerants was investigated in an experimental test facility shown in Fig. 1, which was a vapor compression heat pump water heater composed of three independent flow loops: a refrigerant loop containing the test condenser, a heating water loop, and a cooling water loop. The refrigerant cycle consisted of four main components: the compressor, the condenser, the expansion valve, and the evaporator. The

---

Contributed by the Heat Transfer Division for publication in the JOURNAL OF HEAT TRANSFER. Manuscript received by the Heat Transfer Division November 27, 2002; revision received March 12, 2004. Associate Editor: J. N. Chung.

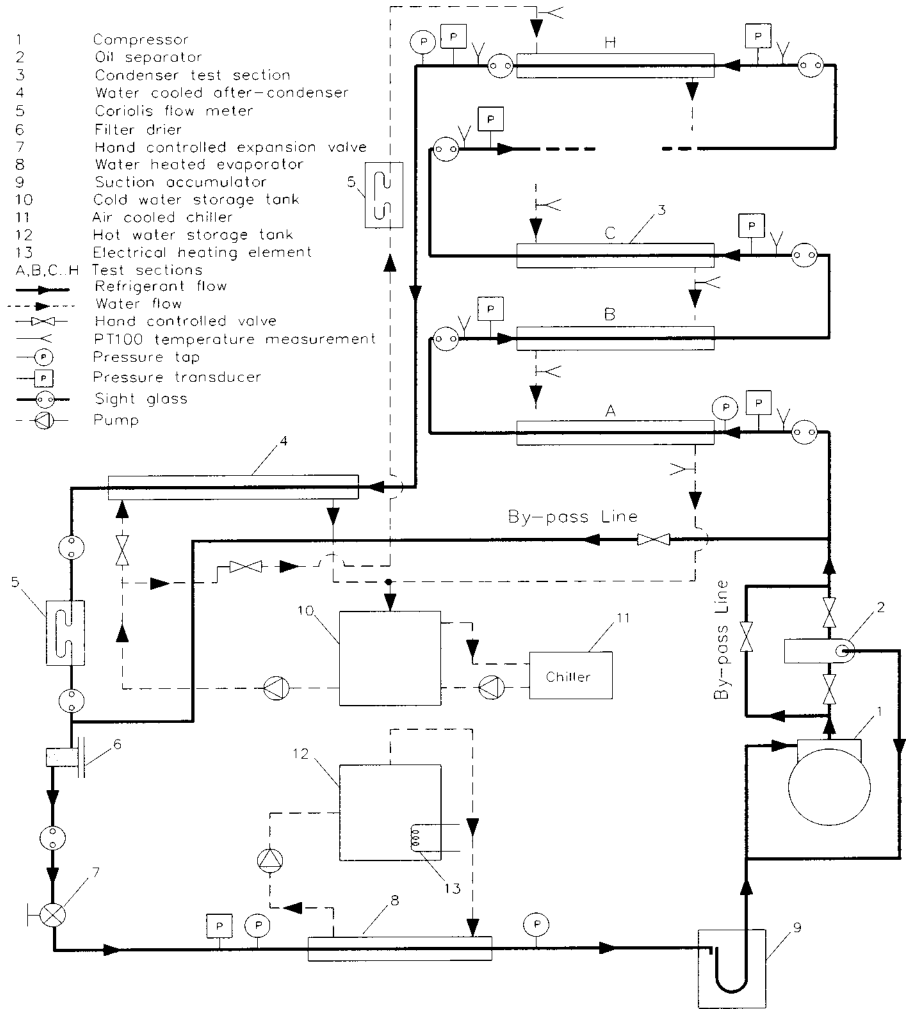

Fig. 1 Schematic representation of the experimental apparatus

compressor was a hermetically sealed, reciprocating type with a nominal power rating of 10 kW. An oil separator was connected to the compressor in parallel with a bypass line. Although oil concentration was not directly measured, the composition of the circulating refrigerant could be inferred by comparing experimental data with expected results from the Refprop refrigerants database [6]. By manually controlling the flow through the bypass line and the oil separator simultaneously, the oil mass fraction in the refrigerant could be controlled. The water-cooled type tube-in-tube condenser consisted of two parts: the test condenser and the after-condenser. The test condenser consisted of eight separate coaxial double tube test sections in series labeled *A*, *B*, *C*, up to *N*, where $N=8$, as shown in Fig. 1. The outer tube of each test section was a hard-drawn copper tube with an inside diameter of 17.27 mm and an outside diameter of 19.05 mm. The inner tubes were either smooth or spiralled microfin tubes as listed in Table 1. Sight-glasses were installed between the test sections in order to monitor visually the refrigerant vapor quality. All test sections were well insulated to minimize heat leakage.

A by-pass line connected in parallel with the test condenser was used to control the refrigerant mass flow rate through the test condenser. The after-condenser was a coiled water-cooled, tube-in-tube condenser, used specifically to ensure that only liquid refrigerant entered the Coriolis mass flowmeter. A filter-drier was placed upstream of a hand-controlled expansion valve, which was used to regulate the refrigerant mass flow rate subsequently evaporating and condensing temperatures and pressures. A suction

Table 1 Geometric parameters of tested inner tubes

Tube number	1	2	3	4
Type	Smooth	Spiral-finned (Microfin 10 deg)	Spiral-finned (Microfin 18 deg)	Spiral-finned (Microfin 37 deg)
Helix angle, β (°)	⋯	10	18	37
Number of fins, N (-)	⋯	60	60	60
Outside diameter (mm)	9.52	9.65	9.55	9.55–9.575
Inside diameter (mm)	8.11	9.06	8.91	8.67
Fin height (mm)	⋯	0.197–0.212	0.198–0.2197	0.182–0.229
Tube wall thickness (mm)	1.3	0.292	0.302–0.312	0.445–0.447
Subsection length (mm)	1.5	1.1	0.9	0.6

Table 2 Uncertainties in experimental variables and results

Quantity	Range	95% Uncertainty Low Mass Flux (300 kg/m^2 s)	95% Uncertainty High Mass Flux (800 kg/m^2 s)
Refrigerant temperature	−27–95°C	0.14 K	0.04
Water temperature	−27–95°C	0.11 K	0.04
Saturation temperature	···	0.12 K	0.02
Log-mean temperature difference		±2.1%	
Temperature difference (water)		±0.438%	
Pressure	0–4000 kPa	0.28%	0.18%
Refrigerant mass flow rate	0–0.9 kg/s (nominal range) 1.9 kg/s (maximum)	0.31%	0.15%
Water mass flow rate	0–0.3 kg/s (nominal range) 0.6 kg/s (maximum)	0.15%	0.40%
Annulus heat transfer coefficient		±4%	±5%
Average heat transfer coefficient		±7%	±40%
Local heat transfer coefficient		±15%	
Annulus heat transfer coefficient		±9%	±11%
Average quality	···	4.58%	1.46%
Viscosity	···	0.10%	0.10%
Density	···	0.03%	0.04%
Tube length	0–10 m	±0.11%	
Tube diameter	0.01–20 mm	±0.125%	
Uncertainty in water heat capacity measurement		±3.39%	

accumulator was placed upstream the compressor to retain the liquid refrigerant and ensure that only vaporous refrigerant flowed to the compressor.

The cooling water cycle consisted of a centrifugal pump circulating the water from a 1000 liter insulated cold-water storage tank through the system at the condensing side. A 15 kW chiller was connected to the storage tank in order to control the cooling water temperature (between 5°C and 25°C). The heating water cycle was composed of a centrifugal pump circulating the water from a 1000 liter insulated hot water storage tank through the system at the evaporating side. A 20 kW electric resistance heater was connected to the storage tank to constantly control the heating water temperature (between 30°C and 40°C). The refrigerant flow rate was measured by means of a Coriolis mass flow meter with an accuracy of ±0.2% situated at the outlet of the test condenser on the refrigerant-side. A second Coriolis mass flow meter (accuracy ±0.2%) placed at the inlet of the test condenser on the water-side was used to measure the cooling water flow rate.

Absolute pressures were measured at the inlet and outlet of each test section by means of two strain-gauge type pressure transducers respectively (accuracy ±0.02%). Two dial pressure gauges with a range of 0 to 3000 kPa (accuracy ±0.2%) were used to monitor absolute pressures, respectively, at the inlet and outlet of the test condenser at the high-pressure side. Temperatures were measured with resistance temperature detectors (RTDs) mounted longitudinally on the outside wall of the tubes (refrigerant and cooling water loops). RTDs of the Pt-100 type (accuracy ±0.1°C) were used in the present study. At each measurement location, two Pt-100s were used, one measuring the temperature at the top and another at the bottom. Temperature values used for data analysis were averages between top and bottom values. All measurement instruments were connected to a data acquisition system firstly for data readings and afterwards for data analysis.

Experimental Procedure

Experiments were conducted for refrigerants R-22, R-134a, and R-407C whose thermodynamic properties were obtained from the Refprop [6] database and which were condensing inside four different hard-drawn test condensers as listed in Table 1. During experiments the mass flux varied between 300 kg/m^2 s and 800 kg/m^2 s, the pressures between 1500 kPa and 1700 kPa, saturation temperatures between 39°C and 41°C, inlet qualities between 85% and 95%, and outlet qualities between 5% and 15%. Only experimental runs with an energy balance less than 1% were considered for data analysis. Uncertainties in experimental variables and results are presented in Table 2. Uncertainties in experimental results were estimated using a propagation-of-error analysis by Kline and McClintock [7].

Data Reduction

Average Heat Transfer Coefficients. Assuming no fouling the average heat transfer coefficients were calculated using the following definition of the overall heat transfer coefficient:

$$h_i=\left(\frac{A_i}{A_o}\left(\frac{1}{U_o}-\frac{1}{h_o}-\frac{d_o\ln\left(\frac{d_o}{d_i}\right)}{2k_w}\right)\right)^{-1} \tag{1}$$

The average annulus heat transfer coefficient h_o was experimentally derived by using the modified Wilson plot technique [8] which was specifically calibrated [9] for the experimental setup used in this study, namely

$$h_o=0.0936\left(\frac{k_o}{d_h}\right)\mathrm{Re}_o^{0.74}\,\mathrm{Pr}_o^{1/3}\left(\frac{\mu_o}{\mu_{wo}}\right)^{0.14} \tag{2}$$

where properties were calculated at the average water bulk temperature in the annulus. The overall heat transfer coefficient based on the outside area of the inner tube was defined by the expression

$$U_o = \frac{Q_{av}}{A_o LMTD} \tag{3}$$

The average heat transfer was the average heat transfer taken between the water and refrigerant sides and the logarithmic mean temperature difference was determined as

$$LMTD = \frac{(t_{\text{sat}} - T_{\text{out}}) - (t_{\text{sat}} - T_{\text{in}})}{\ln\left(\dfrac{t_{\text{sat}} - T_{\text{out}}}{t_{\text{sat}} - T_{\text{in}}}\right)} \tag{4}$$

For pure refrigerants, the saturation temperature was obtained from the average of the refrigerant bulk temperature at the inlet and exit of the condensation test section. For the zeotropic mixture (R-407C), the saturation temperature was deduced using the following correlation of Cavallini et al. [5]:

$$t_{\text{sat}} = t_{\text{dew}} - \Delta t_{\text{glide}}(1 - x) \tag{5}$$

For condensation inside the micro-fin tube, the heat transfer coefficient in the inner tube (Eq. (1)) was based on the inside area of a smooth tube having an inner diameter equal to the maximum diameter of the micro-fin tube (nominal heat transfer area).

Local Heat Transfer Coefficients. Semi-local heat transfer coefficients were determined at the inlet and outlet of each test section using the Eckels and Tesene [10] method

$$h_i = \left(\frac{(t - T)\pi d_i}{\dot{M} C_{po} \dfrac{dT}{dz}} - \frac{d_i}{d_o h_o} - \frac{d_i \ln\left(\dfrac{d_i}{d_o}\right)}{2k_w} \right)^{-1} \tag{6}$$

The water temperature distribution in the annulus was expressed as a function of the axial distance z along the test section and fit to a second power order polynomial. The axial temperature variation dT/dz was then determined from the derivative of the second power order polynomial and evaluated at the water temperature at the respective measurement station.

Vapor qualities at inlet and exit of each test section were calculated at saturation temperature using respectively the following expressions:

$$x_{\text{in}} = \frac{i_{\text{in}} - i_l}{i_v - i_l} \tag{7}$$

$$x_{\text{out}} = \frac{i_{\text{out}} - i_l}{i_v - i_l} \tag{8}$$

The average vapor quality of each test section was then derived

$$x = \frac{x_{\text{in}} + x_{\text{out}}}{2} \tag{9}$$

Experimental Results

Verification of the Experimental Procedure and Data Reduction. To verify the experimental setup and procedure of data reduction, measured values of the average and local heat transfer coefficients of smooth tubes and micro-fin tubes with R-22 were compared to the measurements of Eckels and Tesene [10], Muzzio et al. [11], and Eckels and Unruh [12] at saturation temperatures of 35°C and 40°C over a mass flux range of 58 to 400 kg/m^2 s. It was found that for smooth tubes, the present experimental setup over predicted the average heat transfer coefficients by approximately 6% on average, with a maximum error of 18% at low mass fluxes of 89 kg/m^2 s. For micro-fin tubes, the agreement is better than for smooth tubes. The heat transfer coefficients are over predicted by approximately 2% on average and the maximum error is 3% at a mass flux of approximately 100 kg/m^2 s. Pressure drops were all within 10% of the measurements of Eckels and Tesene [10]. More details on the verification of the experimental procedure and data reduction are given in references [13–15].

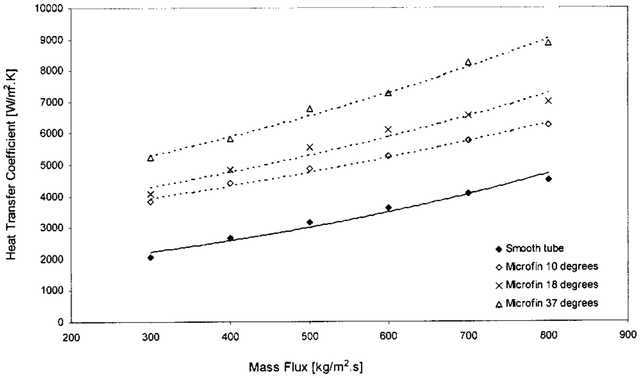

Fig. 2 Average heat transfer coefficients for condensation of R-407C inside micro-fin tubes. (**Uncertainties in average heat transfer coefficient: ±7% at low mass fluxes; ±40% at high mass fluxes; Uncertainties in mass fluxes: ±0.31% for low mass fluxes; ±0.15% for high mass fluxes.**)

Heat Transfer Coefficients. As representative results, Fig. 2 presents average heat transfer coefficients for condensation of R-407C in smooth and micro-fin tubes as a function of mass flux for a smooth tube and micro-fin tubes at different helix angles. The measured values are shown as well as the trend lines. The heat transfer coefficients increase monotonically with an increase of the spiral angle, due to the additional swirling secondary flow that is set up at larger helix angles. These large helix angles cause a distinct redistribution of the condensed liquid around the tube inner-surface, which essentially simulates an annular flow with a tick film that enjoys an accompanying increase in heat transfer. It was also shown [16] that that the micro-fins bring about a heat transfer area increase (compared to a smooth tube) that is proportional to 1/cos(β), which gives 1.02 for β=10 deg, 1.05 for β=18 deg, and 1.25 for β=37 deg. The larger helix angles, therefore, also ensure greater heat transfer areas, and, thus, greater heat transfers.

As the mass flux increased with 166% from 300 kg/m^2 s to 800 kg/m^2 s, the heat transfer coefficients increased with 124% for smooth tubes, and 64%, 69%, and 69% respectively for 10 deg, 18 deg, and 37 deg micro-fin tubes. The increase of the heat transfer coefficients of the micro-fin tubes are therefore approximately constant and is not a strong function of mass flux as the heat transfer coefficients of smooth tubes. This indicates that the high turbulence that is evident at high mass fluxes, results in a suppression of any possible heat transfer enhancement effect of the micro-fin tubes relative to the smooth tube. Although the results in Fig. 2 are only for R-407C, similar results were found for R-22 and R-134a.

In Fig. 3 the enhancement factors of the average heat transfer coefficients are given for the micro-fin tubes in comparison to smooth tubes. The enhancement factor was defined as the ratio of the heat transfer coefficient of the micro-fin tube to the heat transfer coefficient of the smooth tube, with the same temperature difference between the wall and the refrigerant. The enhancement factors are given as function of mass flux for R-22, R-134a, and R-407C for spiral angles of 10 deg, 18 deg, and 37 deg micro-fin tubes. At the lowest mass flux of 300 kg/m^2 s the enhancement factor is the highest while the lowest heat transfer augmentation was observed at the highest mass flux of 800 kg/m^2 s. The reason being that the micro-fin tube ensures that the flow regime stays annular for a longer period before it changes to a stratified/wavy regime. The micro-fins therefore delay the onset of liquid-

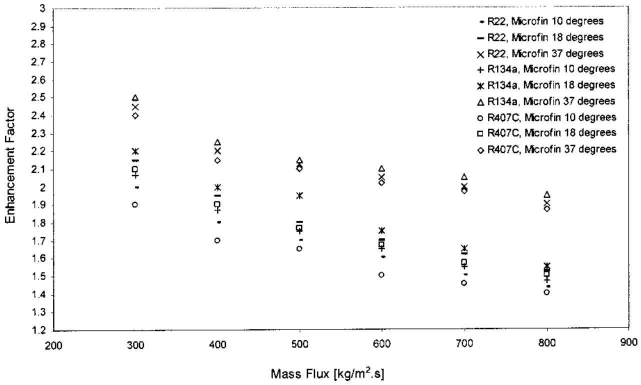

Fig. 3 Enhancement factors for condensation inside micro-fin tubes

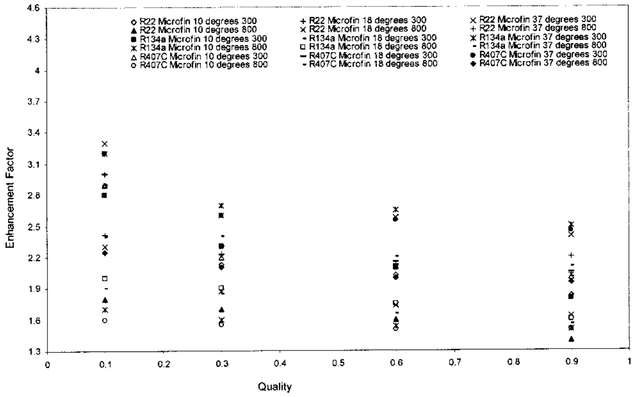

Fig. 5 Local enhancement factors for refrigerants in micro-fin tubes at mass fluxes of 300 kg/m^2 s and 800 kg/m^2 s at three different spiral angles

accumulation at the bottom of the tube. As the mass flux increases, the flow regime remains annular for even a longer period [16]. At a mass flux of 500 kg/m^2 s the enhancement factors are on average approximately 33% higher than at 800 kg/m^2 s. At this same mass flux, the enhancement of the 10 deg micro-fin tube compared to a smooth tube is approximately on average 170% to 180% for an 18 deg, and 220% for a 37 deg micro-fin tube. Furthermore, for a specific helix angle the enhancement factors of the three different refrigerants considered are approximately the same.

In Fig. 4, the semi-local (or sectional) heat transfer coefficients are given for condensation of R-134a inside smooth and micro-fin tubes at spiral angles of 10 deg, 18 deg, and 37 deg, at mass fluxes of 300 kg/m^2 s and 800 kg/m^2 s. Trend lines were fitted through all the experimental values. The data for the refrigerants R-22 and R-407C and for other mass fluxes other than reported in Fig. 4, are available in [15]. All the results show that the heat transfer coefficients increase as the mass flux and vapor quality increase. Also apparent are that the heat transfer coefficients of the micro-fin tubes are all higher than the heat transfer coefficients of the smooth tubes. Furthermore, the heat transfer coefficients increase with spiral angle.

Figure 5 presents local heat transfer enhancement factors relative to smooth tubes at mass fluxes of 300 and 800 kg/m^2 s for all three refrigerants for all three the spiral angles. The heat transfer enhancement factors are the highest at low qualities and the lowest at high qualities. Furthermore, the heat transfer enhancement factors at the lower mass fluxes of 300 kg/m^2 s is higher than at the higher mass fluxes of 800 kg/m^2 s when the same refrigerants and spiral angles are compared. Visual observations of the flow pattern [16] revealed the dominance of intermittent flow in this regime (viz. for $x < 30\%$) with the flow becoming stratified-wavy at very low vapor qualities. The main mechanism of heat transfer in this flow regime is conduction through the liquid film at the top of the tube. This liquid film is very thin, so that the presence of micro-fins reduces the thickness of the film considerably, which also considerably reduces the film conduction resistance. Therefore, a large enhancement factor is obtained under low mass flux conditions. Since wavy (stratified) flow prevailed over the entire vapor quality range, the enhancement factor remained relatively constant with varying vapor quality.

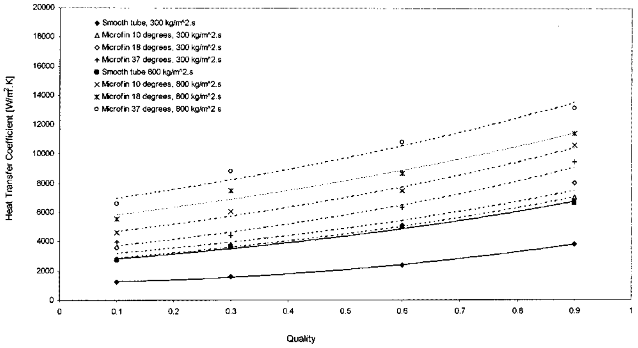

Fig. 4 Local heat transfer coefficients for condensation of R-134a inside micro-fin tubes. (Uncertainties in local heat transfer coefficient: ±15%; Uncertainties in vapor quality: ±4.58% at low mass fluxes; ±1.46% at high mass fluxes.)

At vapor qualities greater than 30%, the enhancement reduces quickly, and then steadies out. The enhancement mechanism with respect to increasing vapor quality may result from an interaction between the micro-fins and the vapor-liquid interface of the fluid in the tube. At low vapor quality the micro-fins are flooded by the condensate, so little or no fin surface is exposed on which surface tension drainage can act. That is, the curvature of the condensate-vapor interface is nearly constant. Then, only vapor shear force is important. In this case, the heat transfer mechanism is the same as for a smooth tube [16].

Therefore, at a vapor quality approximately $x = 0.5$, the thickness of the liquid film is increased when the mass flux is increased. This implies that for $x > 0.5$, the condensate film is sufficiently thin so that part of the fin height penetrates into the vapor region. It is therefore not flooded by condensate. So, the expected increase in convective heat transfer with increase in mass flux is also offset by the increasing thickness of the liquid film (according to $h = k_l/\delta$). At very high vapor qualities and very thin liquid films on the tube surface, the micro-fins may therefore be very effective at mixing the liquid-vapor interface due to their proximity to the vapor-liquid interface. It is also possible to obtain an additional enhancement at very high qualities from surface-tension drainage forces on the micro-fin tips. However, as the liquid accumulates on the surface, both the liquid-vapor interface mixing and the surface tension effects diminish [16].

Therefore, as the vapor quality increases, the flow regime changes from stratified-wavy and intermittent flow to annular flow. In the annular flow regime, the thickness of the annular film is initially large compared to the fin height, which reduces the relative effect of the micro-fins, thus reducing the enhancement factor. As the vapor quality further increases, the thickness of the condensate film is reduced enough so that the fin-effect again becomes important (relative to the conduction effect related to the condensate film thickness). This produces the relatively high enhancement factors at high vapor qualities [16].

The heat transfer enhancement factors also increases as the spiral angle increases, which is directly related to the earlier noted increase of heat transfer coefficient with an increase in the helix angle. It can also be concluded from Fig. 5 that in general the heat transfer enhancement factors of R-134a are the highest, followed

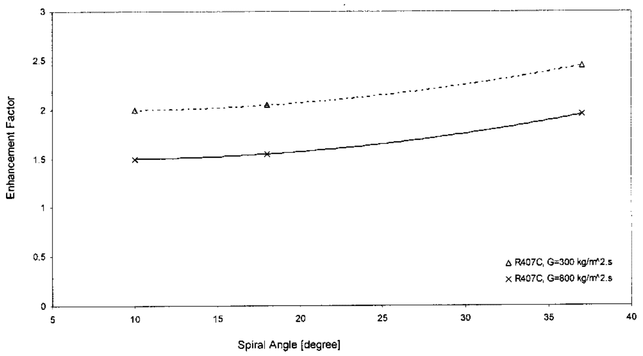

Fig. 6 Enhancement factor versus spiral angle for condensation of R-407C inside micro-fin tubes at mass fluxes of 300 kg/m^2 s and 800 kg/m^2 s

by R-407C and R-22, and that the differences are small. The better condensation performance of R-134a is ascribed mainly to its low reduced vapor pressure and low vapor density (hence, greater vapor specific volume), compared to the higher-pressure refrigerants, R-22 and R-407C.

In Fig. 6, the heat transfer enhancement factor is given for R-407C (similar trend for other refrigerants tested) as function of spiral angle for two different mass fluxes of 300 kg/m^2 s and 800 kg/m^2 s. Again, as was concluded in Fig. 2, the heat transfer enhancement is higher at the lower mass flux of 300 kg/m^2 s than at the higher mass flux of 800 kg/m^2 s. For a spiral angle increase of 10 deg to 18 deg the heat transfer enhancement is moderate, but more substantial when varying the helix angle from 18 deg to 37 deg.

Figure 7 shows the heat transfer enhancement factor increases with spiral angle for different quality values (similar trend for all three refrigerants). At the lowest quality value of 0.1 the heat transfer enhancements are the highest as was also observed in Fig. 5, while the enhancement is the lowest at the highest quality of 0.9. If the mass flux is kept constant at 800 kg/m^2 s the enhancement factor increases as a function of spiral angle, for different vapor qualities, as is shown in Fig. 8. Again, the enhancement factor increases as the spiral angle increases and the highest enhancements occur at the lowest qualities. A different trend was observed at the highest mass flux of 800 kg/m^2 s where a moderate augmentation was observed over the entire vapor quality range. This disparity in enhancement factor depending on vapor quality and mass flux was an indication that in addition to the heat transfer area increase, other factors strongly depending on the flow regime prevailed in each local point of the test condenser caused additional heat transfer augmentation. It appears [15], that additional heat transfer augmentation was produced by (a) the turbulence in the film liquid due to the presence of spiralled micro-fins, and (b) the effect of surface tension forces. These two factors are strong functions of vapor quality and mass flux.

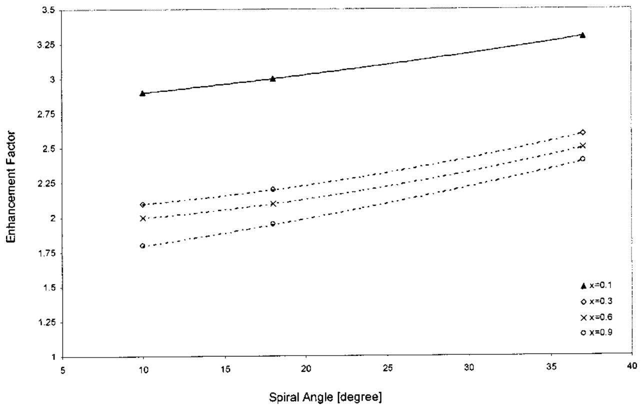

Fig. 7 Enhancement factor versus spiral angle for condensation of R-22 inside micro-fin tubes at 300 kg/m^2 s

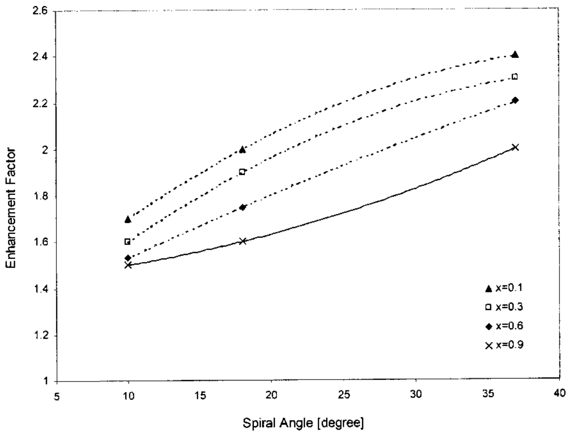

Fig. 8 Enhancement factor versus spiral angle for condensation of R-134a inside micro-fin tubes at a mass flux of 800 kg/m^2 s

Heat Transfer Correlation

A new correlation for the prediction of heat transfer during condensation inside spiralled micro-fin tubes was developed based on experimental results of the present study. The database of experimental results, from which the predictive correlation was generated consisted specifically of measurements for annular and intermittent flow regimes; therefore, the new predictive model is appropriate for annular flow. This model was also used as a good approximation for intermittent flow, which indicates that annular flow models predict refrigeration condensation performance effectively when the flow is of such a nature that mostly annular and intermittent flow are present; and, therefore, also, that the annular flow models effectively capture the flow geometry of intermittent flow [16].

The approach adopted to develop the new predictive correlation consisted of three steps: first, identification from existing smooth in-tube condensation models, the best predictor of experimental results of the present study; second, identification of modifiers to be applied to the selected smooth tube correlation in order to improve the agreement between experimental data and predicted values. The third and most crucial step was to apply modifiers to the proposed new smooth tube correlation in order to adapt it for the prediction of heat transfer during condensation inside spiralled micro-fin tubes. These modifiers had to reflect the influence of geometric parameters of the micro-fin tube. The Akers et al. [17] model, which was identified as the best predictor of current experimental results, was selected as a reference for developing the new predictive correlation. The general form of the new correlation for smooth tubes that corresponds to the Akers model is

$$\mathrm{Nu}\,\mathrm{Pr}_l^{-1/3} = C_1\,\mathrm{Re}_{\mathrm{eq}}^{C_2}\,P_{\mathrm{red}}^{C_3} \tag{8}$$

The value of reduced pressure is informative regarding the variation in fluid properties. At high values of reduced pressure, the liquid and vapor densities become similar, at which point a homogeneous void fraction model is applicable, which assumes that the vapor and liquid phases travel at the same velocity in the condenser tube. This further implies higher values of vapor density and viscosity, and lower values of liquid density and viscosity. The surface tension, which has the interpretation of the work required to increase the interfacial area [16], also decreases as the reduced pressure increases and the phases become more similar. At a given temperature, the reduced pressure is lowest for the

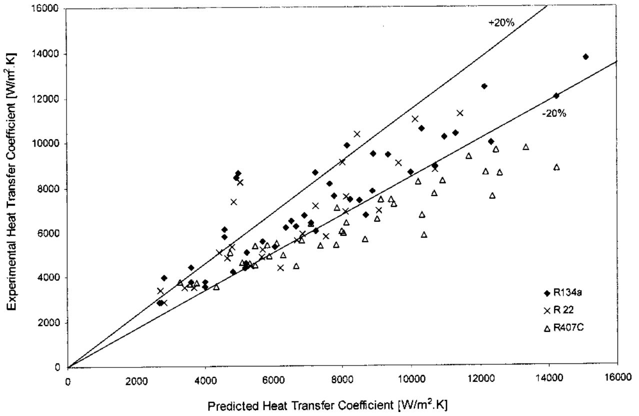

Fig. 9 **Comparison between experimental and predicted heat transfer coefficients for condensation inside smooth and micro-fin tubes**

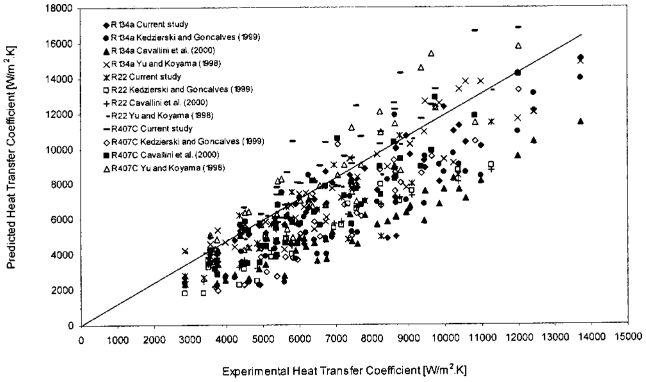

Fig. 10 **Comparison between experimental and predicted heat transfer coefficients calculated from different predictive models for condensation inside spiralled micro-fin tubes. (Uncertainties in local heat transfer coefficient: ±15%.)**

R-134a (i.e., $P_{\text{red}}=0.26$), followed by R-22 (i.e., $P_{\text{red}}=0.31$) and then R-407C (i.e., $P_{\text{red}}=0.36$), calculated at a saturation temperature of 40°C.

The reduced pressure P_{red} was, therefore, added to the original Akers et al. [17] model. This modifier effectively reflected the effect of the inlet pressure of the condensing fluid on the thickness of the condensing liquid film; the thickness of the liquid film being a factor that considerably affects the heat transfer performance during condensation in smooth tubes.

A total of 144 experimental points for the micro-fin tubes from the present study were used for the three refrigerants to determine the constants C_1, C_2, and C_3 by using a power regression analysis. The constants were $C_1=0.0323$, $C_2=0.82$, and $C_3=0.3$, if and when $2<\text{Pr}_l<5$, $0.2<P_{\text{red}}<0.4$, and $\text{Re}_{\text{eq}}>20{,}000$.

The model for condensation inside spiralled micro-fin tubes was derived from the new smooth tube predictive correlation by inserting two new dimensionless parameters J and W. The modifier J accounted for heat transfer surface area increase (being a function of increasing spiral angle) while the modifier W accounted for surface tension force effects. The general form of the new spiralled micro-fin tube predictive correlation was expressed as

$$\text{Nu}\,\text{Pr}_l^{-1/3}=0.0323\,\text{Re}_{\text{eq}}^{0.82}\,P_{\text{red}}^{0.3}[1+C_4 J^{C_5} W^{C_6}] \tag{9}$$

The heat transfer surface area modifier J was defined as the ratio of the actual heat transfer area (A_a) to the nominal heat transfer area (A_n)

$$J=\frac{A_a}{A_n}=1+\frac{2eN}{\pi d_i \cos\beta} \tag{10}$$

The surface tension force modifier W was defined as

$$W=\left(\frac{x}{1-x}\right)\text{Bo} \tag{11}$$

A total of 144 experimental runs from the present study were used for each tested refrigerant (R-22, R-134a, and R-407C) and test condenser to determine the constants C_4, C_5, and C_6 by employing the power regression analysis. The following new predictive correlation was, therefore, generated for condensation inside spiralled micro-fin tubes:

$$h=0.0323\left(\frac{k_1}{d_{eq}}\right)\text{Re}_{\text{eq}}^{0.82}\,\text{Pr}_l^{1/3}P_{\text{red}}^{0.3}\left[1+0.176J^{5.3}\left(\left(\frac{x}{1-x}\right)\text{Bo}\right)^{-0.08}\right] \tag{12}$$

with $C_4=0.176$, $C_5=5.282$, and $C_6=-0.083$.

Figure 9 presents a comparison between experimental and predicted heat transfer coefficients (Eq. (12)). A good agreement was observed as the majority of data points fell within the ±20% deviation zone. Using similar but not exactly comparable data as the fin geometries are not necessary the same, the predictive equation (Eq. 12) was compared to the prediction methods of Cavallini et al. [5], Yu and Koyama [18] and Kedzierski and Goncalves [19]. Figure 10 shows that the Cavallini et al. [5] and Kedzierski and Goncalves [19] models under predict the current experimental results by about 25 and 50% respectively. The Yu and Koyama [18] model over predicts the current experimental results by about 10% while the new predictive model (Eq. (12)) under predicts the current experimental results by about 12%. Taking into account the uncertainties in experimental results, this was an indication that the new predictive correlation was in reasonable agreement with both the pre-mentioned predictive models and the current experimental results.

Conclusion

The effect of the spiral angle on the condensation heat transfer performance of spiralled micro-fin tubes has been investigated in this study and a new correlation was proposed for predicting condensation heat transfer inside smooth and spiralled micro-fin tubes. Tests were conducted for condensation of R-22, R-134a, and R-407C inside smooth and micro-fin tubes having spiral angles of 10, 18, and 37 deg respectively. The mass fluxes ranged between 300 kg/m^2 s and 800 kg/m^2 s and measurements were taken at an average saturation temperature of 40°C.

In general, heat transfer coefficients increased with an increase in mass flux. The highest heat transfer augmentation was observed at the lowest mass flux of 300 kg/m^2 s. The heat transfer augmentation decreased as the mass flux was increased, producing the lowest heat transfer augmentation at the highest mass flux. At lower mass fluxes (ranging between 300 kg/m^2 s to 500 kg/m^2 s), a substantial heat transfer augmentation was observed for the vapor quality ranging between 0.1–0.3 which corresponds to the intermittent flow region. However, a moderate heat transfer augmentation was observed for the vapor quality ranging between 0.4–0.9 which corresponds to the transitional and annular flow region. At higher mass fluxes (ranging between 600–800 kg/m^2 s), a different trend was observed where a moderate heat transfer augmentation occurred over the entire range of vapor quality. The spiraled micro-fins at 37 deg produced the highest heat transfer augmentation while 18 deg spiraled micro-fins produced a moderate heat transfer augmentation.

A predictive correlation for annular flow has been generated from current experimental results. The new correlation is in good agreement with experimental results, the majority of data points falling within a deviation zone of ±20%. The correlation was also tested against other correlations for microfin tubes (although not necessarily with the same fin geometry). However, more investigation is needed in the future to test the credibility of the new correlation and its range of applicability. Furthermore, more data are needed for condensation inside spiralled micro-fin tubes covering a broad range of refrigerants and most importantly a wider range of flow regimes.

Acknowledgment

The authors would like to thank the manufacturer of the micro-fin tubes, Wolverine Tubes Inc. (specifically Petur Thors and Ram Narayanamurthy) and Wieland-Werke AG (Axel Krigsmann) for donating several lengths of micro-fin tubes.

Nomenclature

A = area [m^2]
A_a = actual heat transfer area of the micro-fin tube ($\pi d_{\text{eq}}L = \pi d_i L + 2eNL/\cos\beta$), [m^2]
$A_{\text{cross},a}$ = actual cross sectional area of the micro-fin tube ($\pi d_a^2/4$), [m^2]
A_i = nominal heat transfer area of the micro-fin tube ($\pi d_i L$), [m^2]
A_o = outside surface area of the inner tube ($\pi d_o L$), [m^2]
b = fin thickness [m]
Bo = bond number ($g\rho_l e\pi d_i/8N\sigma$), [-]
C_p = specific heat at constant pressure [J/kg K]
d = tube diameter [m]
d_a = actual diameter of the microfin tube ($d_i + 2Neb/\cos\beta$), [m]
D_i = inside diameter of the outside tube, [m]
d_h = hydraulic diameter ($D_i - d_o$), [m]
d_{eq} = equivalent diameter ($4A_{\text{cross},a}/A_a$), [m]
e = fin height, [m]
g = gravity acceleration [m/s^2]
h = heat transfer coefficient [W/m^2 K]
i = enthalphy [J/kg]
k = thermal conductivity [W/m K]
L = length [m]
LMTD = log mean temperature difference [°C]
$\dot{M}$ = water mass flow rate [kg/s]
$\dot{m}$ = refrigerant mass flow rate [kg/s]
N = number of fins [-]
Q = heat transfer [W]
T = water temperature [°C]
t = refrigerant temperature [°C]
U = overall heat transfer coefficient [W/m^2 K]
x = vapor quality [-]
z = axial distance along the test section [m]
β = spiral angle [deg]
δ = film thickness [m]
ρ = density [kg/m^3]
σ = surface tension [N/m]
μ = viscosity [Pa/s]

Dimensionless Parameters

J = modifier accounting for surface area increase (A_a/A_n)
Nu = Nusselt number [-]
Pr = Prandtl number [-]
P_{red} = reduced pressure ($P_{\text{cond}}/P_{\text{crit}}$), [-]
Re = Reynolds number [-]
Re_{eq} = equivalent Reynolds number $G[(1-x)+x(\rho_l/\rho_v)^{0.5}]d_i/\mu_l$, [-]
W = modifier accounting for surface tension forces effect ($x/(1-x)\text{Bo}$), [-]

Subscripts

av = average
cond = condensing
crit = critical
dew = dew point
eq = equivalent
glide = glide
i = inner (refrigerant-side)
in = inlet
l = liquid
o = outer (water-side)
out = outlet
sat = saturation
v = vapor
w = tube wall
wo = outside wall of inner tube

References

[1] Schlager, L. M., Pate, M. B., and Bergles, A. E., 1990, "Evaporation and Condensation Heat Transfer and Pressure Drop in Horizontal 12.7 mm Micro-fin Tubes With Refrigerant 22," ASME J. Heat Transfer, **112**, pp. 1041–1047.
[2] Yasuda, K., Ohizumi, K., Hori, M., and Kawamata, O., 1990, "Development of Condensing Thermofin-HEX-C Tube," Hitachi Cable Rev., **9**, pp. 27–30.
[3] Chiang, R., 1993, "Heat Transfer and Pressure Drop During Evaporation and Condensation of Refrigerant R-22 in 7.5 mm Diameter Axial and Helical Grooved Tubes," AIChE Symp. Ser., **295**(89), pp. 205–210.
[4] Tatsumi, A. K., Oizumi, K., Hayachi, M., and Itoh, M., 1982, "Application of Inner Grooves Tubes to Air Conditioners," Hitachi Rev., **32**(1), pp. 55–60.
[5] Cavallini, A., Del Col, D., Doretti, L., Longo, G. A., and Rossetto, L., 2000, "Heat Transfer and Pressure Drop During Condensation of Refrigerants Inside Horizontal Enhanced Tubes," Int. J. Refrig., **23**, pp. 4–25.
[6] NIST, 1998, NIST Thermodynamic and Transport Properties of Refrigerants and Refrigerant Mixtures Database (REFPROP Ver. 6.01), National Instruments of Standards and Technology, Gaithersburg, MD.
[7] Kline, S. J., and McClintock, F. A., 1953, "Describing Uncertainties in Single Sample Experiments," Am. Soc. Mech. Eng., **75**, pp. 3–8.
[8] Briggs, D. E., and Young, E. H., 1969, "Modified Wilson Plot Techniques for obtaining Heat Transfer Correlations for Shell and Tube Heat Exchangers," Chemical Engineering Progress Symposium, **92**(65), pp. 35–45.
[9] Coetzee, S., 2000, "The Development of an Experimental Set-Up to Investigate Heat Transfer Enhancement in Tube-in-Tube Heat Exchangers," MEng thesis, Department of Mechanical Engineering, Rand Afrikaans University, Johannesburg, South Africa.
[10] Eckels, S. J., and Tesene, B. A., 1999, "A Comparison of R-22, R-134a, R-410A and R-407C Condensation Performance in Smooth and Enhanced Tubes: Part 1, Heat Transfer," ASHRAE Trans., **105**, pp. 428–441.
[11] Muzzio, A., Niro, A., and Arosio, S., 1998, "Heat Transfer and Pressure Drop During Evaporation and Condensation of HCFC-22 Inside 9.52-mm O.D. Microfin Tubes at Different Geometries," J. Enhanced Heat Transfer, **5**, pp. 39–52.
[12] Eckels, S. J., and Unruh, B. J., 1999, "Local Heat Transfer Coefficients During Condensation of HCFC-22 and R-32/R-125 Mixtures," HVAC&R Res., **5**(1), pp. 59–76.
[13] Smit, F. J., Thome, J. R., and Meyer, J. P., 2002, "Heat Transfer Coefficients During Condensation of the Zeotropic Refrigerant Mixture HCFC-22/HCFC-142b," ASME J. Heat Transfer, **124**(6), pp. 1137–1146.
[14] Smit, F. J., and Meyer, J. P., 2002, "R-22 and Zeotropic R-22/R-142b Mixture Condensation in Microfin, High-Fin, and Twisted Tape Insert Tubes," ASME J. Heat Transfer, **124**(5), pp. 912–921.
[15] Bukasa, J. P. M., 2002, "Heat Transfer Performance During Condensation Inside Spiralled Microfin Tubes," Ph.D. thesis, Department of Mechanical Engineering, Rand Afrikaans University, Johannesburg, South Africa.
[16] Liebenberg, L., 2002, "A Unified Prediction Method for Smooth and Micro-Fin Tube Condensation Performance," Ph.D. thesis, Rand Afrikaans University, Johannesburg, South Africa.
[17] Akers, W. W., Deans, H. A., and Crosser, O. K., 1959, "Condensing Heat Transfer Within Horizontal Tubes," Chemical Engineering Progress Symposium Series, **55**(29), pp. 171–176.
[18] Yu, J., and Koyama, S., 1998, "Condensation Heat Transfer of Pure Refrigerants in Microfin Tubes," *Proceedings International Refrigeration Conference*, Purdue, pp. 325–330.
[19] Kedzierski, M. A., and Goncalves, J. M., 1997, "Horizontal Convective Condensation of Alternative Refrigerants Within a Micro-Fin Tube," NISTIR 6095, U.S. Dept. Commerce, Washington, D.C., p. 74.

D. K. Agarwal
Department of Mechanical Engineering,
Indian Institute of Technology,
Kanpur-208016, India

S. W. J. Welch
Department of Mechanical Engineering,
University of Colorado, Denver,
Colorado-80217, USA

G. Biswas
e-mail: gtm@iitk.ac.in
Mem. ASME,
Department of Mechanical Engineering,
Indian Institute of Technology,
Kanpur-208016, India

F. Durst
Institute of Fluid Mechanics, LSTM,
University of Erlangen-Nuremberg,
Cauer Str. 4, D-91058 Erlangen, Germany

Planar Simulation of Bubble Growth in Film Boiling in Near-Critical Water Using a Variant of the VOF Method

A planar simulation of film boiling and bubble formation in water at 373°C, 219 bar on an isothermal horizontal surface was performed by using a volume of fluid (VOF) based interface tracking method. The complete Navier-Stokes equations and thermal energy equations were solved in conjunction with a interface mass transfer model. The numerical method takes into account the effect of temperature on the transportive thermal properties (thermal conductivity and specific heat) of vapor, effects of surface tension, the interface mass transfer and the corresponding latent heat. The computations provided a good insight into film boiling yielding quantitative information on unsteady periodic bubble release patterns and on the spatially and temporally varying film thickness. The computations also predicted the transport coefficients on the horizontal surface, which were greatly influenced by the variations in fluid properties, compared to calculations with constant properties. [DOI: 10.1115/1.1737779]

Keywords: Boiling, Bubble Growth, Computational, Heat Transfer, Mass Transfer, Surface Tension.

1 Introduction

Numerous publications in the open literature document that there has been a long-lasting interest among the researchers to clarify interface transport mechanisms in liquid-vapor phase change processes. In the past, appropriate studies in this field were carried out experimentally. Albeit having very useful contributions in the development of the subject, the early investigations could not provide the physical details needed for a closer understanding of the bubble formation and the time varying heat transfer characteristics. Experimental studies in boiling have yielded several empirical correlations that are valid for specific cases. Only the advancement of computational techniques have opened up new ways to carry out the investigations in detail on boiling, revealing the nuances of the interface transport processes. The volume of fluid (VOF) method of Hirt and Nichols [1] forms the building block of computations involving two fluids separated by a sharp interface. The VOF method has been modified very successfully by Welch and Wilson [2] to simulate horizontal film boiling. Son and Dhir [3] have also performed complete numerical simulation of the evolution of the vapor-liquid interface during film boiling on a horizontal surface. In another approach, Son and Dhir [4] have modified the level set method of Sussman et al. [5] to perform numerical simulation of film boiling. At low wall superheats, they have observed the upward movement of the interface initiating the vapor bubble formation. Having released the bubble, the interface drops down alternatively at the nodes and anti-nodes of a Taylor wave.

Juric and Tryggvason [6] have performed excellent simulations of film boiling using single field formulation where one set of conservation equations are written for the entire flow field and different phases are treated as one fluid with variable material properties. They have used source terms in the continuity and the energy equations as an enhancement of the method of Unverdi and Tryggvason [7]. Interfacial source terms for surface tension, interface mass transfer and latent heat are added as delta functions that are nonzero at the interface boundary. Banerjee and Dhir [8] have performed direct simulation of evolving interface during sub-cooled film boiling. The simulation provides the shape and growth rates of the interface and the associated thermal behavior.

The overview on numerical simulations of pool boiling has been authoritatively reviewed by Dhir [9]. He pointed out that numerical simulations of evolving liquid-vapor interfaces during a phase change process such as boiling provide significant additional insights into the phenomena. More recently Welch and Rachidi [10] developed another VOF based interface tracking method to explore film boiling on a horizontal surface and considered a conjugate problem between a solid wall and the boiling fluid. They carried out the analysis considering constant thermal properties at the saturation temperature, whereas it has been seen from the NBS/NRC Table (Table 1) that at near critical pressure, the transportive thermal properties of vapor vary significantly with temperature. The present work is an extension of the work by Welch and Rachidi [10] with respect to the variable thermal properties. In this work, we consider a heated wall with a uniform temperature of 388°C, superheated by 15°C relative to the pool of saturated water at near-critical conditions of 373°C, 219 bar ($T_c = 374.15°\text{C}, P_c = 221.29$ bar). The model assumes that location of the bubbles are spaced on a solid surface in a square pattern separated by the Taylor fastest-growing wavelength given by Berenson [11]

$$\lambda_o = 2\pi\sqrt{\frac{3\sigma}{(\rho_l-\rho_g)g}} \tag{1}$$

The bubble diameter and the bubble height in Berenson's model are considered to be proportional to the bubble spacing. However, the characteristic length in the present investigation, for presenting the pertinent dimensionless parameters, such as, Nusselt number has been considered as

$$\lambda = \sqrt{\frac{\sigma}{(\rho_l-\rho_g)g}} \tag{2}$$

Contributed by the Heat Transfer Division for publication in the JOURNAL OF HEAT TRANSFER. Manuscript received by the Heat Transfer Division January 2, 2003; revision received March 5, 2004. Associate Editor: D. B. R. Kenning.

Table 1 Properties from NBS/NRC table for vapor phase

Temperature, °K	*k*, W/mK	c_p, kJ/kgK	μ, Pas
646.15	0.5383	3.520×10^2	3.230×10^{-5}
647.81	0.2502	0.4318×10^2	2.912×10^{-5}
649.48	0.2126	0.2854×10^2	2.825×10^{-5}
651.15	0.1918	0.2227×10^2	2.775×10^{-5}
652.81	0.1777	0.1864×10^2	2.743×10^{-5}
654.48	0.1673	0.1622×10^2	2.720×10^{-5}
656.15	0.1591	0.1448×10^2	2.704×10^{-5}
657.82	0.1524	0.1316×10^2	2.692×10^{-5}
659.48	0.1468	0.1211×10^2	2.683×10^{-5}
661.15	0.1421	0.1126×10^2	2.676×10^{-5}

This three-dimensional geometry is further simplified to planar geometry. In this investigation we explore by the numerical simulations discussed below the nature of the heat transfer processes and particularly the influence of the large variations in the thermal and transport properties of the vapor.

2 Formulation of the Problem

The mass, momentum and energy conservation equations for the incompressible Newtonian fluids for the liquid and vapor phases are given by

$$\frac{\partial U_i}{\partial x_i}=0 \tag{3}$$

$$\rho\left(\frac{\partial U_j}{\partial t}+\frac{\partial U_i U_j}{\partial x_i}\right)=-\frac{\partial p}{\partial x_j}+\frac{\partial}{\partial x_i}\left(\mu\frac{\partial U_j}{\partial x_i}\right) \tag{4}$$

$$\left(\frac{\partial(\rho c_p\theta)}{\partial t}+\frac{\partial(\rho c_p\theta U_j)}{\partial x_j}\right)=\frac{\partial}{\partial x_j}\left(k\frac{\partial\theta}{\partial x_j}\right) \tag{5}$$

Here, U_j, p, c_p, ρ, θ, μ and k are the fluid velocity, pressure, specific heat, density, temperature, viscosity and thermal conductivity, respectively. The dissipation term in the energy equation has been neglected.

2.1 Boundary Conditions. Figure 1 shows the domain of interest for the present investigation. The simulation is planar, two-dimensional. The computational domain is given by ABCD. The boundary conditions are symmetry conditions at the left and right boundaries

$$\text{at } x=0 \text{ and } x=\lambda_o/2: \quad u=0;\ \frac{\partial v}{\partial x}=0;\ \frac{\partial\theta}{\partial x}=0$$

Constant wall temperature condition is used on the solid-fluid interface

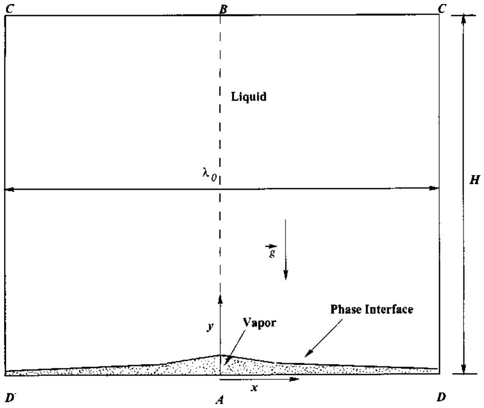

Fig. 1 The domain for the simulation of film boiling

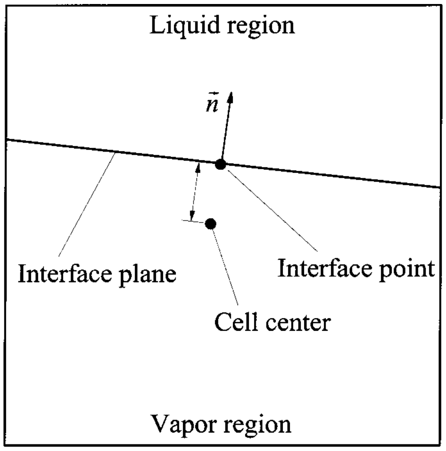

Fig. 2 A typical two phase cell with piecewise linear interface

$$\text{at } y=0 \quad \theta=\theta_{\text{sup}}$$

Outflow boundary conditions are used on the top surface of the domain

$$\text{at } y=H \quad \frac{\partial u}{\partial y}=\frac{\partial v}{\partial y}=\frac{\partial\theta}{\partial y}=0;\ P=P_o$$

The outlet pressure is the saturation pressure less the hydrostatic pressure difference from the initial film level to the outlet. The boundary condition at the vapor liquid interface is of special concern in this study. In order to address this issue, a suitable interface tracking method has been implemented.

2.2 Interface Tracking. The presence of two phases in the fluid requires handling of the phase interface. We advect the interface using enhancement of VOF method of Hirt and Nichols [1] due to Youngs [12]. The method of Youngs is implemented at the end of a time cycle to calculate the new density field using conservation of mass for each cell

$$\frac{\partial}{\partial t}\int_{V_c}\rho dV+\int_{S_c}\rho\mathbf{v}\cdot\mathbf{n}dS=0 \tag{6}$$

where V_c is the cell volume and S_c is the cell surface. The symbol $\mathbf{v}$ is used for the fluid velocity. Once, the new cell densities are found, the cell void fractions are calculated using

$$\alpha=\frac{\rho-\rho_g}{\rho_l-\rho_g} \tag{7}$$

Here, ρ_l and ρ_g are the densities of the saturated liquid and saturated vapor, respectively. The implementation of the method of Youngs has been well documented in Welch and Wilson [2], Rudman [13] and Rider and Kothe [14]. The phase interface is represented by piecewise linear curves. Figure 2 shows a typical two phase cell. The orientation of the curve within each two phase cell is determined using the procedure described by Welch and Rachidi [10] based on LVIRA method of Puckett et al. [15]. The method requires minimization of the function

$$G_{ij}(\mathbf{n})=\sum_{k,l=-1}^{1}\{\alpha_{i+k,j+l}-\hat{\alpha}(\mathbf{n},l)_{i+k,j+l}\}^2 \tag{8}$$

Here $\alpha_{i,j}$ is the actual void fraction of the cell $(i,\,j)$ and $\hat{\alpha}(\mathbf{n},l)_{i,j}$ is the function that maps the line with orientation $\mathbf{n}$ and offset length l into a void fraction of the cell $(i,\,j)$. This constrained

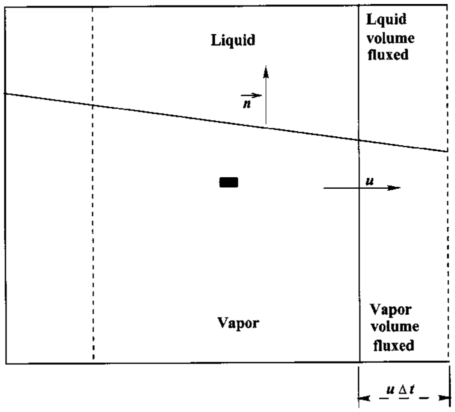

Fig. 3 Schematic of cell flux calculation

minimization of the function $G_{ij}(\mathbf{n})$ is a nonlinear problem requiring an initial estimate for $\mathbf{n}$. This initial $\mathbf{n}$ is the value determined by the modified VOF method of Youngs [12] as

$$\mathbf{n}=\frac{\nabla\alpha}{|\nabla\alpha|} \tag{9}$$

In order to maintain the continuity of the text, LVIRA algorithm is not being discussed here in detail. More information on LVIRA is available in the appendix. Given the orientation of the planar surface that represents the interface in a cell, we determine the location of the oriented surface, such that the surface partitions the cell into liquid and gas regions of correct volume, based upon the void fraction (which is defined as the volume fraction of the liquid) of the cell. Given the location of the planar interface (i.e., knowing $\mathbf{n}$, l) in each two phase cell and the velocity at a junction face between two cells, the mass flux is determined from simple volumetric considerations. Once the mass is fluxed across the cell boundaries in one direction (Fig. 3), the interface is reconstructed before mass is fluxed in the second direction. This is the Direction Split Approach of Rudman [13].

2.3 Jump Conditions at Liquid Vapor Interface. The mass transfer across the interface is modeled following Welch and Rachidi [10]. We consider a computational cell containing a volume of the liquid phase adjacent to a volume of the vapor phase. We write a mass balance for each phase as

$$\frac{d}{dt}\int_{V_g(t)}\rho dV+\int_{S_g(t)}\rho\mathbf{v}.\mathbf{n}dS+\int_{S_I(t)}\rho(\mathbf{v}-\mathbf{v}_I).\mathbf{n}dS=0 \tag{10}$$

$$\frac{d}{dt}\int_{V_l(t)}\rho dV+\int_{S_l(t)}\rho\mathbf{v}.\mathbf{n}dS+\int_{S_I(t)}\rho(\mathbf{v}-\mathbf{v}_I).\mathbf{n}dS=0 \tag{11}$$

Here V_l, S_l, V_g, S_g are the volume and surface of the liquid and vapor regions, respectively. S_I is the phase interface at the common boundary of the two regions, moving with velocity $\mathbf{v}_I$. The normal vector $\mathbf{n}$ points into the liquid phase on S_I. From the above, and taking into account the incompressibility of each phase, and under the situation that the overall volume is time invariant, the conservation of mass statement for the cell volume is determined

$$\int_{S_c}\mathbf{v}.\mathbf{n}dS+\int_{S_I(t)}\|(\mathbf{v}-\mathbf{v}_I)\|.\mathbf{n}dS=0 \tag{12}$$

Here, $\|.\|$ indicates the jump in the variable of interest across the phase interface and S_c is the surface bounding the computational cell. The mass and energy jump conditions at the interface may be estimated as

$$\|\rho(\mathbf{v}-\mathbf{v}_I)\|.\mathbf{n}=0 \tag{13}$$

$$\|\rho h(\mathbf{v}-\mathbf{v}_I)\|.\mathbf{n}=-\|\mathbf{q}\|.\mathbf{n} \tag{14}$$

entails the contribution of jump in the conservation of mass equation as

$$\|(\mathbf{v}-\mathbf{v}_I)\|.\mathbf{n}=\left(\frac{1}{\rho_l}-\frac{1}{\rho_g}\right)\frac{\|\mathbf{q}\|.\mathbf{n}}{h_{lg}} \tag{15}$$

Here, h is the enthalpy and $h_{lg}=h_g-h_l$ is the latent heat of vaporization while $\mathbf{q}$ is the heat flux vector. We assume the phase interface to be at the saturation temperature of the liquid pressure

$$\theta_I=\theta_{\mathrm{sat}}(P_l) \tag{16}$$

The temperature condition in Eq. (16) is a widely used approximation. The work of Son and Dhir [4] justifies this approximation. We neglect kinetic energy and viscous work terms in the energy jump and the viscous dissipation is also neglected.

2.4 Modified Momentum Equation. The momentum equations are augmented using the continuum surface tension model of Brackbill et al. [16] in the following way:

$$\rho(\tilde{\alpha})\left(\frac{\partial\mathbf{v}}{\partial t}+\mathbf{v}.\nabla\mathbf{v}\right)=-\nabla P+\rho(\tilde{\alpha})\mathbf{g}+\nabla\cdot[\mu(\tilde{\alpha})(\nabla\mathbf{v}+(\nabla\mathbf{v})^T)]+\sigma\kappa\nabla\tilde{\alpha} \tag{17}$$

where $\tilde{\alpha}$ is a smoothened void field and κ is the curvature of the surface defined by smoothened void field. The surface tension force is applied to a transition region of nine cells thick centered at the interface. The density and viscosity vary with the void fields as

$$\rho(\tilde{\alpha})=\tilde{\alpha}\rho_l+(1-\tilde{\alpha})\rho_g \tag{18}$$

$$\mu(\tilde{\alpha})=\tilde{\alpha}\mu_l+(1-\tilde{\alpha})\mu_g \tag{19}$$

In the sequel, it can be said that for the interface cells, we use the augmented momentum Eq. (17), the modified conservation of mass Eq. (12) and the energy jump condition given by Eq. (14). The discontinuity of the velocity field, the velocity gradients, and the viscosity are treated by smoothing.

2.5 Numerical Procedure. The spatial discretization of governing equations is obtained using a staggered grid arrangement of Harlow and Welch [17] with scalars located at the cell centers and velocity components located at the center of the cell faces. The convection terms of the momentum equation are discretized by higher order methods using an ENO discretization scheme (see Chang et al. [18]). The convection terms in energy equation are discretized by QUICK [19]. The temporal discretization is described by a semi-implicit forward Euler method. We begin a time cycle by solving the explicit energy equation in the bulk fluid phases

$$\theta^{n+1}=\theta^{n}+\frac{\delta t}{\rho c_p}[-\mathbf{v}.\nabla(\rho c_p\theta)+\nabla(k\nabla\theta)]^n \tag{20}$$

After every time step with the help of new temperature field, thermal conductivity and specific heat at each cells are calculated. The thermal properties and temperature field thus obtained are used to form the interfacial heat flux jump appearing in the mass source term. The continuity and momentum equations are discretized in time as

$$\int_{S_c}\mathbf{v}^{n+1}.\mathbf{n}dS+\int_{S_I(t)}\left(\frac{1}{\rho_l}-\frac{1}{\rho_g}\right)\frac{\|\mathbf{q}^{n+1}\|.\mathbf{n}}{h_{lg}}dS=0 \tag{21}$$

$$\mathbf{v}^{n+1}=\mathbf{v}^n-\delta t(\mathbf{v}.\nabla\mathbf{v})^n-\frac{\delta t}{\rho^n}\{\nabla P^{n+1}+(\rho\mathbf{g})^n+\nabla.[\mu(\nabla\mathbf{v}+(\nabla\mathbf{v})^T)]^n+\sigma(\kappa\nabla\tilde{\alpha})^n\} \tag{22}$$

The velocity for the new time step is eliminated from these discrete equations and resulting pressure equation is solved by an

Table 2 Properties used for constant property simulation

Substance	k, W/mK	c_p , kJ/kgK	μ, Pas
Liquid Water	0.5454	2.18×10^2	4.67×10^{-5}
Water Vapor	0.5383	3.52×10^2	3.23×10^{-5}

iterative method based on a preconditioned conjugate gradient scheme of Van der Vorst [20] that has been implemented by Welch and Rachidi [10]. Once the pressure at the new time level is obtained, the velocity at the new time level is found from the discrete momentum equations and the new density field is found from Eq. (6) as

$$\rho^{n+1}=\rho^n+\delta t\int_{S_c}\rho\mathbf{v}^{n+1}.\mathbf{n}dS \tag{23}$$

As discussed earlier, at this stage LVIRA algorithm is invoked. The cells that are not mixture cells, or are not adjacent to mixture cells, do not require this treatment. Once the new density field is found, the new void fraction may be calculated and the mixture cell interfacial geometry can be updated.

The numerical scheme is based on the explicit time-advancement strategy. The time step is determined from the limit imposed on a capillary wave traveling in an infinite medium [2]. The wave is not allowed to travel more than half a cell width during a time step.

3 Results and Discussion

The simulations were performed with variable and constant thermal properties of the fluid. The variable properties are indicated in Table 1. The constant properties are evaluated at near-critical conditions of 373°C and 219 bar. These properties are given in Table 2. The computational domain chosen for the present simulation is shown in Fig. 1. Since the problem is symmetric, a computational domain with width $\lambda_o/2$ was chosen. In the present simulation the numerical values of λ_o and λ are 2.270 mm and 0.2087 mm, respectively. The height of the domain, H was set as λ_o with initial interface height, δ set to

$$\delta=\frac{\lambda_o}{128}\left\{2+\cos\left(\frac{2\pi x}{\lambda_o}\right)\right\} \tag{24}$$

We first present results of a convergence study undertaken to find an adequate grid resolution. For this, simulations were performed with three grid-meshes, viz., 90×180, 180×360 and 360×720. Figure 4 shows the interfacial shape at the instant of bubble release from the surface for the above-mentioned grid resolutions. We observe that the 180×360 and 360×720 produce nearly identical results; hence, we choose the 180×360 grid for our subsequent simulations. The same simulation run on 180×360 with the time step halved also gives nearly identical results as seen in Fig. 5. Thus the 180×360 grid with the time step used in spatial convergence study provides results converged in time and in space, and it is used for all the subsequent simulations. In the present simulation we considered water near the critical point and the vapor transportive thermal properties (thermal conductivity and specific heat of vapor) varying with temperature. As mentioned earlier, the properties are given in Table 1. The interfacial properties and density are provided by Table 3. At the outset, we present numerical simulations showing growth of the bubble and its release pattern, with constant wall temperature boundary condition of 15°C superheat. We used a data set of thermal properties (from Table 1) containing ten values in the range of 15 deg superheat and interpolated the properties to get intermediate values at any temperature corresponding to the cell temperature.

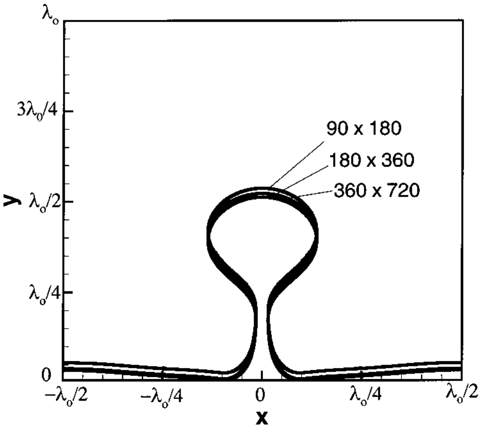

Fig. 4 Bubble interface for three different grid resolutions

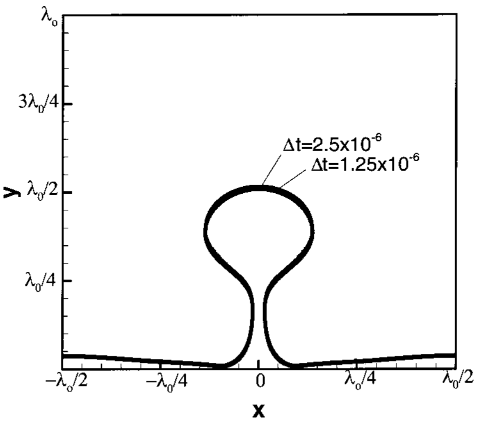

Fig. 5 Bubble interface for two different time steps. Grid resolution is kept as 180×360.

Figure 6 shows the periodic bubble release patterns with growing interface and varying vapor volume. The steady cyclic growth and release of vapor bubbles is usually called ebullition cycle. Starting with a thin vapor layer, gradually the bubble grows bigger. Finally, the bubble reaches a limit at which it detaches. The detached bubble moves upwards and leaves the domain of interest. The released bubble leaves a very thin vapor film near the nodal position on the wall on which it had rested prior to its departure. Due to the vapor production at the interface the thin vapor layer again grows in size. The next bubbles tend to grow at the outer side walls, which are basically the anti-nodes according to the Taylor's wave length.

The ebullition cycle or bubble release cycle is revealed through the sequence of varying interface boundary at different time instants. The mechanism for the repeating pattern can be described in the following way. After the bubble is released from the surface, the vapor left behind experiences a downward force due to surface tension. Subsequently this vapor packet is pushed down towards the film. The vapor packet impinges on the horizontal surface. The surface tension induced flow promotes the movement of pressure gradient driven impinging vapor packet towards the symmetric side walls. The vapor turns upward near the side walls

Table 3 Interfacial properties and density

σ, N/m	h_{lg} , kJ/kg	θ_{sat} , K	P_{sat} , Pa	ρ, kg/m^3 Liquid water	ρ, kg/m^3 Water vapor
0.07×10^{-3}	276.4	646.15	21.9×10^6	402.4	242.7

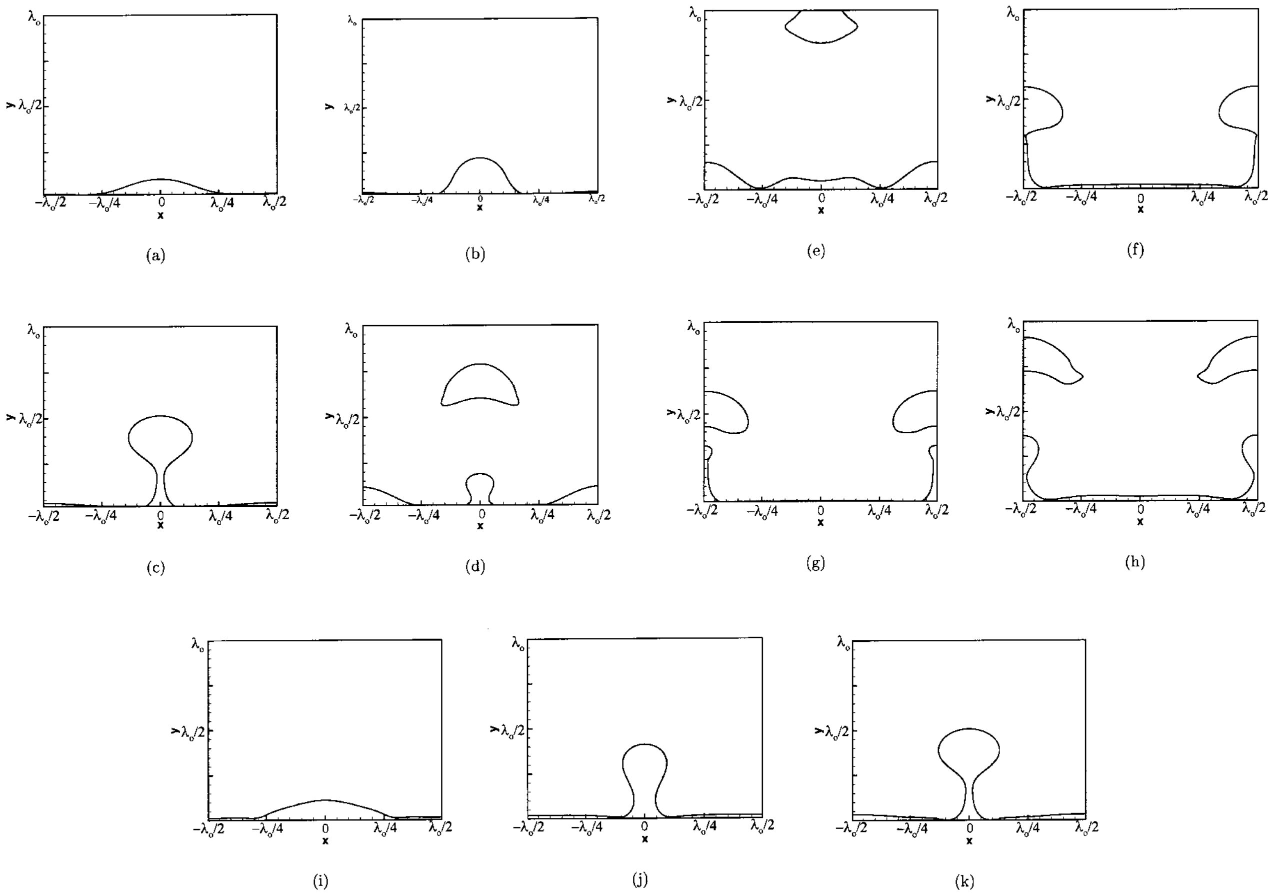

(a) (b) (e) (f)

(c) (d) (g) (h)

(i) (j) (k)

Fig. 6 Bubble release from the constant wall temperature surface for two complete cycles

to initiate an identical bubble release cycle. Similar patterns of bubble release were observed by Son and Dhir [4] in their axisymmetric simulations of saturated film boiling.

Furthermore, the cyclic bubble release pattern can be discerned from Figs. 7 and 8, which show the variation of space averaged wall heat flux with time for constant and variable thermal properties, respectively. For constant thermal properties (Fig. 7), after an initial transient, we observed a cyclic pattern with the time period of 0.27 s. For variable thermal properties (Fig. 8), we found a smaller time period of 0.23 s. Figure 9 shows the variation of interface heat flux with time for both the cases; namely, constant and variable thermal properties. It can be observed that with the variable thermal properties, a higher magnitude of energy is transferred from vapor to liquid. This energy is responsible for conversion of liquid into vapor. Figure 10 shows the variation of fractional vapor volume (vapor volume/(vapor volume and liquid volume)) with time for both the cases. Due to higher vapor generation, the bubble growth rate is faster for the case of variable thermal properties as compared with the constant thermal properties and thus, a smaller time period can be observed in the case of variable thermal properties. Son and Dhir [3] reported the bubble release time-period of the order of 0.1~0.15 s in their numerical simulations using water at 1 atm pressure. The simulations by Son and Dhir [3] were accomplished with the consideration of large degree of superheats, of the order of 100°C. Since in the present work, the degree of superheat is 15°C, a relatively large time period is expected. As mentioned earlier, the vapor generation is higher for the variable property simulation. This observation is well supported by Fig. 9 for heat flux through the liquid-vapor interface. The interface area (in two-dimensional this is a curved line) is used for this calculation. However, the wall heat flux (Figs. 7 and 8) for constant properties is higher then that for the variable properties. There is an apparent contradiction here. This can be explained as the following. Tables 1 and 2 reveal that specific heat (c_p) of the constant property fluid is much higher than the average specific heat of the variable property fluid. As the energy at any phase may be expressed in terms of the enthalpy (c_pT) of that phase, the temperature of the vapor at constant property is much less than that of the vapor at variable property. The higher tem-

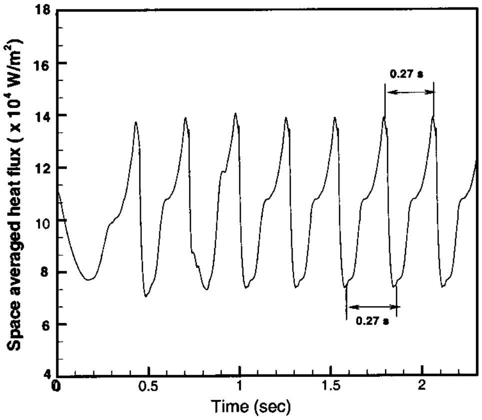

Fig. 7 Fluctuation of space averaged heat flux on the wall surface with constant fluid thermal properties

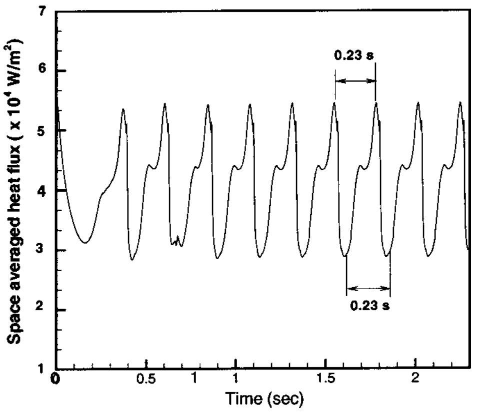

Fig. 8 Fluctuation of space averaged heat flux on the wall surface with variable fluid thermal properties

perature of the vapor (for the case of variable property) sets up a higher temperature gradient at the interface entailing higher vapor generation.

Figures 11(*a*) and (*b*) show the isotherms and interfacial shape during the bubble growth at two different time instants. Each isotherm almost follows the shape of the interface. The spacing between the isotherms is in general uniform. A deeper look into Fig. 11(*a*) reveals slightly nonuniform distribution of the isotherms in the primary bubble. In the primary bubble, the isotherms are a little closely spaced near the neck due to narrowing of the cross-sectional area and the upward motion of vapor.

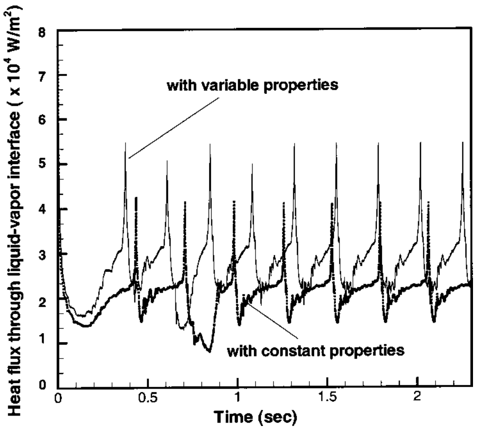

Fig. 9 Fluctuation of liquid-vapor interface heat flux with time

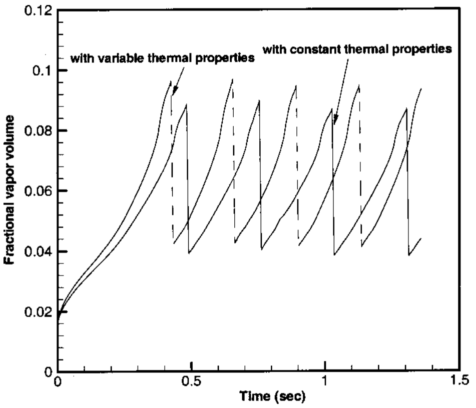

Fig. 10 Variation of fractional vapor volume with time for constant and variable thermal properties

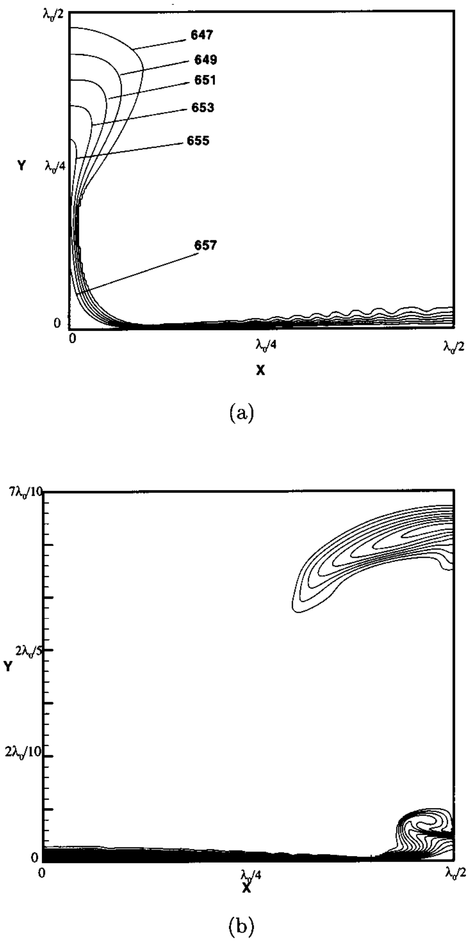

(a)

(b)

Fig. 11 Isotherms for a superheat of $\Delta\theta=15°C$ in the vapor over the computational domain at time instants 0.375 s and 0.625 s, respectively. In (*b*) contour levels are spaced at a temperature difference of 1°C for a range between 647–658°C.

Figure 12 shows the temperature contours within the vapor film on the solid surface, near the location of minimum film thickness, for the degree of superheat 15°C. The uniform spacing between the isotherms indicates that energy transfer from the wall, during film boiling, in this region, is governed primarily by conduction rather than convection. This is further corroborated by Fig. 13, which shows the variation of peak heat flux value with the reciprocal of the minimum film thickness at various time instants. The linear nature of variation indicates that heat flux is inversely proportional to vapor film thickness. In addition, the nature of variation implies the dominance of conduction as mode of heat transfer near the location of the film with minimum thickness.

Figures 14 and 15 show the velocity vectors at different arbitrary time instants, 0.375 and 0.625 s, respectively, for the case of variable thermal properties of the vapor in the computational domain. For clarity, velocity vectors are plotted at the alternative grid points. It can be seen that the upward movement of the interface is much stronger in the primary bubble region (left side symmetric boundary in Fig. 14) than in the region of secondary bubble (right side symmetric boundary in Fig. 14). Figure 15 shows the velocity vectors just after the bubble has relased from right side symmetric boundary. Furthermore, the vapor injected into the primary bubble through the thin film induces vortex motion near the

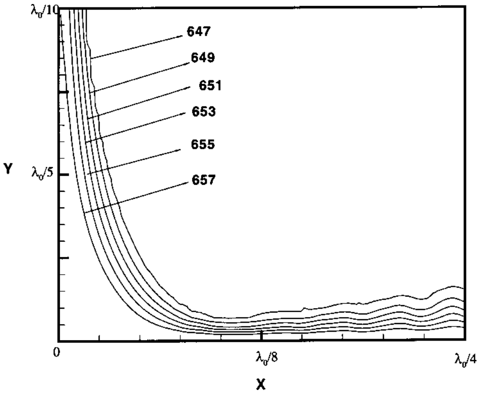

Fig. 12 Isotherms for a superheat of $\Delta\theta = 15°C$ in an enlarged region of Fig. 11(*a*) near the location of minimum film thickness

interface which can be better observed in Figs. 16 and 17. Such observations are quite similar to what have been found by Son and Dhir [3].

The most important quantitative issue of film boiling is the wall heat transfer. Although the wall temperature is constant in the present simulation, the heat flux from the wall varies over the wall surface. Figure 18 shows the distribution of wall heat flux for 15°C superheat at various time instants. We observe that the profile of the heat flux distribution at a particular instant is just reciprocal to that of the vapor film thickness at that instant. The heat flux from the surface is inversely proportional to the vapor film thickness at any wall location. Maximum heat transfer takes place at the location where the film is thinnest. Under the bubble core, very little heat transfer takes place. It is evident that the maximum and minimum heat flux corresponds to minimum and maximum vapor film thickness, respectively. We observe the magnitude of the peak heat flux to increase in passage of time. Consequently, the peak shifts to the right. The figure signifies growth of a bubble at the right symmetric plane. This can be explained in the following way. As the bubble grows, i.e., the interface in the peak region moves upward, the interface at other regions falls to conserve the vapor volume. The vapor generation is unable to offset the conservation of vapor volume by a large magnitude. Thus the film thickness is reduced over most of the wall surface except the region just underneath the bubble core. Furthermore, the location at which the film is the thinnest, moves radially inward (considering the projection of the spherical bubble is circular) on the solid surface as the interface evolves into a fully grown bubble. The radially inward movement of the thinnest layer explains the shift of the peak.

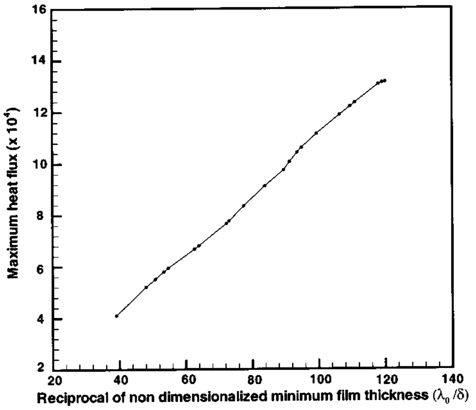

Fig. 13 Variation of peak heat flux value with the reciprocal of minimum film thickness at various time instants

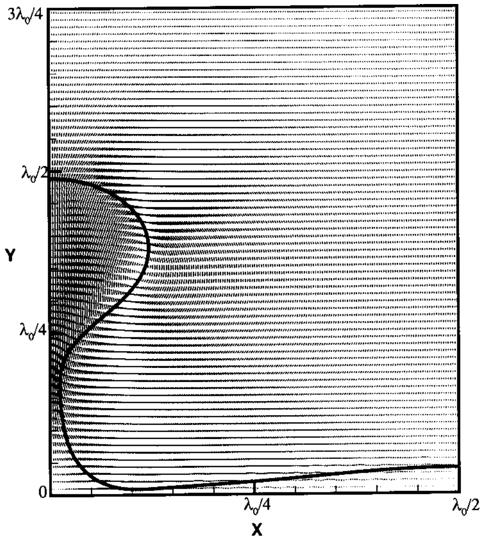

Fig. 14 Velocity vectors for a superheat of $\Delta\theta = 15°$ at time $= 0.375$ s

Further, Fig. 19 shows the same trend in spatial heat flux variations for time instants after the bubble release at the right symmetry boundary, with peak heat flux shifting near to left symmetry boundary. We observe that there is sudden decrease in peak heat flux value just after the bubble release. The space averaged Nusselt number at the solid-fluid interface can be defined as the nondimensional heat flux (or temperature gradient) at the wall in the following way:

$$\overline{\mathrm{Nu}} = \frac{2}{\lambda_o}\int_0^{\lambda_o/2} \frac{\lambda}{(\theta_w - \theta_{\mathrm{sat}})} \left.\frac{\partial\theta}{\partial y}\right|_{y=0} dx \qquad (25)$$

where λ is the characteristic length. Figures 20 and 21 show the evolution of the space averaged Nusselt number with time on the horizontal surface for constant and variable thermal properties, respectively. A cyclic temporal variation (initial transients upto three cycles being ignored) of the space averaged Nusselt number has been observed. We note that during the stage of bubble growth, the space averaged Nusselt number increases. As the interface in the peak region moves upward, the vapor film at another

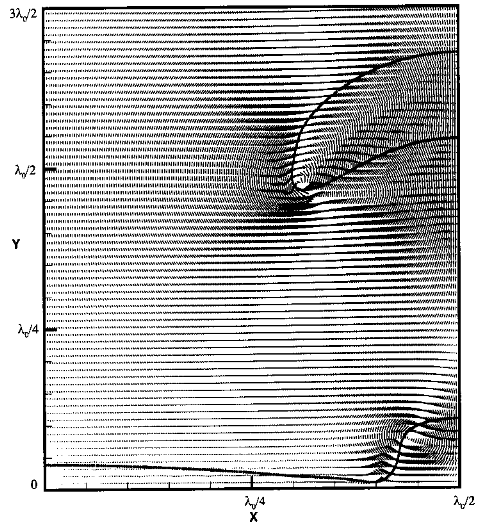

Fig. 15 Velocity vectors for a superheat of $\Delta\theta = 15°$ at time $= 0.625$ s

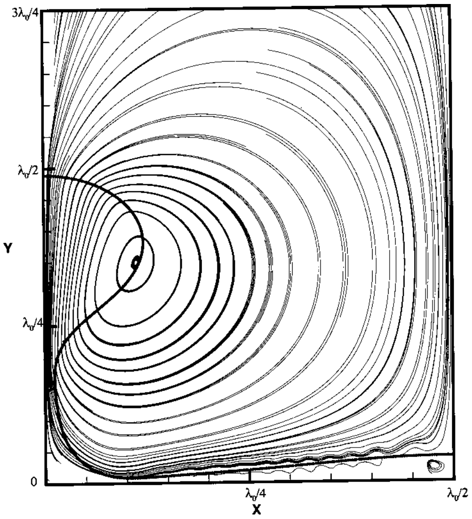

Fig. 16 Streamlines at time = 0.375 s

location of wall becomes extremely thin and thereby entails enhanced heat transfer. Just after the departure of the bubble, the heat transfer rate decreases leading to a sudden drop in Nusselt number which can be seen in the plot. This is because the surface tension, acting as a restoring force, pulls down the interface at the location of the peak, and in turn, the interface in the valley region moves upward. Thus the average film thickness over the major portion on the surface increases leading to a reduction in heat transfer. Thereafter, as the next bubble again starts growing, the Nusselt number increases and this cycle repeats.

Now we compare our time and space averaged Nusselt number values with the predictions made in earlier investigations. The correlations due to Berenson [11] depict the Nusselt numbers constant with time and are not affected by the bubble dynamics unlike the present numerical results. Berenson [11] has predicted the Nusselt number as

$$\mathrm{Nu}=0.42\left\{\frac{\mathrm{Gr}\ \mathrm{Pr}}{\beta}\right\}^{1/4} \tag{26}$$

Here Gr and Pr are the Grashof number and Prandtl number, respectively, defined by

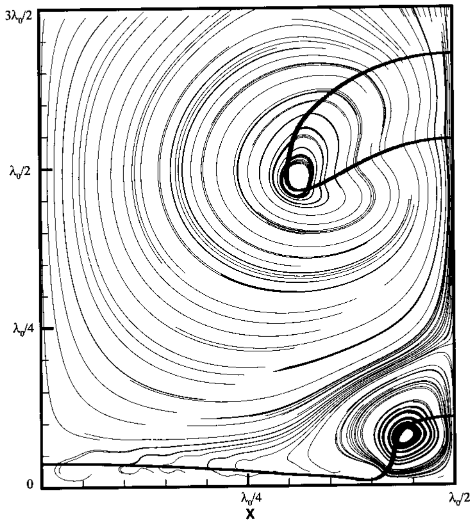

Fig. 17 Streamlines at time = 0.625 s

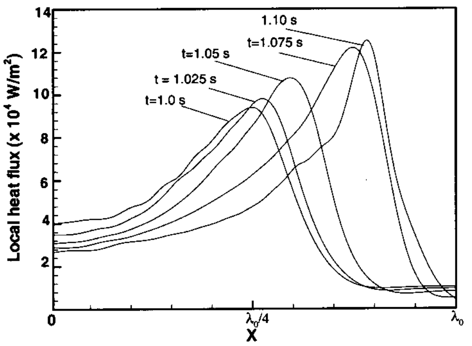

Fig. 18 Variation of heat flux on the wall surface at various time instants before bubble release on right symmetric boundary

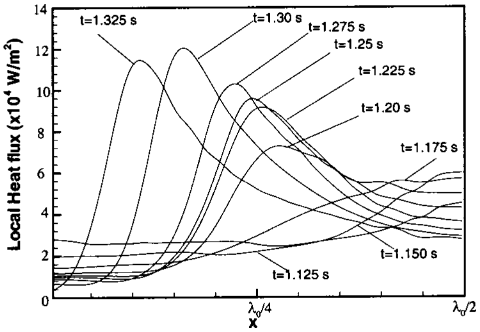

Fig. 19 Variation of heat flux on wall surface at time instants after the bubble release on right symmetric boundary

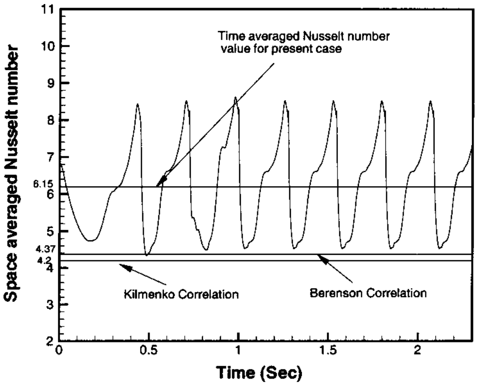

Fig. 20 Nusselt number variation with time (with constant thermal properties)

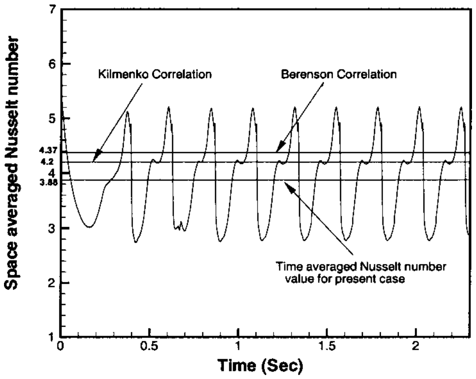

Fig. 21 Nusselt number variation with time (with variable thermal properties)

Table 4 Comparison of predicted Nusselt number with that of Berenson and Klimenko correlation for constant and variable thermal properties

Case	*Nu* (computed)	*Nu* (Berenson model)	*Nu* (Klimenko correlation)	% variation from Berenson	% variation from Klimenko
with variable thermal properties	3.88	4.37	4.20	= −11.2	= −7.6
with constant thermal properties	6.15	4.37	4.20	= +40.7	= +46.4

$$\mathrm{Gr}=\frac{\rho_g^2 g\lambda^3}{\mu_g^2}\left(\frac{\rho_l}{\rho_g}-1\right)$$

$$\mathrm{Pr}=\frac{c_{P_g}\mu_g}{k_g} \tag{27}$$

and β is the ratio of sensible heat to latent heat described as

$$\beta=\frac{c_{P_g}\Delta\theta}{h_{f_g}} \tag{28}$$

Klimenko [21] carried out a somewhat generalized analysis of film boiling on horizontal flat plates. Employing a basic formulation, similar to that Berenson [11], Kilmenko developed a correlation that included data near critical pressure similar to the present numerical study. According to his correlation, Nusselt number data for film boiling on an upward facing horizontal surface was expressed with in ±25 percent as

$$\mathrm{Nu}=1.90\times10^{-1}\mathrm{Gr}^{1/3}\mathrm{Pr}^{1/3}f_1;\quad \text{for } \mathrm{Gr}<4.03\times10^5 \tag{29}$$

$$\mathrm{Nu}=2.16\times10^{-2}\mathrm{Gr}^{1/2}\mathrm{Pr}^{1/3}f_2;\quad \text{for } \mathrm{Gr}>4.03\times10^5 \tag{30}$$

where,

$$\begin{aligned} f_1&=1;\quad \text{for } \beta>0.71\\ &=0.89\beta^{-1/3}\quad \text{for } \beta<0.71\\ f_2&=1;\quad \text{for } \beta>0.50\\ &=0.71\beta^{-1/3}\quad \text{for } \beta<0.50\end{aligned}$$

In Figs. 20 and 21 we compare the span average Nusselt numbers calculated with constant and variable thermal properties to the correlations of Berenson (Eq. (26) and Klimenko (Eq. (29) and (30)). Equation (25) implicitly calculates the Nusselt number with the characteristic length and the thermal conductivity of the vapor evaluated at the wall temperature. The correlations of Berenson and Klimenko both specify that the properties be taken at average film temperature $((T_{\mathrm{wall}}+T_{\mathrm{sat}})/2)$. The time-space average Nusselt numbers for both simulations and both correlations are listed in Table 4, from which it can be seen that there is reasonable agreement between all four values but the simulation with variable properties is closer to the correlations. If the properties in the correlations are evaluated at the wall temperature, the Nusselt numbers for Berenson and Klimenko become 4.80 and 4.36 respectively. This illustrates the shortcomings of attempts to account for the rapid variation in the fluid properties very near the critical point by evaluating them at a single temperature, whether in a correlation or a simulation. The simulation with variable properties takes proper account of their nonlinear variation and defines the Nusselt number in a rational manner. The discrepancies in the results between the values due to correlations and present analysis could also be attributed to the existence of wavelength shorter than the most dangerous wavelength as observed in the experiments of Hosler and Westwater [22]. As also noted by Son and Dhir [3], this difference could be due to the inability of a two-dimensional model to take into account the additional variations pertaining to the interface position. Such variations are expected to provide more efficient flow patterns for vapor removal and thus enhanced heat transfer.

4 Concluding Remarks

The authors have undertaken efforts to carry out investigations of pool boiling with the aim to employ numerical techniques to advance the understanding of bubble formation and the induced fluid motions and consequently their influence on the instantaneous heat transfer characteristics from the wall surface. This numerical investigation provided a nice insight into bubbly film boiling flows, yielding fascinating results. The results of this work revealed

- Successful predictions of bubble growth and heat transfer characteristics for film boiling on a horizontal surface using VOF method.
- The predictions have revealed unsteady periodic nature of bubble growth at the nodes and the anti-nodes.
- Film thickness and heat transfer coefficient are found to vary spatially and temporally during the growth of interface.
- Magnitude and location of maximum heat transfer from the wall surface are found to be dependent on the magnitude and location of minimum film thickness.
- The Nusselt numbers for film boiling (with variable thermal properties) obtained in the present work are only 11.2% and 7.6% lower than those obtained from Berenson's model and Klimeno's correlation respectively.

In the present work, the computations were performed under two-dimensional and symmetric boundary conditions using a predefined separation between regions of bubble formation. In future computations, the restrictive assumption of boundary conditions will be relaxed and a fully three-dimensional prediction must be aimed for.

Appendix

Least Squares Interface Reconstruction Algorithm (LVIRA) is a volume-of-fluid interface reconstruction algorithm for constructing an approximation to the interface at the beginning of every time cycle, given the values of the void fraction $\alpha_{i,j}$. This algorithm produces a linear approximation to the interface which are also continuous across the cell boundaries, in each two phase cell. The interface is uniquely defined by the unit normal, **n**, the orientation of the interface and the offset distance, *l*. Therefore, LVIRA can be understood as a function which returns **n**, *l*, given the void fraction of each two-phase cell.

In the LVIRA the approximate interface in a two phase cell (*i*, *j*) is determined by minimization of the following function in the 3×3 block of cells centered on the (*i*, *j*) cell

$$G_{ij}(\mathbf{n})=\sum_{k,l=-1}^{1}\{\alpha_{i+k,j+l}-\hat{\alpha}(\mathbf{n},l)_{i+k,j+l}\}^2 \tag{31}$$

subject to the constraint at the center cell of the three by three block of cells

$$\alpha_{i,j} = \hat{\alpha}(\mathbf{n}, l)_{i,j} \tag{32}$$

Here, $\alpha_{i,j}$ is the actual void fraction of the cell (i, j) and $\hat{\alpha}(\mathbf{n}, l)_{i,j}$ is the function that maps the line with orientation **n** and offset length l into a void fraction of the cell (i, j). The offset length, l, is obtained by satisfying the constraint. The function $G_{ij}(\mathbf{n})$ is the squared deviation of the actual void fraction from the void fraction given by the mapping using the same line for the entire three by three block of cells centered at cell (i, j). Minimization of this function rotates and translates the line in such a way as to ensure that the mapping is exact for the center cell and that the straight line associated with this mapping is the best fit to the void field for the neighboring cells. The result of the minimization is the calculation of the unit normal and the offset length $(\mathbf{n}, l)$ for the cell at the center of the three by three block. This calculation is performed for all the mixture cells, satisfying the constraints that the mapping $\hat{\alpha}(\mathbf{n}, l)_{i,j}$ returns the actual void fraction. This constrained minimization of the function $G_{ij}(\mathbf{n})$ is a nonlinear problem requiring an initial estimate for **n**. This initial **n** is the value determined by the modified VOF method of Youngs [12] as

$$\mathbf{n} = \frac{\nabla \alpha}{|\nabla \alpha|} \tag{33}$$

We note that this algorithm is second-order method and has the property that it reproduces linear interfaces exactly.

Acknowledgment

The authors are deeply indebted to Prof. David B. R. Kenning of Oxford University for numerous constructive suggestions.

Nomenclature

c_p, c_v = specific heat at constant pressure/volume
Gr = Grashop number
g = gravitational acceleration
H = height of computational domain
h_{lg} = latent heat of vaporization
k = thermal conductivity
l = normal distance from cell center to phase interface
$\overline{N_u}$ = space averaged Nusselt number
n = interface normal vector, pointing into liquid phase
P_o = saturation pressure in excess of hydrostatic pressure
Pr = Prandtl number
p = total pressure
q = heat flux vector
S_c = computational cell boundary surface
S_I = phase interface surface
t = time
u = x component of velocity
U_i, U_j = velocity vectors
V = volume
V_c = cell volume
v = y component of velocity
v = fluid velocity
x = spatial coordinate in the horizontal direction
x_i, x_j = space vectors
y = spatial coordinate in the vertical direction

Greek

α = cell void fraction
$\tilde{\alpha}$ = smoothed void fraction
β = Jakob number
δ = initial film interfacial height from solid wall
δt = time increment
κ = curvature
λ = characteristic length
λ_0 = Taylor fastest growing wavelength
μ = dynamic viscosity
ρ = density
∇ = gradient operator
$\| \|$ = jump symbol
σ = surface tension
θ = temperature
$\Delta\theta$ = wall superheat

Subscripts

I = interface
l = liquid phase
sat = saturation condition
sup = superheated
g = vapor phase

Subscripts

n = values at old time step
$n+1$ = values at new time step

References

[1] Hirt, C. W., and Nichols, B. D., 1981, "Volume of Fluid (VOF) Method For the Dynamics of Free Boundaries," J. Comput. Phys., **39**, pp. 201–225.
[2] Welch, S. W. J., and Wilson, J., 2000, "A Volume of Fluid Bases Method for Fluid Flows with Phase Change," J. Comput. Phys., **160**, pp. 662–682.
[3] Son, G., and Dhir, V. K., 1997, "Numerical Simulation of Saturated Film Boiling on a Horizontal Surface," ASME J. Heat Transfer, **119**, pp. 535–533.
[4] Son, G., and Dhir, V. K., 1998, "Numerical Simulation of Film Boiling Near Critical Pressures With a Level Set Method," ASME J. Heat Transfer, **120**, pp. 183–192.
[5] Sussman, M., Smereka, P., and Osher, S., 1994, "A Level Set Approach for Computing Solutions to Incompressible Two-Phase Flow," J. Comput. Phys., **114**, pp. 146–159.
[6] Juric, D., and Tryggvason, G., 1998, "Computation of Boiling Flows," Int. J. Multiphase Flow, **24**, pp. 387–410.
[7] Unverdi, S. O., and Tryggvason, G., 1992, "A Front-Tracking Method for Viscous, Incompressible, Multi-Fluid Flows," J. Comput. Phys., **100**, pp. 25–37.
[8] Banerjee, D., and Dhir, V. K., 2001, "Study of Subcooled Film Boiling on a Horizontal Disk: Part I-Analysis," ASME J. Heat Transfer, **123**, pp. 271–284.
[9] Dhir, V. K., 2001, "Numerical Simulations of Pool-Boiling Heat Transfer," AIChE J., **47**, pp. 813–834.
[10] Welch, S. W. J., and Rachidi, T., 2002, "Numerical Computation of Film Boiling Including Conjugate Heat Transfer," Numer. Heat Transfer, Part B, **42**, pp. 35–53.
[11] Berenson, P. J., 1961, "Film-Boiling Heat Transfer from a Horizontal Surface," ASME J. Heat Transfer, **83**, pp. 351–358.
[12] Youngs, D. L., 1982, "Time-Dependent Multi-Material Flow With Large Fluid Distortion," *Numerical Methods for Fluid Dynamics*, K. W. Morton and M. J. Baines, eds., Academic Press, New York, pp. 273–285.
[13] Rudman, M., 1997, "Volume-Tracking Methods for Interfacial Flow Calculations," Int. J. Numer. Methods Fluids, **24**, pp. 671–691.
[14] Rider, W. J., and Kothe, D. B., 1998, "Reconstructing Volume Tracking," J. Comput. Phys., **141**, pp. 112–152.
[15] Puckett, E. G., Almgren, A. S., Bell, J. B., Marcus, D. L., and Rider, W. J., 1997, "High-Order Projection Method for Tracking Fluid Interface in Variable Density Incompressible Flows," J. Comput. Phys., **130**, pp. 269–282.
[16] Brackbill, J. U., Kothe, D. B., and Zemach, C., 1992, "A Continuum Method for Modeling Surface Tension," J. Comput. Phys., **100**, pp. 335–354.
[17] Harlow, F. H., and Welch, J. E., 1965, "Numerical Calculation of Time-Dependent Viscous Incompressible Flow of Fluid with Free Surface," Phys. Fluids, **8**, pp. 2182–2189.
[18] Chang, Y. C., Hou, T. Y., Merriman, B., and Osher, S., 1996, "A Level Set Formulation of Eulerian Interface Capturing Methods for Incompressible Fluid Flows," J. Comput. Phys., **124**, pp. 449–464.
[19] Leonard, B. P., 1979, "A Stable and Accurate Convective Modelling Procedure Based on Quadratic Upstream Interpolation," Comput. Methods Appl. Mech. Eng., **57**, pp. 415–438.
[20] Van der Vorst, H. A., 1992, "Bi-CGSTAB: A Fast and Smoothly Converging Variant of Bi-CG for Solution of Non-Symmetric Linear Systems," SIAM J. Sci. Stat. Comput., **12**, pp. 631–644.
[21] Klimenko, V., 1981, "Film Boiling on a Horizontal Plate-New Correlation," ASME J. Heat Transfer, **24**, pp. 69–79.
[22] Hosler, E. R., and Westwater, J. W., 1962, "Film Boiling on a Horizontal Plate," ARS J., **32**, pp. 553–560.

Hysteresis in Liquid Crystal Thermography

M. R. Anderson
e-mail: mike.anderson@ps.ge.com
GE Optimization Services,
1631 Bently Parkway South,
Minden NV 89423

J. W. Baughn
e-mail: jwbaughn@ucdavis.edu
Professor,
Fellow ASME,
Department of Mechanical and Aeronautical Engineering,
University of California, Davis,
One Shields Avenue,
Davis CA 95616

Hysteresis in five different Thermochromic Liquid Crystals (TLCs), both narrow-band and broad-band, has been investigated. All were found to exhibit a similar hysteresis behavior during cooling relative to heating. This hysteresis is characterized by a decrease in reflectivity and a shift in the temperature associated with the peak reflected intensity for each of the R, G, and B components during cooling. This causes a shift in the hue-temperature calibration of the TLC causing temperature biases, when cooled rather than heated, of 20–60% of the useful calibration range. The hysteresis effect increases as the peak temperature during a heating and cooling cycle is increased. Repeatable heating calibrations were obtained when the TLC was cooled below the red start temperature to an apparent low reset temperature. Somewhat repeatable cooling calibrations, different from the heating calibrations, were obtained when the TLC was heated somewhat above the blue stop temperature. A possible explanation of the hysteresis based on the texture of the liquid crystal helices is provided. In addition to hysteresis, a permanent decrease in reflectivity and a shift in the temperature associated with the peak reflected intensity was observed when the TLCs were exposed to extended higher temperatures (60°C–80°C). [DOI: 10.1115/1.1738425]

Keywords: Experimental, Instrumentation, Measurement Techniques, Temperature, Visualization

Background

Early uses of Thermochromic Liquid Crystals (TLCs) to measure temperature used a single color (usually yellow) to produce a single isotherm. [1] and [2] provide an overview of early liquid crystal characteristics and of their use in heat transfer testing. Early applications include those of [3] and [4]. [5] provides a review of five different methods of determining heat transfer coefficients using a narrow-band TLC.

More recently, a range of temperatures have been measured with TLCs by relating the color or hue to temperature. [6] were among the first to obtain R, G, and B information from a single image, which was converted into hue. After calibration, the hue field produces the surface temperature distribution (thermography). [7] also used a hue-capturing technique. The peak intensity has been related to a particular temperature (e.g., [8,9])

Several different representations for hue have been proposed [10]. [11] suggested the following representation, used throughout the present work.

$$\text{Hue}=\arctan\left[\frac{\sqrt{3}(G-B)}{2R-G-B}\right] \tag{1}$$

[11] reports uncertainties of about 7 percent of the useful range. [12] showed that median filtering can reduce the uncertainties significantly (for example, to about 3.7 percent with a 5×5 median filter). [11] suggest that the response of a Chiral Nematic Liquid Crystal (CNLC) may be affected by temperature gradient. [13] explain this affect of the temperature gradient.

There are a number of overviews of the liquid crystalline state (e.g., [14,1,15,2,11,16]). Calamitic liquid crystals are used in the TLCs provided by Hallcrest Inc. and used in all of the results presented here. In the solid state, these liquid crystals are organized like any other crystalline solid. Upon melting, the molecules go into the smectic state, which has a high degree of both orientational and positional order. Upon further heating the liquid crystal passes into the nematic state in which positional order is lost and orientational order is maintained. The chiral nematic (CNLC) state (also referred to as the cholesteric liquid crystal (CLC) state) is made up of thin layers of nematic arrangements stacked on top of each other. Upon further heating the liquid crystal substance passes through the clearing point at which all orientational and positional order is lost and an isotropic liquid is obtained. Typical peak reflected wavelength for TLCs are shown in Fig. 1.

TLCs can be thought of as sheets of molecules laying flat on top of each other with a relative displacement from one sheet to the next. The pitch determines the wavelength of light that is reflected. Theoretically, the wavelength equal to half the pitch is reflected, while all other wavelengths are transmitted through the liquid crystal. As the TLC changes temperature the pitch length changes.

These helical structures can be aligned in several different orientations (or textures) relative to the surface. The two most common textures are focal-conic, in which the centerlines of the helices are aligned parallel to the surface, and planar (or grandjean), in which the centerlines of the helices are aligned perpendicular to the surface, and, therefore, parallel to normal incident light. The focal-conic texture does not possess the combination of optical properties necessary to reflect incident light iridescently [15]. The planar texture tends to form when the liquid crystal is cooled from the isotropic state [2].

To reduce irreversible damage from solvents and UV radiation TLCs are commonly microencapsulated (i.e., the TLC material is encased in a polymer coating, forming spheres). [2] states that when encapsulated, the capsule walls tend to align the structures into the planar texture although patches of focal-conic texture may be present within the capsule; this addition of focal-conic results in a decrease in reflectivity.

TLCs operate at temperatures ranging from −30°C to 150°C and have bandwidths (red start to blue start) which range from 1°C to 50°C. Liquid crystals with bandwidths below 5°C are termed narrow band liquid crystals and those with bandwidths of 5°C or more are termed broadband liquid crystals. The nomenclature used by Hallcrest Inc. is used here to specify the temperature and bandwidth (R24C10W refers to a liquid crystal with a red start of 24°C and a bandwidth of 10°C).

Contributed by the Heat Transfer Division for publication in the JOURNAL OF HEAT TRANSFER. Manuscript received by the Heat Transfer Division July 23, 2001; revision received February 23, 2004. Associate Editor: D. B. R. Kenning.

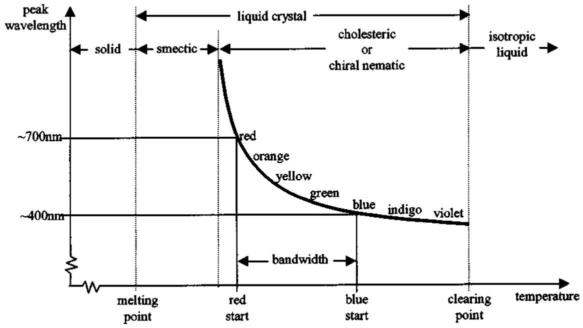

Fig. 1 Typical reflected peak wavelength (color) and molecular state as a function of temperature for a thermochromic liquid crystal substance

Hysteresis. TLCs have often been described as reversible and repeatable ([3,17,18,7,10,19,15] and [16]). [14] suggests liquid crystals are repeatable, and provides graphical data showing that the reflected intensity of a cholesteric liquid crystal decreases when cooled rather than heated, although it is suggested that the reflected color remains unchanged. In general, hysteresis in cholesteric liquid crystals is considered to be rare ([20] and [21]).

Nevertheless, some researchers have described the presence of a hysteresis in cholesteric liquid crystals. [22–24] witnessed a hysteresis in cholesteric liquid crystals used in electro-optical devices. [25] show a hysteresis in the temperature at which phase transitions occur for high-purity cholesteryl oleyl carbonate. [26] examined the thermal hysteresis of a number of liquid crystal mixtures. They measured the reflected intensity as a function of temperature during both heating and cooling (at a rate of up to 10°C/minute) through seven band-pass optical filters. They found many of the mixtures tested exhibited a shift in the temperature at a particular wavelength, which was a strong function of chemical composition. They also found that the magnitude of the hysteresis depended on the relation between the operating range (the start and stop temperatures surrounding a particular measurement) and on the melting point of the mixture. [27] investigated hysteresis in planar layers of cholesteric liquid crystals experimentally, and theoretically, based on the continuum theory of elasticity. They looked at the temperature at which pitch jumps occur, in heating and cooling. They found that the hysteresis depends strongly on the specimen thickness and is a direct consequence of the strong anchoring interaction at the boundaries of the layers. The thicker specimen showed no hysteresis and the thinner specimen showed up to about a 0.5°C bias toward lower temperatures when cooled rather than heated (the CLC used had about a 4°C color play range).

Some researchers have indicated that the rate at which a liquid crystal is heated or cooled may have an effect on its optical properties. [18] using cholesteryl oleyl carbonate (COC) in the development of a fiber-optic temperature sensor showed that the peak reflected intensity decreased as heating rate increased and that the temperature at which the peak occurred increased as the heating rate increased over the range 0.2–1.3°C/min.

The present work is directed toward a study of hysteresis in TLCs, for which there are minimal reports. [28] observed a systematic difference between their heating and cooling TLC calibrations, but attributed this hysteresis to a lack of equilibrium in their apparatus. [29] reports hysteresis in a 25°C start temperature 5°C bandwidth TLC. They found that when cooled rather than heated the reflected hue shifted to lower temperatures and the magnitude of the shift increased as the temperature prior to cooling increased. They measured up to a 0.2°C shift when cooled from 41°C. They advised caution since their uncertainty bounds were on the order of the hysteresis shift.

The present hysteresis investigation was initiated after [30], working with Professor Jones at Oxford University, noticed a hue shift towards lower temperatures and a reduction in saturation and intensity when cooled rather than heated. They felt this was significant and was worthy of future investigation.

A preliminary investigation into the nature of hysteresis for a single TLC was previously carried out by the authors [12]. That investigation, of a microencapsulated R24C10W TLC, showed the existence of a hysteresis when cooled from above the useful colorplay range rather than heated from below the red start temperature. Hysteresis was characterized by a decrease in the TLC reflectivity, (with a decrease in the R, G, and B components captured using an RGB CCD camera), and a shift in the temperature at which the peak R, G and B values occurred. These two effects combine to result in a shift in hue toward lower temperatures when cooled rather than heated. The magnitude of the hysteresis effect increased as the peak temperature prior to cooling increased and resulted in a temperature bias of as much as 1.2°C (or 25 percent of the 5°C useful calibration range). Resetting the TLC below the red start temperature produced repeatable heating calibration results. Resetting the TLC above the useful color play produced repeatable cooling calibration results, although the cooling calibration was different from the heating calibration.

The present investigation tests 4 additional microencapsulated TLCs with 1°C, 5°C, and 10°C bandwidths.

Experimental Setup and Procedure

For these measurements, a 2 cm thick copper calibration block was used to provide a uniform temperature during both heating and cooling. It was airbrushed with a thin coat of Hallcrest BG-1 black paint and then with the microencapsulated TLCs in four different areas of the block. A 10°C wide TLC (R3010W), a 5°C wide TLC (R35C5W), and two 1°C wide TLCs (R35C1W and R50C1W) were used. A piece of gray cardboard was placed on the block within the image area to provide a light intensity reference both during and between runs. The copper block was placed on a coil heater. A black drape was placed over the camera (mounted over and above the block) to minimize room light and reflected light. A single two-foot long T-12 (20W) GE cool white fluorescent light was used as the illumination source. It was located 32 cm from the centerline of the plate and offset by about 45° from the plate normal. A Spectrum EB-74 UV shield was used on the fluorescent bulb to minimize UV radiation. The calibration block temperature was measured using an embedded thermistor. A Sony XC-003 3-chip RGB CCD camera and a Matrox Meteor RGB image acquisition board were used to capture the RGB images, which were saved in TIFF format as 8-bit integer data (scale 0–255) with a resolution of 640×480×3. After focusing the camera, the iris was set to allow maximum luminescence while avoiding saturation. The iris setting was shown to have no effect on the relative magnitude of the R, G, and B, components (since the camera gamma correction was turned off) and therefore no effect on hue [31].

For heating calibrations, the calibration block was brought to a temperature below the liquid crystal color play start temperature. The heater was then adjusted to provide a slow uniform heating rate. The heating rate depended on the bandwidth of the liquid crystal being tested. For the 10°C, 5°C, and 1°C bandwidth liquid crystals, the heating rates did not exceed 0.3°C, 0.2°C, and 0.15°C per minute, respectively. This resulted in temperature variations between the liquid crystal analysis area and the thermistor of less than the 0.01°C and 0.005°C for the 10°C and 1°C bandwidth liquid crystals, respectively [31].

For cooling calibrations, the calibration block was heated to a particular temperature, generally above the liquid crystal color play range, and then cooled throughout the color play using compressed air on the underside of the calibration block. Cooling rate limits were the same as those used in heating.

The image data was processed using MATLAB. MATLABs

RGB2HSV function was used to transform the R, G, and B matrices to a hue matrix. This calculation uses the following algorithm to calculate hue.

$$\begin{aligned} &\text{if } \mathrm{R}>\mathrm{G} \quad \text{and } \mathrm{R}>\mathrm{B} \quad H=\frac{\mathrm{G}-\mathrm{B}}{6(\mathrm{R}-\min(\mathrm{RGB}))} \\ &\text{else} \quad \text{if } \mathrm{G}>\mathrm{B} \quad H=\frac{2+\mathrm{B}-\mathrm{R}}{6(\mathrm{G}-\min(\mathrm{RGB}))} \\ &\text{else} \quad H=\frac{4+\mathrm{R}-\mathrm{G}}{6(\mathrm{B}-\min(\mathrm{RGB}))} \end{aligned} \tag{2}$$

R, G, and B are unsigned 8-bit integers that range from 0 to 255. The resulting hue values range from 0 to 1. This algorithm is equivalent to Eq. (1) but is numerically more efficient since it involves no trigonometric or square root functions. A comparison between the two methods was performed showing a maximum difference in hue of about 0.003, which is negligible compared to our hue standard deviations in TLC images of about 0.01–0.1 [31].

Average values of R, G, B, and hue were obtained from unfiltered data within 10×100-pixel analysis areas. These areas were chosen near the center of each of the areas where the TLC application was highly uniform. Furthermore, these areas were chosen parallel to the light source to minimize variations in luminance from the surface due to varying distances to the light source and to minimize any variations in hue due to illumination angle effects.

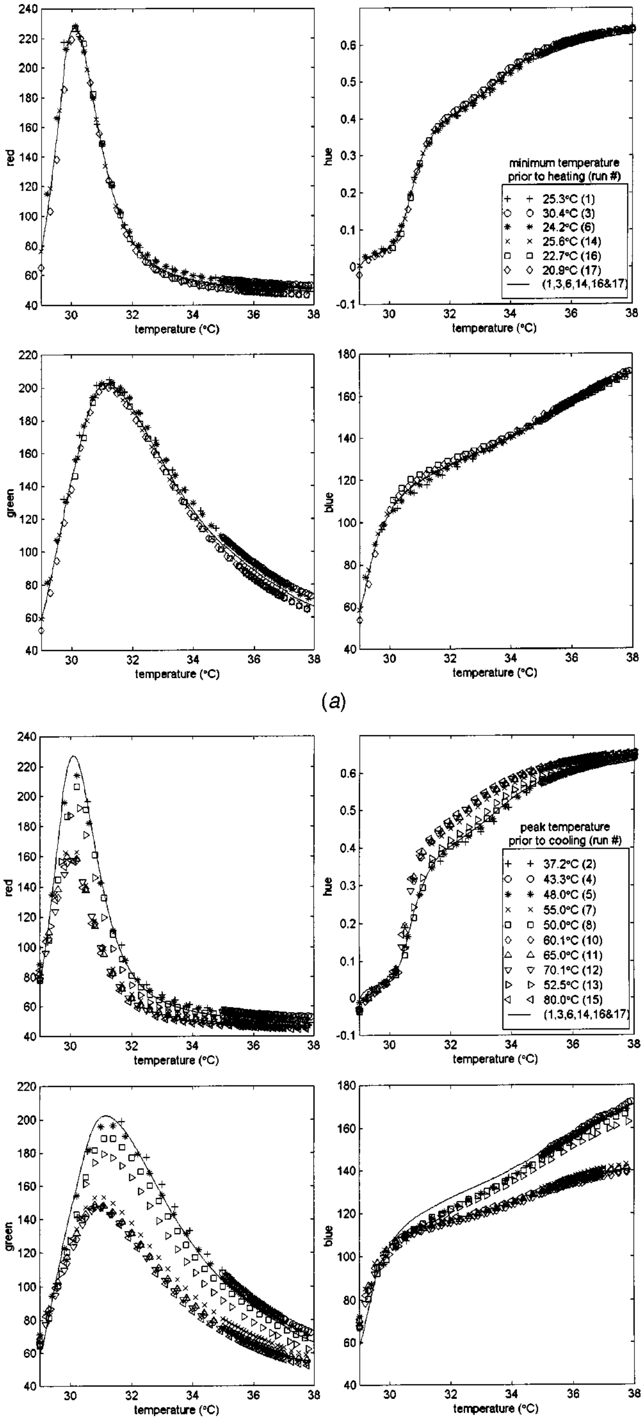

(*a*)

(*b*)

Fig. 2 (*a*) RGB and Hue for R30C10W—Heating; and (*b*) RGB and Hue for R30C10W—Cooling

Experimental Results

Seventeen tests were performed over the course of ten days consisting of seven heating runs and ten cooling runs. Low temperature heating and cooling tests were performed first, and testing progressed to higher temperatures. Low temperature heating and cooling tests were interspersed within the high temperature testing to determine whether or not permanent damage due to excessive heating was taking place.

R, G, B, and hue heating data for the 10°C wide (R30C10W) TLC are shown in Fig. 2(*a*). The temperature prior to heating and the run number are shown in the legend. This data was taken over the course of nine days and is fairly repeatable. There appears to be a slight shift in the data between runs 6 and 14, seen as a slight decrease in the red and green data and a very slight increase in the blue and hue data. Runs 6 and 14 were separated by about five days and the maximum temperature attained by the liquid crystal prior to run 6 was 48°C, whereas, the maximum temperature prior to run 14 was 70°C. Variations due to time or excessive heating may be contributors to this shift. [26] also witnessed a shift in liquid crystal characteristics, which they attributed to high temperature exposure. A single fit curve for each set of heating data is superimposed on each plot.

Cooling data for the same liquid crystal is shown in Fig. 2(*b*) along with the fit curves from the heating data. Note the decrease in R, G, and B values when cooled rather than heated. The magnitude of this decrease is a function of peak temperature prior to cooling; the higher the temperature the greater the decrease. Runs 2, 4, and 5, which represent cooling runs from 37.2°C, 43.3°C, and 48.0°C, respectively, show very little deviation from the heating data. Run 8, which represents cooling from 50°C shows a noticeable decrease in red and green components although the hue data agrees very well with the heating data. Runs 13 and 7, which represent cooling from 52.5°C and 55.0°C, respectively, show progressively larger decreases in red, green and blue components, a shift in the temperature at which the peak R and G occur and a significant shift in hue. Runs 10, 11, 12, and 15 which represent cooling from between 60°C and 80°C also show a significant decrease in red, green and blue components, a shift in R and G peak temperature and a significant shift in hue. These runs, which represent a very wide range of cooling start temperatures, show very good agreement with one another indicating that if cooling begins well above the color play temperature, a repeatable cooling calibration curve can be obtained with uncertainty comparable to that of a heating calibration. The decrease in value is due to a decrease in reflectivity of the TLC, and relative to the background values of about 40 to 50, this corresponds to about a 30 percent reduction in reflectivity when cooled from 80°C rather than heated. The hysteresis results in a maximum offset in the hue-temperature calibration of about 1.2°C corresponding to 20 per-

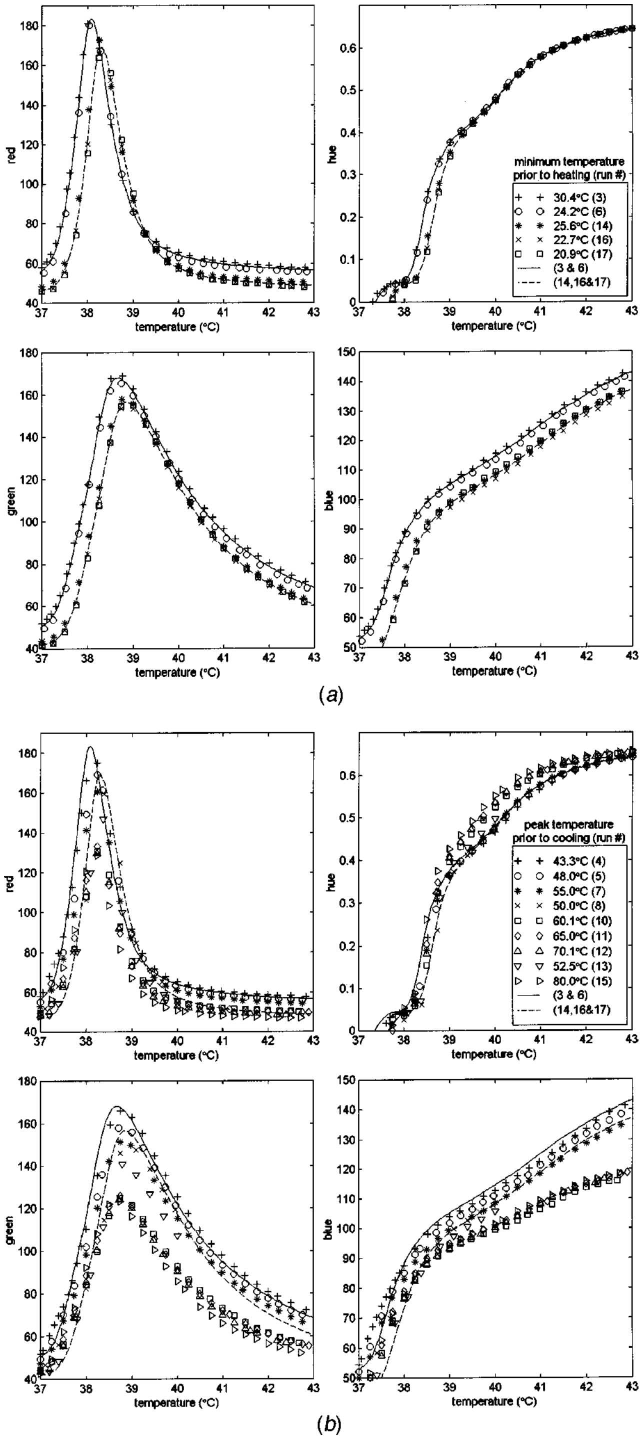

(*a*)

(*b*)

Fig. 3 (*a*) RGB and Hue for R35C5W—Heating; and (*b*) RGB and Hue for R35C5W—Cooling

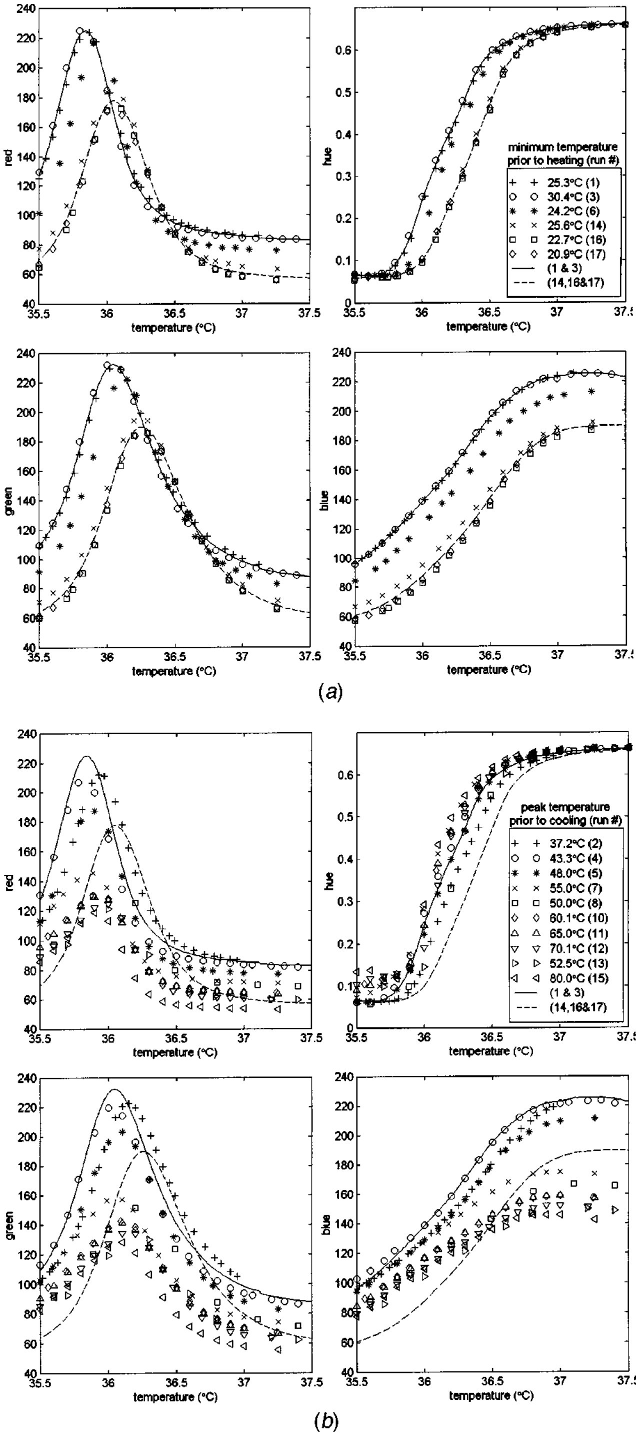

(*a*)

(*b*)

Fig. 4 (*a*) RGB and Hue for R35C1W TLC—Heating; (*b*) RGB and Hue for R35C1W TLC—Cooling

cent of the 6°C useful range from 30°C to 36°C. Even considering the permanent shift between runs 6 and 14, the presence of a hysteresis is unmistakable. This bias is significant compared to uncertainties in TLC thermography, which can be lower than 4 percent of the measurement range [12].

Note that if there were no shift in peak temperature and the red, green, and blue values decreased by either the same amount or by the same percentage at each temperature, then the hue-temperature calibrations would be unaffected (see Eq. (2)).

Heating data for a 5°C wide (R35C5W) TLC is shown in Fig. 3(*a*). The apparent shift in calibration data between runs 6 and 14 is more pronounced here than it was for the 10°C wide R30C10W. Two separate fits are shown for these data, one applied to runs 3 and 6 and one to runs 14, 16, and 17. For each of these two sets, the data are repeatable.

Cooling data for the R35C5W liquid crystal, with the two heating regression curves superimposed, are shown in Fig. 3(*b*). Once again, the higher the peak temperature prior to cooling, the greater the decrease in the R, G, and B components and the greater the shift in hue. Although this hysteresis effect is superimposed on a permanent shift, likely due to the high temperature exposure, useful information can still be extracted. Heating runs 3 and 6, from

Table 1 Reduction in peak R and G values due to hysteresis

TLC	maximum decrease
R24C10W	50%
R30C10W	33%
R35C5W	25%
R35C1W	50%
R50C1W	33%

which one of the regression curves was generated, showed very high repeatability and therefore data between these runs did not experience a permanent shift. Cooling runs 4 and 5, therefore, can be compared directly to this regression. These two cooling runs from 43.3°C and 48°C show a progressive decrease in red, green, and blue values and a very slight shift (not measurable over much of the region) in the hue-temperature calibration. This small shift is in the opposite direction of the hysteresis effects observed in earlier runs. Cooling runs 7 and 8, from 55°C and 50°C each show a similar hysteresis effect. The maximum temperature attained prior to these runs was 55°C. One would expect cooling run 13 from 52.5°C to fall between runs 7 and 8. Data from this run, however, shows significantly lower R, G, and B values. The maximum temperature attained by the block prior to this run was 70°C, which is a likely explanation for this discrepancy. Cooling runs 10, 11, and 12, which represent cooling runs from 60.1°C, 65°C, and 70.1°C respectively, show a large hysteresis effect, and like the R30C10W TLC, show high repeatability. Run 15, which is a cooling run from 80°C shows a slight shift from the other three high temperature cooling runs in red, green, and hue. The peak temperature attained by the block prior to run 15 was 80°C, whereas the peak temperature prior to the other three high temperature runs was 60°C–70°C. The TLC likely incurred additional permanent damage between 70°C and 80°C. The hysteresis for this TLC leads to a maximum offset in the hue-temperature calibration of about 0.6°C corresponding to about 20 percent of the 3°C useful range between 38°C and 41°C.

The two narrow-band TLCs tested (R35C1W and R50C1W) exhibit similar phenomena to that of the broadband TLCs. Heating data for the R35C1W is shown in Fig. 4(*a*) (for the R50C1W see [31]). These narrow-band TLCs showed more pronounced exposure damage than the 10°C and 5°C TLC. There is a greater decrease in red green and blue values as well as a greater temperature shift relative to the useful range. Two heating calibration curves were generated for each of these liquid crystals one for the earlier runs and one for later runs.

Cooling data for the R35C1W is shown in Fig. 4(*b*) and shows the same basic hysteresis trend seen in the broad-band liquid crystals, although it is somewhat harder to distinguish due to the increase in damage effect over that of the broad-band liquid crystals. Data for both liquid crystals show a significant decrease in R, G, and B values as the peak temperature prior to cooling increases. Unlike the broad-band crystals, these data are not grouped as tightly when cooled from higher temperatures (i.e., when cooled from below 80°C, a calibration curve is not as repeatable as one done in heating). Comparing the high temperature cooling hue data to the heating hue data from runs 14, 16, and 17 it is seen that the hysteresis can lead to significant temperature biases. For the 35°C liquid crystal, hysteresis results in a bias up to 0.3°C, which corresponds to 33 percent of the 0.9°C useful temperature range between 35.9°C and 36.8°C. For the 50°C liquid crystal, hysteresis can lead to about a 0.4°C bias corresponding to about 36 percent of the 1.1°C useful range between 49.9°C and 51.0°C. In percent of useful range, the hysteresis bias encountered in the narrow-band liquid crystals tested is significantly higher than that encountered in the broad-band liquid crystals tested.

The reference gray exhibited red, green, and blue variations generally less than 5 out of 150 and variations were proportional for the R, G, and B components indicating no significant change in the spectral characteristics of the illumination source or the imaging system. The variations did not indicate a dependence on heating/cooling direction.

Summary of Hysteresis Results. Each of the five TLCs investigated (the three presented here, the R50C1W in [31] and the R24C10W in [12]), tend to exhibit many of the same features, including a hysteresis when cooled from above their colorplay range rather than heated from below their colorplay start temperature. The R, G, and B values, or reflectivity, of each of the TLCs tend to decrease when cooled from above their color play range rather than heated from below their colorplay start temperature. Furthermore, the values decrease as the peak temperature prior to cooling increases. Table 1 shows the maximum percent reduction in peak R and G values relative to the background values.

These values were calculated from:

$$\text{maximum decrease} = \frac{\text{Rpeak}_{\text{heating}} - \text{Rpeak}_{\text{max cooling}}}{\text{Rpeak}_{\text{heating}} - \text{Rbackground}_{\text{heating}}} \times 100\% \qquad (3)$$

The exposure damage was taken into account and the peak and background values were chosen from runs that appeared to have no increase in exposure damage relative to one another. The decrease in R and G does not seem to be related to the bandwidth of the TLC. The blue component seems to have a comparable decrease, although in many of the runs the peak was outside of the measured temperature range.

This decrease alone is not enough to cause a shift in hue (if the R, G, and B values all decreased by the same amount or by the same percentage of the full scale then hue would not be affected). The hysteresis encountered in this testing resulted in a nonconstant, nonproportional decrease in R, G, and B values (the peaks occur at different temperatures) producing a shift in hue.

In addition to the decrease in R, G, and B values when cooled rather than heated, the R, G, and B curves, and, therefore, the hue curve, go through a displacement in temperature when cooled from different temperatures. The temperature at which the peak R and G occur tends to increase when cooled from just above the top of the useful range and then tends to decrease as the maximum temperature prior to cooling increases. The magnitude of this shift for the various TLCs tested is summarized in Table 2. This table shows the maximum increase and decrease in temperatures that

Table 2 Shift in temperature at which peak R and G values occur due to hysteresis

		Maximum increase			maximum decrease		
TLC	useful calibration range (°C)	temperature shift (°C)	Percent of useful range	cooling start temperature (°C)	temperature shift (°C)	percent of useful range	cooling start temperature (°C)
R24C10W	5	0.3	6%	45	−0.3	−6%	55
R30C10W	6	0.2	3%	50	−0.2	−3%	55
R35C5W	3				−0.2	−7%	52
R35C1W	0.9	0.1	11%	37	−0.15	−17%	80
R50C1W	1.1	−0.05	−5%	55	−0.3	−27%	80

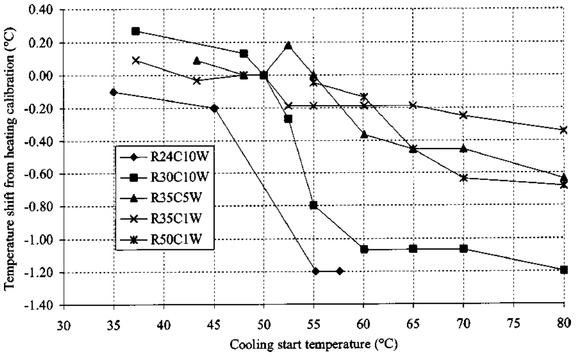

Fig. 5 Temperature shift (or bias) due to hysteresis as a function of cooling start temperature for 5 TLCs (measured at a hue value between 0.4 and 0.5)

the green peak exhibited due to hysteresis (the shift in red peak was comparable). The increases and decreases were taken between heating and cooling runs with the same exposure damage. The shift as a percentage of the calibration range, along with the associated temperature from which cooling started is shown.

Both the nonuniform decrease in R, G, and B components and the shift in temperature, illustrated by the peak R and G shift, contribute significantly to the hysteresis. The temperature shift (or bias) due to hysteresis for the five TLCs investigated is shown in Fig. 5. This graph represents the temperature bias at a hue near 0.4 (which is near the center of the temperature range for each TLC) as a function of maximum temperature prior to cooling. The permanent damage shift, which appears to be related to the prior temperature history of the TLC, was taken into consideration when determining the bias. Temperature biases for each cooling run were determined relative to a heating run with a comparable damage history. As previously discussed, the bias increases as the peak temperature prior to cooling increases. For each of the TLCs tested the bias tends to level off at higher start temperatures and the liquid crystal seems to reset resulting in repeatable cooling calibrations. A summary of the maximum bias exhibited by each TLCs is provided in Table 3.

The temperature prior to cooling at which the reset occurs is particularly important to those employing cooling transient techniques who want to calibrate and test in cooling, and obtain repeatable data with no bias. The hysteresis effect tended to level off at about 0°C to 5°C above the blue stop temperature [31]. The blue stop temperature is difficult to determine with the naked eye and the blue value from the imaging system is needed to determine this temperature. It was approximately 20°C above the top of the useful range for each of the TLCs tested here.

Discussion

These results have shown that there is a definite hysteresis in the calibrations performed using five microencapsulated thermochromic liquid crystals. Two separate hysteresis phenomena have been observed: (1) a decrease in luminance from a TLC coated surface, and (2) a shift in temperature at which the peak R and G occur. The obvious conclusion is that the crystalline structure of the liquid crystal behaves differently depending on whether it has been heated or cooled and also on the maximum temperature prior to cooling. Before making this conclusion, several other possibilities are considered.

Table 3 Maximum temperature bias near middle of hue range

TLC	useful calibration range (°C)	maximum bias (°C)	percent of useful range
R24C10W	5	−1.2	−24%
R30C10W	6	−1.2	−20%
R35C5W	3	−0.6	−21%
R35C1W	0.9	−0.3	−38%
R50C1W	1.1	−0.7	−62%

Could the observed hysteresis be due to the camera or light source? A reference gray was attached to the calibration block for all measurements on four of the TLCs. This reference square did not show an appreciable change in R, G, or B values, especially between heating and cooling. This indicates that neither the camera nor the light source is responsible for the hysteresis. It is unlikely that the light source caused damage to any of the TLCs. The fluorescent light source used was encased in a UV shield to minimize UV output. The exposure damage experienced by the 5°C and 1°C bandwidth liquid crystals does not appear to be gradual as it would be if the damage was due to UV. For example runs 14, 16, and 17 for these three liquid crystals showed very good repeatability, indicating the damage had been incurred prior to these runs and not during these runs.

Could the hysteresis be influenced by the reflectivity of the black paint, the vinyl encapsulating material, or the liquid crystal binder material used to make the liquid crystals adhere to the surface? The luminance from the surface can be broken into two components: one from the background, which encompasses the three materials being considered here, and the other from the liquid crystal itself. When outside of the color play range this background luminance is what is being measured. If the background were being affected by the direction of temperature change (heating versus cooling), we would expect to see this effect outside of the color play range region and not just inside it (i.e., the background values during heating would be shifted relative to the values during cooling) which does not happen (see Figs. 2–4).

Could there have been a lag in the TLC, a lag in the temperature measurement device, a lag in the recording of the temperature relative to the acquisition of the image, or a nonuniform plate temperature? The rate of change of temperature was purposefully chosen to be slow enough that lags would be much less than the shifts encountered [31]. For the 10°C and 5°C bandwidth TLCs the error and uncertainty in the temperature difference between heating and cooling is estimated to be +0.05°C/−0.03°C. This is an order of magnitude lower than the differences in peak temperatures due to hysteresis, which are in the range 0.2°C to 0.3°C. For the 1°C bandwidth TLCs the uncertainty in the temperature difference between heating and cooling is estimated to be +0.04°C/−0.03°C. This is almost an order of magnitude lower than the differences in peak temperatures due to hysteresis, which are in the range 0.15°C to 0.2°C. Variations due to these sources could not account for the shift in peak temperatures summarized in Table 2.

As stated by [2] and by [15], the focal-conic texture tends to form when the liquid crystal is cooled from the isotropic state and the planar texture can form either from mechanical shear of the focal-conic texture or from heating from the smectic phase. It is the planar texture that results in the selective reflection associated with TLCs; the focal-conic texture does not reflect incident light selectively [15]. [2] further states that when encapsulated, the capsule walls tend to align the structures into the planar texture, however, patches of focal-conic texture may be present within the capsule; this addition of focal-conic results in a decrease in reflectivity. [27] found that the hysteresis in temperature at which pitch jumps occur depends strongly on the specimen thickness and is a direct consequence of the strong anchoring interaction at the boundaries of the layers. The thicker specimen showed no hysteresis and the thinner specimen showed up to about a 0.5°C bias toward lower temperatures when cooled rather than heated (the CLC used had about a 4°C color play range). [32] investigated the effect of shear on cholesteric liquid crystals and found that the reflected intensity spectrum decreased in value and spread out in wavelength with shear rate. They offer a mechanical model to explain this behavior in which the axis of each liquid crystal helix is initially perpendicular to the surface under the no-shear condition (planar texture). When a shear is applied the crystals near the surface remain perpendicular while the others shift in orientation resulting in a decrease in reflectivity. Although this hysteresis was due to shear and not temperature the reflectivity behavior is similar to that observed in the present study and the cause of this behavior may be related. Upon heating, the molecules may form a planar texture throughout the microcapsule, while upon cooling, especially from the isotropic liquid state, the molecules may form a planar texture near the surface but a focal-conic texture away from the surface resulting in a decrease in reflectivity. In addition, this increase in focal-conic texture may be the cause of the hue shift towards bluer hues, the other characteristic of hysteresis observed in the present study, for reasons similar to the well known angle effect in TLCs.

Conclusions

It has been shown that each of the five TLCs tested exhibit a similar hysteresis behavior when cooled rather than heated, if the final temperature of heating was high enough relative to the colorplay. Both a decrease in reflectivity of the TLC and a shift in the temperature at which the peak red and green components occur characterize this hysteresis. The combined effects result in a shift in the hue-temperature calibration of the TLC. The magnitude of the hysteresis effects increase with the peak temperature in a heating and cooling cycle. When cooled from near the top of the useful calibration range, the hysteresis effect is small and the hue-temperature calibration data generally fall within the scatter of the heating data. When cooled from higher temperatures, the hysteresis effects increase, resulting in greater deviation from the heating case. At some point the cooling data appear to level off (or reset) providing a somewhat repeatable cooling calibration curve. Repeatable heating data has been obtained when the TLC is cooled below the color play (below the red start temperature). Similarly, repeatable cooling data (not quite as repeatable as the heating data) was obtained in most cases when the TLC is heated above an apparent cooling reset temperature. This temperature appears to be near the end of color play (i.e., when the red, green and blue components all return to their background value) and is higher than the naked eye would suggest (about 20°C to 25°C above the top of the useful range).

The magnitude of the hysteresis can be significant. The broad-band TLCs exhibited maximum biases of about 1.2°C for the 10°C bandwidth TLCs and 0.6°C for the 5°C bandwidth TLC, which are over 20 percent of their useful calibration ranges. The narrow-band TLCs exhibited biases of about 0.3°C and 0.7°C, which correspond to 38 percent and 62 percent of their useful calibration ranges. The uncertainties in temperature for these calibrations were generally an order of magnitude less than the hysteresis effects.

In addition to hysteresis, it was found that the TLCs tested suffered permanent change or damage during their use. A decrease in reflectivity and a shift in temperature at which the peak red and green components occur characterize this damage. It is believed that this damage is related to high temperature exposure. The magnitude of the effect was related to the bandwidth; the smaller the bandwidth the greater the effect.

It is suggested that the hysteresis may be related to the texture of the TLC. The planar texture, in which the axis of the helices are aligned perpendicular to the surface, exhibits iridescent reflection, however the focal-conic texture, in which the axis are aligned parallel to the surface do not. Upon heating from the smectic phase (below color play), liquid crystals tend to align into the planar texture, however when cooled from the isotropic liquid, liquid crystals tend to align into the focal-conic (although near the microcapsule surface the planar texture is exhibited). This reduction in planar texture during cooling may be related to the observed hysteresis.

Data from the current study suggests that there is both a low temperature reset, and a high temperature reset. The low temperature reset is associated with the bottom of color play, which may be associated with the solid-liquid crystal transition point (or melting point), and the high temperature reset at some temperature above color play, which may be associated with the liquid crystal-isotropic liquid transition point (or clearing point). If a TLC remains within its upper and lower reset temperatures then its behavior will depend on the last reset temperature achieved (high or low).

Although hysteresis may be a problem, it can be avoided to some extent by proper use. Calibrations can be done in the same direction and from about the same initial temperature as in the application, starting below or above the color play temperature range. For example, in the transient method some experimenters expose a low temperature (usually room temperature) model to a heated flow (e.g., [33]) and some expose a preheated model to a lower temperature (usually room temperature) flow (e.g., [34]). In either case the calibration should be performed in the same direction as the transient and from similar initial temperatures. For fluctuating temperature measurements avoiding hysteresis is more complex and may not be possible. If the maximum and minimum temperatures remain within the color band, the data suggests that the hue will follow the heating or cooling calibration curve from which the color play initially began and thus that is the calibration curve to use. However, if the temperatures go outside the color play by different amounts during fluctuations, it may be impossible to select an appropriate calibration curve.

Acknowledgments

We would like to thank Dr. James Mayhew, Captain Jason Wolf, and Christopher Gordon for their help with the initial investigation and testing. The support of the Air Force Office of Scientific Research, which provided a University Resident Researcher Program grant for the assignment of Professor Baughn to the USAF Academy, is gratefully acknowledged. We would also like to acknowledge the support and advice of Dr. Aaron Byerley at the USAF Academy and Dr. Richard Rivir of the USAF Wright Laboratory Discussions. Suggestions by Professor Terry Jones (Oxford University) and Professor J. Michael Owen (University of Bath), who visited the USAF Academy under an EOARD WOS grant, were helpful and are greatly appreciated.

Nomenclature

English Symbols

H, Hue = hue (Eq. 1 or 2)
R, G, B = matrices of red, green, and blue components, respectively
Rpeak = peak red value from a TLC image
Rbackground = red value from a TLC image at a temperature outside of color play

Subscripts

heating = during a heating run in which the TLC is heated from a cooler temperature
max cooling = during a cooling run in which the TLC experiences the maximum decrease in reflectivity

Acronyms

TLC = Thermochromic Liquid Crystal
CNLC = Chiral Nematic Liquid Crystal
CLC = Cholesteric Liquid Crystal

References

[1] Moffat, R. J., 1990, ''Experimental Heat Transfer,'' *Proc. 9th Int. Heat Transfer Conference*, Vol. 1, pp. 187–205.

[2] Jones, T. V., 1992, ''The Use of Liquid Crystals in Aerodynamic and Heat Transfer Testing,'' *Transport Phenomena in Heat and Mass Transfer*, Proceedings of the Fourth International Symposium on Transport Phenomena in Heat and Mass Transfer (ISTP-IV), Elsevier, pp. 1242–1273.

[3] Cooper, T. E., Field, R. J., and Meyer, R. J., 1975, ''Liquid-Crystal Thermometry and Its Application to the Study of Convective Heat Transfer,'' ASME J. Heat Transfer, **97**, pp. 442–450.

[4] Hippensteele, S. A., Russell, L. M., and Torres, F. J., 1986, ''Use of a Liquid-Crystal and Heater-Element Composite for Quantitative, High-Resolution Heat-Transfer Coefficients on a Turbine Airfoil Including Turbulence and Surface-Roughness Effects,'' Winter Annual Meeting of the American Society of Mechanical Engineers, Anaheim, CA., Dec. 7–12, pp. 105–120.

[5] Baughn, J. W., 1995, ''Liquid Crystal Methods for Studying Turbulent Heat Transfer,'' Int. J. Heat Fluid Flow, **16**(5), pp. 365–375.

[6] Hollingsworth, D. K., Boehman, A. L., Smith, E. G., and Moffat, R. J., 1989, ''Measurement of Temperature and Heat Transfer Coefficient Distributions in a Complex Flow Using Liquid Crystal Thermography and True-Color Image Processing,'' ASME Collected Papers in Heat Transfer, HTD-Vol 123, pp. 35–42.

[7] Camci, C., Kim, K., and Hippensteele, S. A., 1992, ''A New Hue Capturing Technique for the Quantitative Interpretation of Liquid Crystal Images Used in Convective Heat Transfer Studies,'' ASME J. Turbomach., **114**(4), pp. 765–775.

[8] Kim, Y. W., and Reynolds, S. A., 1995, ''Simultaneous Measurement of Surface Temperature and Heat Flux Using a Composite Slab,'' Exp. Heat Transfer, **8**(4), pp. 281–292.

[9] Wang, Z., Ireland, P. T., and Jones, T. V., 1995, ''An Advanced Method of Processing Liquid Crystal Video Signals From Transient Heat Transfer Experiments,'' ASME J. Turbomach., **117**(1), pp. 184–189.

[10] Farina, D. J., Hacker, J. M., Moffat, R. J., and Eaton, J. K., 1994, ''Illuminant Invariant Calibration of Thermochromic Liquid Crystals,'' Exp. Therm. Fluid Sci., **9**(1), pp. 1–12.

[11] Hay, J. L., and Hollingsworth, D. K., 1996, ''A Comparison of Trichromic Systems for Use in the Calibration of Polymer-Dispersed Thermochromic Liquid Crystals,'' Exp. Therm. Fluid Sci., **12**(1), pp. 1–12.

[12] Baughn, J. W., Anderson, M. R., Mayhew, J. E., and Wolf, J. D., 1999, ''Hysteresis and Uncertainty of Thermochromic Liquid Crystal Temperature Measurement Based on Hue,'' ASME J. Heat Transfer, **121**, pp. 1067-1072.

[13] Ireland, P. T., and Jones, T. V., 2000, ''Liquid Crystal Measurements of Heat Transfer and Surface Shear Stress,'' Meas. Sci. Technol., **11**(7), pp. 969–986.

[14] Fergason, J. L., 1996, ''Liquid Crystals,'' Scientific American, Aug., pp. 77–85.

[15] Hallcrest Inc., 1991, Handbook of Thermochromic Liquid Crystal Technology, Sales Literature, Hallcrest Inc., Glenview, IL.

[16] Stasiek, J., 1997, ''Thermochromic Liquid Crystals and True Color Image Processing in Heat Transfer and Fluid-Flow Research,'' IEEE Commun. Mag., **33**(1–2), pp. 27–39.

[17] Akino, N., Kunugi, T., Ichimiya, K., Mitsushiro, K., and Ueda, M., 1989, ''Improved Liquid-Crystal Thermometry Excluding Human Color Sensation,'' ASME J. Heat Transfer, **111**(4), pp. 558–565.

[18] Zhu, C., and Hieftje, G. M., 1989, ''A New Liquid-Crystal-Based Fiber-Optic Temperature Sensor,'' Appl. Spectrosc., **43**(8), pp. 1333–1336.

[19] Behle, M., Schulz, K., Leiner, W., and Fiebig, M., 1996, ''Color-Based Image Processing to Measure Local Temperature Distributions by Wide-Band Liquid Crystal Thermography,'' Appl. Sci. Res., **56**(2–3), pp. 113–143.

[20] Kelker, H., and Hatz, R., 1980, *Handbook of Liquid Crystals*, Weinheim, Deerfield Beach, FL, p. 607, Chap. 14.

[21] Goodby, J., 1998, ''Phase Structures of Calamitic Liquid Crystals,'' in *Handbook of Liquid Crystals Vol. 2A: Calamitic Liquid Crystals*, J. Demus, J. Goodby, G. W. Gray, H.-W. Spiess, and V. Vill, eds., Wiley-Vch Publishers, Weinheim (Federal Republic of Germany), pp. 3–21.

[22] Melamed, L., and Rubin, D., 1970, ''Electric Field Hysteresis Effects in Cholesteric Liquid Crystals,'' Appl. Phys. Lett., **16**(4), pp. 149–151.

[23] Gruebel, W., 1974, ''Bistability Behavior of Texture in Cholesteric Liquid Crystals in an Electric Field,'' Appl. Phys. Lett., **25**(1), pp. 5–7.

[24] Kawachi, M., and Kogure, O., 1977, ''Hysteresis Behavior of Texture in the Field-Induced Nematic-Cholesteric Relaxation,'' Jpn. J. Appl. Phys., **16**(9), pp. 1673–1678.

[25] Elser, W., Pohlmann, J. L. W., and Boyd, P. R., 1976, ''The Preparation of High-Purity Cholesteryl Oleyl Carbonate,'' Mol. Cryst. Liq. Cryst., **36**, pp. 279–292.

[26] Dixon, G. D., and Scala, L. C., 1970, ''Thermal Hysteresis in Cholesteric Color Responses,'' Mol. Cryst. Liq. Cryst., **10**, pp. 317–325.

[27] Zink, H., and Belyakov, V. A., 1997, ''Temperature Hysteresis of the Change in the Cholesteric Pitch and Surface Anchoring in Thin Planar Layers,'' J. Exp. Theor. Phys., **85**, pp. 58–66.

[28] Kenning, D. B. R., and Yan, Y., 1996, ''Pool Boiling Heat Transfer on a Thin Plate: Features Revealed by Liquid Crystal Thermography,'' Int. J. Heat Mass Transfer, **39**, pp. 3117–3137.

[29] Birrell, D. C., and Eaton, J. K., 1998, ''Liquid Crystal Temperature Measurement for Real-Time Control,'' *Applications of Digital Image Processing XXI*, Proceedings of SPIE—The International Society for Optical Engineering, Andrew G. Tescher, ed., Vol. 3460.

[30] Wang, Z., 1998, personal correspondence.

[31] Anderson, M. R., 1999, ''Thermochromic Liquid Crystal Thermography: Hysteresis, Illumination and Imaging System Effects, Image Processing and Applications,'' Ph.D. dissertation, University of California, Davis.

[32] Ciliberti, D. F., Dixon, G. D., and Scala, L. C., 1973, ''Shear Effects on Cholesteric Liquid Crystals,'' Mol. Cryst. Liq. Cryst., **20**, pp. 27–36.

[33] Metzger, D. E., Bunker, R. S., and Bosch, G., 1991, ''Transient Liquid Crystal Measurement of Local Heat Transfer on a Rotating Disk With Jet Impingement,'' ASME J. Turbomach., **113**(1), pp. 52–59.

[34] Baughn, J. W., and Yan, X, 1991, ''A Preheated-Wall Transient Method for Measurements of the Heat Transfer from a Surface to an Impinging Jet,'' *Heat Transfer in Single Phase Flows*, Proceedings of the 1991 Eurotherm Seminar Nr. 25, pp. 1–7.

Transport in Flat Heat Pipes at High Heat Fluxes From Multiple Discrete Sources

Unnikrishnan Vadakkan

Suresh V. Garimella

Jayathi Y. Murthy

Cooling Technologies Research Center,
School of Mechanical Engineering,
Purdue University, West Lafayette,
IN 47907-2088

A three-dimensional model has been developed to analyze the transient and steady-state performance of flat heat pipes subjected to heating with multiple discrete heat sources. Three-dimensional flow and energy equations are solved in the vapor and liquid regions, along with conduction in the wall. Saturated flow models are used for heat transfer and fluid flow through the wick. In the wick region, the analysis uses an equilibrium model for heat transfer and a Brinkman-Forchheimer extended Darcy model for fluid flow. Averaged properties weighted with the porosity are used for the wick analysis. The state equation is used in the vapor core to relate density change to the operating pressure. The density change due to pressurization of the vapor core is accounted for in the continuity equation. Vapor flow, temperature and hydrodynamic pressure fields are computed at each time step from coupled continuity/momentum and energy equations in the wick and vapor regions. The mass flow rate at the interface is obtained from the application of kinetic theory. Predictions are made for the magnitude of heat flux at which dryout would occur in a flat heat pipe. The input heat flux and the spacing between the discrete heat sources are studied as parameters. The location in the heat pipe at which dryout is initiated is found to be different from that of the maximum temperature. The location where the maximum capillary pressure head is realized also changes during the transient. Axial conduction through the wall and wick are seen to play a significant role in determining the axial temperature variation. [DOI: 10.1115/1.1737773]

Keywords: *Electronics, Heat Pipes, Phase Change, Three-Dimensional, Transient*

Introduction

Heat pipes are widely used in electronics cooling applications, both as efficient heat spreaders and to transport heat to remote heat sinks for dissipation. The analysis of the operation and performance of heat pipes has received a lot of attention, as reviewed in Garimella and Sobhan [1]. For the most part, attention has been focused on the study of either flat or round heat pipes, typically with single heat sources. Recently, there has been increased interest in exploring the use of flat heat pipes as substrates upon which multiple heat generating components would be mounted. In such a configuration, the heat pipe acts both as a heat spreader as well as a conveyer of heat, while also providing the mechanical substructure. The performance of flat heat pipes under these types of heterogeneous and distributed loads is not well understood and forms the subject of the present study.

A number of steady-state analyses of heat pipes, mostly with single heat sources, have been published. Tien and Rohani [2] investigated the effects of vapor pressure distribution on vapor temperature in a cylindrical heat pipe with a single heat source using a stream function vorticity formulation. The analysis indicated that in certain situations the vapor pressure variation plays a significant role in the performance of heat pipes; this work assumed a constant datum pressure at the liquid-vapor interface at the end of the evaporator section. Approximate solutions based on parabolic boundary layer equations were shown to yield inaccurate predictions of the vapor pressure variation at high evaporation and condensation rates. Van Ooijen and Hoogendoorn [3] presented a steady two-dimensional numerical analysis of the vapor core in a horizontal flat heat pipe. The computations were performed at different radial Reynolds numbers and the results were compared with a porous plate model. Though interesting insights into vapor flow patterns were presented, the study did not consider coupled wick/vapor flow, and the evaporator/condenser mass flow rate was assumed to be known *a priori*. Chen and Faghri [4] studied both single and multiple heat sources, albeit in a two-dimensional axi-symmetric cylindrical heat pipe. A coupled analysis of the wall, wick and vapor regions was conducted. Both sodium and water were considered as the working fluids. The solutions are compared against experimental results for the vapor and wall temperature at high and low operating temperatures. For the operating conditions considered, compressibility effects were found to be very important.

Unsteady analyses of heat pipe operation have also been published. Issacci et al. [5] analyzed the transient behavior of vapor flow in heat pipes, taking vapor pressurization into account in determining the change in vapor density. The absolute pressure of the vapor was used as the interface pressure in calculating the temperature at the interface from the saturation condition, and the pressure difference between the vapor and the interface to allow for vaporization or condensation at the interface was not considered. The analysis studied the effect of input heat flux and condensation temperature on vapor core response. Transient two-dimensional computations of cylindrical heat pipes including the wick, vapor and wall were performed by Cao and Faghri [6]. A compressible flow formulation was used to account for the pressurization of the vapor during the transient. The study also investigated the transient response of heat pipes to a pulsed heat input. Issacci et al. [7] studied vapor dynamics during heat pipe start-up. The analysis neglected the convection through the liquid wick and conduction through the wall. The liquid flow in a homogeneous wick heat pipe was studied by Ambrose and Chow [8]. The transient axial distribution of liquid in the wick was analyzed and the results compared to experiments. Dryout was observed when the heat transport was greater than the capillary limit. Tournier and El-Genk [9] developed a two-dimensional model for the transient analysis of heat pipes. The analysis determined the radius of cur-

---

Contributed by the Heat Transfer Division for publication in the JOURNAL OF HEAT TRANSFER. Manuscript received by the Heat Transfer Division June 30, 2003; revision received February 6, 2004. Associate Editor: J. H. Lienhard V.

vature of the liquid meniscus at the liquid-vapor interface. A model for liquid pooling was included. The study assumed a constant temperature in the vapor core. The results were compared to experiments which studied the effect of inclination on the transient performance of heat pipes [10]. The experiments provided temperatures on the wall and the vapor core of the heat pipe in the axial direction. Zhu and Vafai [11] studied the start-up transients in an asymmetrical flat heat pipe, using transient heat conduction equations for the heat pipe wall and wick, and a pseudo-three-dimensional approximation in the vapor region. More recent experimental and numerical analyses of heat pipe performance may be found in [12–18].

Although these studies have established useful models and methodologies for the steady as well as transient simulation of thermal transport in heat pipes, sound models representing flat heat pipe performance under transient conditions and with multiple discrete heat sources on the evaporator section are not readily available.

In recent work by the authors [19], a complete two-dimensional mathematical model was developed to analyze the transient and steady-state performance of flat heat pipes. The model accounted for the pressurization of the vapor core and the coupling of the continuity, momentum and energy equations in the wick and vapor regions. A stable numerical procedure was devised to solve the resulting governing equations. The procedure improved upon the standard sequential solution scheme by recognizing the sensitivity of the mass flow rate at the phase change interface to the interface temperature and pressure, as well as the system pressure. The improved method was shown to perform well over a range of heat inputs, and the predictions showed satisfactory agreement with experiments.

The present work utilizes the numerical method developed in [19] to study the performance of flat heat pipes with multiple discrete heat sources. The effect of heat source strength and separation and their effect on steady as well as transient performance are studied. The simulations are used to assess the possibility of dryout as well as the location at which dryout might first be observed. The maximum pore radius necessary to support the pressure drop at the evaporator interface is obtained from the hydrodynamic pressure variation at the interface.

Mathematical Model

The present three-dimensional analysis includes the liquid wick and the wall in addition to the vapor core. An equilibrium model for heat transfer and a Brinkman-Forchheimer extended Darcy model for fluid flow in the wick region are employed. The density change in the vapor due to pressurization is calculated using the ideal gas state equation. The mass flow rate, temperature and pressure at the interface are determined using an energy balance at the interface in conjunction with kinetic theory and the Clausius-Clapeyron equation. The energy balance at the interface includes convection and conduction on the liquid and vapor sides. Vapor flow, temperature and hydrodynamic pressure fields are computed from coupled continuity/momentum and energy equations in the vapor and wick regions, and a conduction analysis in the wall. The flow of the vapor is assumed as laminar and incompressible. At high heat fluxes, the vapor velocity may be high enough for compressibility effects to become important; these are not accounted for in the present development. Compressibility effects are being included in the formulation as part of ongoing work.

The boundary conditions are of the Neumann type on the evaporator side and of mixed type at the condenser. The model assumes that the wick is saturated with liquid throughout, which is required to prevent dryout. The initial volume fraction of the liquid in the wick is 0.5 (liquid-saturated wick). If the wick were not fully saturated with liquid, vapor would occupy the unsaturated portion of the wick. Estimates of the force needed to expel this trapped vapor from the liquid show it to be significant compared to the force required to move liquid from the condenser to the evaporator. As a result, dryout would occur as soon as vapor displaces the liquid in the wick. This unsaturated condition need not be considered for prediction of the onset of dryout.

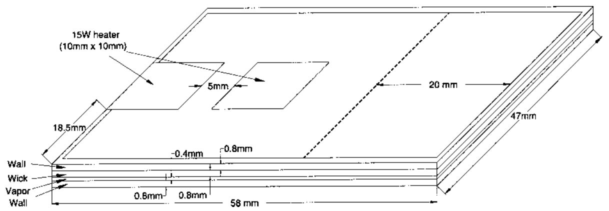

Fig. 1 Schematic diagram of the flat heat pipe investigated; the thickness dimension has been greatly exaggerated in this schematic to delineate the different parts of the heat pipe

The physical dimensions of the flat heat pipe investigated are shown in Fig. 1. The heat pipe dimensions, 47 mm width and 58 mm length with a wall thickness of 0.8 mm on all six sides, simulate those of typical commercially available flat heat pipes. The condenser covers 20 mm of the heat pipe as shown in the figure. The wall and wick are made of copper and the working fluid is water. The porosity, permeability and thermal conductivity of the sintered copper wick are 0.5, 1.43×10^{-11} m^2, and 40 W/mK [20], respectively. The wick is present only on one side of the heat pipe, and the heating and cooling boundary conditions are applied only on this wicked side. Two discrete 10×10 mm heat sources are mounted at a separation distance of 5 mm in the baseline case. The heat input to each heat source is 15 W. Those portions of the heat pipe surface not exposed to the condenser or evaporator boundary conditions are assumed adiabatic. The thermophysical properties of the heat pipe wall, wick and vapor core are given in Table 1. The coolant water temperature and the heat transfer coefficient on the condenser are 287 K and 2604 W/m^2 K, respectively. The initial temperature all through the heat pipe is 287 K and the vapor is assumed to be saturated.

To accommodate changes in the vapor and liquid mass during the transient under the assumption of a liquid-saturated wick, the mass balance of the liquid is handled by modifying the volume-averaged density of the liquid in the wick. All thermophysical properties are assumed constant except for the vapor density, which is found from the operating pressure P_{op} and the local temperature using the perfect gas law. Under these assumptions, the governing equations may be written as shown below, following the development in [19]. The continuity equation for the wick and the vapor core is

$$\varphi\frac{\partial\rho}{\partial t}+\nabla.(\rho V)=0 \tag{1}$$

The term $\partial\rho/\partial t$ accounts for mass addition or depletion in the vapor and liquid spaces. The three-dimensional momentum equations in the wick and the vapor core are

Table 1 Thermophysical properties of the heat pipe material and the working fluid

Copper wall/wick	Thermal conductivity	401 W/m K
	Specific heat	385 J/kg K
	Density	8933 kg/m^3
	Wick conductivity	40 W/m K
Water	Thermal conductivity	0.6 W/m K
	Specific heat	4200 J/kg K
	Density	1000 kg/m^3
	Viscosity	8×10^{-4} N s/m^2
Water vapor	Thermal conductivity	0.0189 W/m K
	Specific heat	1861.54 J/kg K
	Density	0.01 kg/m^3
	Viscosity	8.4×10^{-6} N s/m^2
Water/Vapor	Latent heat	2473 kJ/kg

$$\frac{\partial \rho u}{\partial t}+\nabla.(\rho V u)=-\frac{\partial \varphi p}{\partial x}+\nabla.(\mu \nabla u)-\frac{\mu \varphi}{K}u-\frac{C_E \varphi}{K^{1/2}}\rho|V|u \tag{2}$$

$$\frac{\partial \rho v}{\partial t}+\nabla.(\rho V v)=-\frac{\partial \varphi p}{\partial y}+\nabla.(\mu \nabla v)-\frac{\mu \varphi}{K}v-\frac{C_E \varphi}{K^{1/2}}\rho|V|v \tag{3}$$

$$\frac{\partial \rho w}{\partial t}+\nabla.(\rho V w)=-\frac{\partial \varphi p}{\partial z}+\nabla.(\mu \nabla w)-\frac{\mu \varphi}{K}w-\frac{C_E \varphi}{K^{1/2}}\rho|V|w \tag{4}$$

In the vapor core, permeability $K=\infty$ and porosity $\varphi=1$. The energy equation in the wall, wick and the vapor core is

$$\frac{\partial(\rho C)_m T}{\partial t}+\nabla.[(\rho C)VT]=\nabla.(k_{\text{eff}}\nabla T) \tag{5}$$

Here, $(\rho C)_m$ assumes different values in the wall, wick, and vapor core

$$\text{Wall:}\quad (\rho C)_m=(\rho C)_s$$

$$\text{Wick:}\quad (\rho C)_m=(1-\varphi)(\rho C)_s+\varphi(\rho C)_l$$

$$\text{Vapor core:}\quad (\rho C)_m=(\rho C)_v$$

Also, k_{eff} is the effective conductivity in the region of interest and assumes appropriate values in the wall, wick and vapor core. In the wick, an effective value of 40 W/mK is assumed [20].

The following boundary conditions are imposed on the domain [19].

1. Wick-Vapor Interface: Change of phase from liquid to vapor is assumed to occur at the wick-vapor core interface (Fig. 1). The interface temperature T_i is obtained from the energy balance at the interface

$$-k_{wick}A_i\frac{\partial T}{\partial y}+m_iC_iT_i=-k_vA_i\frac{\partial T}{\partial y}+m_iC_vT_i+m_ih_{fg} \tag{6}$$

Here, $m_i<0$ denotes evaporation, and $m_i>0$ denotes condensation. The interface pressure P_i is obtained from the Clausius-Clapeyron equation, with P_0 and T_0 being reference values

$$\frac{R}{h_{fg}}\ln\left(\frac{P_i}{P_0}\right)=\frac{1}{T_0}-\frac{1}{T_i} \tag{7}$$

The interface mass flux is calculated using kinetic theory [21]

$$\left(\frac{2\sigma}{2-\sigma}\right)\left(\frac{1}{(2\pi R)^{1/2}}\right)\left(\frac{P_v}{(T_v)^{1/2}}-\frac{P_i}{(T_i)^{1/2}}\right)=m_i'' \tag{8}$$

A value for σ of 0.03 [21] is used in this work. The evaporated and condensed mass is assumed to flow normal to the interface when accounting for momentum transport due to evaporation/condensation. In the present formulation, no attempt is made to track the free surface; as a result entrainment effects cannot be computed. Since the velocity computed in the wick region is averaged over both fluid and solid, the mean tangential velocity in the wick at the wick/vapor interface is approximately zero.

2. Wick-Wall and Vapor-Wall Interface: $u=0,\ v=0$
3. Top Wall:

$$\text{Evaporator section:}\quad k_w\frac{\partial T}{\partial y}=q_e \quad 0\leq x\leq L_e$$

$$\text{Adiabatic section:}\quad \frac{\partial T}{\partial y}=0 \quad u=v=0, \quad L_e\leq x\leq L_e+L_a$$

$$\text{Condenser section:}\quad -k_w\frac{\partial T}{\partial y}=h_c(T-T_c) \quad x>L_e+L_a$$

4. Lateral Walls: $u=v=\partial T/\partial x=0$
5. Bottom Wall: $u=v=\partial T/\partial y=0$

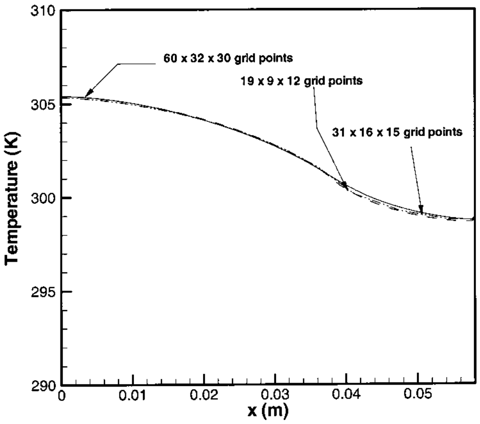

Fig. 2 Steady-state axial wall temperature variation for different mesh sizes at 15–15 W input power ($z/W=0$)

In addition, the following initial conditions are imposed: $T(x,y,0)=T_i$ and $P_{op}(t=0)=P_{\text{sat}}(T_i)$.

Details of the numerical method may be found in [19]. The governing equations are discretized using the finite volume method. The SIMPLE algorithm [22] with a collocated grid is employed. An up-winding scheme is implemented for the convective flux and central differencing for the diffusive flux. The linear equations resulting from the discretization are solved by a line-by-line TDMA. An Euler implicit scheme is used for time differencing.

A variety of tests were run to establish mesh and time-step independence. A baseline case with a heat input to the left and right heat sources of 15 W each (henceforth denoted as 15-15 W for the left-right values) was used. Three different meshes ($x\times y\times z$) were evaluated: $19\times 9\times 12$, $31\times 16\times 15$, and $60\times 32\times 30$. The dependence of the evaporator wall temperature on the mesh size is shown in Fig. 2. The results indicate that changing the number of grids from $19\times 9\times 12$ to $60\times 32\times 30$ changes the wall temperature by 0.10 percent. The corresponding average difference in the total evaporator mass flow rate was 1.22 percent at steady state. As a result of this grid-independence study, the $31\times 16\times 15$ mesh was used for all the results shown here; the wall, wick and vapor regions include 8, 4, and 4 grid points, respectively, in the y-direction. Similar tests varying the time step indicate that a time step of 1 s is adequate. The attainment of steady state is identified in this work as the time at which the heat transfer rate on the condenser side reaches within 0.1% of the value at the evaporator. Within each time step, the computations are stopped when the sum of the absolute values of the residuals for temperature, u, v, and w velocities are less than or equal to 10^{-11}.

Results and Discussion

The transient variation of wall temperature under the center of the far-left heater is shown in Fig. 3. The heat flux supplied to the two heat sources is varied while the heat source separation is held constant at 5 mm. The numerical results reveal a time constant for the heat pipe under consideration to be 6 s. This compares well to an estimated response time of the system from a lumped capacitance analysis of 7.1 s. The relatively low time constant results from the small thermal mass of the heat pipe and the relatively high heat transfer coefficient at the condenser (achieved in the experiments with a cooling water jacket). The time constant is independent of the heat flux applied at the evaporator.

It is clear from Fig. 3 that the temperature under the left heater decreases as its heat input is reduced from 15 to 5 W. In all three cases, the system reaches a steady state at 100 s, independent of the heat input. The transient variation of heat transfer rate on the condenser side for the three different sets of heat input is shown in

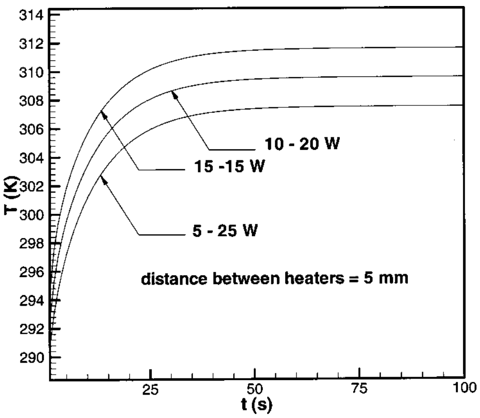

Fig. 3 Transient wall temperature under the far-left heater $(x/L=0.093, y/H=1, z/W=0.5)$ for different power input combinations to the two heaters

Fig. 4. It is clear from the figure that the condenser heat transfer rate is the same for all three distributions of heat input.

Contours of the wall temperature variation on the wicked side of the heat pipe $(y=2.8$ mm$)$ at steady state are shown in Fig. 5. The baseline case is again considered, with equal heat inputs to the two sources. As observed earlier, the maximum temperature occurs at the center of the heat source on the left. Conduction down the side wall is responsible for the maximum temperature not occurring at the left end of this heat source. The temperature decreases with distance away from the heated zone.

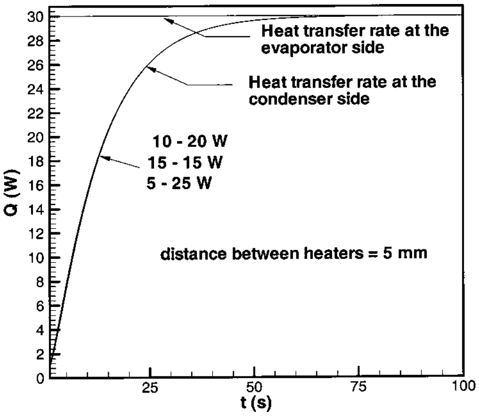

Fig. 4 Transient variation of the heat removal rates at the evaporator (constant Q_{in}) and condenser (Q_{out}) sections for the three heat input combinations

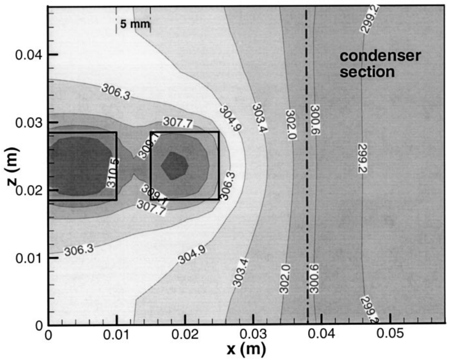

Fig. 5 Temperature contours at the wall $(y/H=1)$ on the wicked side of the heat pipe at an input power of 15–15 W: the condenser section is delineated by the dashed line.

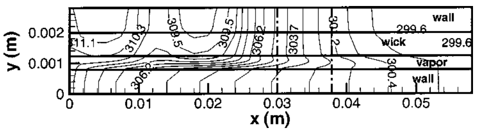

Fig. 6 Temperature distribution at the mid plane $(z/W=0.5)$ of the heat pipe for the baseline case with 15–15 W heat input $(d=5$ mm$)$

The temperature distribution along the vertical midsection $(z=23.5$ mm$)$ of the heat pipe is shown in Fig. 6. Again, the highest temperatures are in the vicinity of the discrete heat sources. In the vapor region, a significant drop of 12°C in temperature along the axial direction is observed, indicating continual energy transfer into the vapor across the liquid-vapor interface. In cases where the effect of convection in the vapor may be dominant over diffusion at the liquid-vapor interface, the vapor temperature variation would be significantly smaller. The Peclet number $(\rho u C_p H_v/k \sim 10-20$ in the present work$)$ of the vapor space governs which of these processes is dominant. The figure also shows a significant drop in temperature through the wick (y-direction), attributable to the low wick thermal conductivity.

The velocities in the wick and vapor core at steady state are shown in Fig. 7. It is clear that there is no "adiabatic" section inside the heat pipe. The v-velocities at the liquid-vapor interface allow a delineation of the actual length of the evaporator and condenser regions at the wick-vapor interface. In the vapor core, the velocity increases in the evaporator region along the axial direction because of mass addition from the interface; similarly, the velocity decreases in the condenser region along the axial direction because of mass depletion. The average liquid velocity is much smaller than the average vapor velocity because of the large differences in density. The analysis also shows that there is no region in the liquid-vapor interface where the interfacial velocity is zero.

Figure 8 shows the transient variation of liquid and vapor pressure drop at the liquid-vapor interface. The pressure drop at any point is calculated by subtracting the absolute pressure at the right end of the condenser section from the actual pressure at the desired location. The sum of the liquid and vapor pressure drops at the liquid-vapor interface gives the capillary pressure head. It is clear from the figure that the maximum pressure drop occurs at the left end of the evaporator. Even though the maximum tem-

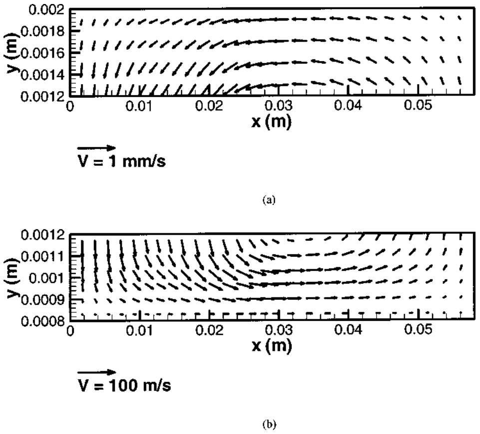

Fig. 7 Velocity vectors in the (*a*) wick and (*b*) vapor core at the mid plane of the heat pipe $(z/W=0.5$, with 15–15 W heat input and $d=5$ mm$)$: note that the velocity scale in the two plots is very different.

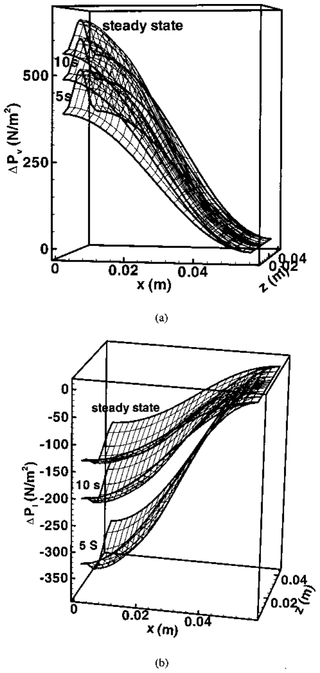

Fig. 8 Transient development of pressure drop in the (*a*) vapor, and (*b*) liquid, at the liquid-vapor interface (heat input = 15–15 W, *d* = 5 mm)

perature does not occur at the left end of the evaporator (as shown in Fig. 5), Fig. 8 shows that the maximum pressure drop is realized at the left end of the evaporator throughout the transient and at steady state.

In the following, the effects of varying the power input to the two heat sources, as well as the separation between the heat sources, on the temperature, velocity and pressure distributions in the heat pipe under transient and steady-state conditions are presented. The effects of these parameters on the overall performance of the heat pipe are also discussed.

Effect of Variation of Heat Input to the Heat Sources. The effect of changing the heat input distribution between the two heat sources (for a fixed total input power) on the temperature contours is shown in Fig. 9. Of the total input power of 30 W, three cases with progressively increasing heat input to the right heat source are considered: (a) 15-15 W (baseline), (b) 10–20 W, and (c) 5–25 W. The end-to-end separation between the heat sources is held constant in this set of results. When the heat inputs to the two sources are equal (case a), the maximum temperature in the heat pipe (311.9 K) occurs at the center of the left heater. However, when the heat input to the heat source on the right is increased from 15 to 20 and 25 W, the location of the maximum temperature (312.5 K for 10–20 W input and 314.2 K for 5–25 W input) shifts to the right heat source, closer to the condenser section.

Figure 10 shows the axial mass flow rate through the wick for the different heat input distributions considered in Fig. 9. The mass flow rate increases with distance away from the condenser end as mass is added by condensation of vapor. So also, the mass flow rate decreases as the evaporator is traversed from right to left due to evaporation of liquid. The effect of the increase in heat input to the right-side heat source is apparent in the reduction of mass flow rate to the left-side heat source in the 5–25 W distribution case. The mass flow rate through the left heater is not tripled when the heat input increases from 5 W to 15 W at this heater. This is because of the effect of heat spreading through the wall and the liquid wick.

Effect of Heat Source Separation. The effect of heat source

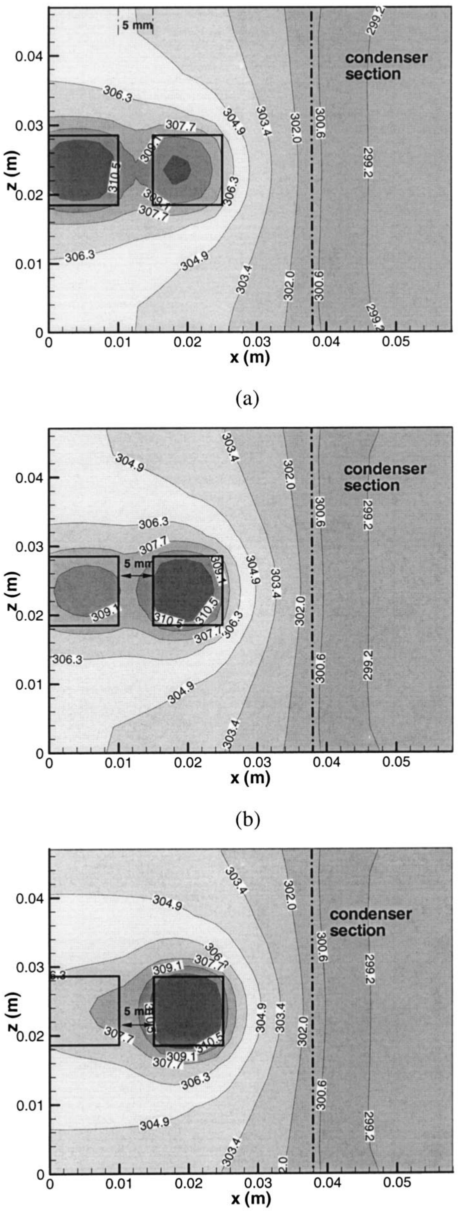

(a)

(b)

(c)

Fig. 9 Temperature contours on the wicked-wall of the heat pipe for heat inputs to the left and right heat sources of (*a*) 15–15 W, (*b*) 10–20 W, and (*c*) 5–25 W (*d* = 5 mm)

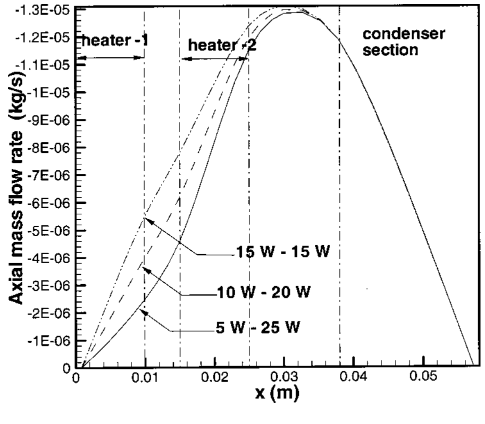

Fig. 10 Axial mass flow rate through the wick (*d* = 5 mm)

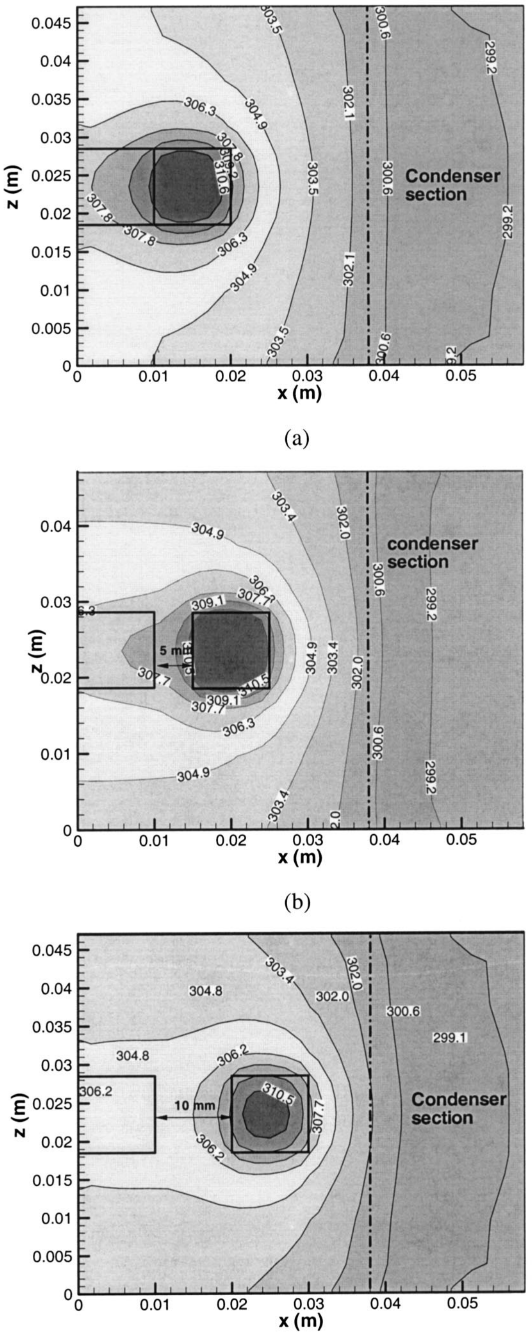

(a)

(b)

(c)

Fig. 11 Temperature contours in the liquid at the liquid-vapor interface for different separation between the heaters (heat input=5–25 W)

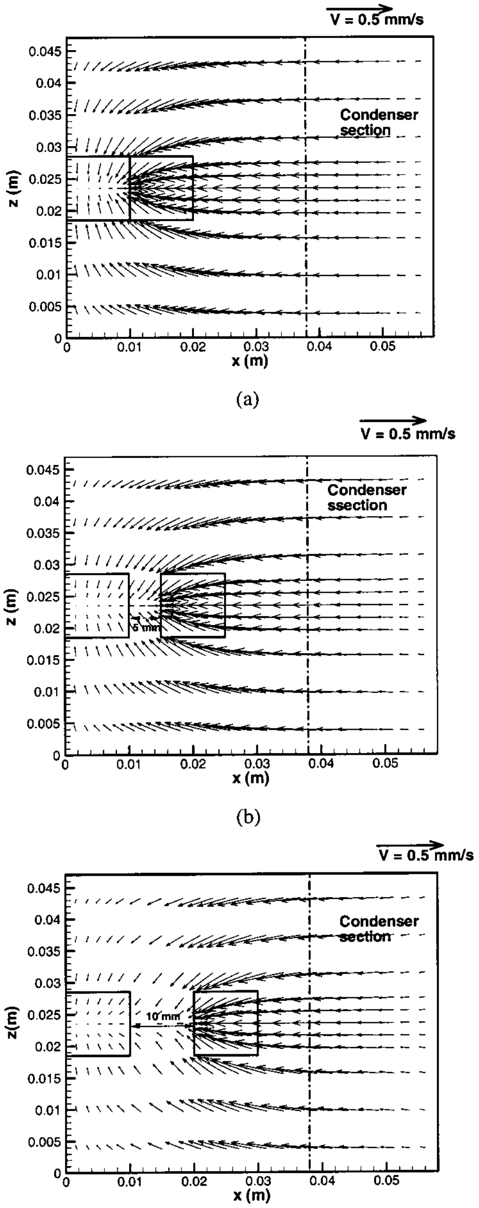

(a)

(b)

(c)

Fig. 12 Liquid velocity vectors in the wick near the liquid vapor interface for different heat source separations (heat input =5–25 W): (*a*) d=0, (*b*) 5, and (*c*) 10 mm.

separation is investigated next, with the power input to the two heat sources held constant at 5 and 25 W for the left and right sources, respectively. The heat source separation is varied through 0, 5 and 10 mm.

As expected, Fig. 11 shows that the maximum temperature always occurs at the center of the right heat source with the higher heat input. This maximum temperature reduces from 312.6 K to 311.4 K as the distance between sources is increased from 0 to 10 mm. As the separation between the sources is increased, the source on the right gets closer to the condenser, explaining this drop in maximum temperature. This temperature dependence with respect to the location of the heat source with respect to the condenser illustrates the importance of axial diffusion through the wall and wick.

Figure 12 illustrates the effect of heat source separation on the mass flow rate through the evaporator. As the high heat input source moves closer to the condenser, the mass flow to the left-side heat source is significantly reduced. This is because of the effect of heat spreading into the condenser region through the wall and the wick when the distance between the heaters is increased. A change in heat source separation from $d=0$ to 10 mm results in a reduction of 54 percent in the mass flow rate to the left-side heat source. The temperature on the left end of the evaporator is decreased when the heat source separation increases, thus reducing the rate of evaporation under the left end.

The location of the maximum velocity at the interface corresponds to the location of the maximum interface temperature. Also, this v-velocity is higher as the heat source separation is

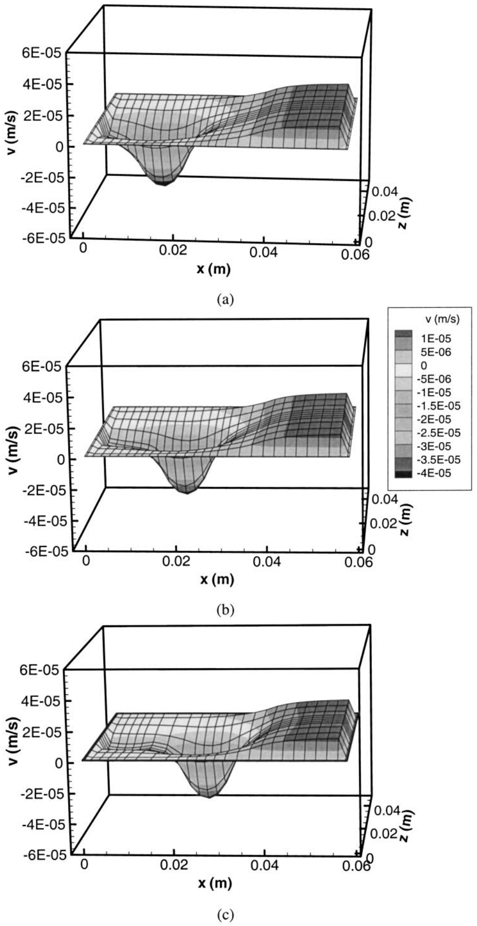

Fig. 13 Normal (v-) velocities in the liquid at the liquid-vapor interface at different heat source separations (heat input =5–25 W): (*a*) d=0, (*b*) 5, and (*c*) 10 mm. The shading denotes contours of *v*-velocity.

reduced, since the maximum wall temperature correspondingly increases. The v-velocity at the liquid-vapor interface is shown in Fig. 13 at the different heat source separations. As the higher-power heat source is moved closer to condenser, the actual "condenser section" penetrates deeper and deeper towards the evaporator section. The actual condensing and evaporating areas at the liquid vapor interface can be determined from Fig. 13.

Figure 14 shows the transient variation of the liquid and vapor pressure drop at the liquid-vapor interface. It is interesting to note that the location of the maximum pressure in the liquid and vapor changes during the transient. The mass flow rate in heat pipe increases during the transient period and reaches a maximum value at steady state. As the dynamic pressure loss increases in response to this increase in the flow rate, and becomes significant, the location of the maximum pressure drop shifts towards the left end of the evaporator. The location of the dryout region during transient startup would thus depend on the transient path adopted.

The axial variation of the liquid and vapor pressure drop at the interface at steady-state conditions is shown in Fig. 15. Once steady state is reached, irrespective of the location of the maximum temperature (and the maximum interface velocity), the maximum pressure drops in the liquid and vapor always occur near the left end of the evaporator. This is because of the significant velocities in the liquid and vapor encountered under the conditions of the present work, which lead to high dynamic pressure losses. When the heat source separation decreases, the mass flow rate to the left end of the evaporator increases (Fig. 12), as do the dynamic pressure losses as seen in Fig. 15.

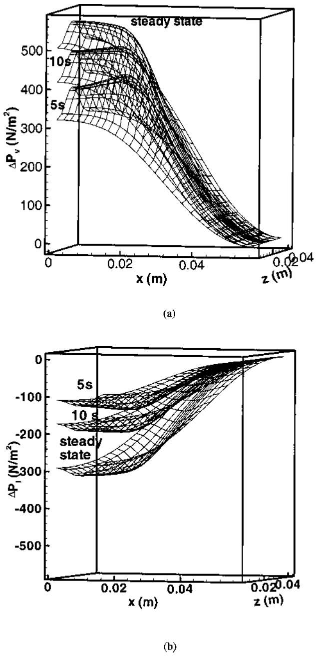

Fig. 14 Transient development of pressure drop in the (*a*) vapor, and (*b*) liquid, at the liquid-vapor interface (heat input 5–25 W and *d*=5 mm)

In the absence of gravity, the sum of the liquid and vapor pressure drops give the total pressure drop at any axial location along the liquid-vapor interface. From Fig. 15 it is possible to determine the required capillary pressure drop by summing the maximum liquid and vapor pressure drops. From the expression for the capillary pressure drop, $\Delta P_c = 2\sigma / r_p$, it is possible to determine the pore radius of the wick that can provide the required capillary pressure drop necessary to prevent dryout. For instance, in the present cases, the steady-state ΔP_c is found to be 1021, 883, and 742 N/m^2 for the 0, 5, and 10 mm separation distances, respectively. The pore radii necessary to support these capillary pressure heads are thus 1.37×10^{-4}, 1.58×10^{-4}, 1.89×10^{-4} m, respectively. For a given pore radius, the present analysis helps to determine the time and location of dryout. The location of dryout is that at which the capillary pressure head has a maximum value. In

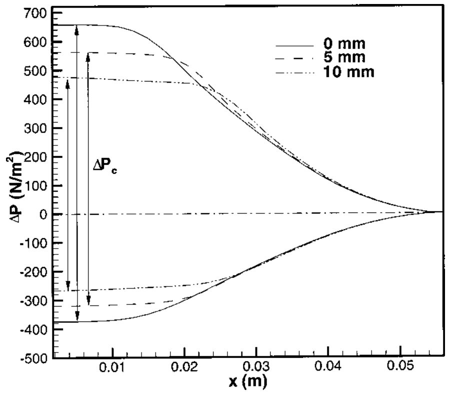

Fig. 15 Pressure drop in the liquid and vapor at the liquid-vapor interface at different heat source separation distances (heat input 5–25 W, *z*/*W*=0.5)

all the three cases studied, the maximum pressure head at steady state occurs at the left end of the evaporator, and this is the point where dryout would occur.

Conclusions

A complete, three-dimensional mathematical model has been developed to analyze the transient and steady-state performance of flat heat pipes, under the action of discrete multiple heat sources. The model accounts for the pressurization of the vapor core and the coupling of the continuity/momentum and energy equations in the wick and vapor regions. The analysis helps to determine the maximum pore radius of the wick allowable while still supporting the total pressure drop in a flat heat pipe. The location of dryout under transient and steady-state conditions can also be estimated.

The analysis highlights the importance of considering axial diffusion through the wall and wick in determining the temperature distribution in flat heat pipes. As the distance between multiple discrete heat sources increases, the maximum temperature in flat heat pipe decreases, resulting in lower liquid and vapor pressure drops.

Acknowledgment

The authors acknowledge the financial support of the members of the Cooling Technologies Research Center (www.ecn.purdue.edu/CTRC), a National Science Foundation Industry/University Cooperative Research Center.

Nomenclature

A = area, m^2
C = specific heat capacity at constant pressure, J/kg K
C_E = Ergun's coefficient, 0.55
d = end-to-end separation between heat sources, m
H = thickness of the heat pipe, m
h_{fg} = latent heat, J/kg
k = thermal conductivity, W/m K
k_{eff} = effective thermal conductivity, W/m K
K = permeability of the porous medium, m^2
L = length of the heat pipe, m
m = mass flow rate, kg/s
m'' = mass flux, kg/m^2 s
M = mass, kg
P = pressure, Pa
q = heat flux, W/m^2
R = gas constant, J/kg K
r = pore radius, m
t = time, s
T = temperature, K
u = longitudinal velocity, m/s
v = transverse velocity, m/s
V = velocity vector, m/s
W = width of the heat pipe, m
w = transverse velocity, m/s
x = axial coordinate; axial distance, m
y = transverse distance, m
Δt = time step, s
Δx = x-direction width of control volume, m
Δy = y-direction width of control volume, m

Greek Symbols

μ = dynamic viscosity, Ns/m^2
ρ = density, kg/m^3
φ = porosity of the wick
σ = accommodation coefficient; surface tension, N/m

Subscripts

0 = reference
a = adiabatic section
c = condenser
i = interface
l = liquid
m = mean value
op = operating pressure
s = solid
sat = saturation condition
v = vapor
w = wall

References

[1] Garimella, S. V., and Sobhan, C. B., 2001, ''Recent Advances in the Modeling and Applications of Nonconventional Heat Pipes,'' *Advances in Heat Transfer*, **35**, pp. 249–308, Chpt. 4.
[2] Tien, C. L., and Rohani, A. R., 1974, ''Analysis of the Effects of Vapor Pressure Drop on Heat Pipe Performance,'' Int. J. Heat Mass Transfer, **17**, pp. 61–67.
[3] Ooijen, V., and Hoogendoorn, C. J., 1979, ''Vapor Flow Calculations in a Flat Heat Pipe,'' AIAA J., **17**, pp. 1251–1259.
[4] Chen, M. M., and Faghri, A., 1990, ''An Analysis of the Vapor Flow and the Heat Conduction Through the Liquid Wick and Pipe Wall in a Heat Pipe with Single or Multiple Heat Sources,'' Int. J. Heat Mass Transfer, **33**, pp. 1945–1955.
[5] Issacci, F., Catton, I., Heiss, A., and Ghoniem, N. M., 1989, ''Analysis of Heat Pipe Vapor Dynamics,'' Chem. Eng. Commun., **85**, pp. 85–94.
[6] Cao, Y., and Faghri, A., 1990, ''Transient Two-Dimensional Compressible Analysis for High-Temperature Heat Pipes with Pulsed Heat Input,'' Numer. Heat Transfer, Part A, **18**, pp. 483–502.
[7] Issaci, F., Catton, I., and Ghoniem, N. M., 1991, ''Vapor Dynamics of Heat Pipe Start-Up,'' ASME J. Heat Transfer, **113**, pp. 985–994.
[8] Ambrose, J. H., and Chow, L. C., 1991, ''Detailed Model for Transient Liquid Flow in Heat Pipe Wicks,'' J. Thermophys. Heat Transfer, **5**, pp. 532–538.
[9] Tournier, J. M., and El-Genk, M. S., 1993, ''A Heat Pipe Transient Analysis Model,'' Int. J. Heat Mass Transfer, **37**, pp. 753–762.
[10] El-Genk, M. S., Huang, L., and Tournier, J. M., 1995, ''Transient Experiments of an Inclined Copper-Water Heat Pipe,'' J. Thermophys. Heat Transfer, **9**, pp. 109–116.
[11] Zhu, N., and Vafai, K., 1998, ''Analytical Modeling of the Startup Characteristics of Asymmetrical Flat-Plate and Disk-Shaped Heat Pipes,'' Int. J. Heat Mass Transfer, **41**, pp. 2619–2637.
[12] Um, J. Y., Chow, L. C., and Baker, K., 1994, ''An Experimental Investigation of Flat Heat Pipe,'' *Fundamentals of Heat Pipes*, **278**, ASME, New York, pp. 21–26.
[13] Chesser, J. B., Peterson, G. P., and Lee, S., 2000, ''A Simplified Method for Determining the Capillary Limitation of Flat Heat Pipes in Electronics Cooling,'' *Proceedings of NHTC'00, 34th National Heat Transfer Conference*, pp. 1–6.
[14] Shimura, T., Sho, H., and Nakamura, Y., 2002, ''The Aluminum Flat Heat Pipe Using Cyclopentane as Working Fluid,'' *Inter Society Conference on Thermal Phenomena*, IEEE, pp. 224–229.
[15] Chien, L., and Chang, C. C., 2002, ''Experimental Study of Evaporator Resistance on Porous Surface in Flat Heat Pipes,'' *Inter Society Conference on Thermal Phenomena*, IEEE, pp. 236–242.
[16] Gillot, C., Avenas, Y., Cezac, N., Poupo, G., Schaeffer, C., and Fournier, E., 2002, ''Silicon Heat Pipes Used as Thermal Spreaders,'' *Inter Society Conference on Thermal Phenomena*, IEEE, pp. 1052–1057.
[17] Xuan, Y., Hong, Y., and Li, Q., 2003, ''Investigation on Transient Behaviors of Flat Heat Pipes,'' Exp. Therm. Fluid Sci., in press.
[18] Rightley, M. J., Tigges, C. P., Givler, R. C., Robino, C. V., Mulhall, J. J., and Smith, P. M., 2003, ''Innovative Wick Design for Multi-Source, Flat Plate Heat Pipes,'' Microelectron. J., **34**(3), pp. 187–194.
[19] Vadakkan, U., Murthy, J. Y., and Garimella, S. V., 2003, ''Transient Analysis of Flat Heat Pipes,'' *Procs. ASME Summer Heat Transfer Conference*, Paper No. HT2003-47349.
[20] Grubb, K., 1999, ''CFD Modeling of a Therma-Base(TM) Heat Sink,'' 8th International FLOTHERM User Conference.
[21] Carey, V. P., 1992, *Liquid-Vapor Phase Change Phenomena*, Hemisphere Publishing Corp., Washington DC.
[22] Patankar, S. V., 1980, *Numerical Heat Transfer and Fluid Flow*, McGraw-Hill, New York.

Thermal and Thermomechanical Phenomena in Picosecond Laser Copper Interaction

Xinwei Wang
e-mail: xwang3@unl.edu
Department of Mechanical Engineering,
N104 Walter Scott Engineering Center,
The University of Nebraska at Lincoln,
Lincoln, Nebraska 68588-0656

Thermal and thermomechanical phenomena in laser metal interaction are of great importance in terms of understanding the underlying mechanisms in laser materials processing, optimizing the efficiency of laser micro-machining, and minimizing laser induced damage. In this work, Molecular Dynamics (MD) simulation is carried out to investigate picosecond laser copper interaction. A method has been developed to account for the laser beam absorption in, and the thermal transport sustained by, free electrons. Superheating is observed, and an evident temperature drop is revealed at the solid-liquid interface, which moves at a speed of 4400 m/s. However, the later phase change from solid to liquid happens in the target simultaneously and no visible movement of solid-liquid interface is observed. The results show that the laser induced stress wave consists of a strong compressive stress and a weak tensile stress. After reflection at the back side of the MD domain, the strong compressive stress becomes a strong tensile stress, which results in a visible drop of the number density of atoms. In the presence of this strong tensile stress, voids have formed in the region near the back side of the MD domain, indicating that the strong tensile stress in laser materials interaction plays an important role in terms of inducing structural damage. [DOI: 10.1115/1.1725092]

Keywords: *Heat Transfer, Laser, Stress, Thermal*

I Introduction

Thermal and thermomechanical phenomena in laser materials interaction have attracted much attention due to the rapid development of lasers and their applications in materials processing. Laser metal interaction differs from laser dielectric interaction in terms of laser absorption and thermal transport mechanisms. In dielectrics, the laser energy is directly absorbed by molecules and the laser induced thermal transport is sustained by the vibration movement of molecules. On the other hand, in metals the laser energy is absorbed by free electrons, thereby resulting in a temperature gradient in electrons and a temperature difference between electrons and the lattice. The lattice is subsequently heating up through the energy exchange between electrons and the lattice [1].

Attributed to ultrafast laser metal heating and the resulting intense structural change, Molecular Dynamics (MD) simulations have been employed to investigate the pertaining thermal and thermomechanical phenomena at atomic levels. By incorporating the energy transfer from electrons to lattice, Häkkinen and Landman [2] have investigated the superheating, melting, and annealing of copper surfaces under picosecond (ps: 10^{-12} second) laser irradiation. Applying the Morse potential [3] to two-dimensional MD simulation, Horiuchi et al. [4] investigated ps laser induced ablation in Fe and compared the results with experiments quantitatively. However, it needs to be pointed out that MD simulations using the Morse potential do not take account of the thermal transport sustained by the movement of free electrons, which accounts for the major thermal transport in metals. In order to account for the thermal transport by free electrons, Ohmura et al. [5] modified the MD simulation using the Morse potential by implementing a forced thermal conduction among atoms. Using this modified MD simulation, they studied the temperature field and laser induced ablation in ps laser Al interaction.

It is worth noting that during laser metal interaction, the laser energy is absorbed by free electrons, and then free electrons transfer the energy to the lattice. This two-step heating has significant effects on laser induced thermal and thermomechanical phenomena [6–8]. In addition, due to the high thermal conductance nature of metals, the limited size of targets in MD simulation imposes much constraint on thermal transport, thereby inducing unrealistic phenomena in laser induced material ablation.

In this work, MD simulation is modified a great deal to study thermal and thermomechanical phenomena in ps laser copper interaction. The laser beam absorption in, and the thermal transport sustained by free electrons, and the energy exchange between electrons and the lattice are taken into account to give a detailed picture of laser copper interaction. Special treatment of boundary conditions at the back side of the MD domain is introduced to simulate a semi-infinite material irradiated by a ps laser pulse. Emphasis is placed on stress wave reflection from the back side of the MD domain and its strong influence on the structural damage. Methodologies of the MD simulation are described in Sec. II and simulation results are presented in Sec. III.

II Simulation Methods

The problem to be addressed is associated with a copper crystal at an initial temperature of 300 K illuminated with a ps laser pulse. The basic procedure is to solve the Newtonian equation for each atom interacting with its neighbors,

$$m_i \frac{d^2 r_i}{dt^2} = \sum_{j \neq i} F_{ij} \tag{1}$$

where m_i and r_i are the mass and position of atom *i*, respectively. F_{ij} is the interaction force between atoms *i* and *j*, which is calculated from the Morse potential as $F_{ij} = -\partial \phi_{ij} / \partial r_{ij}$ with $r_{ij} = r_i - r_j$. The Morse potential ϕ_{ij} takes the form of [3]

$$\phi_{ij} = D(e^{-2\sigma(r_{ij}-r_0)} - 2e^{\alpha(r_{ij}-r_0)}) \tag{2}$$

where D is the dissociation energy, r_0 is the equilibrium distance of atoms, and α is a constant of the dimension of reciprocal distance.

Contributed by the Heat Transfer Division for publication in the JOURNAL OF HEAT TRANSFER. Manuscript received by the Heat Transfer Division March 31, 2003; revision received January 21, 2004. Associate Editor: C. P. Grigoropoulos.

Table 1 Values of the parameters used in the MD simulation [3,10,12–15]

Parameters	Values
Atomic mass, m (kg)	1.055×10^{-25}
Dissociation energy, D (eV)	0.3429
Constant, α (m^{-1})	1.3588×10^{10}
Lattice constant of copper, a (nm)	0.361
Equilibrium distance, r_0 (nm)	0.2866
Time step, δt (fs)	5
Electron-lattice coupling, G ($\mathrm{W/m^3\cdot K}$)	4.8×10^{16}
Volumetric specific heat of free electrons, C_e ($\mathrm{J/m^3\cdot K}$)	2.1×10^{4}
Thermal conductivity of free electrons, k_e ($\mathrm{W/m\cdot K}$)	386
Volumetric specific heat of lattice, C_l ($\mathrm{J/m^3\cdot K}$)	3.439×10^{6}
Laser beam absorption depth, τ (nm)	12.60
t_0 (ps)	10
t_1 (ps)	3
Laser fluence, E ($\mathrm{J/m^2}$)	2000

Values of these parameters used in the calculation are listed in Table 1. In the calculation, the half-step leap-frog scheme, a modification to the velocity Verlet algorithm [9], is employed to solve the movement of atoms with a time step of 5 fs (fs: 10^{-15} second). When the distance between atoms exceeds a certain value r_c, namely the cutoff distance, the interaction between them is negligible, and no force computation is necessary. The cutoff distance is chosen to make sure that the neglected interaction force is much smaller than the typical force between atoms. In this work, it is found that a cutoff distance of 0.684 nm is appropriate in terms of the uncertainty and computation time requirement. At this distance, the potential of an atomic-pair is less than 1% of the well depth of the Morse potential. The force between two atoms of a distance of 0.684 nm is less than 0.2% of the force (the typical force) between two nearest neighboring atoms in equilibrium positions.

Pulsed laser heating in the target is achieved in two steps. First, the laser beam is absorbed by free electrons following the equation [1,6]

$$C_e\frac{\partial T_e}{\partial t}=k_e\frac{\partial^2 T_e}{\partial z^2}-G(T_e-T_l)+I\cdot\tau^{-1}\cdot e^{-z/\tau} \tag{3}$$

where C_e, T_e, and k_e are the volumetric specific heat, temperature, and thermal conductivity of free electrons, respectively. T_l stands for the lattice temperature, G is the electron-lattice coupling constant, and z is the direction normal to the target surface. Equation (3) describes the evolution of the temperature of free electrons under thermal diffusion, laser heating, and electron-lattice coupling. The laser beam is assumed to be absorbed exponentially with a characteristic absorption depth τ. The wavelength of the laser beam is presumed to be 0.8 μm, which is the wavelength of the Ti:sapphire ps laser. At this wavelength, the absorption depth τ in copper is 12.60 nm [10]. The laser intensity assumes a Gaussian temporal distribution in the form of

$$I=I_0e^{-(t-t_0)^2/t_1^2} \tag{4}$$

where t_0 and t_1 are taken as 10 ps and 3 ps, respectively, indicating that the laser pulse has an FWHM (full width at half maximum) of 5 ps centered at 10 ps. In this paper, the laser intensity used in Eqs. (3) and (4) is the one absorbed by the material rather than the incident laser intensity before reflection. Therefore, no reflectivity is used in Eq. (3).

In the second step of laser heating, the energy of free electrons is transferred to the lattice through electron-lattice coupling [1,6]

$$C_l\frac{\partial T_l}{\partial t}=k_l\frac{\partial^2 T_l}{\partial z^2}+G(T_e-T_l) \tag{5}$$

where C_l and k_l are the volumetric specific heat and the thermal conductivity of the lattice, respectively.

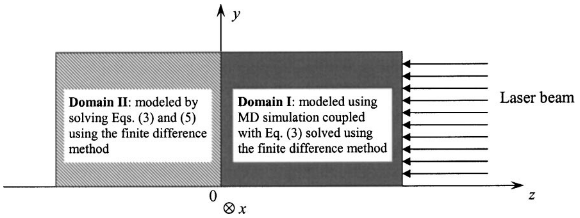

Fig. 1 Schematic of the computational domain

The schematic of the computational domain is shown in Fig. 1. An extra space is added above the target, which allows macromotion of atoms in the positive z-direction. The target is divided into two domains I and II as shown in Fig. 1. In Domain I the laser beam is absorbed and the target experiences intense thermal transport and phase change. In this domain, the movement of atoms is solved using MD simulation, which is described by Eq. (1). Since MD simulation can not capture the thermal transport by free electrons, Eq. (3) is solved using the finite difference method in this domain to predict the thermal transport by electrons. Equation (3) is integrated with MD simulation through the energy exchange between electrons and atoms (lattice). The lattice heating through the energy exchange with free electrons is achieved by exciting the kinetic energy of atoms in MD simulation, which is fulfilled by scaling the velocity of copper atoms with a factor χ

$$\chi=\left[1+\frac{\Delta t\cdot G(T_e-T_l)\cdot\Delta V}{\frac{1}{2}\sum_{i=1}^{N}m_i\cdot[(\nu_{i,1}-\overline{\nu_1})^2+(\nu_{i,2}-\overline{\nu_2})^2+(\nu_{i,3}-\overline{\nu_3})^2]}\right]^{1/2} \tag{6}$$

where $\nu_{i,j}$ and $\overline{\nu_j}$ ($j=1,2,3$) are velocities of atom i and the average velocity in the x, y, and z directions for atoms in a layer of volume ΔV normal to the laser beam. N is the number of atoms within the layer and Δt is the time step. The new velocity $\nu'_{i,j}$ of atom i is calculated as

$$\nu'_{i,j}=(\nu_{i,j}-\overline{\nu_j})\cdot\chi+\overline{\nu_j}\quad j=1,2,3 \tag{7}$$

When density changes, such as void formation in the target, the electron-lattice coupling constant G is adjusted by multiplying a factor, which is the ratio of the local density to the full density of copper. In addition, the specific heat, density, and thermal conductivity of electrons are adjusted in the same manner. The density and specific heat of the lattice are computed by the MD simulation automatically, which directly tracks the movement of atoms. During the preparation of this paper, it came to our knowledge that laser-metal interaction was studied using the similar method as that described in this paper [11,12]. In these studies, the model developed by Häkkinen and Landman [2] was employed which added an extra term in Eq. (1) to account for the energy exchange between electrons and the lattice. Treatment of this lattice-electron coupling is different from the atomic velocity scaling described by Eq. (7) in this work, and does not the meet the requirement of momentum conservation, which may cause undesirable atomic movement.

In Domain II as shown in Fig. 1, heat transfer is calculated by solving Eqs. (3) and (5) using the finite difference method. This semi-infinite solid copper plays the role of conducting the heat away from Domain I, which experiences intense phase change. For atoms close to the back side of Domain I, two extra forces arise in the presence of the semi-infinite solid copper. One force originates from the static interaction between the MD domain and the semi-infinite solid sample. The static interaction represents the interaction between atoms in Domain I and those in Domain II when there is no stress in space. We place a layer of static atoms with a thickness of the cutoff distance in Domain II next to the interface between Domains I and II. The force exerted by atoms in

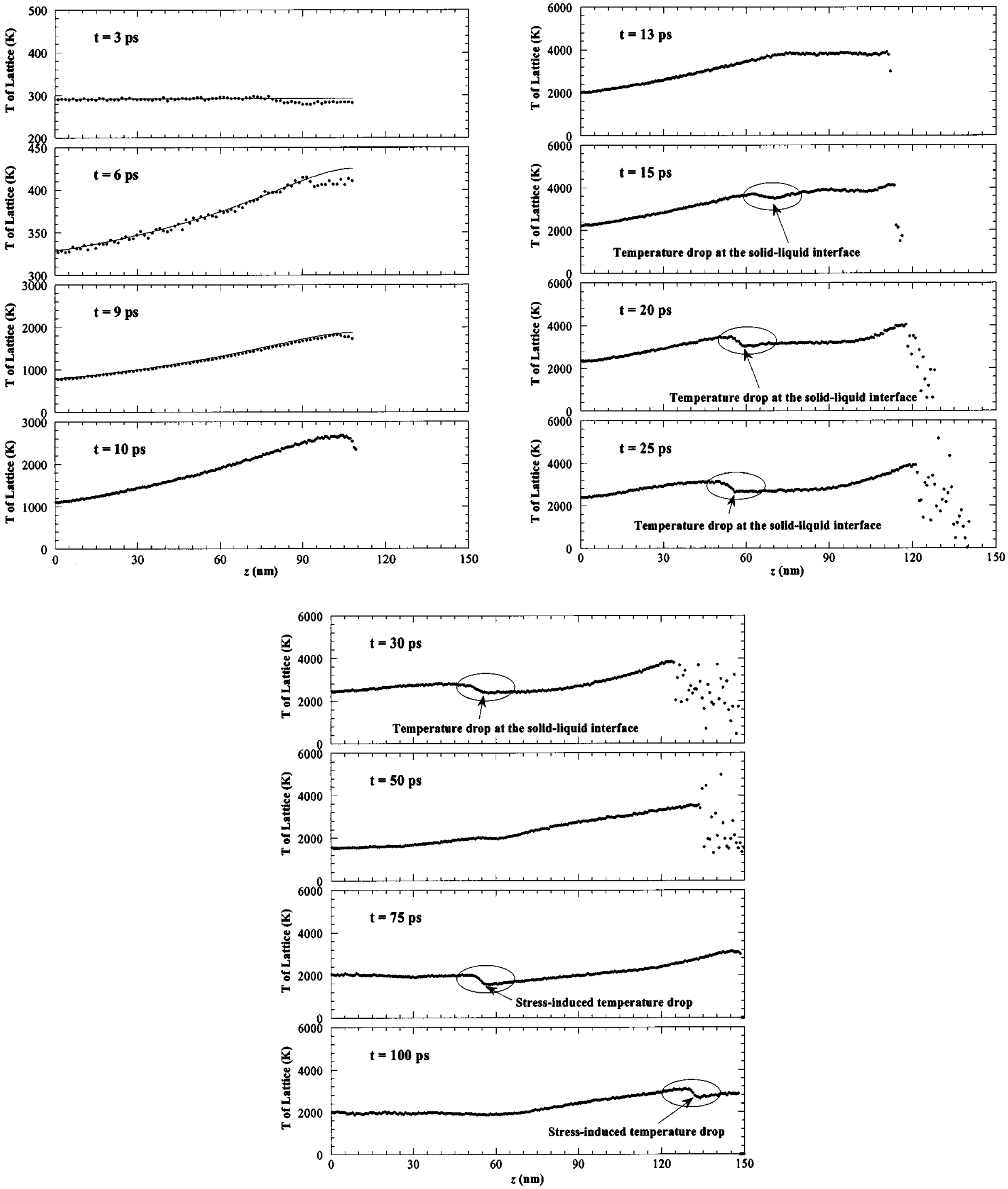

Fig. 2 The temperature distribution of lattice at different times. Solid line: numerical computation using the finite difference method; dots: MD simulation.

Domain II on those in Domain I represents the static interaction. The other force exerted on atoms in Domain I close to the interface between Domains I and II is induced by the stress wave propagation in the *z*-direction and is in the form of [13]

$$F_s = -\rho v c \cdot A/N \qquad (8)$$

where ρ is the density of the target, v is the average velocity in the z direction for atoms within one small layer close to the back side, and c is the speed of the stress wave in the z-direction. A is the cross-sectional area of the target, and N is the number of atoms within the small layer close to the back side of Domain I. Periodic boundary conditions are implemented on boundaries in the x and y directions and free boundary conditions on boundaries in the z-direction.

When solving Eq. (3) in Domain I and Eqs. (3) and (5) in Domain II, constant properties are used, which are evaluated at 300 K. In the MD simulation part, introduction of Eq. (3) is used to consider the effect of heat transfer by electrons, which could not be accounted for by the classical MD simulation. It is true that the properties such as thermal conductivity and specific heat of electrons are temperature dependent. This paper presents our first step to study laser-metal interactions and we assume these prop-

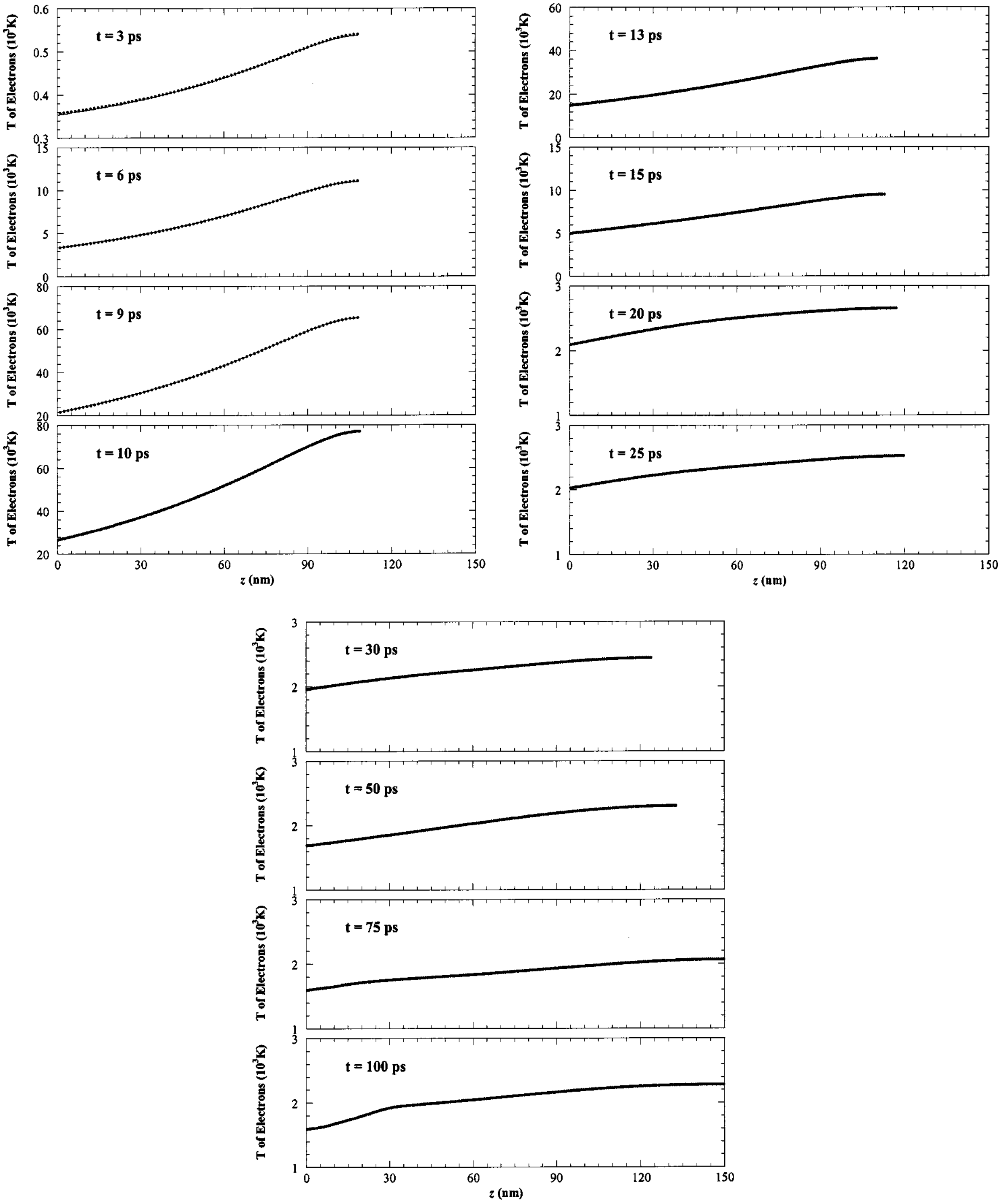

Fig. 3 The temperature distribution of electrons at different times. Solid line: numerical computation using the finite difference method; dots: MD simulation.

erties constant to simply the computation and provide a general picture about the physical processes underlying laser-metal interaction. These assumptions may affect the simulation results to a certain extent, but will not alter the general conclusions made in the paper, which is intended to provide qualitative interpretations of laser-metal interaction. In the laser-copper interaction studied in this work, intense phase change takes place in the material, which absorbs substantial thermal energy from electrons. This will reduce the uncertainty in heat conduction induced by the assumption of constant properties of electrons. Equations (3) and (5) are solved to obtain the temperature distribution in Domain II as specified in Fig. 1. Domain II is used to conduct the thermal energy from the MD domain (Domain I). The temperature distribution in Domain II is largely influenced by the thermal conductivity of electrons and the density and specific heat of the lattice. Therefore, the assumption of constant specific heat of electrons in Domain II has little effect on temperature distribution while at most times electrons and the lattice have close temperatures. In addition, the density and specific heat of the lattice and the thermal conductivity of electrons from 300 K to the melting point are pretty much constant.

Before laser heating starts, the sample is thermalized for 100 ps

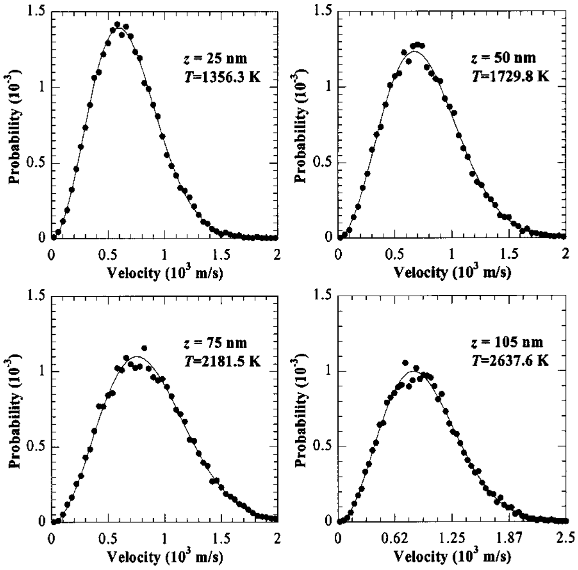

Fig. 4 Velocity distribution in comparison with the Maxwellian distribution at different locations during laser heating (t =10 ps). The temperature shown in the figure is the local temperature used for calculating the Maxwellian distribution. Dots: MD simulation; solid line: Maxwellian distribution.

to reach thermal equilibrium. In this calculation, the MD domain is initially constructed based on the fcc lattice structure with the (100) surface facing the laser beam. Values of the parameters used in the simulation are listed in Table 1 [3,10,14–17]. The computation is conducted on a two-processor workstation using OpenMP (open multiple processing) as the algorithm for parallel computation. Before conducting simulation of laser-copper interaction, we calculate the specific heat and melting point of copper to obtain the idea about the accuracy of the Morse potential in terms of predicting the behavior of copper. The specific heat of copper is calculated by adding a certain amount of energy to a copper system and observing the final temperature increase. The specific heat is calculated to be 405 J/kg·K at 300 K, which is close to the experimental result of 385 J/kg·K [17]. The melting point of copper is obtained by increasing the temperature of a copper system until the regular lattice structure is completely destroyed. We find that the Morse potential predicts a melting point of 2090 K, higher than the experimental value of 1385 K [17].

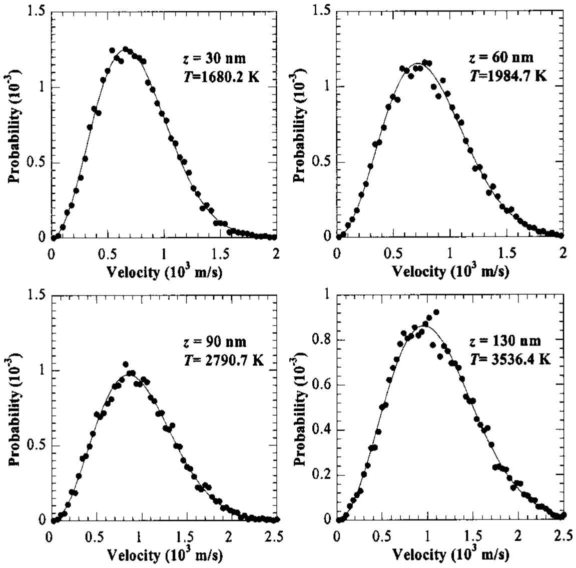

Fig. 5 Velocity distribution in comparison with the Maxwellian distribution at different locations after laser heating (t =50 ps). The temperature shown in the figure is the local temperature used for calculating the Maxwellian distribution. Dots: MD simulation; solid line: Maxwellian distribution.

III Results and Discussion

In this work, the target for MD simulation is constructed to have 45, 45, and 300 fcc (face-centered cubic) unit cells in the x, y, and z-directions, respectively. A total of 2,430,000 atoms are tracked in the simulation. Measurements of the MD domain are 16.245 nm in the x and y directions, and 108.3 nm in the z-direction. The computational domain has the same size as the target in the x and y-directions. In the z-direction, the computational domain is taken as 2.608 μm to capture atoms escaping from the target surface during the time of computation. The laser pulse assumes a fluence (E) of 2000 J/m^2, which is estimated to be high enough to induce phase change and material ablation. At this laser fluence, the constant (I_0) in the temporal laser intensity expressed by Eq. (4) is $I_0 = E/(\sqrt{\pi} t_1) = 37.6126$ GW/cm^2.

III.1 Temperature Distribution in the Target. The temperature distribution in the lattice is displayed in Fig. 2. For the purpose of comparison, Eqs. (3) and (5) have been solved in Domain I using the finite difference method before phase change takes place. The results obtained using the finite difference method are shown at 3, 6, and 9 ps at which little or no phase change is observed. It is much pronounced that before phase change takes place, the MD simulation and the finite difference method are in good agreement in terms of predicting laser heating and thermal transport. Beyond 9 ps, phase change originates so only the MD simulation results are presented in Fig. 2. Before 13 ps, the temperature of the lattice experiences a continuous increase. However, it is important to note that when the lattice temperature reaches about 3850 K (t = 13 ps), no further temperature increase is observed. This phenomenon is clearly demonstrated by the temperature distribution at 13 ps for which a flat region of 3850 K is observed. The phase change from solid to liquid (detailed in III.2) absorbs a great deal of energy deposited by the laser beam, thereby suppressing further increase of the lattice temperature.

A close look at Fig. 2 reveals that starting from 15 ps (just after laser heating), a temperature drop appears in the spatial distribution. This temperature drop becomes abrupt at 20 and 25 ps, which is marked by circles in Fig. 2. As will be discussed below, this temperature drop originates from the phase change from solid to liquid. Further study finds that the location of this abrupt temperature change is the same as the location of the solid-liquid interface. The energy absorbed by the liquid during phase change explains the temperature drop observed in Fig. 2. At 13 ps in Fig. 2, a sudden temperature drop is not visible although a solid-liquid interface is observed in Fig. 6. This is because that at 13 ps, the material is still experiencing intense laser heating, which can provide the energy needed for melting. In addition, we find that before (including) 12 ps, no clear solid-liquid interface is observed although the front of the material is being melted. It is the movement of the solid-liquid interface (meaning melting is taking place) that induces the local temperature drop. At 13 ps, the solid-liquid interface starts to move, which takes time to induce the local temperature drop.

We study the melting point of the copper modeled using the Morse potential and find that this potential overpredicts the melting point and reports a value of 2090 K, higher than the melting point of copper [17]. At the solid-liquid interface, it is observed that the local temperature is greatly above 2000 K, exceeding the modeled melting point. Super heating has also been observed in the recent work by Schäfer et al. [11]. In addition to the temperature change resulting from phase change before 75 ps, another sudden temperature change has been observed after phase change

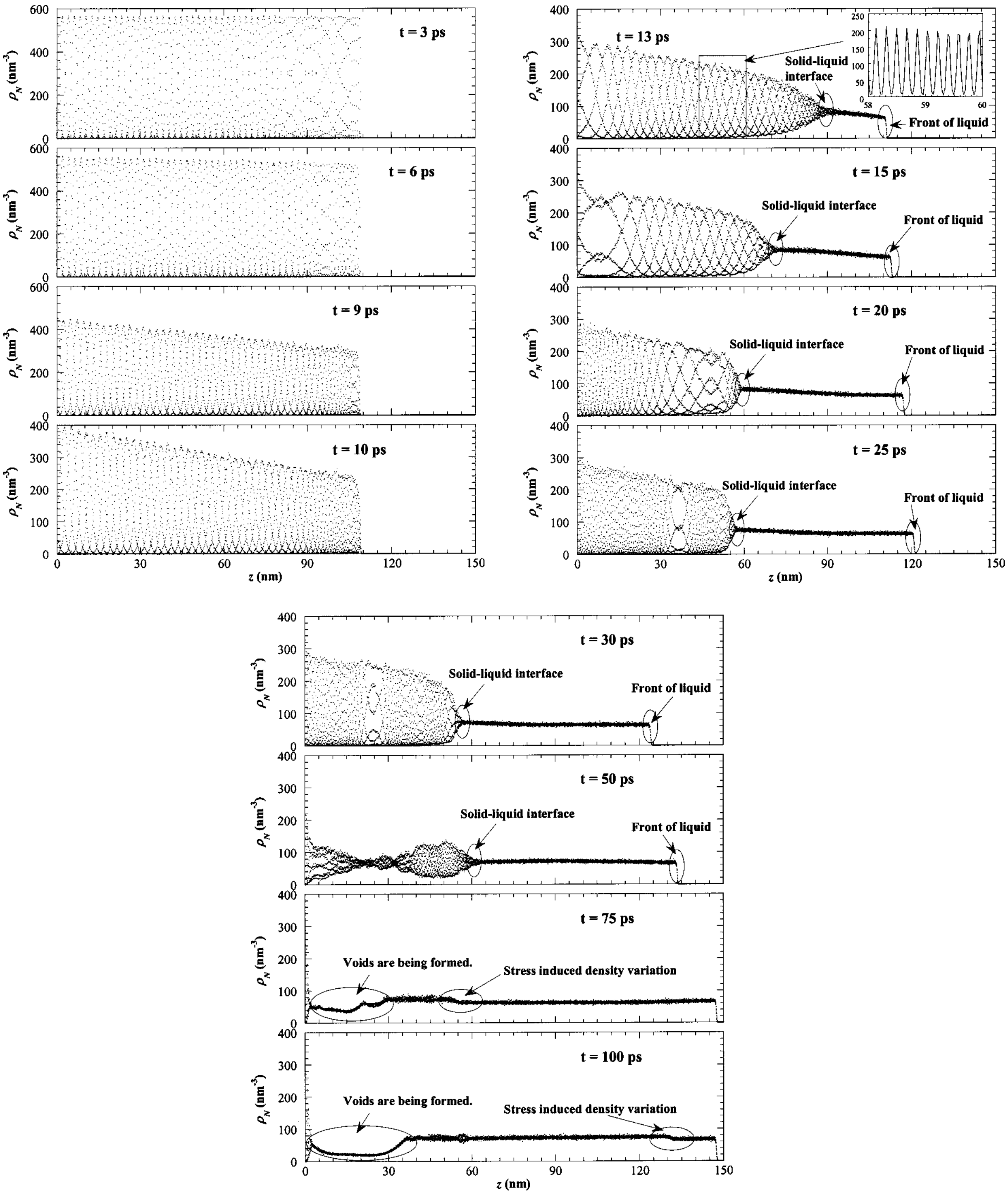

Fig. 6 Number density distribution in space at different times

finishes, which is marked by circles in Fig. 2 at 75 and 100 ps. This temperature change is a direct consequence of the sharp stress variation in space and will be discussed in III.3.

Presented in Fig. 3 is the temperature distribution of electrons. At 3, 6, and 9 ps, the MD simulation results are compared with those obtained with the finite difference method, and good agreements are observed. The temperature of electrons is characterized with a maximum level of about 78,000 K at 10 ps. At 15 ps (just after laser heating), the electron temperature quickly decreases to 10,000 K due to the intense energy exchange with the relatively cold lattice. From 15 ps to 20 ps, the temperature of electrons quickly decays to below the lattice temperature. Subsequently, electrons play the role of cooling the lattice and transferring the energy to the inside of the target.

When calculating the energy transfer from electrons to atoms in Domain I, the technique (Eqs. (6) and (7)) used to excite the kinetic energy of atoms meets the requirement of momentum conservation, but could disturb the local thermal equilibrium. The use of temperature to describe laser induced heating and thermal transport within the target can be justified by looking into the thermal equilibrium of the target during and after laser heating. Figure 4 shows the velocity distribution at different locations at 10

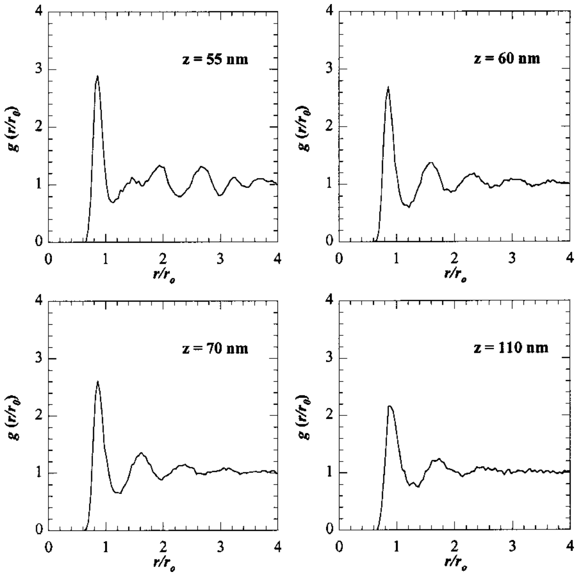

Fig. 7 In-plane radial distribution function at different locations for $t=20$ ps

ps (during laser heating). Also shown in Fig. 4 is the Maxwellian distribution in comparison with the MD results. It is evident that the velocity distribution of atoms follows the Maxwellian distribution closely, even at the very front of the target ($z=105$ nm). The equilibrium status of the target after laser heating is examined by comparing the velocity distribution of atoms with the Maxwellian distribution at different locations, including the front of the target ($z=130$ nm) at 50 ps. The comparison is presented in Fig. 5, which shows a good agreement between the atomic velocity distribution and the Maxwellian distribution, thereby confirming the existence of thermal equilibrium within the target and justifying the use of temperature.

III.2 Structural Change of the Target. In this section, the structural change within the target is investigated by looking into the number density distribution of atoms in space and the radial distribution function at different locations.

The number density is a measure of the number of atoms per unit volume. Its variation in space reflects the structural variation of the target [18]. Figure 6 presents the number density distribution at different times. In Fig. 6, no obvious solid-liquid interface is observed before 10 ps. At 13 ps, melting has happened, and a clear solid-liquid interface is evident, which is circled in the plot. The number density distribution in solid (to the left of the circle) has a regular pattern and is detailed in the inset. The periodically varying number density is attributed to the regular structure of the lattice. To the right of the circle is liquid, and its number density is uniform, which is a result of the random distribution of liquid atoms in space. It is apparent in Fig. 6 that the solid-liquid interface is moving toward the solid, meaning more solid is being melted. At the same time, a visible movement of the liquid front toward the right is observed, which is circled in the plot. When solid melts, its density becomes less, and the volume of the material will expand, thereby inducing the toward-out movement of the liquid front. The number density distribution at 50 ps reveals that solid and liquid structures co-exist in the rear part of the target, meaning melting takes place in this region simultaneously and is not characterized by a clear movement of the solid-liquid interface. This phenomenon could be attributed to the small thickness of the target and the boundary condition applied to the interface between Domains I and II. For instance, the reflected stress wave from the interface can strongly disturb the material close to the interface, making them melt simultaneously. We have performed large-scale parallel MD simulations to study this boundary and thickness effect. The target used is about 1.234 μm (consisting of more than 27 million atoms), which is more than ten times the thickness of the target studied in this work. In this extended study, no finite difference domain is added below the MD domain and a free boundary condition is employed. The results show that melting is characterized with a rapid movement of the solid-liquid interface, and no simultaneous melting is observed.

At 75 ps, the target has been melted completely, and the visible low number density in space is attributed to the formation of voids within the liquid. More details will be discussed in III.4. Furthermore, an insignificant, yet visible number density variation is observed at 75 and 100 ps. This number density change originates from the sharp stress change in space and is explained in detail in III.3. Based on locations of the solid-liquid interface and the front of liquid at 13 and 20 ps, it is estimated that during this period, the solid-liquid interface moves at a speed of 4400 m/s, and the front of the liquid moves out at a speed of 860 m/s. The calculated speed of the solid-liquid interface (~4400 m/s) is close to the sound speed in the [100] direction in copper (4364 m/s) [10]. Similar high-speed movement of the melt front was observed in the MD simulation about picosecond laser-copper interaction [11]. In that work, Schäfer et al. [11] reported a melt front velocity of the order of $1\text{-}2\times10^3$ m/s in a copper irradiated with a laser pulse of 0.5 ps duration and 680 J/m^2 fluence (absorbed).

In addition to the number density distribution, the radial distribution function also reflects the structure of the target. In this work, the in-plane radial distribution function $g(r/r_0)$ [18] is studied, which is a ratio of the number of atoms at a distance r from a given atom to the number of atoms at the same distance in an ideal gas with the same density. Figure 7 presents the in-plane radial distribution function at 20 ps. It is revealed that to the left of the solid-liquid interface, the radial distribution function is characterized with a number of peaks ($z=55$ nm), which are attributed to the regular structure of the solid. At locations of 60 nm and 70 nm (to the right of the solid-liquid interface), the short range order structure is still preserved while the long-range order is disappearing. This is reflected by the diminishing peaks at the long distance ($r/r_0=3$ or greater), meaning the materials are losing the long-range order structure. At the front of the liquid ($z=110$ nm), a typical liquid structure is observed, which is characterized by the two short-range peaks in the radial distribution function.

III.3 Stress Evolution in the Target. During laser material interaction, a stress wave will be generated and propagate toward the inside of the material. In this work, the stress is calculated based on the velocity and position of atoms. In the work by Wang and Xu [19], the stress was calculated by directly evaluating the atomic interaction force across a cross section of interest. Although the trend and amplitude of the stress were captured, substantial noise was observed in the calculation results. In this work, the stress is averaged over a small domain to suppress the statistical uncertainty following the equation

$$\sigma_{mn}=-\frac{1}{\Delta V}\left(\sum_{j\neq i}^{N} r_{ij,m}F_{ij,n}+\delta_{mn}\cdot Nk_BT\right) \tag{9}$$

where $r_{ij,m}$ and $F_{ij,n}$ are the distance and force between atoms i and j in the m and n directions, respectively. N is the number of atoms within a small domain of a volume ΔV. δ_{mn} is the delta function, which is 1 for $m=n$ and 0 for $m\neq n$. In the beginning of laser heating, the normal stress is the same in the x, y and z directions, and the shear stress is negligible. However, when voids are formed in the target, the shear stress becomes appreciable and the normal stress is not the same in the x, y and z directions. This issue will be addressed elsewhere. In this work, only the normal stress in the z direction (the laser irradiation direction) is discussed in detail. Figure 8 shows the stress wave generation and propagation in the copper target. At 3 ps, laser

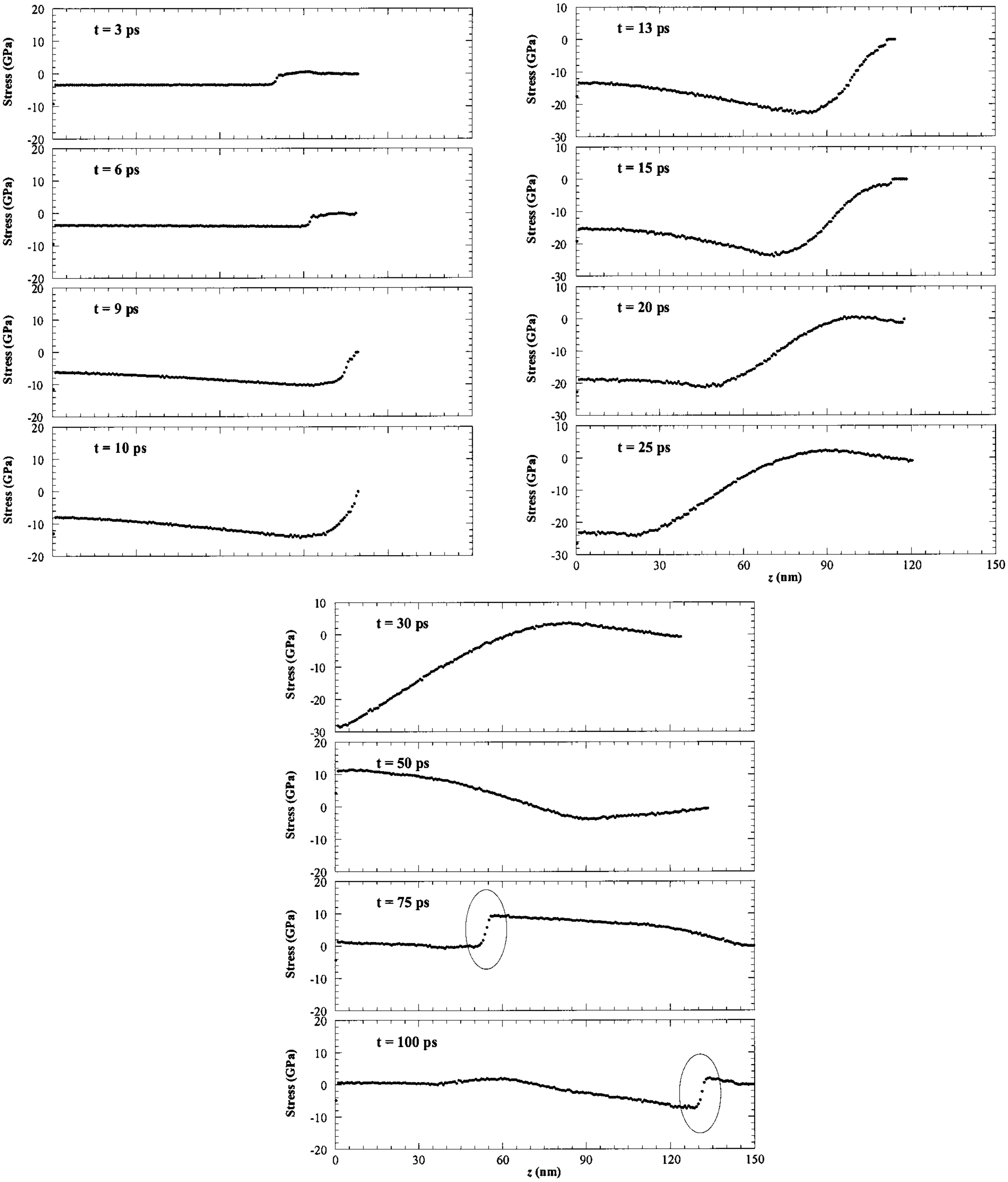

Fig. 8 Stress distribution in space at different times

heating is weak, and the visible non-zero stress originates from the initial construction of the target. At 9 ps, it is seen that a compressive stress has been generated in the near surface region. From 9 ps to 20 ps, the stress wave experiences an emerging process. At 25 ps, it is apparent that the stress wave consists of a strong compressive stress (~25 GPa) and a weak tensile stress (~3 GPa). This stress wave generation has the same characteristic as the one revealed in ps laser argon interaction [19]. In the MD simulation, we carefully monitor the development and propagation of the initial non-zero stress and find that this stress is induced by the design of the initial sample. This stress propagates in space with the same amplitude and does not cause structural damage. In addition, we conduct large-scale parallel MD simulation and observe the similar behavior of the nonzero initial stress. In the large-scale MD simulation, we used a much larger target (1.234 μm of thickness). A similar nonzero initial stress was observed with the same amplitude as the one observed in this paper. Our large-scale MD simulation with free boundary conditions indicates similar stress as the one observed in this work before reflection at the back side of the MD domain. This ensures that the large compressive stress observed in this work arises from the laser-material interaction and is not an amplification of the initial stress by the boundary conditions.

At 30 ps in Fig. 8, the compressive stress has reached the back

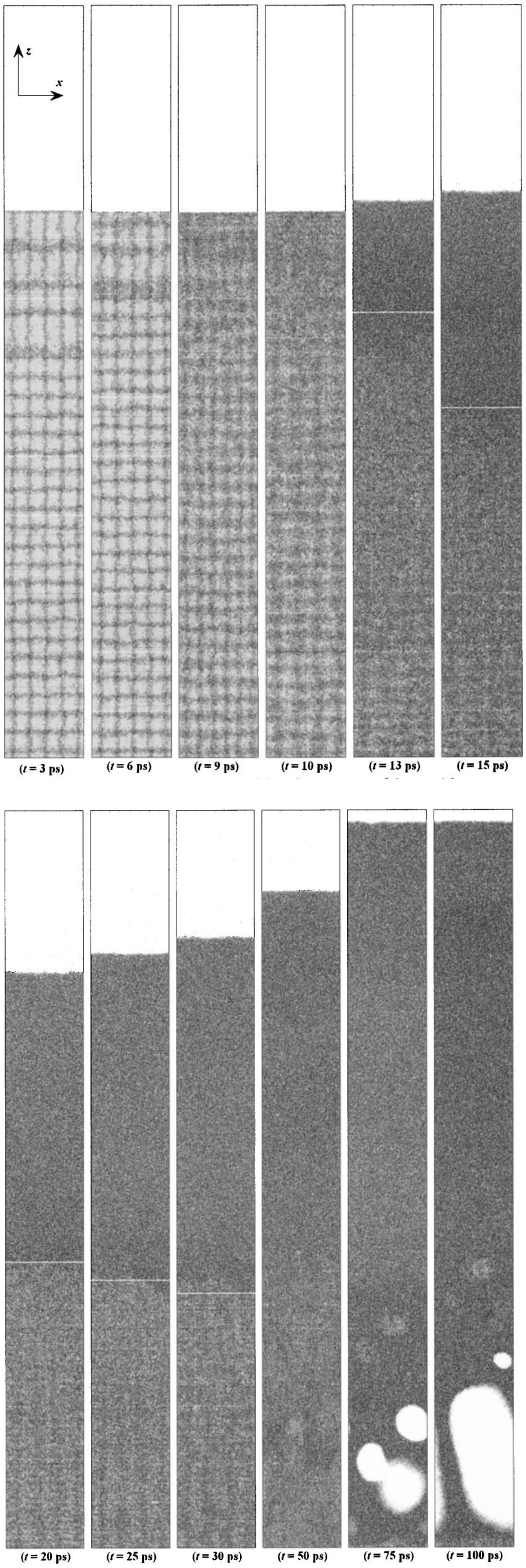

Fig. 9 Snapshot of atomic positions in the space of $0<x<16$ nm, $7.37<y<8.87$ nm, and $0<z<150$ nm. The horizontal white lines mark the approximate position of the solid-liquid interface.

side of the MD domain and is being reflected back. The boundary condition introduced by Eq. (8), which is intended to eliminate the reflection of the stress wave, could not eliminate the stress wave reflection completely. The speed c used in Eq. (8) is taken as 4364 m/s by assuming the target is a solid copper at room temperature [10]. On the other hand, in Figs. 2, 6, and 8 it is evident that when the stress wave reaches the back side ($t=30$ ps), the target is at a much elevated temperature (~2400 K) and has been melted partially. Based on the location of the peak compressive stress at 13 and 25 ps, it is estimated that the stress wave is traveling at a speed of about 5000 m/s, a little higher than the one used in Eq. (8). In addition, because of the much elevated temperature in Domain I, the spacing between atoms in this domain changes much, which is much different from the constant atomic spacing used in Domain II. Therefore, this structure mismatch will have a contribution to the wave reflection at the interface. Nevertheless, the boundary condition expressed by Eq. (8) does reduce the stress wave reflection, which is dictated by the smaller magnitude of the reflected stress (~10 GPa) compared with the larger magnitude of the incident stress (~28 GPa).

In Fig. 8, it is evident that after reflection, the compressive stress becomes a tensile stress. It has been observed in previous research that with a free boundary condition at the back side of the target, the stress wave is completely reflected [19]. After reflection, the speed of the stress wave reduces to 3080 m/s, much smaller than the speed of the incident stress wave. This could be explained by the fact that after 75 ps, the target has been melted completely, and the liquid sustains a lower wave speed than the solid does. Propagation of the reflected tensile stress is characterized with a substantial dissipation. At 75 ps, the tensile stress has a magnitude of 10 GPa located at 55 nm, while after only 25 ps, its magnitude decays to 2 GPa after traveling only about 77 nm. This reveals the fact that liquid has a limited capability of sustaining tensile stress waves. In addition, our careful study of the wave propagation from 75 ps to 100 ps reveals that there is a strong interaction between the reflected stress wave and the incident stress wave. This is because the stress generated by laser heating has a great span in space, making the reflected wave interact with the incident wave, complicating the stress distribution in space. At 75 and 100 ps, one abrupt change of the stress in space is observed, which is marked with circles in Fig. 8. This abrupt stress change could be attributed to some stress reflection at the interface between Domains I and II and the interaction between the reflected stress and the incident stress. This abrupt stress change means a rapid temporal stress variation at the local position, thereby inducing the sudden temperature change observed in Fig. 2. This temperature change is related to the local stress as [19]

$$\partial T_l/\partial t \sim -B/(B+4/3\cdot G)\cdot \beta_T T_0/(\rho c_p)\cdot \partial\sigma/\partial t \tag{10}$$

Equation (10) has been discussed by Wang and Xu in detail elsewhere [19]. In this stress-temperature relation, B, G, β_T, ρ, c_p are the bulk and shear moduli, the thermal expansion coefficient, density and specific heat of the material, respectively. In addition to the induced temperature variation, the abrupt stress change marked in Fig. 8 at 75 and 100 ps also induces a visible variation of the number density of atoms, which is marked in Fig. 6. The tensile stress intends to pull the material apart, thereby inducing a visible number density drop.

III.4 Snapshots of Atomic Positions. Figure 9 presents the snapshots of atomic positions at different times with each dot representing one atom. For the purpose of illustration, only the domain of $0<x<16$ nm, $7.37<y<8.87$ nm, and $0<z<150$ nm is displayed in Fig. 9. It is apparent that at 3 and 6 ps, a regular structure is observed. Although the regular lattice structure is still preserved at 9 and 10 ps, atoms spread more in space, especially in the near surface region. This is because the temperature of the target is increasing due to laser heating, thereby resulting in a more intense random movement of atoms and spreading them more in space. This reduction of the structural regularity explains the decay of the peak number density of atoms, especially in the near surface region as observed at 9 and 10 ps in Fig. 6. At 13 ps, it is apparent that in the near surface region, positions of atoms become completely random, meaning the target has lost the regularity of the structure, and solid no longer exists in this region.

At 20, 25, and 30 ps, a clear solid-liquid interface is much pronounced, which is marked with a white horizontal line. In the liquid region, atoms become random in space, and the picture looks dark. On the other hand, the picture looks light in the solid region due to the regular position of atoms in space. An interesting phenomenon is observed at 75 and 100 ps, which is characterized with voids formed inside the liquid. The tensile stress has a great contribution to the formation of voids because the tensile stress intends to pull the atoms apart in the material. At 75 and 100 ps, the material is liquid which has limited capability of sustaining tensile stress and the atoms inside are easy to be pulled apart. The existence of this tensile stress is a direct consequence of the reflection of the compressive stress at the back side of the MD domain. This suggests that in laser materials interaction, especially for thin films deposited on substrates or for free-standing thin films, the reflection of the compressive stress at the back side of the film makes the compressive stress become tensile; this tensile stress could result in a structural damage in the region close to the back side.

IV Conclusion

In this work, MD simulation was carried out to investigate the thermal and thermomechanical phenomena in ps laser copper interaction. Superheating was observed, and the early period of phase change from solid to liquid was characterized with a solid-liquid interface movement at a speed of 4400 m/s. However, the latter phase change from solid to liquid happened in the target simultaneously with no visible movement of solid-liquid interface. The results showed that the laser induced stress wave consisted of a strong compressive stress and a weak tensile stress. The strong tensile stress emerging after stress wave reflection at the back side of the MD domain exceeded the limitation that can be sustained by the target and intended to pull the material apart. As a direct consequence, voids were formed in the interior of the liquid near the back side of the MD domain, indicating that the strong tensile stress in laser materials interaction played an important role in inducing structural defect in the target. Propagation of this strong tensile stress was characterized with a remarkable decay, which could be attributed to the limited capability of liquid to sustain tensile stress waves and the interaction between the reflected and incident stress waves.

Acknowledgment

Financial support for this work from the College of Engineering and Technology and the Department of Mechanical Engineering at the University of Nebraska–Lincoln (UNL) is greatly acknowledged. This work is also partially supported by the Research Council of UNL through the Faculty Seed Grant. The author thanks Dr. Xianfan Xu of Purdue University and Dr. David A. Willis of the Southern Methodist University for their helpful discussions.

Nomenclature

A = cross-sectional area
B = bulk modulus
C_e = volumetric specific heat of free electrons
C_l = volumetric specific heat of lattice
c = stress wave speed
D = dissociation energy
F = interaction force between atoms
F_s = the force induced by stress wave propagation
G = electron-lattice coupling factor; shear modulus
g = radial distribution function
I = laser beam intensity
I_0 = constant in the laser intensity temporal distribution
k_e = thermal conductivity of free electrons
k_l = thermal conductivity of lattice
m = atomic mass
N = number of atoms
r = atomic position
r_c = cutoff distance
r_0 = equilibrium distance
T_e = temperature of free electrons
T_l = temperature of lattice
t = time
t_0 = time constant in the laser intensity temporal distribution
t_1 = time constant in the laser intensity temporal distribution
ν = velocity
x = coordinate in the x direction
y = coordinate in the y direction
z = coordinate in the z direction

Greek Symbols

α = constant in the Morse potential
β_T = thermal expansion coefficient
ϕ = Morse potential function
ρ = density
σ = stress
τ = laser beam absorption depth

Subscripts

i = index of atoms

References

[1] Anisimov, S. I., Kapeliovich, B. L., and Perelman, T. L., 1974, ''Electron Emission from Metal Surfaces Exposed to Ultra-short Laser Pulses,'' Sov. Phys. JETP, **39**, pp. 375–377.
[2] Häkkinen, H., and Landman, U., 1993, ''Superheating, Melting, and Annealing of Copper Surfaces,'' Phys. Rev. Lett., **71**, pp. 1023–1026.
[3] Girifalco, L. A., and Weizer, V. G., 1959, ''Application of the Morse Potential Function to Cubic Metals,'' Phys. Rev., **114**, pp. 687–690.
[4] Horiuchi, K., Ishiyama, M., Hasebe, T., Yukimura, K., and Imaida, Y., 1998, ''A Fundamental Study of Excimer Laser Ablation Using Experimental and MD Simulation Method,'' Mater. Chem. Phys., **54**, pp. 201–204.
[5] Ohmura, E., Fukumoto, I., and Miyamoto, I., 1999, ''Modified Molecular Dynamics Simulation on Ultrafast Laser Ablation of Metal,'' presented at the International Congress on Applications of Lasers and Electro-Optics, Laser Institute of America, Orlando, pp. 219–228.
[6] Qiu, T. Q., and Tien, C. L., 1993, ''Heat Transfer Mechanisms During Short-Pulse Laser Heating of Metals,'' ASME J. Heat Transfer, **115**, pp. 835–841.
[7] Tang, D. W., and Araki, N., 1996, ''The Wave Characteristics of Thermal Conduction in Metallic Films Irradiated by Ultra-short Laser Pulses,'' J. Phys. D, **29**, pp. 2527–2533.
[8] Wang, X., and Xu, X., 2002, ''Thermoelastic Wave in Metal Induced by Ultrafast Laser Pulses,'' J. Therm. Stresses, **25**, pp. 457–473.
[9] Allen, M. P., and Tildesley, D. J., 1987, *Computer Simulation of Liquids*, Clarendon Press, Oxford.
[10] Lide, D. R., 1994, *CRC Handbook of Chemistry and Physics: A Ready-Reference Book of Chemical and Physical Data*, Section 12, CRC Press, Boca Raton, FL.
[11] Schäfer, C., Urbassek, H. M., and Zhigilei, L. V., 2002, ''Metal Ablation by Picosecond Laser Pulses: A Hybrid Simulation,'' Phys. Rev. B, **66**, pp. 1–8.
[12] Ivanov, D. S., and Zhigilei, L. V., 2003, ''Combined Atomistic-Continuum Modeling of Short-pulse Laser Melting and Disintegration of Metal Films,'' Phys. Rev. B, **68**, pp. 1–22.
[13] Zhigilei, L. V., and Garrison, B. J., 1999, ''Pressure Waves in Microscopic Simulations of Laser Ablation,'' Mater. Res. Soc. Symp. Proc., **538**, pp. 491–496.
[14] Kittel, C., 1976, *Introduction to Solid State Physics*, 5th ed., John Wiley & Sons, New York.
[15] Lide, D. R., and Kehiaian, H. V., 1994, *CRC Handbook of Thermophysical and Thermochemical Data*, CRC Press, Boca Raton, FL.
[16] Tzou, D. Y., 1996, *Macro- to Microscale Heat Transfer-The Lagging Behavior*, Taylor and Francis, Washington.
[17] Incropera, F. P., and Dewitt, D. P., 2002, *Fundamentals of Heat and Mass Transfer*, 5th ed., John Wiley & Sons, New York.
[18] Wang, X., and Xu, X., 2002, ''Molecular Dynamics Simulation of Heat Transfer and Phase Change During Laser Material Interaction,'' ASME J. Heat Transfer, **124**, pp. 265–274.
[19] Wang, X., and Xu, X., 2003, ''Molecular Dynamics Simulation of Thermal and Thermomechanical Phenomena in Picosecond Laser Material Interaction,'' Int. J. Heat Mass Transfer, **46**, pp. 45–43.

Fluid-Dynamic Analysis and Optimization of the Quenching Process for Hardening of Change-Speed Gears Using DOE–ANOVA Method

Paolo M. Congedo
e-mail: paolo.congedo@unile.it

Antonio Ficarella

Domenico Laforgia

Dipartimento di Ingegneria
Dell'Innovazione-Crea,
Università Degli Studi di Lecce,
via per Arnesano,
Lecce, Italy, I-73100

This investigation deals with the fluid-dynamic behavior of the hardening process for change-speed gears, where a Nitrogen high pressure flow is used for quenching. At the end of the process, the gears showed a high planarity error due to a slow and non-homogeneous cooling process. A detailed fluid-dynamic calculation was performed to identify some possible technical improvements, such as varying some design parameters including the geometry configuration of the quenching chamber and the operating conditions. Three performance indexes have been defined to synthesize the quality of the hardening process and their trends have been evaluated as a function of the design and operative configuration by a DOE–ANOVA statistical analysis to obtain the best configuration. [DOI: 10.1115/1.1731355]

Keywords: *Forced Convection, Heat Transfer, Modeling, Processing, Unsteady*

Introduction

The mechanical components of a gearbox must strictly satisfy the quality requirements to achieve high tensile strength and long fatigue life, as today required by the automotive manufacturers to guarantee superior performances of the vehicles. Hardening is an extremely important aspect in gears production: at the end of the quenching phase in the gear hardening machine, defects such as high planarity errors must be avoided to guarantee high quality gears [1].

The fluid dynamic behavior of the quenching process affects heavily the planarity error shown by the gears. The cooling of the gears is performed using a high-pressure flow of Nitrogen. In particular, the gears located at the bottom of the quenching chamber (Fig. 1) show high values of the planarity defects; those defects are mainly due to a nonuniform cooling due to a Nitrogen flow, that is not homogeneously diffused, as shown in [2]. In fact, these gears are located downstream of the main cooling flow, where Nitrogen is characterized by a higher temperature (600 K and more) because of the heat subtracted from the gears encountered upstream.

Nevertheless, small differences in the quenching process (in terms of heat transfer rate) of different gears can be accepted, while differences in the cooling strength on the surfaces of the same gears are harmful for they cause the planarity errors. Planarity errors arise when the quenching process is too slow (due to the downstream increase of temperature of the Nitrogen flow), and, at the same time, surfaces of the same gear experience different cooling rates because of a nonuniform temperature distribution of the Nitrogen flow around the gear.

Several studies performed in the field of industrial and applied fluid dynamics [3] and [4] show that the use of fluid dynamic simulations, accompanied by some experimental data, are very useful to understand the fluid dynamic behavior and to optimize the design and operating parameters of the analyzed production processes.

Several designs and operating parameters influence the phenomena under investigation: the operating pressure inside the chamber, the swirl velocity component of the Nitrogen intake, the radial restriction of the chamber section, called C in Fig. 1, and the wall slope, called D in Fig. 1. The reduction of the gears defects can be achieved by improving the control of the cooling process, obtaining the same quenching strength for all of the gears independent of the location in the quenching chamber, and a good cooling homogeneity on the different surfaces of the same gear.

In the present work, the fluid dynamic behavior of the quenching process inside a gear hardening machine was analyzed in detail, and a process optimization was carried out in order to reduce the planarity error of the gears surfaces. In a previous work [2], some calculations were performed using an axial-symmetric model and the main operating and geometrical parameters of the process were characterized. The limit was that the axial-symmetric model neglected the heat rate exchanged by the Nitrogen flowing between gears. In the following, full three-dimensional simulations will be presented. In particular, the present work has been developed through the following steps.

- The behavior of the quenching chamber in the actual configuration has been investigated by a fluid dynamic numerical simulation code. The results have been correlated to the measured level of defects of the gears in different zones of the chamber.
- The numerical simulation errors have been evaluated using the procedure suggested in [5] and [6]; different grid refinements have been considered to identify the right balance between the number of computational cells and the time required for the convergence of the calculations.
- Further, using Taguchi approach [7], a design of experiment (DOE) procedure has been performed to assess the significance of the influence of design and operating parameters on the performance of the industrial process under investigation.
- Some parameters were defined to evaluate the quality of the quenching process, as the value of the cooling strength, the homogeneity of the quenching process for different gears, and the cooling homogeneity for the different surfaces of the same gear.

Contributed by the Heat Transfer Division for publication in the JOURNAL OF HEAT TRANSFER. Manuscript received by the Heat Transfer Division November 1, 2002; revision received February 4, 2004. Associate Editor: K. S. Ball.

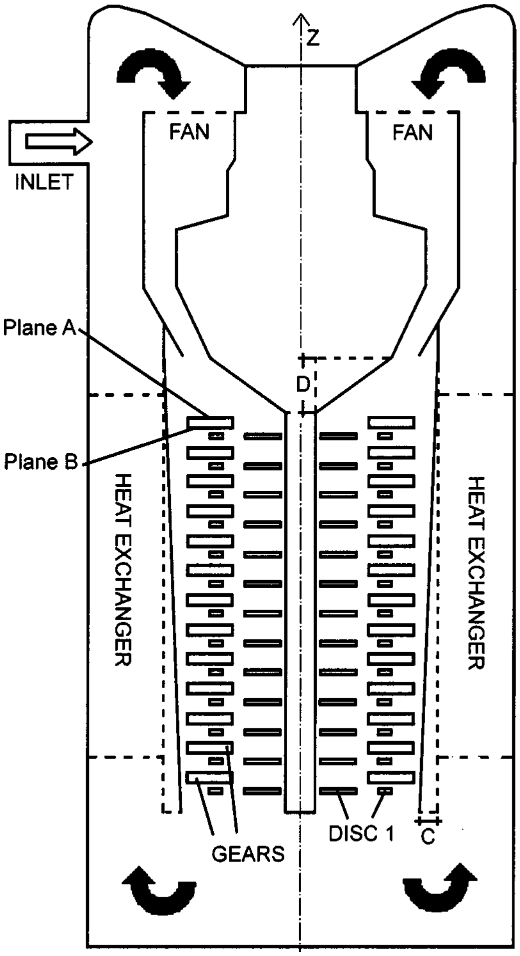

Fig. 1 Geometrical configuration

- Several numerical simulations were performed using the CFD code Fluent 6.1.22.
- The results were analyzed and discussed using an Analysis of Variance (ANOVA) technique [8] and [9].

The Quenching Process

The quenching at the end of the hardening is a very fast cooling process after a controlled heating of a mechanical component above a suitable temperature. Generally, quenching consists of an immersion of the components in some fluid as water, oil, polymer solution, salt or forced air flow. The heating process temperature is above the austenitizing temperature, above the so-called A_{c3} point for hypoeutectoid steels, and above Ac_{cm} point for hypereutectoid steels [10]. The heating temperature should not be increased to avoid the formation of bigger austenitic grains. After heating, the gear rests at the aforementioned temperature until gaining a completely austenitic structure; this structure is characterized by a face-centered cubic crystal structure, where carbon atoms are trapped in the octahedral interstitial sites (the so-called solid solution γ).

The last step of the hardening process consists of a fast cooling with a velocity higher than the upper critical one [11], to obtain a martensitic structure. The crystal structure evolves into a body-centered tetragonal one, while the carbon atoms do not have time to diffuse and take up the free spaces available, the edges and the centers of the two bases of the elementary cell. The martensitic structure is characterized by great hardness and brittleness. By the following tempering treatment, it is possible to modify the strength and hardness of steel in a wide field.

The heating temperature and the heat transfer rate affect heavily the results of the quenching of the mechanical components. Defects such as planarity errors can grow when different zones of the same component experience different quenching treatments.

Actual Configuration of the Quencing Chamber

A section of the actual configuration of the quenching chamber is shown in Fig. 1 (geometrical parameters C and D are equal to 0); it consists of a vertical chamber with a vertical z-axis, in which the gears are placed on drilled metal discs around a central tubular mount. Each metal disc (13 in all), shown in detail in Fig. 2, has eight gears and is rotated by 22.5 deg with respect to the previous one, in order to avoid the formation of preferential paths for the Nitrogen flow and to improve the turbulence level of the flow. The gears are numbered from the bottom (gears at disc no. 1) to the top of the chamber (gears at disc no. 13). No difference has been considered between the gears of the same disc and the assumption is that gears placed on the same disc experience the same cooling process (geometrical periodicity). Then, Nitrogen, from a storage vessel under a pressure of about 2 MPa, is injected into the chamber until the equilibrium pressure between the storage vessel and the quenching chamber is reached. The final operating pressure is 1.85 MPa, while the initial Nitrogen and gear temperatures are 300 K and 800 K, respectively. Then, a fan is operated to help Nitrogen circulation to continue the cooling process to subtract heat from gears and exchange it with the heat exchanger (see Fig. 1), keeping the Nitrogen temperature at suitable values for a fast cooling. The heat exchanger consists of horizontal tubes covering the quenching chamber. The operating internal fluid is water with an inlet temperature of 288 K. The behavior of the heat exchanger has been neglected in such an analysis, considering only its effect on the Nitrogen inlet temperature inside the quenching chamber. After four minutes, the pressure is reduced to 0.4 MPa for an additional six minutes. In Table 1 and Table 2, the geometrical properties and the material properties of the quenching chamber are shown, respectively. The steel properties have been considered to be constant, neglecting variations with phase and temperature.

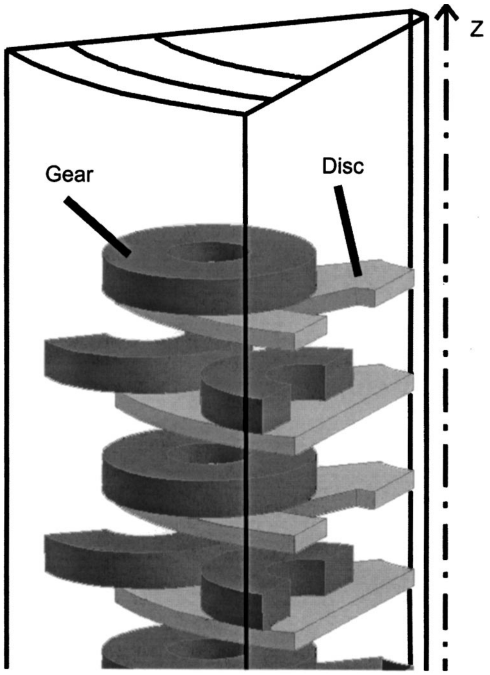

Fig. 2 A detail of drilled metallic discs around a central tubular mount where the gears are placed

Table 1 Geometrical dimensions and operating conditions

QUENCHING CHAMBER	
Axial height to chamber internal diameter ratio	2.21
FAN	
Fan diameter to chamber internal diameter ratio	0.31
Number of cycles	3000 rpm
Efficiency	0.80
Pressure gap	1035 Pa
TEMPERATURES	
Chamber initial temperature	300 K
Gears initial temperature	800 K
Cooling gas initial temperature	300 K

Table 2 Materials properties

GEARS	
Material	Steel
Density (g/m^3)	8030
Roughness height (m)	0.0001
Roughness constant	0.3
Specific Heat (J/kg K)	502
Thermal Conduc. (W/m K)	16.27
Emissivity	0.1
QUENCHING CHAMBER WALL and DISCS	
Material	Steel
Density (g/m^3)	8030
Specific Heat (J/kg K)	502
Thermal Conduc. (W/m K)	16.27
Roughness height (m)	0
Roughness constant	0.5
Emissivity	0.2
COOLING GAS (N$_2$)	
Material	Nitrogen
Viscosity (kg/m s)	1.663E-5
Specific Heat (J/kg K)	1041
Perfect gas coeff. (J/kg K)	724
Thermal Conductivity (W/m K)	0.0242
Absorption coefficient	0.01

Planarity Errors and Experimental Data

The measurement of the planarity errors was allowed by a ZEISS three-dimensional measuring the *z*-coordinates of a reference circle placed on plane B of each gear (see Fig. 1). The difference between the measured maximum and minimum values is the planarity error. In Fig. 3 the planarity errors of the actual configuration are shown as a function of the position inside the chamber for different operating pressures. Each dot in the plot represents the average planarity error of the eight gears placed on disc. Looking at the Fig. 3 it is clear that the planarity errors increase going through the chamber, in fact the highest planarity errors correspond to the gears placed at the bottom of the chamber (lower disc numbers). The Fig. 4 shows planarity errors as a function of the operating pressure.

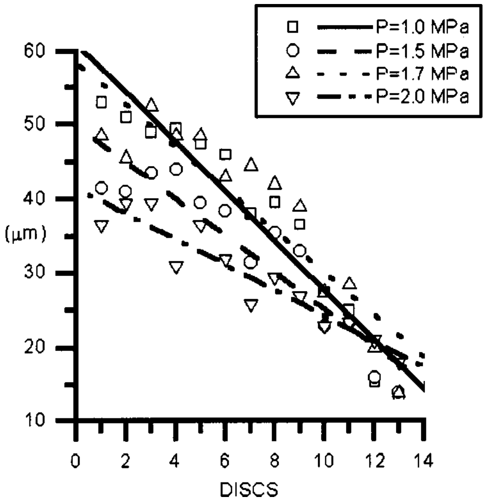

Fig. 3 Experimental data for the actual configuration: gears planarity errors versus the position varying the operating pressure

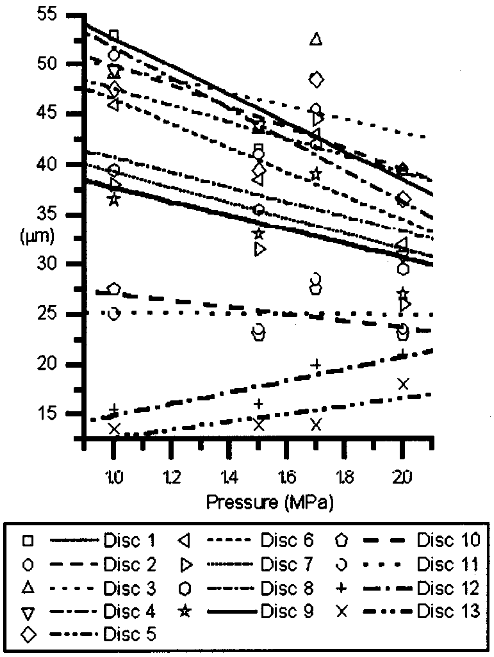

Fig. 4 Experimental data for the actual configuration: gear planarity errors versus the operating pressure

The planarity errors decrease when the operating pressure increases, with the exception of gears placed on discs 12 and 13. Increasing the operating pressure results in a flow with a higher heat capacity. With a higher heat capacity, the flow has a greater cooling effect on the surfaces that it flows over. The flow over the gears on discs 12 and 13 is not uniform, since they are near the inlet. Thus, the heat transfer rates from those gears is not uniform and as the cooling capability of the flow is increased, the temperature nonuniformities increase as do the planarity errors. Overall, though, the planarity errors decrease because the flow has a greater cooling capacity at the bottom of the chamber and the gears are more uniformly cooled away from the chamber inlet.

Design and Operating Parameters

With the actual process configuration, some gears show an unacceptable planarity error, due to improper cooling. In particular, the low-number gears, at the bottom of the chamber, showed the worst defects. These gears are located downstream with respect to the main Nitrogen flow. Different configurations in terms of geometric and operating conditions have been investigated. Some preliminary two-dimensional analyses [1] suggest the presence of some preferential paths for the Nitrogen flow, bypassing gears and reducing the effective heat exchange. Figure 5 shows a Nitrogen flow close to the wall, bypassing completely the gears and arriving at the bottom of the chamber with a small temperature increase. The two-dimensional analysis allows a preliminary identification of the parameters that affect significantly the quenching process. In particular, four design, and operating parameters have been identified: the operating pressure P inside the quenching chamber during the first 4 min, the swirl velocity component of inlet Nitrogen $\cos v_x$, the normalized radial restriction l (which is equal to twice the radial restriction C normalized by the chamber internal diameter, see Fig. 1) and the normalized wall slope d at

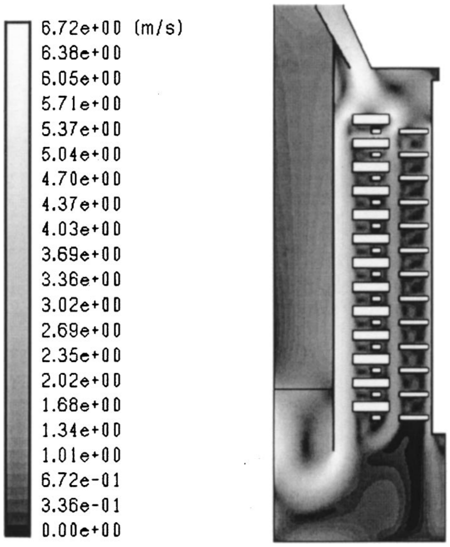

Fig. 5 Contours of velocity magnitude for the original configuration [2]

the inlet section inside the quenching chamber (which is equal to the wall slope D normalized by the chamber internal diameter, see Fig. 1).

The Numerical Model

The numerical simulations of the performances of the quenching chamber of the hardening machine were performed using the fluid-dynamic code FLUENT Rel. 6.1.22. Geometrical data, material properties, boundaries, and initial conditions are summarized in Table 1 and Table 2. Simulation parameters are listed in Table 3. All the other parameters, not shown in the tables, had the default values.

For the turbulence modeling, the original k-ε turbulence model is a popular choice. The k-ε turbulence model has been adopted since it is relatively robust and computationally inexpensive. The standard k-ε model has become the workhorse of practical engineering flow calculations in the time since it was proposed by Launder and Spalding [10]. This is the simplest complete turbulence model in which the solution of two separate transport equations allows the turbulent velocity and length scales to be independently determined. Its popularity is due to its robustness, economy, and reasonable accuracy for a wide range of turbulent flows. In the derivation of the k-ε model, it was assumed that the flow is fully turbulent, and the effects of molecular viscosity are negligible. The standard k-ε model is therefore valid only for fully turbulent flows, which is the case of the present simulations. It is well established that the eddy viscosity models, such as the k-ε model do not correctly reflect the sensitivity of turbulent stresses to streamline curvature and body forces, strong transport effects, etc. In these cases Reynolds stress models (RSM) have to be used.

Table 3 Settings of the numerical simulations

Solver	3D double precision
Numerical Scheme:	segregated
Linearization:	implicit
Discretization Scheme:	Second order upwind
Time:	Unsteady
Space:	3D
Turbulence Model	Standard κ-ε
Wall treatment:	Standard wall functions
Radiation model	Discrete Ordinates (DO)

Table 4 Grids properties

N°	1	2	3
Type	Fine	Medium	Coarse
No. of Cells	372,011	53,703	11,837
No. of Faces	778,565	116,275	26,003
No. of Nodes	84,458	14,458	3411
Cells dim. (mm)	6.25–7.5	12.5–15	25–30
Wall YPlus min.	0	0	0
Wall YPlus max.	621.435	1190.011	1457.43
Cell equiangle Skew max.	3.96E−4	5.216E−4	1.05E−2
Cell equiangle Skew max.	0.8317	0.83132	0.9459
Cell equivolume Skew max.	7.05E−7	6.878E−7	1.54E−4
Cell equivolume Skew max.	0.8118	0.8182	0.9594

The flow in examination is without swirl, adverse pressure gradient, recirculation, and large streamline curvature so the use of standard k-ε model can be a good choice.

The discrete ordinates radiation model (DO) has been chosen because the code FLUENT doesn't permit to use the Surface-to-Surface model with periodic boundary conditions. The DO model solves the radiative transfer equation for a finite number of discrete solid angles. With optical thickness aL (the absorption coefficient a per the appropriate length scale L) close to 0 (<1) and localized heat sources (gears), the DO model is reasonably efficient. All surfaces have been assumed diffuse-gray, because of the complexity of the radiation phenomena an overall hemispheric emissivity has been chosen. Values of emissivities and absorption coefficient have been reported in Table 2.

The fourth-order dependence of the radiative heat flux on temperature suggests that the radiative heat flux is maximum at the beginning of the process and it suggests that gears placed at the bottom of the chamber (at higher temperatures) suffer a bigger radiative heat flux. In other words, the gears exchanging a smaller convective heat transfer rate exchange a bigger radiative heat transfer rate (because of higher temperature), reducing the nonuniformity of the quenching process between the gears.

The computational grids have been created using the preprocessor GAMBIT 1.3; tetrahedral elements were used. The geometry of the chamber shows a rotational periodicity of 45 deg, allowing the reduction of the modeled volume and the reduction of the calculation time. The typical calculation time of each simulation, using about 54,000 cells, is 10 hours on a Compaq Alpha XP 900 CPU. Monotonic convergence of the obtained numerical solution is an essential requirement; moreover, the estimation of the grid-dependent uncertainty of the computational results has to be performed to assess the ordered discretization error. The Roache method based on Richardson extrapolation has been used [5] and [6]. Roache suggests the use of the grid convergence index (GCI) to obtain an evaluation of the grid induced error. An analogue analysis has been done considering the time step as a time grid spacing to investigate the time step-dependence uncertainty.

The GCI index gives a measure of the percentage the computed value is away from the value of the asymptotic numerical value. For the present work, three different grid refinement levels have been considered, as showed in Table 4. Considering three grid levels, the values for the GCI indexes can be evaluated as follows:

$$\mathrm{GCI}_{1-2}=\frac{F_s|\varepsilon_{1-2}|}{(r_{1-2}^{p}-1)} \text{ with fine and medium grids} \tag{1}$$

$$\mathrm{GCI}_{2-3}=\frac{F_s|\varepsilon_{2-3}|}{(r_{2-3}^{p}-1)} \text{ with coarse and medium grids; where} \tag{2}$$

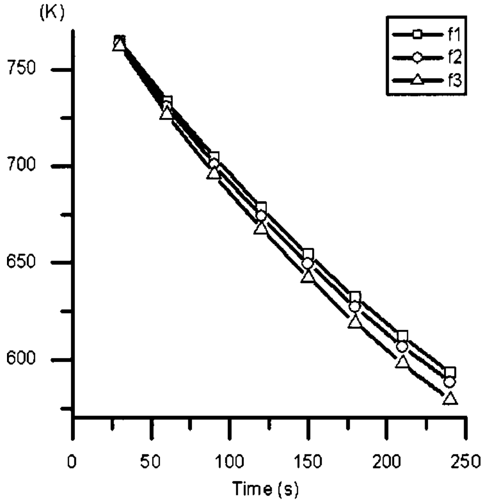

Fig. 6 Volume average temperature of the gear no. 1 versus time varying the grid spacing

F_s is a factor of safety and for the comparison of three grids is equal to 1.25; with

$$h_1 < h_2 < h_3 \tag{3}$$

$$\varepsilon_{n-n+1} = \frac{f_{n+1} - f_n}{f_n} \tag{4}$$

$$r_{n-n+1} = \frac{h_{n+1}}{h_n} \tag{5}$$

$$p = \frac{\ln \dfrac{f_{n+2} - f_{n+1}}{f_{n+1} - f_n}}{\ln r} \tag{6}$$

where p is the order of convergence; h is the grid spacing; and f is the value of the solution.

It is important that the solution of the considered grid level is in the asymptotic range; it happens if the following auditing ratio is equal to 1. It means that increasing the number of cells does not change the value of the solution f.

$$\frac{\mathrm{GCI}_{2-3}}{r^p\,\mathrm{GCI}_{1-2}} \cong 1 \tag{7}$$

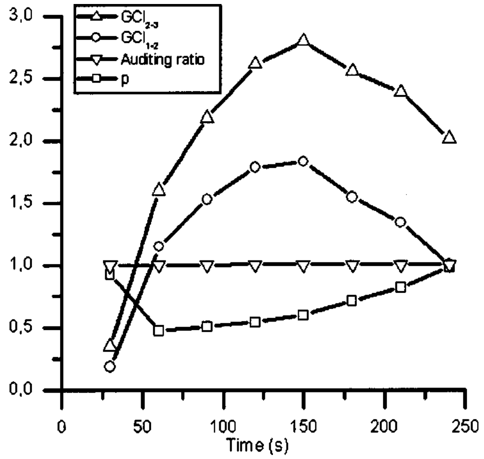

Fig. 7 Grid convergence indexes, auditing ratio and order of convergence versus time (grid spacing analysis)

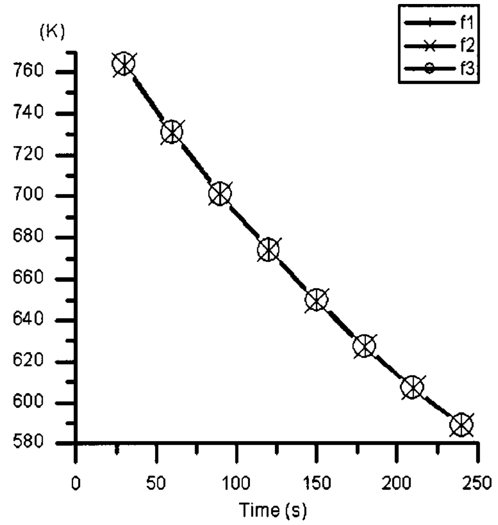

Fig. 8 Volume average temperature of the gear no. 1 versus time varying the time step

Using the finest grid, the evaluated value of the solution is

$$f = f_1 + \frac{f_1 - f_2}{r_{1-2}^p - 1} + \mathrm{GCI}_{1-2} \ \text{percent} \tag{8}$$

For the present work, the volume averaged temperature of the gear no. 1 (Fig. 1) has been chosen as a comparison parameter. In Fig. 6 such a temperature is plotted as function of time for different grid spaces. In detail, f1 curve represents the temperature calculated with the finest grid, f2 curve with the medium grid, and f3 with coarsest one. The curves show a little divergence with increasing time. In Fig. 7 the grid convergence indexes, the order of convergence and the auditing ratio are reported. It is important to verify that the auditing ratio is really close to 1. An analogue observation can be done looking at Fig. 8 and Fig. 9 where the results as function of the time step are reported. That is, f1 curve represents the temperature calculated with the smallest time step (0.5 s), f2 curve with the medium time step (1 s) and f3 with the greatest time step (2 s). Such curves are overlap completely and the auditing ratio trend in Fig. 9 confirms that the solution is in asymptotic range.

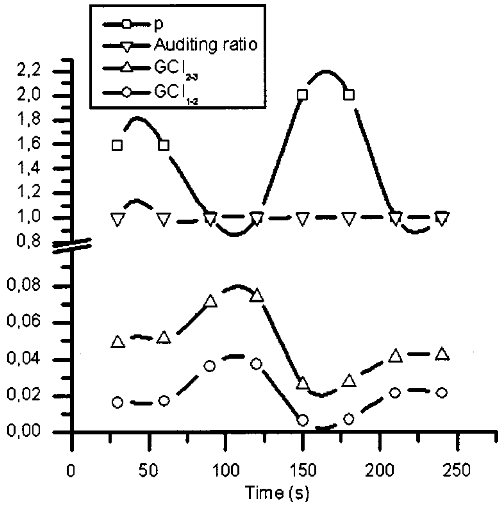

Fig. 9 Grid convergence indexes, auditing ratio and order of convergence versus time (time step analysis)

Table 5 Variation range of analysis parameters

Parameter	Range of variation (four levels)
Operating pressure	[1.25 MPa, 2.0 MPa]
$\cos v_x$	[0,0.61]
$\cos v_y$	−0.5 (constant)
$\cos v_z$	[0.86,0.61]
l	[0,0.056]
d	[0,0.168]

Optimization Methodology

A sensitivity analysis has been performed to assess the influence of design and operating parameters of the quenching chamber on the performance of the hardening process. In particular, four design parameters have been selected to set the sensitivity analysis: the operating pressure inside the quenching chamber during the first four minutes, the swirl velocity component of inlet Nitrogen $\cos v_x$, the normalized radial restriction l, and the normalized wall slope d at the inlet section inside the quenching chamber. Regarding the setting of the inlet velocity, the analysis has been performed assuming a constant velocity magnitude and velocity component $\cos v_y$, changing $\cos v_x$, and calculating the last component $\cos v_z$. In Table 5 the ranges of variation of each parameter are shown.

A good hardening process needs a high heat transfer rate to increase the material tenacity and, at the same time, a cooling homogeneity on the external surfaces to avoid high planarity error. Three performance indexes have been considered to allow the comparison between different designs and operating configurations, like a measure of the heat transfer rate, the cooling homogeneity (in terms of homogeneous temperature distribution) between the surfaces of each gears, the cooling homogeneity between the gears placed at different location.

Indexes of Performance. Three different performance indexes have been defined; in detail, the first index is a measure of the average heat transfer rate of the gears, the second index is a measure of the cooling homogeneity between gears anywhere placed inside the chamber, the last one is a measure of the cooling homogeneity between the surfaces of the same gears. The analysis has been done comparing the results of the gears at the bottom (gear 01), in the middle (gear 07) and at the top of the chamber (gear 13), so in the following description of the performance indexes, the gear subscript is i (1,7,13). Referring to the nodes the subscript j is used varying in the interval $[1,\ldots,n]$. The subscript indicating time is k and it can assume the following values: 30, 60, 90, 120, 150, 180, 210, 240. In the following equations the definition of the performance indexes are given:

$T_{i,\mathrm{Average},k}$ is the volume average temperature of gear i at the time k (see Table 6).

$$T_{i,\mathrm{Average},k}=\frac{\sum_{j=1}^{n}T_{i,j,k}}{n} \tag{9}$$

$T_{i,\mathrm{StaDev},k}$ is the temperature standard deviation of gear i at the time k (see Table 6).

$$T_{i,\mathrm{StaDev},k}=\sqrt{\frac{\sum_{j=1}^{n}(T_{i,j,k}-T_{i,\mathrm{Average},k})^2}{n}} \tag{10}$$

$T_{i,CV,k}$ is the coefficient of variation of temperature of gear i at the time k (see Table 6).

$$T_{i,CV,k}=\frac{T_{i,\mathrm{StaDev},k}}{T_{i,\mathrm{Average},k}}100 \tag{11}$$

Table 6 Indexes of performance of the single gear

CONFIGURATION 01									
	Time step (s)								
GEAR No. 1	30	60	90	120	150	180	210	240	
Temp. (K)	748.4	699.6	659.7	626.5	598.6	574.9	554.6	537.2	
	746.7	697.8	658.0	624.9	597.1	573.5	553.3	536.1	
	…	…	…	…	…	…	…	…	
Average	750.1	710.2	675.6	645.5	619.2	596.1	575.8	558.0	
St. Dev.	11.8	15.2	17.4	18.6	19.1	19.1	18.7	18.0	C.V. time Average
C.V.	1.6	2.1	2.6	2.9	3.1	3.2	3.2	3.2	2.7

Table 7 Indexes of performance of the configuration

CONFIGURATION 01									
	Time Step (s)								
	30	60	90	120	150	180	210	240	
	Temperature averages inside the gears (K)								
Gear no. 1	750.1	710.2	675.6	645.5	619.2	596.1	575.8	558.0	
Gear no. 7	747.6	705.7	669.5	638.2	611.1	587.5	566.9	549.0	
Gear no. 13	688.0	614.4	561.4	523.2	495.3	475.1	460.3	449.5	
Average	728.6	676.7	635.5	602.3	575.2	552.9	534.3	518.8	INDEX 1
St. Dev.	35.1	54.1	64.2	68.6	69.3	67.5	64.3	60.2	INDEX 2
C.V.	4.8	8.0	10.1	11.4	12.0	12.2	12.0	11.6	10.3
	C.V. coefficients per each gear								C.V. Average
Gear no. 1	1.6	2.1	2.6	2.9	3.1	3.2	3.2	3.2	2.7
Gear no. 7	1.6	2.1	2.4	2.7	2.8	2.9	2.9	2.9	2.5
Gear no. 13	2.8	2.5	2.1	1.7	1.3	1.0	0.8	0.6	1.6
								INDEX 3	2.3

Table 8 Design of experiment table (no radiation)

	Operating pressure (MPa)	cos v_x	Mass flow rate (kg/s)	l	d	INDEX 01	INDEX 02	INDEX 03
Conf. 01	1.25	0.00	2.22	0.000	0.000	538.2	11.2	2.5
Conf. 02	1.50	0.22	2.66	0.000	0.056	521.4	11.5	2.6
Conf. 03	1.75	0.43	3.10	0.000	0.112	504.3	11.5	2.8
Conf. 04	2.00	0.61	3.54	0.000	0.168	492.1	11.2	3.1
Conf. 05	1.50	0.43	2.66	0.019	0.000	506.4	10.3	2.5
Conf. 06	1.25	0.61	2.22	0.019	0.056	522.3	9.8	2.7
Conf. 07	2.00	0.00	3.54	0.019	0.112	479.9	9.3	2.7
Conf. 08	1.75	0.22	3.10	0.019	0.168	491.6	9.6	2.7
Conf. 09	1.75	0.61	3.10	0.037	0.000	477.0	8.4	2.6
Conf. 10	2.00	0.43	3.54	0.037	0.056	468.3	8.3	2.6
Conf. 11	1.25	0.22	2.22	0.037	0.112	511.2	8.4	2.3
Conf. 12	1.50	0.00	2.66	0.037	0.168	494.0	8.1	2.4
Conf. 13	2.00	0.22	3.54	0.056	0.000	458.2	6.7	2.2
Conf. 14	1.75	0.00	3.10	0.056	0.056	467.7	6.6	2.1
Conf. 15	1.50	0.61	2.66	0.056	0.112	478.8	7.1	2.3
Conf. 16	1.25	0.43	2.22	0.056	0.168	496.6	7.1	2.3

Index 1. $T_{\text{Average,Average,240}}$ is the average of the mean temperatures of all gears at the end of the process (240 s) and it is a measure of the heat transfer rate during the treatment (see Table 7).

$$T_{\text{Average,Average,240}}=\frac{\sum_{i=1}^{13}T_{i,\text{Average,240}}}{3} \tag{12}$$

$T_{\text{DevSta,Average},k}$ is the standard deviation of the average temperatures of all gears at the time k (see Table 7).

$$T_{\text{DevSta,Average},k}=\sqrt{\frac{\sum_{i=1}^{13}(T_{i,\text{Average},k}-T_{\text{Average,Average},k})^2}{n}} \tag{13}$$

$T_{CV,\text{Average},k}$ is the coefficient of variation of the average temperatures of all gears at the time k and it is a measure of the cooling homogeneity between the gears at the time k (see Table 7).

$$T_{CV,\text{Average},k}=\frac{T_{\text{StaDev,Average},k}}{T_{\text{Average,Average},k}}100 \tag{14}$$

Index 2. $T_{CV,\text{Average,Average}}$ is the average in time of the coefficients of variations of the gears average temperatures and it is a measure of the cooling homogeneity between gears during the whole process (see Table 7).

$$T_{CV,\text{Average,Average}}=\frac{\sum_{k=30}^{240}T_{CV,\text{Average},k}}{8} \tag{15}$$

Index 3. $T_{\text{Average},CV,\text{Average}}$ is the average of the coefficients of variations of the temperature of each gear at each time and it is a measure of the cooling homogeneity inside the volume of the gear through the whole process (see Table 7).

$$T_{\text{Average},CV,\text{Average}}=\frac{\sum_{i=1}^{13}\sum_{k=30}^{240}T_{i,CV,k}}{3\cdot 8} \tag{16}$$

For a better understanding of the definitions above, Table 6 and Table 7 have been used. The definitions of the indexes of optimization will be given for the first configuration in Table 6, for the others the definitions have been done analogously. In Table 6 the temperatures of the nodes (in the table only the temperatures of the first two nodes are reported, for clarity) of the gear no. 1 (at the bottom) are reported in column for each time step. The temperature average at the bottom of the table represents the temperature volumetric average of the gear no. 1. The Coefficient of Variation (C.V.) is the temperature volumetric average divided by the standard deviation multiplied by 100 (percent). The C.V. time average represents an index of cooling homogeneity between the nodes of the gear no. 1 during the process. Repeating for the gears no. 7 and no. 13, Table 7 has been obtained. At the top of the table the row corresponding to the gear no. 1 is the row of the temperature volumetric average defined in Table 6, for the gears no. 7 and no. 13 analogously. Now the temperature average for each time step is the volumetric average between all gears, in particular the

Table 9 Design of experiment table (with radiation model)

	Operating pressure (MPa)	cos v_x	Mass flow rate (kg/s)	l	d	INDEX 01	INDEX 02	INDEX 03
Conf. 01	1.25	0.00	2.22	0.000	0.000	518.8	10.3	2.3
Conf. 02	1.50	0.22	2.66	0.000	0.056	505.2	10.5	2.4
Conf. 03	1.75	0.43	3.10	0.000	0.112	491.3	10.5	2.6
Conf. 04	2.00	0.61	3.54	0.000	0.168	481.4	10.3	2.9
Conf. 05	1.50	0.43	2.66	0.019	0.000	493.3	9.5	2.3
Conf. 06	1.25	0.61	2.22	0.019	0.056	506.5	9	2.5
Conf. 07	2.00	0.00	3.54	0.019	0.112	471.5	8.7	2.5
Conf. 08	1.75	0.22	3.10	0.019	0.168	481.2	8.9	2.5
Conf. 09	1.75	0.61	3.10	0.037	0.000	469.3	7.8	2.4
Conf. 10	2.00	0.43	3.54	0.037	0.056	462	7.7	2.4
Conf. 11	1.25	0.22	2.22	0.037	0.112	497.7	7.8	2.1
Conf. 12	1.50	0.00	2.66	0.037	0.168	483.5	7.6	2.2
Conf. 13	2.00	0.22	3.54	0.056	0.000	453.6	6.4	2.1
Conf. 14	1.75	0.00	3.10	0.056	0.056	461.7	6.3	2
Conf. 15	1.50	0.61	2.66	0.056	0.112	471.3	6.6	2.1
Conf. 16	1.25	0.43	2.22	0.056	0.168	486.1	6.7	1.9

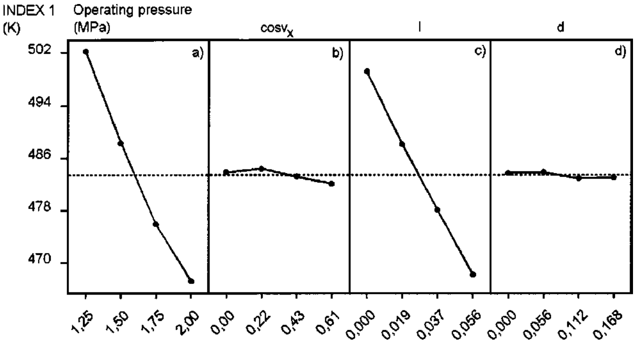

Fig. 10 Main effects on performance index 1 (heat transfer rate) versus the design parameters

value measured at 240 s is an index of the heat exchanged during all the treatment. In other words, the lower is this value, called index 1, the faster is the cooling process.

Also C.V. coefficients calculated between the gears are shown and they represent indexes of cooling homogeneity between the gears for each time step. The C.V. coefficient time average is the index 2, representing the cooling homogeneity between the gears averaged between the time steps. The lower index 2 is, the more similar are the cooling processes encountered by each of the gears, independent of their axial position.

At the bottom of the Table 7 the row corresponding to the gear no. 1 is the row of the C.V. coefficients in Table 6 calculated for each time step. The C.V. coefficients time average is the index 3, representing the cooling homogeneity inside a gear averaged between all gears and in time. The lower the index is, the more homogeneous is the cooling process of different zones of the same gear.

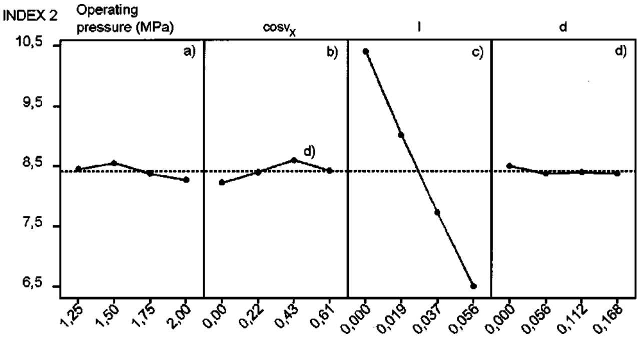

Fig. 11 Main effects on performance index 2 (cooling homogeneity between gears) versus the design parameters

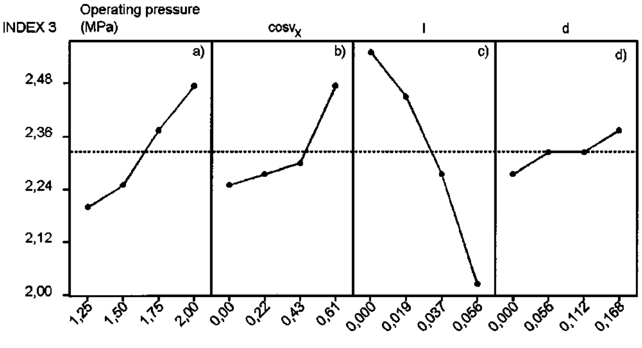

Fig. 12 Main effects on performance index 3 (cooling homogeneity inside each gears) versus the design parameters

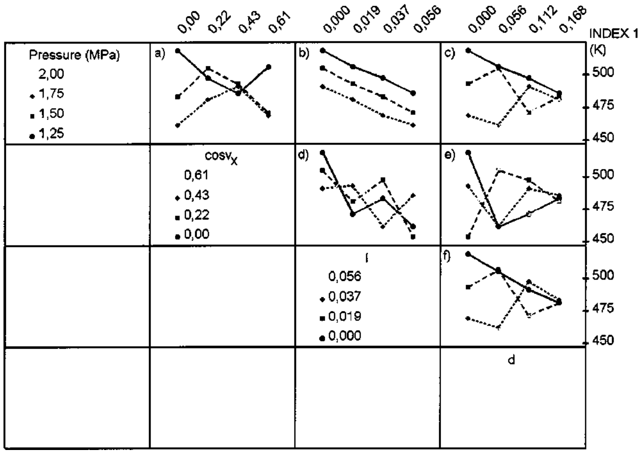

Fig. 13 Design parameters interaction effects on index 1 (heat transfer rate)

Design of Experiment. Using a Design of Experiment (DOE) methodology the cases to be simulated have been reduced to 16. In the present investigation the Taguchi method with 4 factors on 4 levels (L16) has been used [7]. If more than one parameter has to be investigated, the number of possible combinations is the number of levels, over which each parameter has been discretized,

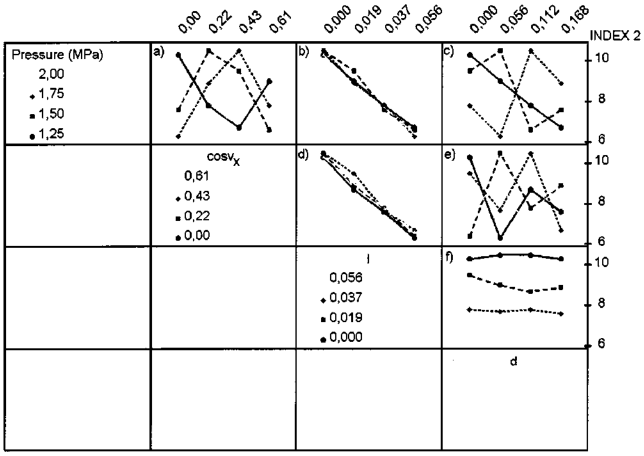

Fig. 14 Design parameters interaction effects on index 2 (cooling homogeneity between gears)

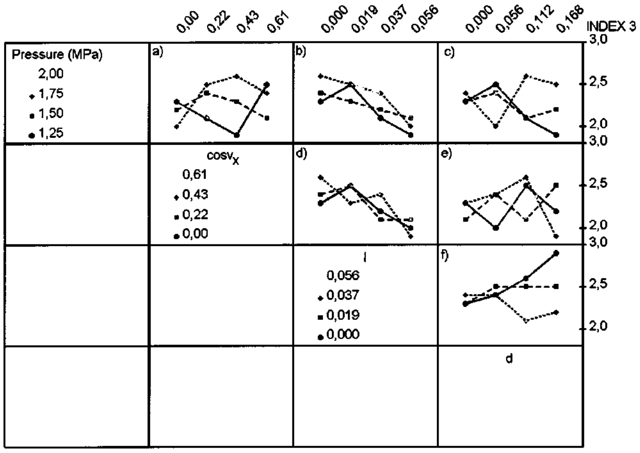

Fig. 15 Design parameters interaction effects on index 3 (cooling homogeneity inside each gears)

Table 10 Convective heat flux coefficients $(W/m^2\,K)$

	Time Step (s)							
Conf. 01	30	60	90	120	150	180	210	240
Gear no. 1	85.94	81.42	77.16	73.06	69.08	65.21	61.94	57.70
Gear no. 7	91.33	86.50	81.85	77.30	72.83	68.44	64.12	59.88
Gear no. 13	212.75	184.80	157.80	132.00	108.10	86.74	68.35	53.02
Conf. 13	30	60	90	120	150	180	210	240
Gear no. 1	185.58	165.12	144.98	125.28	106.46	88.99	73.25	59.47
Gear no. 7	166.85	150.88	165.04	119.35	104.07	89.54	76.05	63.84
Gear no. 13	296.03	238.13	183.05	134.46	94.93	64.95	43.41	28.54

elevated to the number of parameters. This means that even with few parameters and few levels (for example, 4 parameters on 4 levels) the number of combinations can be really high (256). The DOE gives the possibility to reduce the number of experiments needed to find the main parameters and to define their influence by eliminating the combinations not giving any further information. Of course, it is important to understand what parameters have the strongest influence on the phenomena. Neglecting one of these will invalidate the analysis. In particular, the right range of variation of each parameter has to be chosen.

In Table 8 (no radiation) and Table 9 (with radiation) the variables of DOE analysis (independent parameters) have been listed in the first five columns (excluding the mass flow rate). The value of the mass flow rate corresponding to a particular value of operating pressure are reported keeping constant the fan characteristics. The values of the calculated indexes of performances show that the lower are the indexes corresponding to a configuration, the better is the behavior of that configuration in terms of heat transfer rate and/or homogeneity. By comparing Tables 8 and 9, a first important consideration is that all indexes of performance are lower using the radiation model, in other words the hypothesis to neglect the radiation model is careful for the analysis. Looking at the results of the simulations (Table 9), configurations 13, 14, and 16 seem to be the best ones. In particular, configuration 13 shows the lowest value of the index 1 (heat transfer rate), configuration 14 shows similar cooling process of all gears (the lowest value of index 2) and configuration 16 shows the best cooling process in terms of homogeneity inside each gear (the lowest value of index 3). Comparing the three configurations it can be seen that the differences between the values of the indexes 2 and 3 are really small while index 1 differs by 8°C and 33°C, respectively. The first analysis suggests that configuration 13 is the best one.

More information can be obtained with the following analysis. In Fig. 10 the index 1 (the minimum temperature after a treatment of 240 s) is shown as function of the independent parameters. It can be noted that the independent parameters d and $\cos v_x$ do not seem to have any influence on the index, while parameters l and P show a great influence on the minimum temperature. Each one of these last parameters contribute about 30 K. In Fig. 13(b), the curves describing the interaction between l and P are parallel indicating the absence of a contribution due to the interaction. That is important because it means that operating on both parameters at the same time, the whole contribution is doubled (about 60 K). Besides, looking at the square of the interaction l-d it is clear that with high values of l it is better to use d lower in order to obtain the minimum of temperature.

In Fig. 11 the behavior of the index 2 (cooling homogeneity between gears) is shown as a function of the independent parameters. This index seems to be independent of the independent parameters with the exception of the parameter l. In particular, when parameter l increases, index 2 decreases in accordance with the index 1. The parallelism of curves in Figs. 14(b), (d), and (f) shows that there are no contributions due to the interaction between parameter l and the others.

Index 3, which indicates the cooling homogeneity inside the gears, is plotted as a function of the independent parameters in Fig. 12. The figure shows that the range of variation of index 3 as a function of the parameters is a maximum with the parameter l. Furthermore, in Fig. 12(c), it is shown that increasing the parameter l results in a decrease in the value of index 3, which is beneficial. Increases in any of the other independent parameters (P, $\cos v_x$, and d) result in a larger value of index 3 (Figs. 12(a), (b), and (d)), which is not desirable. Furthermore, for large values of the parameter l, index 3 becomes relatively insensitive to changes

Table 11 ANOVA analysis of the index 1

	INDEX 1	Operating pressure (MPa)	$\cos v_x$	l	d	Residuals
MAX	518.8	1.25	0.22	0	0.056	
MIN	453.6	2	0.61	0.056	0.112	
	Degrees of Freedom	3	3	3	3	
	Variance	936.03	3.937	707.737	0.867	0.357
	F	2624.38	11.037	1984.31	2.4299	
	Fisher Test (%)	100	96.04	100	75.75	

Table 12 ANOVA analysis of the index 2

	INDEX 2	Operating pressure (MPa)	$\cos v_x$	l	d	Residuals
MAX	10.81	1.5	0.43	0	0	
MIN	6.1375	2	0	0.056	0.168	
	Degrees of Freedom	3	3	3	3	3
	Variance	0.0542	0.094	11.27	0.014	0.0092
	F	5.909	10.27	1229.9	1.545	
	Fisher Test (%)	91.07	95.64	100	63.54	

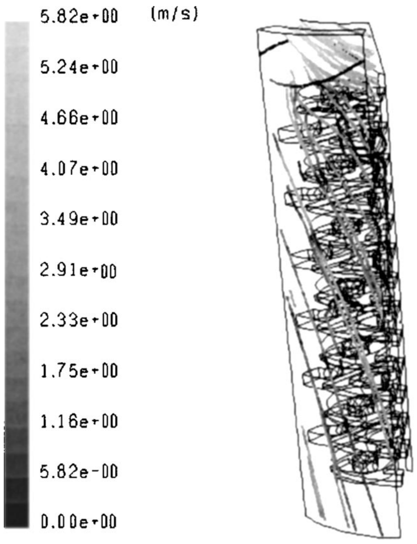

Fig. 16 Nitrogen path lines with configuration 4

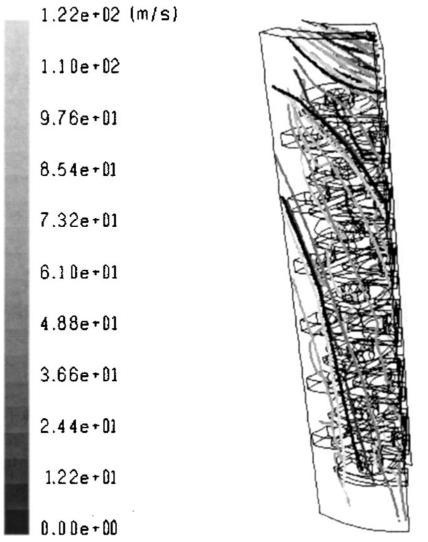

Fig. 17 Nitrogen path lines with configuration 15

in value of the other parameters. This is shown in Fig. 15, where index 3 is relatively constant over the range of d (Fig. 15(f)) and also over the range of $\cos v_x$ (Fig. 15(d)) for $l=0.056$. Since the dependence of index 3 on d and $\cos v_x$ is negligible (for large l) or actually increases slightly as d and $\cos v_x$ increase (which is undesirable), the analysis suggests setting these parameters to their minimum values. As for the operating pressure, even though it has little influence on index 3 (Fig. 15(b)) for $l=0.056$, it has a significant effect on index 1. Higher values of P result in significantly lower values of index 1 (Fig. 10(a)), which is very desirable. Thus, the analysis suggest setting P to its maximum value.

In Table 10 the convective heat flux coefficients are reported as function of time and gear for configuration 1 (one of the worst) and configuration 13 (one of the best). The coefficients corresponding to configuration 13 are significantly higher than the others and there are high values also for the gears placed at the bottom of the chamber. It means that these gears suffer a sufficiently fast normalizing process.

Statistical Analysis ANOVA. In the industrial field, the ANOVA analysis is one of the most important techniques used for the optimization of processes and systems [9]. An ANOVA statistical analysis allowed the determination of the main dependences of the indexes defined above. For clarity, the parameters fixed by the user will be called ''independent parameters,'' and the parameters calculated by the simulations will be called dependent parameters. The operating pressure and the parameters $\cos v_x$, l and d defined above are the independent ones, while the dependent parameters are the indexes of performance. Analysis of variance is a powerful and popular technique for analyzing data, as shown by DeGroot [8]. The concept of ANOVA is really quite simple: to compare different sources of variance and make inferences about their relative sizes. It is fundamental that an experiment is designed properly for the data to be useful. The Analysis of Variance (ANOVA) is a useful system to check the main influence of a factor and the eventual contribution due to its interaction with the others.

In Table 11 the ANOVA analysis of index 1 is shown. For a fast cooling, index 1 has to be as low as possible, so the minimum value shows the best set of design parameters to get this single optimization. In particular, the analysis of sensitivity by a Fisher test [8,9], confirms that the parameters l and P have a great influence (highest values) on index 1 variation. Such a test suggests that the performance in function of the index 1 can be improved by varying the parameters l and P and with a smaller contribution from $\cos v_x$. The parameter d seems to have less influence on index 1. Finally, the optimization of index 1 suggests choosing the highest values for the parameters l, P, and $\cos v_x$. About the parameter $\cos v_x$, a high value increases the swirl at the top of the chamber creating a helicoidal flow, which can penetrate more easily between the gears with a better heat exchange.

In Table 12 the ANOVA analysis of index 2 is shown. The best value is the minimum, for which the cooling process is more homogeneous between the gears. Fisher coefficients suggest that parameters 1 and $\cos v_x$ have more influence on index 2 variation following by the parameter P. The minimum value of index 2 is obtained with the highest of value of each parameter with the exception of cosvx, for which the minimum value is chosen. The choice of the minimum value of $\cos v_x$ is confirmed from Fig. 16 and Fig. 17. The figures represent the Nitrogen path lines with the configurations 4 and 15 (see Table 8 and Table 9). The configurations have the maximum value of $\cos v_x$ and the minimum and maximum values of the normalized radial restriction l, respectively. Both of them show Nitrogen path lines aligned with the axis at the bottom of the chamber, losing the swirl components of velocity through the chamber. This effect is more pronounced for larger values of l. A high value of $\cos v_x$ is useless because it only

Table 13 ANOVA analysis of the index 3

	INDEX 3	Operating pressure (MPa)	$\cos v_x$	l (mm)	d (mm)	Residuals
MAX	2.9	2	0.61	0	0.168	
MIN	1.775	1.25	0	0.056	0	
	Degrees of Freedom	3	3	3	3	3
	Variance	0.0617	0.0417	0.212	0.0067	0.0017
	F	37	25	127	40	
	Fisher Test (%)	99.28	98.73	99.88	85.76	

serves to increase the heat transfer rate of the gears at the top of the chamber, and increases the differences in heat transfer rates for the gears at the bottom.

In Table 13 there is the ANOVA analysis of index 3. Such an index is a measure of the cooling homogeneity average inside a gear, and its best value is the minimum. This value is obtained with the highest value of the parameter *l*, a medium value of the parameter *P*, and the minimum values of the parameters *d* an $\cos \mathrm{v}_x$. The Fisher test suggests that all of the parameters have a great influence on the behavior of such a index with the exception of parameter *d*.

Finally, the analysis suggests a configuration average of the configurations optimizing the indexes of performance, with the values of the parameters *l* and *P* close to the maximum and the parameters *d* and $\cos \mathrm{v}_x$ close to the minimum $(\mathrm{l}=0.056,\ d=0.093,\ P=18.3\ \mathrm{MPa},\ \cos \mathrm{v}_x=0.2)$.

Conclusions

A numerical model to simulate the behavior of the quenching chamber in a hardening machine has been applied to identify the best design configuration to reduce the planarity defects due to a too fast and not homogeneous quenching process. A numerical analysis has been carried out using a design of experiments method developed with the Taguchi method $(l=16)$. Three indexes of performance have been defined in order to compare the configurations in terms of heat transfer rate, similar cooling processes of the gears placed anywhere inside the chamber, and the volumetric average of cooling homogeneity inside a gear. Such analysis allowed the comparison of sixteen different configurations and the following ANOVA analysis characterized the trends of indexes of performance as functions of the geometrical and operating independent parameters. In particular, an analysis of sensitivity has been performed by the Fisher test in order to evaluate what parameters have more influence on the process. The analysis showed that by operating on the radial restriction *l* and the operating pressure *P* it is possible to change the performance of the process significantly. The best configuration has been suggested $(l=0.056,\ d=0.093,\ P=18.3\ \mathrm{MPa},\ \cos \mathrm{v}_x=0.2)$.

Acknowledgment

The authors wish to thank the company GETRAG–Bari, Italy, for their contribution.

Nomenclature

$\cos \mathrm{v}_x$ = swirl velocity cosine of inlet Nitrogen flux
D = wall slope at the inlet section
f_n = value of the solution for nth grid
H = alumina height
h_n = grid spacing for *n*th grid
L = section radial restriction
P = order of convergence
r = grid refinement ratio
$\mathrm{BY_n}$ = *n*th crossing section of Nitrogen
F_s = factor of safety
$\mathrm{GCI_{coarse}}$ = grid convergence index for the coarsest grids
$\mathrm{GCI_{fine}}$ = grid convergence index for the finest grids
P = operating pressure
$T_{i,\mathrm{Average},k}$ = volume average temperature of gear no. *i* at the time *k*
$T_{i,\mathrm{StaDev},k}$ = temperature standard deviation of gear no. *i* at the time *k*
$T_{i,CV,k}$ = coefficient of variation of temperature of gear no. *i* at the time *k*
$T_{\mathrm{Average,Average,240}}$ = average of the average temperatures of all gears at the end of the process (240 s) and it is a measure of the heat transfer rate
$T_{\mathrm{DevSta,Average},k}$ = standard deviation of the average temperatures of all gears at the time *k*
$T_{CV,\mathrm{Average},k}$ = coefficient of variation of the average temperatures of all gears at the time *k*
$T_{CV,\mathrm{Average,Average}}$ = average in time of the coefficients of variations of the gears average temperatures
$T_{\mathrm{Average},CV,\mathrm{Average}}$ = average of the coefficients of variations of the temperature of each gear at each time
ε = relative error

References

[1] Mgbokwere, C., and Callabresi, M., 2000, ‘‘Numerical Simulation of a Heat-Treated Ring Gear Blank,’’ ASME J. Eng. Mater. Technol., **122**, pp. 305–314.
[2] Congedo, P. M., Ficarella, A., and Laforgia, D., 2001, ‘‘Analisi Termo-Fluidodinamica di un Processo di Normalizzazione di Ruote Dentate all’interno di un Forno di Tempra,’’ Proc. 56° Congresso Nazionale ATI, Napoli, Italy, **3**, pp. 13–24.
[3] Sima, M. A., and Harris, J. A., 1999, ‘‘Numerical Modeling of Flow in a Vertical Cooling Crystallizer,’’ ASME J. Fluids Eng., **121**, pp. 148–155.
[4] Jahnke, C. C., and Valentine, D. T., 1998, ‘‘Recirculation Zones in a Cylindrical Container,’’ ASME J. Fluids Eng., **120**, pp. 680–684.
[5] Roache, P. J., 1994, ‘‘Perspective: A Method for Uniform Reporting of Grid Refinement Studies,’’ ASME J. Fluids Eng., **116**, pp. 405–413.
[6] Roache, P. J., 1998, *Verification and Validation in Computational Science and Engineering*, Hermosa Publishers, Albuquerque, New Mexico.
[7] Roy, R. K., 2001, *Design of Experiments Using the Taguchi Approach*, Wiley-Interscience, NY.
[8] DeGroot, M. H., and Schervish, M. J., 2002, *Probability and Statistics*, Addison Wesley, Chap. 10.
[9] Montgomery, D. C., and Runger, G. C., 1999, Applied Statistics and Probability for Engineers, John Wiley & Songs.
[10] Launder, B. E., and Spalding, D. B., 1972, *Lectures in Mathematical Models of Turbulence*, Academic Press, London, England.
[11] Nicodemi, W., 1991, *Metallurgia*, Masson Editore, Italy.

Role of Phonon Dispersion in Lattice Thermal Conductivity Modeling

J. D. Chung
Assistant Professor
e-mail: jdchung@sejong.ac.kr
Department of Mechanical Engineering,
Sejong University,
Seoul, 143-147,
Korea

A. J. H. McGaughey
Graduate Student
e-mail: amcgaugh@umich.edu

M. Kaviany
Professor
ASME Fellow
e-mail: kaviany@umich.edu

Department of Mechanical Engineering,
University of Michigan,
Ann Arbor, MI 48109-2125

The role of phonon dispersion in the prediction of the thermal conductivity of germanium between temperatures of 2 K and 1000 K is investigated using the Holland approach. If no dispersion is assumed, a large, nonphysical discontinuity is found in the transverse phonon relaxation time over the entire temperature range. However, this effect is masked in the final prediction of the thermal conductivity by the use of fitting parameters. As the treatment of the dispersion is refined, the magnitude of the discontinuity is reduced. At the same time, discrepancies between the high temperature predictions and experimental data become apparent, indicating that the assumed heat transfer mechanisms (i.e., the relaxation time models) are not sufficient to account for the expected thermal transport. Molecular dynamics simulations may be the most suitable tool available for addressing this issue. [DOI: 10.1115/1.1723469]

Keywords: *Conduction, Heat Transfer, Modeling, Properties*

1 Introduction

The thermal conductivity of dielectric crystals (where phonons dominate the thermal transport) has been theoretically investigated since the works of Debye [1] and Peierls [2]. The exact or even numerical prediction of the thermal conductivity is a formidable task. This is due to the complexity of the Boltzmann transport equation (BTE), which is the basis for most solution techniques. Analytical thermal conductivity models have been developed based on the single mode relaxation time (SMRT) approximation in the BTE with different degrees of complexity [3,4]. In SMRT models, a single relaxation time is associated with each phonon mode, and describes how that mode would respond if excited while all others remain at equilibrium. The temperature and frequency dependencies of the relaxation times are assumed, and the predictions must be fit to the experimental data.

Callaway [3] developed an SMRT model that can successfully predict the low temperature thermal conductivity of germanium. This approach uses the Debye approximation, which assumes that there is no phonon dispersion and that the longitudinal and transverse polarizations behave identically. Holland [4] extended the work of Callaway by separating the contributions of longitudinal acoustic (LA) and transverse acoustic (TA) phonons, including some phonon dispersion, and using different forms of the relaxation times. Better high temperature agreement was found for germanium than with the Callaway model. The Holland model has been refined to include further detail on the phonon dispersion and relaxation times [5–7]. The added complexities lead to more fitted parameters. One could argue that the resulting better fits with the experimental data are due to this increase in the number of fitted parameters, and not to an improvement of the actual physical model.

This study examines the impact of refining the phonon dispersion model beyond the Debye approximation for germanium using an SMRT approach. Consideration is given to the distinction between the group and phase velocities, their frequency dependencies, and the rigorous treatment of impurity scattering. In the context of the improved dispersion model, some issues with the Holland relaxation time model are addressed.

2 Thermal Conductivity Model

By solving the BTE and using the Fourier law of conduction, the thermal conductivity of germanium, assuming an isotropic crystal, and neglecting the contributions of optical phonons, has been predicted to be of the form [4]

$$k=\frac{1}{6\pi^2}\left[\int_0^{\omega_{mL}} c_v\frac{v_{g,L}}{v_{p,L}^2}\tau_L\omega_L^2 d\omega_L +2\left(\int_0^{\omega_1} c_v\frac{v_{g,T}}{v_{p,T}^2}\tau_{T0}\omega_T^2 d\omega_T+\int_{\omega_1}^{\omega_{mT}} c_v\frac{v_{g,T}}{v_{p,T}^2}\tau_{TU}\omega_T^2 d\omega_T\right)\right]. \tag{1}$$

The first term corresponds to longitudinal (L) phonons, and the second and third terms to transverse (T) phonons (two degenerate branches). Here, c_v is the quantum-harmonic specific heat per normal mode and τ is a SMRT. The forms of τ are given in [4]. The upper limits of the first and third integrals are the angular frequencies of the phonon branches at the edge of the first Brillouin zone. For the transverse phonons, the frequency ω_1 is that at the center of the first Brillouin zone. The phonon group velocity, v_g, is defined as $\partial\omega/\partial\kappa$, where ω is the angular frequency and κ is the wave number. The phonon phase velocity, v_p, is defined as ω/κ.

3 Phonon Dispersion Models

Experimental results for the phonon dispersion of the acoustic modes of germanium in the [100] direction, at a temperature of 80 K, are shown in Figs. 1(a) and 1(b) [8]. The horizontal axis is a dimensionless wave number, which is obtained by normalizing the wave number against its value at the edge of the first Brillouin zone, i.e., $\kappa^*=\kappa/\kappa_m=\kappa/(2\pi/a)$. For germanium at a temperature of 80 K, the value of a is 5.651 Å [8]. To allow for the use of Eq. (1), which assumes isotropic dispersion, this direction is used in the subsequent analysis. The temperature dependence of the dispersion [9] is not considered. The experimental data at a temperature of 80 K are used for all calculations. To assess the importance of accurately modeling the dispersion, five different models are examined.

Contributed by the Heat Transfer Division for publication in the JOURNAL OF HEAT TRANSFER. Manuscript received by the Heat Transfer Division June 13, 2003; revision received January 9, 2004. Associate Editor: G. Chen.

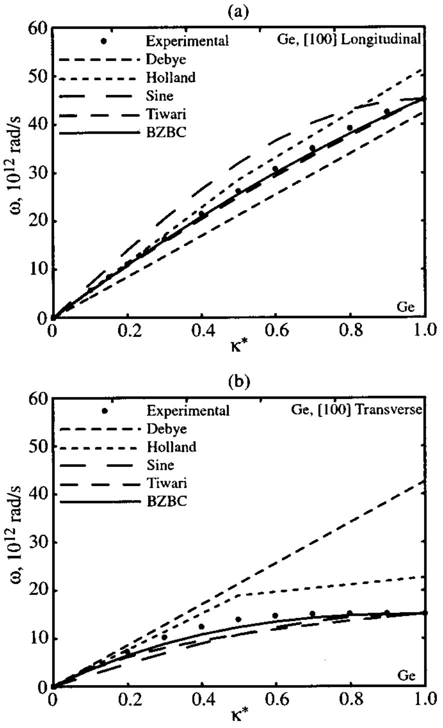

Fig. 1 Germanium phonon dispersion in the [100] direction. Experimental data [8] and five models used in this study for (*a*) LA phonons and (*b*) TA phonons.

3.1 Debye Model. From experimental data at low frequencies, the phonon frequency is proportional to its wave number such that

$$\omega = v_{0g}\kappa, \tag{2}$$

where the subscript 0 refers to the low frequency limit, i.e., $\kappa \rightarrow 0$, and v_{0g} is the low frequency limit of the phonon group velocity. The Debye dispersion model uses Eq. (2) for all frequencies, and does not distinguish between the LA and TA phonons. Note that in this case $v_p = v_g$, so that in Eq. (1), v_g/v_p^2 becomes $1/v_g$. The specification of v_{0g} is somewhat arbitrary. One possibility is [3]

$$\frac{1}{v_{0g}} = \frac{1}{3}\left(\frac{1}{v_{0g,L}} + \frac{2}{v_{0g,T}}\right), \tag{3}$$

where $v_{0g,L}$ and $v_{0g,T}$ are obtained from the experimental data. Using that of Nilsson and Nelin [8], we get 5142 m/s and 3391 m/s for $v_{0g,L}$ and $v_{0g,T}$, respectively, which give a v_{0g} value of 3825 m/s.

3.2 Holland Model. Holland [4] separated the contributions of LA and TA phonons, and included a partial effect of phonon dispersion by splitting each branch into two linear segments. The change in the slope (and thus the phonon velocities) is assumed to occur at a κ^* value of 0.5. As taken from the experimental data of Nilsson and Nelin [8], the phonon velocities $v_{0g,L}$, $v_{0g,T}$, $v_{0.5g,L}$, and $v_{0.5g,T}$ are 5142 m/s, 3391 m/s, 4152 m/s, and 678 m/s, where the subscript 0.5 refers to the segment between κ^* values of 0.5 and 1. Note that the change in slope implies that v_g is not equal to v_p in the second region. This effect was neglected by Holland, but is included in the current study.

3.3 Sine Function Model. In the sine function model, the phonon dispersion relation for each polarization is approximated by that of a linear monatomic chain as [10]

$$\omega_i = \omega_{mi}\sin\left(\frac{\pi\kappa_i^*}{2}\right), \tag{4}$$

where the label i can be L or T (this notation holds for the rest of the dispersion models). The critical drawback of this model is the nonrealistic behavior at low frequencies ($\kappa \rightarrow 0$) where the asymptotic velocities

$$v_{0g,i} = \left.\frac{\partial\omega_i}{\partial\kappa_i}\right|_{\kappa_i\rightarrow 0} = \frac{\pi\omega_{mi}}{2\kappa_{mi}} \tag{5}$$

are different from the experimental results. For $v_{0g,L}$ and $v_{0g,T}$, we obtain 6400 m/s and 2130 m/s, compared to the experimental values of 5142 m/s and 3391 m/s.

3.4 Tiwari Model. In the Tiwari model [5], the dispersion is assumed to be of the form

$$\kappa_L = \frac{\omega_L}{v_{0g,L}}(1+\alpha\omega_L) \quad \text{and} \quad \kappa_T = \frac{\omega_T}{v_{0g,T}}(1+\beta\omega_T^2), \tag{6}$$

where α and β are constants, given in [5]. Note that these equations satisfy the Brillouin zone boundary conditions

$$\kappa_i(\omega_i = 0) = 0 \quad \text{and} \quad \left.\frac{\partial\kappa_i}{\partial\omega_i}\right|_{\omega_i=0} = \frac{1}{v_{0g,i}}. \tag{7}$$

This model does not show the observed experimental behavior of

$$\left.\frac{\partial\omega_T}{\partial\kappa_T}\right|_{\kappa_T^*\rightarrow 1} = 0 \tag{8}$$

at the edge of the Brillouin zone, as seen in Fig. 1(*b*).

3.5 Present Study. We introduce a new model for the dispersion, referred to hereafter as the Brillouin zone boundary condition (BZBC) model. A quadratic wave number dependence for LA phonons and a cubic wave number dependence for TA phonons are used. This model is a modification of the Tiwari model, in that the boundary conditions given by Eqs. (7) and (8), and $\omega_i(\kappa_{mi}) = \omega_{mi}$, are applied. The resulting dispersion relations are

$$\begin{aligned} \omega_L &= v_{0g,L}\kappa_m\kappa^* + (\omega_{mL} - v_{0g,L}\kappa_m)\kappa^{*2} \\ \omega_T &= v_{0g,T}\kappa_m\kappa^* + (3\omega_{mT} - 2v_{0g,T}\kappa_m)\kappa^{*2} \\ &\quad + (v_{0g,T}\kappa_m - 2\omega_{mT})\kappa^{*3}. \end{aligned} \tag{9}$$

3.6 Comparison of Dispersion Models. A comparison of the five dispersion models, along with the experimental data for germanium [8], is shown in Figs. 1(*a*) and 1(*b*). For the both the longitudinal and transverse polarizations, both the Tiwari and BZBC models match the experimental data reasonably well over most of the first Brillouin zone. The agreement is not as good for the transverse polarization above κ^* values of 0.7 due to the plateau behavior, which is difficult to fit with a low order polynomial. The other dispersion curves are unsatisfactory. Of the Tiwari and BZBC models, the BZBC curve gives the best agreement with the experimental data. We note than none of these dispersion relations will be consistent with the experimental phonon density of states due to the isotropic assumption. Additionally, the integral of the volumetric density of states will not go to the expected value of $3n$, where n is the volumetric density of unit cells. In order for this to occur, one would need to set the dispersion with this result in mind. For these calculations, we are more concerned with matching the experimental dispersion data.

While the Tiwari and BZBC dispersion curves show some similarities, significant differences become apparent when the quantity they affect in the thermal conductivity expression, v_g/v_p^2, is considered. This is shown in Figs. 2(*a*) and 2(*b*). The deviation is most significant for the TA phonons near the edge of Brillouin zone, and will result in an over prediction of the high frequency contribution to the thermal conductivity by the Tiwari model. This

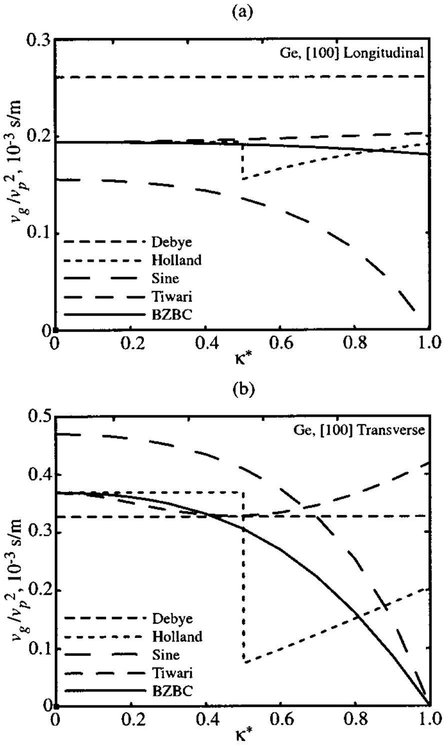

Fig. 2 v_g/v_p^2 **for the five dispersion models plotted as a function of normalized wave number for (*a*) LA phonons and (*b*) TA phonons.**

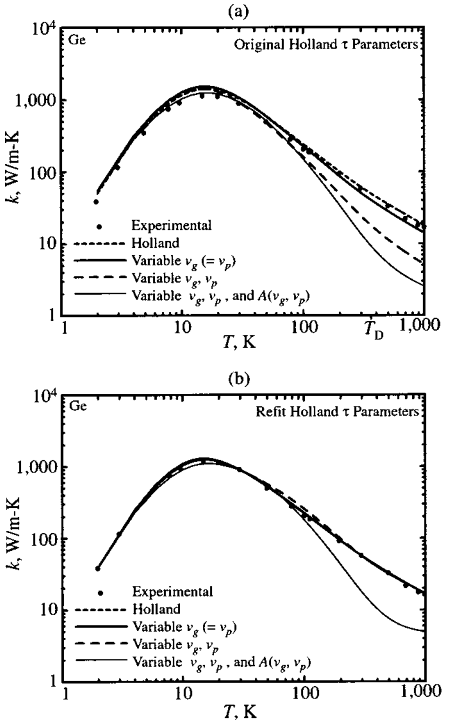

Fig. 3 Effect of refining the treatment of the dispersion on the prediction of the thermal conductivity of germanium. (*a*) Based on the original Holland fitting parameters, and (*b*) predictions refit to the experimental data.

deviation is because the appropriate boundary condition at the edge of the Brillouin zone (Eq. (8)) has not been enforced in the Tiwari model.

3.7 Impurity Scattering. The value of the thermal conductivity is sensitive to impurities, which include the isotopic content of an otherwise pure crystal [11]. The impurity relaxation time, τ_I, is given by [12,13]

$$\frac{1}{\tau_I}=\frac{V_0\Sigma_i f_i[1-(M_i/M)]^2}{4\pi v_g v_p^2}\omega^4, \tag{10}$$

where V_0 is the average volume of a unit cell, f_i is the fractional concentration of species i, M is the average atomic mass, and M_i is the atomic mass of species i. At low frequency, where $v_g \sim v_p \sim v_{0g}$, the relaxation time displays an ω^{-4}-dependence (i.e., Rayleigh scattering). Due to phonon dispersion, such an assumption will not be valid at higher frequencies, and will lead to an overestimation of the thermal conductivity.

4 Thermal Conductivity Prediction

4.1 Role of Dispersion. The accuracy of the thermal conductivity model described in section 2 depends on the nature of the phonon dispersion and relaxation time models. To isolate the effects of dispersion, the relaxation time model used in the subsequent calculations is fixed to that of Holland [4].

In Figs. 3(*a*) and 3(*b*), the effect of including the difference between the phonon group and phase velocities on the prediction of the thermal conductivity of germanium is shown. The experimental data are taken from Holland [4]. The predicted values in Fig. 3 correspond to (i) the Holland model, that is, no distinction between v_g and v_p and a linear two region treatment, (ii) no distinction between v_g and v_p, but using the frequency dependence of the group velocity, (iii) different and frequency dependent v_g and v_p, and (iv) same as (iii), plus rigorous treatment of the impurity scattering by distinguishing between v_g and v_p. In (ii)–(iv), the velocities are calculated with the BZBC dispersion model. In (i)–(iii) the impurity scattering is calculated with $v_g = v_p = v_{0g}$ for each polarization.

In Fig. 3(*a*), the relaxation time model and fitting parameters originally obtained by Holland are used. In Fig. 3(*b*), the curves have been refit to the experimental data. From Fig. 3(*a*), it is evident that the fitting parameters are not universal, and strongly dependent on the dispersion model. Thus, to use the values obtained by Holland, one must also use that dispersion model. However, as shown in Fig. 3(*b*), by refitting the relaxation time parameters, excellent agreement with the experimental data can be obtained in all cases, except when the impurity scattering is rigourously modeled. In this case, the predicted thermal conductivity becomes lower than the experimental data, especially at high temperatures. Under the Holland dispersion, the plateau in the TA dispersion curve is not properly addressed, and the TA phonons make a significant contribution to the thermal conductivity at high temperatures. Here, with the proper modeling of the TA phonons, this contribution is reduced and as such, the role of TA phonons should be reassessed. The effect is not seen at low temperatures, where it is the lower frequency phonons that dominate the thermal transport.

4.2 Role of Relaxation Time Model. The use of a rigorous model for the phonon dispersion has led to an apparent failure of the Holland SMRT approach at high temperatures. The explanation for this must lie in the forms of the relaxation times used. While exact expressions for the relaxation times can be developed [14], their evaluation is extremely difficult due to the required knowledge of the phonon dispersion and three-phonon interactions. Approximate expressions are generally based on low frequency asymptotes [3,4], and yet are often applied over the entire temperature and frequency ranges.

Even with the observed disagreement, the importance of modeling the dispersion can still be shown. The Holland relaxation times are plotted in Fig. 4(*a*) at a temperatures of 80 K for the four

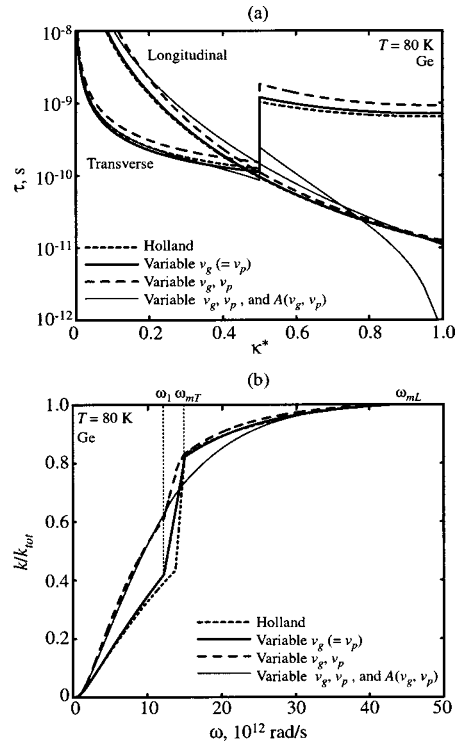

Fig. 4 (*a*) Three phonon relaxation times for refit data from Fig. 3(*b*) at $T=80$ K. (*b*) Cumulative frequency dependence of the thermal conductivity for refit data from Fig. 3(*b*) at $T=80$ K. The thermal conductivity is plotted as a percentage of the total value for each case. The curves show three distinct regions. The transition between the first and second regions takes place at ω_1, where the form of the TA relaxation time changes. The transition between the second and third regions occurs at ω_{mT}, after which there is no contribution from TA phonons [see Eq. (1)].

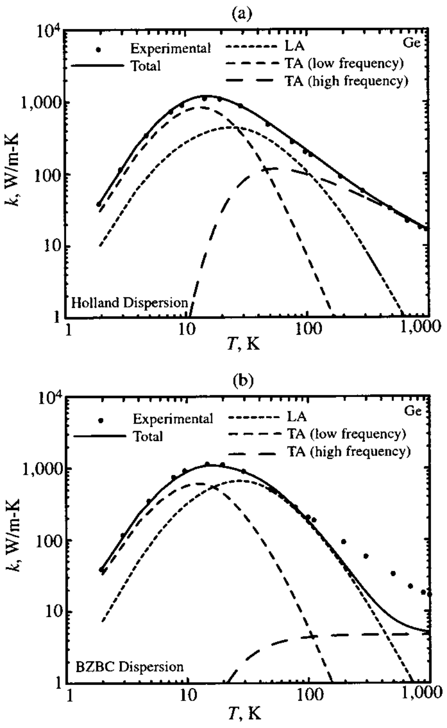

Fig. 5 Contributions of LA and TA phonon branches to the thermal conductivity based on (*a*) Holland dispersion model, and (*b*) BZBC dispersion model.

cases shown in Fig. 3(*b*). The most striking feature of these results is the large discontinuity in the TA relaxation time when κ^* is equal to 0.5, where the functional form is assumed to change (see Eq. (1)). As the temperature increases, the size of the discontinuity increases. For example, at a temperature of 900 K, the discontinuity covers four orders of magnitude. The size of the discontinuity decreases as the treatment of the dispersion is refined. This suggests that the observed behavior is more realistic. Such discontinuities are also found in other relaxation time models [5,6]. In theory, one would expect the relaxation time curves to be continuous, and this has been found in molecular dynamics simulations of the Lennard-Jones face-centered cubic crystal [15].

The effect of the fitting parameters in the relaxation time model can also be demonstrated by plotting the cumulative frequency dependence of the thermal conductivity. This is shown for the same four cases as Fig. 4(*a*) in Fig. 4(*b*). Note that the thermal conductivity is normalized against the total value for each case. As the treatment of the dispersion is refined, the thermal conductivity curves become smoother.

4.3 Transverse and Longitudinal Phonon Contributions

The relative contributions of LA and TA phonons to the total heat flow at high temperatures have not been fully resolved. As shown in Fig. 5(*a*), the Holland model predicts that the TA phonons are the dominant heat carriers at high temperatures, even though they have lower group velocities than LA phonons. This result was supported by Hamilton and Parrott [16] using calculations based on a variational method, which does not involve the SMRT approximation. Mazumder and Majumdar [17] ascertained that above 100 K, TA phonons are the primary carriers of energy in silicon (which has the same crystal structure as germanium) using Monte Carlo simulations. However, their calculations were based on the original Holland relaxation times for silicon, which may have contributed to this conclusion. Asen-Palmer et al. [7] have concluded that while the heat flow in germanium above the maximum is primarily due to TA phonons, the LA Umklapp processes cannot be ignored (as they are in the Holland formulation). Ju and Goodson [18] have suggested that LA phonons are the dominant heat carriers in silicon near room temperature. Sood and Roy [6] ascertained that LA phonons dominate heat transport in germanium at high temperatures.

In Fig. 5(*b*), the relative contributions of LA and TA phonons to the thermal conductivity predicted by the BZBC dispersion model (with refit relaxation time parameters) are shown. Compared to the results of Fig. 5(*a*), the role of TA phonons is quite different when the dispersion and impurity scattering are rigorously modeled. We find a thermal conductivity of 5.2 W/m-K at a temperature of 1,000 K, while the experimental value is 17 W/m-K. The high frequency TA phonons cannot contribute much to the thermal conductivity of germanium because of their low group velocity, which appears directly in the thermal conductivity expression, and also results in a high impurity scattering rate. We note that the expected electronic contribution to the thermal conductivity of germanium at a temperature of 1,000 K is 4 W/m-K [19], which is not sufficient to explain the predicted discrepancy.

5 Summary

While the Holland approach to phonon thermal conductivity modeling has been used for more than forty years, some of its physical features are masked by the necessary use of fitting parameters. Previous work has thus only shown the qualitative validity of the SMRT approach. Using molecular dynamics simulations, it has recently been shown that the SMRT approach is also quantitatively valid for Lennard-Jones crystals, through careful calculation of the relaxation times, and inclusion of the effects of temperature on the phonon dispersion [15]. This suggests that the analytical approach described here is valid, but must include accurate, physical modeling of the phonon dispersion and relaxation times. In this study, we have addressed the issue of the phonon dispersion (albeit isotropic, and neglecting any temperature effects) for germanium, using an existing relaxation time model.

Compared to the standard Debye approach, the rigorous treatment of the phonon dispersion has two effects, namely, (i) the use of v_g/v_p^2 in Eq. (1) instead of $1/v_g$, and (ii) enhancement of the impurity scattering rate, τ_I by using $1/v_p^2 v_g$ instead of $1/v_g^3$ in Eq. (10). As shown in Fig. 3(*b*), the effects of refining the dispersion are masked by the fitting parameters required in this approach for all cases except when the impurity scattering is properly modeled. Through examination of the relaxation times and the cumulative frequency dependence of the thermal conductivity, as shown in Figs. 4(*a*) and 4(*b*), the underlying behavior is found to be nonphysical, but improves as the treatment of the dispersion is refined.

To make up the difference in the experimental and predicted thermal conductivities, we suggest inclusion of two heat transfer mechanisms, namely, an optical phonon component [20] and/or an increased contribution of high frequency LA phonons. The role of LA phonons has been investigated to some extent in the past, but not in the context of an accurate dispersion model. We note that one must be very careful when using and/or formulating relaxation time models, as they should be continuous, and not contain abrupt order of magnitude changes. Molecular dynamics simulations appear to be the most promising source of such relations [15].

Acknowledgment

This work was supported by Korea Research Foundation grant KRF-2002-005-D20001 (JDC), the U.S. Department of Energy, Office of Basic Energy Sciences grant DE-FG02-00ER45851, and the Natural Sciences and Engineering Research Council of Canada (AJHM).

References

[1] Debye, P., 1914, *Vortrage uber die kinetische Theorie der Materie und der Elektrizitat*, Teubner, Berlin.
[2] Peierls, R., 1997, ''On the Kinetic Theory of Thermal Conduction,'' *Selected Scientific Papers of Sir Rudolf Peierls With Commentary*, Dalitz, R. H. and Peierls, R., eds., World Scientific, Singapore, pp. 15–48.
[3] Callaway, J., 1959, ''Model for Lattice Thermal Conductivity at Low Temperatures,'' Phys. Rev., **113**, pp. 1046–1051.
[4] Holland, M. G., 1963, ''Analysis of Lattice Thermal Conductivity,'' Phys. Rev., **132**, pp. 2461–2471.
[5] Tiwari, M. D., and Agrawal, B. K., 1971, ''Analysis of the Lattice Thermal Conductivity of Germanium,'' Phys. Rev. B, **4**, pp. 3527–3532.
[6] Sood, K. C., and Roy, M. K., 1993, ''Longitudinal Phonons and High-Temperature Heat Conduction in Germanium,'' J. Phys.: Condens. Matter, **5**, pp. 301–312.
[7] Asen-Palmer, M., Bartkowski, K., Gmelin, E., Cardona, M., Zhernov, A. P., Inyushkin, A. V., Taldenkov, A., Ozhogin, V. I., Itoh, K. M., and Haller, E. E., 1997, ''Thermal Conductivity of Germanium Crystals With Different Isotopic Compositions,'' Phys. Rev. B, **56**, pp. 9431–9447.
[8] Nilsson, G., and Nelin, G., 1971, ''Phonon Dispersion Relations in Ge at 80 K,'' Phys. Rev. B, **3**, pp. 364–369.
[9] Dove, M. T., 1993, *Introduction to Lattice Dynamics*, Cambridge, Cambridge.
[10] Kittel, C., 1996, *Introduction to Solid State Physics*, Wiley, New York.
[11] Geballe, T. H., and Hull, G. W., 1958, ''Isotopic and Other Types of Thermal Resistance in Germanium,'' Phys. Rev., **110**, pp. 773–775.
[12] Klemens, P. G., 1958, ''Thermal Conductivity and Lattice Vibrational Modes,'' Solid State Phys., **7**, pp. 1–98.
[13] Slack, G. A., 1957, ''Effect of Isotopes on Low-Temperature Thermal Conductivity,'' Phys. Rev., **105**, pp. 829–831.
[14] Ziman, J. M., 2001, *Electrons and Phonons*, Oxford, Oxford.
[15] McGaughey, A. J. H., and Kaviany, M., 2004, ''Quantitative Validation of the Boltzmann Transport Equation Thermal Conductivity Model Under the Single Mode Relaxation Time Approximation,'' Phys. Rev. B, **69**, 094303, pp. 1–12.
[16] Hamilton, R. A., and Parrott, J. E., 1969, ''Variational Calculation of the Thermal Conductivity of Germanium,'' Phys. Rev., **178**, pp. 1284–1292.
[17] Mazumder, S., and Majumdar, A., 2001, ''Monte Carlo Study of Phonon Transport in Solid Thin Films Including Dispersion and Polarization,'' ASME J. Heat Transfer, **123**, pp. 749–759.
[18] Ju, Y. S., and Goodson, K. E., 1999, ''Phonon Scattering in Silicon Films With Thickness of Order 100 nm,'' Appl. Phys. Lett., **74**, pp. 3005–3007.
[19] Slack, G. A., and Glassbrenner, C., 1960, ''Thermal Conductivity of Germanium From 3 K to 1020 K,'' Phys. Rev., **120**, pp. 782–789.
[20] McGaughey, A. J. H., and Kaviany, M., 2004, ''Thermal Conductivity Decomposition and Analysis Using Molecular Dynamics Simulations. Part II. Complex Silica Structures,'' Int. J. Heat Mass Transfer, **47**, pp. 1799–1816.

Kiari Boulama

Nicolas Galanis
e-mail address: nicolas.galanis@usherbrooke.ca

THERMAUS,
Génie Mécanique,
Université de Sherbrooke,
Sherbrooke J1K 2R1, QC,
Canada

Analytical Solution for Fully Developed Mixed Convection Between Parallel Vertical Plates With Heat and Mass Transfer

Exact analytical solutions for fully-developed, steady-state laminar mixed convection with heat and mass transfer between vertical parallel plates are presented. The thermal boundary conditions are UWT or UHF while the concentration at each wall is assumed to be uniform but not necessarily the same. The solution for the UWT case depends on a single parameter which combines the effects of thermal and solutal buoyancy. In the UHF case it depends on three independent parameters, the ratio of the thermal Grashof number to the Reynolds number, the ratio of the solutal Grashof number to the Reynolds number, and the wall heat flux ratio. [DOI: 10.1115/1.1737774]

Keywords: *Analytical, Heat Transfer, Laminar, Mass Transfer, Mixed Convection*

Introduction

Heat and mass transfer in mixed convection occurs in many industrial processes and natural phenomena. It has therefore been the subject of many detailed, mostly numerical studies for different flow configurations [1–3]. In the following we focus on analytical solutions in the fully developed flow region.

For pure thermal laminar mixed convection, the limiting case of fully developed flow has been investigated often and the corresponding hydrodynamic and thermal fields have been determined analytically. Thus, Aung and Worku [4] presented an exact solution for fully developed mixed convection in a parallel-plate vertical channel and compared it to their numerical results for developing flow at great distances from the duct entry. In that study the fluid enters the channel from below with uniform velocity and temperature while the two plates are kept at different constant temperatures superior to that of the entering fluid. Therefore, the fluid near the hot wall is accelerated upwards and, in order to satisfy the overall mass conservation, the flow near the cool wall decelerates. For pronounced buoyancy effects, this situation leads to flow reversal. Hamadah and Wirtz [5] extended this study by examining different thermal boundary conditions and obtained the velocity and temperature profiles as well as expressions for the Nusselt numbers. More recently, a similar study was reported by Barletta and Zanchini [6]. Particular attention was paid by these authors to the proper choice of the reference temperature in the Boussinesq expansion of density and the instability of the proposed analytical solution has been extensively discussed.

In natural convection, Gebhart and Pera [7] reported an analytical solution for the simultaneous heat and mass transfer problem along a vertical wall. Temperature and mass fraction of some diffusing species were imposed on the wall and the coupled mass, momentum, energy and species conservation equations were solved. The similarity method adopted by these authors made it possible to obtain solution covering both the developing and the fully developed flow regions. But, as it is now perfectly established, similarity solutions exist only under certain limited conditions. As far as the fully developed flow region is concerned, Nelson and Wood [8] resolved the governing mass, momentum, heat and species conservation equations in an inclined channel subjected to various thermal and solutal boundary conditions. The solution method was analogous to that adopted in the treatment of the thermal mixed convection problem [4–6] and an exact solution was obtained when the uniform wall temperature (UWT) and concentration (UWC) boundary conditions were considered. In the case of uniform wall heat and mass fluxes (UH/MF); however, the velocity profile was approximated by a symmetric parabola and the corresponding expressions for the temperature and mass fraction profiles were calculated.

The aim of the present work is to extend these earlier results to mixed convection involving simultaneous heat and mass transfer. We consider laminar steady-state upward flow of a mixture of two non-reacting components between a two-parallel-plate vertical channel with asymmetrical thermal and mass fraction conditions at the walls. Such solutal boundary conditions have been often used in the literature to model very thin liquid films on solid walls or transpiring porous walls [1,2]. The thermal boundary conditions are UWT and UHF. Analytical expressions for the fully developed velocity, temperature and concentration profiles as well as for the friction coefficients, the Nusselt and Sherwood numbers, are given. Criteria for the existence of flow reversal are also specified.

Mathematical Formulation

The flow field and the transfer processes are two-dimensional, time-independent, and fully developed. The fluid properties are constant except for the density in the gravity force which is

$$\rho=\rho_1[1-\beta_T(T-T_1)-\beta_M(\omega-\omega_1)] \tag{1}$$

Viscous dissipation has been usually neglected in the literature. Gebhart and Pera [7] as well as Nelson and Wood [8] stated that this hypothesis is valid for flows of small vertical extent relatively to the atmospheric scale height. Furthermore, Gebhart and Pera [7] established that the species diffusion due to temperature gradients (Soret effect) and the diffusion of energy due to concentration differences (enthalpy interdiffusion and Dufour effects) are negligible when the concentration of the diffusing species is very small compared to that of the other species. This is the case when water vapor diffuses in dry air. Besides, an order of magnitude analysis in the specific cases under consideration in this paper has revealed that species flux due to the concentration gradient is at least 200 times larger than that due to the Soret effect. Similarly, heat conduction is approximately 100 times larger than enthalpy

---

Contributed by the Heat Transfer Division for publication in the JOURNAL OF HEAT TRANSFER. Manuscript received by the Heat Transfer Division July 22, 2003; revision received February 27, 2004. Associate Editor: P. S. Ayyaswamy.

diffusion, 10^3 larger than the Dufour effect and 10^7 larger than viscous dissipation. Consequently, as in all the studies cited above, all these effects are neglected in this text.

Finally, if the boundary layer assumptions are adopted, the following relations apply in the fully-developed region:

$$v=0, \quad \frac{\partial u}{\partial x}=0, \quad \frac{\partial p}{\partial y}=0, \quad \frac{\partial p}{\partial x}=\frac{dp}{dx}=\text{const} \tag{2}$$

Thus, the dimensionless momentum equation in the stream-wise direction is

$$-\frac{dP}{dX}+\frac{\partial^2 U}{\partial Y^2}+\frac{\text{Gr}_T}{\text{Re}}\theta+\frac{\text{Gr}_M}{\text{Re}}W=0 \tag{3}$$

with $U=0$ at $Y=0$ and $Y=0.5$. As pointed out by Barletta and Zanchini [6], this equation is exact in the UWT case but in the UHF case it is valid only if the axial derivative of the density is small.

Analogously, because of the first order boundary conditions ($W=0$ at $Y=0$ and $W=1$ at $Y=0.5$), the fully developed solutal conditions imply that

$$\frac{\partial W}{\partial X}=0 \tag{4}$$

Therefore, the dimensionless species conservation equation is

$$\frac{d^2 W}{dY^2}=0 \tag{5}$$

The expressions for the dimensionless temperature θ, the Grashof number Gr_T and the energy conservation equation depend on the thermal boundary conditions. Thus, for isothermal walls ($T_2>T_1$)

$$\theta=\frac{(T-T_1)}{(T_2-T_1)}, \quad \text{Gr}_T=\frac{g\beta_T(T_2-T_1)D_h^3}{\nu^2} \tag{6}$$

The corresponding boundary conditions are

$$\theta(Y=0)=0, \quad \theta(Y=0.5)=1 \tag{7}$$

Furthermore, for fully developed flow

$$\frac{\partial \theta}{\partial X}=0 \tag{8}$$

The dimensionless energy conservation equation for UWT is then

$$\frac{\mathrm{d}^2\theta}{\mathrm{d}Y^2}=0 \tag{9}$$

On the other hand, for uniform heat fluxes at the walls ($q_2 \geqslant |q_1|$ with positive values indicating that heat is supplied to the fluid)

$$\theta=\frac{(T-T_1)}{q_2 D_h/\lambda}, \quad \text{Gr}_T=\frac{g\beta_T q_2 D_h^4}{\lambda\nu^2} \tag{10}$$

with the boundary conditions

$$\left.\frac{\partial\theta}{\partial Y}\right|_{Y=0}=-\frac{q_1}{q_2}, \quad \left.\frac{\partial\theta}{\partial Y}\right|_{Y=0.5}=1 \tag{11}$$

and, for thermally developed flow

$$\frac{\partial T}{\partial x}=\frac{q_1+q_2}{\rho C_p u_m b}$$

The dimensionless energy conservation equation in this second case is then

$$\frac{d^2\theta}{dY^2}=2\left(1+\frac{q_1}{q_2}\right)U \tag{12}$$

It should be noted at this point that the entering fluid temperature (T_0) used as reference in Eq. (1) and in the definition of θ by both Aung and Worku [4] as well as Hamadah and Wirtz [5] allows comparisons with the numerical solution of the developing flow problem at great distances from the entry, but is rather bizarre as far as the fully developed flow is concerned. Instead, Barletta and Zanchini [6] set the reference temperature equal to the arithmetic mean temperature over the cross section of the duct. In the present study, we adopt the temperature of the cooler wall as reference, because it is physically convenient and leads to simple expressions for the thermal boundary conditions. In particular, the value of the dimensionless temperature at this wall is $\theta(Y=0)=\theta_1=0$.

Solution for Isothermal Walls. The temperature and mass fraction profiles are easily obtained by double-integration of Eqs. (5) and (9) and application of the appropriate boundary conditions. Thus,

$$\theta(Y)=2Y \tag{13}$$

$$W(Y)=2Y \tag{14}$$

These expressions are then replaced in the momentum equation which upon integration gives

$$U(Y)=\frac{dP}{dX}\left(\frac{Y^2}{2}-\frac{Y}{4}\right)-\frac{\text{Gr}_T+\text{Gr}_M}{\text{Re}}\left(\frac{Y^3}{3}-\frac{Y}{12}\right) \tag{15}$$

The pressure gradient here is unknown and must be evaluated by the overall mass conservation equation

$$\int_0^{0.5} U dY=0.5 \tag{16}$$

which yields

$$\frac{dP}{dX}=-48+\frac{\text{Gr}_T+\text{Gr}_M}{2\,\text{Re}} \tag{17}$$

The velocity profile is therefore given by

$$U(Y)=\frac{\text{Gr}_T+\text{Gr}_M}{\text{Re}}\left(-\frac{Y^3}{3}+\frac{Y^2}{4}-\frac{Y}{24}\right)-24Y^2+12Y \tag{18}$$

This equation indicates that the fully developed velocity profile is independent of the entry conditions and depends only on the combined buoyancy parameter $(\text{Gr}_T+\text{Gr}_M)/\text{Re}$. Moreover, it should be noted that the forced convection Poiseuille profile is recovered by simply equating the combined buoyancy parameter to zero in this expression.

Equation (18) can further be used to calculate mathematically the conditions of flow reversal. In fact, flow reversal occurs when the slope of the velocity profile near the cold wall ($Y=0$) becomes negative

$$\left.\frac{dU}{dY}\right|_{Y=0}<0 \tag{19}$$

which translates into

$$\frac{\text{Gr}_T+\text{Gr}_M}{\text{Re}}>288 \tag{20}$$

Equations (10) and (11) and the previously obtained velocity profile (Eq. (18)) can also be used to derive the following expressions for the bulk temperature and mass fraction:

$$\theta_b=\int_0^{0.5} U\theta dY=\frac{1}{2}+\frac{\text{Gr}_T+\text{Gr}_M}{2880\,\text{Re}} \tag{21}$$

$$W_b=\int_0^{0.5} UWdY=\frac{1}{2}+\frac{\mathrm{Gr}_T+\mathrm{Gr}_M}{2880\,\mathrm{Re}} \tag{22}$$

Finally, the temperature (Eq. (13)), concentration (Eq. (14)) and velocity (Eq. (18)) profiles, together with the calculated bulk temperature (Eq. (21)) and mass fraction (Eq. (22)), are used to derive the following analytical expressions for the friction coefficients and the heat and mass transfer rates on the two walls:

$$\mathrm{Re}\,C_{f1}=12-\frac{\mathrm{Gr}_T+\mathrm{Gr}_M}{24\,\mathrm{Re}} \quad \text{and} \quad \mathrm{Re}\,C_{f2}=12+\frac{\mathrm{Gr}_T+\mathrm{Gr}_M}{24\,\mathrm{Re}} \tag{23}$$

$$\mathrm{Nu}_1=-\frac{4}{1+\dfrac{\mathrm{Gr}_T+\mathrm{Gr}_M}{1440\,\mathrm{Re}}} \quad \text{and} \quad \mathrm{Nu}_2=\frac{4}{1-\dfrac{\mathrm{Gr}_T+\mathrm{Gr}_M}{1440\,\mathrm{Re}}} \tag{24}$$

$$\mathrm{Sh}_1=-\frac{4}{1+\dfrac{\mathrm{Gr}_T+\mathrm{Gr}_M}{1440\,\mathrm{Re}}} \quad \text{and} \quad \mathrm{Sh}_2=\frac{4}{1-\dfrac{\mathrm{Gr}_T+\mathrm{Gr}_M}{1440\,\mathrm{Re}}} \tag{25}$$

Solution for Uniform Heat Fluxes at the Walls. By double-differentiating the momentum conservation equation (Eq. (3)) with respect to the variable Y and using the mass fraction profile (Eq. (14)) and the energy conservation equation (Eq. (12)), one obtains the fourth order differential equation:

$$\frac{d^4U}{dY^4}=-2\,\frac{\mathrm{Gr}_T}{\mathrm{Re}}\left(1+\frac{q_1}{q_2}\right)U \tag{26}$$

or

$$\frac{d^4U}{dY^4}=-4\xi^4U \quad \text{where} \quad \xi=\left[\frac{\mathrm{Gr}_T}{2\,\mathrm{Re}}\left(1+\frac{q_1}{q_2}\right)\right]^{1/4} \tag{27}$$

The parameter ξ is real since $q_2 \geqslant |q_1|$ (i.e., the net heating effect is positive). The general solution of Eq. (27), therefore, leads to the following velocity profile:

$$\begin{aligned} U=&C_1\exp(\xi Y)\cos(\xi Y)+C_2\exp(-\xi Y)\cos(\xi Y)\\ &+C_3\exp(\xi Y)\sin(\xi Y)+C_4\exp(-\xi Y)\sin(\xi Y) \end{aligned} \tag{28}$$

By applying the hydrodynamic (no-slip) boundary conditions at $Y=0$ and $Y=0.5$, two algebraic relations for the four unknown constants C_1, C_2, C_3 and C_4 are obtained. Two more relations result from the application of the corresponding thermal (imposed wall heat flux) boundary conditions to the derivative of Eq. (3) with respect to Y. Some typical values of these constants are given in Table 1.

Once the velocity profile is obtained, the momentum conservation equation (Eq. (3)) is applied at $Y=0$ where $\theta=W=0$ and yields the pressure gradient

$$\frac{dP}{dx}=2\xi^2(C_3-C_4) \tag{29}$$

Equation 3 can finally be used to derive the following expression for the dimensionless temperature:

$$\begin{aligned} \theta=\frac{\mathrm{Re}}{\mathrm{Gr}_T}\Bigg\{&2\xi^2(C_3-C_4)-2\,\frac{\mathrm{Gr}_M}{\mathrm{Re}}\,Y-\xi^2[-4C_1\cosh(\xi Y)\sin(\xi Y)\\ &+2C_3\exp(\xi Y)\cos(\xi Y)-2C_4\exp(-\xi Y)\cos(\xi Y)]\Bigg\} \end{aligned} \tag{30}$$

As for the case of isothermally heated walls, the criteria of flow reversal can be analytically evaluated from the velocity profile (Eq. (28)) in terms of variables C_1, C_2, C_3, and C_4. Thus,

Table 1 Typical values of constants C_1, C_2, C_3, and C_4 as defined in Eq. 28

	$C_1=-C_2$	C_3	C_4
	$\mathrm{Gr}_M/\mathrm{Re}=250$ and $q_1/q_2=-0.5$		
$\mathrm{Gr}_T/\mathrm{Re}=1$	177.5086	−137.8252	−214.9714
$\mathrm{Gr}_T/\mathrm{Re}=500$	2.1634	0.4281	−6.1325
$\mathrm{Gr}_T/\mathrm{Re}=1000$	1.3510	0.6994	−5.9501
$\mathrm{Gr}_T/\mathrm{Re}=2000$	0.7366	0.7989	−6.4187
	$\mathrm{Gr}_M/\mathrm{Re}=250$ and $q_1/q_2=0.5$		
	$C_1=-C_2$	C_3	C_4
$\mathrm{Gr}_T/\mathrm{Re}=1$	77.8988	−54.8365	−99.2572
$\mathrm{Gr}_T/\mathrm{Re}=500$	0.5250	0.3876	−0.8043
$\mathrm{Gr}_T/\mathrm{Re}=1000$	0.1937	0.3323	0.0551
$\mathrm{Gr}_T/\mathrm{Re}=2000$	0.0069	0.2293	0.8218
	$\mathrm{Gr}_M/\mathrm{Re}=250$ and $q_1/q_2=1.0$		
	$C_1=-C_2$	C_3	C_4
$\mathrm{Gr}_T/\mathrm{Re}=1$	62.7733	−42.7679	−81.1855
$\mathrm{Gr}_T/\mathrm{Re}=500$	0.3202	0.3198	0.3206
$\mathrm{Gr}_T/\mathrm{Re}=1000$	0.0836	0.2385	1.3346
$\mathrm{Gr}_T/\mathrm{Re}=2000$	−0.0294	0.1405	2.3085

$$\left.\frac{dU}{dY}\right|_{Y=0}<0 \quad \text{implies} \quad 2C_1+C_3+C_4<0 \tag{31}$$

Analogously, expressions for the bulk temperature and bulk concentration are calculated from Eqs. (28), (30), and (14). These expressions are not as simple as those obtained in the case of isothermal walls and are not reproduced in this text. The friction coefficients, Nusselt and Sherwood numbers are given in terms of the constants C_1, C_3, and C_4, and the bulk values θ_b and W_b by the following expressions:

$$\mathrm{Re}\,C_{f1}=\xi(2C_1+C_3+C_4)$$

and

$$\begin{aligned} \mathrm{Re}\,C_{f2}=\xi\{&2C_1[\sinh(\xi/2)\sin(\xi/2)+\cosh(\xi/2)\cos(\xi/2)]\\ &-C_3\exp(\xi/2)[\cos(\xi/2)+\sin(\xi/2)]\\ &+C_4\exp(-\xi/2)[\sin(\xi/2)-\cos(\xi/2)]\} \end{aligned} \tag{32}$$

$$\mathrm{Nu}_1=\frac{|q_1/q_2|}{\theta_1-\theta_b} \quad \text{and} \quad \mathrm{Nu}_2=\frac{1}{\theta_2-\theta_b} \tag{33}$$

$$\mathrm{Sh}_1=-\frac{2}{W_b} \quad \text{and} \quad \mathrm{Sh}_2=\frac{2}{1-W_b} \tag{34}$$

Some typical values of these parameters are presented in the section ''Results and Discussion'' of the present paper.

Validation

The model presented here has been successfully validated for negligible solutal buoyancy ($\mathrm{Gr}_M=0$) by comparison with the previously published results referred to in the introduction. In the case of isothermal walls, the analytical solution for velocity and temperature profiles as well as the axial pressure gradient and the flow reversal criterion are exactly the same as those obtained by Aung and Worku [4] if the same nondimensionalization technique were used. The friction coefficients and Nusselt numbers were not calculated by these earlier researchers.

In the case of uniform wall heat fluxes without mass transfer, the formulation adopted is exactly the same as that used by Barletta and Zanchini [6] and the results are identical. The dimensionless temperature profiles also match perfectly (the two nondimensionalization techniques differ only by a constant) and the Nusselt numbers (Table 1 of [6]) are exactly reproduced by the present study.

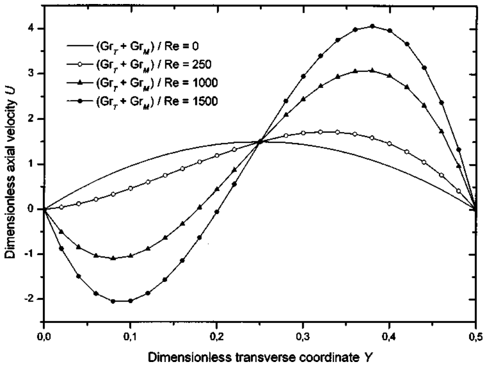

Fig. 1 UWT: Representative velocity profiles for different values of the combined buoyancy parameter $(Gr_T + Gr_M)/Re$

Results and Discussion

Isothermal Walls. In this case the results depend on the value of only one parameter, the combined buoyancy parameter $(Gr_T + Gr_M)/Re$. Representative velocity profiles are shown in Fig. 1 for different values of this parameter. For $(Gr_T + Gr_M)/Re = 0$, the Poiseuille parabolic profile is recovered. With increasing values of the combined buoyancy parameter, the flow accelerates near the hot wall. This phenomenon is accompanied by a flow deceleration near the cooler wall, and, for values of $(Gr_T + Gr_M)/Re$ higher than the previously established limit value of 288 (Eq. (20)) the flow reverses its sign. The region of flow reversal becomes larger as $(Gr_T + Gr_M)/Re$ increases but at the centerline the velocity is never negative. In fact the value of the dimensionless axial component of the velocity vector at mid-channel is independent of $(Gr_T + Gr_M)/Re$. This result which is illustrated in the figure can be derived directly from the velocity profile (Eq. (18)).

Figure 2 illustrates the variation of the friction coefficients with the combined buoyancy parameter. Starting from the pure forced convection value of 12, the friction coefficient near the hot wall increases linearly when the buoyancy parameter increases or, equivalently, when the flow in that region is accelerated. On the other hand the friction coefficient near the cooler wall decreases linearly, becomes negative when the flow direction changes, and continues to decrease when the combined buoyancy parameter increases. It is finally worth noting that our Fig. 2 is analogous to Fig. 3 of [4] when the solutal Grashof number is equal to zero.

The expressions for the bulk temperature (Eq. (21)) and Nusselt numbers (Eqs. (24)) reduce to Eqs. (11*a*) and (11*b*) of Hamadah and Wirtz [5] when only thermal buoyancy effects are considered. As pointed out by Aung and Worku [4], the bulk temperature is always higher than the cold wall temperature (i.e., $Nu_1 < 0$) and can even become higher than that of the hot wall when $(Gr_T + Gr_M)/Re > 1440$. In the latter case, Nu_2 is negative even though heat is supplied to the fluid. Figure 3 shows that the absolute value of the Nusselt number for the cooler wall diminishes monotonically when the combined buoyancy parameter increases. On the other hand, Nu_2 initially increases as buoyancy effects become more important. The occurrence of a fluid bulk temperature equal to that of the hotter wall gives rise to a discontinuity in Nu_2 with positive infinite values when $(Gr_T + Gr_M)/Re$ is very close but inferior to 1440, and negative infinite values of Nu_2 for values of the buoyancy parameter very close but superior to 1440. The corresponding heat fluxes which have very high absolute values occur from the wall to the fluid when $(Gr_T + Gr_M)/Re < 1440$ and in the opposite direction when $(Gr_T + Gr_M)/Re > 1440$. The expressions for the Sherwood numbers (Eqs. (25)) are identical to those of the Nusselt numbers (Eqs. (24)). This result is consistent with the heat and mass transfer analogy and Fig. 3 together with the corresponding discussion apply for both Sherwood and Nusselt numbers.

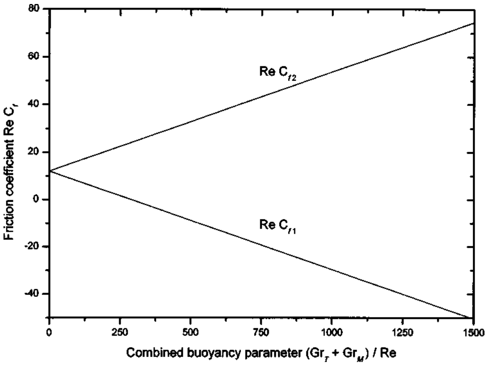

Fig. 2 UWT: Effects of the combined buoyancy parameter $(Gr_T + Gr_M)/Re$ on the friction coefficients

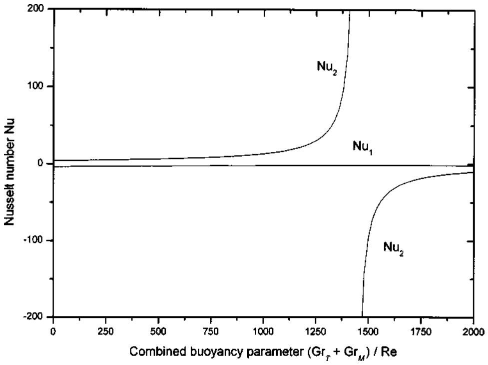

Fig. 3 UWT: Effects of the combined buoyancy parameter $(Gr_T + Gr_M)/Re$ on the Nusselt (or Sherwood) numbers

Uniform Wall Heat Fluxes. At this point, it is recalled that $q_2 \geqslant |q_1|$ for the obtained solution to be valid (see Eqs. (27) and (28)). However, q_1 can be positive (the fluid is then heated from both walls) or negative (the fluid is cooled from the wall at $Y = 0$ and heated from the wall at $Y = 0.5$.

In this case, the velocity and temperature profiles (Eqs. (28) and (30)) as well as the dimensionless transfer rates (Eqs. (32), (33), and (34)) depend on the values of three parameters: the two buoyancy parameters Gr_T/Re, Gr_M/Re, and the wall heat flux ratio q_1/q_2.

First of all the pure thermal buoyancy effects are investigated. In Fig. 4(*a*) the dimensionless velocity profile is plotted for different values of Gr_T/Re and symmetrical heating conditions $(q_1/q_2 = 1)$. Increasing Gr_T/Re induces flow acceleration near both walls and consequently flow deceleration in the centerline of the channel. Eventually this tendency can lead to flow reversal at the centerline but the corresponding value of Gr_T/Re is of questionable physical signification (see discussion by Barletta and Zanchini [6] on stability). This tendency to flatten the velocity profile induces a more homogenous distribution of the temperature across the channel width (Fig. 4(*b*)). The fluid temperature is always lower than the wall temperatures and, consequently, the bulk temperature is also lower than the wall temperatures. Both velocity and temperature profiles are symmetrical when $q_1/q_2 = 1$.

For the same symmetrical thermal boundary conditions, Figs. 5(*a*) and 5(*b*) indicate that the velocity and temperature profiles become more and more distorted as solutal buoyancy effects increase. As seen in Fig. 5(*a*), the flow accelerates near the wall with the higher mass fraction W and decelerates near the other wall leading eventually to flow reversal. Recall that the flow reversal condition (Eq. (31)) involves each of the three independent parameters Gr_T/Re, Gr_M/Re, and q_1/q_2 while in the isothermal case (Eq. (20)) it depended only on the combined buoyancy pa-

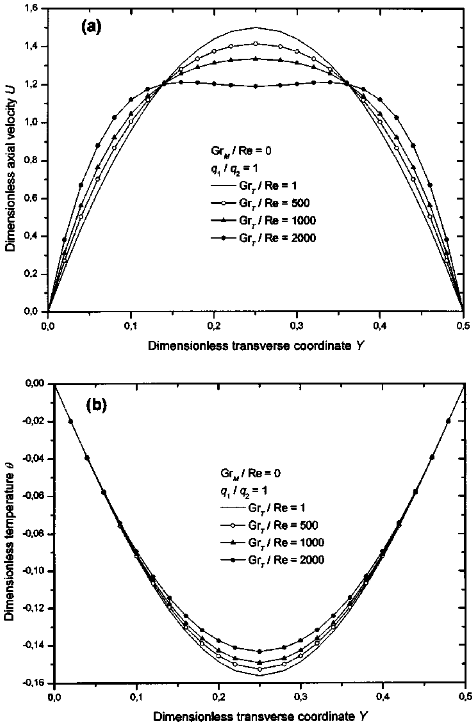

Fig. 4 UHF: Effects of the thermal buoyancy parameter $\mathrm{Gr}_T/\mathrm{Re}$ on (*a*) the velocity, and (*b*) the temperature profiles

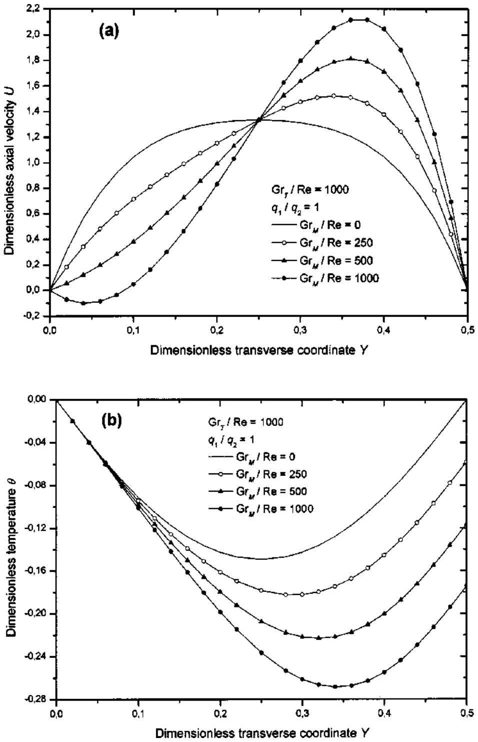

Fig. 5 UHF: Effects of the solutal buoyancy parameter $\mathrm{Gr}_M/\mathrm{Re}$ on (*a*) the velocity, and (*b*) the temperature profiles

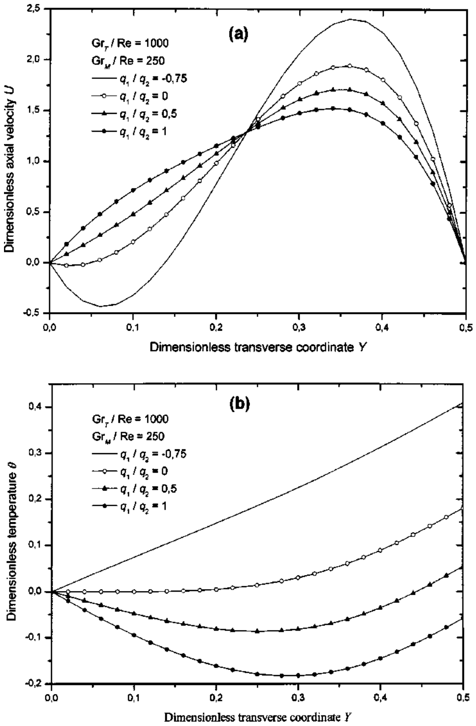

Fig. 6 UHF: Effects of the wall heat flux ratio q_1/q_2 on (*a*) the velocity, and (*b*) the temperature profiles

rameter. It should also be noted in Fig. 5(a) that the dimensionless axial velocity at the centerline of the channel is independent of the value of $\mathrm{Gr}_M/\mathrm{Re}$.

Figure 5(*b*) shows that the temperature profile slopes on both walls remain constant in accordance with the imposed thermal boundary conditions (Eq. (11)). As $\mathrm{Gr}_M/\mathrm{Re}$ increases, wall 2 becomes increasingly cooler relatively to wall 1. This observation can be explained by the fact that the axial convective heat transport near the right wall becomes more and more important (Fig. 5(*a*)). For $\mathrm{Gr}_M/\mathrm{Re}=0$, the fluid bulk temperature is much lower than that of the two walls. As $\mathrm{Gr}_M/\mathrm{Re}$ increases it approaches that of wall 2. Eventually the fluid bulk temperature can exceed that of wall 2 but is always lower than that of wall 1.

Figures 6(*a*) and 6(*b*) illustrate the effects of the wall heat flux ratio on the velocity and temperature profiles for given values of the two buoyancy parameters. It is shown that when q_1/q_2 diminishes, the flow near wall 2 is more and more accelerated and flow reversal is observed in the vicinity of wall 1. Meanwhile wall 2 becomes increasingly hotter relatively to wall 1 and the temperature profile approaches a linear distribution. The limiting case of $q_1/q_2=-1$ cannot be obtained from Eqs. (28) and (30). However in this case Eq. (12) reduces to the energy conservation equation for the isothermal case (Eq. (9)) as pointed out by Barletta and Zanchini [6] for pure thermal convection. Therefore, the solution for $q_1/q_2=-1$ depends only on the combined buoyancy parameter (see Figs. 1, 2, 3). The fluid bulk temperature can be higher than either or both wall temperatures as pointed out by Aung and Worku [4] for pure thermal convection.

Figure 7(*a*) illustrates the influence of the thermal buoyancy parameter on the friction coefficients of the two walls. The values of the two friction coefficients become increasingly different as $\mathrm{Gr}_T/\mathrm{Re}$ increases. The difference between $\mathrm{Re}\,\mathrm{C}_{f1}$ and $\mathrm{Re}\,\mathrm{C}_{f2}$ diminishes when q_1/q_2 increases. This influence of q_1/q_2 is more pronounced when $\mathrm{Gr}_T/\mathrm{Re}$ is large and vanishes in the absence of thermal buoyancy effects.

The effects of the solutal buoyancy parameter on the friction

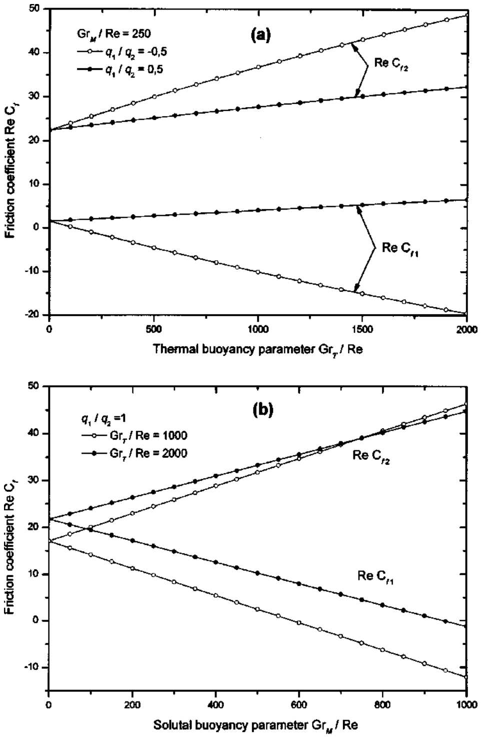

Fig. 7 UHF: Effects of (*a*) the thermal buoyancy parameter $\mathrm{Gr}_T/\mathrm{Re}$, and (*b*) the solutal buoyancy parameter $\mathrm{Gr}_M/\mathrm{Re}$ on the friction coefficients

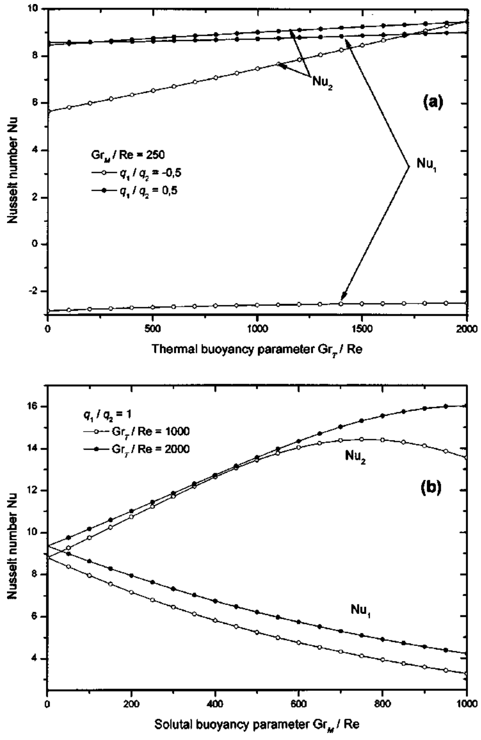

Fig. 9 UHF: Effects of (*a*) the thermal buoyancy parameter $\mathrm{Gr}_T/\mathrm{Re}$, and (*b*) the solutal buoyancy parameter $\mathrm{Gr}_M/\mathrm{Re}$ on the Nusselt numbers

coefficients are shown in Fig. 7(*b*) for two values of $\mathrm{Gr}_T/\mathrm{Re}$ and $q_1/q_2=1$. As $\mathrm{Gr}_M/\mathrm{Re}$ decreases, the friction coefficient of wall 2 decreases while that of wall 1 increases, consistently with the velocity profiles of Fig. 5(*a*). When $\mathrm{Gr}_M/\mathrm{Re}$ becomes zero, the values of the two friction coefficients are identical. Furthermore as $\mathrm{Gr}_T/\mathrm{Re}$ decreases, this unique value also decreases and in the limit $\mathrm{Gr}_T/\mathrm{Re}=0$ it becomes equal to 12 which is the value for forced convection.

Figure 8 shows the effects of the wall heat flux ratio on the friction coefficients. The two friction coefficients start far apart when q_1/q_2 is small and converge towards intermediate values as q_1/q_2 increases. This behavior is easily understandable when Fig. 8 is related to Fig. 6(*a*) where it was shown that increasing q_1/q_2 reduces the distortion in the shape of the velocity profile. Since $\mathrm{Gr}_M/\mathrm{Re}\neq 0$ (the velocity profile is not symmetrical) the values of the two friction coefficients at $q_1/q_2=1$ are not equal.

Figures 9(*a*), 9(*b*), and 10 illustrate, respectively, the effects of the thermal buoyancy parameter, the solutal buoyancy parameter and the wall heat flux ratio on the Nusselt numbers. As for the isothermal case, positive Nusselt numbers indicate that the wall temperature is higher than that of the fluid while negative values indicate that the fluid bulk temperature is higher than that of the wall. Specifically, Fig. 9(*a*) for $\mathrm{Gr}_M/\mathrm{Re}=250$ shows that Nu_2 increases with $\mathrm{Gr}_T/\mathrm{Re}$. This increase can be explained by the fact that θ_b approaches θ_2 when thermal buoyancy effects increase (see Fig. 6). At low values of $\mathrm{Gr}_T/\mathrm{Re}$, Nu_2 increases with q_1/q_2. Similarly, for the same value of $\mathrm{Gr}_M/\mathrm{Re}$ and $q_1/q_2=0.5$, Nu_1 is positive since $\theta_b<\theta_1$ (Eq. (33)) and increases with $\mathrm{Gr}_T/\mathrm{Re}$. However, for $q_1/q_2=-0.5$, Nu_1 is negative and its absolute value diminishes as $\mathrm{Gr}_T/\mathrm{Re}$ increases.

Figure 9(*b*) indicates that the Nusselt number for wall 1 is positive and monotonically decreases as $\mathrm{Gr}_M/\mathrm{Re}$ increases. This result can be predicted from Fig. 5(*b*) which indicates that the bulk temperature decreases relatively to θ_1 when $\mathrm{Gr}_M/\mathrm{Re}$ increases. On the other hand, the behavior of Nu_2 cannot be deduced directly from Figs. 5(*a*) and 5(*b*) because both θ_b and θ_2

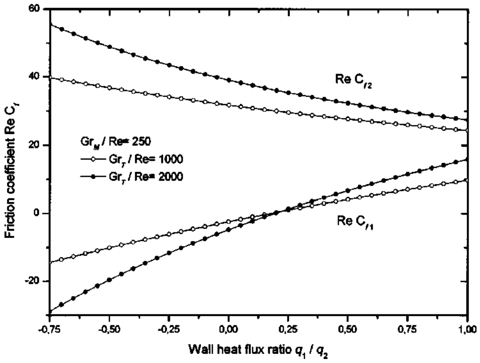

Fig. 8 UHF: Effects of the wall heat flux ratio q_1/q_2 on the friction coefficients

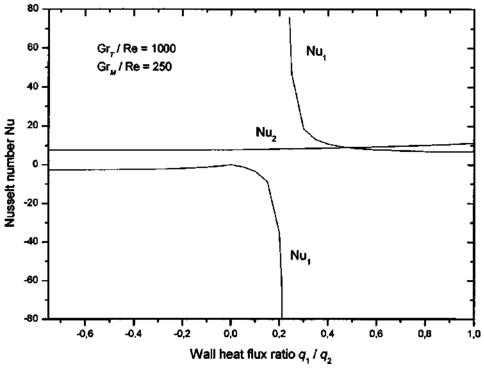

Fig. 10 UHF: Effects of the wall heat flux ratio q_1/q_2 on the Nusselt numbers

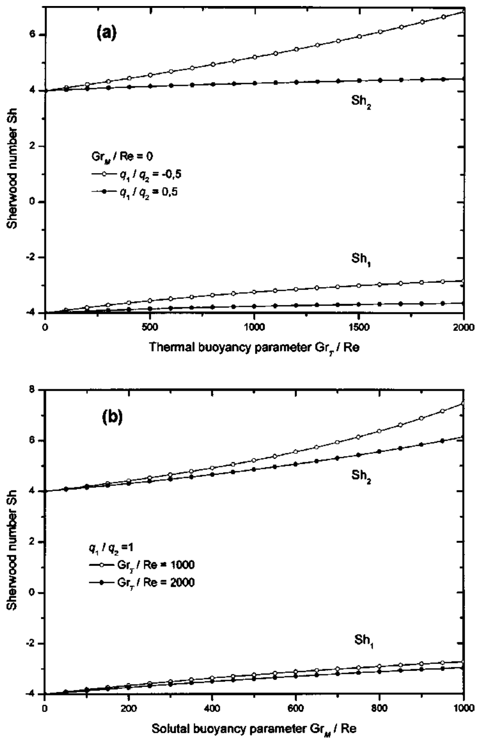

Fig. 11 UHF: Effects of (*a*) the thermal buoyancy parameter $\mathrm{Gr}_T/\mathrm{Re}$, and (*b*) the solutal buoyancy parameter $\mathrm{Gr}_M/\mathrm{Re}$ on the Sherwood numbers

vary (accordingly to Eq. (33) the Nusselt number depends on the difference between these two temperatures) and Fig. 9(*b*) reveals that Nu_2 may reach a maximum value as $\mathrm{Gr}_M/\mathrm{Re}$ increases.

Figure 10 shows that the Nusselt number for wall 2 varies very little as the wall heat flux ratio increases. Its value remains always positive consistently with Eq. (33) since $\theta_2 > \theta_b$ for all values of q_1/q_2 and this combination of buoyancy parameters (see Fig. 6). On the other hand Nu_1 starts from a negative value when $q_1/q_2 = -0.75$ consistently with Eq. (33) because $\theta_b > 0$ (see Fig. 6 (*b*)). As $|q_1/q_2|$ decreases, θ_b decreases too, and the variation of the Nusselt number is not easily predictable. However, as θ_b approaches zero, Nu_1 tends to $-\infty$. As q_1/q_2 increases further, θ_b becomes negative, therefore Nu_1 is positive. It remains positive but decreases monotonically with q_1/q_2.

Finally, Figs. 11(*a*), 11(*b*), and 12 respectively show the effects of the thermal buoyancy parameter, the solutal buoyancy parameter and the wall heat flux ratio on the Sherwood numbers. Figure 11(*a*) shows that the Sherwood numbers increase with $\mathrm{Gr}_T/\mathrm{Re}$. This effect is more important for lower values of q_1/q_2. Similarly, Fig. 11(*b*) indicates that the Sherwood numbers for the two walls start from the forced convection values and increase regularly with $\mathrm{Gr}_M/\mathrm{Re}$. As expected this effect is more pronounced for lower values of $\mathrm{Gr}_T/\mathrm{Re}$. Finally, Fig. 12 indicates that for the given values of $\mathrm{Gr}_M/\mathrm{Re}$ and $\mathrm{Gr}_T/\mathrm{Re}$, the wall Sherwood numbers decrease when the ratio q_1/q_2 increases. This decrease is more important for larger values of $\mathrm{Gr}_T/\mathrm{Re}$.

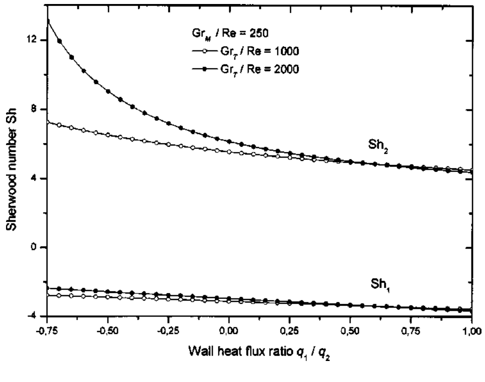

Fig. 12 UHF: Effects of the wall heat flux ratio q_1/q_2 on the Sherwood numbers

The above remarks concerning the effects of the three controlling parameters on the solution should not be generalized. For other combinations of $\mathrm{Gr}_T/\mathrm{Re}$, $\mathrm{Gr}_M/\mathrm{Re}$, and q_1/q_2, the model should be applied in order to obtain these effects.

Conclusion

The analytical solution for upward, fully developed, laminar, and time-independent mixed convection heat and mass transfer in a vertical channel has been derived following an approach formerly used by Aung and Worku [4], Hamadah and Wirtz [5], and Barletta and Zanchini [6] for pure thermal mixed convection. When the solutal buoyancy effects are neglected, the obtained results are identical to those reported by these researchers for corresponding conditions. When asymmetrical and uniform temperatures and concentrations are imposed at the walls the solutions depend on the combined buoyancy parameter $(\mathrm{Gr}_T + \mathrm{Gr}_M)/\mathrm{Re}$. If however the thermal boundary conditions are changed to UHF the solutions depend on the three independent parameters: $\mathrm{Gr}_T/\mathrm{Re}$, $\mathrm{Gr}_M/\mathrm{Re}$, and q_1/q_2. In both cases analytical expressions for velocity, temperature, and mass fraction profiles are obtained and the conditions of flow reversal are analyzed. Furthermore, typical friction coefficients, as well as Nusselt and Sherwood numbers are presented for different values of the controlling parameters. The figures reveal that buoyancy effects significantly improve heat and momentum transfer rates near heated walls.

The solution presented for the UHF case is valid when the net heating effect is positive but an analogous solution can be obtained for opposing thermal buoyancy forces from Eq. (26).

Acknowledgment

The financial support of this work by the Natural Sciences and Engineering Research Council of Canada is gratefully acknowledged.

Nomenclature

b = channel width [m]
C_f = coefficient of friction$=\tau/(0.5\rho u_0^2)$
C_p = specific heat at constant pressure $[\mathrm{J\,kg^{-1}\,K^{-1}}]$
D = mass diffusivity $[\mathrm{m^2\,s^{-1}}]$
D_h = hydraulic diameter$=2b$ [m]
g = gravitational acceleration $[\mathrm{m\,s^{-2}}]$
Gr_T = thermal Grashof number (as defined by Eqs. 6 and 8)
Gr_M = solutal Grashof number$=g\beta_M(\omega_2-\omega_1)D_h^3/\nu^2$
h = coefficient of heat transfer $[\mathrm{W\,m^{-2}\,K^{-1}}]$
h_M = coefficient of mass transfer $[\mathrm{kg\,m^{-2}\,s^{-1}}]$
Nu = Nusselt number$=hD_h/\lambda$
p = static pressure [Pa]
P = dimensionless pressure$=(p+\rho g x)/\rho u_0^2$
Re = Reynolds number$=u_m D_h/\nu$
q = imposed wall heat flux $[\mathrm{W\,m^{-2}}]$
Sh = Sherwood number$=h_M D_h/D$
T = temperature [K]
u, v = axial and transverse components of velocity vector $[\mathrm{m\,s^{-1}}]$
U, V = dimensionless components of velocity vector $U = u/u_0$ and $V = vD_h/\nu$
W = dimensionless mass fraction of diffusing species$=(\omega-\omega_1)/(\omega_2-\omega_1)$

x, y = axial and transverse coordinates [m]
X, Y = dimensionless axial and transverse coordinates $X = x/(D_h \text{Re})$ and $Y = y/D_h$

Greek Letters

β_M = solutal expansion coefficient [−]
β_T = thermal expansion coefficient [K^{-1}]
λ = thermal conductivity [$W\,m^{-1}\,K^{-1}$]
ν = kinematic viscosity [$m^2\,s^{-1}$]
τ = wall shear stress [$N\,m^{-2}$]
ρ = density [$kg\,m^{-3}$]
θ = dimensionless temperature (as defined by Eqs. 6 and 8)
ω = mass fraction of diffusing species [kg of diffusing species/kg of mixture]

Subscripts

0 = value at duct entrance ($x = 0$)
1 = value on cold wall ($y = 0$)
2 = value on hot wall ($y = b$)
b = bulk value

References

[1] Orfi, J., and Galanis, N., 2002, ‘‘Developing Laminar Convection With Heat and Mass Transfer in Horizontal and Vertical Tubes,’’ Int. J. Therm. Sci., **41**(4), pp. 319–331.

[2] Yan, W. M., 1995, ‘‘Transport Phenomena of Developing Laminar Mixed Convection Heat and Mass Transfer in Inclined Rectangular Ducts,’’ Int. J. Heat Mass Transfer, **38**(15), pp. 2905–2914.

[3] Ali Cherif, A., and Daïf, A., 1999, ‘‘Étude numérique du transfert de chaleur et de masse entre deux plaques planes verticales en présence d’un film liquide binaire ruisselant sur l’une des plaques chauffée,’’ Int. J. Heat Mass Transfer, **42**(13), pp. 2399–2418.

[4] Aung, W., and Worku, G., 1986, ‘‘Theory of Fully Developed, Combined Convection Including Flow Reversal,’’ ASME J. Heat Transfer, **108**(2), pp. 485–488.

[5] Hamadah, T. T., and Wirtz, R. A., 1991, ‘‘Analysis of Laminar Fully Developed Mixed Convection in a Vertical Channel With Opposing Buoyancy,’’ ASME J. Heat Transfer, **113**(2), pp. 507–510.

[6] Barletta, A., and Zanchini, E., 1999, ‘‘On the Choice of Reference Temperature for Fully Developed Mixed Convection in a Vertical Channel,’’ Int. J. Heat Mass Transfer, **42**(16), pp. 3169–3181.

[7] Gebhart, B., and Pera, L., 1971, ‘‘The Nature of Vertical Natural Convection Flows Resulting From the Combined Buoyancy Effects of Thermal and Mass Diffusion,’’ Int. J. Heat Mass Transfer, **14**(12), pp. 2025–2050.

[8] Nelson, D. J., and Wood, B. D., 1989, ‘‘Fully Developed Combined Heat and Mass Transfer Natural Convection Between Parallel Vertical Plates With Asymmetric Boundary Conditions,’’ Int. J. Heat Mass Transfer, **32**(9), pp. 1789–1792.

Analysis of Variable Porosity, Thermal Dispersion, and Local Thermal Nonequilibrium on Free Surface Flows Through Porous Media

Bader Alazmi
Department of Mechanical Engineering,
Kuwait University,
P.O. Box 5969,
Safat 13060 Kuwait

Kambiz Vafai
e-mail: vafai@engr.ucr.edu
University of California, Riverside,
Department of Mechanical Engineering,
A363 Bourns Hall,
Riverside, CA 92521-0425

Characteristics of momentum and energy transport for free surface flows through porous media are explored in this study. Effects of variable porosity and an impermeable boundary on the free surface front are analyzed. In addition, effects of thermal dispersion and local thermal nonequilibrium (LTNE) are also analyzed. Pertinent parameters such as porosity, Darcy number, inertia parameter, Reynolds number, particle diameter, and solid-to-fluid conductivity ratio are used to investigate the significance of the above mentioned effects. Results show that considering the effect of variable porosity is significant only in the neighborhood of the solid boundary. The range of parameters which enhance the dispersion and LTNE effects are prescribed. Finally, it is shown that adding the effect of thermal dispersion to LTNE increases the sensitivity of LTNE between the two phases. [DOI: 10.1115/1.1723470]

Keywords: *Convection, Heat Transfer, Porous Media*

1 Introduction

Incompressible free surface fluid flow in porous media has been the subject of many studies in the last few decades because of its importance in many applications such as geophysics, die filling, metal processing, agricultural and industrial water distribution, oil recovery techniques, and injection molding. One of the earliest studies in this field was performed by Muskat [1] who considered a one-dimensional Darcy's flow model to analyze the linear encroachment of two fluids in a narrow channel. Recently, an analytical solution for linear encroachment in two immiscible fluids in a porous medium was presented in Srinivasan and Vafai [2]. They obtained a closed form solution, for the temporal free surface fluid front, that accounts for boundary and inertia effects. Their results show that for higher permeabilities Muskat's model underestimates the total time needed for the encroaching fluid to reach the end of the channel. Furthermore, they show that implementing their analytical solution is essential for cases of low mobility ratios.

Later on, Chen and Vafai [3] investigated the free surface transport through porous media numerically using the Marker and Cell method. They extended the study of Srinivasan and Vafai [2] to include free surface energy transport in their investigation. Another study performed by Chen and Vafai [4] considered interfacial tension effects on the free surface transport in porous media. Their results show that surface tension can be neglected for high Reynolds number flows.

Additional effects such as variable porosity, thermal dispersion and LTNE have been shown to be quite significant for a number of practical situations and were not studied in the earlier related works [1–4]. Vafai [5,6] and Vafai et al. [7] investigated analytically and experimentally the effect of variable porosity on fluid flow and heat transfer in porous media. It has been shown that the channeling effect can be significant at the neighborhood of solid boundaries. Several other studies considered the effect of thermal dispersion in porous media such as Amiri and Vafai [8], Hwang et al. [9]. It is found that ignoring the effect of thermal dispersion might lead to inaccurate predictions of heat transfer for some practical applications. The assumption of local thermal equilibrium between the solid and fluid phases is not valid for some engineering applications where temperature discrepancies exist between the phases. LTNE in porous media has been investigated by many researchers such as Lee and Vafai [10], Quintard and Whitaker [11] and Quintard et al. [12]. Quintard and Whitaker [13] analyzed the mass flux boundary condition at a moving fluid-fluid interface. Their analysis suggests a mass jump condition for a singular surface at the moving boundary which depends on the concentration at the interface. Recently, the same authors [14] have considered the problem of dissolution of an immobile phase caused by mass transfer to a second phase which generates a moving free surface between the two phases. In [13,14], a general shape of the free surface front is used in the analysis to derive the volume averaged governing equations and boundary conditions. However, it is practically reasonable to assume a flat free surface at the interface of the two phases. Therefore, the main objective of this study is to investigate the effects of variable porosity, thermal dispersion and LTNE on the free surface fluid flow and heat transfer through porous media.

2 Analysis

Geometry and Physical properties are chosen to be similar to those given in previous related studies [2,3] for the purpose of comparison. Description of the system under consideration is shown in Fig. 1. The volume-averaged governing equations are given as [15] follows:

Continuity Equation.

$$\nabla \cdot \langle V \rangle = 0 \tag{1}$$

Momentum Equation.

$$\frac{\rho_f}{\varepsilon} \langle (V\nabla) V \rangle = -\frac{\mu_f}{\mathrm{K}} \langle V \rangle - \frac{\rho_f F \varepsilon}{\sqrt{\mathrm{K}}} [\langle V \rangle \langle V \rangle] J + \frac{\mu_f}{\varepsilon} \nabla^2 \langle V \rangle - \nabla \langle P \rangle^f \tag{2}$$

Contributed by the Heat Transfer Division for publication in the JOURNAL OF HEAT TRANSFER. Manuscript received by the Heat Transfer Division April. 19, 2003; revision received January 21, 2004. Associate Editor: J. N. Chung.

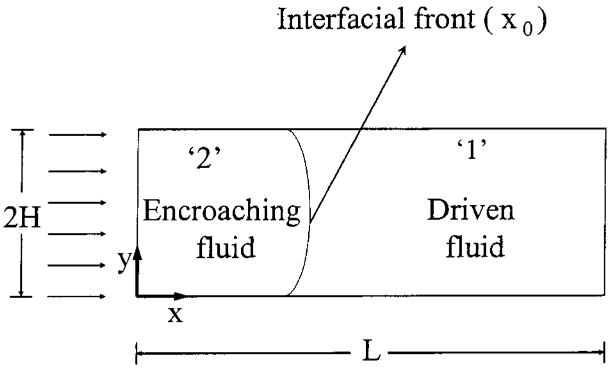

Fig. 1 Schematic diagram of the free surface front and the corresponding coordinate system

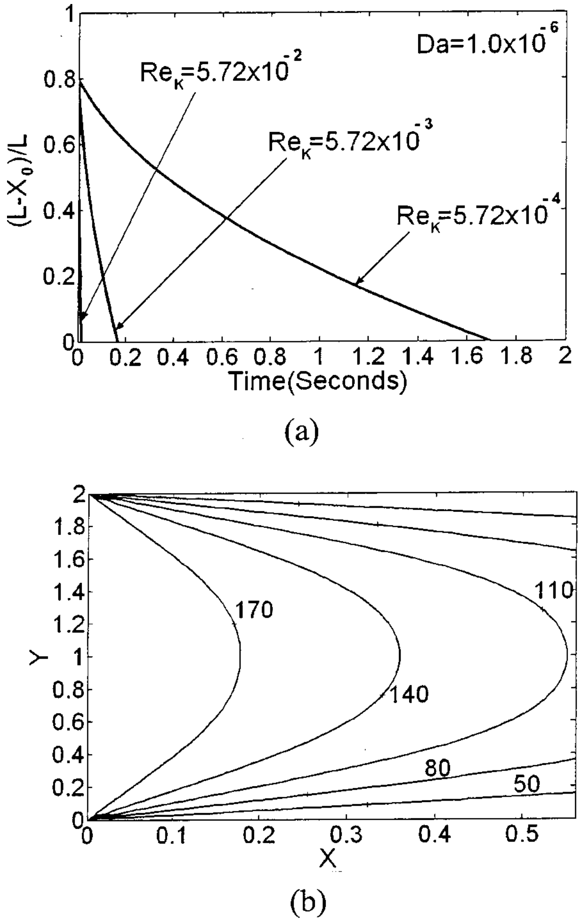

Fig. 2 Comparison between the present results and the numerical results in Chen and Vafai [3]: (a) temporal free surface distribution using constant Darcy number; and (b) temperature contours for $\mathrm{Re}_K=5.72\times10^{-4}$, $\mathrm{Da}=1.0\times10^{-6}$ at $t=0.5$ s

Fluid Phase and Solid Phase Energy Equations[8].

$$\langle\rho_f\rangle^f c_f\langle V\rangle\nabla\langle T_f\rangle^f=\nabla(k_{f\,\mathrm{eff}}\nabla\langle T_f\rangle^f)+h_{sf}a_{sf}(\langle T_s\rangle^s-\langle T_f\rangle^f) \tag{3}$$

$$0=\nabla(k_{s\,\mathrm{eff}}\nabla\langle T_s\rangle^s)-h_{sf}a_{sf}(\langle T_s\rangle^s-\langle T_f\rangle^f) \tag{4}$$

The fluid-to-solid heat transfer coefficient and the specific surface area are expressed as [8]

$$h_{sf}=\frac{k_f}{d_p}\left[2+1.1\mathrm{Pr}^{1/3}\left(\frac{\rho_f u d_p}{\mu_f}\right)^{0.6}\right] \tag{5}$$

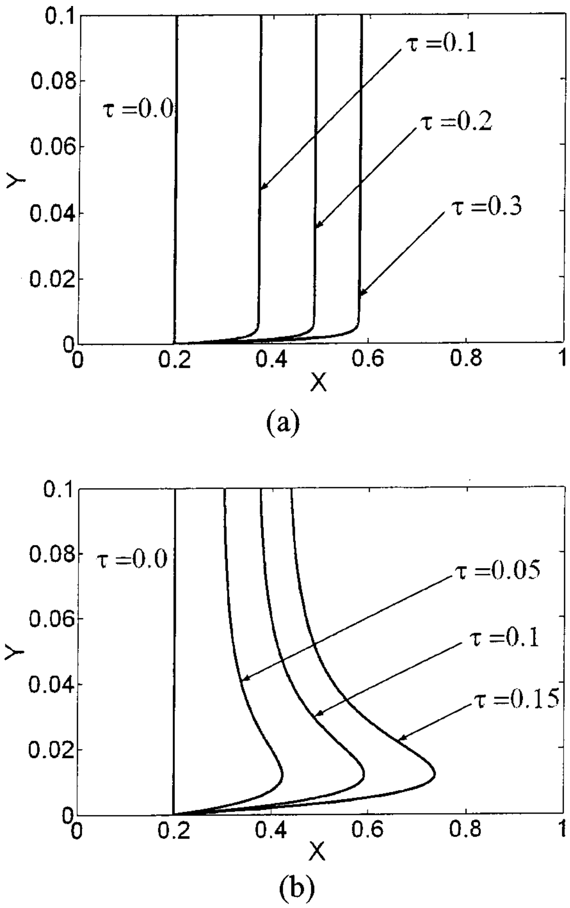

Fig. 3 Progress of the interfacial front for (a) constant porosity category with $\mathrm{Da}=1.0\times10^{-6}$, $\varepsilon=0.8$, $\Lambda=10.0$, and $\mathrm{Re}=100$; and (b) variable porosity category with $\varepsilon_\infty=0.45$, $b=0.98$, $c=2.0$, $\mathrm{Re}=100$, and $d_P/H=0.05$

$$a_{sf}=\frac{6(1-\varepsilon)}{d_p} \tag{6}$$

Effective conductivities of both phases are defined as

$$k_{f\,\mathrm{eff}}=\varepsilon k_f \tag{7}$$

$$k_{s\,\mathrm{eff}}=(1-\varepsilon)k_s \tag{8}$$

When effects of thermal dispersion are present, axial and lateral effective conductivities of the fluid phase can be represented, respectively, as [8]

$$(k_{f\,\mathrm{eff}})_x=\left[\varepsilon+0.5\mathrm{Pr}\left(\frac{\rho_f u d_p}{\mu}\right)\right]k_f \tag{9}$$

$$(k_{f\,\mathrm{eff}})_y=\left[\varepsilon+0.1\mathrm{Pr}\left(\frac{\rho_f u d_p}{\mu}\right)\right]k_f \tag{10}$$

Furthermore, when variation of porosity near the impermeable boundaries is present, porosity, permeability and the geometric function F may be expressed as [5,6]

$$\varepsilon=\varepsilon_\infty\left[1+b\exp\left(\frac{-cy}{d_p}\right)\right] \tag{11}$$

$$\mathrm{K}=\frac{\varepsilon^3 d_p^2}{150(1-\varepsilon)} \tag{12}$$

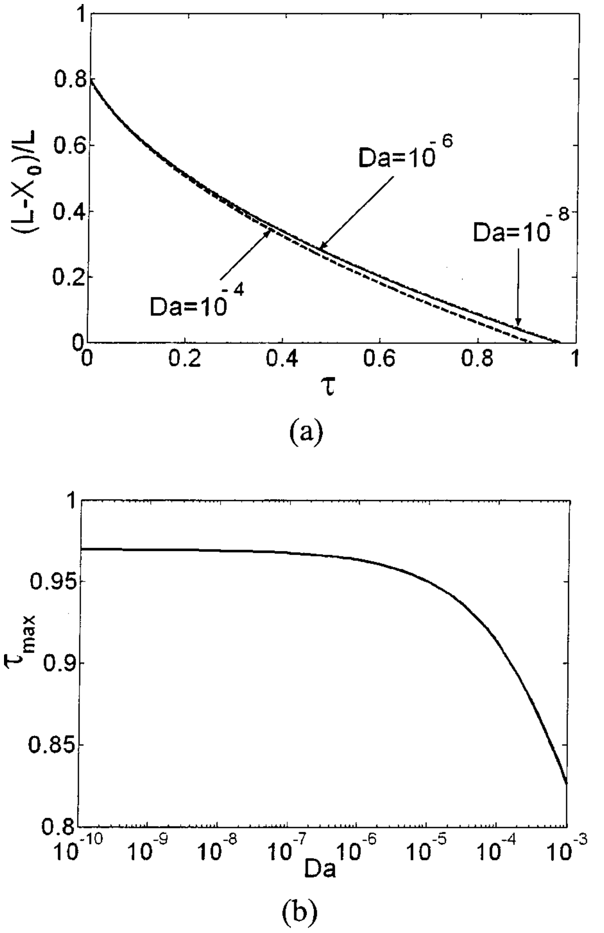

(a)

(b)

Fig. 4 Effect of Darcy number for the constant porosity category using $\Lambda=10.0$, Re=100 and $\varepsilon=0.8$ on (a) the temporal free surface front; and (b) the total time to reach the channel exit ($\tau_{\max}$)

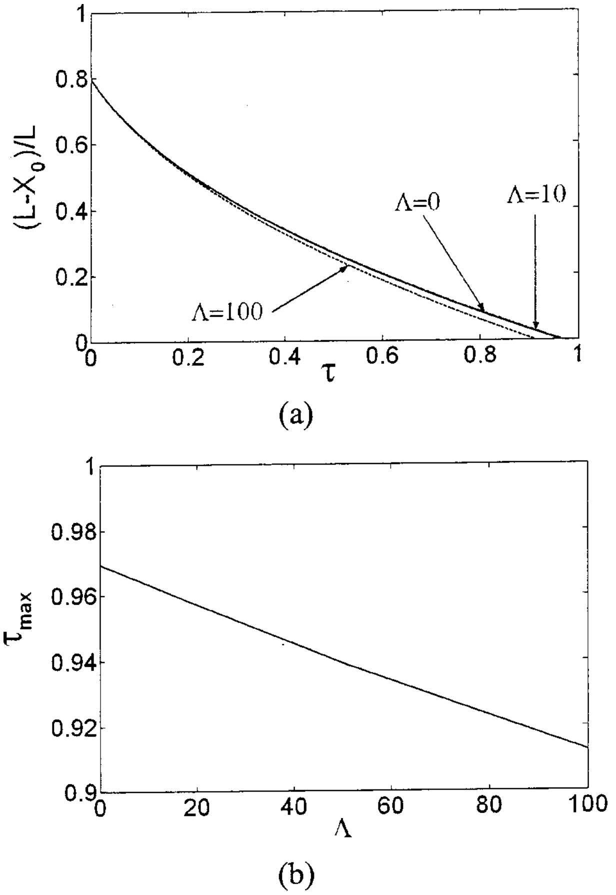

(a)

(b)

Fig. 5 Effect of Inertia parameter for the constant porosity category using $\varepsilon=0.8$, Da$=1.0\times10^{-6}$ and Re=100: (a) On the temporal free surface front; and (b) On the total time to reach the channel exit ($\tau_{\max}$)

$$F=\frac{1.75}{\sqrt{150\varepsilon^3}} \tag{13}$$

Results are presented in terms of the average Nusselt numbers ($\overline{\mathrm{Nu}}_f$ and $\overline{\mathrm{Nu}}_s$). Local Nusselt numbers for both phases are [8]

$$\mathrm{Nu}_f=-\frac{4H}{\langle T_f\rangle_w^f-\langle T_f\rangle_m^f}\left(\frac{\partial\langle T_f\rangle^f}{\partial y}\right)_{y=0} \tag{14}$$

$$\mathrm{Nu}_s=-\frac{4H}{\langle T_s\rangle_w^s-\langle T_s\rangle_m^s}\left(\frac{\partial\langle T_s\rangle^s}{\partial y}\right)_{y=0} \tag{15}$$

where $\langle T_f\rangle_m^f$ and $\langle T_s\rangle_m^s$ are the volume averaged mean fluid and solid temperatures, respectively.

As mentioned earlier, boundary and initial conditions are taken exactly similar to previous studies [2,3].

Initial Condition.

$$\text{At } t=0,\quad u=v=0,\quad \text{and}\quad T=T_\infty \tag{16}$$

Boundary Conditions.

$$\text{At } x=0,\quad p=p_e,\quad v=0,\quad T=T_e \tag{17}$$

$$\text{At } x=x_0,\quad p=p_\infty,\quad \frac{\partial u}{\partial x}=0,\quad -k_{\mathrm{eff}}\frac{\partial T}{\partial x}=h(T-T_\infty) \tag{18}$$

$$\text{At } y=0{,}2H,\quad u=v=0,\quad T=T_w \tag{19}$$

It is possible to compare the present numerical results to the modified analytical solution given in [3]. The modified analytical solution in [3] is presented in terms of the driven fluid physical properties. However, it is more appropriate to express the solution in terms of the encroaching fluid physical properties. Also, in order to compare the numerical results to the analytical results it is assumed that the viscosity of the driven fluid is smaller for this comparison than the viscosity of the encroaching fluid. As such the modified analytical solution is re-written in a simpler form

$$\frac{x_0}{L}=\frac{-\omega+\sqrt{\left[\omega+(1-\omega)\left(\frac{x_i}{L}\right)\right]^2+(1-\omega)\frac{2\mathrm{K}_2\Delta p}{\varepsilon\mu_2L^2}t}}{(1-\omega)} \tag{20}$$

The above equation, Eq. (20), is only a rearranged format of the solution given in [3] and the new mobility ratio (ω) is the inverse of the one defined in [3]. The present mobility ratio, which is assumed to have a very small value, is defined as

$$\omega=\frac{\mu_1}{\mu_2} \tag{21}$$

Based on the appearance of Eq. (20), we also define a dimensionless time (τ) as

$$\tau=\gamma t \tag{22}$$

where

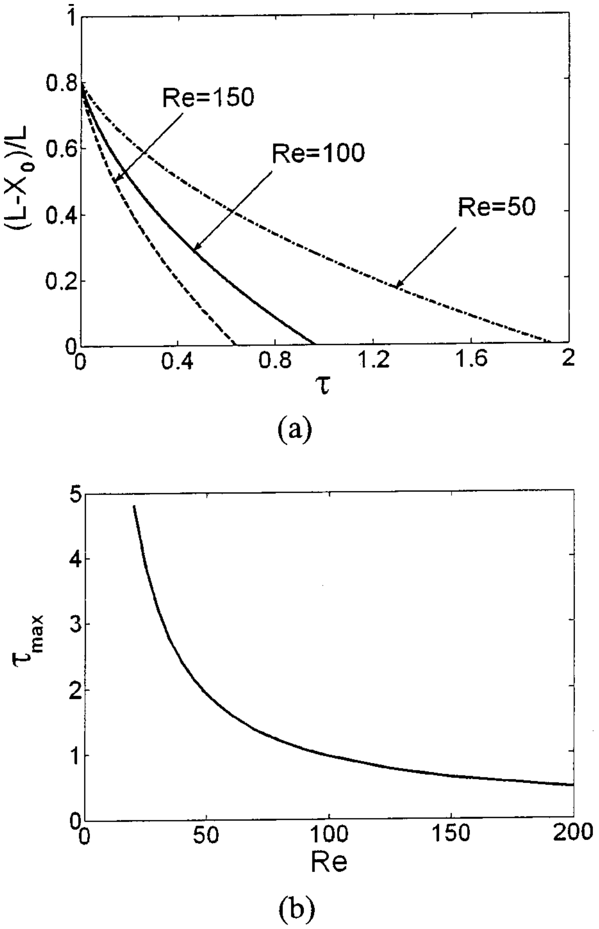

Fig. 6 Effect of Reynolds number for the constant porosity category using $\varepsilon=0.8$, Da$=1.0\times10^{-6}$ and $\Lambda=10.0$: (a) the temporal free surface front; and (b) the total time to reach the channel exit ($\tau_{\max}$)

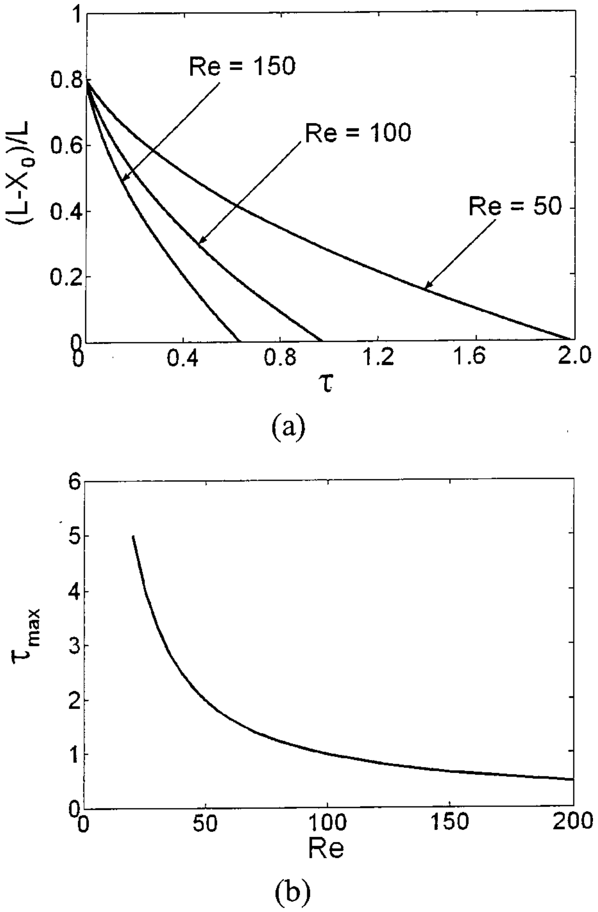

Fig. 7 Effect of Reynolds number for the variable porosity category using $\varepsilon_{\infty}=0.45$, $b=0.98$, $c=2.0$, and $d_P/H=0.05$ on (a) the temporal free surface front; and (b) the total time to reach the channel exit ($\tau_{\max}$)

$$\gamma=\frac{2K_2\Delta p}{\varepsilon\mu_2L^2} \tag{23}$$

In the above equation, the pressure difference is calculated according to the relation given in Vafai and Kim [16]. Permeability is related to the Darcy number for the constant porosity category while it can be calculated using Eq. (12) for the variable porosity category. Water is considered as the encroaching fluid in the present study.

3 Numerical Solution

Variable grids in the y-direction and constant grids in the x-direction were implemented in the prediction of the flow and temperature fields. Mesh refinements in the vicinity of the free surface front were also applied. This procedure is called interface capturing technique (ICT). It is similar to the one given in Sharif and Wiberg [17]. However, the finite difference method is used in the present study instead of the finite element method used in [17]. ICT eliminates the need for interpolations and extrapolations in the process of predicting the velocity and temperature fields. Since all the nodes coincide with the free surface, the two coupled energy equations are solved using the alternating direction implicit (ADI) method. An iterative solution is required since the two energy equations are coupled.

The requirement that the variation of velocity and temperature distributions is less than 10^{-6} between any two consecutive iterations is employed as the criterion for convergence. Numerical experiments were performed to assure grid independent results. A grid size of 201×501 was found to provide grid independent results. Due to the presence of symmetry and in order to save a considerable amount of CPU time, numerical computations were performed for the lower half of the physical domain.

In order to verify the accuracy of the present numerical results, comparisons with previous analytical and numerical results are presented in Fig. 2. Figure 2(a) shows comparison between the present numerical results and the modified analytical solution, using a mobility ratio value of zero ($\omega=0$), for the free surface front position. Inputs used to generate Fig. 2(a) were taken to be the same as the ones given in (Fig. 4 of Chen and Vafai [3]). The same is done in Fig. 2(b) which displays the comparison between the current numerical temperature distributions and previous corresponding results in Chen and Vafai [3]. Excellent agreement is found between the present numerical results and results given in Chen and Vafai [3]. Note that the analytical solution given in [2] has been revised by Vafai and Alazmi [18]. They identified some typos in the analytical solution [2] and formulated a modified accurate analytical solution for the problem of linear encroachment in two immiscible fluid systems in a porous medium.

Numerical accuracy for results of velocity, temperature and the average Nusselt number (Nu) was assessed by varying the convergence criteria and the mesh size of the computational domain. Changing the convergence criterion from the utilized value of 10^{-6} to 10^{-8} always results in a deviation less than 0.5%, 0.2% and 0.1% in velocity, temperature and Nu results respectively. On the other hand, mesh refinements of 401×1001 are found to cause

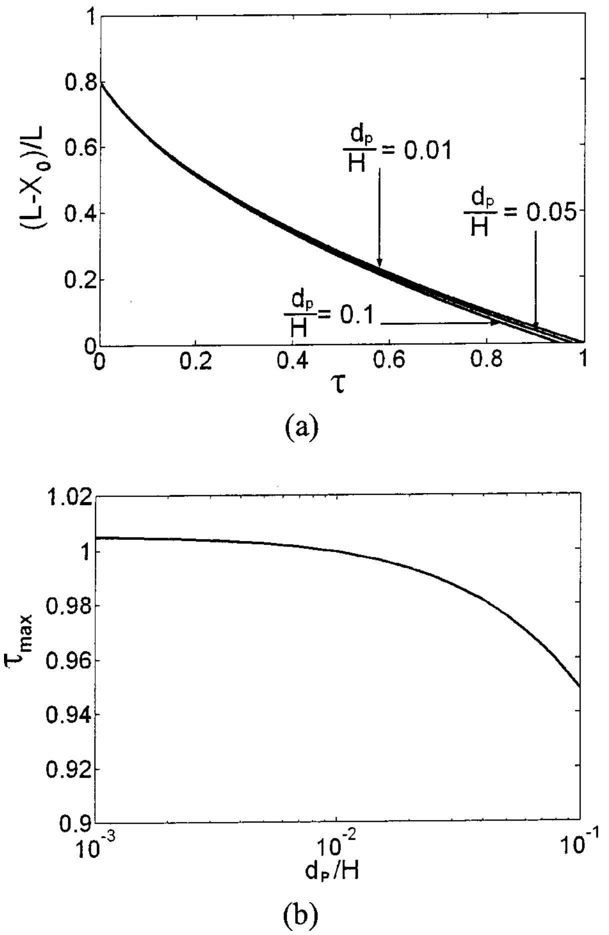

Fig. 8 Effect of particle diameter for the variable porosity category using $\varepsilon_\infty=0.45$, $b=0.98$, $c=2.0$, and Re=100 on (a) the temporal free surface front; and (b) the total time to reach the channel exit (τ_{max})

the results of velocity, temperature and Nu to deviate from those of the utilized mesh size of 201×501 by less than 0.8%, 0.3%, and 0.2%, respectively.

4 Results and Discussion

To show the effect of utilizing the constant porosity assumption, results for both constant and variable porosity will be discussed here. Figure 3(a) shows the progress of the interfacial front using constant porosity as a function of time while Fig. 3(b) shows the same using variable porosity. For both cases the flow is assumed to have the same initial position. However, the development of the variable porosity flow is different than the one using constant porosity. It is evident that the effect of variable porosity, which is the case for a number of engineering applications, is more prominent in the neighborhood of the solid boundary. This phenomenon is called the channeling effect which was discussed in detail in [5–6] and will not be discussed here. Our goal here is to analyze the effects of pertinent parameters such as porosity, Darcy number and Reynolds number on the residence time, τ_{max}, for the encroaching fluid under both constant and variable porosity conditions.

4.1 Constant Porosity. For the constant porosity category, the reference value of dimensionless time τ is based on the choice of intermediate values for the pertinent parameters. These reference values are 0.8 for the porosity, 10^{-6} for the Darcy number, 100 for the Reynolds number and 10 for the inertia parameter. For a wide range of Darcy number values, 10^{-10} to 10^{-6} in the present study, it is found that the required τ_{max} to reach the end of the channel is almost the same. However, higher Darcy numbers allow the fluid to reach the end of the channel in a shorter time as shown in Fig. 4. Effect of inertia parameter (Λ) on the temporal free surface front location is displayed in Fig. 5. It is found that the inertia parameter has less influence on the results when other parameters are fixed. The inertia parameter and τ_{max} show an inversely linear proportional relation as shown in Fig. 5(b). As expected, Reynolds number has the most significant effect on the progress of the free surface front. Its effect is shown in Fig. 6 where higher Reynolds numbers require significantly shorter time for the fluid to reach the end of the channel.

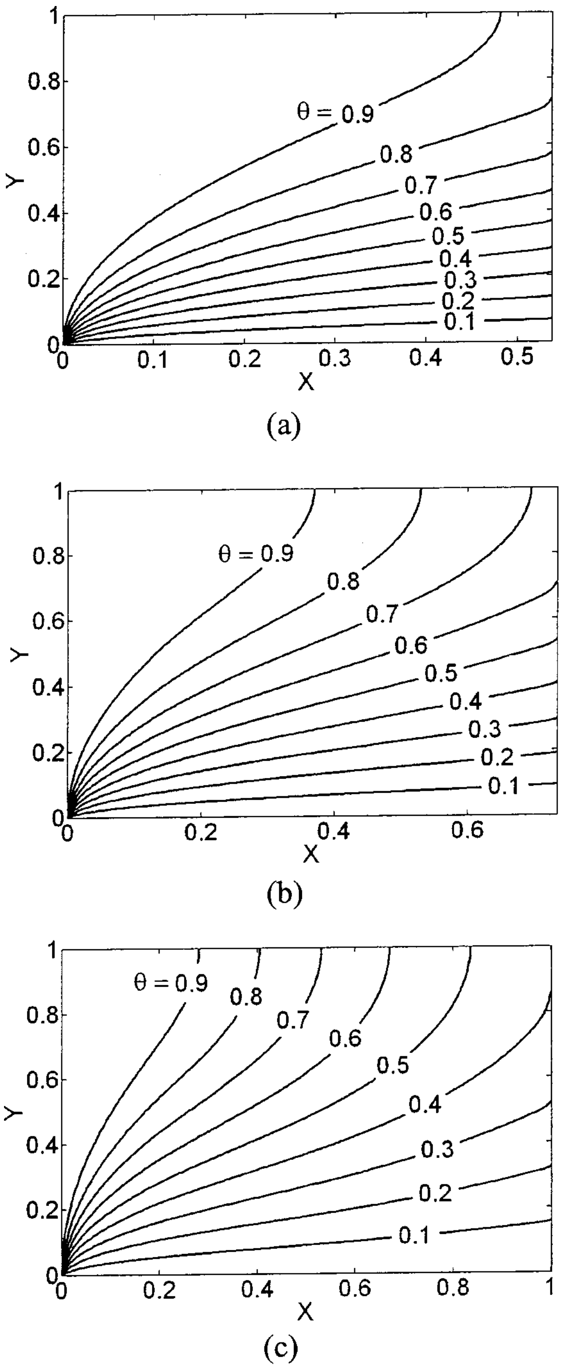

Fig. 9 Temporal dimensionless temperature profiles including thermal dispersion effects, $\varepsilon=0.8$, Da=10^{-6}, Re=100, $\Lambda=10$, $\kappa=15.0$, and $d_P/H=0.05$: (a) $\tau=0.25$, (b) $\tau=0.5$, and (c) $\tau=\tau_{max}$

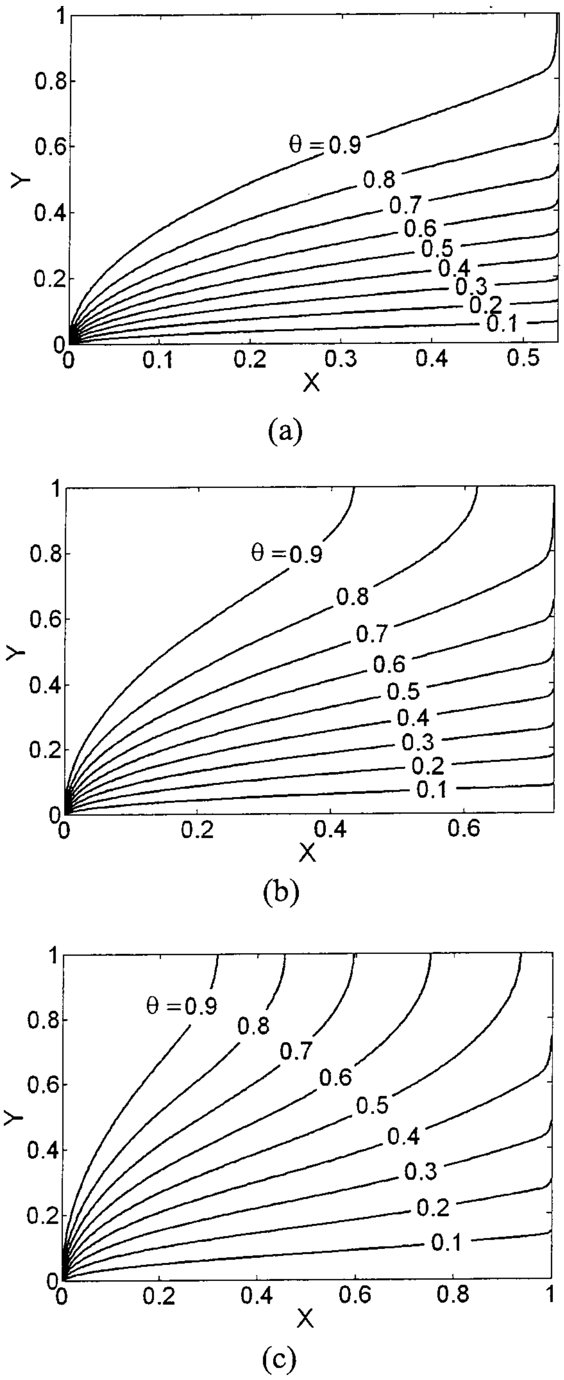

Fig. 10 Temporal dimensionless temperature profiles excluding thermal dispersion effects, ε=0.8, Da=10^{-6}, Re=100, Λ=10, κ=15.0, and d_P/H=0.05: (a) τ=0.25, (b) τ=0.5, and (c) $\tau=\tau_{\max}$

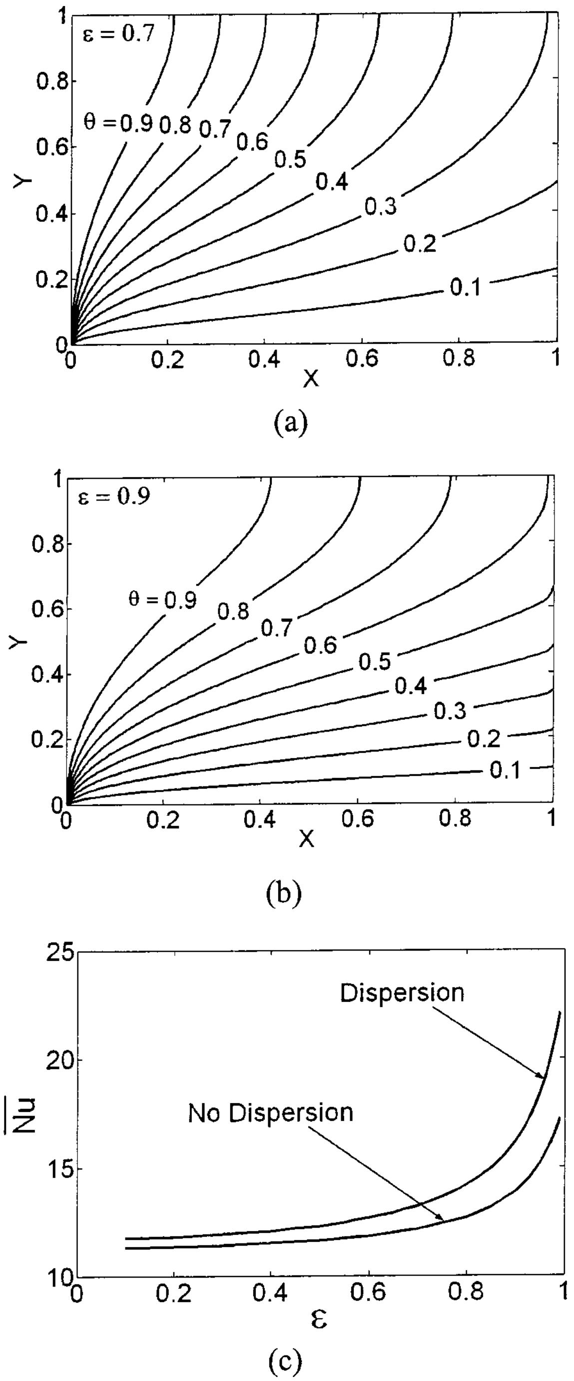

Fig. 11 Effect of porosity for the thermal dispersion category using Da=10^{-6}, Re=100, Λ=10, κ=15.0, and d_P/H=0.05 on (a) dimensionless temperature profiles using ε=0.7, (b) dimensionless temperature profiles using ε=0.9, and (c) total Nusselt number

4.2 Variable Porosity. For the variable porosity category, the reference value of dimensionless time τ is also based on the choice of intermediate values for the pertinent parameters. These reference values are 0.45 for the free stream porosity, 100 for the Reynolds number, and 0.05 for ratio of particle diameter to channel height. As mentioned earlier, permeability, Darcy number, the geometric function (*F*) and pressure gradient depend on the choice of the pertinent parameters for the variable porosity category. It is found that parameters (b) and (c) in Eq. (11) affect the velocity profile but have insignificant effect on the location of the free surface front. Typical values for parameters (b) and (c) are assumed based on a previous study [5].

Results of the effect of the Reynolds number in Fig. 7 for the variable porosity category and for the constant porosity category given in Fig. 6 reveal that the general behavior of the relation between the free surface position and Reynolds number is not affected by introducing the effect of variable porosity. Particle diameter appears in the expressions for the variable porosity (Eq. 11) and the permeability expression (Eq. 12). It is found that

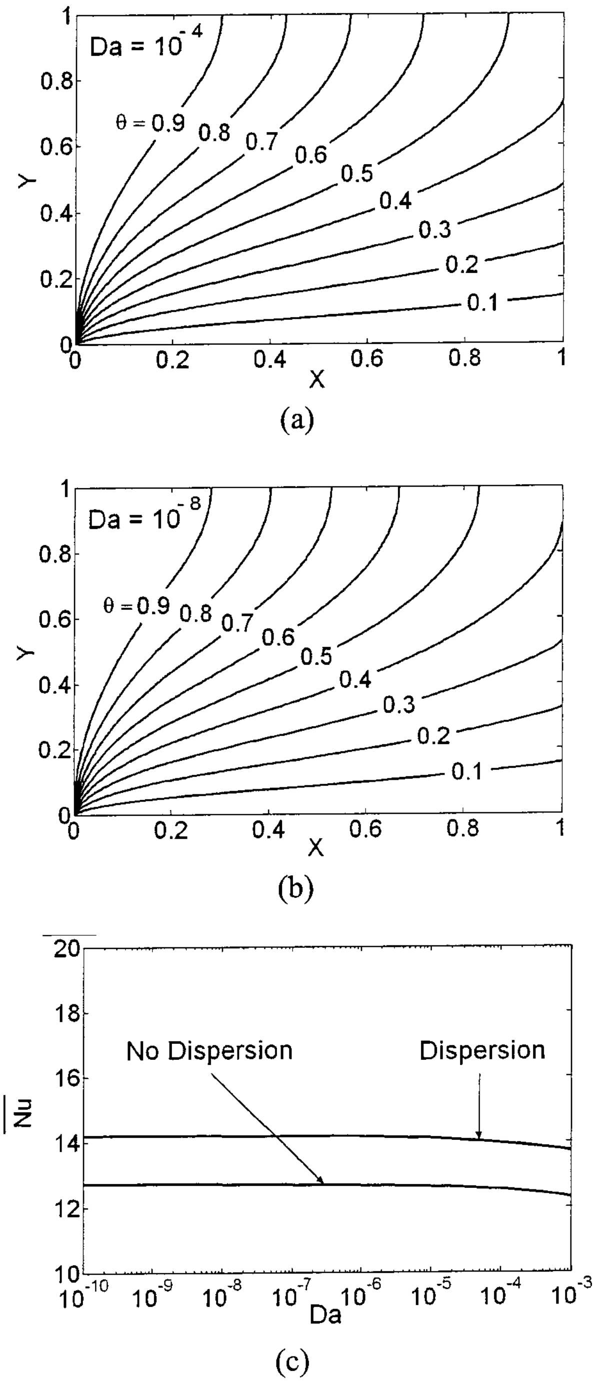

Fig. 12 Effect of Darcy number for the thermal dispersion category using ε=0.8, Re=100, Λ=10, κ=15.0, and d_P/H=0.05 on (a) dimensionless temperature profiles using Da=10^{-4}, (b) dimensionless temperature profiles using Da=10^{-8}, and (c) total Nusselt number

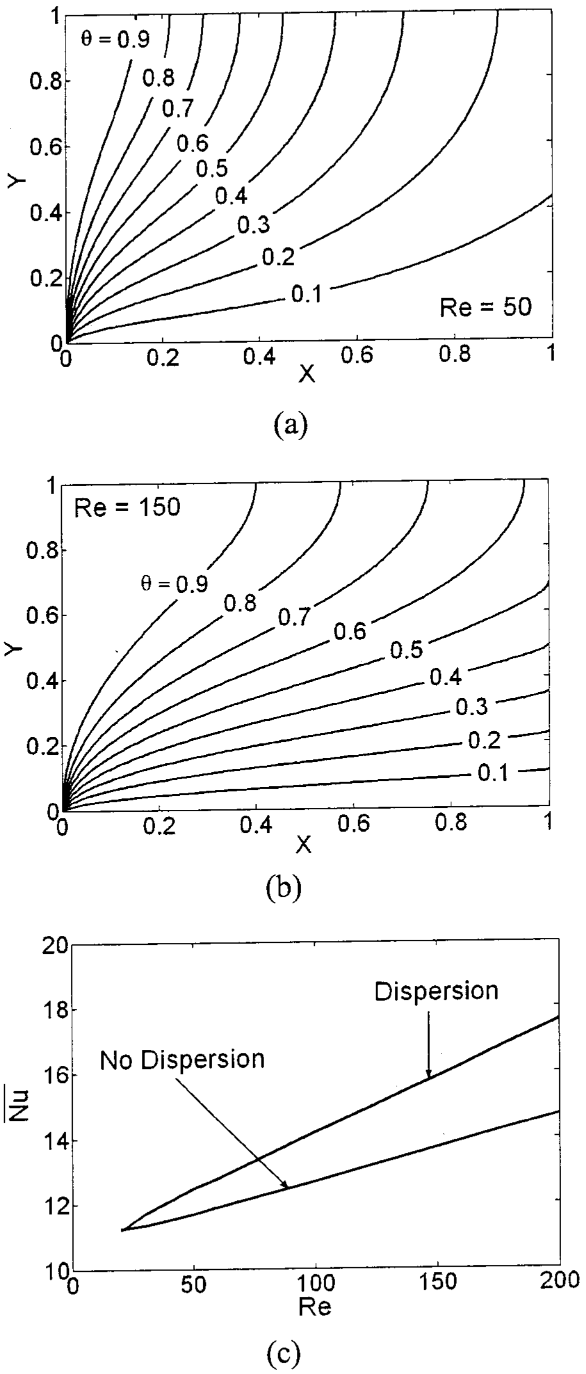

Fig. 13 Effect of Reynolds number for the thermal dispersion category using ε=0.8 Da=10^{-6}, Λ=10, κ=15.0, and d_P/H=0.05 on (a) dimensionless temperature profiles using Re=50, (b) dimensionless temperature profiles using Re=150, and (c) total Nusselt number

changing the particle diameter has an insignificant effect on the results. However, the influence of changing the particle diameter on the permeability is more significant. Particle diameter affects the value of Darcy number through the definition of permeability. Therefore, it is reasonable to compare the results of Fig. 8 for the particle diameter and the ones in Fig. 4 for the effects of variations in the Darcy number. The effect of Darcy number in Fig. 4 for the constant porosity category is more pronounced than the effect of variations in the particle diameter given in Fig. 8 for the variable porosity category.

4.3 Thermal Dispersion. The effect of thermal dispersion on the thermal characteristics of the free surface are analyzed in this section. Thermal equilibrium between the two phases is assumed. Introducing the effect of thermal dispersion in the energy equation in general favors conduction over convection. In other words, supplementing dispersion effects to the energy equation gives thermal conduction more dominance. This can be seen by comparing the temporal dimensionless temperature profiles in Figs. 9 and 10. Figure 9 illustrates the development of the temperature field with time with thermal dispersion effects included

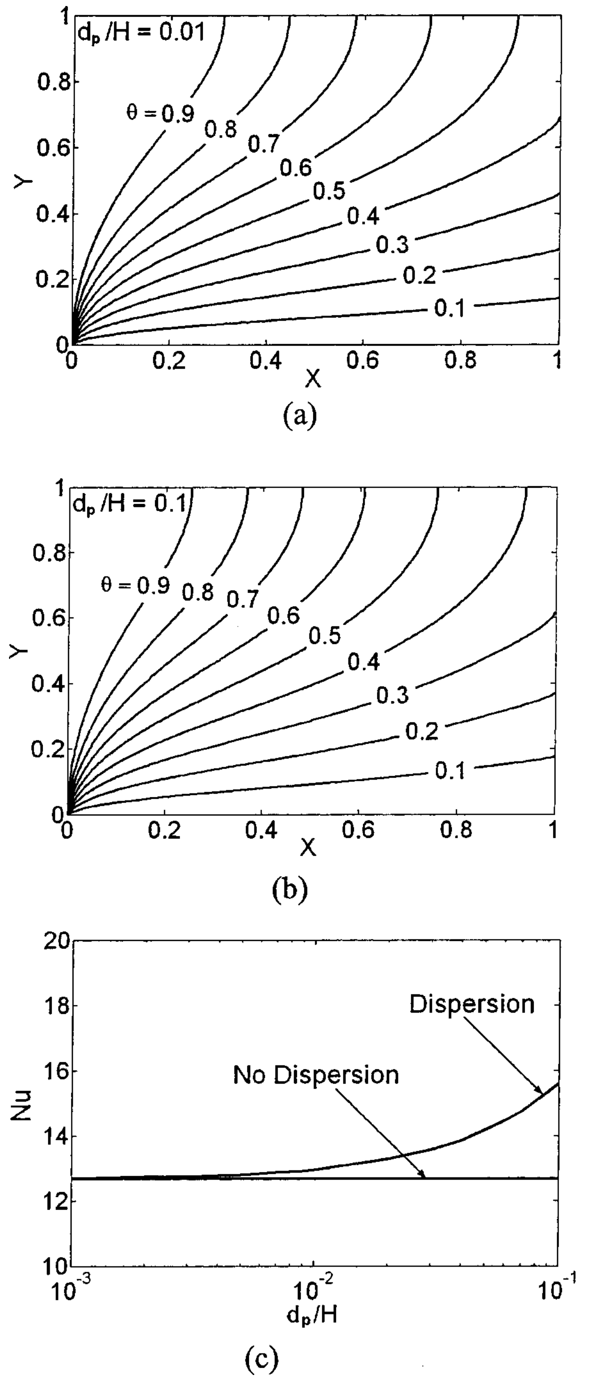

Fig. 14 Effect of particle diameter for the thermal dispersion category using ε=0.8 Da=10^{-6}, Re=100, Λ=10, and κ=15.0 on (a) dimensionless temperature profiles using d$_P$/H=0.01, (b) dimensionless temperature profiles using d_P/H=0.1, and (c) total Nusselt number

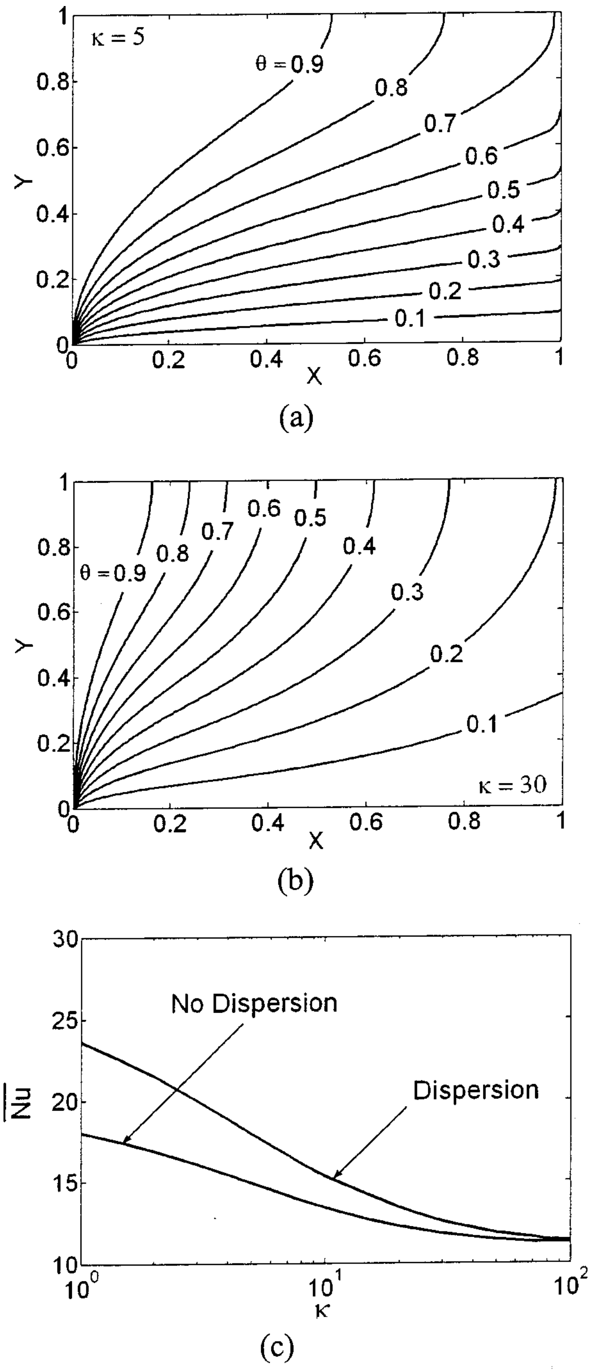

Fig. 15 Effect of solid-to-fluid thermal conductivity ratio, κ, for the thermal dispersion category using ε=0.8 Da=10^{-6}, Re =100, Λ=10, and d_P/H=0.05 on (a) dimensionless temperature profiles using κ=5.0, (b) dimensionless temperature profiles using κ=30.0, and (c) total Nusselt number

while Fig. 10 shows the same with thermal dispersion effects excluded while all other input parameters are kept the same. It is found that the total time taken to reach the end of the channel is the same for both cases.

Temperature contours and average Nusselt number curves for different values of porosity are shown in Fig. 11. It can be seen that higher porosity allows further thermal penetration of the encroaching fluid into the channel. Also, higher porosities result in higher Nusselt numbers as shown in Fig. 11(c). In addition, the difference between the two Nusselt numbers (with and without dispersion) widens as porosity increases. Therefore, effect of thermal dispersion becomes more pronounced at higher porosities.

Temperature contours for relatively small and larger Darcy numbers are quite similar as seen in Figs. 12(a) and 12(b). Overall heat transfer characteristics are almost unaffected. The two Nusselt numbers, with and without the effect of dispersion, are almost the same for different Darcy numbers as shown in Fig. 12(c). However, both curves show a slight decrease as Da increases while keeping the same difference. Therefore, effect of Darcy number with the presence of thermal dispersion is relatively in-

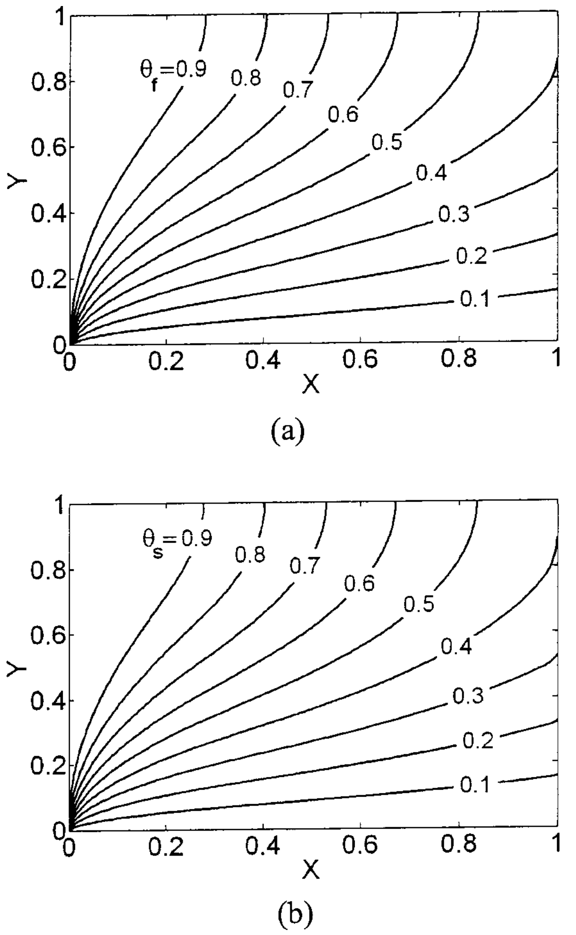

Fig. 16 Dimensionless temperature profiles for the LTNE category using ε=0.8, Da=10^{-6}, Re=100, Λ=10, κ=15.0, and d_P/H=0.05: (a) fluid phase; and (b) solid phase

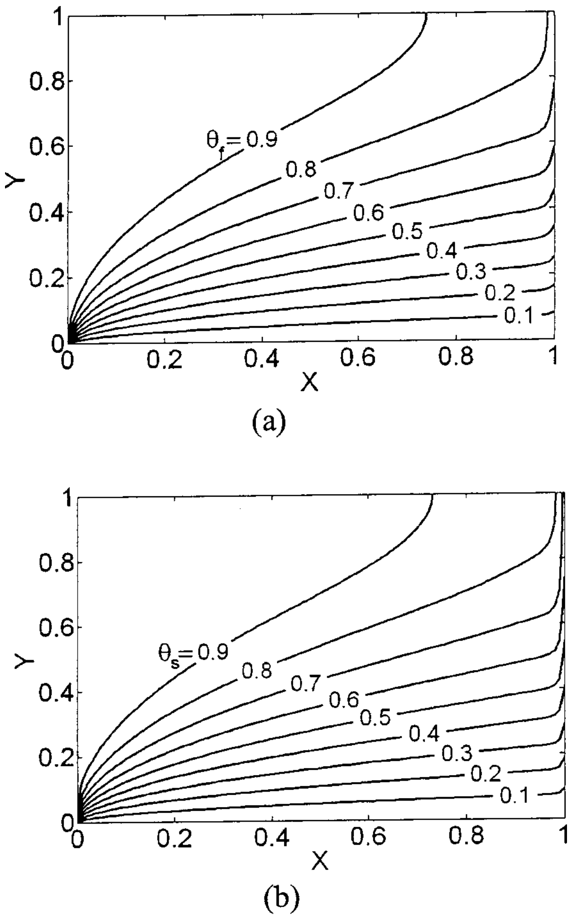

Fig. 17 Dimensionless temperature profiles for the LTNE category using ε=0.9, Da=10^{-8}, Re=200, Λ=100, κ=5.0, and d_P/H=0.1: (a) fluid phase; and (b) solid phase

significant. Inertial parameter variation were also found to have an insignificant effect on the temperature distributions.

Effect of Reynolds number with the presence of thermal dispersion on temperature contours is shown in Figs. 13(a) and 13(b). As expected, heat transfer by convection is more dominant at higher Reynolds numbers. Reynolds number influence, with and without the presence of thermal dispersion, on the Nusselt number is depicted in Fig. 13(c). As can be seen the effect of thermal dispersion is relatively insignificant at very small Reynolds numbers. However, as Reynolds number increases, the effect of thermal dispersion becomes more pronounced. Figure 14 reveals that it is only important to account for the thermal dispersion effects for larger values of d_p.

Figures 15(a) and 15(b) present effect of solid-to-fluid conductivity ratio on temperature profiles when thermal dispersion effect is included. As can be seen in Fig. 15 temperature contours undergo a drastic change as this ratio changes. In Fig. 15(a) where a relatively smaller conductivity ratio is considered, the convective mode is more dominant since the effective conductivity is relatively smaller. As can be seen in Fig. 15(c), neglecting the thermal dispersion effect is a reasonable assumption only for relatively high conductivity ratios.

4.4 Local Thermal Nonequilibrium.

In previous sections, local thermal equilibrium (LTE) between the solid and fluid phases was assumed. Figure 16 displays dimensionless temperature contours, under LTNE conditions while accounting for thermal dispersion. It is noted that temperatures of both phases are almost indistinguishable when moderate pertinent input parameters are used. When limiting input parameters are used as in Fig. 17, temperature difference between the two phases becomes more pronounced.

Effect of porosity variations on the average Nusselt numbers on LTNE is shown in Fig. 18. Figure 18(a) shows this effect while neglecting thermal dispersion. As can be seen the relatively small difference between the two Nusselt numbers remains constant as porosity changes. This is not the case when thermal dispersion effect is accounted for as demonstrated in Fig. 18(b). It is worth noting that the solid phase Nusselt number is almost the same with and without the effect of thermal dispersion.

Figure 19 shows the effect of Darcy number on the LTNE. For higher Darcy numbers, the two phases tend to reach thermal equilibrium as their Nusselt numbers intersect. Involvement of thermal dispersion enhances the effect of LTNE between the two phases as shown in Fig. 19(b). The inertia parameter effect is not significant on the Nusselt numbers as shown in Fig. 20, however, thermal dispersion widens the difference between the two Nusselt numbers as the inertia parameter changes. Once again, the solid phase Nusselt numbers are almost the same regardless of the presence or absence of thermal dispersion effects.

Increasing the Reynolds number increases the LTNE between the two phases with and without the effect of thermal dispersion. The involvement of thermal dispersion increases the sensitivity of LTNE to Reynolds number. The relation between the Nusselt numbers and Reynolds number remains linear for all cases even with the assumption of LTE as in Fig. 13. Particle diameter variations with and without the presence of thermal dispersion do not affect significantly the solid phase Nusselt numbers. However,

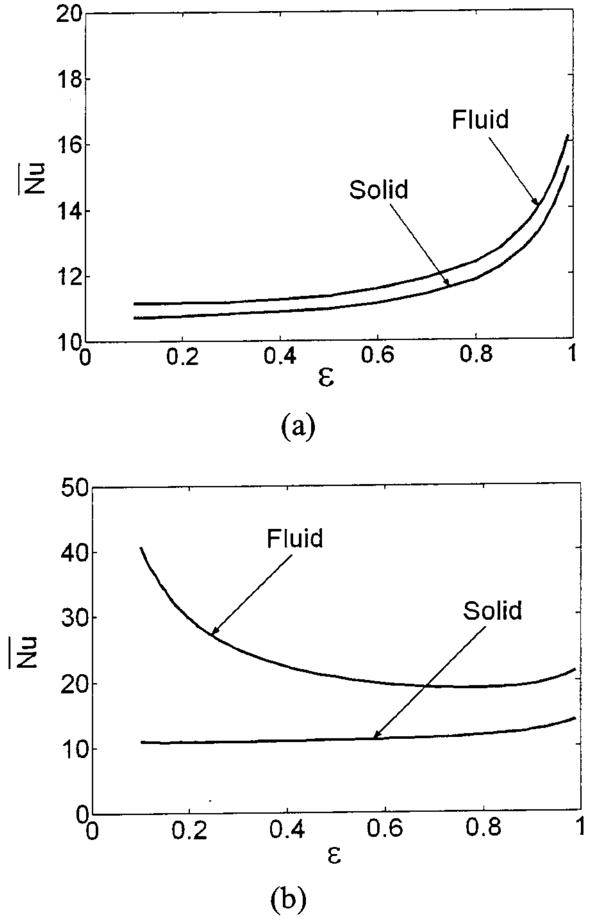

Fig. 18 Effect of porosity on average Nusselt numbers for the LTNE category, $\mathrm{Da}=10^{-6}$, Re=100, $\Lambda=10$, $\kappa=15.0$, and $d_P/H=0.05$: (a) excluding thermal dispersion effects; and (b) including thermal dispersion effects

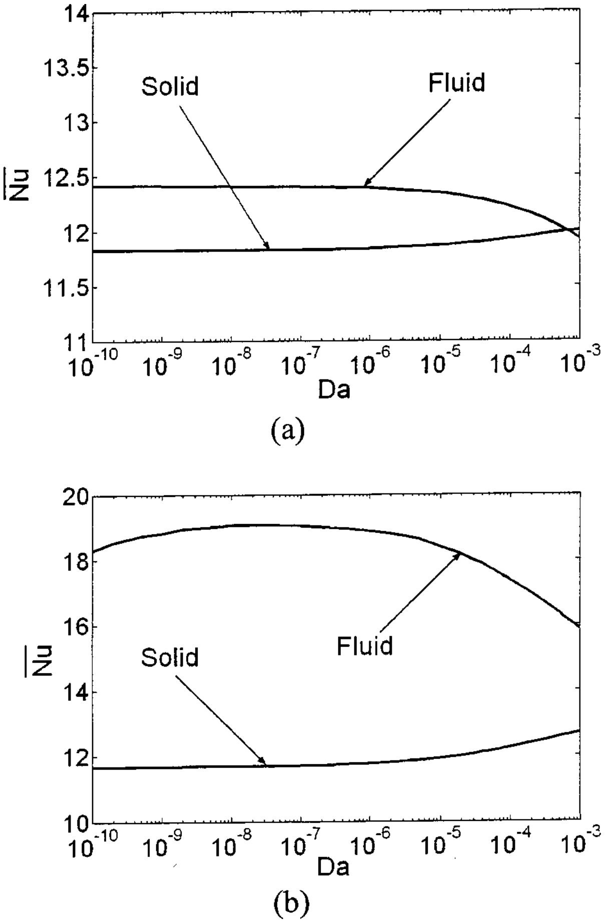

Fig. 19 Effect of Darcy number on average Nusselt numbers for the LTNE category, $\varepsilon=0.8$, Re=100, $\Lambda=10$, $\kappa=15.0$, and $d_P/H=0.05$: (a) excluding thermal dispersion effects; and (b) including thermal dispersion effects

fluid phase Nusselt numbers increase as the value of particle diameter increases. Again, including thermal dispersion effects increases the response of the fluid phase Nusselt number to the changes in the particle diameter.

When thermal dispersion is not included, higher solid-fluid conductivity ratios cause a slight increase in the difference between the two Nusselt numbers. On the other hand, the difference between the two Nusselt numbers is almost constant when thermal dispersion effect is considered. It is worth noting that all Nusselt numbers decrease as the solid-to-fluid conductivity ratio increases for the same reasons discussed in the previous section.

5 Conclusions

A comprehensive analysis of variable porosity, thermal dispersion and local thermal nonequilibrium on free surface transport through porous media is presented in this study. Effects of pertinent parameters such as porosity of the porous medium, Darcy number, Inertia parameter, Reynolds number, particle diameter and solid-to-fluid conductivity ratio, on the momentum and thermal transport are analyzed and discussed. It is found that variable porosity effects can be quite substantial in the neighborhood of the solid boundaries. It is also shown that the thermal dispersion has a substantial effect on the thermal transport process. LTNE between the two phases is found to be more pronounced when thermal dispersion effect is included. Changes in porosity, Darcy number, Reynolds number and particle diameter on free surface transport are characterized and quantified. Therefore, ignoring these effects can lead to inaccurate estimations of the free surface problem.

Nomenclature

a_{sf} = specific surface area of the packed bed, $[\mathrm{m}^{-1}]$
b, c = porosity variation parameters, Eq. (11)
c_p = specific heat at constant pressure, $[\mathrm{J\,kg^{-1}\,K^{-1}}]$
d_p = particle diameter [m]
Da = Darcy number, $\mathrm{K/H^2}$
F = geometric function defined in Eq. (13)
h_{sf} = fluid-to-solid heat transfer coefficient, $[\mathrm{W\,m^{-2}\,K^{-1}}]$
H = half the height of the channel, [m]
J = unit vector aligned along the pore velocity
k = thermal conductivity, $[\mathrm{W\,m^{-1}\,K^{-1}}]$
K = permeability $[\mathrm{m}^2]$
L = length of the channel, [m]
Nu = local Nusselt number
$\overline{\mathrm{Nu}}$ = average Nusselt number
P = pressure, $[\mathrm{N/m^2}]$
Pr = Prandtl number, $\mu\, c_{Pf}/k_f$
Re = Reynolds number, $u_\infty H/\nu_f$
Re_K = particle Reynolds number, $u_c K^{1/2}/\nu$
T = temperature, [K]
u = velocity in x-direction, $[\mathrm{m\,s^{-1}}]$
x_0 = free surface front location, [m]
x, y = Cartesian coordinates, [m]
X, Y = non-dimensional coordinates, x/H and y/H

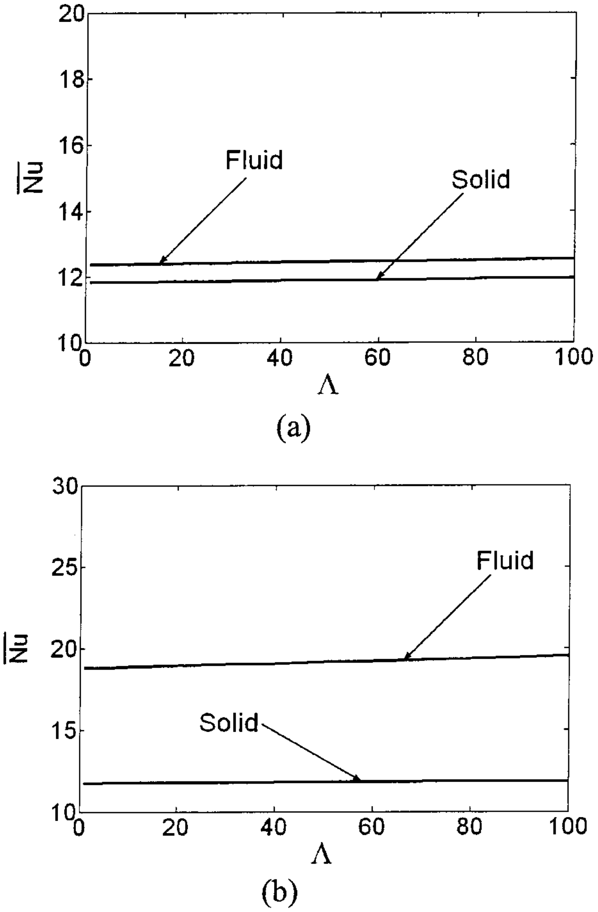

(a)

(b)

Fig. 20 Effect of Inertia parameter on average Nusselt numbers for the LTNE category, $\varepsilon=0.8$, Da$=10^{-6}$, Re$=100$, $\kappa=15.0$, and $d_P/H=0.05$: (a) excluding thermal dispersion effects; and (b) including thermal dispersion effects

Greek Symbols

α = thermal diffusivity, $[\mathrm{m^2\,s^{-1}}]$
ε = porosity
γ = parameter
κ = solid-to-fluid thermal conductivity ratio, k_s/k_f
Λ = Inertia parameter, $\varepsilon^{3/2}\mathrm{Fu}_\infty H/\nu_f$
μ = kinematics Viscosity, $[\mathrm{kg\,m^{-1}\,s^{-1}}]$
ν = dynamic viscosity, $[\mathrm{m^2\,s^{-1}}]$
θ = dimensionless temperature, $[(T_w-T)/(T_w-T_e)]$
ρ = density, $[\mathrm{kg\,m^{-3}}]$
τ = dimensionless time, Eq. (22)

Subscripts

c = convective component
e = inlet
eff = effective property
f = fluid
m = mean
max = maximum
s = solid
w = wall
∞ = free stream

Other Symbols

$\langle\ \rangle$ = "local volume average" of a quantity

References

[1] Muskat, M., 1937, *The Flow of Homogeneous Fluids Through Porous Media*, Edwards, Ann Arbor, MI.
[2] Srinivasan, V., and Vafai, K., 1994, "Analysis of Linear Encroachment in Two-Immiscible Fluid Systems in a Porous Medium," ASME J. Fluids Eng., **116**, pp. 135–139.
[3] Chen, S. C., and Vafai, K., 1996, "Analysis of Free Surface Momentum and Energy Transport in Porous Media," Numer. Heat Transfer, Part A, **29**, pp. 281–296.
[4] Chen, S. C., and Vafai, K., 1997, "Non-Darcian Surface Tension Effects on Free Surface Transport in Porous Media," Numer. Heat Transfer, Part A, **31**, pp. 235–254.
[5] Vafai, K., 1984, "Convective Flow and Heat Transfer in Variable-Porosity Media," J. Fluid Mech., **147**, pp. 233–259.
[6] Vafai, K., 1986, "Analysis of the Channeling Effect in Variable Porosity Media," ASME J. Energy Resour. Technol., **108**, pp. 131–139.
[7] Vafai, K., Alkire, R. L., and Tien, C. L., 1985, "An Experimental Investigation of Heat Transfer in Variable Porosity Media," ASME J. Heat Transfer, **107**, pp. 642–647.
[8] Amiri, A., and Vafai, K., 1994, "Analysis of Dispersion Effects and Non-Thermal Equilibrium, Non-Darcian, Variable Porosity, Incompressible Flow Through Porous Media," Int. J. Heat Mass Transfer, **37**, pp. 939–954.
[9] Hwang, G. J., Wu, C. C., and Chao, C. H., 1995, "Investigation of Non-Darcian Forced Convection in an Asymmetrically Heated Sintered Porous Channel," ASME J. Heat Transfer, **117**, pp. 725–732.
[10] Lee, D. Y., and Vafai, K., 1999, "Analytical Characterization and Conceptual Assessment of Solid and Fluid Temperature Differentials in Porous Media," Int. J. Heat Mass Transfer, **42**, pp. 423–435.
[11] Quintard, M., and Whitaker, S., 1995, "Local Thermal Equilibrium for Transient Heat Conduction: Theory and Comparison With Numerical Experiments," Int. J. Heat Mass Transfer, **38**, pp. 2779–2796.
[12] Quintard, M., Kaviany, M., and Whitaker, S., 1997, "Two-Medium Treatment of Heat Transfer in Porous Media: Numerical Results for Effective Properties," Adv. Water Resour., **20**, pp. 77–94.
[13] Quintard, M., and Whitaker, S., 1995, "The Mass Flux Boundary Condition at a Moving Fluid-Fluid Interface," Ind. Eng. Chem. Res., **34**, pp. 3508–3513.
[14] Quintard, M., and Whitaker, S., 1999, "Dissolution of an Immobile Phase During Flow in Porous Media," Ind. Eng. Chem. Res., **38**, pp. 833–844.
[15] Vafai, K., and Tien, C. L., 1981, "Boundary and Inertia Effects on Flow and Heat Transfer in Porous Media," Int. J. Heat Mass Transfer, **24**, pp. 195–203.
[16] Vafai, K., and Kim, S. J., 1989, "Forced Convection in a Channel Filled With a Porous Medium: An Exact Solution," ASME J. Heat Transfer, **111**, pp. 1103–1106.
[17] Sharif, N. H., and Wiberg, N. E., 2002, "Adaptive ICT Procedure for Non-Linear Seepage Flows With Free Surface in Porous Media," Commun. Numer. Methods Eng., **18**, pp. 161–176.
[18] Vafai, K., and Alazmi, B., 2003, "On the Line Encroachment in Two-Immiscible Fluid Systems in a Porous Medium," ASME J. Fluids Eng., **125**, pp. 738–739.

Estimation of Average and Local Heat Transfer in Parallel Plates and Circular Ducts Filled With Porous Materials

A. Haji-Sheikh
Department of Mechanical and Aerospace Engineering,
The University of Texas at Arlington,
Arlington, Texas 76019-0023

Accurate estimation of heat transfer to a fluid passing through a porous medium located between impermeable walls is of practical interest. Generally, the numerical computation of heat transfer to porous media can become time consuming and correlations are needed to enable practitioners to determine this quantity rapidly. In this paper, correlations for two cases are considered: one when porous materials are between two parallel plates and the other when they are within a circular pipe. This presentation includes correlations for both local and average heat transfer coefficients in these two passages for incompressible laminar flow. These correlations require knowledge of local and average heat transfer for unobstructed fluid flowing through these passages with sufficient accuracy. Because existing correlations lack sufficient accuracy, this presentation includes an appendix that emphasizes correlations for heat transfer to fluids passing through unobstructed parallel plate channels and also for circular pipes. [DOI: 10.1115/1.1735769]

Keywords: *Channel Flow, Entrance, Flow, Forced Convection, Heat Transfer, Laminar, Porous Media*

Introduction

A study of flow in porous passages is of interest in the heat transfer community. The fundamentals of flow in porous media are well documented by Nield and Bejan [1], Kaviany [2], and Vafai [3]. The solution for heat transfer in developing sections of porous plate channels and circular tubes is available in the literature. The solutions to these types of problems are numerically tedious. This paper reports simple approximate relations that permit quick but approximate results. Studies of developing temperature fields in parallel plate channels and circular ducts are in Nield et al. [4]. These references are valuable in the development of the exact series solution presented here.

This work concerns the computation of heat transfer for incompressible laminar flow passing through parallel plate channels and circular ducts, each having constant wall temperatures and filled with saturated porous materials. Furthermore, it is assumed that the effect of frictional heating and axial heat conduction is negligible, the porous materials are saturated, and the thermophysical properties have constant values.

The exact series solution requires the computation of a set of eigenvalues and the numerical computation of certain eigenvalues can become a formidable task. In practice, it may not be possible to compute a large number of eigenvalues with relative ease. To verify the accuracy of the series solution, the use of an alternative method of analysis becomes necessary. The closed-form solution that uses the method of weighted residuals is selected [5]. This latter method of solution provides comparable accuracy over an extended range of variables. For a finite number of eigenvalues, the method of weighted residuals provides results with comparable accuracy at larger values of the axial coordinate [6]. Because it is based on variational calculus and the minimization principle, it yields significantly higher accuracy than the exact solution near the thermal entrance region with the same number of eigenvalues. In addition, standard-computing packages can produce all eigenvalues with ease instead of getting them one at a time. This technique facilitates the extension of the series solution further toward the thermal entrance point.

Working Relations

Heat transfer to a fully developed flow through a porous media confined within an impermeable wall is of interest in this study. This paper considers heat transfer in parallel plate channels, Fig. 1(a), and circular pipes, Fig. 1(b), in the absence of volumetric heat source, and axial heat conduction. The Brinkman momentum equation for a fully developed flow is

$$\mu_e \nabla^2 u - \frac{\mu}{K} u - \frac{\partial p}{\partial x} = 0 \tag{1}$$

Here, a fluid flows in the direction of x and the Laplace operator takes different forms depending on the shape of the passages. The energy equation in its reduced form is

$$u \frac{\partial T}{\partial x} = \frac{k}{\rho c_p} \nabla^2 T + \frac{1}{\rho c_p} S \tag{2}$$

where S is the classical volumetric heat source that includes the contribution of frictional heating. Various theories concerning the form of S are in Nield et al. [4]. Setting $S=0$ further reduces the energy equation for the specific cases considered here. Equations (1) and (2) in conjunction with the given wall and entrance conditions provide velocity and temperature fields. The energy balance on a differential fluid element produces the relation $hC(T_w - T_b) = \rho U A (dT_b/dx)$ where T_w is the constant wall temperature and $T_b = T_b(x)$ is the local bulk or mean temperature of the fluid,

$$T_b = \frac{1}{A} \int_A \left(\frac{u}{U} \right) T dA \tag{3}$$

Let L_c be a characteristic length selected depending on the shape of a passage and U to designate the average fluid velocity in the passage. For a parallel plate channel, Fig. 2(a), $L_c = H$ where $2H$ is the distance between plates and for a circular pipe, Fig. 2(b),

---

Contributed by the Heat Transfer Division for publication in the JOURNAL OF HEAT TRANSFER. Manuscript received by the Heat Transfer Division July 29, 2003; revision received February 20, 2004. Associate Editor: N. K. Anand.

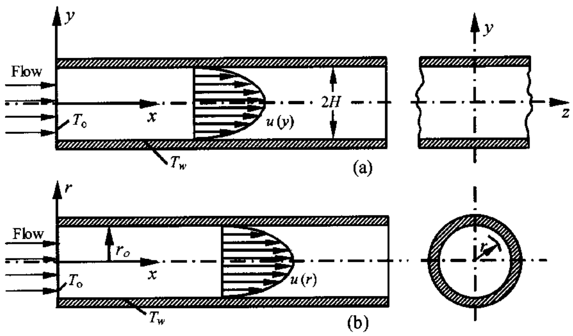

Fig. 1 Schematic of a flow (a) parallel plate channel and (b) circular pipe

$L_c = r_o$ where r_o is the radius of the pipe. This produces the working relation for computing the dimensionless local heat transfer coefficient hL_c/k as

$$\frac{hL_c}{k} = -\left(\frac{\bar{A}}{\bar{C}}\right)\left[\frac{dT_b(\bar{x})/d\bar{x}}{T_w - T_b(\bar{x})}\right] = -\left(\frac{\bar{A}}{\bar{C}}\right)\left[\frac{d\theta_b(\bar{x})/d\bar{x}}{\theta_b(\bar{x})}\right] \qquad (4a)$$

where $\bar{x} = x/(\mathrm{Pe}L_c)$, $\mathrm{Pe} = \rho c_p L_c U/k$, $\bar{A} = A/L_c$, $\bar{C} = C/L_c$, and $\theta_b(x) = [T_b(\bar{x}) - T_w]/(T_i - T_w)$ in which T_i and T_w are constant inlet fluid and wall temperatures, respectively. Equation (4a) yields the local Nusselt number, $\mathrm{Nu}_D = hD_h/k$

$$\frac{hD_h}{k} = -\left(\frac{D_h^2}{4L_c^2}\right)\left[\frac{d\theta_b(\bar{x})/d\bar{x}}{\theta_b(\bar{x})}\right] \qquad (4b)$$

where $D_h = 4A/C$ is the hydraulic diameter. Using the definition of average heat transfer coefficient,

$$\bar{h} = \frac{1}{x}\int_0^x h\,dx \qquad (5a)$$

Eqs. (4a–b) yield

$$\frac{\bar{h}L_c}{k} = -\left(\frac{\bar{A}}{\bar{C}}\right)\left[\frac{\ln\theta_b(\bar{x})}{\bar{x}}\right] \qquad (5b)$$

and the corresponding average Nusselt number, $\overline{\mathrm{Nu}}_{\mathrm{D}} = \bar{h}D_h/k$, as

$$\frac{\bar{h}D_h}{k} = \left(\frac{D_h^2}{4L_c^2}\right)\left[\frac{\ln\theta_b(\bar{x})}{\bar{x}}\right] \qquad (5b)$$

Equations (1) through (5) were used to obtain data as referenced quantities for evaluation of the approximate correlations.

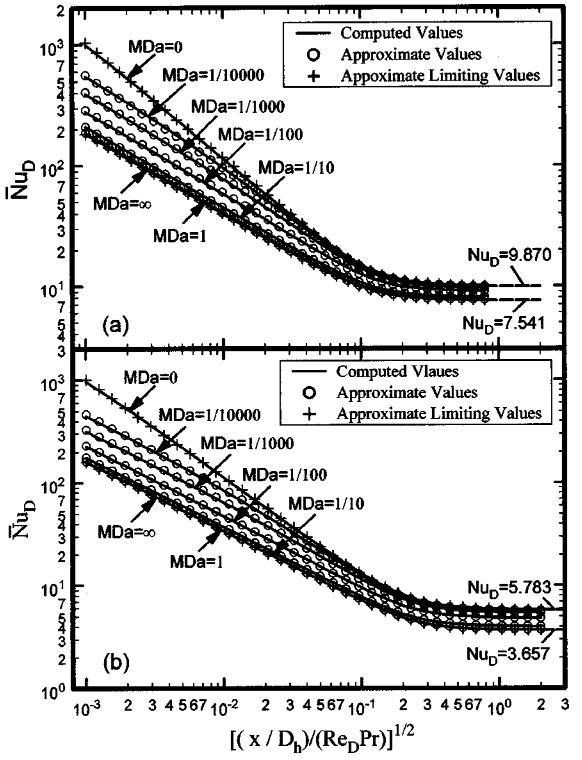

Fig. 2 A comparison of data from correlation with the computed data for average heat transfer coefficient: (a) in parallel plate channels; and (b) in circular pipes.

Average Heat Transfer Coefficient

The following analysis reports results using the definition of dimensionless average heat transfer coefficients. The correlation of the average heat transfer coefficient appears first for the two ducts under consideration and the correlations for the local heat transfer coefficient will follow in a separate section.

Parallel Plate Channels. The first flow model considers a steady and hydrodynamically fully developed flow between two impermeable parallel plates, $2H$ apart, see Fig. 1. The computation begins by considering the Brinkman momentum equation

$$\mu_e\frac{\partial^2 u}{\partial y^2} - \frac{\mu}{K}u - \frac{\partial p}{\partial x} = 0 \qquad (6a)$$

whose solution, when $\omega = 1/\sqrt{M\mathrm{Da}}$, $M = \mu_e/\mu$, and $\mathrm{Da} = K/H^2$, is

$$\frac{u}{U} = \frac{\omega}{\omega - \tanh(\omega)}\left[1 - \frac{\cosh(\omega\bar{y})}{\cosh(\omega)}\right] \qquad (6b)$$

The temperature distribution, assuming local thermal equilibrium, is governed by the energy equation

$$u\frac{\partial T}{\partial x} = \frac{k}{\rho c_p}\frac{\partial^2 T}{\partial y^2} \qquad (7a)$$

The simultaneous solution of these equations produces the temperature field and subsequently the heat transfer coefficient. When $\theta = (T - T_w)/(T_i - T_w)$, $L_c = H$, $\bar{y} = y/H$. $\bar{x} = (x/H)/\mathrm{Pe}$, and $\mathrm{Pe} = \rho c_p HU/k$, Eq. (7$a$) takes the form

$$\frac{u}{U}\frac{\partial\theta}{\partial\bar{x}} = \frac{d^2\theta}{d\bar{y}^2} \qquad (7b)$$

whose solution using the separation of variables technique is

$$\theta = \sum_{m=1}^{\infty} B_m Y_m(\bar{y}) e^{-\lambda_m^2\bar{x}} \qquad (8a)$$

The eigenfunction $Y_m(\bar{y})$ is

$$Y_m(\bar{y}) = \sum_{n=0}^{\infty} c_n(\bar{y})^n \qquad (8b)$$

and the coefficients $c_1, c_2, \cdots$ are obtainable from the recursive relation [6],

$$c_0 = 1, \quad c_1 = 0, \quad c_{n+2} = -\frac{\omega^2\psi_m(c_n - d_n)}{(n+2)^2 - (n+2)} \qquad (9a)$$

where $\psi_m = (\lambda_m^2/\omega)/[\omega - \tanh(\omega)]$ contains the eigenvalue λ_m and

$$d_n = \sum_{j=0}^{n} c_j a_{n-j},$$

and

$$a_i = \begin{cases} \dfrac{(\omega)^i}{\cosh(\omega)}\left(\dfrac{1}{i!}\right) & \text{when } i \text{ is even} \\ 0 & \text{when } i \text{ is odd} \end{cases} \qquad (9b)$$

A major task is the computation of the eigenvalues in order to satisfy the condition $Y_m(\overline{y})=0$ when $\overline{y}=1$. Once $Y_m(\overline{y})$ is known, a classical orthogonality condition applies

$$\int_0^1 \left(\frac{u}{U}\right) Y_m(\overline{y}) Y_n(\overline{y}) d\overline{y} = \begin{cases} 0 & \text{when } n \neq m \\ N_m & \text{when } n = m \end{cases} \qquad (9c)$$

where

$$N_m = \int_0^1 \left(\frac{u}{U}\right)[Y_m(\overline{y})]^2 d\overline{y} = \frac{1}{2\lambda_m}\left[\frac{\partial Y_m(\overline{y})}{\partial \overline{y}}\right]_{\overline{y}=1} \times \left[\frac{\partial Y_m(\overline{y})}{\partial \lambda_m}\right]_{\overline{y}=1} \qquad (9d)$$

to be used in the computation of B_m,

$$B_m = \frac{A_m}{N_m} = \frac{1}{N_m}\left[\int_0^1 \left(\frac{u}{U}\right) Y_m(\overline{y}) d\overline{y}\right]$$

$$= -\frac{1}{N_m \lambda_m^2}\left[\frac{\partial Y_m(\overline{y})}{\partial \overline{y}}\right]_{\overline{y}=1}$$

$$= -\left(\frac{2}{\lambda_m}\right) \Big/ \left[\frac{\partial Y_m(\overline{y})}{\partial \lambda_m}\right]_{\overline{y}=1} \qquad (10)$$

Haji-Sheikh and Vafai [6] reported a parametric study of the local and average heat transfer coefficients using the aforementioned procedure. The solution was compared to an alternative solution technique with comparable accuracy (see Table 3 in [6]). Since the average heat transfer coefficient is of practical interest, it receives primary consideration. The computed average Nusselt number data appear as solid lines in Fig. 2(a) for different MDa values. The line for $M\text{Da}=\infty$ describes the average heat transfer coefficient in unobstructed channels, $\overline{\text{Nu}}_D^*(x)$. As MDa approaches 0, the solid lines in Fig. 2(a) show a relatively rapid change of the slopes at small values of x. The following relation, for developing the average heat transfer coefficient, performs well at large and small values of MDa:

$$\overline{\text{Nu}}_D(x, M\text{Da}) = \Psi(x, M\text{Da}) \times \overline{\text{Nu}}_D^*(x) \qquad (11)$$

The presentation of a correlation for the function $\Psi(x, M\text{Da})$ is the main objective of this work. It is an empirical equation that was developed by curve fitting using the actual computed data and their limiting values. This function has the following form;

$$\Psi(x, MDa) \cong \frac{\text{Nu}_D(\infty)}{\text{Nu}_D^*(\infty)} + \frac{C_1 \times \left(\dfrac{x/D_h}{\text{Pr Re}_D}\right)^{-1}}{1 + C_2 \times \left(\dfrac{x/D_h}{\text{Pr Re}_D}\right)^{-m}} \qquad (12a)$$

where $\text{Nu}_D^*(\infty)=7.541$. The other coefficients C_1, C_2, and m depend on the value of MDa and they are approximated as

$$C_1 = \frac{0.023}{1 + 88(M\text{Da})^{0.85}} \qquad (12b)$$

$$C_2 = 0.0033 + \frac{0.0051}{1 + 500(M\text{Da})^{0.5}} \qquad (12c)$$

and

$$m = 0.97 - \frac{0.17}{1 + 3000(M\text{Da})^{0.8}} \qquad (12d)$$

Moreover, an estimate of the heat transfer coefficient under a thermally fully developed condition is

$$\text{Nu}_D(\infty) \cong \text{Nu}_D^*(\infty) + \frac{2.328}{1 + 22(M\text{Da})^{3/4}} \qquad (13)$$

where $\text{Nu}_D^*(\infty)=7.541$ is the heat transfer coefficient under a fully developed condition for a free flowing fluid in a parallel plate channel.

Equation (12a) was derived using a targeted accuracy of ±5 percent. To maintain this level of accuracy, the term $\overline{\text{Nu}}_D^*(x)$ in Eq. (11) must be accurate to well below these self-imposed limits. Various functional forms were examined and the best two are presented as an illustration. The following two equations are selected to accomplish the task of providing $\overline{\text{Nu}}_D^*(x)$ for a fluid flowing in a channel free from porous materials; they are

$$\overline{\text{Nu}}_D^*(x) = 7.541 + \frac{1.32 \times \left(\dfrac{x}{D_h}\dfrac{1}{\text{Pr Re}_D}\right)^{-0.355}}{1 + 64.2 \times \left(\dfrac{x}{D_h}\dfrac{1}{\text{Pr Re}_D}\right)^{3/4}} \qquad (14a)$$

and

$$\overline{\text{Nu}}_D^*(x) \cong 7.541 + \frac{1.55 \times \left(\dfrac{x/D_h}{\text{Pr Re}_D}\right)^{-0.344}}{\left[1 + 3.4\sqrt{\dfrac{x/D_h}{\text{Pr Re}_D}}\right]^4} \qquad (14b)$$

A nonlinear regression procedure was used to determine the values of the coefficients in Eqs. (14a–b) and then they were adjusted for simplicity of the presentation without significant loss of accuracy. Equation (14a) yields an estimated Nusselt number within ±1.5 percent and Eq. (14b) within ±0.84 percent of the computed data. The percent error throughout this presentation is defined by comparing the approximate Nusselt number from a correlation with a numerically computed Nusselt number using the relation

$$\%\text{Error} = [(\overline{\text{Nu}})_{\text{approx.}} - (\overline{\text{Nu}})_{\text{numer.}}] \times 100/(\overline{\text{Nu}})_{\text{numer.}}$$

To demonstrate the expected accuracy of the correlation given by Eq. (12a), Fig. 2(a) is prepared wherein this correlation is compared with the numerically acquired average heat transfer data. The solid lines are from the result obtained following the solution of the system of equations and their respective boundary conditions while the discrete circular data are the results of this approximate presentation. The data in Fig. 2(a) show that the predicted data, using Eq. (12a), agree well with the computed data obtained by solving Eqs. (6) and (7) using Mathematica [7]. As can be inferred from the graph, the error is less than the size of the radius of the circular symbols (~3 percent), often within ±2 percent or smaller. Generally, there is also an inherent source of error in the correlation leading to the value of the heat transfer coefficient in the absence of porous material. Because this correlation, e.g., Eq. (11), uses the correlation given by Eq. (14a) or (14b), it is appropriate to emphasize their accuracy. As shown in Fig. 3(a), the error distribution for the correlations given by Eq. (14b) remains within ±0.84 percent over a broad range of the dimensionless axial coordinate. However, Eq. (14a) provides a slightly better accuracy when $(x/D_h)/(\text{Pr Re}_D) > 10^{-2}$.

Circular Pipes. The computation of heat transfer to a fluid passing through a porous medium bounded by an impermeable circular wall is the subject of the next investigation. The procedure to obtain an average heat transfer coefficient requires the solution momentum equation and energy equation in cylindrical coordinates. In cylindrical coordinates, the Brinkman momentum equation is

$$\mu_e\left(\frac{\partial^2 u}{\partial r^2}+\frac{1}{r}\frac{\partial u}{\partial r}\right)-\frac{\mu}{K}u-\frac{\partial p}{\partial x}=0 \tag{15a}$$

where r is the local radial coordinate and x is the axial coordinate. The solution of Eq. (21a) when $\omega=1/\sqrt{M\mathrm{Da}}$, $M=\mu_e/\mu$, and $\mathrm{Da}=K/r_\mathrm{o}^2$, is

$$\frac{u}{U}=\frac{\omega \mathrm{I}_0(\omega)}{\omega \mathrm{I}_0(\omega)-2\mathrm{I}_1(\omega)}\left[1-\frac{\mathrm{I}_0(\omega\overline{r})}{\mathrm{I}_0(\omega)}\right] \tag{15b}$$

The steady-state form of the energy equation in cylindrical coordinates assuming local thermal equilibrium is

$$u\frac{\partial T}{\partial x}=\frac{k}{\rho c_p}\left(\frac{\partial^2 T}{\partial r^2}+\frac{1}{r}\frac{\partial T}{\partial r}\right) \tag{16a}$$

When $\theta=(T-T_w)/(T_i-T_w)$, $L_c=r_\mathrm{o}$, $\overline{r}=r/r_\mathrm{o}$. $\overline{r}=(r/r_\mathrm{o})/\mathrm{Pe}$, and $\mathrm{Pe}=\rho c_p r_\mathrm{o} U/k$, Eq. (22$a$) becomes

$$\frac{u}{U}\frac{\partial\theta}{\partial\overline{x}}=\frac{\partial^2\theta}{\partial\overline{r}^2}+\frac{1}{\overline{r}}\frac{\partial\theta}{\partial\overline{r}} \tag{16b}$$

whose solution is

$$\theta=\sum_{m=1}^{\infty}B_m R_m(\overline{r})e^{-\lambda_m^2\overline{x}} \tag{17a}$$

The eigenfunction $R_m(\overline{r})$ is

$$R(\eta)=\sum_{n=0}^{\infty}c_n(\overline{r})^n \tag{17b}$$

and the coefficients c_1, c_2,$\cdots$ are obtainable from the recursive relation [6],

$$c_0=1,\quad c_1=0,\quad c_{n+2}=-\frac{\omega^2\psi_m(c_n+d_n)}{(n+2)^2} \tag{18a}$$

where $\psi_m=(\lambda_m^2/\omega)\mathrm{I}_0(\omega)/[\omega\mathrm{I}_0(\omega)-2\mathrm{I}_1(\omega)]$ that includes the eigenvalues λ_m and

$$d_n=\sum_{j=0}^{n}c_j a_{n-j},$$

and

$$a_i=\begin{cases}\dfrac{(\omega/2)^i}{I_0(\omega)}\left[\dfrac{1}{(i/2)!}\right]^2 & \text{when } i \text{ is even}\\ 0 & \text{when } i \text{ is odd}\end{cases} \tag{18b}$$

Again, the major task is the computation of eigenvalues λ_m^2 in order to satisfy the condition $R_m(\overline{r})=0$ when $\overline{r}=1$. Once $R_m(\overline{r})$ in known, a classical orthogonality condition applies

$$\int_0^1\left(\frac{u}{U}\right)\overline{r}R_m(\overline{r})R_n(\overline{r})d\overline{r}=\begin{cases}0 & \text{when } n\neq m\\ N_m & \text{when } n=m\end{cases} \tag{18c}$$

where

$$N_m=\int_0^1\left(\frac{u}{U}\right)\overline{r}[R_m(\overline{r})]^2d\overline{r}=\frac{1}{2\lambda_m}\left[\frac{\partial R_m(\overline{r})}{\partial\overline{r}}\right]_{\overline{r}=1}\times\left[\frac{\partial R_m(\overline{r})}{\partial\lambda_m}\right]_{\overline{r}=1} \tag{18d}$$

and therefore, the coefficient B_m for inclusion in Eq. (17a) is

$$\begin{aligned}B_m=\frac{A_m}{N_m}&=\frac{1}{N_m}\int_0^1\left(\frac{u}{U}\right)\overline{r}R_m(\overline{r})d\overline{r}\\ &=-\frac{1}{N_m\lambda_m^2}\left[\frac{\partial R_m(\overline{r})}{\partial\overline{r}}\right]_{\overline{r}=1}\\ &=-\left(\frac{2}{\lambda_m}\right)\bigg/\left[\frac{\partial R_m(\overline{r})}{\partial\lambda_m}\right]_{\overline{r}=1}\end{aligned} \tag{19}$$

A solution using this exact analysis agrees well with an alternative numerical solution that uses the method of weighted residuals (see Table 4 in [6]). The solution of this system of equations requires a high degree of precision.

That same methodology described for parallel plate channels is to be used to estimate the average heat transfer coefficient for flow in circular pipes. For fluid flow in porous passages, as in the previous case, this study suggests selecting the relation

$$\overline{\mathrm{Nu}}_D(x,M\mathrm{Da})=\Psi(x,M\mathrm{Da})\times\overline{\mathrm{Nu}}_D^*(x) \tag{20}$$

The value of $\Psi(x,M\mathrm{Da})$, obtained similar to that described for parallel plate channels, is

$$\Psi(x,MDa)=\frac{\mathrm{Nu}_D(\infty)}{\mathrm{Nu}_D^*(\infty)}+\frac{C_1\times\left(\dfrac{x/D_h}{\mathrm{Pr}\,\mathrm{Re}_D}\right)^{-1}}{1+C_2\times\left(\dfrac{x/D_h}{\mathrm{Pr}\,\mathrm{Re}_D}\right)^{-m}} \tag{21a}$$

where $\mathrm{Nu}_D^*(\infty)=3.657$. The other coefficients depend on $M\mathrm{Da}$ and they are

$$C_1=\frac{0.0031}{1+800(M\mathrm{Da})^{0.88}} \tag{21b}$$

$$C_2=0.0011+\frac{0.0089}{1+20(M\mathrm{Da})^{1/4}} \tag{21c}$$

and

$$m=0.97-\frac{0.17}{1+2400(M\mathrm{Da})^{2/3}} \tag{21d}$$

while the heat transfer coefficient under thermally fully developed condition is

$$\mathrm{Nu}_D(\infty)\cong\mathrm{Nu}_D^*(\infty)+\frac{2.126}{1+30(M\mathrm{Da})^{3/4}} \tag{22}$$

where $\mathrm{Nu}_D^*(\infty)=3.657$ is the heat transfer coefficient under fully developed conditions for free flowing fluids in parallel plate channels.

The value of $\overline{\mathrm{Nu}}_D^*(x)$ for classical tube flow is obtainable by using a correlation similar to Eq. (14b), that is

$$\overline{\mathrm{Nu}}_D^*(x)=3.657+\frac{1.403\times\left(\dfrac{x/D_h}{\mathrm{Pr}\,\mathrm{Re}_\mathrm{D}}\right)^{-0.342}}{\left[1+2.537\times\sqrt{\dfrac{x/D_h}{\mathrm{Pr}\,\mathrm{Re}_\mathrm{D}}}\right]^3} \tag{23}$$

Also, the Hausen correlation [8] below can perform the task of providing

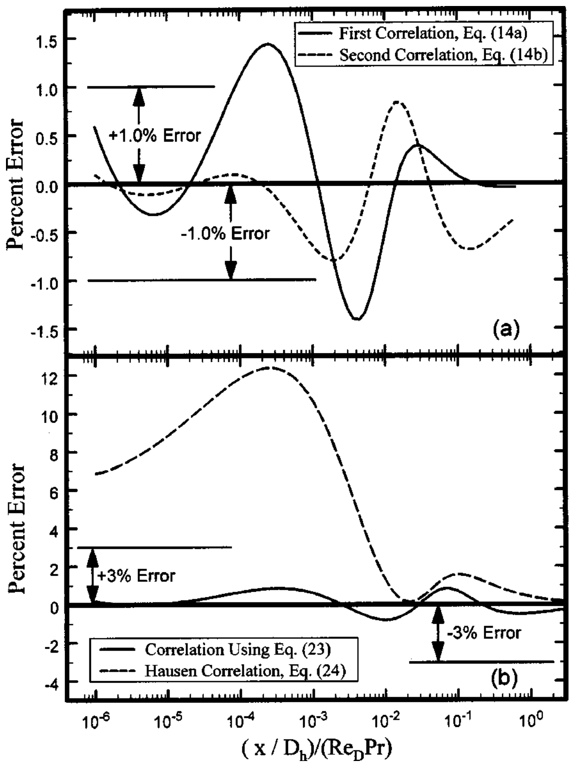

Fig. 3 Errors in the Value of $\overline{\mathrm{Nu}}_D^*$: (a) in parallel plate channels using Eqs. (11*a–b*); and (b) in circular pipes using Eqs. (23,24).

$$\overline{\mathrm{Nu}}_D^*(\infty)=3.66+\frac{0.0668\times\left(\dfrac{x/D_h}{\mathrm{Pr}\,\mathrm{Re}_D}\right)^{-1}}{1+0.04\times\left(\dfrac{x/D_h}{\mathrm{Pr}\,\mathrm{Re}_D}\right)^{-2/3}} \tag{24}$$

The next task is to compare the estimated average heat transfer coefficients obtainable from Eqs. (20–22) with the numerically obtained data from the exact analysis. Figure 2(b) shows this comparison. The solid lines are from the numerical solution of the system of governing equations with their respective boundary conditions [6]. The discrete circular data are from the estimated values from the relations presented here. The data in Fig. 2(b) show that the approximate data from the correlation agree remarkably well with the numerically computed data. As before, the error is less than the size of the radius of the circular symbols, within ±3 percent. Accurate heat transfer data can be realized from these correlations if accurate values for $\overline{\mathrm{Nu}}_D^*(x)$ are available. For this reason, Fig. 2(b) is prepared to show the accuracy of correlations given by Eqs. (23) and (24). The solid line in Fig. 3(b) shows the percent error when using Eq. (23). Depending on the range of interest, the error is typically within ±0.84 percent. The dash line describes the expected error when using the Hausen correlation, Eq. (24). The error can exceed 12 percent at the smaller values of the dimensionless axial coordinate, $(x/D_h)/(\mathrm{Pr}\,\mathrm{Re}_D)$. Accordingly, depending on the range of interest, one can obtain accurate data within ±0.84 percent.

The data presented here describe Graetz-type problems for two different flow passages. Accurate computation of the thermally developing temperature in these passages is a demanding task. Indeed, the effect of the porosity further complicates the numerical evaluations. For this reason, the correlation presented here can be a valuable tool in practical applications that require sizing of devices under a developing heat transfer condition.

Local Heat Transfer Coefficient

The local heat transfer coefficient is also obtainable using a nonlinear curve-fitting scheme. Such tools are readily available in standard packages. The variation of the local heat transfer coefficient as a function of $(x/D_h)/(\mathrm{Re}_D\,\mathrm{Pr})$ for these two ducts is similar to those shown in Figs. 2(a–b). There is also a relatively large change of slope as one goes from $M\mathrm{Da}=10^{-4}$ to zero. However, using Eq. (11) for the parallel plate channel or Eq. (20) for circular pipes, this transition difficulty is significantly reduced. The correlations described earlier, Eqs. (11) and (20), indeed provide satisfactory values for heat transfer coefficients for any finite value of $M\mathrm{Da}$ once the heat transfer coefficient for $M\mathrm{Da}=\infty$ is known. An attempt was made to obtain a functional relation with a form similar to Hausen's correlation, Eq. (22). The result was satisfactory for each value of $M\mathrm{Da}$; however, the secondary correlation of the computed coefficient with $M\mathrm{Da}$ as a parameter was not satisfactory. Correlations that estimate the local heat transfer coefficients for these two ducts are in the next sections.

Parallel Plate Channels. A similar procedure used for the average heat transfer coefficient was used. The methodology required a few modifications. The modified correlation has the form

$$\mathrm{Nu}_D(x,M\mathrm{Da})=\mathrm{Nu}_D^*(x)\times\Psi(x,M\mathrm{Da}) \tag{25}$$

Again, the presentation of the function $\Psi(x,M\mathrm{Da})$ is the main objective of this work. The empirical equation was developed by nonlinear curve fitting of numerically acquired data. Equation (12*a*) was selected for this curve fitting and the computed new set of constants,

$$C_1=\frac{0.00053}{1+20(M\mathrm{Da})^{0.75}} \tag{26a}$$

$$C_2=0.00044+\frac{0.004}{1+10{,}000(M\mathrm{Da})^{1/8}}+\frac{0.00165}{[1+0.025(M\mathrm{Da})^{-2/3}]^{1/2}} \tag{26b}$$

and

$$m=1.0-\frac{0.24}{[1+82(M\mathrm{Da})^{1/4}]^{1/2}} \tag{26c}$$

are computed for insertion in Eq. (12*a*).

Moreover, a nonlinear regression was used to accomplish the task of providing the value of the local Nusselt number, $\mathrm{Nu}_D^*(x)$, in the absence of porous materials. The initial effort was directed toward an equation that has a form similar to that of the Hausen relation, Eq. (24), for circular pipes; however, the error was larger than expected. Different function forms were examined. The form of Eq. (14*b*) performed satisfactorily but with different coefficients,

$$\mathrm{Nu}_D^*(x)=7.54+\frac{0.78\times\left(\dfrac{x/D_h}{\mathrm{Pr}\,\mathrm{Re}_D}\right)^{-0.362}}{\left[1+69\times\left(\dfrac{x/D_h}{\mathrm{Pr}\,\mathrm{Re}_D}\right)^{3/4}\right]^2} \tag{27}$$

A nonlinear regression followed by some manual adjustment determined the coefficients in Eq. (27). It is also possible, as an example, to use Eqs. (11) and (14*b*) to get an estimation of the local heat transfer coefficient. By designating the dimensionless axial coordinate as $\tilde{x}=(x/D_h)/(\mathrm{Re}_D\,\mathrm{Pr})$, following appropriate differentiation and a minor refinement of coefficients, one obtains

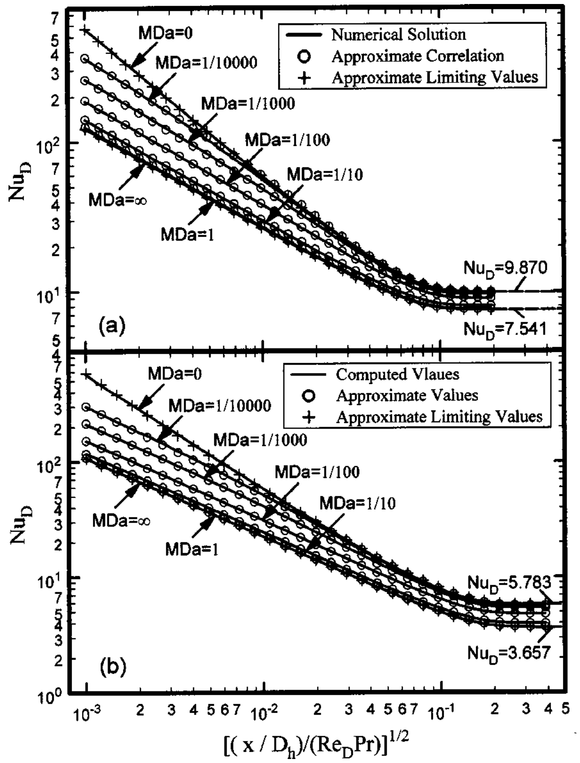

Fig. 4 A comparison of data from correlation with the computed data for local heat transfer coefficient: (a) in parallel plate channels; and (b) in circular pipes.

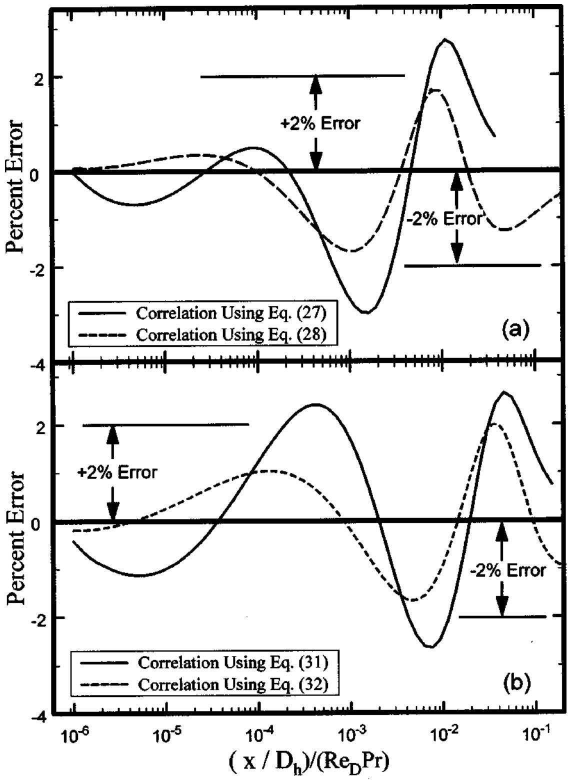

Fig. 5 Errors in the Value of Nu_D^*: (a) in parallel plate channels using Eqs. (27,28); and (b) in circular pipes using Eqs. (31,32).

$$\begin{aligned}\mathrm{Nu}_D^*(\tilde{x}) &= \overline{\mathrm{Nu}}_D^*(\tilde{x}) + \tilde{x}\,d[\overline{\mathrm{Nu}}_D^*(\tilde{x})]/d\tilde{x} \\ &= 7.541 + \frac{1.557\times(\tilde{x})^{-0.344}}{[1+3.47\sqrt{\tilde{x}}]^4}\left[\frac{1-3.47\sqrt{\tilde{x}}}{1+3.47\sqrt{\tilde{x}}} - 0.344\right]\end{aligned} \tag{28}$$

Figure 4(a) is prepared to show a general view of the accuracy of these correlations for the local heat transfer coefficient as a function of MDa. The data show that, in general, the targeted accuracy of ±5 percent is satisfied over the range of plotted data. As in the previous case, Eq. (27) or Eq. (28) needs to provide data for classical flow in parallel plate channels with accuracy within the range of errors for data in Fig. 4(a). Accordingly, Eqs. (27) and (28) are compared with numerically acquired data and percent error is plotted in Fig. 5(a). This figure shows that the expected errors in these correlations could generally be larger than those reported for the average heat transfer coefficient. Equation (27) has a simpler form while Eq. (28) has a slightly better accuracy. The error when using Eq. (27) is within ±3 percent whereas the error when using Eq. (28) is smaller, within ±1.7 percent. The correlations given by Eq. (27) or (28) are suitable to obtain approximate heat transfer data for flow through parallel plate channels and to get $\mathrm{Nu}_D^*(x)$ for inclusion in Eq. (25). This implies that the prediction for the local heat transfer coefficient for flow in a channel filled with porous materials may contain a slightly larger error than that for the average heat transfer coefficient.

Cylindrical Pipes. For cylindrical passages, Eq. (21*a*) needs additional modifications in order to satisfy the imposed error criterion of ±5 percent. The modified form of the $\Psi(x,M\mathrm{Da})$ function used in this correlation is

$$\Psi(x,M\mathrm{Da}) = \frac{\mathrm{Nu}_D(\infty)}{\mathrm{Nu}_D^*(\infty)} + C_3\times\left[\frac{C_1\times\left(\dfrac{x}{D_h}\dfrac{1}{\mathrm{Pr\,Re}_D}\right)^{-1}}{1+C_2\times\left(\dfrac{x}{D_h}\dfrac{1}{\mathrm{Pr\,Re}_D}\right)^{-m}}\right]^n \tag{29a}$$

The coefficients C_1, C_2, and m remain as given by Eqs. (21*b*–*d*) while the new coefficients, C_3 and n, are

$$C_3 = 42 + 80(M\mathrm{Da})^{0.61} \tag{29b}$$

and

$$n = 1.9 + \frac{0.5}{1+400\sqrt{M\mathrm{Da}}} \tag{29c}$$

Figure 4(b) shows the values of the local Nusselt number plotted as a function of the dimensionless axial coordinate. As before, the solid lines represent the reference values computed numerically. The circular symbols are the approximate values obtained using the correlation

$$\mathrm{Nu}_D(x,M\mathrm{Da}) = \mathrm{Nu}_D^*(x)\times\Psi(x,M\mathrm{Da}) \tag{30}$$

when $\Psi(x,M\mathrm{Da})$ is taken from Eqs. (29*a*–*c*). Finally, it is necessary to present a prediction for the value of $\mathrm{Nu}_D^*(x)$. Among various formulations attempted, the following correlation performed satisfactorily,

$$\mathrm{Nu}_D^*(x) = 3.657 + \frac{0.70\times\left(\dfrac{x}{D_h}\dfrac{1}{\mathrm{Pr\,Re}_D}\right)^{-0.362}}{\left[1+17\times\left(\dfrac{x}{D_h}\dfrac{1}{\mathrm{Pr\,Re}_D}\right)^{2/3}\right]^2} \tag{31}$$

Table 1 Summary of the coefficients in the $\Psi(x,M\mathrm{Da})$ factor, Eq. (33), for the Nusselt number correlations

Channel Descriptions	C_1	C_2	C_3	m	n
Parallel Plates, $\overline{\mathrm{Nu}}_D$	$0.023/(1+88\times M\mathrm{Da}^{0.85)}$	$0.0033+0.0051/(1+500\times M\mathrm{Da}^{0.5})$	1	$0.97-0.17/(1+3000\times M\mathrm{Da}^{4/5})$	1
Parallel Plates, Nu_D	$0.00053/(1+20\times M\mathrm{Da}^{0.75})$	$0.00044+0.004/(1+10{,}000\times M\mathrm{Da}^{1/8})+0.00165/(1+0.025\times M\mathrm{Da}^{-2/3})^{1/2}$	1	$1-0.24/(1+82\times M\mathrm{Da}^{1/4})^{1/2}$	1
Circular Pipes, $\overline{\mathrm{Nu}}_D$	$0.0031/(1+800\times M\mathrm{Da}^{0.88})$	$0.0011+0.0089/(1+20\times M\mathrm{Da}^{1/4})$	1	$0.97-0.17/(1+2400\times M\mathrm{Da}^{2/3})$	1
Circular Pipes, $\overline{\mathrm{Nu}}_D$	$0.0031/(1+800\times M\mathrm{Da}^{0.88})$	$0.0011+0.0089/(1+20\times M\mathrm{Da}^{1/4})$	$42+80\times M\mathrm{Da}^{0.61}$	$0.97-0.17/(1+2400\times M\mathrm{Da}^{2/3})$	$1.9+0.5/(1+400\sqrt{M\mathrm{Da}})$

One can also perform a proper differentiation of Eq. (23) to obtain the following relations:

$$\begin{aligned}\mathrm{Nu}_D^*(\tilde{x}) &= \overline{\mathrm{Nu}}_D^*(\tilde{x}) + \tilde{x}\,\mathrm{d}[\overline{\mathrm{Nu}}_D^*(\tilde{x})]/d\tilde{x} \\ &= 3.657 + \frac{1.403\times(\tilde{x})^{-0.342}}{[1+2.537\sqrt{\tilde{x}}]^4}\left[\frac{1-1.27\sqrt{\tilde{x}}}{1+2.537\sqrt{\tilde{x}}} - 0.342\right]\end{aligned} \tag{32}$$

where $\tilde{x} = (x/D_h)/(\mathrm{Re}_D\,\mathrm{Pr})$.

The solid line plotted in Fig. 5(b) designates the percent error when using the correlation given by Eq. (31). The dash line in Fig. 5(b) indicates the distribution of the error using Eq. (32), also plotted over a relatively large range of dimensionless axial coordinate. The error when using Eq. (31) is within ± 2.7 percent while the error when using Eq. (32) is within ± 2 percent. This figure shows that any one of these two correlations can provide the local heat transfer coefficient data with sufficient accuracies. They can be implemented to provide the values for $\mathrm{Nu}_D(x)$, using Eqs. (29–30). This will facilitate the computation of the local heat transfer coefficient for flow through porous materials imbedded in a circular pipe.

Summary

The correlations presented earlier followed a two-step procedure. The first step is to select a value for $M\mathrm{Da}$ and provide a correlation for that parameter. A nonlinear regression conveniently provides the needed coefficient for a selected functional form and this process is repeated for other $M\mathrm{Da}$ values. As expected, the computed coefficients would depend on the selected $M\mathrm{Da}$ values. The second step was to find simple relations that relate these coefficients. This second step necessitated the examination of different functional forms in the first step. Moreover, the process of correlating these coefficients was simpler for the average Nusselt number. Also, as can be seen from Figs. 2(a–b), the error for the average Nusselt number is less than the size of the symbols, within ± 3 percent. Whereas, the radius of a symbol in Figs. 4(a–b) is ~ 3.8 percent of the value of local Nusselt number; therefore the error for the local heat transfer coefficients is generally within ± 4 percent over the range of plotted data.

The solution for heat transfer to fully developed flow through unobstructed passages is well known. The issue is finding a multiplying function that can be used to get the heat transfer coefficient through a fluid saturated passage, e.g., from Eq. (11). For the two passages presented here, the function $\Psi(x,M\mathrm{Da})$, in Eqs. (12*a*), (21*a*), (29*a*), has a similar form,

$$\Psi(x,M\mathrm{Da}) = \frac{\mathrm{Nu}_D(\infty)}{\mathrm{Nu}_D^*(\infty)} + C_3\times\left[\frac{C_1\times\left(\dfrac{x}{D_h}\,\dfrac{1}{\mathrm{Pr}\,\mathrm{Re}_D}\right)^{-1}}{1+C_2\times\left(\dfrac{x}{D_h}\,\dfrac{1}{\mathrm{Pr}\,\mathrm{Re}_D}\right)^{-m}}\right]^n \tag{33}$$

For each case studied here, the coefficients C_1, C_2, C_3, m, and n are deterministic. According to Eq. (13), the first term on the right side of Eq. (33), for a parallel plate channel, reduces to

$$\frac{\mathrm{Nu}_D(\infty)}{\mathrm{Nu}_D^*(\infty)} \cong 1 + \frac{0.309}{1+22(M\mathrm{Da})^{3/4}} \tag{34a}$$

and according to Eq. (22) for a circular pipe becomes

$$\frac{\mathrm{Nu}_D(\infty)}{\mathrm{Nu}_D^*(\infty)} \cong 1 + \frac{0.581}{1+30(M\mathrm{Da})^{3/4}}. \tag{34b}$$

All other coefficients have numerical values that depend on $M\mathrm{Da}$. Secondary correlations to estimate these coefficients, for all $M\mathrm{Da}$ between 0 and ∞, appeared earlier and are summarized in Table 1. For the four cases reported here, Table 1 serves as a tool for quick identification of the coefficients C_1, C_2, C_3, m, and n for insertion in Eq. (33).

Conclusion

The initial objective to set up correlations that would enable one to obtain relatively accurate local and average heat transfer data for flow through selected porous channels has been achieved. One objective in this study is to have correlations that provide relatively accurate results for a broad range $0 \leqslant M\mathrm{Da} \leqslant \infty$. This condition and the second objective of having an error of ± 5 percent, with a relatively high probability, determined the selection of the forms of these correlations. The forms of these correlations make it necessary to evaluate the accuracy of the existing correlations for flow through unobstructed channels, that is, for $M\mathrm{Da} = \infty$. For this reason existing correlations are revisited and additional studies are included in the appendix.

Nomenclature

A = area, m^2
A_m, B_m = coefficients
C = duct contour, m
C_1, C_2 = coefficients
c_j = coefficients
Da = Darcy number, K/L_c^2
D_h = hydraulic diameter, m

Table A.1.a Selected eigenvalues, λ_m, coefficients A_m, and norms N_m for laminar flow through parallel plate channels

m	λ_m	$A_m \times 10^3$	N_m	m	λ_m	$A_m \times 10^3$	N_m
1	1.37302	758.102	0.631315	26	83.0105	−6.09124	0.589063
2	4.62942	−177.639	0.593791	27	86.2765	5.82307	0.589062
3	7.89409	95.0026	0.590715	28	89.5425	−5.57603	0.589061
4	11.1596	−63.3752	0.589884	29	92.8085	5.34777	0.589060
5	14.4254	46.9552	0.589548	30	96.0745	−5.13627	0.589060
6	17.6912	−36.9987	0.589380	31	99.3405	4.93980	0.589059
7	20.9571	30.3595	0.589285	32	102.606	−4.75684	0.589058
8	24.2230	−25.6376	0.589225	33	105.872	4.58608	0.589058
9	27.4890	22.1191	0.589185	34	109.138	−4.42637	0.589057
10	30.7549	−19.4029	0.589158	35	112.404	4.27668	0.589057
11	34.0209	17.2471	0.589138	36	115.670	−4.13613	0.589056
12	37.2868	−15.4975	0.589123	37	118.936	4.00393	0.589056
13	40.5528	14.0511	0.589111	38	122.202	−3.87936	0.589055
14	43.8188	−12.8368	0.589102	39	125.468	3.76180	0.589055
15	47.0848	11.8040	0.589095	40	128.734	−3.65069	0.589055
16	50.3507	−10.9155	0.589089	41	132.000	3.54553	0.589054
17	53.6167	10.1437	0.589084	42	135.266	−3.44585	0.589054
18	56.8827	−9.46745	0.589080	43	138.532	3.35126	0.589054
19	60.1487	8.87040	0.589077	44	141.798	−3.26138	0.589054
20	63.4146	−8.33969	0.589074	45	145.064	3.17587	0.589053
21	66.6806	7.86507	0.589072	46	148.330	−3.09444	0.589053
22	69.9466	−7.43828	0.589069	47	151.596	3.01680	0.589053
23	73.2126	7.05259	0.589068	48	154.862	−2.94270	0.589053
24	76.4786	−6.70246	0.589066	49	158.128	2.87192	0.589053
25	79.7446	6.38329	0.589065	50	161.394	−2.80423	0.589053

H = channel dimension in Fig. 1(a), m
h = local heat transfer coefficient W/m$^2\cdot$K
$\bar{h}$ = average heat transfer coefficient, W/m$^2\cdot$K
K = permeability, m^2
k = effective thermal conductivity, W/m$\cdot$K
M = μ_e/μ
N_m = norm
$\overline{\mathrm{Nu}}_\mathrm{D}$ = Nusselt number, hD_e/k
Nu^*_D = Reference Nusselt number
Pe = Peclet number, $\rho c_p L_c U/k$
p = pressure, Pa
Re_D = Reynolds number, $\rho U D_h/\mu$
r = radial coordinate
r_o = pipe radius, m
T = temperature, K
T_b = bulk temperature, K
T_i = inlet temperature, at $x=0$, K
T_w = wall temperature, K
u = velocity, m/s
U = average velocity, m/s
x = axial coordinate, m
$\bar{x}$ = $x/(\mathrm{Pe}L_\mathrm{c})$
$\tilde{x}$ = $(x/D_h)/(\mathrm{Re_D\,Pr})$
y, z = coordinates, m
$\bar{y}$ = y/H

Greek

γ_m = eigenvalues
θ = $(T-T_w)/(T_i-T_w)$
λ_m = eigenvalues
μ = fluid viscosity, N$\cdot$s/m^2
μ_e = effective viscosity, N$\cdot$s/m^2
ρ = density, kg/m^3
Ψ = auxiliary function, see Eq. (12*a*)
ψ = a parameter

Appendix

The correlations presented here require knowledge of relatively accurate data for flow through unobstructed channels, $M\mathrm{Da}=\infty$. For example, a temperature solution based on Eqs. (6) and (7), for parallel plate channels when $M\mathrm{Da}=\infty$, can describe the variation of the $\overline{\mathrm{Nu}}^*_D(x)$. The relation for a fully developed velocity profile for inclusion in Eq. (7*b*) is

$$\frac{u}{U}=\frac{3}{2}\left[1-\left(\frac{y}{H}\right)^2\right] \tag{A.1}$$

where $2H$ is the spacing between two plates and U is the average velocity. The solution of the energy equation, Eq. (7*b*), is essentially the same as that described by Eqs. (8–10), the coefficients c_n given by Eq. (9*a*) must be modified. These coefficients are $c_0=1$, $c_2=-3\gamma_m^2/4$, $c_1=c_3=c_5=\cdots=0$ and the remaining. c_n values are obtainable from the following recursive relation

Table A.1.b Referenced heat transfer values for parallel plate ducts when $M\mathrm{Da}=\infty$

$(x/D_h)(1/\mathrm{Pr\,Re}_D)$	hD_h/k	$\bar{h}D_h/k$	$(T_b-T_w)/(T_i-T_w)$
5.0×10^{-7}	154.26	232.76	0.99953
1.0×10^{-6}	122.93	184.55	0.99926
2.0×10^{-6}	97.538	146.42	0.99883
5.0×10^{-6}	71.830	107.83	0.99785
0.00001	56.999	85.557	0.99658
0.00002	45.245	67.890	0.99458
0.00005	33.379	50.027	0.99004
0.0001	26.560	39.736	0.98423
0.0002	21.188	31.598	0.97504
0.0005	15.830	23.416	0.95425
0.001	12.822	18.752	0.92774
0.002	10.545	15.125	0.88604
0.005	8.5167	11.623	0.79258
0.01	7.7405	9.8249	0.67503
0.02	7.5495	8.7133	0.49804
0.05	7.5407	8.0103	0.20148
0.1	7.5407	7.7755	0.44592×10^{-1}
0.2	7.5407	7.6581	0.21842×10^{-2}
0.5	7.5407	7.5877	0.25671×10^{-6}
1	7.5407	7.5642	0.72389×10^{-13}
2	7.5407	7.5524	0.57561×10^{-26}
5	7.5407	7.5454	0.28941×10^{-65}

Table A.2.a Selected eigenvalues λ_m, coefficients A_m, and norms N_m for laminar flow through circular pipes

m	λ_m	$A_m \times 10^4$	$N_m \times 10^3$	m	λ_m	$A_m \times 10^4$	$N_m \times 10^3$
1	1.91227	2773.74	187.868	26	72.5965	−6.32349	4.87014
2	4.72279	−604.913	75.0397	27	75.4249	5.93319	4.68750
3	7.54722	276.037	46.8842	28	78.2534	−5.58005	4.51808
4	10.3740	−162.237	34.0942	29	81.0818	5.25939	4.36047
5	13.2016	108.494	26.7872	30	83.9102	−4.96722	4.21349
6	16.0295	−78.4785	22.0596	31	86.7386	4.70018	4.07609
7	18.8576	59.8457	18.7505	32	89.5670	−4.45540	3.94737
8	21.6858	−47.4034	16.3046	33	92.3955	4.23039	3.82653
9	24.5140	38.6387	14.4233	34	95.2239	−4.02303	3.71287
10	27.3423	−32.2067	12.9312	35	98.0523	3.83146	3.60577
11	30.1706	27.3316	11.7188	36	100.881	−3.65409	3.50467
12	32.9990	−23.5385	10.7144	37	103.709	3.48949	3.40909
13	35.8273	20.5227	9.86848	38	106.538	−3.33645	3.31859
14	38.6557	−18.0809	9.14638	39	109.366	3.19387	3.23276
15	41.4841	16.0728	8.52276	40	112.194	−3.06080	3.15126
16	44.3125	−14.3992	7.97875	41	115.023	2.93638	3.07377
17	47.1409	12.9880	7.50002	42	117.851	−2.81986	3.00000
18	49.9693	−11.7857	7.07549	43	120.680	2.71056	2.92969
19	52.7977	10.7522	6.69644	44	123.508	−2.60789	2.86260
20	55.6261	−9.85634	6.35594	45	126.337	2.51131	2.79851
21	58.4545	9.07424	6.04840	46	129.165	−2.42032	2.73723
22	61.2829	−8.38691	5.76924	47	131.993	2.33449	2.67857
23	64.1113	7.77926	5.51471	48	134.822	−2.25343	2.62238
24	66.9397	−7.23911	5.28170	49	137.650	2.17679	2.56849
25	69.7681	6.75656	5.06757	50	140.479	−2.10423	2.51678

Table A.2.b Referenced heat transfer values for circular pipes when M Da$=\infty$

$(x/D_h)(1/\mathrm{Pr}\,\mathrm{Re}_D)$	hD_h/k	$\overline{h}D_h/k$	$(T_b-T_w)/(T_i-T_w)$
5.0×10^{-7}	129.74	204.34	0.99959
1.0×10^{-6}	106.08	160.47	0.99936
2.0×10^{-6}	84.334	127.05	0.99898
5.0×10^{-6}	61.877	93.334	0.99814
0.00001	48.914	73.869	0.99705
0.00002	38.637	58.429	0.99534
0.00005	28.254	42.812	0.99147
0.0001	22.279	33.810	0.98657
0.0002	17.559	26.683	0.97888
0.0005	12.824	19.501	0.96175
0.001	10.130	15.384	0.94032
0.002	8.0362	12.152	0.90736
0.005	6.0015	8.9432	0.83622
0.01	4.9161	7.1552	0.75111
0.02	4.1724	5.8146	0.62803
0.05	3.7100	4.6406	0.39530
0.1	3.6581	4.1556	0.18971
0.2	3.6568	3.9063	0.43935×10^{-1}
0.5	3.6568	3.7566	0.54583×10^{-3}
1	3.6568	3.7067	0.36376×10^{-6}
2	3.6568	3.6817	0.16155×10^{-12}
5	3.6568	3.6668	0.14152×10^{-31}

$$c_n=\frac{3(c_{n-4}-c_{n-2})\gamma_m^2}{2n(n-1)} \quad \text{for } n=4,6,\cdots$$

The proper values of γ_m must make $Y_m(1)=0$ in order to satisfy the boundary condition at $y=H$. These roots will be ordered and called γ_1, γ_2,$\cdots$. Then, the mth eigenvalue $\lambda_m=\gamma_m$ defines the function $Y_m(\overline{y})$, Eq. (8*b*), for insertion in Eq. (8*a*) while Eq. (10) provides the coefficient $B_m=A_m/N_m$. The first 50 values of λ_m, A_m, and N_m are in Table A.1.a. Once the temperature solution is known, Eqs. (4) and (5) give the local and average Nusselt numbers. Samples of computed average and local Nusselt numbers are in Table A.1.b.

A similar procedure defines the temperature distribution in circular pipes. The fully developed velocity profile to be inserted in Eq. (16*b*) is

$$\frac{u}{U}=2\left[1-\left(\frac{r}{r_o}\right)^2\right] \tag{A.2}$$

where r_o is the radius of the pipe, and U is the average velocity. The solution of Eq. (16*b*), is similar to that described by Eqs. (17–19), the coefficients c_n given by Eq. (18*a*) must be modified. These new coefficients are $c_0=1$, $c_2=-\gamma_m^2/2$, and $c_1=c_3=c_5=\cdots=0$. and the remaining c_n values are obtainable from the recursive relation

$$c_n=(c_{n-4}-c_{n-2})\gamma_m^2/n^2 \quad \text{for } n=4,6,\cdots$$

As before, a proper value of γ_m must make $R_m(1)=0$ in order to satisfy the boundary condition at $r=r_o$. These roots are designated as γ_1, γ_2,$\cdots$ and the corresponding eigenvalues λ_m are obtained from the relation $\lambda_m=\gamma_m/\sqrt{2}$. For each eigenvalue λ_m, Eq. (17*b*) provides the eigenfunctions $R_m(\overline{r})$ for insertion in Eq. (17*a*). The next step is the determination of coefficients $B_m=A_m/N_m$ from Eq. (19) also for insertion in Eq. (17*a*). The first 50 values of λ_m, A_m, and N_m are in Table A.2.a. In addition, Table A.2.b is prepared to show samples of computed average and local Nusselt numbers.

To get the first few eigenvalues, a marching technique provides a bound on the location of each eigenvalue. Then, two second-order Newton iterations are sufficient to compute an eigenvalue with sufficient accuracy. These eigenvalues assume nearly uniform spacing beyond the 30th eigenvalue. This observation simplifies the determination of eigenvalues beyond γ_{30}. For a parallel plate channel, the spacing between the adjacent γ_m values rapidly approaches $\sqrt{32/3}$ while the spacing between the γ_m values for a circular pipe rapidly approaches 4. As an illustration, for circular pipes, the 30th eigenvalue has a value of 118.666939596 and the 330th eigenvalue is 1318.666677673; therefore, the average spacing between two successive eigenvalues is equal to ~3.9999991. This simplifies the computational procedure because, for the larger eigenvalues, a single second-order Newton iteration is sufficient for these eigenfunctions to assume their proper values with an error between 10^{-9} to 10^{-23}.

The numerically computed local and average Nusselt number data in Tables A.1.a and A.1.b are highly accurate; the error is in the last digit appearing in these tables mainly due to truncation. At small values of *x*, as many as 400 eigenvalues were computed in order to get accurate heat transfer data for parallel plate ducts and 500 eigenvalues were used to get accurate data for circular pipes.

References

[1] Nield, D. A., and Bejan, A., 1999, *Convection in Porous Media*, 2nd ed., Springer-Verlag, New York.

[2] Kaviany, K., 1991, *Principles of Heat Transfer in Porous Media*, Springer-Verlag, New York.

[3] Vafai, K., ed., 2000, *Handbook of Porous Media*, Marcel Dekker, New York.

[4] Nield, D. A., Kuznetsov, A. V., and Xiong, M., 2003, ''Thermally Developing Forced Convection in a Porous Medium: Parallel Plate Channel With Walls at Uniform Temperature, With Axial Conduction and Viscous Dissipation Effects,'' Int. J. Heat Mass Transfer, **46**, pp. 643–651.

[5] Beck, J. V., Cole, K., Haji-Sheikh, A., and Litkouhi, B., 1992, *Heat Conduction Using Green's Functions*, Hemisphere Publ. Corp., Washington D.C.

[6] Haji-Sheikh, A., and Vafai, K., 2004, ''Analysis of Flow and Heat Transfer in Porous Media Imbedded Inside Various-Shaped Ducts,'' Int. J. Heat Mass Transfer, **47**, pp. 1889–1905.

[7] Wolfram, S., 1999, *The Mathematica Book*, Fourth Edition, Cambridge University Press, Cambridge, UK.

[8] Burmeister, L. C., 1993, *Convective Heat Transfer*, Second Edition, John Wiley & Sons, Inc., New York.

Polymer Electrolyte Fuel Cells With Porous Materials as Fluid Distributors and Comparisons With Traditional Channeled Systems

S. M. Senn

D. Poulikakos

Laboratory of Thermodynamics in Emerging Technologies,
Institute of Energy Technology,
Swiss Federal Institute of Technology Zurich,
ETH Zentrum, CH-8092 Zurich, Switzerland

In this study, a novel concept is investigated, according to which the traditional ribbed flow delivery systems are replaced with permeable porous fluid distributors, which circumvent a number of known performance hindering drawbacks. A thorough single-phase model, including the conservation of mass, momentum, energy, species, and electric current, using Butler-Volmer kinetics, is numerically solved in three dimensions, to investigate the impact of different flow configurations on the performance of hydrogen fuel cells. It is found that cells with porous gas distributors generate substantially higher current densities and therefore are more advantageous with respect to mass transfer. Another advantage of porous flow distributors is the potential for higher power densities and reduced stack weight. [DOI: 10.1115/1.1738424]

Keywords: Computational, Energy Conversion, Modeling, Porous Media, Fuel Cells

1 Introduction

Polymer electrolyte fuel cells (PEFC) have the potential to become firmly established as a competitive form of electric power generation in a host of engineering applications, such as powering of vehicles, portable power systems, and remote power generations. Even though low temperature fuel cells have very high theoretical efficiencies, there are several challenges to overcome in the way of making the PEFC a competitive, efficient and environmentally friendly alternative energy conversion device. Current issues in PEFC research are strongly interdisciplinary and are related to transport phenomena, thermal management, water management, electrochemistry, materials, and manufacturing.

Numerical modeling provides an improved understanding of the fundamental transport phenomena inside the fuel cell and therefore allows for efficient, scientifically based optimization which is necessary to aid the PEFC on the road to success. Therefore, substantial research effort has been focused on the development of mathematical models and their analytical or numerical solution during the last decade. One-dimensional models [1–4], pseudo-two-dimensional models [5–8] as well as fully two-dimensional models [9–13] are not able to predict with the needed accuracy the three-dimensional transport phenomena in a PEFC, and, therefore, are not ideally appropriate for design or material optimization. Three-dimensional modeling [14–19] is crucial to capture performance-limiting effects such as mass transfer limitations to and from the portion of the diffusion layer which is not covered by flow channels as well as Ohmic losses in the membrane-electrode assembly. In most of these three-dimensional models [14–18] the catalyst layers are modeled as infinitely thin interfaces, whereas in [19] the finite size of the catalyst layers was considered. The existence of two different electric potential fields, i.e., a solid potential field governing the electron flux and a membrane potential field governing the proton flux is not accounted for. A two-dimensional approach is used for the membrane in [15–17]. In contrast, the present mathematical model accounts for the finite thickness of the catalyst layers as well as of the membrane and the governing equations inside each of these layers are solved in three dimensions. Two different electric potential fields are considered, i.e., a solid potential field and a membrane potential field. In addition, kinetic gas theory is used to determine the thermal conductivity of the gas mixture, which strongly depends on the mixture composition.

The mathematical model is solved for porous flow distributors, put forth by Bejan and co-workers [20,21], as well as for the classical parallel and serpentine flow distributors, for the sake of comparison. Validation of the code at different operating pressures and temperatures was performed using experimental data from Ticianelli et al. [22]. Parallel and serpentine flow-fields exhibit limited reactant/product mass transfer to and from the part of the diffusion and catalyst layer which is not covered by flow channels (i.e., under the current collector ‘‘shoulders’’). This effect is most distinct on the cathode side due to the low diffusivity of oxygen. Removal of water vapor from these regions is also limited. In this paper it is shown that porous flow distributors circumvent this drawback which is particular to ribbed flow-fields and therefore are more advantageous in terms of mass transfer.

Porous materials such as carbon or metal foams are available at porosities up to 98% which implies the possibility of a reduction in stack weight—a key quantity for applications in transportation. However, the higher the porosity of the foam, the lower the effective electrical conductivity is. On the other hand, mass transfer limitations are higher at the lower porosities due to reduced effective species diffusivities. Parametric studies are performed to investigate these interactions. Finally, appropriate foam materials currently available on the market are suggested.

2 Mathematical Model

Transport phenomena in the PEFC are described by the formulation of mass, momentum, energy, species, and electric current conservation equations. The method of local volume averaging [23–26] is applied to equations governing transport in porous media which means that the equations are spatially smoothed over a

---

Contributed by the Heat Transfer Division for publication in the JOURNAL OF HEAT TRANSFER. Manuscript received by the Heat Transfer Division August 25, 2003; revision received February 26, 2004. Associate Editor: S. P. Vanka.

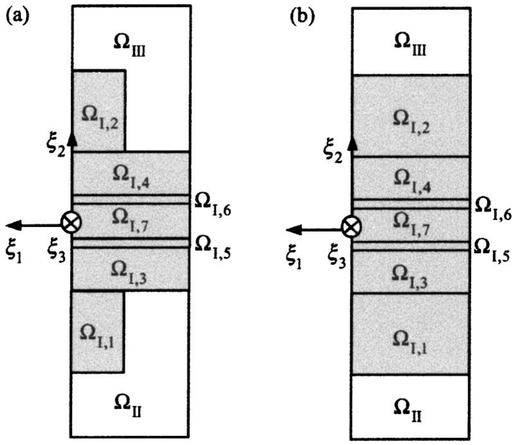

Fig. 1 Schematic drawing of the partition of the computational domain $\Omega=\Omega_I\cup\Omega_{II}\cup\Omega_{III}$. (a) Cell with a channeled flow-field. (b) Cell with a porous gas distributor. The domain Ω consists of the fluid subdomain Ω_I (flow channels $\Omega_{I,1}$ and $\Omega_{I,2}$ in (a); porous gas distributors $\Omega_{I,1}$ and $\Omega_{I,2}$ in (b); diffusion layers $\Omega_{I,3}$, $\Omega_{I,4}$; catalyst layers $\Omega_{I,5}$, $\Omega_{I,6}$; membrane $\Omega_{I,7}$), the solid subdomain Ω_{II} including the current collector on the cathode side and the solid subdomain Ω_{III} including the current collector on the anode side. The flow direction is indicated with ξ_3

representative elementary volume. Its diameter has to be much larger than the pore diameter as well as much smaller than the macroscopic dimension of the corresponding porous layer. The computational domain Ω consists of three coupled subdomains Ω_{I}, Ω_{II}, and Ω_{III}, as shown in Fig. 1. The first subdomain Ω_{I} (fluid subdomain) incorporates flow channels, gas diffusion layers, catalyst layers, and the membrane. Inhomogeneous distributions of material properties inside this subdomain are defined in order to account for different physical layers. Mass, momentum, energy, species, and electric current conservation is formulated for this subdomain. The second and third subdomain (solid subdomains), Ω_{II} and Ω_{III}, include the current collector on the cathode and anode side, respectively, for which conservation of energy and electric current is formulated. Rates of electrochemical reactions in the catalyst layers are described by Butler-Volmer equations.

An ideal gas mixture is assumed inside the fluid subdomain Ω_{I},

$$p=\frac{\rho}{M}RT, \quad p=p_i/x_i, \quad \rho=\sum_{i=1}^{N}\rho_i, \quad M=\sum_{i=1}^{N}x_iM_i, \tag{1}$$

where pressure is defined in terms of partial pressure and mole fraction of species *i*, mixture density is expressed in terms of mass concentrations and mixture molecular weight is given by the molecular weight of individual species. For the ideal gas mixture, the specific enthalpy is a function of temperature and species mass fractions,

$$h(T,\omega_1,\ldots,\omega_N)=\sum_{i=1}^{N}\omega_ih_i(T), \tag{2}$$

where specific enthalpies h_i of individual species, defined as the sum of the enthalpy of formation at the standard reference state and the sensible enthalpy, depend on temperature only and are approximated using *JANAF* tables [27]. In the following, volume-averaged conservation equations are formulated to describe transport in porous media. Mass conservation for the ideal gas mixture reads

$$\underline{\nabla}\cdot(\varepsilon\rho\underline{v})=0. \tag{3}$$

For a porosity of $\varepsilon=1$, mass conservation of a free-stream gas mixture is recovered. Momentum conservation is written as

$$\underline{\nabla}\cdot(\varepsilon\rho\underline{v}\,\underline{v})=-\underline{\nabla}(\varepsilon p)-\underline{\nabla}\cdot(\varepsilon\underline{\underline{\tau}})-\frac{\mu}{\kappa}\varepsilon^2\underline{v} \tag{4}$$

with the stress tensor

$$\underline{\underline{\tau}}=-\mu(\underline{\nabla}\,\underline{v}+(\underline{\nabla}\,\underline{v})^T)+\frac{2}{3}\mu(\underline{\nabla}\cdot\underline{v})\underline{\underline{I}}. \tag{5}$$

The last term in Eq. (4) represents an additional source term, Darcy's drag, for porous media regions in order to account for increased flow resistance. Note that Eq. (4) is a generalized form of Darcy's law [23–26]. For $\varepsilon=1$ and $\kappa\to\infty$, momentum conservation for a free-stream gas mixture is recovered. The local dynamic viscosity of the gas mixture

$$\mu=\sum_{i=1}^{N}\frac{x_i\mu_i}{\sum_{j=1}^{N}x_j\Theta_{ij}} \tag{6}$$

with

$$\Theta_{ij}=\frac{1}{\sqrt{8}}\left(1+\frac{M_i}{M_j}\right)^{-1/2}\left[1+\left(\frac{\mu_i}{\mu_j}\right)^{1/2}\left(\frac{M_j}{M_i}\right)^{1/4}\right]^2 \tag{7}$$

is determined based on the Chapman-Enskog theory, extended to multicomponent gas mixtures at low density [28–30]. Within this framework, dynamic viscosities of individual species are given as

$$\mu_i=2.6693\cdot10^{-6}\frac{\sqrt{10^3\cdot M_iT}}{\varpi_i^2\Omega_{\mu,i}}. \tag{8}$$

The volume-averaged conservation equation of energy is written as [30]

$$\underline{\nabla}\cdot(\varepsilon\rho h\underline{v})=-\underline{\nabla}\cdot\underline{q}-(\varepsilon\underline{\underline{\tau}}:\underline{\nabla}\,\underline{v})+\underline{v}\cdot\underline{\nabla}(\varepsilon p)-J\eta+\frac{\underline{i}_s\cdot\underline{i}_s}{\sigma_s}+\frac{\underline{i}_f\cdot\underline{i}_f}{\sigma_f} \tag{9}$$

where

$$\underline{q}=-k_{\mathrm{eff}}\underline{\nabla}T+\sum_{i=1}^{N}h_i\underline{j}_i \tag{10}$$

is the heat flux, accounting for heat conduction and energy transport by species diffusion. The second term on the right hand side of Eq. (9) manifests the irreversible rate of viscous dissipation and the third term includes the reversible rate compression work. The fourth term accounts for electric work due to volumetric electric current transfer between the solid potential field Φ_s and the pore potential field Φ_f in the catalyst layers, where the volumetric transfer current density J is given by Eqs. (23) and (26) below and η is the overpotential. This term appears only in the catalyst layers. The fifth term stands for Joule heating due to electron flux and the last term accounts for Joule heating due to proton flux in the catalyst layers and the membrane. Heat generation due to reactions, i.e., conversion of chemical energy to heat energy, is implicitly accounted for in Eq. (9) through the fourth term on the right hand side, since enthalpy h_i is defined as the sum of the enthalpy of formation at the standard reference state and the sensible enthalpy [30]. The effective thermal conductivity in porous media is determined based on the variational approach using composite spheres for macroscopically homogeneous and isotropic multiphase materials, as introduced by Hashin and Shtrikman [31], where the higher bound reads

$$k_{\mathrm{eff}}=\frac{1}{\dfrac{1-\varepsilon}{3k_s}+\dfrac{\varepsilon}{2k_s+k_f}}-2k_s. \tag{11}$$

Note that $k_{\mathrm{eff}}(\varepsilon=1)=k_f$ and $k_{\mathrm{eff}}(\varepsilon=0)=k_s$ applies. The thermal conductivity of the fluid phase strongly depends on the composition of the gas mixture and is determined within the framework of the Chapman-Enskog theory [32], i.e.,

$$k_f=\sum_{i=1}^{N}\frac{x_i k_i}{\sum_{j=1}^{N} x_j \Theta_{ij}}. \tag{12}$$

Conservation of species reads

$$\underline{\nabla}\cdot(\varepsilon\rho\omega_i\underline{v})=-\underline{\nabla}\cdot\underline{j}_i+r_i,\quad i\in[1,2,3,\ldots,N] \tag{13}$$

with the diffusive flux of species i,

$$\underline{j}_i=-\rho D_{i,\mathrm{eff}}\underline{\nabla}\omega_i. \tag{14}$$

Note that the species source terms r_i on the right hand side of Eq. (13) only appear in the catalyst layers. Effective diffusion coefficients account for reduced mass transport in porous media and are determined in terms of the free-stream diffusion coefficients,

$$D_{i,\mathrm{eff}}=\varepsilon^{\tau}D_i, \tag{15}$$

according to the Bruggeman correction [23,25]. The diffusion coefficient of species i,

$$D_i=\frac{1-x_i}{\sum_{j=1,j\neq i}^{N}\dfrac{x_j}{D_{ij}}}, \tag{16}$$

is expressed in terms of binary diffusion coefficients which in turn are obtained from the Chapman-Enskog theory [30,33],

$$D_{ij}=0.018829\,\frac{\sqrt{T^3\left(\dfrac{1}{10^3\cdot M_i}+\dfrac{1}{10^3\cdot M_j}\right)}}{p\varpi_{ij}^2\Omega_{D,ij}}. \tag{17}$$

Note that Eq. (17) is written here in terms of quantities with SI units as declared in the nomenclature. The electric current flow through the cell is due to electron flux in the current collectors, the solid phase of the gas diffusion layers, the solid phase of the catalyst layers and due to proton flux in the polymer electrolyte phase of the catalyst layers and the membrane. The electron flux is governed by the electric potential field Φ_s and the proton flux is governed by the electric potential field Φ_f. The steady conservation equation of electric current in conjunction with Gauss's law for irrotational electric fields leads to

$$\underline{\nabla}\cdot\underline{i}_s=-\underline{\nabla}\cdot(\sigma_s\underline{\nabla}\Phi_s)=\begin{cases}+J^+, & \text{cathode catalyst layer}\\ -J^-, & \text{anode catalyst layer}\\ 0, & \text{else}\end{cases} \tag{18}$$

and

$$\underline{\nabla}\cdot\underline{i}_f=-\underline{\nabla}\cdot(\sigma_f\underline{\nabla}\Phi_f)=\begin{cases}-J^+, & \text{cathode catalyst layer}\\ +J^-, & \text{anode catalyst layer}\\ 0, & \text{else}\end{cases} \tag{19}$$

From the sum of Eqs. (18) and (19),

$$\underline{\nabla}\cdot\underline{i}_s+\underline{\nabla}\cdot\underline{i}_f=0, \tag{20}$$

it is seen that conservation of charge is accomplished. Electrochemical surface reaction rates are determined with Butler-Volmer equations [34,35]. The surface specific transfer current in the catalyst layer on the cathode side is given then as

$$i^+=i_0^+\left\{\exp\left[\frac{\alpha_a^+F}{RT}(\Phi_s-\Phi_f)\right]-\exp\left[-\frac{\alpha_c^+F}{RT}(\Phi_s-\Phi_f)\right]\right\} \tag{21}$$

with the overpotential $\eta=\Phi_s-\Phi_f$, where the exchange current density

$$i_0^+=-i_0^{\mathrm{ref}+}\left(\frac{c_{O_2,w}}{c_{O_2,w}^{\mathrm{ref}}}\right)^{\gamma_{O_2}}\left(\frac{c_{H_2O,w}}{c_{H_2O,w}^{\mathrm{ref}}}\right)^{\gamma_{H_2O}} \tag{22}$$

is expressed in terms of the reference current density and the reactant and product concentrations $c_{i,w}=\omega_{i,w}\rho/M_i$ at the interface. Multiplying with the surface to volume ratio a^+ in the catalyst layer leads to the volumetric transfer current density

$$J^+=a^+i^+ \tag{23}$$

on the cathode side, where a^+ is a direct representation of catalyst loading. Similarly, electrochemical reaction rates on the anode side are expressed as

$$i^-=i_0^-\left\{\exp\left[\frac{\alpha_a^-F}{RT}(\Phi_s-\Phi_f)\right]-\exp\left[-\frac{\alpha_c^-F}{RT}(\Phi_s-\Phi_f)\right]\right\} \tag{24}$$

$$i_0^-=i_0^{\mathrm{ref}-}\left(\frac{c_{H_2,w}}{c_{H_2,w}^{\mathrm{ref}}}\right)^{\gamma_{H_2}} \tag{25}$$

and

$$J^-=a^-i^-. \tag{26}$$

The stoichiometric reactant coefficients of the cathode reaction

$$\frac{1}{4}O_2+H^++e^-\rightarrow\frac{1}{2}H_2O \tag{27}$$

and of the hydrogen oxidation on the anode side

$$\frac{1}{2}H_2\rightarrow H^++e^- \tag{28}$$

are needed to couple the surface specific transfer current density to mass transfer at the solid-fluid interface in the catalyst layers. This is written as

$$M_{O_2}\frac{i^+}{4F}=+\rho D_{O_2,\mathrm{eff}}\frac{\omega_{O_2}-\omega_{O_2,w}}{d^+} \tag{29}$$

and

$$M_{H_2O}\frac{i^+}{2F}=-\rho D_{H_2O,\mathrm{eff}}\frac{\omega_{H_2O}-\omega_{H_2O,w}}{d^+} \tag{30}$$

where ω_i denotes the mass fraction of species i in the middle of the fluid pore, $\omega_{i,w}$ is the mass fraction at the solid-fluid interface where surface reactions occur, d^+ is the average pore diameter and $D_{i,\mathrm{eff}}/d^+$ represents the mass transfer coefficient. Numerical solution of the set of nonlinear Eqs. (21), (22), and (29) for $\omega_{i,w}$ [36] allows to determine the volumetric source terms

$$r_{O_2}=-a^+\rho D_{O_2,\mathrm{eff}}\frac{\omega_{O_2}-\omega_{O_2,w}}{d^+} \tag{31}$$

and

$$r_{H_2O}=-a^+\rho D_{H_2O,\mathrm{eff}}\frac{\omega_{H_2O}-\omega_{H_2O,w}}{d^+} \tag{32}$$

which are used in Eq. (13). Similarly, formulation of these constraints on the anode side yields

$$M_{H_2}\frac{i^-}{2F} = +\rho D_{H_2,\mathrm{eff}}\frac{\omega_{H_2}-\omega_{H_2,w}}{d^-} \tag{33}$$

and

$$r_{H_2} = -a^-\rho D_{H_2,\mathrm{eff}}\frac{\omega_{H_2}-\omega_{H_2,w}}{d^-}. \tag{34}$$

For determining the proton conductivity σ_f in the membrane, the correlation by Springer et al. [1] is used,

$$\sigma_f = 100\exp\left[1286\left(\frac{1}{303}-\frac{1}{T}\right)\right](0.005139\lambda - 0.00326) \tag{35}$$

where the water content in the membrane

$$\lambda = \begin{cases} 0.043+17.81\zeta - 39.85\zeta^2 + 36.0\zeta^3 & \text{for } 0<\zeta\leq 1 \\ 14+1.4(\zeta-1) & \text{for } 1<\zeta\leq 3 \end{cases} \tag{36}$$

is correlated in terms of the water activity

$$\zeta = \frac{x_{H_2O}p}{p_{\mathrm{sat}}}. \tag{37}$$

The saturation pressure of water vapor is approximated with [1]

$$\begin{aligned} \log_{10}(p_{\mathrm{sat}}10^{-5}) = &-2.1794+0.02953(T-273.15) \\ &-9.1837\times 10^{-5}(T-273.15)^2 \\ &+1.4454\times 10^{-7}(T-273.15)^3 \end{aligned} \tag{38}$$

3 Numerical Solution

3.1 Models and Boundary Conditions. The performance of fuel cells with porous flow distributors is numerically investigated and compared with fuel cells having either parallel or serpentine flow-fields. For the cell with the parallel flow-field, one single half-channel assembly is modeled in three dimensions, as shown in Fig. 1(a), using symmetry boundary conditions at $\xi_1 = \xi_{1,\min}$ and $\xi_1 = \xi_{1,\max}$. Dirichlet boundary conditions are used for temperature on the top, bottom, and front sides with a constant value corresponding to the temperature of the inlet gas streams. These settings represent the case of a perfectly cooled flow-field. Newman boundary conditions with zero flux are used for Φ_f on $\partial\Omega$. At the top and bottom boundaries of the channel, Dirichlet boundary conditions with constant values are set for Φ_s, where zero-flux conditions are applied to the inlet and outlet front. The difference between the top and bottom boundary condition value of Φ_s is obviously the sum of all the potential losses inside the cell. Constant mass flow rates and fixed pressure boundary conditions are applied to inlets and outlets, respectively. The serpentine flow-field is of quadratic shape; its width is equal to the length of the parallel flow-field and therefore includes exactly seven connected channels. For the porous flow distributors, no variations in the direction of ξ_1 are assumed, cf. Fig. 1(b). Therefore, it is modeled in two dimensions.

3.2 Solution Method. The coupled set of partial differential equations is numerically solved with a finite-volume central scheme on a structured grid using the licensed solver CFD-ACE distributed by CFDRC of Huntsville, USA. Coupling of the set of partial differential equations including the strongly non-linear Butler-Volmer equations requires advanced source term linearization techniques [37]. Algebraic multigrid solver is used in conjunction with a convergence criterion of 1×10^{-10}. A first order upwind scheme is chosen to obtain a preliminary numerical solution for the model with the serpentine flow-field consisting of 647,360 finite volumes, which is further used as an initial condition for the application of the central scheme.

The computational grid of the two-dimensional model of the porous gas distributor consists of 2700 cells. By increasing the cell number to 5400 (10,800), the average current density increases by 5.9×10^{-4}% (7.6×10^{-4}%). When comparing species contours, the three grids yield practically indistinguishable results. For the three-dimensional model of the parallel flow-field, a computational grid consisting of 43,200 cells is used. By increasing the cell number to 86,400 (172,800), the average current density increases by 0.015% (0.022%). Again, comparison of species contours yields practically indistinguishable results. The grid resolution of the serpentine flow-field (647,360 cells) is consistent with the one of the parallel flow-field.

4 Validation

The mathematical model is validated on a wide range of operating conditions using data from experiments conducted at Los Alamos National Laboratory, cf. Ticianelli et al. [22]. In their work, the effect of temperature and of pressure on the cell potential-current density behavior was investigated as part of a comprehensive analysis of electrode kinetics of single cells. Among other things, cell potential-current density measurements were recorded at 323 K and 1/1 Atm (inlet pressure at anode/inlet pressure at cathode), 323 K and 3/5 Atm, 353 K and 3/5 Atm, for Prototech electrodes (20 wt% Pt/C in supported electrocatalyst plus 50 nm sputtered film of Pt, 0.45 mg/cm^2 of Pt), as shown in Fig. 2. The numerical results in Fig. 2 were obtained from the three-dimensional parallel flow-field. Corresponding geometry data are given in Table 1, material properties and operating con-

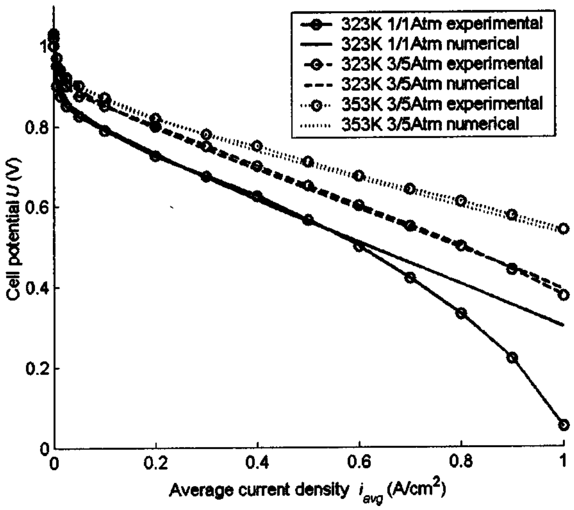

Fig. 2 Comparison of numerical results with experimental results from Ticianelli et al. [22]. Polarization curves for three different operating conditions: (1) 323 K, 1/1 Atm; (2) 323 K, 3/5 Atm; and (3) 353 K, 3/5 Atm

Table 1 Geometry data for the half-channel assembly representing the parallel flow-field

Current collector thickness (mm)*	0.762
Gas channel thickness (mm) [11]	0.762
Gas diffuser thickness (mm) [11]	0.254
Catalyst layer thickness (mm) [11]	0.0287
Membrane thickness (mm) [11]	0.230
Gas channel length L (mm)*	10.6681
Gas channel width (half-width) (mm)*	0.762 (0.381)
Current collector width (half-width) (mm)*	0.762 (0.381)

*assumed

Table 2 Material properties for the membrane-electrode assembly and the current collector

Porosity of the diffusion layers, ε [11,3]	0.4
Porosity of the catalyst layers, ε [11,3]	0.4
Porosity of the membrane, ε [11,3]	0.28
Permeability of the diffusion layers, κ (m^2) [11]	1.76×10^{-11}
Permeability of the catalyst layers, κ (m^2) [11]	1.76×10^{-11}
Permeability of the membrane, κ (m^2) [11,3]	1.8×10^{-18}
Tortuosity of the diffusion and catalyst layers, τ [11,3]	1.5
Solid thermal conductivity	
of the diffusion layers, k_s ($W\,m^{-1}\,K^{-1}$) [44]	169
of the catalyst layers, k_s ($W\,m^{-1}\,K^{-1}$) [44]	169
of the current collector, k_s ($W\,m^{-1}\,K^{-1}$) [44]	169
Solid electrical conductivity	
of the diffusion layers, σ_s ($\Omega^{-1}\,m^{-1}$) [3,22]	53
of the catalyst layers, σ_s ($\Omega^{-1}\,m^{-1}$) [3,22]	53
of the current collector, σ_s ($\Omega^{-1}\,m^{-1}$) [44]	1.25×10^5

ditions are listed in Table 2 and Table 3, respectively. Material properties of graphite are used for the current collector plates. The reference current densities and Tafel constants listed in Table 3 were obtained by calibration at low current densities, because they are not known from the experiment. Since the performance of the cell is rate-limited at low current densities, this is a valid procedure. The open-circuit potentials reported by Ticianelli et al. [22] were used to determine the cell potentials.

The comparison shows good agreement between numerical and experimental results, especially at 323 K and 3/5 Atm, 353 K and 3/5 Atm. For the case with 323 K and 1/1 Atm, cell performance is over-predicted at current densities higher than 0.6 A/cm^2. This bound corresponds to the maximum power output of the cell. The discrepancy is assumed to appear due to the fact that the current mathematical model does not take into account effects caused by water vapor condensation which are highest at the high current densities. The presence of liquid water blocking the pores of the gas diffusion and catalyst layers is expected to add additional mass transport limitations [38–40]. At the higher temperature and pressure levels, these limitations become significant at current densities higher than 1 A/cm^2 [22] due to enhanced species diffusivities and electrochemical reaction rates.

5 Numerical Results and Discussion

In cells with ribbed flow distributors, the mass transfer rate to and from the reacting zones under the current collector shoulders is reduced compared to the mass transfer rate to zones under the flow channels, due to longer diffusion paths. This phenomenon is most prominent on the cathode side of fuel cells operated with air and hydrogen due to the low diffusivity of oxygen in nitrogen. For saturated inlet streams, the diffusivity of hydrogen in water vapor is much higher and therefore the issue of mass transfer limitations on the anode side is of minor importance. The limitations on the cathode side manifest themselves in reduced oxygen mole fractions, increased mole fractions of water vapor and increased overpotential losses (activation and concentration) under the current collector shoulders, as shown clearly in Figs. 3(b) and 4(b). Obviously, removal of water vapor from these regions is also limited. Therefore, a higher saturation level is observed under the shoulders which is expected to lead to further mass transfer limitations due to pores clogged with liquid water which cannot be captured since the current model does not account for condensation. Therefore, the performance assessment of the porous flow distributors with respect to the ribbed flow distributors is expected to be a conservative one, especially at the higher current densities where the saturation level is highest. It is shown in Figs. 3(a) and 4(a) that the mole fraction of oxygen in the reacting zone under the shoulders can be markedly smaller (approximately down to half) compared to the concentration under the flow channels. In addition, a significant reduction in the oxygen concentration in the downstream region of the serpentine flow distributor of Fig. 4(a) is observed.

Replacing the traditional ribbed flow distributors with distributors made out of a porous medium eliminates the above mentioned drawback of mass transfer nonuniformity, since the diffusion layers are continuously covered with the bulk flow through the permeable porous matrix. Therefore, the oxygen mole fraction and all other quantities vary in the flow direction ξ_3 only, cf. Fig. 5, and not in the cross-direction ξ_1.

There are three key properties of the porous medium of the flow distributors which need consideration in this context: porosity, permeability, and effective electrical conductivity. High permeability and porosity of the foam are required to avoid excessive pressure drop in the flow-field. However, the higher the porosity, the lower the effective electrical conductivity, which results in increased Ohmic losses across the foam. Further, mass transfer through the porous matrix is limited at lower porosities due to reduced effective diffusivities, as a consequence of the Bruggeman correction [see Eq. (15)]. Both, pressure drop and Ohmic losses need to be minimized to maximize overall fuel cell efficiency.

In order to explore the influence of each quantity parametric studies have been performed on the porous flow distributors. It is seen from Fig. 6 that the porous gas distributors can generate up to 13% higher average current densities than the parallel flow-field. This improvement is achieved for porosities higher than 0.7. If the effective electrical conductivity of the foam is about two thousandths of the conductivity of the solid material, then the same average current density is obtained from the porous gas distributors as from the parallel flow-field, for foam porosities higher than 0.7. Mass transfer limitations due to reduction of foam porosity can be neglected at porosities higher than 0.7 but become important at lower values. If the electrical conductivity of the

Table 3 Operating conditions and kinetic constants

	Anode	Cathode
Relative humidity of inlet streams [11,3]	1	1
N_2/O_2 mole fraction of dry air		0.79/0.21
O_2 stoichiometric flow ratio [11]		2.8 A/cm^2 equivalent
H_2 stoichiometric flow ratio [11]	2.6 A/cm^2 equivalent	
Anodic transfer coefficient α_a*	1/2	3/2
Cathodic transfer coefficient α_c*	1/2	3/2
Concentration exponent γ_{H_2} [18]	1/2	
Concentration exponent γ_{O_2} [18]		1
Concentration exponent γ_{H_2O} [18]		0
Reference current density $a^- i_0^{\mathrm{ref}-}/(c_{H_2,w}^{\mathrm{ref}})^{\gamma_{H_2}}$*		2.92×10^7 $(A/m^3)/(mol/m^3)^{1/2}$
Reference current density $a^+ i_0^{\mathrm{ref}+}/[(c_{O_2,w}^{\mathrm{ref}})^{\gamma_{O_2}}(c_{H_2O,w}^{\mathrm{ref}})^{\gamma_{H_2O}}]$*		1.05×10^3 $(A/m^3)/(mol/m^3)$

*calibration parameter

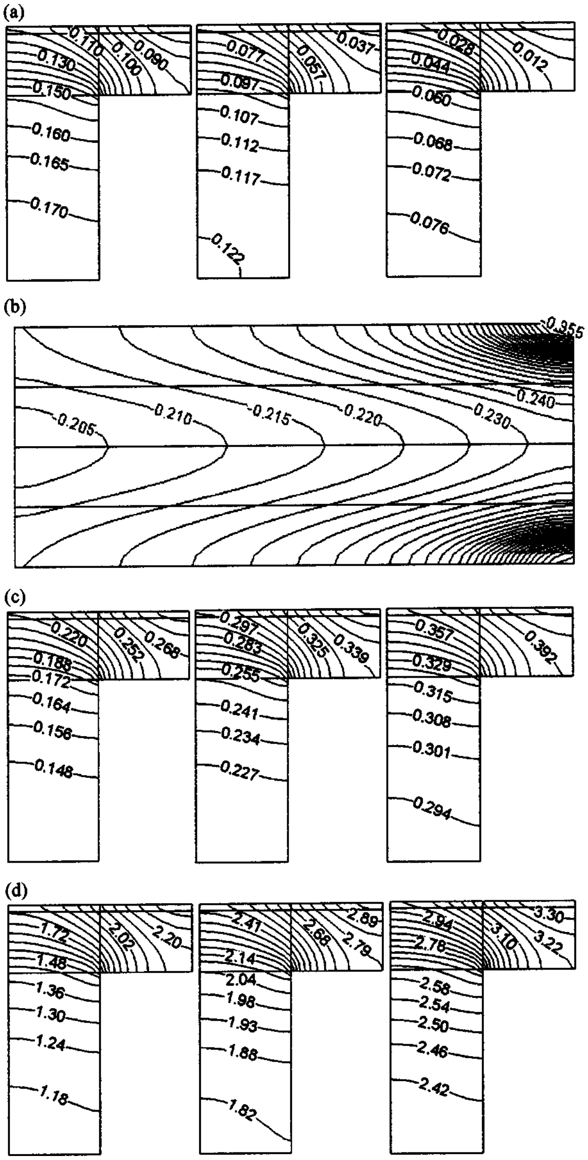

Fig. 3 Parallel flow-field at 323 K, 1/1 Atm and $U=0.3$ V. (a) Cross-sectional distribution of the oxygen mole fraction x_{O_2} in three different planes, i.e., $\xi_3=0.1\,L$ (left side), $\xi_3=0.5\,L$ (middle) and $\xi_3=0.9\,L$ (right side). The subdomains $\Omega_{l,1}$, $\Omega_{l,3}$, and $\Omega_{l,5}$ are shown from the bottom to the top. (b) Distribution of the overpotential $\eta=\Phi_s-\Phi_f$ in the middle of the cathode catalyst layer ($\xi_2=-129.35\,\mu$m). The picture is shrunk in the flow direction ξ_3. (c) Cross-sectional distribution of the water vapor mole fraction x_{H_2O} in the three planes, i.e., $\xi_3=0.1\,L$ (left side), $\xi_3=0.5\,L$ (middle) and $\xi_3=0.9\,L$ (right side). (d) Cross-sectional distribution of the relative humidity $x_{H_2O}p/p_{\text{sat}}$ in the three planes, i.e., $\xi_3=0.1\,L$ (left side), $\xi_3=0.5\,L$ (middle), and $\xi_3=0.9\,L$ (right side)

foam is 10^3 times smaller than that of the solid matrix, Ohmic losses are dominant compared to the losses caused by these mass transfer limitations, as shown in Fig. 6.

Reticulated vitreous carbon (RVC) [41] is one example of a potential material to be used as a porous fluid distributor, due to its high electrical conductivity and low resistance to flow. It is available down to a recommended thickness of 1.5 mm with a maximum of 100 pores per inch (ppi). The performance of reticulated vitreous carbon ($\varepsilon=0.9$, 100 ppi, $\kappa=1.76\times10^{-9}\,\text{m}^2$, $\sigma_s=1{,}250\,\Omega^{-1}\,\text{m}^{-1}$) is marked by a cross-marker in Fig. 6.

Polarization curves for cells with the porous flow distributors are given in Fig. 7 for different effective electrical conductivities of the foam and constant foam porosity and permeability. For performance assessment of the porous flow distributors, the numerically obtained polarization curve of the parallel flow-field is given in the same graph in conjunction with the corresponding experimentally obtained curve [22]. These two curves are the same as the lowest curves in Fig. 2. With increasing electrical conductivity of the foam, the polarization curve is shifted upwards and therefore higher cell power output is achieved. If the effective electric foam conductivity is higher than about 0.2% of the conductivity of the solid material, then the cell power output from the porous gas distributors is higher than the one from the parallel flow-field. At lower conductivities, Ohmic losses across the foam increase such that the parallel flow-field becomes more advantageous in terms of cell power output. The performance of reticulated vitreous carbon is also shown as a specific example.

Phase change and transport of liquid water driven by pressure, capillary, and gravity forces are not considered in the present model. Consequently, transport of liquid water through the membrane by means of electro-osmotic drag is also not accounted for. The effect of electro-osmotic drag in the membrane is expected to cause a higher water saturation level in the cathode catalyst layer which may lead to further mass transport limitations for gas species to the reaction sites due to enhanced blocking of pores by liquid water [39]. Mazumder and Cole recently showed with their three-dimensional mathematical model accounting for transport and formation of liquid water [37,39] that in the investigated cases the effect of electro-osmotic drag on cell performance is not significant.

Pressure drops of 1.56 Pa (0.315 Pa), 74.2 Pa (13.4 Pa), and 9.40 Pa (1.92 Pa) are obtained for the cathode (anode) side of the parallel, serpentine, and macro-porous flow-field ($\varepsilon=0.9$, $\kappa=1.76\times10^{-9}\,\text{m}^2$, $\sigma=1{,}250\ \Omega^{-1}\,\text{m}^{-1}$, $U=0.5\,\text{V}$), respectively. Hence, pressure drop in the porous gas distributor is roughly an order of magnitude higher than in the parallel flow-field but an order of magnitude lower than in the serpentine flow-field. Experimental and numerical studies on flow characteristics in metal foams [42,43] also report that the pressure drop in flows through high porosity porous foams is not prohibitingly high.

6 Conclusions

A thorough mathematical model describing the transport phenomena in a PEFC has been presented and numerically solved. A central point of the study was to investigate the performance of porous flow distributors as a possible replacement for the currently used ribbed flow distributors of various shapes. As a consequence, the solution of both porous and ribbed flow distributors was accomplished, which allowed for the necessary comparisons. Numerical results were validated against experimental data from Ticianelli et al. [22]. Mass transfer limitations in cells with ribbed flow-fields such as parallel and serpentine flow-fields were investigated. It has been shown numerically that porous gas distributors are advantageous in terms of mass transfer and therefore exhibit substantially higher cell performance. Reticulated vitreous carbon has been suggested as one example of a potential porous material to be used in this context. The replacement of ribbed flow-fields with macro-porous gas distributors would also allow for a reduction in stack weight. Finally, the manufacturing cost could be substantially reduced since the expensive process of machining the ribbed flow-field would no longer be necessary.

Acknowledgment

This work has been supported by the Swiss Federal Office of Energy (BFE) under contract No. 87,100 (program manager Dr. A. Hintermann). Helpful discussions with Dr. S. Haferl during the

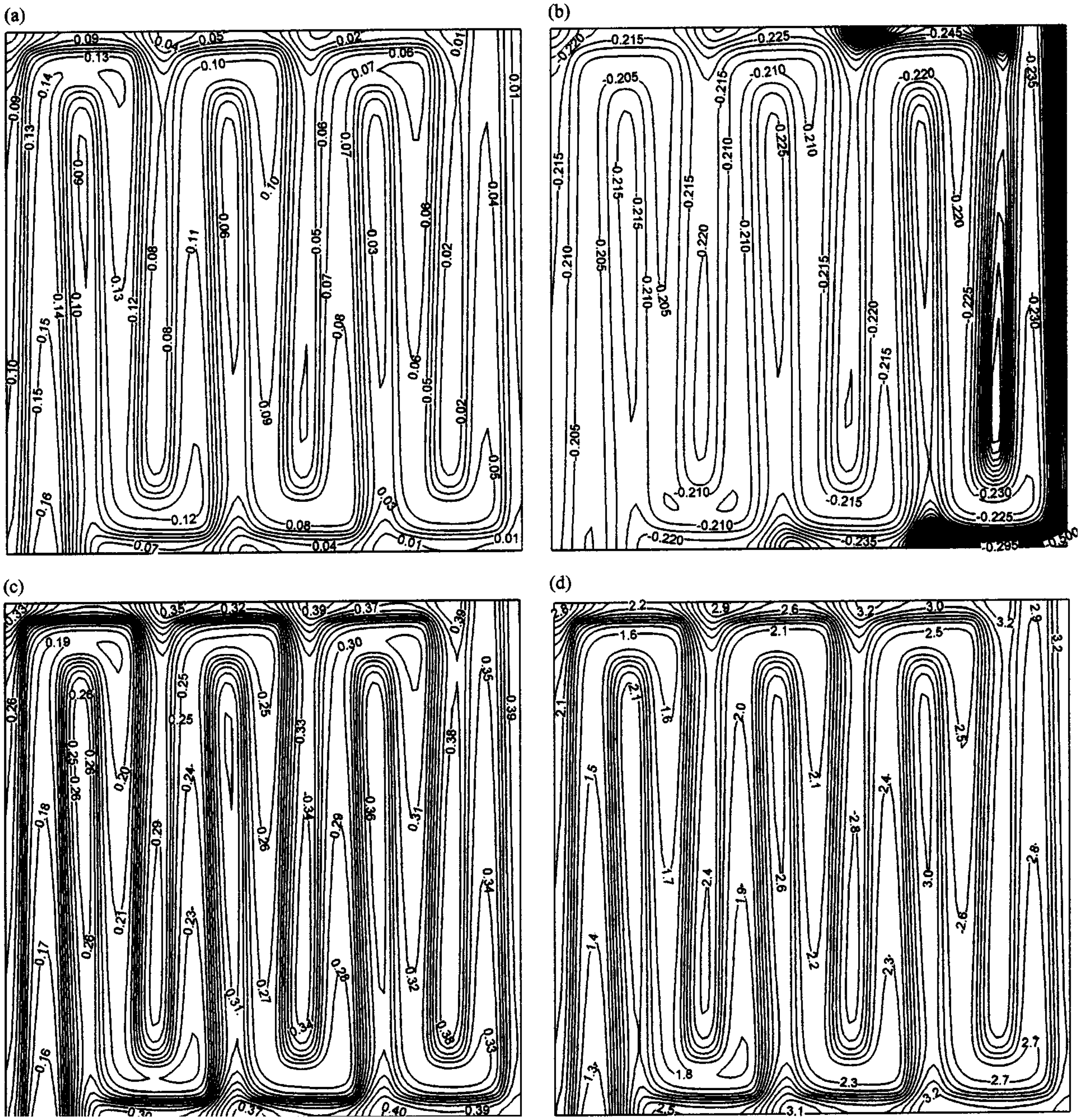

Fig. 4 Serpentine flow-field at 323 K, 1/1 Atm, and $U=0.3$ V. (a) Distribution of the oxygen mole fraction x_{O_2} in the middle of the cathode diffusion layer ($\xi_2=-270.7\ \mu$m). (b) Distribution of the overpotential $\eta=\Phi_s-\Phi_f$ in the middle of the cathode catalyst layer ($\xi_2=-129.35\ \mu$m). (c) Distribution of the water vapor mole fraction x_{H_2O} in the middle of the cathode diffusion layer ($\xi_2=-270.7\ \mu$m). (d) Distribution of the relative humidity $x_{H_2O}p/p_{\mathrm{sat}}$ in the middle of the cathode diffusion layer ($\xi_2=-270.7\ \mu$m)

early stages of the work are gratefully acknowledged. CFD Research Corporation of Huntsville, USA, is also acknowledged for allowing the use of their software.

Nomenclature

Latin Letters

a = effective surface to volume ratio ($\mathrm{m^2\,m^{-3}}$)
c = molar concentration ($\mathrm{mol\,m^{-3}}$)
D_i = binary diffusivity of i in a multicomponent mixture ($\mathrm{m^2\,s^{-1}}$)
D_{ij} = diffusivity of the pair $i-j$ in a binary mixture ($\mathrm{m^2\,s^{-1}}$)
d = average pore diameter (m)
F = Faraday constant, 96485.309 ($\mathrm{C\,mol^{-1}}$)
h = specific enthalpy of gas mixture ($\mathrm{J\,kg^{-1}}$)
$\underline{\underline{I}}$ = identity matrix ($-$)
i = electric current density ($\mathrm{A\,m^{-2}}$)
i_0 = exchange current density ($\mathrm{A\,m^{-2}}$)
i_0^{ref} = reference current density ($\mathrm{A\,m^{-2}}$)
$\underline{i}$ = electric current density ($\mathrm{A\,m^{-2}}$)
J = transfer current density ($\mathrm{A\,m^{-3}}$)
$\underline{j}_i$ = diffusive flux of species i ($\mathrm{kg\,m^{-2}\,s^{-1}}$)
k = thermal conductivity ($\mathrm{W\,m^{-1}\,K^{-1}}$)
L = channel length (m)
M = molecular weight ($\mathrm{kg\,mol^{-1}}$)
N = total number of species ($-$)

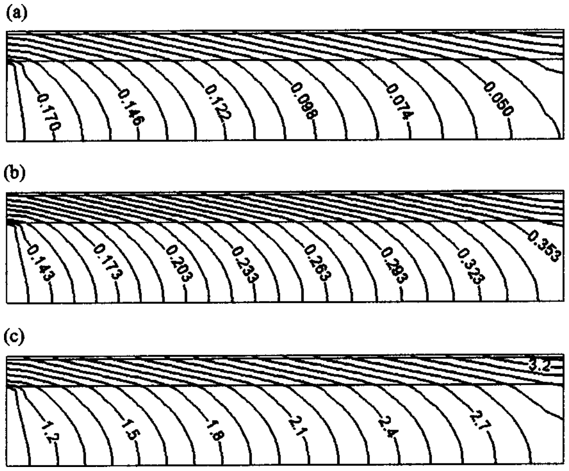

Fig. 5 Porous gas distributor at 323 K, 1/1 Atm, $U=0.3\,\mathrm{V}$, $\varepsilon=0.9$, $\kappa=1.76\times10^{-9}\,\mathrm{m}^2$, and $\sigma=1{,}250\ \Omega^{-1}\,\mathrm{m}^{-1}$. (a) Distribution of the oxygen mole fraction x_{O_2} throughout the cell ($\xi_1=\mathrm{const.}$). The picture is shrunk in the flow direction ξ_3. (b) Distribution of the water vapor mole fraction x_{H_2O} in the same plane. (c) Distribution of the relative humidity $x_{H_2O}p/p_{\mathrm{sat}}$ in the same plane

p = pressure (Pa)
$\underline{q}$ = heat flux ($\mathrm{W\,m^{-2}}$)
r_i = reaction source term of species i ($\mathrm{kg\,m^{-3}\,s^{-1}}$)
R = universal gas constant, 8.314510 ($\mathrm{J\,K^{-1}\,mol^{-1}}$)
T = temperature (K)
U = cell potential (V)
$\underline{v}$ = mixture velocity ($\mathrm{m\,s^{-1}}$)
x_i = mole fraction of species i (−)

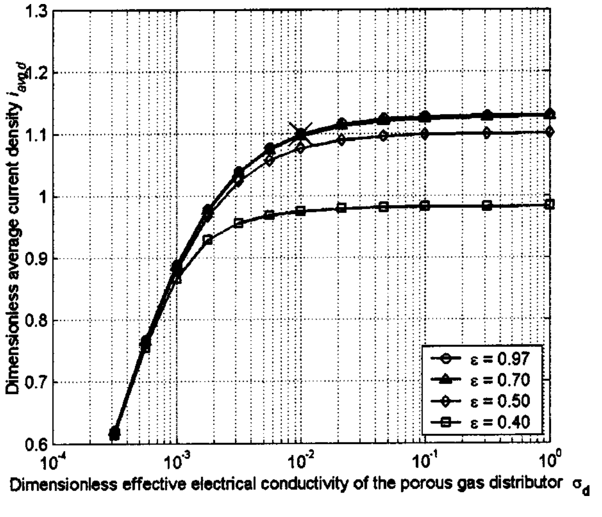

Fig. 6 Average current density of a fuel cell with a porous gas distributor for different effective electrical conductivities and porosities ε of the foam at 323 K, 1/1 Atm, $U=0.5\,\mathrm{V}$, and $\kappa=1.76\times10^{-9}\,\mathrm{m}^2$. The effective electrical foam conductivity σ_s is nondimensionalized with the electrical conductivity of the solid material ($125{,}000\ \Omega^{-1}\,\mathrm{m}^{-1}$), i.e., $\sigma_d=\sigma_s/(125{,}000\,\Omega^{-1}\,\mathrm{m}^{-1})$. The average current density i_{avg} of the cell with the porous gas distributor is nondimensionalized with the average current density obtained from the parallel flow-field operated at identical conditions, i.e., $i_{\mathrm{avg},d}=i_{\mathrm{avg}}/(0.62\,\mathrm{A/cm}^2)$. The position of a cell in which reticulated vitreous carbon ($\varepsilon=0.9$, 100 ppi) is used for the porous gas distributors is indicated by the cross-marker

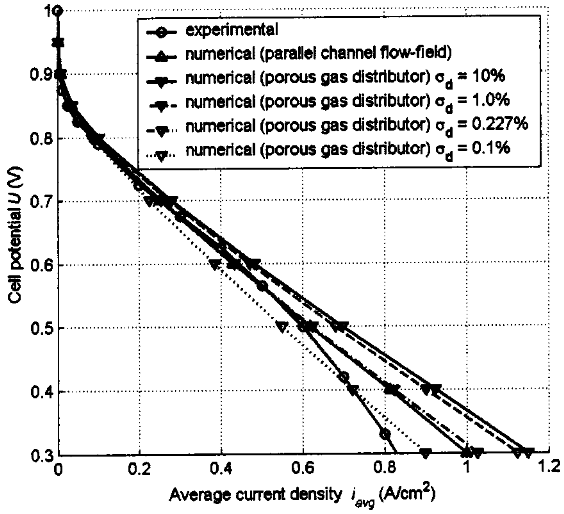

Fig. 7 Polarization curves. Comparison of the parallel channel flow-field with the porous gas distributors for different effective electrical conductivities σ_s of the foam at 323 K, 1/1 Atm, $\varepsilon=0.9$, $\kappa=1.76\times10^{-9}\,\mathrm{m}^2$ with $\sigma_d=\sigma_s/(125{,}000\,\Omega^{-1}\,\mathrm{m}^{-1})$. The position of reticulated vitreous carbon ($\varepsilon=0.9$, 100 ppi) is indicated as a specific example

Greek Letters

α_a = anodic transfer coefficient (−)
α_c = cathodic transfer coefficient (−)
γ = concentration exponent (−)
ε = porosity (−)
ζ = water activity (−)
η = overpotential (V)
κ = permeability (m^2)
λ = water content in the membrane
μ = dynamic viscosity ($\mathrm{Pa\cdot s}$)
ρ = mixture density ($\mathrm{kg\,m^{-3}}$)
ρ_i = mass concentration of species i ($\mathrm{kg\,m^{-3}}$)
σ = electrical conductivity ($\Omega^{-1}\,\mathrm{m}^{-1}$)
τ = tortuosity (−)
$\underline{\underline{\tau}}$ = stress tensor ($\mathrm{N/m^2}$)
Φ = electric potential (V)
ω_i = mass fraction of species i (−)
ϖ = collision diameter (Angstroem)
Ω_D = collision integral (−)
Ω_μ = collision integral (−)

Subscripts

avg = averaged
d = dimensionless
eff = effective
f = fluid
i = species i
j = species j
max = maximum
min = minimum
s = solid
sat = saturation
w = fluid-solid interface, wall

Superscripts

$+$ = cathode
$-$ = anode
ref = reference

References

[1] Springer, T. E., Zawodzinski, T. A., and Gottesfeld, S., 1991, ''Polymer Electrolyte Fuel Cell Model,'' J. Electrochem. Soc., **138**(8), pp. 2334–2342.

[2] Bernardi, D. M., and Verbrugge, M. W., 1991, ''Mathematical Model of a Gas-Diffusion Electrode Bonded to a Polymer Electrolyte,'' AIChE J., **37**(8), pp. 1151–1163.

[3] Bernardi, D. M., and Verbrugge, M. W., 1992, ''A Mathematical Model of the Solid-Polymer-Electrolyte Fuel Cell,'' J. Electrochem. Soc., **139**(9), pp. 2477–2491.

[4] Springer, T. E., Wilson, M. S., and Gottesfeld, S., 1993, ''Modeling and Experimental Diagnostics in Polymer Electrolyte Fuel Cells,'' J. Electrochem. Soc., **140**(12), pp. 3513–3526.

[5] Fuller, T. F., and Newman, J., 1993, ''Water and Thermal Management in Solid-Polymer-Electrolyte Fuel Cells,'' J. Electrochem. Soc., **140**(5), pp. 1218–1225.

[6] Nguyen, T. V., and White, R. E., 1993, ''A Water and Heat Management Model for Proton-Exchange-Membrane Fuel Cells,'' J. Electrochem. Soc., **140**(8), pp. 2178–2186.

[7] Yi, J. S., and Nguyen, T. V., 1998, ''An Along-the-Channel Model for Proton Exchange Membrane Fuel Cells,'' J. Electrochem. Soc., **145**(4), pp. 1149–1159.

[8] Yi, J. S., and Nguyen, T. V., 1999, ''Multicomponent Transport in Porous Electrodes of Proton Exchange Membrane Fuel Cells Using the Interdigitated Gas Distributors,'' J. Electrochem. Soc., **146**(1), pp. 38–45.

[9] Gurau, V., Liu, H., and Kakac, S., 1998, ''Two-Dimensional Model for Proton Exchange Membrane Fuel Cells,'' AIChE J., **44**(11), pp. 2410–2422.

[10] Singh, D., Lu, D. M., and Djilali, N., 1999, ''A Two-Dimensional Analysis of Mass Transport in Proton Exchange Membrane Fuel Cells,'' Int. J. Eng. Sci., **37**(4), pp. 431–452.

[11] Um, S., Wang, C. Y., and Chen, K. S., 2000, ''Computational Fluid Dynamics Modeling of Proton Exchange Membrane Fuel Cells,'' J. Electrochem. Soc., **147**(12), pp. 4485–4493.

[12] He, W., Yi, J. S., and Nguyen, T. V., 2000, ''Two-Phase Flow Model of the Cathode of PEM Fuel Cells Using Interdigitated Flow Fields,'' AIChE J., **46**(10), pp. 2053–2064.

[13] Natarajan, D., and Nguyen, T. V., 2001, ''A Two-Dimensional, Two-Phase, Multicomponent, Transient Model for the Cathode of a Proton Exchange Membrane Fuel Cell Using Conventional Gas Distributors,'' J. Electrochem. Soc., **148**(12), pp. A1324–A1335.

[14] Zhou, T., and Liu, H., 2000, ''3-D Model of Proton Exchange Membrane Fuel Cells,'' *Proceedings of the ASME Heat Transfer Division*, **366-1**, pp. 43–49.

[15] Shimpalee, S., and Dutta, S., 2000, ''Numerical Prediction of Temperature Distribution in PEM Fuel Cells,'' Numer. Heat Transfer, Part A, **38**(2), pp. 111–128.

[16] Dutta, S., Shimpalee, S., and Van Zee, J. W., 2000, ''Three-Dimensional Numerical Simulation of Straight Channel PEM Fuel Cells,'' J. Appl. Electrochem., **30**, pp. 135–146.

[17] Dutta, S., Shimpalee, S., and Van Zee, J. W., 2001, ''Numerical Prediction of Mass-Exchange Between Cathode and Anode Channels in a PEM Fuel Cell,'' Int. J. Heat Mass Transfer, **44**(11), pp. 2029–2042.

[18] Berning, T., Lu, D. M., and Djilali, N., 2002, ''Three-Dimensional Computational Analysis of Transport Phenomena in a PEM Fuel Cell,'' J. Power Sources, **106**(1–2), pp. 284–294.

[19] Um, S., and Wang, C. Y., 2000, ''Three-Dimensional Analysis of Transport and Reaction in Proton Exchange Membrane Fuel Cells,'' *Proceedings of the ASME Heat Transfer Division—2000*, HTD-Vol. 366-1, pp. 19–25.

[20] Nield, D. A., and Bejan, A., 1992, *Convection in Porous Media*, Springer, New York.

[21] Bejan, A., 2000, *Shape and Structure, From Engineering to Nature*, Cambridge University Press, Cambridge.

[22] Ticianelli, E. A., Derouin, C. R., and Srinivasan, S., 1988, ''Localization of Platinum in Low Catalyst Loading Electrodes to Attain High Power Densities in SPE Fuel Cells,'' J. Electroanal. Chem., **251**(2), pp. 275–295.

[23] Dagan, G., 1989, *Flow and Transport in Porous Formations*, Springer, Berlin.

[24] Bear, J., and Bachmat, Y., 1990, *Introduction to Modeling of Transport Phenomena in Porous Media*, Kluwer Academic Publishers, Dordrecht.

[25] Kaviany, M., 1995, *Principles of Heat Transfer in Porous Media*, second ed., Springer, New York.

[26] Whitaker, S., 1999, *The Method of Volume Averaging*, Kluwer Academic Publishers, Dordrecht.

[27] Stull, D. R., and Prophet, H., 1971, *JANAF Thermochemical Tables*, second ed., NSRDS-NBS 37, National Bureau of Standards, Washington.

[28] Curtiss, C. F., and Hirschfelder, J. O., 1949, ''Transport Properties of Multicomponent Gas Mixtures,'' J. Chem. Phys., **17**(6), pp. 550–555.

[29] Wilke, C. R., 1950, ''A Viscosity Equation for Gas Mixtures,'' J. Chem. Phys., **18**(4), pp. 517–519.

[30] Bird, R. B., Stewart, W. E., and Lightfoot, E. N., 1960, *Transport Phenomena*, Wiley, New York.

[31] Hashin, Z., and Shtrikman, S., 1962, ''A Variational Approach to the Theory of the Effective Magnetic Permeability of Multiphase Materials,'' J. Appl. Phys., **33**(10), pp. 3125–3131.

[32] Mason, E. A., and Saxena, S. C., 1958, ''Approximate Formula for the Thermal Conductivity of Gas Mixtures,'' Phys. Fluids, **1**(5), pp. 361–369.

[33] Chapman, S., and Cowling, T. G., 1990, *The Mathematical Theory of Non-Uniform Gases*, third ed., Cambridge University Press, Cambridge.

[34] Newman, J. S., 1991, *Electrochemical Systems*, second ed., Prentice Hall, New Jersey.

[35] Atkins, P., and de Paula, J., 2002, *Atkins' Physical Chemistry*, seventh ed., Oxford University Press, New York.

[36] Mazumder, S., and Lowry, S. A., 2001, ''The Treatment of Reacting Surfaces for Finite-Volume Schemes on Unstructured Meshes,'' J. Chem. Phys., **173**(2), pp. 512–526.

[37] Mazumder, S., and Cole, J. V., 2003, ''Rigorous 3-D Mathematical Modeling of PEM Fuel Cells, I. Model Predictions without Liquid Water Transport,'' J. Electrochem. Soc., **150**(11), pp. A1503–1509.

[38] Wang, C. Y., and Cheng, P., 1997, ''Multiphase Flow and Heat Transfer in Porous Media,'' Adv. Heat Transfer, **30**, pp. 93–196.

[39] Mazumder, S., and Cole, J. V., 2003, ''Rigorous 3-D Mathematical Modeling of PEM Fuel Cells, II. Model Predictions With Liquid Water Transport,'' J. Electrochem. Soc., **150**(11), pp. A1510–1517.

[40] Berning, T., and Djilali, N., 2003, ''A 3D, Multiphase, Multicomponent Model of the Cathode and Anode of a PEM Fuel Cell,'' J. Electrochem. Soc., **150**(12), pp. A1589–1598.

[41] 2002, Duocel RVC Physical Characteristics Data Sheet, ERG Materials and Aerospace, Oakland, CA.

[42] Boomsma, K., and Poulikakos, D., 2002, ''The Effects of Compression and Pore Size Variations on the Liquid Flow Characteristics in Metal Foams,'' J. Fluids Eng., **124**(1), pp. 263–272.

[43] Boomsma, K., and Poulikakos, D., 2001, ''On the Effective Thermal Conductivity of a Three-Dimensionally Structured Fluid-Saturated Metal Foam,'' Int. J. Heat Mass Transfer, **44**(4), pp. 827–836.

[44] Kuchling, H., 1991, *Taschenbuch der Physik*, Fachbuchverlag Leipzig, Leipzig.

Heat Transfer to Water-Oxygen Mixtures at Supercritical Pressure

S. N. Rogak

D. Faraji

Department of Mechanical Engineering,
University of British Columbia,
2324 Main Mall, Vancouver, BC,
Canada, V6T 1Z4

The constant pressure heat capacity and forced convection heat transfer coefficient of water/oxygen mixtures were measured in a horizontal, smooth, electrically-heated tube. For the supercritical pressure (25 MPa) considered, flow rates (0.76–2.04 kg/min), heat fluxes (21–290 kW/m^2) and temperatures (330–430°C), the flow in the 6.2 mm ID tube was fully turbulent. The fluid was distilled water and up to 9 wt % oxygen. The water/oxygen mixture and the above experimental conditions are relevant to supercritical water oxidation systems (SCWO). At subcritical temperatures the oxygen/water mixture is almost immiscible and the flow is two-phase. Just below the critical temperature, the fluid becomes single-phase. By measuring bulk and surface temperatures, for a given flow rate, heat flux and oxygen content, both the heat capacity and heat transfer coefficient for the mixture were measured. The water-oxygen system is a highly non-ideal mixture, and small amounts of oxygen significantly reduce the temperature at which maximum heat transfer occurs. Despite the multi-phase nature of the flow at temperatures well below the critical temperature (i.e., $<$360°C), the presence of small quantity of oxygen has little effect on the heat transfer. At supercritical temperatures where the flow is single-phase and gas-like, the presence of oxygen has little effect on the heat transfer coefficient. However, at near-critical temperatures, the addition of small amounts of oxygen results in a dramatic change in the heat transfer. Firstly, the magnitude and temperature for the peak heat transfer decrease, consistent with changes in heat capacity. Secondly, heat transfer is deteriorated at moderate heat flux, mostly but not exclusively on the top surface of the tube. [DOI: 10.1115/1.1731329]

Keywords: *Convection, Experimental, Heat Transfer, Multi-Component, Multi-Phase*

Introduction

Supercritical fluids have found increasing application in industrial processes. In recent years, supercritical water power systems have received renewed interest with the need for greater power plant efficiency [1]. Now, a wide range of chemical processes such as particle formation, extractions and foam manufacture employ supercritical fluids such as CO_2 and hydrocarbons. In chemical waste remediation, toxic organics are mixed with oxygen in supercritical water (Supercritical Water Oxidation, SCWO), resulting in innocuous ‘‘combustion’’ products [2–5]. In most of these applications, heat transfer to the process fluid occurs at supercritical pressure and sub- and supercritical temperatures.

The problem of forced convection heat transfer to a pure fluid near the critical point received much attention from the 1950’s [6,7] through the 1970’s, as reviewed by Hall [8], Jackson and Hall [9] and Polyakov [10]. The fundamentals are well understood, and may be applied to supercritical CO_2, water or other fluids, however numerical predictions of heat transfer near the critical point remain unsatisfactory. Discrepancies in predictions of heat transfer coefficient from different correlations are often a factor of 2 or more for near-critical water [11]. This is partly because the measurements lack accuracy, and also because the measurements were correlated with water properties that have changed over the years. For example, the conductivity of water at 23 MPa and 378°C differs by about 25 percent in the IAWPS-95 Scientific Formulation and the 1985 NBS Steam Tables [12]. Two additional factors further complicate heat transfer near the critical point. Firstly, in a variable property flow, fully-developed flow may not be achieved even in a long tube with constant heat flux. Secondly, the very large density differences and low viscosities in a near-critical fluid give rise to buoyancy flows at surprisingly high flow velocities in small tubes. For example, Bazargan [11] applied the correlation of Petukhov et al. [13] to argue that in occasions researchers have treated buoyancy-affected flows as pure forced convection. He measured the onset of buoyancy-affected heat transfer in the same test facility used in this paper. For instance, at a flow rate of 0.78 kg/min ($G=432$ kg/m^2/s) and a heat flux of 300 kW/m^2, heat transfer coefficients at the bottom of the tube were over two times those on the upper surface for sub- and near-critical temperatures.

Heat transfer to near-critical multi-component systems has received much less attention. Knowledge of the heat transfer coefficients for multi-component mixtures is needed to optimize heat transfer equipment design in SCWO. Also, extreme corrosion and fouling may occur in SCWO systems over a narrow range of temperatures, often just below the critical temperature [5]. This makes the prediction of the wall temperatures crucial. In this paper, we examine heat transfer to water/oxygen mixtures at supercritical pressure from sub to supercritical temperatures. The water/oxygen mixture is of particular importance in SCWO, in which the process fluid containing several percent of oxygen by weight along with other compounds, may be heated at constant pressure from room temperature to supercritical temperatures.

Accurate thermodynamic property data for water/oxygen mixtures are needed for modeling and correlation of experiments. With appropriate property modeling, for single-phase supercritical mixtures, one expects good agreement from pure-fluid correlations. However, at subcritical temperatures, several phases may be present, and close to the critical temperature, property modeling is challenging. The only published PVTx data for supercritical pressures were provided by Japas and Franck [14]. Measurements were not made for the pressures most commonly encountered in SCWO (23–26 MPa), so it is necessary to either interpolate their measurements directly or use a fitted equation of state (EOS). For example, Saur et al. [15] used an EOS developed by Christoforakos and Franck [16] to compute mixture density and heat capacity at temperatures well above the critical temperature. Viscosity and thermal conductivity were obtained as deviations from values for

---

Contributed by the Heat Transfer Division for publication in the JOURNAL OF HEAT TRANSFER. Manuscript received by the Heat Transfer Division February 7, 2003; revision received February 4, 2004. Associate Editor: S. Acharya.

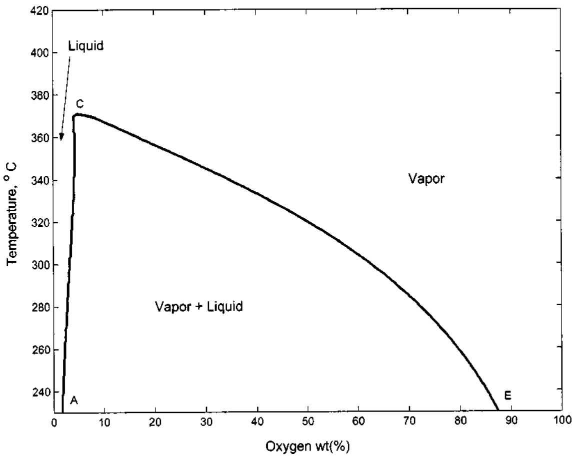

Fig. 1 Phase diagram for the water-oxygen system at 25 MPa, as predicted by the RKS Equation of State [17]

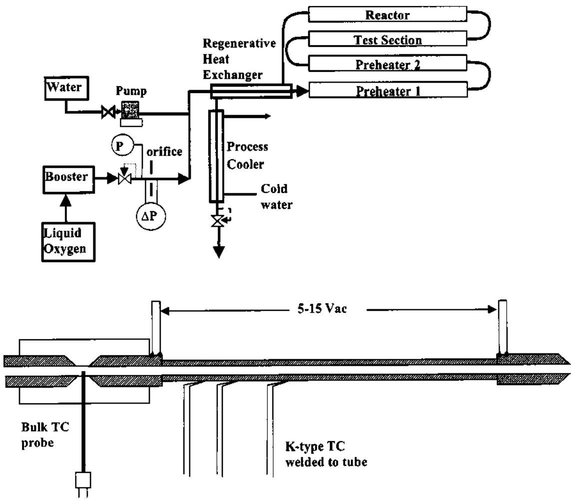

Fig. 2 Process diagram for the UBC SCWO pilot plant (above) and schematic of the first half of the test section (below)

low density gases. Wang [17] calculated the phase boundary, constant pressure heat capacity and density of water/oxygen mixture using Hard Sphere and Redlich-Kwong-Soave (RKS) equations. Oh et al. [18] calculated thermodynamic and transport properties for SCWO fluids (water, ethanol, isopropyl alcohol, nitrogen, oxygen, and carbon dioxide) using the RKS EOS. Although property prediction in the near-critical regime remains very challenging, previous work has established that the water-oxygen system will be highly non-ideal at these conditions, and consequently very sensitive to small changes in the oxygen fraction.

The effect of addition of few percent oxygen to water at supercritical conditions is shown by examining Wang's predictions at 25 MPa from the RKS EOS, optimized to fit the nearest data from Japas and Franck (Fig. 1). The phase curve divides liquid, vapor and liquid-vapor regions from each other. Point C is the intersection of the critical curve with the 25 MPa plane. Curve AC and CE represent the oxygen fraction in the liquid phase and the oxygen fraction in the vapor phase, respectively. For example, at 310°C, the vapor is approximately 58 percent oxygen by weight while the liquid contains approximately 3 percent O_2. From the diagram it is clear that at a few percent oxygen, at subcritical temperatures, the mixture will have two phases. A mixture with 3 wt% oxygen will have two phases at temperatures less than about 310°C, while an 8 wt% oxygen mixture will have two phases for temperatures less than about 370°C. There is considerable uncertainty in interpolating existing measurements for these conditions from Fig. 1. Because of these uncertainties in mixture properties the experimental data cannot be reduced to traditional non-dimensional form (i.e., Nusselt Number versus Reynolds Number).

The UBC/NORAM SCWO pilot plant has been used in three studies of water-oxygen mixtures. Rogak [19] reported heat capacity measurements showing that the addition of few percent oxygen lowers the peak heat capacity and the pseudo-critical temperature of the fluid; the temperature of maximum heat capacity. This trend confirms available PVTx data and EOS modeling. Boskovic [20] made heat transfer coefficient measurements in the same system, and showed that the effect of oxygen on heat capacity and heat transfer coefficients are nearly identical. This may be because turbulent heat transfer coefficient depends very strongly on heat capacity, and because fluid volumetric properties are correlated with heat capacity. The third study from which preliminary results have been reported by Rogak et al. [21] uses significantly better temperature calibration procedures and a more accurate pressure control. The present paper includes the measurements in [21], but also adds new experimental results for broader range of heat fluxes.

Experimental System

Process Configuration. The experiments were conducted in the UBC/NORAM SCWO pilot plant (Fig. 2). The main heat transfer elements of the SCWO system were the regenerative heat exchanger, two pre-heaters, the test section, the reactor, and the process cooler. The process cooler was 6.1 m of 9.5 mm stainless steel tube. All other tubing was made of Alloy 625 (6.2 mm ID and 9.5 mm OD). An electrical current through the tube wall provided the heat to the system. The power was supplied from silicon-controlled rectifiers (SCR).

A 550 L cylindrical storage tank supplied the system with distilled water. Water was pressurized with a triplex plunger pump and oxygen was pressurized using an air-operated booster. The power was transmitted from the SCR panel through two step-down transformers to each preheater. The preheaters were controlled separately from the SCR panel. The power to preheater 1 was adjusted manually while the power to preheater 2 was equipped with a feedback temperature controller. Between the horizontal preheater 2 and the test section was an insulated, unheated section of tube bending through 180 deg with a 0.25 m bend radius. We note this because this bend and the bulk thermocouple probes are the only obstructions that might hinder the development of stratified or slug flow prior to the test section. The heating for the test section was achieved in the same way as for the preheaters, but power control was always manual. The test section was made from four horizontal tube sections. The two main sections (1.52 m each) were electrically heated while two shorter sections (0.3 m), placed at the inlet and the outlet of the test section, are not heated. All the surface and bulk thermocouples were located in the test section. The regenerative heat exchanger is designed to recover approximately 30 kW of power from the test section outlet. The tubing is insulated in 0.15 m×0.15 m boxes of ceramic board.

Pressure Measurement and Control. The gauge pressure was measured using a pressure transducer (GP50 model 211-C), located at the entrance to the test section. The output is a signal ranging between 0–5 V proportional to the pressure. The pressure transducer was calibrated using a digital calibrator (Cole Parmer model 68036-Series). The uncertainty of the pressure measurement, considering errors in data acquisition, and variations in pressure along the test section was approximately 0.1 percent.

In the work reported by Rogak [19] and Boskovic [20], a conventional TESCOM back-pressure regulator was used and accurate pressure control was a problem. In this study, the pressure was controlled with a custom gas-backed pressure regulator. This was constructed by modifying the conventional TESCOM back-pressure regulator to operate with a high pressure nitrogen connected to a conventional 2-stage regulator. Hysteresis caused by O-ring friction in the conventional regulator was greatly reduced, so that pressure variations during the course of an experiment were less than 0.1 percent, even when the outlet flow varied. Gas-backed regulators are available commercially, but we are not aware of their use in the SCWO systems.

Temperature Measurement. All thermocouples used to measure the surface and bulk temperatures in the test section were of K-type thermocouples (Chromel-Alumel) with twisted shielded extension wire. The surface temperatures were measured in 29 locations on the test section: 19 thermocouples were evenly placed and spot welded to the top and bottom surface of the first portion of the test section and 10 thermocouples were spot welded only to the top surface of the second portion of the test section. The bulk fluid temperature was measured in three unheated (isothermal) portions of the test section. The bulk fluid thermocouples were inserted inside the fluid through a high-pressure tee-fittings such that the tip of the thermocouple was located at the center of the test section. These fittings were placed at the inlet, outlet and midsection of the test section. This setup provides an approximate ''mixing-cup temperature,'' and small errors resulting from the cross-tube temperature profile are partially cancelled by calibrating thermocouples and heat flux using pure-water measurements. The bulk thermocouples were calibrated by measuring the saturation temperature of the pure water at known pressures. In this procedure, the fluid temperature and pressure were set above the critical temperature and pressure was decreased to values below the critical pressure (without adjusting the total power input to the system). The fluid in the test section was in the saturated state during the entire calibration procedure. The bulk thermocouple measurements of the saturated water were compared with the known saturation temperature for that pressure. The bulk measurements were consistently 3–4°C higher than the saturation temperature. Boskovic's [20] heat capacity measurements indicated that the measured temperatures were approximately 2°C higher. This is essentially consistent with the 2-phase calibrations in this study. For our recent measurements, the thermocouple readings are corrected according to the calibration, resulting in a temperature uncertainty of no more than ±1°C and the ability to resolve temperature differentials ($T_w - T_b$) of approximately 0.5°C.

Surface temperature measurements presented here have been calibrated by adjusting the test section power until the corrected bulk inlet and outlet temperatures difference was zero. At this point, the net heat flux to the test section must be zero and all surface temperatures should be the same as the bulk temperatures. The temperature deviation was used to correct surface temperature measurements. This procedure is not perfect, and therefore heat transfer coefficients at low heat flux near the critical point, where heat transfer coefficients are high, have a large uncertainty. For example, a 0.5°C error in wall temperature would result in only 5 percent error when $h \sim 7\ \mathrm{kW/m^2/°C}$ and heat flux $Q = 70\ \mathrm{kW/m^2}$ but about 50 percent error when $h \sim 70\ \mathrm{kW/m^2/°C}$.

Heat Flux Measurement. Heat flux to the water-oxygen mixture was calculated relative to pure water measurements. System pressure, flow rate, inlet temperature and electric power in the test section were fixed. The outlet temperature in the test section was recorded and the heat flux into in the test section was calculated using the enthalpy i of pure water [20] as follows:

$$Q = \dot{m}(i_{b,\mathrm{out}} - i_{b,\mathrm{in}}) \tag{1}$$

This procedure determines the net heat flux to the test section at system parameters, therefore eliminating the need to estimate the heat losses. In Boskovic's MASc thesis [20], a transient heat loss model was calibrated against a pure water measurements with an unheated test section. Boskovic's results may have depended on unmeasured details, such as the way insulation packing was changed after servicing the test section. Considering these complications, we decided to run pure-water calibrations every day before investigating the water-oxygen mixtures. Using the well-established IAPWS-95 water properties, it is possible to determine an apparent heat flux for each temperature. Due to measurement noise and thermocouple error, the apparent heat flux is not perfectly constant, but we observed no significant trend with temperature (for the range 350–410°C) and therefore used the average heat flux for the subsequent experiments. Figure 3(a) shows the water heat capacity calculated using a single value for the heat flux. Averaged over the full temperature range, the measured heat capacity must be close to the IAPWS-95 values, but the fact that the measurements show the correct location for the peak heat capacity provides some confidence in the measurements for the water-oxygen mixture.

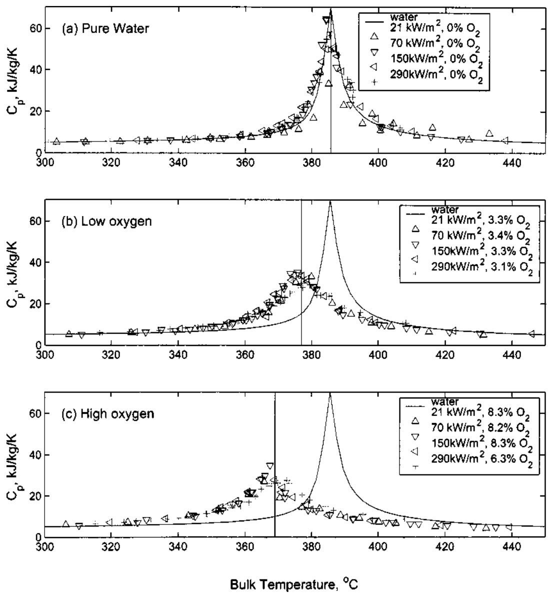

Fig. 3 Measured heat capacity compared with the IAPWS correlation for water [12]. Flow rate can be found from Table 1 for specified values of heat flux and oxygen content.

Flow Rate Measurement. The flow rate of cold water was measured with a graduated cylinder and a stopwatch at the system outlet. Oxygen flow was measured using a differential pressure transmitter (Foxboro model IDP10) installed across an orifice plate downstream of the booster. The orifice was calibrated by running the oxygen through a valve and a dry gas meter at atmospheric pressure. The volumetric flow and transmitter output were measured to an accuracy of about 1 percent during the calibration, but variations in supply pressure and temperature during the experiments increased the uncertainty to approximately 5 percent.

Heat Capacity Measurement. Heat capacity was calculated as

$$C_p = Q/\dot{m}(T_{b,\mathrm{out}} - T_{b,\mathrm{in}}) \tag{2}$$

where Q is the power supplied to the working fluid, $T_{b,\mathrm{out}}$ is the bulk temperature at the test section outlet and $T_{b,\mathrm{in}}$ is the bulk temperature at the test section inlet. The mean value of inlet and outlet temperature was used as the nominal temperature for reporting C_p values. It should be noted that for sub-critical temperature, two phases may exist. The thermodynamic state of the mixture is nevertheless fixed by temperature, pressure and the overall mole fraction, according to the Gibbs Phase Rule. Thus, the measured C_p incorporates the phase change enthalpy and the heat capacity of each phase, but it is still a well-defined thermodynamic property of the mixture.

Heat Transfer Coefficient Measurement. The thermocouples were welded to the outer surface of the tube. Technically it is not feasible to measure the inner wall temperature in a small-bore tube without affecting the flow pattern. Thus, the inside temperature was estimated from outside temperature by solving the radial heat conduction equation, assuming uniform heat generation in the tube and an insulated outer surface. The conductivity of the tube wall was 14 W/m/K for the temperature range in this study. The effect of this correction was to increase apparent heat transfer coefficients by up to 30 percent, and the uncertainty in the correction itself was possibly 30 percent, resulting in an uncertainty of about 9 percent in heat transfer coefficient.

The local heat transfer coefficient depends on the local bulk temperature. The bulk temperature was estimated from an energy balance $Q = m\Delta i$, as follows:

$$\Delta i = C_p (T_{b,(j+1)} - T_{b,j}), \quad T_{b,i+1} = \frac{Q\Delta x}{L\dot{m}C_p} + T_{b,i} \tag{3}$$

where C_p is heat capacity for water-oxygen mixtures and $T_{b,i}$ and $T_{b,(i+1)}$ are bulk temperatures at axial position j and $j+1$, respectively, Q is power supplied to fluid, L is the heated test section length, and Δx axial distance between thermocouples. The bulk temperatures were calculated assuming constant heat capacity over the test section length. This linear interpolation resulted in an error when the heat capacity varied significantly over the test section length. In the worst case for the experiments reported, the bulk temperature increases about 8°C along the test section length and the heat capacity changed by almost 30 percent. Assuming a linear variation in heat capacity, i.e., quadratic variation in temperature, the error introduced by Eq. (3) can be shown to be about 0.3°C.

After determining the inside wall and bulk temperatures, the local heat transfer coefficient was obtained by

$$h = \frac{q}{(T_w - T_b)} \tag{4}$$

where $q = Q/A$, and A is the heated area.

Results

Table 1 summarizes the experiments performed in the present study. The experiments were performed at 25 MPa and water flow rates of 0.76–2.04 kg/min. The heat flux varied from 21 kW/m^2 to 290 kW/m^2. Oxygen content in the flow varied from 3.1 percent to 8.3 percent of the overall flow rate. A typical experiment started by setting water flow rate and the pressure of the system. The system inlet temperature was then set to 300°C and the heat flux in the test section was fixed. The oxygen was introduced into the system and data were recorded. Then the inlet temperature to the test section was increased in increments of 5, 10, or 20°C depending on the run. The experiments were carried out up to inlet temperature of 450°C or when the surface temperature in the test section exceeded 550°C.

Table 1 Parameters of experiments reported in this study

Heat Flux kW/m^2	Flow Rate kg/min	Oxygen %	Pressure MPa	Run #
21	0.76	0	25.2	87–101
21	0.76	3.3	25.2	123–136
21	0.76	8.3	25.2	137–151
70	0.78	0	24.8	35–47
70	0.76	3.4	25.1	152–168
70	0.78	8.2	25.0	61–74
150	0.76	0	25.1	75–86
150	0.76	3.3	25.1	102–112
150	0.76	8.3	25.1	113–122
150	2.04	0	25.2	169–178
290	2.20	0	25.1	179–197
290	2.04	3.1	25.5	198–209
290	2.04	3.2	25.1	210–225
290	2.04	6.3	25.3	226–241

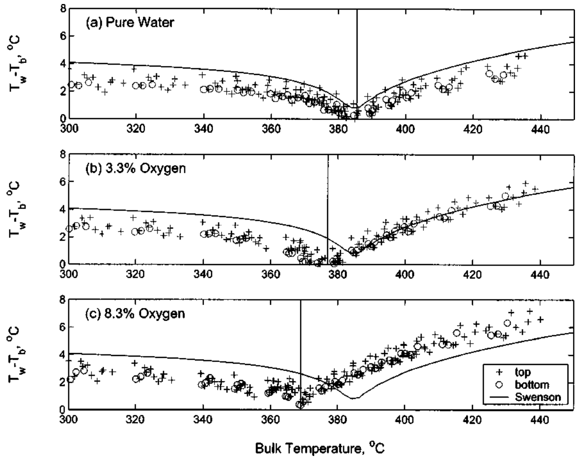

Fig. 4 Wall-bulk temperature differentials for low heat flux experiments (21 kW/m^2) at 0.78 kg/min water flow

Figure 3(b) shows the effect of addition of a small amount of oxygen (about 3 percent) in the overall mixture heat capacity at 25 MPa. Compared to the heat capacity of pure water, the C_p of the mixture has been reduced and its peak temperature has shifted to a lower temperature. The C_p measurements are only a function of the oxygen content and insensitive to the test section power as required of thermodynamic properties. Figure 3(c) (8 percent to 9 percent O$_2$) further illustrates this fact and shows further shifting of the peak C_p to lower temperature. Note that in Fig. 3(b) the oxygen content for 290 kW/m^2 measurements is 6.3 percent and the temperature at which the peak C_p occurs is consistent with the trend in the measurements.

Figure 4 compares the top and bottom wall-bulk temperature differences (proportional to h^{-1}) for low and high oxygen content, at a water flow of 0.78 kg/min and heat flux of 21 kW/m^2. The top and bottom tube wall temperatures are nearly same. The effect of the oxygen is to lower the temperature at which minimum temperature difference occurs. For reference, the position of the maximum mixture heat capacity is shown on the graphs. The minimum temperature difference is less than 1°C, and therefore subject to significant uncertainty, but it is apparent that oxygen has reduced the magnitude of the peak heat transfer coefficients. Predictions from the pure water correlation of Swenson et al. [22] are shown for comparison.

At 70 kW/m^2 (Fig. 5), the temperature difference is much easier to measure. Comparing Fig. 5(a), (b), and (c) it is observed that temperatures at the top of the tube are higher for subcritical bulk temperatures for low oxygen content. However at higher oxygen content the top and bottom temperatures show no difference. At supercritical temperatures the top and bottom temperatures are the same regardless of the amount of oxygen in the system. The most striking effect of oxygen is to introduce a region of deteriorated heat transfer on the top surface of the tube, at bulk temperatures below where C_p is at maximum. There is no evidence of heat transfer deterioration at the bottom surface for this heat flux. The stratification of flow is the most plausible explanation for this effect.

Figure 6 shows that at 150 kW/m^2, the top/bottom temperature differences for water are larger and extend to supercritical temperatures. Again, the oxygen-water system shows more severe deteriorated heat transfer in the near critical region. The top/bottom temperature differences exhibited by the water-oxygen system at sub-critical conditions are less pronounced than for pure water. This is surprising, because at these temperatures we can be con-

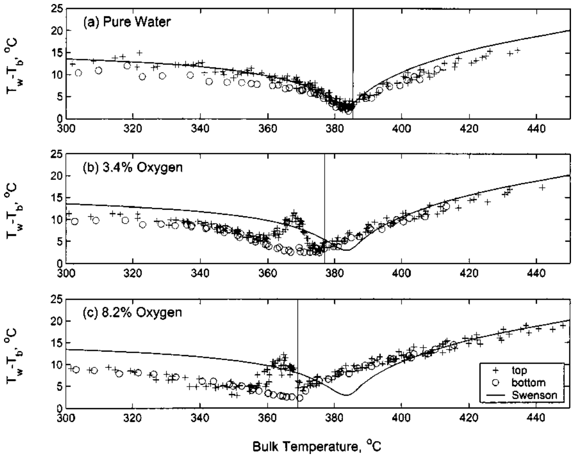

Fig. 5 Wall-bulk temperature differentials for moderate heat flux experiments (70 kW/m^2) at 0.76–0.78 kg/min water flow

fident that the oxygen is present mainly as a separate phase with a density 20 percent of the density of water. However, it should be noted that the water flow has been held constant in these measurements, so flow velocities for the mixtures are slightly higher than for pure water. At this heat flux the heat transfer deterioration has expanded to the bottom of the tube as is evident from the graphs.

Figure 7 shows the effect of increasing the water flow to over 2 kg/min and increasing the heat flux to 290 kW/m^2 (near the maximum allowed by the facility). As expected, the higher flow has reduced the stratification for the pure water system. Surprisingly, with oxygen present, the stratification at subcritical temperatures is just as pronounced as at lower velocities, and now heat transfer deterioration is more pronounced at the tube bottom. Although there are only a handful of temperature measurements indicating this deterioration, the magnitude of the deterioration is over 5°C, and therefore very reliably detected by our system. Near-duplicate runs (b) and (c) exhibit the same behavior.

Figure 8 presents all of the measurements more conventionally as heat transfer coefficients. In order to make the graphs clearer, the temperatures have been filtered with a moving box average. The top surface temperatures are 8 point moving average while the bottom surface temperature are 3 point averages. The difference in the number of averaged point between the top and bottom is because there were three times as many thermocouples on the top surface.

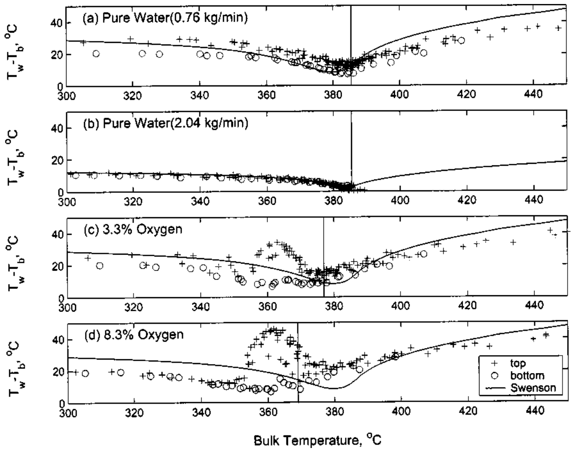

Fig. 6 Wall-bulk temperature differentials for high heat flux experiments (150 kW/m^2). Water flow rate is 0.76 kg/min except as noted.

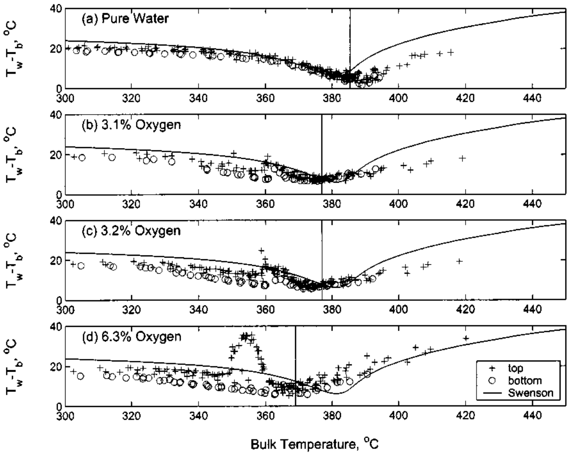

Fig. 7 Wall-bulk temperature differentials for high heat flux experiments (290 kW/m^2) at over 2 kg/min water flow

Measurements of Boskovic [19] also showed a hint of heat transfer deterioration at subcritical temperatures, on the bottom of the tube. Many of her runs showed distinct deterioration at the top of the tube surface, although it was not clear at the time the thesis was written whether this was real or an artifact of the measurements.

The fact that there can be deterioration at the bottom of the tube suggests that some mechanism other than density stratification is involved. While it is possible that some fluid properties of the mixture are changing abruptly at the point of deterioration, it

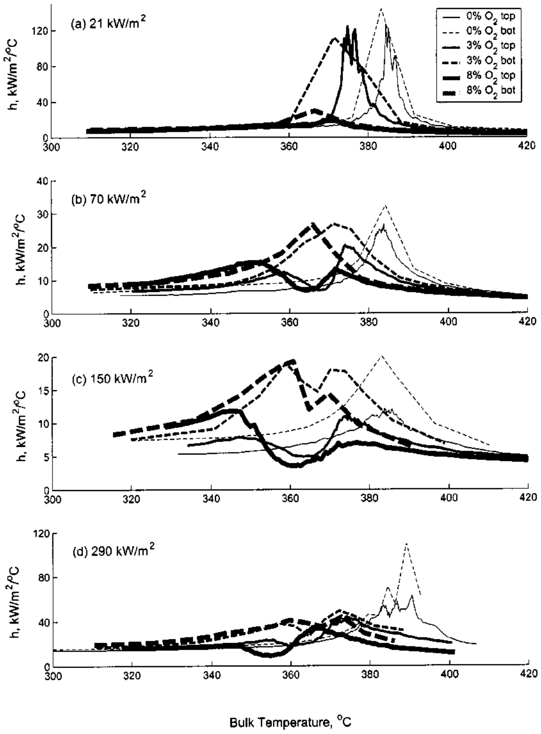

Fig. 8 Summary of heat transfer coefficients as a function of oxygen content and heat flux. As shown in Table 1: experiments at 21, 70, and 150 kW were run with approximately 0.78 kg/min water flow, while the experiments at 290 kW/m^2 were run at 2.04 kg/min.

should be noted that from equation of state modeling [16,17], mixture density and heat capacity vary smoothly, as they do for pure water. Deterioration of heat transfer can occur in accelerating flows, but this would not be expected for pure water at the conditions of our experiment.

Multiphase flow effects are probably important for the subcritical temperatures. At the lower flow rate, the velocity is just under 1 m/s (Re~40,000 for pure water), while at the higher flow rate, the velocity is just over 2 m/s (Re~100,000). For these velocities in a 6.2 mm pipe, traditional flow maps would suggest that slug flow is present. As the critical temperature is approached, however, one expects the slugs to disperse as velocities increase and inter-phase properties decrease. We believe that much more work would be needed to model the flow in the near-critical region.

Conclusions

The constant-pressure heat capacity, C_p, and local forced convection heat transfer coefficient, h, for supercritical water-oxygen mixtures flowing inside horizontal smooth tubes were obtained experimentally. Data were obtained for a pressure of 25 MPa and water flow rates of 0.76 to 2.0 kg/min, at low heat fluxes of up to 290 kW/m^2. Oxygen flow was 0 to 9 wt % of the total mixture flow. For a given flow and power, C_p was determined from the bulk temperature in a heated tube. The heat transfer coefficient was determined from the difference in bulk and wall temperatures.

Despite the multi-phase nature of the flow at temperatures well below the critical temperature (i.e., $<360°C$), the presence of small quantity of oxygen has little effect on the heat transfer. At supercritical temperatures where the flow is single-phase and gas-like, the presence of oxygen has little effect on the heat transfer coefficient. However, at near-critical temperatures, the addition of small amounts of oxygen results in a dramatic change in the heat transfer. Firstly, the magnitude and temperature for the peak heat transfer decrease, consistent with changes in heat capacity. Secondly, heat transfer is deteriorated at moderate heat flux, mostly but not exclusively on the top surface of the tube. This peculiar effect is might be due to an altered (possibly, finer) distribution of the two phases prior to complete miscibility, but without accurate mixture properties, this hypothesis should be tested in experiments measuring velocities and bubble distributions. Until the phenomenon is better understood, engineers must be extremely cautious when using conventional heat transfer correlations in SCWO design.

Acknowledgment

The authors gratefully acknowledge the financial assistance of NSERC, and Noram Engineering and Constructors Ltd. Mr. Alex Podut developed the detailed design of the gas-backed pressure regulator used in this work, and Mr. Mohammad Khan provided assistance with the experiments reported here.

References

[1] Oka, Y., Koshizuka, S., Jevremovic, T., and Okano, Y., 1995, ''System Design of Direct-Cycle Supercritical Water Cooled Fast Reactors,'' Nucl. Technol., **109**, pp. 1–10.

[2] Thomason, T. B., and Modell, M., 1984, ''Supercritical Water Destruction of Aqueous Wastes,'' Hazard. Waste, **1**, pp. 453–246.

[3] Tester, J. W., Holgate, H. R., Armellini, F. J., Webley, P. A., Killilea, W. R., Hong, G. T., and Barner, H. E., 1993, ''Supercritical Water Oxidation Technology: Process Development and Fundamental Research,'' *Emerging Technologies in Hazardous Waste Management*, D. W. Tedder and F. G. Pohland, eds., ACS Symposium Series 518, ACS, Washington, DC, pp. 35–76.

[4] Gloyna, E. F., and Lixiang, L., 1995, ''Supercritical Water Oxidation Research and Development Update,'' Environ. Prog., **14**, pp. 182–192.

[5] Kritzer, P., and Dinjus, E., 2001, ''An Assessment of Supercritical Water Oxidation (SCWO): Existing Problems, Possible Solutions and New Reactor Concepts,'' Chem. Eng. J., **83**, pp. 207–214.

[6] Deissler, R. G., 1954, ''Heat Transfer and Fluid Friction for Fully Developed Turbulent Flow of Air and Supercritical Water With Variable Fluid Properties,'' Trans. ASME, pp. 73–85.

[7] Miropolski, L., and Shitsman, M. E., 1957, ''Heat Transfer to Water and Steam at Variable Specific Heat (in Near-Critical Region),'' Soviet Physics, **27**(10), pp. 2359–2372.

[8] Hall, W. B., 1971, ''Heat Transfer Near the Critical Point,'' *Advances in Heat Transfer*, I. F. Irvine, Jr. and J. P. Hartnett, eds., Academia Press.

[9] Jackson, J. D., and Hall, W. B., 1979, ''Forced Convection Heat Transfer to Fluids at Supercritical Pressure,'' *Turbulent Forced Convection in Channel and Bundles*, Hemisphere, New York, **12**, pp. 563–599.

[10] Polyakov, A. F., 1991, ''Heat Transfer Under Supercritical Pressures,'' Adv. Heat Transfer, **21**, pp. 2–51.

[11] Bazargan, M., 2001, ''Forced Convection Heat Transfer to Turbulent Flow of Supercritical Water in a Round Horizontal Tube,'' Ph.D. thesis, UBC.

[12] Wagner, W., and Pruß, A., 2002, ''The IAPWS Formulation 1995 for the Thermodynamic Properties of Ordinary Water Substance for General and Scientific Use,'' J. Phys. Chem. Ref. Data, **31**, p. 387.

[13] Petukhov, B. S., Polyakov, A. F., Kuleshohov, V. A., and Sheckter, Y. L., 1974, ''Turbulent Flow and Heat Transfer in Horizontal Tubes With Substantial Influence of Thermo-Gravitational Forces,'' *Proc. 5th Int. Heat Transfer Conf.*, Paper No. NC4.8. ASME, New York.

[14] Japas, M. L., and Franck, E. U., 1985, ''High Pressure Equilibria and PVT-Data of the Water-Oxygen System Including Water-Air to 673 K and 250 MPa,'' Ber. Bunsenges. Phys. Chem., **89**, pp. 1286–1274.

[15] Saur, A. M., Behrendt, F., and Franck, E. U., 1993, ''Calculation of High Pressure Counterflow Diffusion Flames Up to 3000 Bar,'' Ber. Bunsenges. Phys. Chem., **97**, pp. 900–908.

[16] Christoforakos, M., and Franck, E. U., 1986, ''An Equation of State for Binary Fluid Mixtures to High Temperatures an High Pressure,'' Ber. Bunsenges. Phys. Chem., **90**, pp. 780–788.

[17] Wang, S., 2001, ''Properties of Supercritical Water-Oxygen Mixtures,'' M.Sc. thesis, UBC.

[18] Oh, C. H., Kochan, R. J., and Beller, J. M., 1997, ''Numerical Analysis and Data Comparison of a Supercritical Water Oxidation Reactor,'' AIChE J., **43**, pp. 1672–1636.

[19] Rogak, S., 2000, ''Measurements of the Constant-Pressure Heat Capacity of Water-Oxygen Mixtures at Near-Critical Conditions,'' *Proc. Of the 13th International Conference on the Properties of Water and Steam*, P. R. Tremaine, P. G. Hill, D. E. Irish, and P. V. Balakrishnan, eds., NRC Research Press, pp. 149–156.

[20] Boskovic, S., 2001, ''Measurements of Heat Capacities and Heat Transfer Coefficient of Water-Oxygen Mixtures at Near Critical Conditions,'' M.A.Sc. thesis, UBC.

[21] Rogak, S. N., Boskovic, S., and Faraji, D., 2002, Proc. ASME Int. Mechanical Engineering Congress & Exposition, Paper IMECE2002-34314.

[22] Swenson, H. S., Carver, J. R., and Kakarla, C. R., 1965, ''Heat Transfer to Supercritical Water in Smooth-Bore Tubes,'' ASME J. Heat Transfer, pp. 477–484.

Manish Mishra
e-mail: mishra_md@yahoo.com
Mechanical Engineering Department,
Indian Institute of Technology, Kharagpur,
India, 721302

P. K. Das
e-mail: pkd@mech.iitkgp.ernet.in
Department of Mechanical Engineering,
Indian Institute of Technology, Kharagpur,
India, 721302

Sunil Sarangi
e-mail: ssarangi@hijli.iitkgp.ernet.in
Cryogenic Engineering Center,
Indian Institute of Technology, Kharagpur,
India, 721302

Transient Behavior of Crossflow Heat Exchangers With Longitudinal Conduction and Axial Dispersion

Transient temperature response of the crossflow heat exchangers with finite wall capacitance and both fluids unmixed is investigated numerically for step, ramp and exponential perturbations provided in hot fluid inlet temperature. Effect of two-dimensional longitudinal conduction in separating sheet and axial dispersion in fluids on the transient response has been investigated. Conductive heat transport due to presence of axial dispersion in fluids have been analyzed in detail and shown that presence of axial dispersion in both of the fluid streams neutralizes the total conductive heat transport during the energy balance. It has also been shown that the presence of axial dispersion of high order reduces the effect of longitudinal conduction. [DOI: 10.1115/1.1738422]

Keywords: *Conduction, Heat Exchangers, Modeling, Transient, Unsteady*

Introduction

Heat exchangers are generally designed to meet certain performance requirements under steady operating conditions. However, transient response of heat exchangers needs to be known for designing the control strategy of different HVAC systems, cryogenic and chemical process plants. Problems such as start-up, shutdown, failure, and accidents have motivated investigations of transient thermal response in crossflow heat exchangers. It also helps the designer to find a solution of the time dependent temperature problems, essential for thermal stress analyses. Besides, transient testing techniques are often adopted for determining the thermal characteristics of heat exchangers. In these experiments one of the fluid streams is subjected to a specified perturbation in inlet temperature while the response at the outlet is recorded. Using this information, thermal characteristics of heat exchangers can be predicted if a suitably developed mathematical model is available.

In the past few decades numerous attempts have been made for modelling the dynamic behavior of heat exchangers. The researchers not only considered heat exchangers of different types but also proposed various methodologies. A pioneering effort [1] for modelling the dynamic behavior of an air-to-gas plate-fin type crossflow heat exchanger has been done. Based on a number of simplified assumptions like negligible local heat storage in the gas and air stream, the energy balance equations were formulated and solved using finite difference technique taking a specific example. The basic set of three differential equations for the simulation of transient heat exchange in a crossflow heat exchanger was proposed [2] and five independent nondimensional parameters were identified. Next one of the fluids is assumed to be mixed, which renders the temperature variation in that stream one-dimensional and greatly simplifies the problem. Further simplifications were sought assuming a large wall capacitance and finally an approximate analytical solution was obtained using integral heat balance technique.

Based on the basic model [2] different researchers have analyzed the transient response of crossflow heat exchangers relaxing one or more number of approximations. A step change of inlet temperature was considered and solution was obtained by finite difference technique using a transformation of variables [3,4]. While infinite capacitance of one of the fluids was assumed in the former work, large wall capacitance was considered in the latter. On the other hand an analysis [5] has been forwarded for fluid streams of negligible capacitance subjected to step, ramp, and exponential inputs. They studied the effect of longitudinal conduction in the separator sheet and observed a deterioration of thermal performance of the heat exchanger.

Parallel efforts were also made to find out the dynamic response of heat exchangers analytically, using Laplace transform technique. The response of gas-to-gas heat exchanger with large core capacitance in case of step input have been analyzed [6,7]. The work has been extended [8] and the two-dimensional temperature response as integrals of modified Bessel's function in space and time for a transient response with any arbitrary initial and inlet conditions were obtained. The results were presented for step, ramp, and exponential inputs. Later the assumption of large wall capacitance is relaxed [9,10] and the temperature response was derived for a deltalike perturbation in temperature as well as step input. The solution is again simplified [11] for the limiting case of small capacitance of the fluid stream compared to the core.

In all of the above works the transient response has been obtained by two or three-fold Laplace transform. Next the temperature fields have been obtained by inversion of the resulting Laplace equations. The task of inverting the transformed temperatures in the physical domain becomes progressively difficult with the increase in the number of simultaneous equations as well as independent variables. This has motivated the investigators to use single Laplace transform along with numerical inversion. A single Laplace transform is used in conjunction with the power series technique for determining the response of crossflow heat exchangers with large and finite core capacitance respectively [12,13].

So far all the analysis made for the prediction of dynamic behavior of crossflow heat exchangers are based on the assumption of ideal plug flow. However, in reality the flow field will have nonuniformities in the form of eddies, turbulent fluctuations and recirculating as well as stagnant fluid zones. This presents a significant deviation from the plug flow, but cannot also be considered as a situation where complete longitudinal mixing is present. The thermal dispersion phenomena in the fluid closely resemble conduction of heat with different time and space scales. The space and time scales of thermal dispersion are small compared to the dimension of the heat exchanger and the time scale of convective

---

Contributed by the Heat Transfer Division for publication in the JOURNAL OF HEAT TRANSFER. Manuscript received by the Heat Transfer Division January 13, 2003; revision received March 2, 2004. Associate Editor: N. K. Anand.

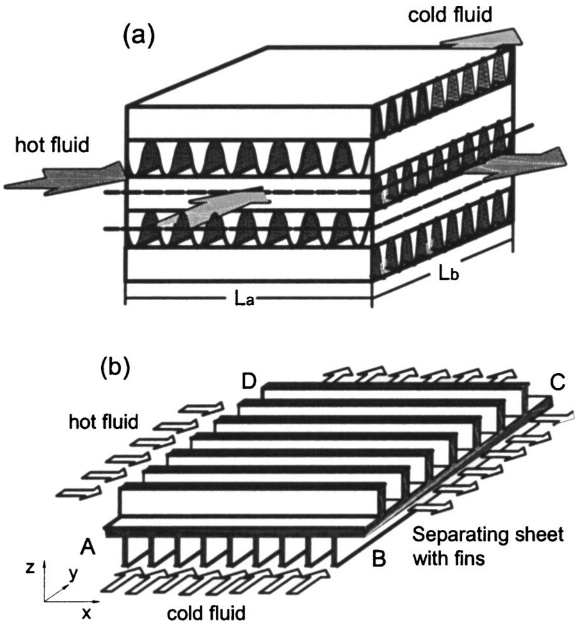

Fig. 1 Crossflow heat exchanger (a) schematic representation, and (b) symmetric module considered for analysis

transport. An approximate analysis of the real situation can be made assuming a Fourier type apparent axial conduction. The axial dispersion model for the transport of mass in a fluid flowing through a conduit was originated [14] and analyzed in general [15]. Exploiting the similarity between heat and mass transfer this model was extended for thermal transport and was implemented for the analysis of regenerators [16] and heat exchangers [17,18]. All of these studies report a significant change in the heat exchanger performance, if the effect of axial dispersion is included. An analytical solution [19] was given for the temperature effectiveness and temperature distribution in crossflow heat exchangers with axial dispersion in one fluid. This analysis shows that the influence of axial dispersion on temperature effectiveness is significant for $\mathrm{Pe}<20$, particularly when the heat exchanger is in balanced condition. Further, the effect increases with the increase in NTU.

The present work investigates the transient performance of a direct transfer, single pass crossflow heat exchanger. The temperature response of the fluid streams as well as the separator plate has been obtained by solving the conservation equations by finite difference formulation for step, ramp as well as exponential variation in the hot fluid inlet temperature. The analysis has been done for the generalized case of unmixed fluid streams and finite capacitances of fluids and metal wall. Effect of various parameters particularly the two-dimensional conduction in wall, axial dispersion in fluids as well as their combined effect on the dynamic performance of the heat exchanger has been studied over a wide range.

Mathematical Formulation

A direct-transfer, two-fluid, crossflow, multilayer plate-fin heat exchanger is shown schematically in Fig. 1(a). The two fluids exchange thermal energy through a separating solid plate while flowing through this heat exchanger in directions normal to each other. The hot stream is subjected to a specified temperature variation at the inlet, while the cold stream enters the heat exchanger with a known constant temperature. Following assumptions are made for the mathematical analysis:

1. Both the fluids are single phase, unmixed and do not contain any volumetric source of heat generation.
2. The exchanger shell or shroud is adiabatic and the effects of the asymmetry in the top and bottom layers are neglected. Therefore the heat exchanger may be assumed to comprise of a number of symmetric sections as shown by dotted lines in Fig. 1(a) and in details in Fig. 1(b).
3. The thermo-physical properties of both the fluids and wall are constant and uniform.
4. The primary and secondary areas of the separating plate have been lumped together, so that the variation of its temperature is two-dimensional.
5. The thermal resistance on both sides comprising of film heat transfer coefficient of primary and secondary surfaces and fouling resistance are constant and uniform.
6. Dispersion coefficient of the fluid streams remains constant.
7. Heat transfer area per unit base area and surface configurations are constant.
8. Variation of temperature in the fluid streams in a direction normal to the separating plate (z-direction) is neglected.

Conservation of energy for wall and the two fluid streams considering longitudinal conduction in separating sheet and the axial dispersion in fluids can be expressed as follows:

$$MC\frac{\partial t_w}{\partial \tau}=(hA)_a(t_a-t_w)+(hA)_b(t_b-t_w)+k\delta L_aL_b\frac{\partial^2 t_w}{\partial x^2}+k\delta L_aL_b\frac{\partial^2 t_w}{\partial y^2} \tag{1}$$

$$(hA)_a(t_w-t_a)=(LA_c\rho c)_a\frac{\partial t_a}{\partial \tau}+L_a(mc)_a\frac{\partial t_a}{\partial x}-A_{ca}D_aL_a\frac{\partial^2 t_a}{\partial x^2} \tag{2}$$

$$(hA)_b(t_w-t_b)=(LA_c\rho c)_b\frac{\partial t_b}{\partial \tau}+L_b(mc)_b\frac{\partial t_b}{\partial y}-A_{cb}D_bL_b\frac{\partial^2 t_b}{\partial y^2} \tag{3}$$

Equations (1)–(3) can be expressed in nondimensional form as follows:

$$\frac{\partial T_w}{\partial \theta}=T_a+RT_b-(1+R)T_w+\lambda_aN_a\frac{\partial^2 T_w}{\partial X^2}+\lambda_bN_bR\frac{\partial^2 T_w}{\partial Y^2} \tag{4}$$

$$V_a\frac{\partial T_a}{\partial \theta}=T_w-T_a-\frac{\partial T_a}{\partial X}+\frac{N_a}{Pe_a}\frac{\partial^2 T_a}{\partial X^2} \tag{5}$$

$$\frac{V_b}{R}\frac{\partial T_b}{\partial \theta}=T_w-T_b-\frac{\partial T_b}{\partial Y}+\frac{N_b}{Pe_b}\frac{\partial^2 T_b}{\partial Y^2} \tag{6}$$

where nondimensional terms are defined as

$$X=\left[\frac{hA}{mc}\right]_a\frac{x}{L_a}=N_a\frac{x}{L_a},\quad Y=\left[\frac{hA}{mc}\right]_b\frac{y}{L_b}=N_b\frac{y}{L_b},\quad \text{where } N=\frac{hA}{mc}$$

$$\theta=\frac{(hA)_a\tau}{MC},\quad T=\frac{t-t_{b,\mathrm{in}}}{t_{\mathrm{REF}}-t_{b,\mathrm{in}}}$$

where t_{REF} is a reference temperature$=(t_{a,\mathrm{in}})_{\max}$.

$$\text{Conductance Ratio,}\quad R=\frac{(hA)_b}{(hA)_a},$$

$$\text{Capacitance Ratio,}\quad V=\frac{LA_c\rho c}{MC}$$

$$\text{Longitudinal Heat Conduction Parameter,}\quad \lambda_a=\frac{k\delta L_b}{L_a(mc)_a},$$

$$\lambda_b = \frac{k\,\delta L_a}{L_b (mc)_b}$$

$$\text{Axial Dispersive Peclet number, } \mathrm{Pe} = \frac{(mc)L}{A_c D}$$

NTU is defined as

$$\frac{1}{\mathrm{NTU}} = C_{\min}\left[\frac{1}{(hA)_a} + \frac{1}{(hA)_b}\right] \tag{7}$$

Further, N_a and N_b can be expressed as a function of nondimensional heat exchanger parameters namely number of transfer units (NTU), conductance ratio (R), and capacity rate ratio $[E = (mc)_b/(mc)_a]$. For $C_a = C_{\min}$

$$N_a = \mathrm{NTU}\left[1 + \frac{1}{R}\right], \quad N_b = \frac{\mathrm{NTU}}{E}(R+1) \tag{8}$$

and for $C_b = C_{\min}$

$$N_a = E\mathrm{NTU}\left[1 + \frac{1}{R}\right], \quad N_b = \mathrm{NTU}(1+R) \tag{9}$$

The initial temperature of the hot fluid, cold fluid and the separating sheet are all equal to the ambient temperature, and so also the inlet temperature of the cold fluid. Then Eqs. (1)–(3) are subjected to

$$T_a(X,Y,0) = T_b(X,Y,0) = T_w(X,Y,0) = 0 \tag{10}$$

Assuming the adiabatic boundary conditions at the fluid exit and at the edges of the separating sheets

$$\left.\frac{\partial T_a(X,Y,\theta)}{\partial X}\right|_{X=N_a} = 0, \tag{11}$$

$$\left.\frac{\partial T_b(X,Y,\theta)}{\partial Y}\right|_{Y=N_b} = 0, \tag{12}$$

$$\left.\frac{\partial T_w(X,Y,\theta)}{\partial X}\right|_{X=0} = \left.\frac{\partial T_w(X,Y,\theta)}{\partial X}\right|_{X=N_a} = \left.\frac{\partial T_w(X,Y,\theta)}{\partial Y}\right|_{Y=0}$$

$$= \left.\frac{\partial T_w(X,Y,\theta)}{\partial Y}\right|_{Y=N_b} = 0 \tag{13}$$

Inlet temperature of hot fluid is subjected to an external perturbation as

$$T_a(0,Y,\theta) = \phi(\theta), \tag{14}$$

while inlet temperature of cold fluid remains unchanged as

$$T_b(X,0,\theta) = 0. \tag{15}$$

Solution may be obtained for any arbitrarily specified temperature function $\phi(\theta)$. However, dynamic response of heat exchanger is generally looked for step, ramp and exponential variation of temperature. Such variation may occur during operations or they may be especially created for the purpose of transient testing of heat exchangers. Though a ramp or an exponential function gives a continuous increase in temperature, such an increase for a prolonged duration is not feasible in reality. For instance the initial temperature rise may have the ramp or exponential nature in both designed and unforeseen transients, but the maximum value of temperature rise will generally not be unlimited. This aspect has not been considered by earlier researchers [5,9], who have considered the continuous increase of temperature during the entire period of operation for both ramp and exponential functions. In the present case instead of continuous increase a limit of maximum temperature has been provided. The functional form of $\phi(\theta)$ is expressed as follows:

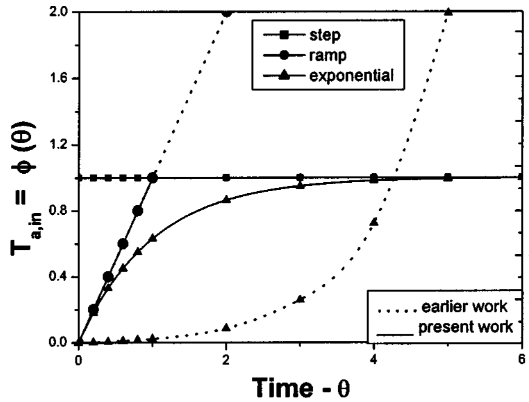

Fig. 2 **Schematic representation of perturbation [$\phi(\theta)$] in inlet temperature of hot fluid**

$$\phi(\theta) = \begin{cases} 1; & \text{for step input} \\ \begin{bmatrix} \alpha\theta, & \theta \leqslant 1 \\ 1, & \theta > 1 \end{bmatrix}; & \text{for ramp input} \\ 1 - e^{-\alpha\theta}; & \text{for exponential input} \end{cases} \tag{16}$$

where α is assumed to be unity in the present analysis.

The pictorial representation of the inlet temperature functions both as considered by the earlier researchers and as taken in the present work are depicted in Fig. 2.

Method of Solution

The conservation equations are discretised using the implicit finite difference technique [20]. Forward difference scheme is used for time derivatives, while upwind scheme and central difference scheme are used for the first and second-order space derivatives, respectively. The difference equations along with the initial and boundary conditions are solved using Gauss-Seidal iterative technique. The convergence of the solution has been checked by varying the number of space grids and size of the time steps. It has been observed that the space grids 50×50 along with time steps 50 give the grid independence. The solution gives the two-dimensional temperature distribution for both of the fluids as well as the separator plate. Additionally, one may calculate the mean exit temperatures as follows:

$$\overline{T_{a,ex}} = \frac{\int_0^{Na} T_{a,ex} u\,dy}{\int_0^{Na} u\,dy} \quad \text{and} \quad \overline{T_{b,ex}} = \frac{\int_0^{Nb} T_{b,ex} v\,dx}{\int_0^{Nb} v\,dx} \tag{17}$$

To check the validity of the numerical scheme, the results of the present investigation have been compared with available analytical results. For balanced gas-to-gas crossflow heat exchangers, the variation of exit temperature is available [8] in the absence of core longitudinal conduction and fluid axial dispersion for a conductance ratio of 1 using Laplace transform. Figure 3 depicts excellent agreements between the results of present investigation and those obtained analytically [8] for step, ramp and exponential inputs. It needs to be mentioned that for the comparison of the results the definition of ramp and exponential inputs prescribed in the present work has not been followed. They have been taken as suggested in [8].

Results and Discussions

Performance of the heat exchanger was studied over a wide range of parameters as well as for a sufficient time duration so that steady state conditions are obtained for each individual excitation. The results have been obtained for the range of NTU from 1 to 8,

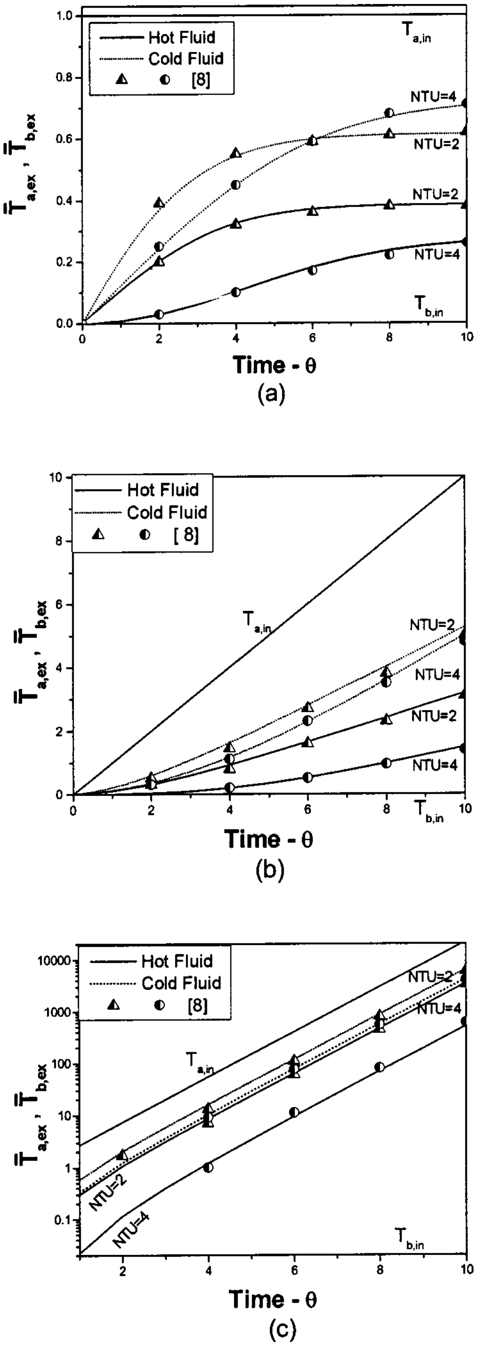

Fig. 3 Comparison of the solutions with the analytical results [8]: (a) step, (b) ramp, and (c) exponential inputs for $E=R=1$, $V=\lambda=0$, and Pe$=\infty$

λ from 0 to 0.025, Pe from 1 to ∞, V from 0 to 10, E from 0.5 to 2, and R from 0.1 to 10. Some of the salient results are discussed below.

Two-Dimensional Temperature Distribution. The temperature of the fluid streams as well as separator plate will continuously change in x-y plane till the heat exchanger attains steady state. The temperature profiles at any intermediate time steps can be obtained with the help of present scheme. Figure 4 shows some typical results of temperature variation of the wall and the two fluids at $\theta=1$ for different input functions.

As the instantaneous value of $\phi(\theta)$ decides the hot fluid inlet temperature, it is 1 for both step and ramp functions, while it is much lower for exponential function at $\theta=1$. Thereafter for all the three cases the hot fluid temperature decreases gradually till it reaches the exit plane. Interestingly, the exit temperature of the hot fluid is highest in case of step input, lowest in ramp input, while it has some intermediate value for exponential input. This indicates the temperature variation for exponential input is more uniform compared to the previous two cases. The wall temperature at the inlet plane of hot fluid is highest for step input, while, ramp and exponential cases are in diminishing order. The cold fluid temperature builds up gradually, as it receives the stored thermal energy from the separating sheet. In the present example cold fluid temperature is more or less uniform over the entire area and is marginally different from its inlet value. This is due to the fact that time step $\theta=1$ considered here is too small to produce any appreciable change in the temperature of the cold stream. However, the effect of input disturbance can still be appreciated as one may note relatively higher temperature in case of step input, the highest point of temperature being at corner D (Fig. 1(b)). The similar profiles can be drawn for different time levels, which can give the complete insight of the temperature variation at different portion of the heat exchanger at transient condition. The temperature profiles may be useful in thermal expansion and stress analysis needed for the mechanical design of the heat exchanger. The variation of plate temperature is of particular interest for mechanical design.

Effect of Aspect Ratio. The effect of NTU on the transient performance of crossflow heat exchanger has been studied by most of the researchers [5,9]. However, the ratio of the length to breadth or the aspect ratio may influence the transient performance of such heat exchangers even if NTU is kept constant. Such investigation for crossflow heat exchangers has so far not been made. From Eqs. (8)–(9) and the definition of X and Y, the aspect ratio of the heat exchanger Y/X can be equated to N_b/N_a and hence to R/E. Thus for $E=1$, the effect of change in R will also give the effect of change in aspect ratio of the heat exchanger as shown in Fig. 5 for step, ramp and exponential inputs at different time levels. Figure 5 shows that with the increase in aspect ratio, i.e., the length of travel of cold fluid, the steady-state condition is reached early by both the fluid streams for a step input. This can be understood as the reduction in flow length/area of hot fluid, gives smaller area of heat transfer available for the fluid where disturbance is provided. Similar results are also observed for ramp and exponential inputs.

Effect of Heat Capacity Rate Ratio. As temperature transients are imparted to hot fluid, which has a higher heat capacity, the effect of disturbances will die out easily for $E<1$, i.e., when $(mc)_a>(mc)_b$. Or in other words the cold fluid with a lower thermal capacity will behave like a gas following the transients of the other fluids closely and will reach the steady state within a small duration. This behavior is depicted for step input in Fig. 6. Temperature responses for ramp and exponential inputs are not much different from those shown in this figure. A few more important observations may also be made from this figure. The difference between the exit temperatures of the two streams increases both during transient and at the steady state for a low value of heat capacity rate ratio. However, this effect diminishes very quickly with the increase in E. At a low value of E, the crossflow heat exchanger may exhibit an interesting behavior. As the temperature of the cold stream increases rapidly, at the beginning of the transients cold stream exit temperature may be higher than that of hot stream though at the steady state there is a reversal of this. This crossover of temperature curves for both $E=1$ and 2 can be noticed from Fig. 6 for step change in input. Similar behavior is obtained for ramp and exponential responses due to specific nature of the input functions.

Effect of Heat Capacity Ratio. When the heat capacity ratio ($V=LA_c\rho c/MC$) is small the effect of wall thermal capacity is more and the time taken to transfer the heat from one fluid to the other is less, so the mean exit temperature of the fluids quickly

(A) Step

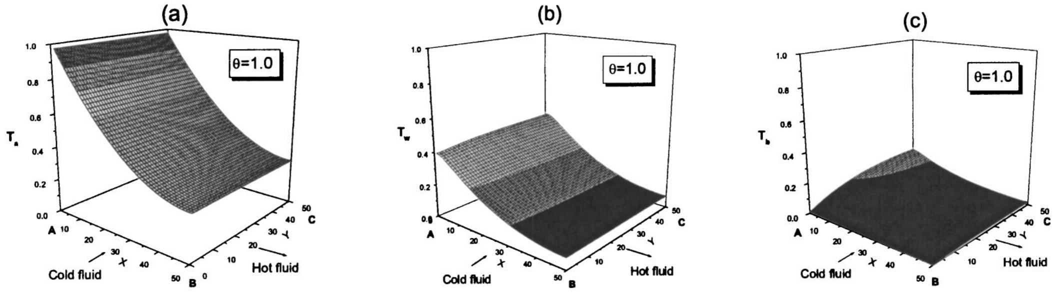

(B) Ramp

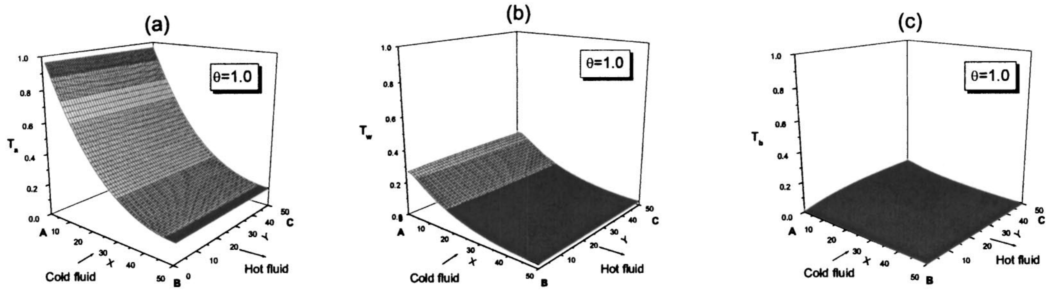

(C) Exponential

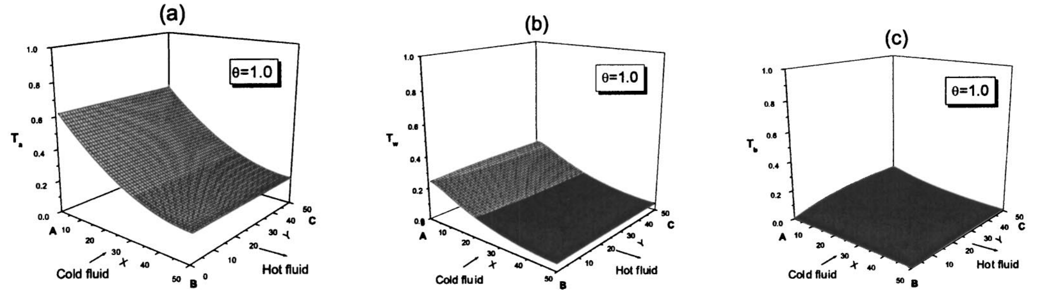

Fig. 4 Two-dimensional temperature distribution of (a) hot fluid, (b) wall, and (c) cold fluid at time $\theta=1$, for (A) step, (B) ramp, and (C) exponential inputs with $E=R=V=\text{Pe}=1$, NTU=2, $\lambda=0.025$ with no flow transients

reaches the steady state value. As the capacitance ratio is increased, more time is taken by the fluid to reach the steady state (Fig. 7(a)). In the presence of longitudinal conduction in wall and axial dispersion in fluids the effect of change of heat capacity ratio is not that much predominant (Fig. 7(b)). The difference in mean exit temperatures due to increase in V is less and also it takes much smaller time to reach to its steady state value compared to the case when the effect of core longitudinal conduction and the fluid axial dispersion is absent. The effect is similar for step, ramp and exponential inputs.

Effect of Axial Dispersion. Nonuniformity in flow at the molecular level comes into picture due to eddy diffusion in the axial direction. This effect may be taken care of by modifying the ideal plug-flow model. An apparent axial heat conduction or axial dispersion term is introduced into the energy balance. Due to presence of molecular conductivity and conductivity due to eddy diffusion, an apparent heat conductivity or diffusion coefficient is considered, which leads to a dimensionless parameter termed as axial dispersive Peclet number ($\text{Pe}=mcL/A_cD$). A smaller value of Pe corresponds to a highly dispersive flow and $\text{Pe}\rightarrow\infty$ leads to the ideal plug flow model, while Pe other than ∞ represents axial dispersion in the fluid stream. One of the aims of the present work is to study the effect of axial dispersion of the fluids on the dynamic performance of heat exchangers in details. In the presence of axial dispersion there is an additional mode of heat transport in the direction of fluid flow. This not only changes the local and spatial temperature of the fluid streams, but may also have a significant effect on the energy balance. It is of particular interest to study the effect when the Peclet numbers are different for the two fluid streams. In the limiting condition this may lead to a situation when one of the fluids may have a high axial dispersion, while the effect is absent ($\text{Pe}=\infty$) in the other fluid.

In general the designers try to select the dimensions of the heat exchangers such that maximum exchange of energy takes place between the streams. This will result in a small temperature gradient in the individual fluid streams at the exit of the heat exchanger. It is the usual practice to impose a zero flux condition at the exit of the heat exchanger. Thermal energy will be transported away from the heat exchanger only through advection, whereas at the entry to the heat exchanger ''conductive'' heat transport will also be present. An elaborate study of these effects on the performance of crossflow heat exchangers has been made and the salient results are presented below.

The effects of variation of Pe on dynamic behavior of hot and

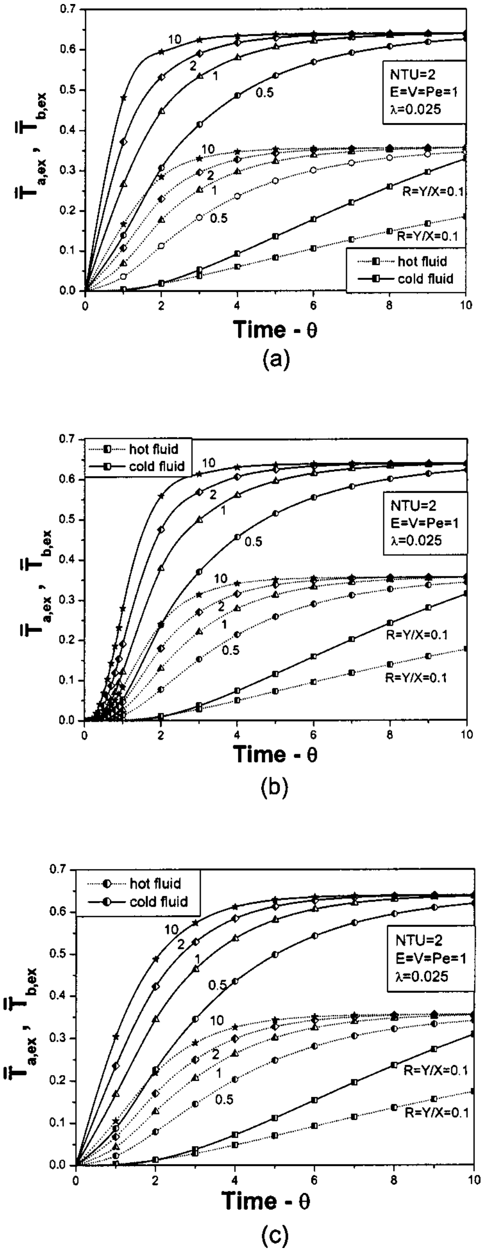

Fig. 5 Effect of aspect ratio (*Y*/*X*) on mean exit temperature of both the fluids with (a) step, (b) ramp, and (c) exponential inputs without longitudinal conduction and axial dispersion

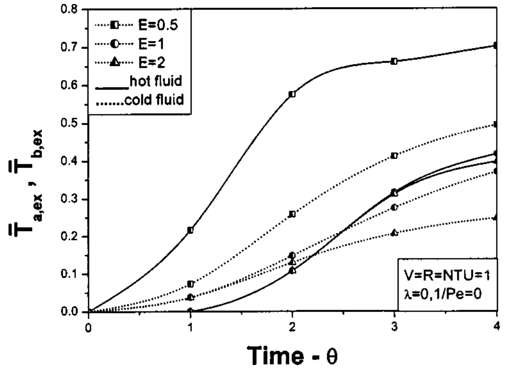

Fig. 6 Effect of heat capacity rate ratio on mean exit temperature of both the fluids for step input

cold fluids can be studied from Fig. 8. In the first investigation both the fluid streams are assumed to have identical Pe (Fig. 8(a)). On decreasing Pe, the mean exit temperature of hot fluid increases showing reduction in the amount of heat transfer. Pe=1 leads to highly dispersive condition. The phenomena in the cold fluid is same in the initial phase, afterwards the mean exit temperature decreases with the reduction in Pe, which again indicates the less amount of heat transfer and in turn, deterioration in performance. The amount of deterioration in cold fluid is comparatively less compared to that in hot fluid in all the cases. Due to the phenomena involved with axial dispersion as described earlier, the fluid exit temperatures reach the steady state faster at low Pe, i.e., with high axial dispersion. The behavior is similar for step, ramp and exponential inputs. For a quick assessment of the energy balance one may refer to Fig. 8(a) in which the hot and the cold fluid temperatures are separately depicted on left and right hand coordinates respectively. For all the values of Peclet number, to start with, the exit temperatures of the fluid streams exhibit a large difference indicating sufficient storage of thermal energy in the separating plate. Gradually, as one approaches towards steady state this difference decreases. For Pe=1 it may be noted that the exit temperature curves coincide with each other indicating attainment of steady state where $T_{a,ex}=0.638$ and $T_{b,ex}=0.355$ (at $\theta=10$). Summation of these two temperatures tends to unity, which indicates that convective heat gain of one of the fluids is perfectly balanced by convective heat loss of the other. Though longer duration is needed to reach the steady state (as depicted in Fig. 8(a)) convective heat balance is satisfied in all the cases (not shown in the figure). From Fig. 8(b) it can be seen that convective

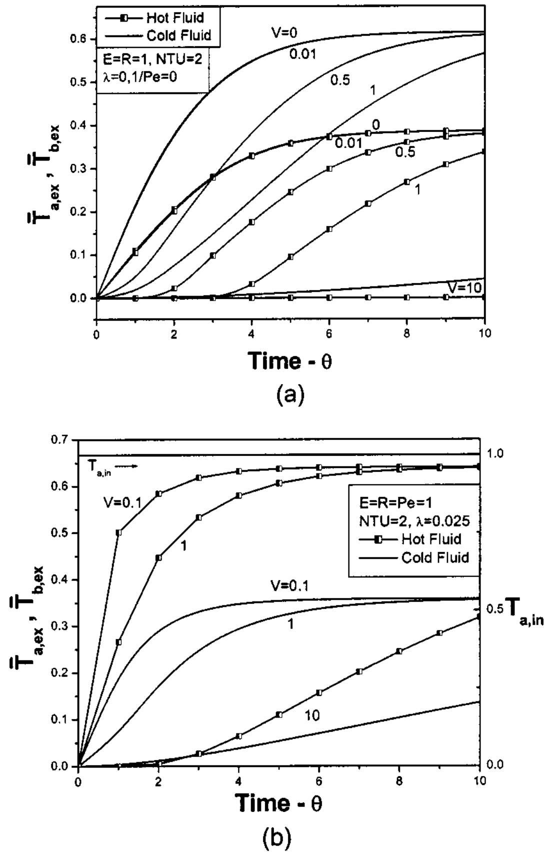

Fig. 7 Effect of fluid capacitance ratio on step response of mean exit temperature of hot and cold fluids (a) without longitudinal conduction and axial dispersion, and (b) with longitudinal conduction and axial dispersion

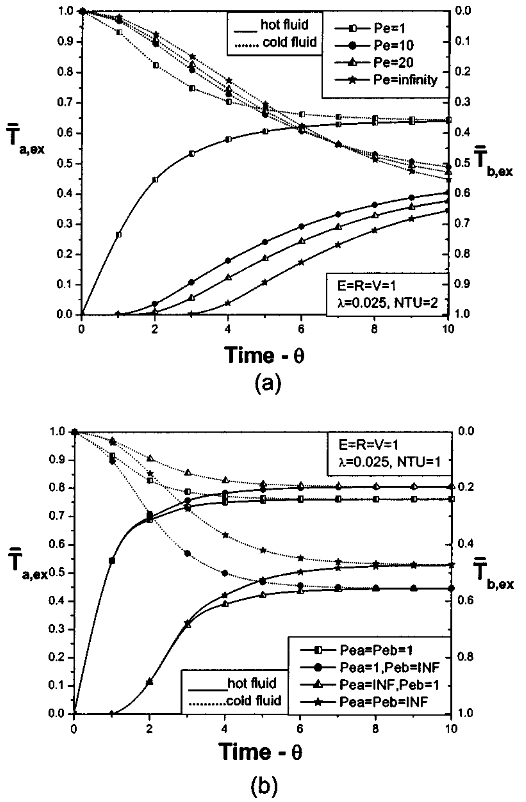

Fig. 8 Effect of axial dispersive Peclet number, Pe on mean exit temperature of both the fluids

heat balance is satisfied when Peclet number of both the fluid streams are of the same order. This includes all the cases from high axial dispersion to zero axial dispersion. However, when the axial dispersions are of different magnitudes in the fluid streams energy balance cannot be obtained considering only the convective heat transfer.

In practice the axial dispersive Peclet number of the fluid streams may have different values. To study the effect two different situations are considered. In the first case axial dispersion is present only in hot fluid while in the second case axial dispersion is present only in cold fluid. A part of the energy will be transported by conductive transport from or to the fluid having an axial dispersion. The value of conductive heat transfer will decrease with Peclet number as shown in Fig. 9. The hot fluid entering the heat exchanger gain energy due to this phenomenon, while the entering cold fluid will lose energy. It may be noted that at a particular Pe, the gain is equal to the loss. This gives a perfect convective heat balance as shown in Figs. 8 and 10. In Fig. 10 the cold fluid exit temperature has been plotted as a function of hot fluid exit temperature. A diagonal joining the corners (1,0) and (0,1) has been drawn. When the steady state is located in this diagonal, a convective heat balance is indicated between the two streams. This is the case when both the fluids have identical Peclet numbers (points A and H in the figure). When axial dispersion is absent in the fluids, the steady state located at point A indicates the minimum cold fluid exit temperature and the maximum exit temperature for the hot fluid for cases when both the streams are having identical Peclet numbers. With the decrease of Pe, exit temperature of cold fluid increases, while there will be an equal decrease in the exit temperature of hot fluid. A theoretical bound of the exit temperatures for such cases may be obtained from point A to R.

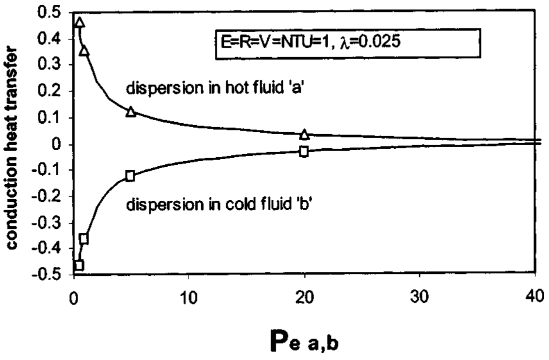

Fig. 9 Conductive heat transfer due to axial dispersion in any of the fluid streams

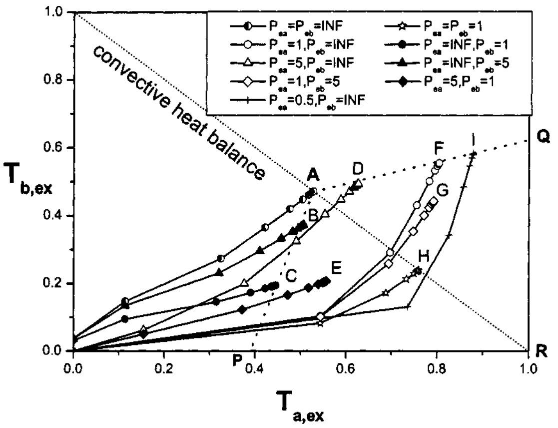

Fig. 10 Mean exit temperature of hot and cold fluids due to axial dispersion for step change in hot fluid inlet temperature

When the Peclet number of the fluids are not identical, the steady state will not be located on AR. When axial dispersion is present only in the hot fluid some additional amount of thermal energy will enter the stream due to temperature gradient at the inlet of the heat exchanger. Finally, a large portion of it will be transferred to the cold stream. The steady states (D,F,I) will be located on a line AQ indicating an increase in the cold fluid exit temperature. On the other hand if axial dispersion is present only in the cold fluid, it will lose certain amount of thermal energy while entering the exchanger. This will reduce the mean exit temperature of the cold fluid and will locate the steady-state positions on a line AP below AR. Therefore, Fig. 10 gives a convenient way of representing steady state operation of a crossflow heat exchanger in the presence of axial dispersion. The steady states will be located on a space bounded by the lines AP, PR, RQ, and QA. Line AR denotes identical Peclet numbers for both the fluids, value of Pe decreasing from A to R. AQ and AP are lines of infinite Pe for the hot and cold fluids, respectively. When axial dispersion of different orders are present in hot and cold fluids, the steady state will be located either in ΔAQR or in ΔAPR. For example, G is located inside ΔAQP; it indicates the steady state for $Pe_a < Pe_b$. On the other hand E indicates the reverse situation.

Longitudinal Conduction in Wall. Longitudinal conduction in case of conventional heat exchangers is often an insignificant effect. But for compact heat exchangers used in cryogenics and similar applications, it may result in serious performance deterioration. It has been shown [9] that for crossflow heat exchanger the deterioration is significant only at higher NTU's (8 or more) and it increases with the increase in NTU. As the NTU values are very high for cryogenic heat exchangers (sometimes as high as 500) because of high effectiveness, consideration of longitudinal conduction becomes essential in such equipments. Moreover, cryogenic and other compact heat exchangers have short conduction

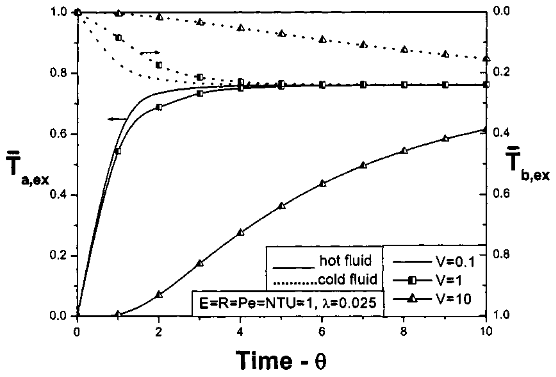

Fig. 11 Effect of capacitance ratio on step response of hot and cold fluid mean exit temperatures

lengths, which further enhances the effect of longitudinal conduction. In spite of the above facts extensive investigation has not been made to study the effect of longitudinal conduction on dynamic performance of compact crossflow heat exchangers. The sole work on this aspect is due to [9], which gives the effect of longitudinal conduction assuming large core capacity and negligible axial dispersion. In the present study it is intended to investigate the effect of longitudinal conduction in the presence of axial dispersion as well as for finite value of the core capacitance. Figure 11 depicts the response of crossflow heat exchanger in the presence of core longitudinal conduction and axial dispersion for different values of core capacity. Though the mean exit temperatures at steady state are identical in all the cases, temperature of both the fluid streams exhibit significant difference in the transient phase for a change of capacitance ratio from 10 to 1. This clearly shows the effect of core capacitance on the performance of heat exchanger. It is interesting to note that the effect of capacitance ratio reduces as its value is decreased. Moreover, at a low value of capacitance ratio steady state is reached much faster.

From the previous figure it has been seen that the axial conduction in the wall influences the performance of the heat exchanger during the transient period. However, the combined effect of longitudinal conduction and axial dispersion is not clear from this. To study the combined effect of both these phenomena transient response of the heat exchanger was computed for the four cases namely (i) without longitudinal conduction and axial dispersion, (ii) with longitudinal conduction only, (iii) with both longitudinal conduction and axial dispersion, and (iv) with axial dispersion only. The changes in mean exit temperatures for the case (ii) and (iv) with respect to the case (i) and (iii) respectively have been computed. As the results obtained for step, ramp and exponential excitation depict similar trend, only step response has been presented in Fig. 12. Effect of longitudinal conduction is different for hot and cold fluids. In both the cases the effect of longitudinal conduction becomes prominent with the increase in NTU. In general, Initially the mean exit temperature of hot fluid increases at a rapid rate in the presence of longitudinal conduction. Subsequently, it decreases and ultimately reaches to steady-state value. This gives a peak at all the values of NTU. It signifies that the effect of longitudinal conduction cannot be neglected during the transient conditions. Presence of axial dispersion along with longitudinal conduction gives the same behavior but the magnitude of the change is much smaller than that with pure longitudinal conduction.

The mean exit temperature of cold fluid exhibits a more complex behavior in the presence of axial dispersion. In general, there is decrease in the cold fluid exit temperature in the presence of longitudinal conduction. The relative change in temperature during the initial period of transients is more. Numerical value of the change in cold fluid exit temperature initially increases and then decreases finally leading to a steady-state value. In the presence of axial dispersion the change in temperature first increases positively and finally assumes a small negative value. Axial dispersion in the cold stream diminishes the effect of longitudinal conduction.

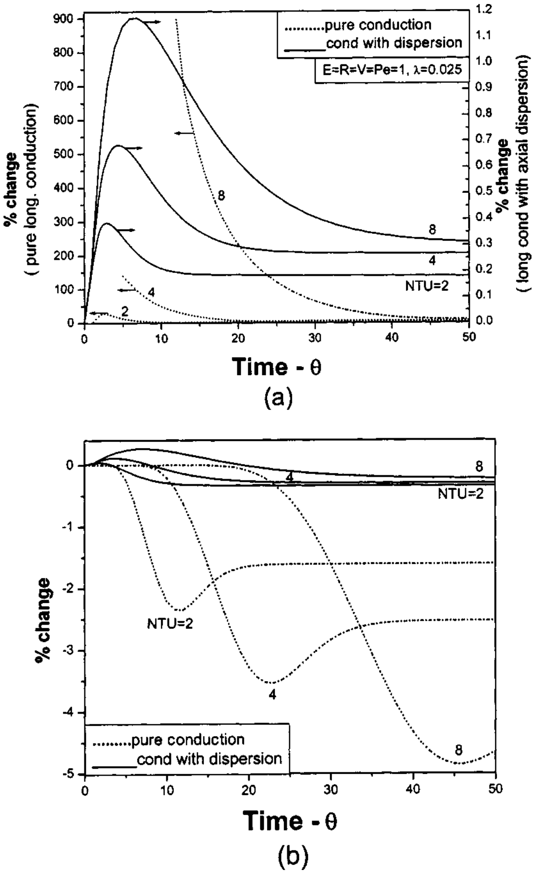

Fig. 12 Change in exit temperature of (a) hot and (b) cold fluid due to longitudinal conduction with and without fluid axial dispersion for step input

Conclusion

A numerical scheme has been developed for determining the transient behavior of crossflow heat exchangers using finite-difference method. Dynamic performance of the heat exchanger has been studied in response to step, ramp, and exponential excitation given to the inlet temperature of the hot fluid. Contrary to the conventional practice ramp and exponential input functions have been modified so that they reach a predefined maximum within a stipulated time period and then remain constant. The modified functions represent the transients generally observed in practice. Transient behavior has been obtained for a combined effect of finite core capacity, two-dimensional longitudinal conduction in wall and axial dispersion in fluids. Two-dimensional temperature distributions of the two fluids and the separating sheet may be obtained from the simulation to form the basis of detailed mechanical design. Conductive heat transport due to the presence of axial dispersion in fluids have been analyzed in detail and shown that presence of axial dispersion in both the fluid streams neutralises the total conductive heat transfer during the energy balance. It has also been shown that the presence of axial dispersion of high order reduces the effect of longitudinal conduction up to some extent. It has been observed that the longitudinal conduction plays an important role with the increase in NTU, similarly fluid axial dispersion is important when Pe is smaller. Both the conditions are very common in the case of compact crossflow heat exchangers having small sizes and working at high NTU and low values of Reynolds number. The detailed study of transient performance of crossflow heat exchangers will be useful for the detailed thermal and mechanical design and control of systems having such heat exchangers at different practical situations.

Nomenclature

A = area of heat transfer, m^2
A_c = area of cross-section, m^2
c, cp = specific heat of fluid, J/kg-K
C = specific heat of the wall material, J/kg-K
D = diffusion coefficient, W/m-K
E = capacity rate ratio$=(\mathrm{mc})_b/(\mathrm{mc})_a$
G = mass flux velocity, kg/m^2-s
h = heat transfer coefficient, W/m^2-K
k = thermal conductivity of the separating sheet, W/m-K
L = heat exchanger length, m
m = mass flow rate of fluid, kg/s
M = mass of the separating sheet, kg
N = hA/mc, dimensionless
NTU = number of transfer units, Eq. (7)
Pe = axial dispersive Peclet number$=(mc)L/A_cD$
R = conductance ratio$=(hA)_b/(hA)_a$
t = temperature, °C
$\underline{\mathrm{T}}$ = $t-t_{b,\mathrm{in}}/t_{\mathrm{REF}}-t_{b,\mathrm{in}}$, dimensionless temperature
T = mean dimensionless temperature
u, v = velocity in x and y direction
V = capacitance ratio$=\mathrm{LA}_c\rho c/\mathrm{MC}$
x, y = space direction
X = $(hA/mc)_a x/L_a$, dimensionless length
Y = $(hA/mc)_b y/L_b$, dimensionless length

Greek Letters

θ = $(hA)_a\tau/MC$, dimensionless time
ρ = density, kg/m^3
λ = longitudinal heat conduction parameter, $\lambda_a=k\delta L_b/L_a(mc)_a$, $\lambda_b=k\delta L_a/L_b(mc)_b$
δ = thickness of the separating sheet, m
τ = time, s
$\phi(\cdot)$ = perturbation in hot fluid inlet temperature

Subscripts

a = hot fluid
b = cold fluid
w = wall
in = inlet
ex = exit
max = maximum
min = minimum

References

[1] Dusinberre, G. M., 1959, ''Calculation of Transients in a Crossflow Heat Exchanger,'' ASME J. Heat Transfer, **81**, pp. 61–67.
[2] Myers, G. E., Mitchell, J. W., and Norman, R. F., 1967, ''The Transient Response of Crossflow Heat Exchangers, Evaporators, and Condensers,'' ASME J. Heat Transfer, **89**, pp. 75–80.
[3] Myers, G. E., Mitchell, J. W., and Lindeman, Jr., C. P., 1970, ''The Transient Response of Heat Exchangers Having an Infinite Capacitance Rate Fluid,'' ASME J. Heat Transfer, **92**, pp. 269–275.
[4] Yamashita, H., Izumi, R., and Yamaguchi, S., 1978, ''Analysis of the Dynamic Characteristics of Crossflow Heat Exchanger With Both Fluids Unmixed,'' Bull. JSME, **21**, pp. 479–485.
[5] Kou, H. S., and Yuan, P., 1994, ''Effect of Longitudinal Separator Sheet Conduction on the Transient Thermal Response of Crossflow Heat Exchangers With Neither Gas Mixed,'' Numer. Heat Transfer, Part A, **25**, pp. 223–236.
[6] Romie, F. E., 1983, ''Transient Response of Gas-to-Gas Crossflow Heat Exchangers With Neither Gas Mixed,'' ASME J. Heat Transfer, **105**, pp. 563–570.
[7] Gvozdenac, D. D., 1986, ''Analytical Solution of the Transient Response of Gas-to-Gas Crossflow Heat Exchanger With Both Fluids Unmixed,'' ASME J. Heat Transfer, **108**, pp. 722–727.
[8] Spiga, G., and Spiga, M., 1987, ''Two-Dimensional Transient Solutions for Crossflow Heat Exchangers With Neither Gas Mixed,'' ASME J. Heat Transfer, **109**, pp. 281–286.
[9] Spiga, G., and Spiga, M., 1988, ''Transient Temperature Fields in Crossflow Heat Exchangers With Finite Wall Capacitance,'' ASME J. Heat Transfer, **110**, pp. 49–53.
[10] Spiga, G., and Spiga, M., 1992, ''Step Response of the Crossflow Heat Exchanger With Finite Wall Capacitance,'' Int. J. Heat Mass Transfer, **35**(2), pp. 559–565.
[11] Romie, F. E., 1994, ''Transient Response of Crossflow Heat Exchangers With Zero Core Thermal Capacitance,'' ASME J. Heat Transfer, **116**, pp. 775–777.
[12] Chen, H. T., and Chen, K. C., 1991, ''Simple Method for Transient Response of Gas-to-Gas Cross-Flow Heat Exchangers With Neither Gas Mixed,'' Int. J. Heat Mass Transfer, **34**(11), pp. 2891–2898.
[13] Chen, H. T., and Chen, K. C., 1992, ''Transient Response of Crossflow Heat Exchangers With Finite Wall Capacitance,'' ASME J. Heat Transfer, **114**, pp. 752–755.
[14] Taylor, G., 1954, ''The Dispersion of Matter in Turbulent Flow Through a Pipe,'' Proc. R. Soc. London, Ser. A, **A-223**, pp. 447–468.
[15] Dankwerts, P. V., 1953, ''Continuous Flow Systems—Distribution of Residence Times,'' Chem. Eng. Sci., **2**(1), pp. 1–13.
[16] Sarangi, S., and Baral, H. S., 1987, ''Effect of Axial Conduction in the Fluid on Cryogenic Regenerator Performance,'' Cryogenics, **27**, pp. 505–509.
[17] Roetzel, W., and Xuan, Y., 1992, ''Analysis of Transient Behavior of Multipass Shell and Tube Heat Exchangers With the Dispersion Model,'' Int. J. Heat Mass Transfer, **35**(11), pp. 2953–2962.
[18] Das, S. K., and Roetzel, W., 1995, ''Dynamic Analysis of Plate Heat Exchangers With Dispersion in Both Fluids,'' Int. J. Heat Mass Transfer, **38**(6), pp. 1127–1140.
[19] Luo, X., and Roetzel, W., 1998, ''Theoretical Investigation on Cross-flow Heat Exchangers With Axial Dispersion in One Fluid,'' Rev. Gen. Therm., **37**, pp. 223–233.
[20] Ozisic, M. N., 1994, *Computational Methods in Heat Transfer*, CRC Press, London.

Fabrication and Performance of a Pin Fin Micro Heat Exchanger

Christophe Marques

Kevin W. Kelly
e-mail: kelly@me.lsu.edu

Mechanical Engineering Department,
2508 CEBA,
Louisiana State University,
Baton Rouge, LA 70803, USA

Nickel micro pin fin heat exchangers can be electroplated directly onto planar or non-planar metal surfaces using a derivative of the LIGA micromachining process. These heat exchangers offer the potential to more effectively control the temperature of surfaces in high heat flux applications. Of particular interest is the temperature control of gas turbine engine components. The components in the gas turbine engine that require efficient, improved cooling schemes include the gas turbine blades, the stator vanes, the turbine disk, and the combustor liner. Efficient heating of component surfaces may also be required (i.e., surfaces near the compressor inlet to prevent deicing). In all cases, correlations providing the Nusselt number and the friction factor are needed for such micro pin fin heat exchangers. Heat transfer and pressure loss experimental results are reported for a flat parallel plate pin fin micro heat exchanger with a staggered pin fin array, with height-to-diameter ratios of 1.0, with spacing-to-diameter ratios of 2.5 and for Reynolds numbers (based on the hydraulic diameter of the channel) from 4000 to 20,000. The results are compared to studies of larger scale, but geometrically similar, pin fin heat exchangers. To motivate further research, an analytic model is described which uses the empirical results from the pin fin heat exchanger experiments to predict a cooling effectiveness exceeding 0.82 in a gas turbine blade cooling application. As a final point, the feasibility of fabricating a relatively complex micro heat exchanger on a simple airfoil (a cylinder) is demonstrated. [DOI: 10.1115/1.1731341]

Keywords: Cooling, Finned Surfaces, Heat Transfer, Heat Exchangers, Microstructures

1 Background

1.1 Motivation. A major component in the development of advanced gas turbine engines is the increase of turbine inlet temperatures. Associated with this drive for higher turbine inlet temperatures is the need for more effective blade cooling strategies. Consequently, there is a significant ongoing effort in the gas turbine industry, federal laboratories, and academia directed at improving blade cooling technology.

Current cooling technology relies primarily on a combination of internal cooling through serpentine ribbed coolant passages that are integrally cast in the turbine blades and film cooling where a coolant is injected through a series of coolant holes on the blade surfaces. Due to the need for improved blade cooling, researchers are focusing attention on optimizing every aspect of the current technology. This includes depositing a protective coating on the blade surface, optimizing the shape and orientation of the rib turbulators in the coolant passages, exploring film cooling hole shapes and coolant injection angles, optimizing the location of the coolant holes, etc. The advances in this field have been encouraging and have led to, for example, thermal barrier coatings (TBC) on blade surfaces, the use of shaped holes for film cooling, and internal rib turbulators with V-orientations [1–4].

An important figure of merit used to quantify the thermal performance of a cooling scheme in a gas turbine is the cooling effectiveness, ε. The cooling effectiveness [1] is defined in Eq. (1).

$$\varepsilon=\frac{T_G-T_{\text{shroud}}}{T_G-T_C} \tag{1}$$

T_G corresponds to the characteristic temperature of gases surrounding the turbine blade. T_{shroud} is the temperature of the outer surface of the heat exchanger. T_C is the temperature at which the coolant is injected into the heat exchanger. The values taken by ε can vary between 0.0 and 1.0 depending upon the value of T_{shroud}. An effective cooling scheme provides a relatively high value of ε with a relatively low coolant-to-surrounding gases mass flow rate ratio. The typical range of ε in advanced cooling schemes for gas turbine blades is from 0.3 to 0.7 [5]. Improving significantly upon these numbers implies an increased cooling capability, and the potential to increase the allowable turbine inlet gas temperature and
pressure.

Enhancing heat transfer with increasingly complex internal cooling schemes usually causes increased pressure losses. This penalty has to be included in the assessment of the performance. Therefore, an overall thermal performance parameter is defined as [1]:

$$\eta=\frac{(\mathrm{Nu}/\mathrm{Nu}_o)}{(f/f_o)^{0.3}} \tag{2}$$

Nu and f are, respectively, average values of the Nusselt number and friction factor of the cooling scheme studied. The values with the subscripts are associated with a reference case. Values of η greater than 1.0 mean that the geometry studied has a better performance than the reference geometry.

The capability of electroplating nickel micro pin fin heat exchangers directly on planar or non-planar metal surfaces using a derivative of the LIGA micromachining process has been demonstrated [6–7]. A new method to fabricate a micro pin fin heat exchanger directly on a metal surface [8] is described in this paper that possibly provides increased latitude with respect to fabricating fine-scaled heat exchangers onto gas turbine components. The fabrication procedure involves electrodepositing a moderately dense array of microstructures (nickel or nickel-alloy) directly onto a surface with a nickel-alloy shroud on top. While the "double wall" concept is not new, the manufacturing approach is new, offering a wider range of micro feature dimensions that can be fabricated. A schematic of the concept for the case of a turbine blade is shown in Fig. 1, where the outer shroud is joined to the blade core by a field of microstructures. The nickel-alloy outer shroud is a few hundred micrometers thick. The gap separating the

---

Contributed by the Heat Transfer Division for publication in the JOURNAL OF HEAT TRANSFER. Manuscript received by the Heat Transfer Division July 24, 2003; revision received February 4, 2004. Associate Editor: P. M. Ligrani.

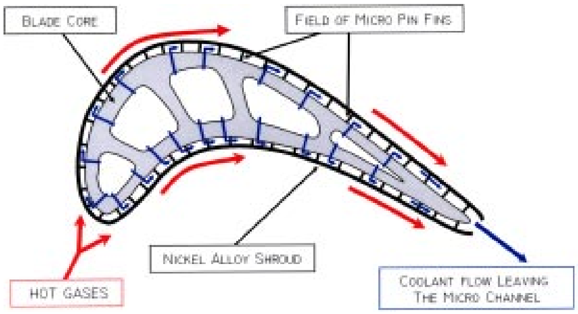

Fig. 1 Concept of a micro heat exchanger on the metal blade surface

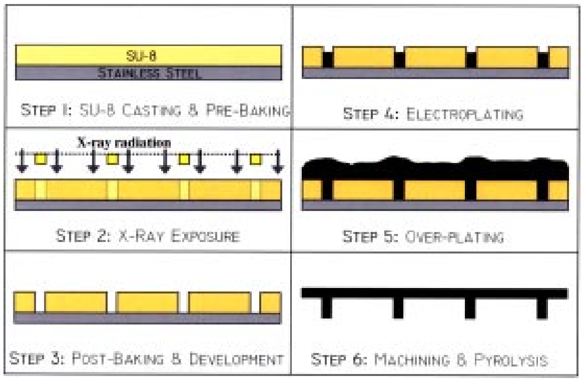

Fig. 2 A modified version of the LIGA manufacturing process

shroud and the internal core of the turbine blade ranges between from 100 to 1000 μm. The diameter of the microstructures can range from 50 μm to a few hundred micrometers, and the spacing between the microstructures is variable. The cross-sectional shape of the microstructures is arbitrary. In a gas turbine blade scenario, coolant (compressed air bled from the compressor) is directed through the core of the blade and into the micro pin fin heat exchanger via coolant holes located at several chord locations through the blade surface. The micro heat exchanger removes heat effectively from the outer shroud, maintaining the shroud temperature at a relatively low value.

The reasons why the micro pin fin heat exchanger is so effective are numerous: (i) their presence increases the wetted surface area available to heat transfer; (ii) they promote higher turbulence levels by breaking up boundary layers which causes mixing and creates higher convective heat transfer coefficients between endwalls and fluid; and (iii) the wetted surface area associated with the fins (where the flow configuration is typically referred as ‘‘cylinder in cross-flow’’ by Zhukauskas [9]) is characterized by convective heat transfer coefficients 3 to 4 times greater than for a smooth wall.

The expectation is that such a heat exchanger can effectively control the temperature of the exposed outer surface of the blade, even in high heat flux scenarios. The primary goal of this paper is to quantify the performance (Nusselt numbers and friction factors) of such a micro pin fin heat exchanger. Significant demonstrated improvements in effectiveness could motivate efforts to use micro pin fin arrays in gas turbine blade-cooling scenarios, independent of the manufacturing approach.

1.2 Heat Transfer With Pin Fin Heat Exchangers. Pin fin heat exchangers are defined in the context of this paper as two parallel plates (endwalls) connected by fields of cylindrical fins, with height-to-diameter ratios (h/d) in the range of 1 to 4. Coolant is pumped into the channel between the two endwalls while heat is transferred through one or both sides.

Since the early 1980s, numerous investigations have been motivated by the fact that banks of pin fins are used in the internal cooling channels at the trailing edge of turbine blades. In that case, pin fin height-to-diameter ratios are usually on the order of unity due to manufacturing constraints of internally cooling turbine blades [10]. In several publications, related work usually deals with quantifying heat transfer and/or pressure drop across arrays of circular pin fins. Major fundamental research studying geometrical parameters was conducted by authors such as Zhukauskas [9], Van Fossen [11], Metzer [12–13] and Chyu [14–16]. Important geometrical aspects are pin height-to-diameter ratio [9], array orientation (in-line or staggered) [14–15], fin cross-sectional shape [16], size of gap atop an array of fins (for partial length pin fins) [16–17], convergence of the channel [18], lateral flow ejection in pin fin channels [10], etc.

One key conclusion from the survey is the fact that geometry (h/d, spacing-to-diameter ratio of the pins) is a crucial parameter in determining heat transfer and friction factors. A second finding is that available heat transfer models are usually empirical because mathematical models for heat transfer or friction drag have not been developed yet for pin fin heat exchangers. This is due to the fact that for cylinder arrays where h/d is of the order of unity, the interaction between cylinder and endwall is very strong [14] and reliable analytical or numerical models for this endwall-pin fin interaction do not exist. Experimental studies [15] have indicated that the convective heat transfer coefficient at the endwall-fluid interface is only about 10 percent to 20 percent less than the values at the pin-fluid interface and much greater, by a scale factor of about 4, than would exist if the posts were not present (the parallel plate case) for Reynolds numbers (based on maximal velocity and pin fin diameter) from 5000 to 25,000.

The micro pin fin heat exchanger analyzed in this study is similar in pattern and design, but of smaller scale than pin fin heat exchangers that have been previously investigated [10,12–15]. The micro heat exchanger consists of a staggered pin fin array with the same height-to-diameter ratio of 1.0 and spacing-to-diameter ratio of 2.5 used in the previous work of Chyu [15]. Chyu's research uses the heat/mass transfer analogy which makes his study equivalent to an isothermal boundary condition problem where both endwalls are heated.

1.3 Fabrication of a Micro Pin Fin Heat Exchanger Using LIGA. The typical LIGA micromachining process [19–21] has been modified to fabricate micro heat exchangers. The manufacturing process [8] is shown in Fig. 2 and described as the following steps:

1. A layer of NANO™ SU-8 2075 [22] x-ray resist is cast onto a flat sandblasted stainless steel plate. The photoresist is pre-baked at 105°C and then flycut to the desired thickness, which typically corresponds to the desired height of the microstructures.
2. The SU-8 is exposed to x-rays using a gold absorber-on-graphite membrane mask containing the appropriate pin fin array geometry.
3. The SU-8 is post-baked at 96°C to allow the photoresist to crosslink in those regions exposed to radiation, then developed in NANO™ SU-8 developer [22].
4. The exposed and developed photoresist layer is used as a template in a subsequent electroplating process to define the shape of nickel microstructures. At first, the electroforming process fills up the voids in the SU-8.
5. Eventually the nickel microstructures merge when the SU-8 layer no longer constrains the electroplating process.
6. Once the nickel electroform is de-anchored from the stainless steel plate, the uneven overplated shroud is machined to the desired thickness. Then, the crosslinked SU-8 is removed by pyrolysis at 500°C.

A heat exchanger comprising a plate (or endwall) and a stag-

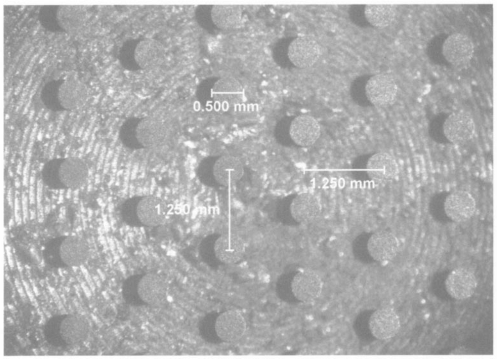

Fig. 3 Top view of the nickel micro pin fin heat exchanger

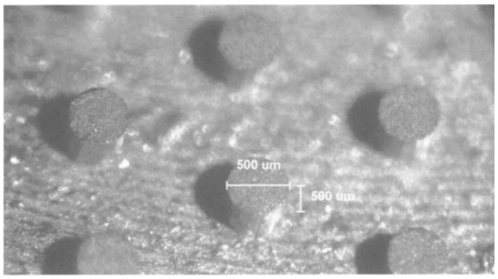

Fig. 4 Three-dimensional view of the nickel microstructures

gered array of pin fins was fabricated using the process described above. A 500 μm layer of SU-8 2075 was used in place of poly-(methyl methacrylate) (PMMA), the typical positive photoresist used in the LIGA process. The motivation for using SU-8 comes from the fact that SU-8 is approximately 200 times more sensitive to x-ray radiation than PMMA [23] which significantly reduces the exposure dose, hence the exposure time. SU-8 being a negative tone photoresist, x-ray lithography generates cross-linking within those regions that are exposed to radiation, making it insoluble in the SU-8 developer. The gold absorber mask was a graphite membrane covered with a 5.0 cm by 5.0 cm array of staggered 500 μm diameter gold x-ray absorber features spaced by a distance of 1.25 mm from center-to-center in both directions. The heat exchanger was successfully electroformed using a low-stress nickel sulfamate solution. The final height of the micro pin fins is 500 μm (the thickness of the SU-8 photoresist) while the post diameter and spacing correspond to the dimensions of the gold dots located on the x-ray mask. The lateral dimensions of the heat exchanger endwall are both 5 cm and the thickness is 2.54 mm. Pictures of the heat exchanger are provided in Figs. 3 and 4.

The final pin fin heat exchanger is created by clamping a 3.2 mm thick stainless steel plate to the array of pins electroplated onto the nickel plate. Both the stainless steel and the nickel plates have the same lateral dimensions.

2 Experimental Apparatus and Test Procedure

Experiments have been carried out to quantify the performance of the planar micro pin fin heat exchanger described in the previous section. The performance of this heat exchanger is compared to that of a similar heat exchanger without micro posts, i.e., flat parallel plates spaced 500 μm apart. The difference in performances isolates the enhancement associated with the pin fins.

2.1 Material Selection. The experimental apparatus is comprised of the following materials:

Aluminum 6061-$T6$: This metal was used to manufacture the heating block. The thermal conductivity is 165 W/m·K and varies by 10 percent as a function of temperature during the subsequent experiments.

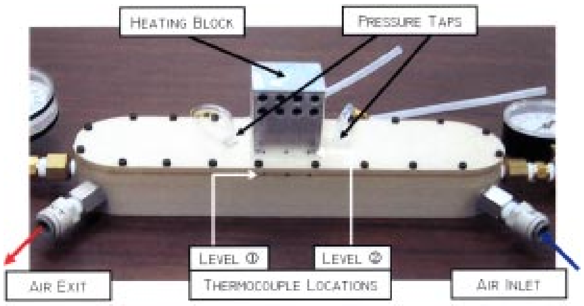

Fig. 5 Assembled apparatus

Virgin PEEK (PolyEtherEther-Ketone): This material was chosen to manufacture the upper and lower body parts of the apparatus. It has good strength, and the low thermal conductivity (0.25 W/mK) helps reduce the heat leakage rate.

Superflex™ Clear RTV Silicone Adhesive sealant (from Loctite Corp.): This silicone was used as a sealant between the heating block and the upper part of the apparatus. It has a low viscosity, so the film joining the heating block to the upper part of the apparatus is very thin.

Stainless steel 316: This metal was used to manufacture the lower plate used for both micro pin fin and parallel plate heat exchangers as well as the upper plate and shims used to create the parallel plate heat exchanger. The temperature dependent thermal conductivity is around 13.5 W/m·K and varies by 10 percent in the range of use.

Calsil (Calcium Silicate): This material was used to insulate the aluminum block from the ambient air. The thermal conductivity is 0.047 W/m·K.

A finite element model solving the steady state three dimensional heat equation in the materials comprising the upper body part of the experimental apparatus was performed on ANSYS 5.7 [8]. This model was used to estimate the percentage of heat losses (i.e., the percentage of energy input to the heaters that does not transfer into the fluid) during the heat transfer experiments. The predicted heat losses range from 10 to 6 percent for the parallel plate experiments and from 6 to 4 percent for the pin fin heat exchanger experiments.

2.2 Experimental Apparatus Description. The heat exchanger is sandwiched between the lower and upper halves of the experimental apparatus, which are screwed together as depicted in Fig. 5. After flowing through a pressure regulator and a filter, the

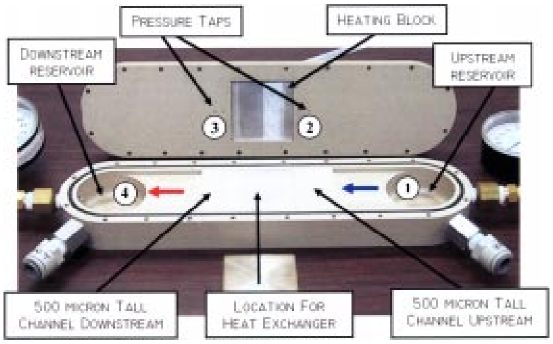

Fig. 6 Open view of apparatus

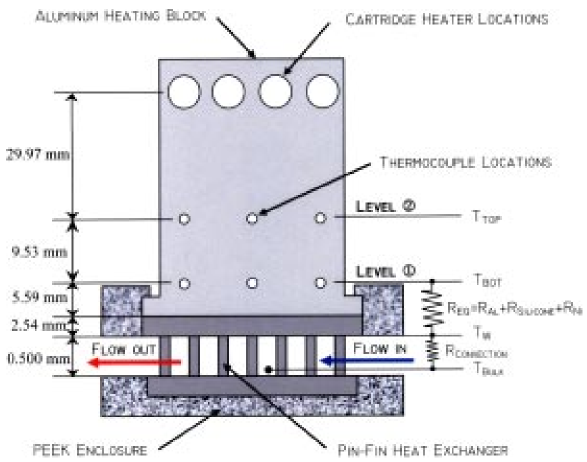

Fig. 7 Schematic of thermal resistances within the heat exchanger

coolant enters a 5 cm diameter and 2 cm deep reservoir machined into one end of the lower half of the PEEK apparatus (Fig. 6) and flows through a channel with rectangular cross section (5.0 cm wide and 3.2 mm high). The volumetric flow rate of the coolant is measured with a 2–25 SCFM (0.06–0.71 m^3/min) range direct-reading spring-loaded flow meter.

The channel height decreases to 500 μm (equal to the gap between the plates of the micro heat exchanger) a distance of 3.1 cm upstream of the entrance to the micro heat exchanger (Fig. 6). Recesses in both the upper and lower halves of the experimental apparatus are machined to accommodate the thickness of both the upper and lower plates of the heat exchanger (Fig. 6). These recesses allow the inner surfaces of the top and bottom plates of the heat exchanger to be flush with the upper and lower surfaces of the channel.

A schematic of the heat exchanger section of the assembled apparatus is shown in Fig. 7. Energy is transferred to the coolant through the upper surface of the heat exchanger which is tightly clamped to the bottom surface of the heating block. A 100 μm thick layer of thermally conductive silicone paste (OMEGATHERM® 201 with thermal conductivity of 2.3 W/m·K, from Omega Engineering Inc.) is used at the heating block-heat exchanger interface in order to minimize the contact resistance. The energy is supplied by four 120V–250W electric resistance cartridge heaters inserted into the aluminum block located directly above the heat exchanger (Fig. 5). Access for eight heaters can be seen in Fig. 5, but only four heaters were used in the holes located 45 mm from the heat exchanger. The total electrical power can be varied using a potentiometer and monitored using a digital wattmeter/multimeter. A small step in the cross section of the heating block is used to position and support the heater within the upper half of the apparatus. Above the step, the cross section of the heating block is 4.83 cm by 4.83 cm, below the step the cross section is 5 cm by 5 cm, which matches the footprint of the heat exchanger. The heaters, located within the block, are a sufficient distance from the heat exchangers to insure one dimensional conductive heat transfer within the block. In addition, the aluminum block is insulated to ensure that a very large percentage of the electrical energy is transferred to the coolant.

The 500 μm height of the channel remains constant through the longitudinal span of micro heat exchanger until 3.8 mm downstream of the heat exchanger (Fig. 6). At this point the height of the flow channel increases again to 3.2 mm before emptying into a downstream reservoir with same dimensions as the upstream reservoir.

As illustrated in Fig. 6, the inlet and exit temperatures of the coolant can be measured by thermocouples located, respectively, in the upstream reservoir (location ①) and downstream reservoir (location ④). The temperature profile within the aluminum block is obtained within two planes (marked as level ① and level ② in Figs. 5 and 7) perpendicular to the direction of the heat flow. Temperatures are measured inside of the 6 holes, 1.6 mm in diameter, drilled in the spanwise direction at three downstream locations and at both elevations. By varying the insertion depth of the thermocouple, the temperature can be measured at any spanwise location of the three possible downstream locations. Pressure taps located 12.7 mm upstream and 12.7 mm downstream of the heat exchanger (respectively marked as location ② and location ③ in Fig. 6) provide the static pressure drop. The pressure difference ΔP between the taps is quantified using a differential pressure transducer coupled to a strain gage meter. The upstream and downstream reservoir gage pressures as well as the upstream tap gage pressure are measured using spring loaded pressure gages.

2.3 Test Procedure. A series of experiments were conducted with both the pin fin heat exchanger and the parallel plate heat exchanger with compressed air used as a coolant. Results were obtained as a function of volumetric flow rate corresponding to a range of Reynolds numbers from 4000 to 20,000. Each flow rate was set and maintained to the desired value using the pressure regulator.

For each heat transfer experiment, the combined output power from the four resistance heaters was set to approximately 100 Watts using the potentiometer connected to the wattmeter.

For a given heat exchanger configuration, flow rate, pressure and temperature data acquisition was collected after steady state conditions were attained. Steady state was reached when the monitored temperature at the center of the heating block became constant. The pressures and temperatures of the coolant were recorded in all instrumented locations mentioned in the previous section.

Thermocouple measurements were taken within the aluminum block at levels ① and ② shown in Figs. 5 and 7. These measurements are used to quantify the heat flux through the top plate and the fluid-heat exchanger interface temperature. Throughout all experiments, temperatures inside the heating block at level ② were uniform within ±0.2°C (±0.5 percent) and within ±0.5°C (±1.0 percent) at level ①. Therefore, the heat transfer within the aluminum block just above the heat exchanger is well approximated as one-dimensional and the steady state temperature at a given level can be accurately characterized by a single temperature measurement in the middle of the heating block. In addition, one can assume that a very close approximation of a constant temperature boundary condition exists at the coolant-heat exchanger interface.

Regarding pressure loss experiments, the data acquisition procedure is similar to above, except that no power was supplied to the cartridge heaters and the experiments were performed at ambient temperature.

For the comparative parallel plate heat exchanger experiments, 500 μm thick shims were inserted to separate the two stainless steel plates. The thickness of the upper stainless steel plate was 2.54 mm (the same as the thickness of the electroplated nickel plate used in the pin fin heat exchanger).

3 Data Reduction

In the micro heat exchanger experiments that will be discussed, the coolant experiences significant increases of both sensible and kinetic energy as a result of heat transfer within the heat exchanger and pressure drop across the heat exchanger. For such cases, the rate of heat transfer $\dot{Q}$ is proportional to the difference in total temperature between the inlet and exit of the heat exchanger, as shown by a first law analysis of the control volume of the heat exchanger.

$$\dot{Q}=\dot{m}\left[C_P(T_3-T_2)+\frac{1}{2}(V_3^2-V_2^2)\right]=\dot{m}C_P(TT_3-TT_2) \quad (3)$$

where the total temperatures are defined by

$$TT_2 = T_2 + \frac{V_2^2}{2C_P} \tag{4}$$

$$TT_3 = T_3 + \frac{V_3^2}{2C_P} \tag{5}$$

The quantities $\dot{m}$, V, and C_P respectively denote the mass flow rate, velocity, and specific heat at constant pressure of the coolant.

Due to the much larger channel cross sections at locations ① and ④, the coolant velocity (kinetic energy) at locations ① and ④ is negligible. Assuming heat transfer is negligible between locations ① and ②, it is easy to show that TT_2 is equal to T_1, the static temperature at location ①. With the same set of assumptions, TT_3 is equal to T_4, the static temperature at location ④. Therefore, the heat transfer rate equation can be modified as given by Eq. (6) below

$$\dot{Q} = \dot{m} C_P (T_4 - T_1) \tag{6}$$

Given the relatively constant surface temperature boundary condition associated with these experiments, the average difference between the coolant-heat exchanger interface temperature T_w and the coolant temperature decays exponentially, [24]. The value of the average difference, known as the log mean temperature difference ΔT_{lm}, is defined by Eq. (7).

$$\Delta T_{lm} = \frac{(T_w - T_1) - (T_w - T_4)}{\ln\left(\frac{T_w - T_1}{T_w - T_4}\right)} \tag{7}$$

In this study, the average convective heat transfer coefficient h_w at the coolant-heat exchanger interface is defined as

$$h_w = \frac{\dot{Q}}{A_{\text{heat}} \Delta T_{lm}} \tag{8}$$

A_{heat} is the area of contact (5 cm by 5 cm) between the heating block and the heat exchanger, not the total wetted surface area actually available for heat transfer. Therefore A_{heat} is the same for both the parallel plate and micro pin fin heat exchangers. ΔT_{lm}, the log mean temperature difference is calculated using Eq. (7). The methods to measure $\dot{Q}$ and T_w, the average coolant-heat exchanger interface temperature, are discussed subsequently.

It is important to notice that Chyu's studies, which involve the naphthalene sublimation technique and the heat/mass transfer analogy, do not need to incorporate the compressibility effects of the present study.

Convective heat transfer coefficients are functions of geometry, Reynolds number, and Prandtl number. The Reynolds number Re used herein and defined in Eq. (9) is based on the average minimal velocity of the coolant V and the hydraulic diameter of the micro channel D_h, which is twice the height H of the gap. The quantities ρ, μ, and A respectively designate the density, dynamic viscosity and cross-sectional area of the coolant flow.

$$\text{Re} = \frac{\rho V D_h}{\mu} \quad \left(\text{or } \text{Re} = \frac{\dot{m} D_h}{A \mu}\right) \quad \text{where } D_h = 2H \tag{9}$$

The average Nusselt number defined below customarily presents the convective heat transfer coefficient in the dimensionless form with k designating the thermal conductivity of the coolant.

$$\text{Nu} = \frac{h_w D_h}{k} \tag{10}$$

In order to determine h_w, the unknowns $\dot{Q}$ and T_w have to be determined for each mass flow rate of coolant and each heat exchanger configuration.

$\dot{Q}$, the total amount of heat transferred to the coolant, can be determined by three different ways:

1. Quantify the heat leakage from the aluminum block with a finite element model: The quantity $\dot{Q}_{\text{electric}}$ is the wattmeter reading of the total electrical power dissipated by the heaters. According to specifications provided by the wattmeter manufacturer, the relative uncertainty of the measured quantity is ±2 percent. The variable β, which represents the percentage of heat lost to the surroundings, is calculated with the ANSYS heat transfer finite element model of the upper part of the experimental apparatus. The range of values taken by β depends on the heat exchanger type (pin fin or parallel plate) and the mass flow rate of coolant, as mentioned earlier in section 2.1. The rate of heat transfer to the coolant, $\dot{Q}_{\text{ANSYS}}$, is defined in Eq. (11). The final relative uncertainty on the calculation of $\dot{Q}_{\text{ANSYS}}$ is estimated to be ±5 percent.

$$\dot{Q}_{\text{ANSYS}} = \left(1 - \frac{\beta}{100}\right) \dot{Q}_{\text{electric}} \quad \text{where}$$
$$\beta = f(\text{Re, heat exchanger type}) \tag{11}$$

2. Measure conduction heat transfer through the upper surface of the heat exchanger: By using the temperatures measured above the heat exchanger at level ① and level ②, referred to as T_{bot} and T_{top} in Fig. 7. These temperatures, coupled with the known thermal conductivity of the metal k_{Al}, the cross section of the aluminum block A_{heat} and the distance $d_{\text{top-bot}}$ between level ① and level ②, provide the necessary inputs to Eq. (12) to calculate $\dot{Q}_{\text{conduction}}$, the rate of heat transferred by conduction to the upper surface of the heat exchanger. Using the Kline and McClintock method [25], the relative uncertainty of this technique ranges from 19 percent to 21 percent for both the parallel plate and micro pin fin heat exchangers, at any given coolant mass flow rate. The reasons for this high uncertainty will be explained later.

$$\dot{Q}_{\text{conduction}} = \frac{A_{\text{heat}} k_{\text{Al}} (T_{\text{top}} - T_{\text{bot}})}{d_{\text{top-bot}}} \tag{12}$$

3. Measure the enthalpy rise of the coolant: A final method to calculate the energy supplied to the coolant is to measure the enthalpy rise of the coolant, as described by Eq. (13). The relative uncertainty of $\dot{Q}_{\text{convection}}$ calculated using the Kline and McClintock method [25], increases monotonically from 4 percent to 12.5 percent with decreasing coolant mass flow rate.

$$\dot{Q}_{\text{convection}} = \dot{m} C_P (T_4 - T_1) \tag{13}$$

The first method described above provides an estimate of the total amount of heat transferred to the coolant with the lowest amount of uncertainty. Therefore, $\dot{Q}_{\text{ANSYS}}$ represents the best estimate of the heat transferred to the coolant. The other estimates of heat transfer, $\dot{Q}_{\text{conduction}}$ and $\dot{Q}_{\text{convection}}$ are provided to show consistency between all three approaches.

The last unknown in Eq. (8), T_w, is found using a one-dimensional series of thermal resistances connecting the horizontal plane with thermocouple holes at level ① and the coolant-heat exchanger interface. The validity of this one-dimensional heat transfer model was verified using a finite element study that yielded a model accuracy ranging from 1 percent to 3 percent. As depicted in Fig. 7, this series of thermal resistances consists of:

- a conduction resistance through the aluminum R_{Al}
- a contact resistance through the thin layer of thermally conductive silicone paste $R_{silicone}$, at the heat exchanger-aluminum interface
- a conductive resistance through the nickel (or stainless steel) upper plate of the heat exchanger R_{Ni} (or R_{SS})

R_{Al} and R_{silicone} are equal to 0.34 and 0.43 $\text{cm}^2 \cdot \text{K/W}$, respectively. The thermal resistance through the top plate of the nickel heat exchanger, R_{Ni}, is equal to 0.28 $\mathrm{cm}^2\cdot\mathrm{K/W}$ while the corresponding resistance through the stainless steel top plate of the parallel plate heat exchanger, R_{SS}, is equal to 1.88 $\mathrm{cm}^2\cdot\mathrm{K/W}$. The total resistance for each case is the sum of the three resistances in series, as shown below in Eqs. (14) and (15). The value of R_{eq} for the pin fin heat exchanger is 1.05 $\mathrm{cm}^2\cdot\mathrm{K/W}$, while for the parallel plate heat exchanger, R_{eq} is equal to 2.65 $\mathrm{cm}^2\cdot\mathrm{K/W}$.

$$R_{\mathrm{eq}}=\frac{l_{\mathrm{Al}}}{k_{\mathrm{Al}}}+\frac{l_{\mathrm{silicone}}}{k_{\mathrm{silicone}}}+\frac{l_{\mathrm{Ni}}}{k_{\mathrm{Ni}}} \quad \text{for pin fin heat exchanger} \tag{14}$$

$$R_{\mathrm{eq}}=\frac{l_{\mathrm{Al}}}{k_{\mathrm{Al}}}+\frac{l_{\mathrm{silicone}}}{k_{\mathrm{silicone}}}+\frac{l_{\mathrm{SS}}}{k_{\mathrm{SS}}} \quad \text{for parallel plate heat exchanger} \tag{15}$$

Equation (16) (see Fig. 7) can be used to solve for T_w at any volumetric flow rate of coolant.

$$T_w=T_{\mathrm{bot}}-\frac{\dot{Q}}{A_{\mathrm{heat}}}R_{\mathrm{eq}} \tag{16}$$

The friction factor in the heat exchanger is a function of Reynolds number and geometry. When the flow is incompressible, its value is a nondimensional definition of the pressure drop ΔP_{HE} in the heat exchanger given by

$$f=\frac{\Delta P_{HE}}{0.5(\rho V^2)}\frac{D_h}{L} \tag{17}$$

When compressibility is important, the value of ρV^2 can vary greatly between inlet and exit of the heat exchanger. For such a case, the friction factor is best expressed as a function of the pressure gradient dP/dx given in Eq. (18).

$$f=\frac{dP}{0.5\rho(x)V(x)^2}\frac{D_h}{dx} \tag{18}$$

Assuming air is an ideal gas of constant R_{air} and neglecting the changes in coolant temperature, Eq. (18) can be integrated along any segment of the micro channel where the internal geometry (thus the friction factor) is uniform.

In the case of the smooth channel (parallel plate heat exchanger), the geometry of the micro channel is uniform from location ② to location ③ (i.e., the succession of the 12.7 mm long inlet development channel, the micro pin fin heat exchanger, and the 12.7 mm long exit development channel). Integration of Eq. (18) between the pressure taps located at ② and ③ of Fig. 6 results in Eq. (19), the expression of the friction factor $f_o(\mathrm{Re})$ for a given Reynolds number in the smooth channel configuration. The quantities T_{ave} and L_{2-3} are respectively the coolant average temperature and the distance between location ② and location ③.

$$f_o(\mathrm{Re})=\frac{(P_2^2-P_3^2)A^2}{R_{\mathrm{air}}T_{\mathrm{ave}}\dot{m}^2}\frac{D_h}{L_{2-3}} \tag{19}$$

To obtain $f(\mathrm{Re})$ for the micro pin fin heat exchanger, Eq. (18) is integrated from the inlet to the exit of the heat exchanger because the internal geometry of the heat exchanger is different from the internal geometry of the inlet and exit development channels. The result of the integration is Eq. (20) where P_{inlet}, P_{exit}, $L_{\text{inlet-exit}}$, and T_{ave} are respectively the coolant inlet pressure, exit pressure, average temperature and the streamwise dimension of the heat exchanger.

Table 1 Pressure loss calculations for the micro pin fin heat exchanger

Quantity	Mathematical Model
$\Delta P_{\mathrm{inlet}}$	$\frac{f_o(\mathrm{Re})\rho_2 V_2^2 L_{2\text{-inlet}}}{2D_h}$
P_{inlet}	$P_2-\Delta P_{\mathrm{inlet}}$
ΔP_{exit}	$\frac{f_o(\mathrm{Re})\rho_3 V_3^2 L_{\text{exit-3}}}{2D_h}$
P_{exit}	$P_3+\Delta P_{\mathrm{exit}}$

$$f(\mathrm{Re})=\frac{(P_{\mathrm{inlet}}^2-P_{\mathrm{exit}}^2)A^2}{R_{\mathrm{air}}T_{\mathrm{ave}}\dot{m}^2}\frac{D_h}{L_{\text{inlet-exit}}} \tag{20}$$

In order to calculate P_{inlet} and P_{exit}, one must realize that the differential pressure ΔP_{23} between the two pressure tap locations ② and ③ measured by the pressure transducer is the sum of three main components:

1. $\Delta P_{\mathrm{inlet}}(=P_2-P_{\mathrm{inlet}})$: the pressure drop associated with the frictional losses in the smooth inlet development channel.
2. $\Delta P_{HE}(=P_{\mathrm{inlet}}-P_{\mathrm{exit}})$: the pressure drop corresponding to the frictional losses within the heat exchanger only.
3. $\Delta P_{\mathrm{exit}}(=P_{\mathrm{exit}}-P_3)$: the exit pressure drop associated with the frictional losses in the smooth exit development channel.

Table 1 summarizes how P_{inlet} and P_{exit} are calculated with $L_{2\text{-inlet}}$ and $L_{\text{exit-3}}$ being respectively the length of the 500 μm high inlet and the 500 μm high exit development channels. The components $\Delta P_{\mathrm{inlet}}$ and ΔP_{exit} are calculated using the value of $f_o(\mathrm{Re})$ for smooth channels and lead to the determination of P_{inlet} and P_{exit}. Equation (20) can then be used to compute the value of the friction factor for the pin fin heat exchanger as a function of Re.

4 Results and Discussion

Repeatability for all the test runs was within 5 percent. The raw data collected during the experiments was reduced according to the equations described above and the results are provided in Tables 2–5.

Nusselt number and friction factor experimental results as a function of Reynolds number are plotted respectively in Figs. 8 and 9 with error bars determined using the Kline and McClintock method [25]. As expected, the presence of the pin fins has a dramatic effect on both heat transfer and pressure losses.

4.1 Heat Transfer Results.

From Tables 2 and 4 the following trends are observed:

- The temperatures within the heating block (T_{bot}, T_{top}, and T_w) decrease as the mass flow rate (Reynolds number) increases for both the micro pin fin and parallel plate heat exchangers.

Table 2 Heat transfer results for the parallel plate heat exchanger ($\dot{Q}_{\mathrm{electric}}=100$ W)

$\dot{m}$ (kg/s)	Re	T_1 (°C)	T_4 (°C)	T_{bot} (°C)	T_{top} (°C)	T_w (°C)	$\dot{Q}_{\mathrm{ANSYS}}$ (W)	$\dot{Q}_{\mathrm{conduction}}$ (W) (%$\dot{Q}_{\mathrm{ANSYS}}$)	$\dot{Q}_{\mathrm{convection}}$ (W) (%$\dot{Q}_{\mathrm{ANSYS}}$)	h_w (W/m^2 K)	Nu
0.0023	4200	20.1	55.5	145.1	147.5	134.9	88.5	107(121)	80(90)	358	11.6
0.0045	9100	18.0	37.9	86.7	89.1	76.2	93.8	107(114)	90(97)	769	27.3
0.0068	14,000	18.0	31.8	70.1	72.4	59.5	97.2	103(106)	94(97)	1101	40.1
0.0091	18,800	18.2	28.7	61.2	63.5	50.6	97.2	103(106)	95(98)	1407	52.0

Table 3 Pressure loss results for the parallel plate heat exchanger

$\dot{m}$ (kg/s)	Re	T_1 (°C)	T_4 (°C)	ΔP_{HE} (kPa)	f
0.0017	3700	20.6	20.8	2	0.026
0.0028	6100	20.6	20.8	7	0.031
0.0040	8700	20.6	20.7	12	0.031
0.0051	11,200	20.5	20.6	17	0.032
0.0062	13,800	20.4	20.7	21	0.029
0.0074	16,200	20.5	20.7	26	0.029
0.0085	18,700	20.3	20.6	30	0.032
0.0096	21,200	20.5	21.0	34	0.032

Table 5 Pressure loss results for the micro pin fin heat exchanger

$\dot{m}$ (kg/s)	Re	T_1 (°C)	T_4 (°C)	ΔP_{HE} (kPa)	f
0.0017	3700	20.3	20.5	47	0.640
0.0028	6100	20.0	21.1	83	0.490
0.0040	8700	19.9	20.5	134	0.498
0.0051	11,200	19.9	20.4	185	0.512
0.0062	13,700	20.1	20.0	223	0.477
0.0076	16,800	20.1	19.7	288	0.515
0.0088	19,300	20.1	19.7	315	0.479

- The heat transfer to the coolant (most accurately quantified by $\dot{Q}_{ANSYS}$) increases with mass flow rate (Reynolds number) for both the micro pin fin and parallel plate heat exchangers.
- The temperatures within the heating block at a given Reynolds number are much lower for the case of the micro pin fin heat exchanger.

These trends are explained by the facts that (i) for either heat exchanger geometry, the convective thermal resistance decreases monotonically as the Reynolds number increases, and (ii) convective thermal resistance associated with the micro heat exchanger is much less than that of the parallel plate heat exchanger. As the convective resistance decreases (whether due to geometry or Reynolds number), the temperatures within the heating block decrease, thereby reducing the amount of heat loss through the insulation.

In all the experiments (both parallel plate and micro pin fin), the electric power supplied to the heaters was 100 W. Tables 2 and 4 provide estimates of heat transferred to the coolant using each of the three methods described earlier by Eqs. (11–13). $\dot{Q}_{ANSYS}$ is the most accurate estimate of the *actual* heat transfer to the coolant.

For both sets of experiments, the agreement is excellent between $\dot{Q}_{\mathrm{convection}}$ and $\dot{Q}_{\mathrm{ANSYS}}$. The values are within 3 percent, except at the lowest flow rate, where the agreement is within 10 percent and 7 percent, respectively, for the parallel and pin fin cases. However, at the lowest volumetric flow rate, the relative uncertainty associated with the estimated convective heat transfer to the coolant is relatively high (±12.5 percent) so this calculation is not reliable. The reason for this high uncertainty is the fact that the volumetric flow rate is relatively small and comparable to the uncertainty of the measurement.

Additionally, for all the experimental runs the calculated heat transferred by conduction to the top plate of the heat exchanger is very close to or greater than 100 percent of $\dot{Q}_{\mathrm{ANSYS}}$. The explanation for values greater than 100 percent originates from the fact that the thermocouples measure the temperatures T_{top} and T_{bot} anywhere inside the 1.6 mm diameter holes located at level ① and level ②. This measurement creates relative uncertainties up to 17 percent in the distance between the two elevations which propagate into the calculation of $\dot{Q}_{\mathrm{conduction}}$.

In summary, at higher flow rates, $\dot{Q}_{\mathrm{ANSYS}}=\dot{Q}_{\mathrm{conduction}}=\dot{Q}_{\mathrm{convection}}$. This conclusion validates the temperature measurements in both the aluminum heating block and the air coolant stream. Also, it validates the assumption that the average heat flux over the entire heating block is well represented by the measured heat flux at the center of the heating block.

The Nusselt numbers obtained in this study are plotted in Fig. 8 with error bars. According to the graph, the presence of the micro pin fins enhances the heat transfer by a factor of 4.1 to 5.5 over the range of Reynolds number studied 4000 to 20,000. Surface roughness effects have not been included in the analysis since the relative surface roughness is negligible. Also displayed are experimental results from Kays and Crawford [26] for fully developed turbulent flow between parallel plates, with one side heated and the other insulated. In addition Fig. 8 shows the plot of a correlation from Incropera and DeWitt [24] valid for turbulent fully developed flow in circular tubes adapted for parallel plates (Eq. (21)).

$$\mathrm{Nu}_o=\frac{(f_o/8)(\mathrm{Re}-1000)\mathrm{Pr}}{1+12.7(f_o/8)^{0.5}(\mathrm{Pr}^{2/3}-1)} \qquad \begin{array}{c} f_o=0.316\,\mathrm{Re}^{1/4}\\ 0.5<\mathrm{Pr}<2000\\ 3000\leqslant\mathrm{Re}\leqslant 2\cdot 10^4 \end{array} \tag{21}$$

It appears that the experimental results for parallel plates are within 13 percent of the correlations from Incropera and DeWitt and within 18 percent of the data from Kays and Crawford. This very good match corroborates the reliability of the experimental apparatus and the validity of all the heat transfer experimental data. For turbulent flows, the convective heat transfer coefficient is the same whether one side of the heat exchanger is heated or both because the thermal boundary layer profile is similar.

Pin fin heat exchanger results are compared to Chyu's correlation [15] which corresponds to a heat transfer system in which the wetted surface is entirely isothermal and comprised of seven rows of posts with same array configuration as in the present study. Using the characteristic length scales defined in this study, Chyu's correction is given by Eq. (22):

$$\mathrm{Nu}=0.645\,\mathrm{Re}^{0.583}\,\mathrm{Pr}^{0.4} \qquad 6000\leqslant\mathrm{Re}\leqslant 30{,}000 \tag{22}$$

The Nusselt numbers computed in this study are in general higher than Chyu, diverging from very close agreement at a Reynolds number of around 6000 to 40 percent greater at a Reynolds number of 19,200.

Table 4 Heat transfer results for the micro pin fin heat exchanger ($\dot{Q}_{\mathrm{electric}}=100$ W)

$\dot{m}$ (kg/s)	Re	T_1 (°C)	T_4 (°C)	T_{bot} (°C)	T_{top} (°C)	T_w (°C)	$\dot{Q}_{ANSYS}$ (W)	$\dot{Q}_{\mathrm{conduction}}$ (W) (% $\dot{Q}_{\mathrm{ANSYS}}$)	$\dot{Q}_{\mathrm{convection}}$ (W) (% $\dot{Q}_{\mathrm{ANSYS}}$)	h_w (W/m^2 K)	Nu
0.0023	4500	20.5	58.7	73.0	75.5	69.0	93.3	112(120)	87 (93)	1468	51.8
0.0045	9400	20.3	40.4	46.6	49.0	42.6	93	107(115)	91 (97)	4186	154.9
0.0068	14,300	20.4	34.1	39.5	41.7	35.4	96	98(102)	93 (97)	6623	248.7
0.0091	19,200	20.6	31.5	36.9	39.2	32.8	96.3	103(107)	99(103)	7628	287.9

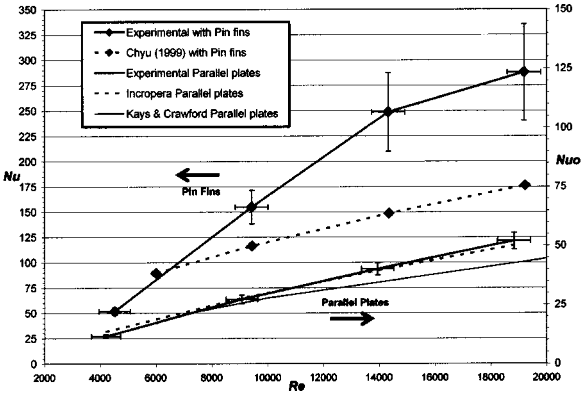

Fig. 8 Nusselt number as a function of Reynolds number

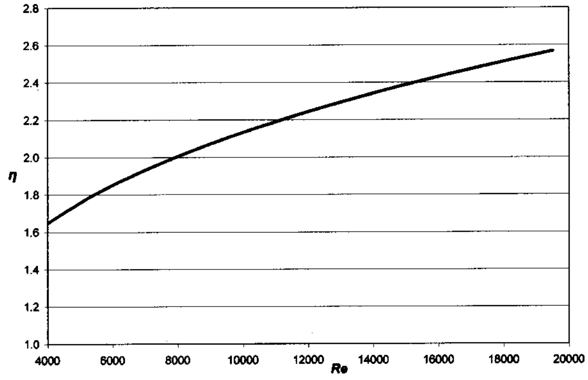

Fig. 10 Overall thermal performance parameter as a function of Reynolds number

The Nu–Re power correlation suggested for tested micro pin fin heat exchanger is given in Eq. (23).

$$\mathrm{Nu}=0.0022\,\mathrm{Re}^{1.221}\,\mathrm{Pr}^{0.4} \quad 4500 \leqslant \mathrm{Re} \leqslant 19{,}200 \tag{23}$$

As a final note, the micro pin fin heat exchanger has 36 percent more surface area than the parallel plate heat exchanger. This increase in wetted area represents a relatively insignificant contribution towards the measured 300–450 percent increase in heat transfer associated with the presence of the micro pin fins. Therefore, the major causes of heat transfer improvement are, as listed in the introduction of this paper (i) the enhanced mixing created by the micro pin fins which generates higher levels of turbulence, and (ii) the greater heat transfer coefficient associated to the geometry of the micro pin fins.

4.2 Pressure Loss Results. The experimental friction factors, which correspond to the data in Tables 3 and 5, are plotted in Fig. 9 with error bars. According to the graph, the presence of the micro pin fins increases the friction factor by a factor of 15 to 20 over the range of Reynolds number studied.

The correlation from Incropera and DeWitt [24] valid for turbulent fully developed flow in circular tubes adapted for parallel plates is shown in Eq. (24) and is also plotted in Fig. 9.

$$f_o=0.316\,\mathrm{Re}^{1/4} \quad \mathrm{Re} \leqslant 2\cdot 10^4 \tag{24}$$

It appears that the experimental results for parallel plates are within 15 percent of agreement with the correlated data from Incropera and DeWitt for Reynolds numbers ranging from 6200 to 19,000. Immediately outside of this range the discrepancies exceed 20 percent. Again, the very good match within a large range of Reynolds numbers confirms the reliability of the experimental apparatus and the validity of the pressure loss experimental data.

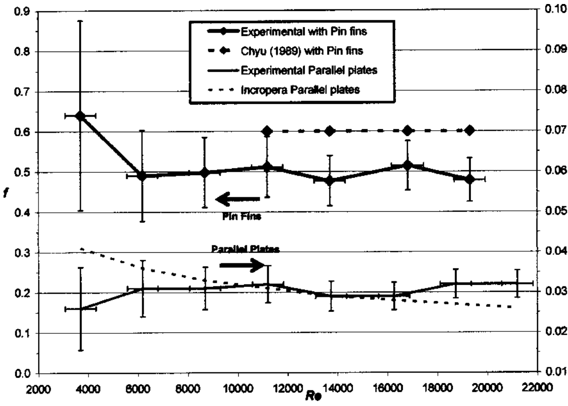

Fig. 9 Friction factor as a function of Reynolds number

In addition, pin fin heat exchanger results are compared to Chyu's experimental friction factor [14] which is approximately equal to 0.6 over the range of Reynolds numbers from 11,200 to 19,300 once the characteristic lengths defined in this study are consistently applied. The micro pin fin heat exchanger results are estimated to be within 26 percent of Chyu's data.

In conclusion, the experimental data is reliable, validated both by the results obtained with the parallel plate heat exchanger and by reasonable agreement with the pin fin heat exchanger results obtained by Chyu.

4.3 Overall Thermal Performance. As explained in the introduction, the performance of micro pin fin heat exchangers can only be assessed after including the penalty effects related to friction losses. The overall thermal performance parameter η as defined in Eq. (2) was calculated and plotted in Fig. 10.

According to the plot, at any Reynolds number η is larger than 1.0 meaning that the micro pin fin heat exchanger performance always exceeds the parallel plate counterpart. Since η increases (from 1.65 to 2.57) with increasing Reynolds numbers, the micro pin fin heat exchanger is best applied when mass flow rates of coolant are the largest.

The logical continuation of this research would be to optimize the pin fin array configuration in order to produce the best performance.

5 Model Prediction for Gas Turbine Blade Cooling

One long-term goal of this research effort is to more effectively cool gas turbine components with complex shapes (such as airfoils). The following model scenario sketched in Fig. 11 was developed to predict the cooling effectiveness of the flat micro pin fin heat exchangers in a gas turbine application.

The assumption is made that a heat exchanger consisting of a pin fin array identical to that described earlier covers a turbine blade airfoil. The outer surface (or shroud) of the airfoil is heated via radiation and convection by combustion gases at T_G. The effective convective heat transfer coefficient at the combustion gas-shroud interface is labeled as h_{external}. Air from the compressor enters the micro heat exchanger at a temperature T_C and pressure P_C typical of modern gas turbine engines. The mass flow rate of coolant per unit width of the channel and the specific heat at constant pressure are respectively $\dot{m}'$ and C_P. The temperature of the coolant T_{coolant}, increases as the coolant travels through the heat exchanger. The effective convective heat transfer coefficient h_w couples the heat transfer between the shroud and the coolant.

In this model, one-dimensional conduction in the shroud and an adiabatic boundary condition at the blade surface are assumed. An average overall heat transfer coefficient per unit width of the channel U can be defined as shown in Eq. (25) after neglecting the conductive thermal resistance in the shroud (this assumption is reasonable when the shroud thickness is in the order of 500 μm).

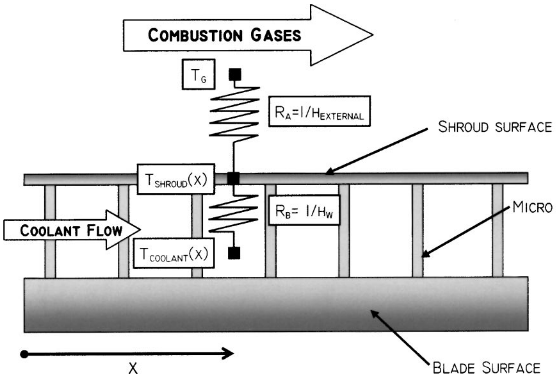

Fig. 11 Schematic of thermal resistances in the turbine blade model

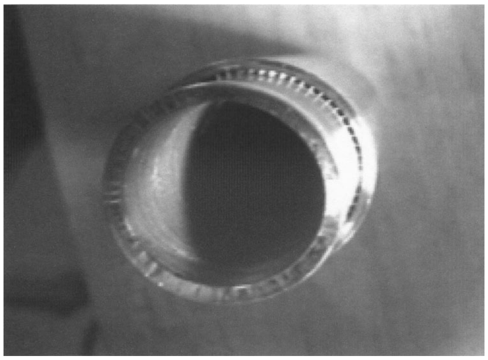

Fig. 12 Curved heat exchanger on a stainless steel tube

$$U=\frac{1}{\frac{1}{h_w}+\frac{1}{h_{\text{external}}}} \tag{25}$$

An energy balance applied to the coolant using the first law of thermodynamics yields a differential equation which was solved in Eq. (26) for $T_{\text{coolant}}(x)$, the temperature of the coolant as a function of the downstream location *x*. The use of thermal resistances yields Eq. (27), which provides the temperature of the shroud $T_{\text{shroud}}(x)$. Both $T_{\text{coolant}}(x)$ and $T_{\text{shroud}}(x)$ are functions of the mass flow rate per unit width of the channel $\dot{m}'$.

$$T_{\text{coolant}}(x)=T_G-(T_G-T_C)\exp\left(\frac{-Ux}{\dot{m}'C_P}\right) \tag{26}$$

$$T_{\text{shroud}}(x)=\frac{T_G h_{\text{external}}+T_{\text{coolant}}(x)h_w}{h_{\text{external}}+h_w} \tag{27}$$

In a typical gas turbine T_G, T_C, P_C, and h_{external} are respectively 2200 K, 700 K, 20 atmospheres [1] and 2500 $\text{W/m}^2\cdot\text{K}$. By using values for h_w from Table 4 (air cooled micro pin fin heat exchanger results), the cooling effectiveness $\varepsilon(x)$ defined in Eq. (1) was predicted at two distances $x_1=1$ cm and $x_2=2$ cm downstream from the coolant injection location. The summarized results of the model provided in Table 6 show that the shroud temperature varies, as expected, with mass flow rate and the distance *x* from the coolant injection point. If the shroud temperature at $x_1=1.0$ cm is chosen as the characteristic temperature of the shroud, then the analysis above provides cooling effectiveness values ranging from $\varepsilon=0.47$ to $\varepsilon=0.82$. The optimal combination of mass flow rate and heat exchanger design is a function of numerous variables (material properties, mission, etc.). This analysis is beyond the scope of this paper.

6 Curved Heat Exchanger on a Cylinder

To demonstrate the feasibility of the manufacturing process on non-planar surfaces, a curved micro pin fin heat exchanger was successfully manufactured onto the surface of a tube, which represents a first order approximation of the leading edge of a turbine blade [8]. A modified LIGA micro machining procedure similar to that described previously was developed to electroplate a nickel shroud of thickness 500 μm around a stainless steel tube with outer diameter equal to 19.1 mm. The shroud is supported by an in-line array of micro pin fins 500 μm in height, 200 μm in diameter and 1000 μm apart in both directions.

A picture of one such completed airfoil is shown in Fig. 12 and an SEM of the cross section of the actual heat exchanger on a tube is shown in Fig. 13. Heat transfer tests have been recently been performed to quantify the cooling effectiveness of such a heat exchanger. A detailed description of these tests and the results will be presented at a later date.

7 Summary and Conclusions

This research has successfully completed the following goals:

- A flat micro pin fin heat exchanger was manufactured according to pre-established design specifications that preserved dimensional similarity with previous, larger scale studies.
- At any Reynolds number, the overall thermal performance parameter, η is strictly larger than 1.0, meaning that the micro pin fin heat exchanger performance always exceeds the parallel plate counterpart.
- An apparatus was fabricated to quantify the performance of micro pin fin array heat exchangers. Nusselt numbers and friction factor values over a range of Reynolds numbers from 4500 to 19,200 were obtained. These values are in reasonable agreement with Chyu's results. The suggested correlation for the Nusselt number is given by:

$$\text{Nu}=0.0022\,\text{Re}^{1.221}\,\text{Pr}^{0.4} \quad 4500\leqslant\text{Re}\leqslant 19{,}200$$

A model was developed to predict the cooling effectiveness of the micro pin heat exchanger in a gas turbine blade cooling scenario. Cooling effectiveness values ranging from 0.47 to 0.82 were obtained over a range of coolant Reynolds numbers from 4500 to 19,200.

The logical continuations of this study could be expressed as follows:

- The pin fin array configuration should be optimized in order to produce the best performance
- The manufactured curved micro pin fin heat exchanger on a tube will be tested in a high temperature aerodynamic facility.

Table 6 Model Predictions for gas turbine blade cooling ($x_1=1$ cm and $x_2=2$ cm)

$\dot{m}'$ (kg/m·s)	h_w (W/m^2 K)	$T_{\text{coolant}}(x_1)$ (K)	$T_{\text{coolant}}(x_2)$ (K)	$T_{\text{shroud}}(x_1)$ (K)	$T_{\text{shroud}}(x_2)$ (K)	$\varepsilon(x_1)$	$\varepsilon(x_2)$
0.085	3032	906	1084	1491	1588	0.47	0.41
0.171	8727	848	982	1149	1253	0.70	0.63
0.258	13,892	809	910	1021	1107	0.79	0.73
0.342	15,875	785	865	977	1046	0.82	0.77

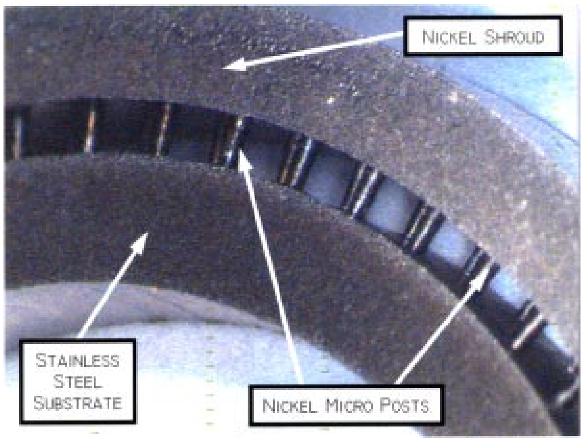

Fig. 13 Curved heat exchanger sliced with a wire EDM machine

Acknowledgment

The authors would like to express thanks to the Defense Advanced Research Project Agency (DARPA) for providing the bulk of the funding for this research. They would also like to thank the Center for Advanced Microstructures and Devices (CAMD), which receives funding from the State of Louisiana. CAMD was indispensable in carrying out certain parts of the LIGA process.

The contributions of the talented Paul Rodriguez and Fred McKenzie at the Chemical Engineering Machine Shop as well as John Parker at the International Mezzo Technologies Inc. Machine Shop are gratefully acknowledged.

Nomenclature

A = coolant flow cross-sectional area
A_{heat} = heating block-heat exchanger contact area
C_P = coolant specific heat at constant pressure
d = distance
D_h = hydraulic diameter, $2H$
f = average friction factor, $2dPD_h/\rho V^2 dx$
h = average convective heat transfer coefficient
H = micro channel height
k = coolant thermal conductivity
l = conduction characteristic length
L = streamwise dimension
$\dot{m}$ = coolant mass flow rate
Nu = average Nusselt number, $h_w D_h/k$
P = static pressure
$\dot{Q}$ = heat rate transferred to the coolant
$\dot{Q}_{\text{ANSYS}}$ = heat rate calculated with ANSYS 5.7
$\dot{Q}_{\text{conduction}}$ = heat rate transferred by conduction
$\dot{Q}_{\text{convection}}$ = heat rate transferred by conduction
Q_{electric} = electrical power dissipated by the heaters
R = thermal resistance in series
R_{air} = air ideal gas constant
Re = Reynolds number, $\rho V D_h/\mu$
T = static temperature
T_{coolant} = coolant temperature in gas turbine engine
T_{shroud} = heat exchanger shroud temperature in gas turbine engine
TT = total temperature, $T+V^2/2C_p$
U = average overall heat transfer coefficient per unit width
V = average coolant velocity in maximum flow area
x = downstream location

Greek Symbols

β = percentage of heat lost to the surroundings
ε = cooling effectiveness
ρ = coolant density
μ = coolant dynamic viscosity
η = overall thermal performance parameter

Subscripts

1 = upstream reservoir (Fig. 6)
2 = upstream pressure tap (Fig. 6)
3 = downstream pressure tap (Fig. 6)
4 = downstream reservoir (Fig. 6)
Al = aluminum
ave = average
bot = level ① in heating block (Figs. 5 and 7)
C = inlet coolant in gas turbine engine conditions
eq = equivalent
exit = heat exchanger exit
external = combustion gas-heat exchanger shroud interface
G = combustion gases in gas turbine engine conditions
HE = heat exchanger
inlet = heat exchanger inlet
lm = log mean
Ni = nickel
o = parallel plate heat exchanger
silicone = thermally conductive silicone paste
SS = stainless steel
top = level ② in heating block (Figs. 5 and 7)
w = coolant-heat exchanger interface

References

[1] Han, J. C., Dutta, S., and Ekkad, S., 2001, *Gas Turbine Heat Transfer and Cooling Technology*, Taylor and Francis.
[2] Eckert, E. R. G., and Hartnett, J. P., 1979, *Studies in Heat Transfer: A Festschrift for E. R. G. Eckert*, McGraw-Hill, pp. 1–16.
[3] Karni, J., and Goldstein, R. J., 1990, ''Surface Injection Effect on Mass Transfer From a Cylinder in Crossflow: A Simulation of Film Cooling in the Leading Edge Region of a Turbine Blade,'' ASME J. Turbomach., **112**, pp. 418–427.
[4] Shen, J. R., Wang, Z., Ireland, P. T., Jones, T. V., and Byerley, A. R., 1996, ''Heat Transfer Enhancement Within a Turbine Blade Cooling Passage Using Ribs and Combinations of Ribs With Film Cooling Holes,'' ASME J. Turbomach., **118**, pp. 428–434.
[5] Lakshminarayana, B., 1996, *Fluid Dynamics and Heat Transfer of Turbomachinery*, John Wiley & Sons, Inc., p. 677.
[6] Marques, C., 1997, ''Heat Transfer of a Microstructure-Covered Cylinder in Crossflow,'' M.S. thesis, Louisiana State University, Baton Rouge, LA.
[7] Marques, C., Desta, Y., Rogers, J., Murphy, M., and Kelly, K., 1997, ''Fabrication of High-Aspect-Ratio Microstructures on Planar and Nonplanar Surfaces Using a Modified LIGA Process,'' Journal of MEMS, , pp. 329–336.
[8] Marques, C., 2003, ''Manufacturing and Analysis of a LIGA Heat Exchanger for the Surface of a Tube: A Cooling Simulation of the Leading Edge Region of A Turbine Blade,'' Ph.D. dissertation, Louisiana State University, Baton Rouge, LA.
[9] Zhukauskas, A., 2004, ''Heat Transfer From Tubes in Cross Flow,'' Adv. Heat Transfer, **8**, pp. 116–133.
[10] Lau, S. C., Han, J. C., and Kim, Y. S., 1989, ''Turbulent Heat Transfer and Friction in Pin Fin Channels With Lateral Flow Ejection,'' ASME J. Heat Transfer, **111**, pp. 51–58.
[11] VanFossen, G. J., 1982, ''Heat Transfer Coefficients for Staggered Arrays of Short Pin Fins,'' ASME J. Eng. Power, **104**, pp. 268–274.
[12] Metzger, D. E., Fan, C. S., and Haley, S. W., 1984, ''Effects of Pin Shape and Array Orientation on Heat Transfer and Pressure Loss in Pin Fin Arrays,'' ASME J. Eng. Gas Turbines Power, **106**, pp. 252–257.
[13] Metzger, D. E., Berry, R. A., and Bronson, J. P., 1982, ''Developing Heat Transfer in Rectangular Ducts With Staggered Arrays of Short Pin Fins,'' ASME J. Heat Transfer, **104**, pp. 700–706.
[14] Chyu, M. K., 1990, ''Heat Transfer and Pressure Drop for Short Pin-Fin Arrays With Pin-Endwall Fillet,'' ASME J. Heat Transfer, **112**, pp. 926–932.
[15] Chyu, M. K., Hsing, Y. C., Shih, T. I.-P., and Natarajan, V., 1999, ''Heat Transfer Contributions of Pins and Endwall in Pin-Fin Arrays: Effects of Thermal Boundary Condition Modeling,'' ASME J. Turbomach., **121**, pp. 257–263.
[16] Chyu, M. K., Yen, C. H., Ma, W., and Shih, T. I.-P., 1999, ''Effects of Flow Gap Atop Pin Elements on the Heat Transfer From Pin Fin Arrays,'' Presented at the International Gas Turbine & Aeroengine Congress & Exhibition, Indianapolis, June 7–10, 1999.

[17] Arora, S. C., and Abdel-Messeh, W., 1990, ''Characteristics of Partial Length Circular Pin Fins as Heat Transfer Augmentors for Airfoil Internal Cooling Passages,'' ASME J. Turbomach., **112**, pp. 559–565.
[18] Brigham, B. A., 1984, ''The Effect of Channel Convergence on Heat Transfer in a Passage With Short Pin Fins,'' NASA-TM-83201.
[19] Becker, E. W., Ehrfeld, W., Hagmann, P., Maner, A., and Munchmeyer, D., 1986, ''Fabrication of Microstructures With High Aspect Ratios and Great Structural Heights by Synchrotron Radiation Lithography, Galvanoforming, and Plastic Molding (LIGA Process),'' Microelectron. Eng., **4**, pp. 35–56.
[20] Bley, P., Menz, W., Bacher, W., Feit, K., Harmening, M., Hein, H., Mohr, J., Schomburg, W., and Stark, W., 1991, ''Application of the LIGA Process in Fabrication of Three-Dimensional Mechanical Microstructures,'' Microprocess 91, 1991 International Microprocess Conference, S. Namba and T. Tsurushima, ed., pp. 384–389.
[21] Hagmann, P., Ehrfeld, W., and Vollmer, H., 1989, ''Fabrication of Microstructures With Extreme Structural Heights by Reaction Injection Molding,'' Makromol. Chem., Macromol. Symp., **24**, pp. 241–251.
[22] Photoresists and Developers, http://www.microchem.com
[23] Jian, L., Desta, Y. M., Aigeldinger, G., Bednarzik, M., Loechel, B., and Goettert, J., 2003, ''SU-8 Based Deep X-Ray Lithography/LIGA,'' *Micromachining and Microfabrication Process Technology VIII*, SPIE Proceedings, **4979**, pp. 394–401.
[24] Incropera, F. P., and DeWitt, D. P., 1996, *Introduction to Heat Transfer*, 3rd ed., John Wiley & Sons, New York.
[25] Holman, J. P., 1978, *Experimental Methods For Engineers*, 3rd ed., McGraw-Hill Inc., pp. 41–50.
[26] Kays, W. M., and Crawford, M. E., 1993, *Convective Heat and Mass Transfer*, 3rd ed., McGraw Hill, p. 344.

Effect of Substrate Temperature on Splashing of Molten Tin Droplets

Navid Z. Mehdizadeh

Mehdi Raessi

Sanjeev Chandra
e-mail: chandra@mie.utoronto.ca

Javad Mostaghimi

Department of Mechanical and Industrial
Engineering,
University of Toronto,
Toronto, Ontario, Canada, M5S 3G8

Tin droplets (0.6 mm diameter) impacting on a polished stainless steel surface were photographed. Droplet impact velocity was varied from 10–40 m/s and substrate temperature from 80–260°C. A molten metal droplet generator was used to produce uniform sized tin droplets. The stainless steel test surface was mounted on the end of a rotating flywheel, giving it linear velocities of up to 40 m/s. A CCD video camera was used to photograph droplets impinging on the substrate. By synchronizing the ejection of a single droplet with the position of the rotating arm and triggering of the camera, different stages of droplet impact were photographed. On a cold surface (20°C) fragments from the periphery of the droplet broke off and flew off the surface during impact. At a high surface temperature (240°C) there was much less splashing and the droplet formed a roughly circular splat. The transition from splashing to circular splats took place at a substrate temperature of approximately 160°C. A three-dimensional model of droplet impact and solidification was used to simulate droplet splashing. Numerical results agreed qualitatively with photographs of droplet splashing. Simulations showed that freezing around the edges of droplets creates instability and triggers splashing. [DOI: 10.1115/1.1737778]

Keywords: *Droplet, Experimental, Heat Transfer, Impingement, Melting, Solidification*

1 Introduction

When a molten metal droplet hits a solid plate and freezes, the shape of the flattened, solidified splat that is formed depends on the temperature of the plate. Figure 1 shows aluminum splats produced by wire arc spraying, a widely used coating process in which an electric arc is struck between the tips of two continuously fed wires. A high velocity air jet directed at the gap between the wires strips off droplets of molten metal and propels them onto the surface being coated. In the study [1] from which Fig. 1 was taken droplet diameters ranged from 16 to 25 μm and velocities from 100 to 125 m/s. Droplets that landed on a polished stainless steel plate at 25°C formed irregular shaped splats (Fig. 1(a)), while those impinging on a plate heated to 350°C produced almost perfectly circular splats (Fig. 1(b)).

Why does surface temperature affect splat shape? The answer to this question is of much more than academic interest since coating quality depends on the shape of individual splats [2]. Fragmented splats produce porous coatings with low adhesion strength. Splashing—defined as disintegration of a single droplet upon impact to produce satellite droplets such as those visible in Fig. 1(a)—reduces deposition efficiency (the fraction of the coating material which adheres to the surface) because smaller droplets bounce off the surface. The effect of varying substrate temperature is not well understood in the thermal spray industry. Coating applicators cool components during spraying to avoid thermal distortion, but rarely make any further effort to monitor or control substrate temperature. Appropriate thermal management may offer ways of improving coating quality and reducing wastage, but it is not presently clear what optimum surface temperature should be maintained during spraying.

Controlling the properties of deposits made by accumulation of molten metal droplets is also of interest in other applications than thermal spray coating. In microcasting [3–5], complete objects are built up by depositing droplets in a stipulated pattern. The metallurgical properties of parts made with this technique depend on the shape and temperature history of individual droplets [5].

The transformation from fragmented deposits to circular ''disk splats'' as surface temperature rises is well documented [6–11] for a wide range of metals and ceramics. Some researchers [9] have conjectured that freezing around the edges of an impinging droplet makes it splash: liquid flowing out from the center of a drop jets upwards when it hits a solidified rim. Delaying solidification, either by raising surface temperature or increasing thermal contact resistance at the droplet-substrate interface, is expected to suppress splashing. Others [10,11] contend that molten droplets superheat volatile compounds on the surface, which evaporate so explosively that they shatter the drops. Preheating the surface removes these contaminants. Since these two mechanisms are not mutually exclusive, it is quite possible that both influence splat shape.

Several studies have studied splashing of liquid drops where solidification did not occur. Much of the literature has been reviewed by Rein [12]. Photographs have shown that fluid instabilities around the edges of the spreading liquid film lead to the development of fingers that detach to form satellites drops [13]. Increased surface roughness is known to enhance fluid instabilities and promote splashing [14]. The solidified layer appears to act in much the same way, creating obstacles under the drop that perturb liquid flow.

Part of the difficulty in identifying the mechanism responsible for droplet splashing is that no one has directly observed impact of thermal spray particles: we have to infer details of impact dynamics from splat photographs such as those in Fig. 1. Several papers (e.g., [15,16]) have presented photographs of molten metal droplets impacting on a surface, but these have typically been of large (2–3 mm diameter) droplets falling under their own weight onto a surface with relatively low impact velocities (1–4 m/s). Weber numbers ($\mathrm{We}=\rho V_0^2 D_0/\sigma$), which measure the ratio of droplet kinetic energy to surface energy, were typically less than

---

Contributed by the Heat Transfer Division for publication in the JOURNAL OF HEAT TRANSFER. Manuscript received by the Heat Transfer Division June 24, 2003; revision received March 10, 2004. Associate Editor: C. Amon.

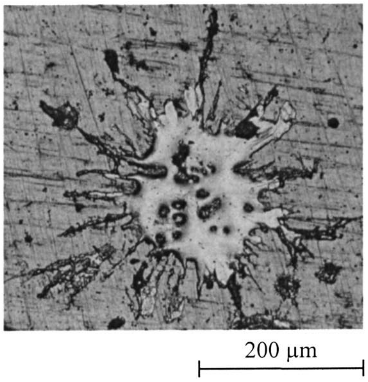

a) T_s=25°C

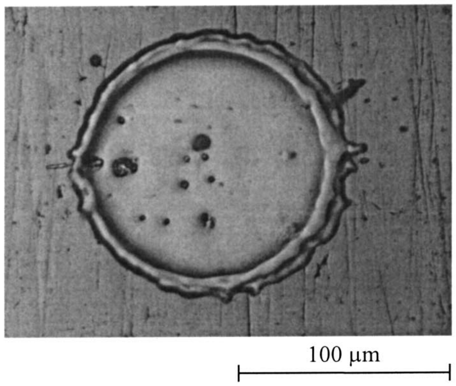

b) T_s=350°C

Fig. 1 Shape of aluminum splats produced by wire arc spraying (D_0=16–25 μm, V_0=100–125 m/s)

10^3 and Reynolds numbers ($\mathrm{Re}=\rho V_0 D_0/\mu$), which measure the ratio of inertial forces to viscous forces were less than 10^4. The molten part of impacting drops did not have enough momentum to surmount a solidified rim so that freezing around the edges of droplets suppressed splashing [16].

Molten droplets in a wire arc spray typically hit a surface with both Re and We$\sim 10^4$. Whereas Re is the same order of magnitude as in previous single droplet impact experiments [15,16], We is much larger. The mechanism triggering splashing under thermal spray conditions may be quite different from that observed at lower We. Computer simulations [17] support the hypothesis that outward flowing liquid is diverted upwards when it hits a solid layer. Fluid instabilities force the jetting liquid sheet to disintegrate.

The objective of our study was to photograph impact of molten metal droplets at high Weber and Reynolds numbers. We used a combination of experiments and numerical simulation to determine the effect of varying both impact velocity and substrate temperature on droplet dynamics.

It is difficult to accelerate a droplet to high enough impact velocities to obtain Weber numbers typical of thermal spray processes. We chose to accelerate the test surface by mounting it on the rim of a flywheel rotating in the horizontal plane. Droplets produced by a generator mounted above the edge of the flywheel fell vertically under their own weight and were hit by the surface moving horizontally at high speed. In this study we photographed splashing of molten tin droplets on a stainless steel surface. Droplet diameter (0.6 mm) and surface roughness (0.03 μm) were kept constant while impact velocity (10–40 m/s) and substrate temperature (80–260°C) were varied. Weber numbers ranged from 8.0×10^2 to 1.3×10^4 and Reynolds number from 2.3×10^4 to 9.2×10^4. A three-dimensional model that simulates fluid flow and heat transfer, developed earlier by Pasandideh-Fard et al. [18] and Bussmann et al. [19], was used to simulate droplet impact and solidification and obtain insight into the cause of splashing.

2 Experimental Method

A molten metal droplet generator [20] was used to produce uniform sized molten tin droplets. Figure 2 shows a schematic of the system. The main body of the generator was made of stainless steel. A band heater (Model HBA-202040, Omega Company, Stamford, Connecticut) was used to maintain the chamber temperature above the melting point of tin. A temperature controller (Model CN9000A, Omega Company, Stamford, Connecticut) and a thermocouple were connected to the heater to monitor the conditions. The chamber was filled with tin shot (99 percent pure, Aldrich Chemical Company, Milwaukee, Wisconsin).

A commercially available synthetic sapphire nozzle with a 178 μm orifice was inserted into a hole drilled through the other wall of the chamber and sealed in place with Teflon tape. Teflon O-rings sealed both bottom and top of the chamber. A T-fitting was connected to the top plate, so that one outlet acted as a vent while the other was connected to a nitrogen tank whose outlet pressure was varied from 125–200 KPa. A solenoid valve (Model 8262G202, Convalve Company, Toronto, Ontario) was placed between the nitrogen tank and chamber. When the solenoid valve opened briefly (8–15 ms) a pressure pulse was sent to the chamber forcing a molten tin droplet out through the nozzle. The pressure in the chamber was then relieved by gas escaping through the vent hole, preventing more droplets from being ejected. By this method single droplets could be produced on demand by sending a signal to the circuit controlling the solenoid valve.

To prevent oxidation of tin droplets emerging from the droplet generator an aluminum pipe with an inner diameter of 10 mm was attached to the bottom of the chamber. Nitrogen was injected into this pipe to shield droplets from the atmospheric oxygen. The

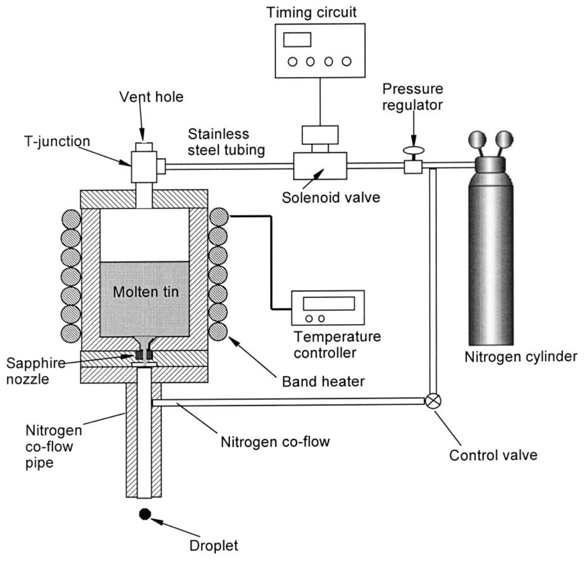

Fig. 2 Schematic diagram of the molten tin droplet generator

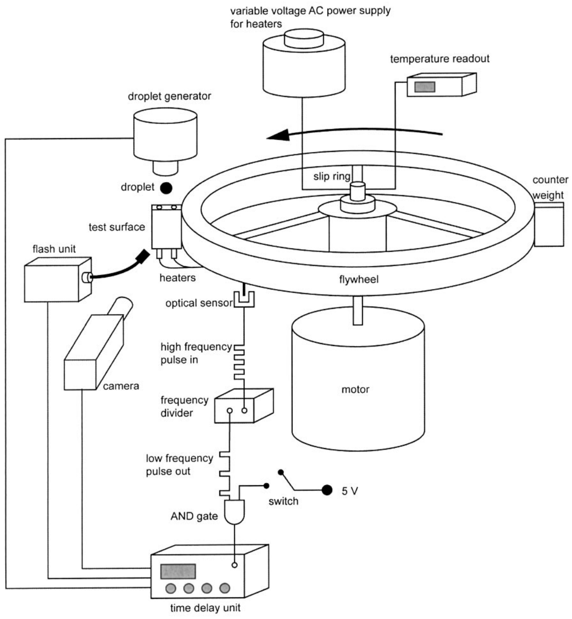

Fig. 3 Schematic diagram of the experimental apparatus

volume flow rate of nitrogen was adjusted until it was just enough to prevent oxidation. The effect of oxidation on droplet formation was immediately obvious since it produced non-spherical, teardrop shaped droplets.

The test surfaces on which molten metal droplets impinged were stainless steel coupons (38.1 mm long, 25.4 mm wide and 0.51 mm thick) polished on a metallurgical wheel to a mirror finish with average surface roughness 0.05 μm. Test coupons were mounted on a 9.5 mm thick aluminum plate with the same length and width as the coupons, which was bolted to the outer rim of a 406.4 mm diameter aluminum flywheel. Another identical plate was attached to the opposite side of the flywheel to act as a counterweight. A vertical rod inserted through the hub of the flywheel was connected to the shaft of a variable speed DC motor (model MS 3130-04/T, Dynetic Systems, Elk River, MN) through a flexible coupling (see Fig. 3). By varying the voltage applied to the motor, rotational speeds of up to 3500 rpm were obtained, giving the test surface linear velocities of up to 80 m/s. The whole system was mounted on a vibration isolation table.

A slip ring (Model S4, Michigan Scientific, Charlevoix, MI) was mounted on the upper end of the flywheel shaft and used to carry electric power to the test surface and thermocouple signals from it. The stationary part of the slip ring was fixed to a support frame. To heat the substrate two 120 W cartridge heaters (Omega Engineering Co., Stamford, CT) were inserted into holes in the aluminum plate backing the test coupons. A Chromel-Alumel thermocouple was inserted into the center of the plate with its tip touching the stainless steel coupon. The rear surface and sides of the aluminum plate were insulated to minimize heat losses due to convection to the air and conduction to the flywheel. By varying the voltage applied to the heaters the temperature of the test surface could be controlled. The temperature of the surface was allowed to reach steady state while rotating before depositing drops on it. Spatial temperature variations from one side of the test surface to the other when it was moving were less than 5°C.

A CCD video camera (Sensicam, Optikon Corporation Ltd., Kitchener, Ontario) was used to photograph droplet dynamics during impact. It had an intensified CCD chip capable of recording 30 frames per second with a resolution of 1280×1024 pixels. The camera could also superimpose up to ten images in every frame, each with an exposure time as short as 0.1 μs, separated by delays that varied from 0 to 1 ms (selectable in 0.1 μs time steps). A 0.1 μs exposure time was short enough to capture the deformation of the droplet during the impact, without any blurring caused by the extremely fast motion of the substrate. To hit a falling droplet with the moving substrate, and to photograph its impact, three events had to be synchronized with the position of the arm: ejection of a droplet, triggering of the camera, and triggering of a flash to provide illumination. An optical sensor was used to pick up the signal caused by the flywheel rotation. This signal was then used to trigger the camera, flash, and droplet generator. Since the frequency of this signal was too high to directly drive the droplet generator, it first passed through a frequency divider, which reduced the frequency by a factor that varied from 2 to 32, depending on the rotational speed of the arm. The low frequency signal formed one input of an AND gate (see Fig. 2).

When we were ready to take a photograph we pressed a switch which activated the second input of the AND gate, so that the pulses at the other input were transmitted to a time delay unit. The rising edge of each pulse provided a reference we used to time all other events. The digital time delay generator (Model DG 535, Stanford Research Systems, Sunnyvale, California) controlled the timing of three subsequent actions with pico-second resolution. We made droplets collide with the substrate by varying the delay between the reference pulse and triggering of the droplet generator. Each droplet was ejected from the generator and fell to a position coincident with the center of the test surface just as the arm approached the droplet. The droplet velocity as it exited the generator was less than 1 m/s, small enough to reasonably assume impact was normal to the surface even for the lowest velocities in our experiments, 10 m/s. Tin droplets did not adhere to the stainless steel surface after impact but were thrown off by centrifugal forces.

The flash (Model MVS 7000, EG&G Corp., Salem, Massachusetts) timing was adjusted so that droplet impact was illuminated by a 10 μs long burst of light. While the flash was on, the camera was activated to take a single 0.1 μs exposure of an impacting droplet. By varying the time at which the camera was triggered, different stages of droplet impact were recorded, and the entire process of droplet impact reconstructed from a sequence of such pictures. This single-shot method was used instead of a high-speed camera because it provided high-resolution photographs in which satellite droplets were clearly visible.

The entire process of droplet impact and spreading takes between 100 to 200 μs. The repeatability of photographs was only about ± 20 μs, which was approximately the interval between successive frames in a sequence of photographs. Therefore, it was not possible to assign an exact time to each frame. This was not a serious shortcoming, as we did not make any time resolved measurements from photographs. They were used only to observe the shape of droplets as they splashed.

In our experiments we accelerated the substrate to achieve high velocity impact. This technique did not exactly replicate a spray coating application, where droplets are accelerated by a high velocity gas flow before they impact on the surface. Nevertheless, we do not expect the gas velocity to have any significant effect on droplet shape or impact dynamics, because the viscous shear force exerted by the surrounding gas on a droplet is much less than the surface tension force that keeps it spherical. The capillary number ($\mathrm{Ca} = \mu V_0/\sigma$) gives the relative magnitudes of viscous and surface tension forces. For a tin droplet traveling with a velocity $V_0 = 100$ m/s we estimated $\mathrm{Ca} \sim 10^{-3}$, showing that the shear exerted by the surrounding gas is relatively small even at high velocities.

A droplet colliding with a rotating surface is acted upon by both centrifugal and Coriolis forces. An order-of-magnitude analysis

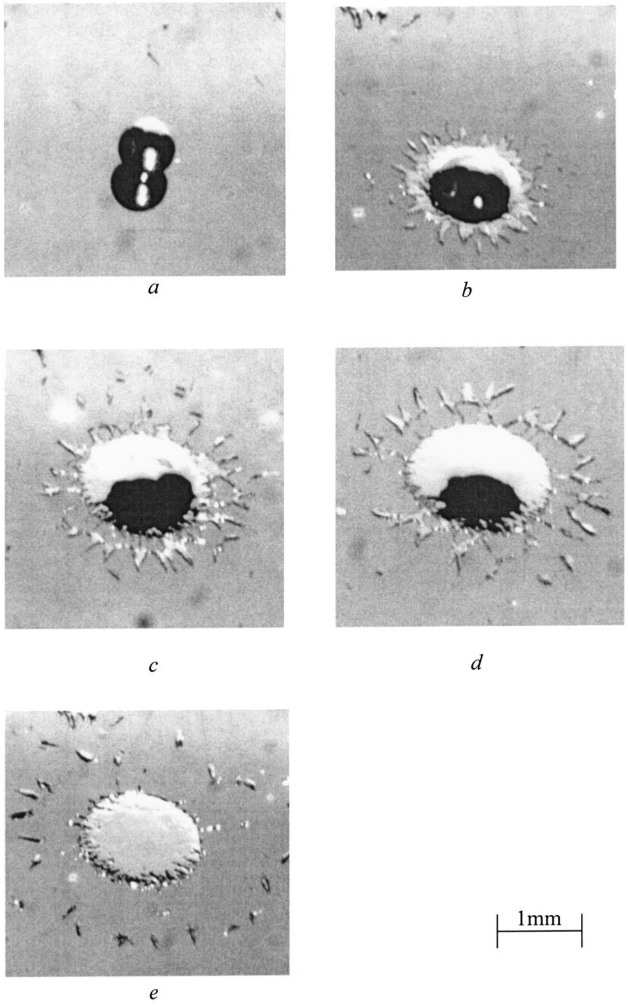

Fig. 4 Impact of 0.6 mm tin droplets with a velocity of 10 m/s on a stainless steel surface with a surface temperature of 20°C (Re=2.3×10^4, We=8×10^2)

[21] of the Navier-Stokes equations in which they appear as additional body forces, showed that for $D_0/R_f \ll 1$ (where R_f is the distance between the center of the droplet and center of rotation) both centrifugal and Coriolis forces may be neglected, which was the case in our experiments.

3 Results and Discussion

3.1 Photographs of Droplet Impact. Figure 4 illustrates the spreading of a 0.6 mm molten tin droplet impacting with a velocity of 10 m/s on a stainless steel surface at a temperature of 20°C, photographed with a camera inclined at an angle of 45° to the substrate. The frames are labeled *a* to *e*, representing successive stages of impact. Triangular protrusions formed around the periphery of the droplet (Fig. 4(b)) as it spread. These protrusions then detached from the rim forming tin fragments that flew outwards (Fig. 4(c)). A roughly circular, solid splat was left on the surface (Fig. 4(e)). The pattern of splashing was quite different from that observed at lower impact velocities, where finger shaped perturbations formed and detached forming satellite droplets around the edge [16].

Suppressing solidification—by increasing substrate temperature above the melting point of tin (232°C)—prevented droplet splashing at an impact velocity of 10 m/s. Figure 5 shows a 0.6 mm molten tin droplet landing with a velocity of 10 m/s on a stainless steel surface. The experimental conditions were exactly the same

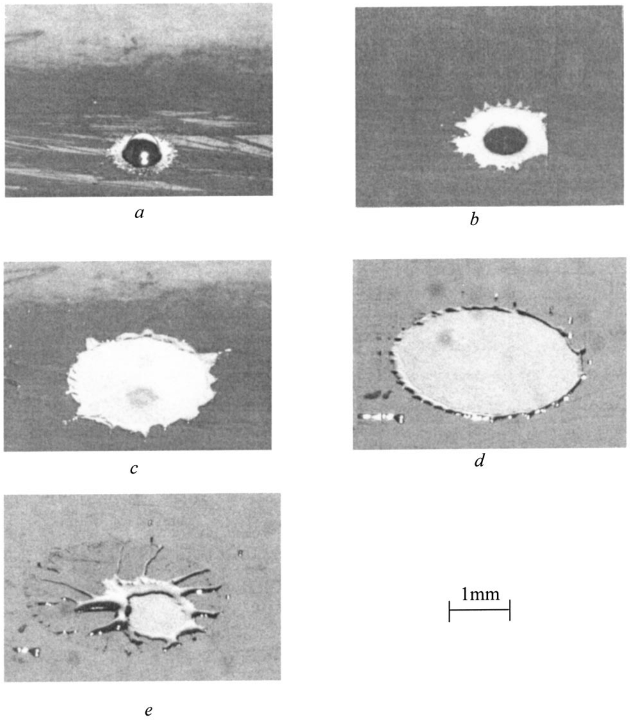

Fig. 5 Impact of a 0.6 mm tin droplets with a velocity of 10 m/s on a stainless steel surface with a surface temperature of T_s =240°C (Re=2.3×10^4, We=8×10^2)

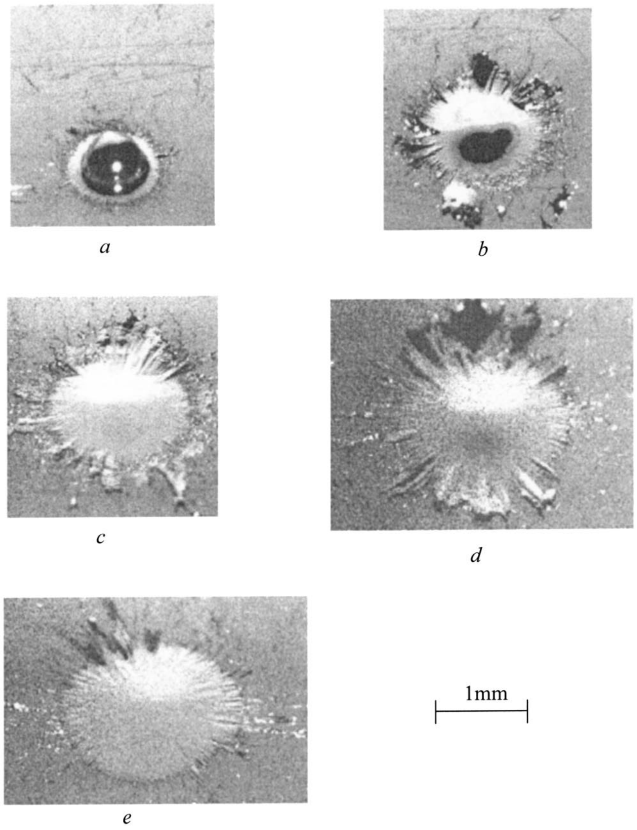

Fig. 6 Impact of a 0.6 mm tin droplets with a velocity of 40 m/s on a stainless steel surface with a surface temperature of T_s =20°C (Re=9.3×10^4, We=1.3×10^4)

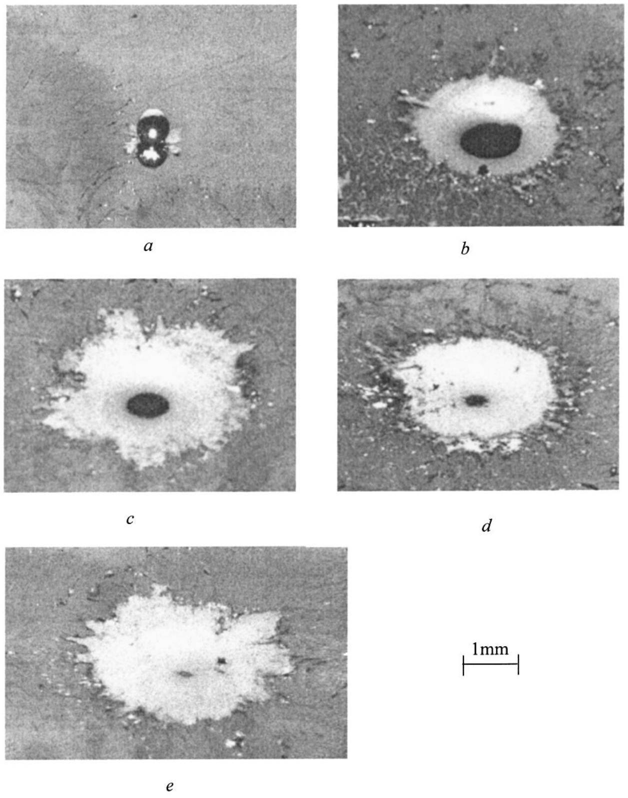

Fig. 7 Impact of a 0.6 mm tin droplets with a velocity of 40 m/s on a stainless steel surface with a surface temperature of $T_s = 240°C$ ($Re = 9.3 \times 10^4$, $We = 1.3 \times 10^4$)

Table 1 Properties of molten tin

Property	ρ (Kg/m^3)	ν (m^2/s)	σ (N/m)	k (W/mK)	c_p (J/kgK)
Value	6970	2.7×10^{-7}	0.526	33.6	244

as those in Fig. 4, except that the substrate temperature was raised to 240°C. The droplet smoothly spread out into a thin disk (Fig. 5(d)) with small fingers forming at regular intervals around its edge. Fingers are created due to Rayleigh-Taylor instability, which occurs when the surface of a spreading droplet undergoes large deceleration [22,23]. Surface tension pulled back the molten tin (Fig. 5(e)), so that there was almost no splashing, with only the tips of a few fingers detaching. The final position of the liquid was asymmetrical due to centrifugal forces that drew the liquid to one side.

Increasing impact velocity enhanced splashing. Figure 6 shows the impact of a 0.6 mm molten tin droplet with a velocity of 40 m/s on a surface at 20°C. At this high impact velocity splashing was much more pronounced than it was at 10 m/s (compare with Fig. 4), producing a cloud of debris ahead of the spreading rim. Violent fragmentation of droplets occurred immediately after impact (Fig. 6(b)). Large sections of the droplet flew off the surface (Fig. 6(d)) instead of the small fragments seen in Fig. 4. A small circular splat remained on the surface (Fig. 6(e)).

At high impact velocities droplets splashed even on a hot substrate. When a droplet hit a 240°C surface with a velocity of 40 m/s (Fig. 7) there was some break-up around its periphery (Fig. 7(b–d)), though less than that observed during impact on a cold surface (compare with Fig. 6). There was no discernible formation of fingers and no recoil of the droplet, unlike that seen at lower impact velocity, and a roughly circular splat with irregular edges (Fig. 7(e)) remained on the substrate.

3.2 Numerical Simulation. To model solidification and splashing of molten metal droplets we used a three-dimensional model of droplet impact and solidification developed by Pasandideh-Fard et al. and Bussmann et al. [18,19]. The model has been discussed in detail in previous publications [17–19,24], so it is described only very briefly here. The model solves the mass, momentum and energy conservation equations, discretized using a finite volume technique on a three-dimensional, Eulerian structured grid. Fluid flow was assumed to be Newtonian, laminar and incompressible. The Volume-of-Fluid (VOF) algorithm was used to track the free surface of the droplet. Surface tension was incorporated as a component of the body force acting on the fluid free surface using the Continuum Surface Force (CSF) model [19,25]. An adiabatic boundary condition was applied at the droplet free surface.

The model requires a value for thermal contact resistance (R_c) at the droplet-substrate interface, that we had no way of measuring in these experiments. Previous measurements have shown that contact resistance under impinging droplets decreases as impact speed is raised, varying from 5×10^{-6} °C/W for tin droplets impacting with a velocity of 1 m/s to 10^{-6} °C/W at 4 m/s [16]. Lacking experimental data at higher velocities we tried using $R_c = 5 \times 10^{-7}$ °C/W and found that predicted droplet shapes agreed with photographs; all simulations shown in this paper were done using this value. Advancing and receding contact angles at the liquid-solid contact lines were set to 140 deg and 40 deg, respectively, based on measurements by Aziz and Chandra [16], who found that contact angles did not depend on impact velocity.

Only a quarter segment of each droplet was simulated and the entire droplet reconstructed by reflecting the results about planes of symmetry. The computational domain was a cube with sides 6 times droplet radius and height 3 times radius. Based on a mesh refinement study [18,24], the mesh size was chosen to be 1/22 of the droplet radius. Previous experience [15,17,18,24], confirmed here, showed that predicted droplet shapes do not change significantly when the computational grid is made smaller. However, once a droplet splashes and small satellite droplets detach, some of them are of the same size as the mesh spacing. Our simulations, therefore, do not give reliable information about the shapes of these secondary droplets and are meant only to model the deformation of the main droplet. Numerical computations were performed on an AMD Athlon 1.4 GHz PC and the maximum CPU time was 24 hours. Properties of tin used in calculations are given in Table 1 [26].

Figure 8 shows simulated images of 0.6 mm tin droplets, initially at 233°C, impinging with an impact velocity of 40 m/s onto stainless steel surfaces with initial temperatures (a) 80°, (b) 180°, and (c) 260°C, respectively. Each column shows a droplet during successive stages of impact on a surface at a given initial temperature. To show clearly the extent of solidification in the computer generated images the liquid was made transparent, with a light gray color. Solid layers were assigned a darker shade of gray. Substrate temperature distributions are given in Fig. 9 for substrate temperatures of (a) 80°C and (b) 180°C, at the same times as those in Fig. 8. Temperature distributions were not given for a substrate at 260°C, where impact was almost isothermal. In Fig. 9 liquid portions of droplets are shown in white and solid in black.

During impact on a substrate at 80°C (Fig. 8(a)), solidification started first along the edges of the spreading drop ($t = 22\ \mu s$), where it first contacted the colder substrate. The temperature distribution in the substrate was essentially one-dimensional, with the substrate a very short distance beyond the edges of the drop at its original temperature of 80°C (see Fig. 9(a) $t = 22\ \mu s$). The highest temperature gradient, and consequently the highest heat flux from the droplet, was along its edge. The band of solid material grew wider (Fig. 8(a), $t = 34\ \mu s$) and freezing also started at the center of the drop, which had been longest in contact with the

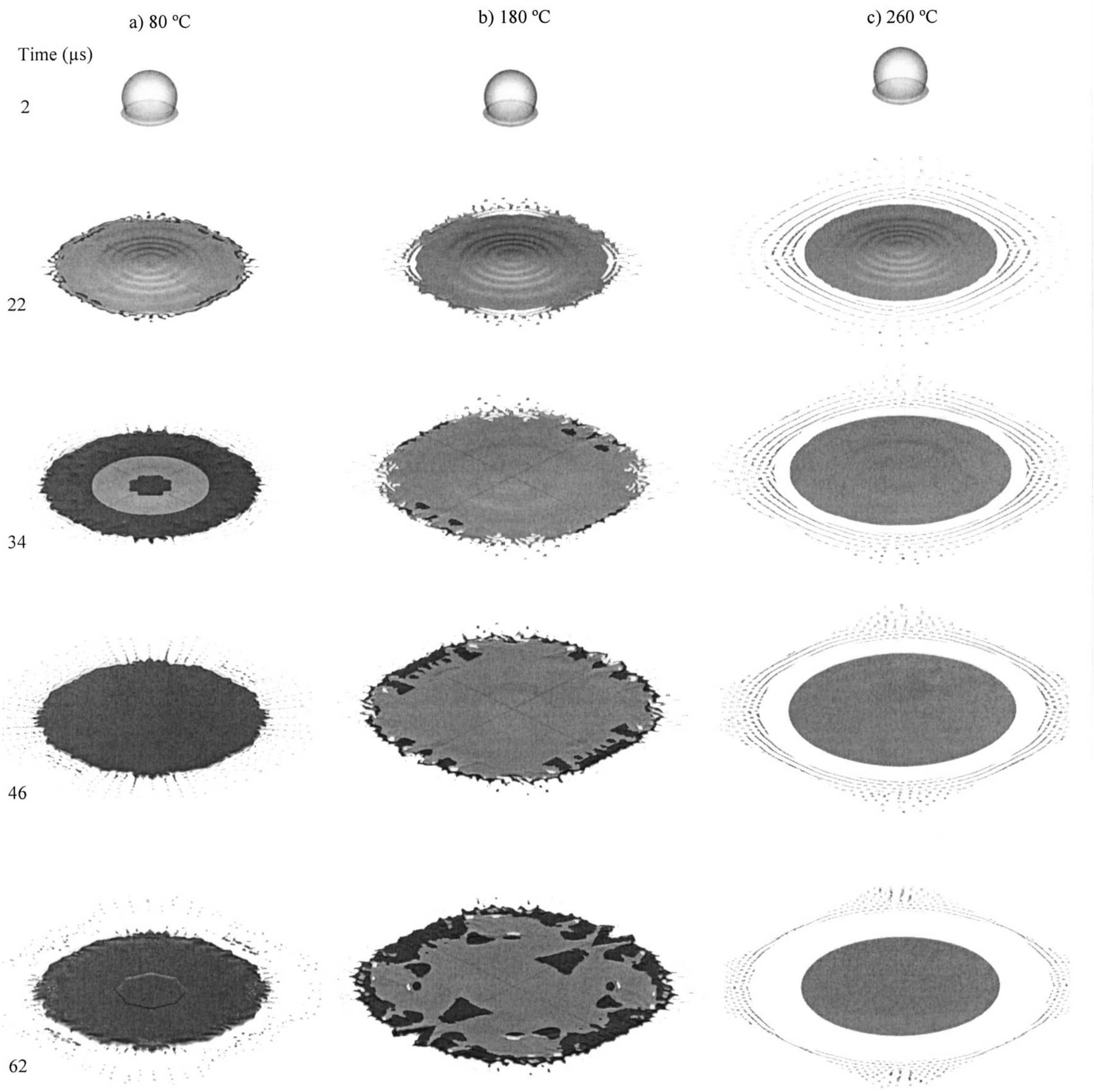

Fig. 8 Computer generated images of 0.6 mm diameter tin droplets at 233°C impacting with a velocity of 40 m/s onto stainless steel substrates at initially temperature: (a) 80, (b) 180, and (c) 260°C

substrate. Liquid jetted over the solidified layer along the droplet rim and broke up into droplets (Fig. 9(a), $t=34\,\mu$s). By $t=46\,\mu$s the bottom of the droplet was entirely solidified, but a film of liquid remained on top of it and continued to flow outwards, forming fingers of liquid around the periphery of the drop that detached and broke-up to form satellite droplets.

At a higher substrate temperature, 180°C, solidification was delayed until $t=34\,\mu$s and was visible only around the fringes of the droplet. In this case too the lowest surface temperature was just beyond the edge of the drop (Fig. 9(b)). The droplet spread to a greater extent than it did on the surface at 80°C. There was clearly less splashing in this case because there was no solidified outer rim to perturb the liquid flow. By the time there was significant solidification the droplet has already spread to its maximum extent ($t=62\,\mu$s) and liquid velocities were very low.

When substrate temperature was raised above the melting point of tin (Fig. 8(c)) no solidification occurred and the droplet spread to form a smooth disk. Rings of molten tin detached along the rim of the droplet, leaving a disk of molten metal in the center.

How well do our numerical simulations capture the mechanism of droplet splashing? Figure 10 shows comparisons between photographs of splats at their maximum spread and corresponding simulations at temperatures of temperatures (a) 80°, (b) 150°, and (c) 260°C. At the lowest temperature, 80°C, thin radial fingers projecting from the splat are visible in both the photograph and simulated image. Bussmann et al. [24] simulated fingering around the edges of liquid droplets—without solidification—by artificially perturbing the velocity field after impact to initiate the growth of fingers. We did not do that in this case, since solidification around the droplet edges was enough to trigger an instability that produced fingering. Raising the surface temperature to 150°C reduced the number of fingers, leaving an irregular shaped splat (Fig. 10(b)). Above the melting point, at a substrate temperature of 260°C, the splat was almost perfectly circular, though material that had detached was visible around the splat.

Explosive vaporization of contaminants on the surface, principally adsorbed water, has been proposed as one possible mechanism that causes splashing of impacting drops [10,11]. Though this mechanism is possible in thermal spray applications where droplets of very high melting point materials impact the substrate, it is unlikely to be significant in our experiments with tin droplets. Simulations of droplet impact on a surface initially at 20°C showed that substrate temperature always remained below 100°C, precluding rapid vaporization of water.

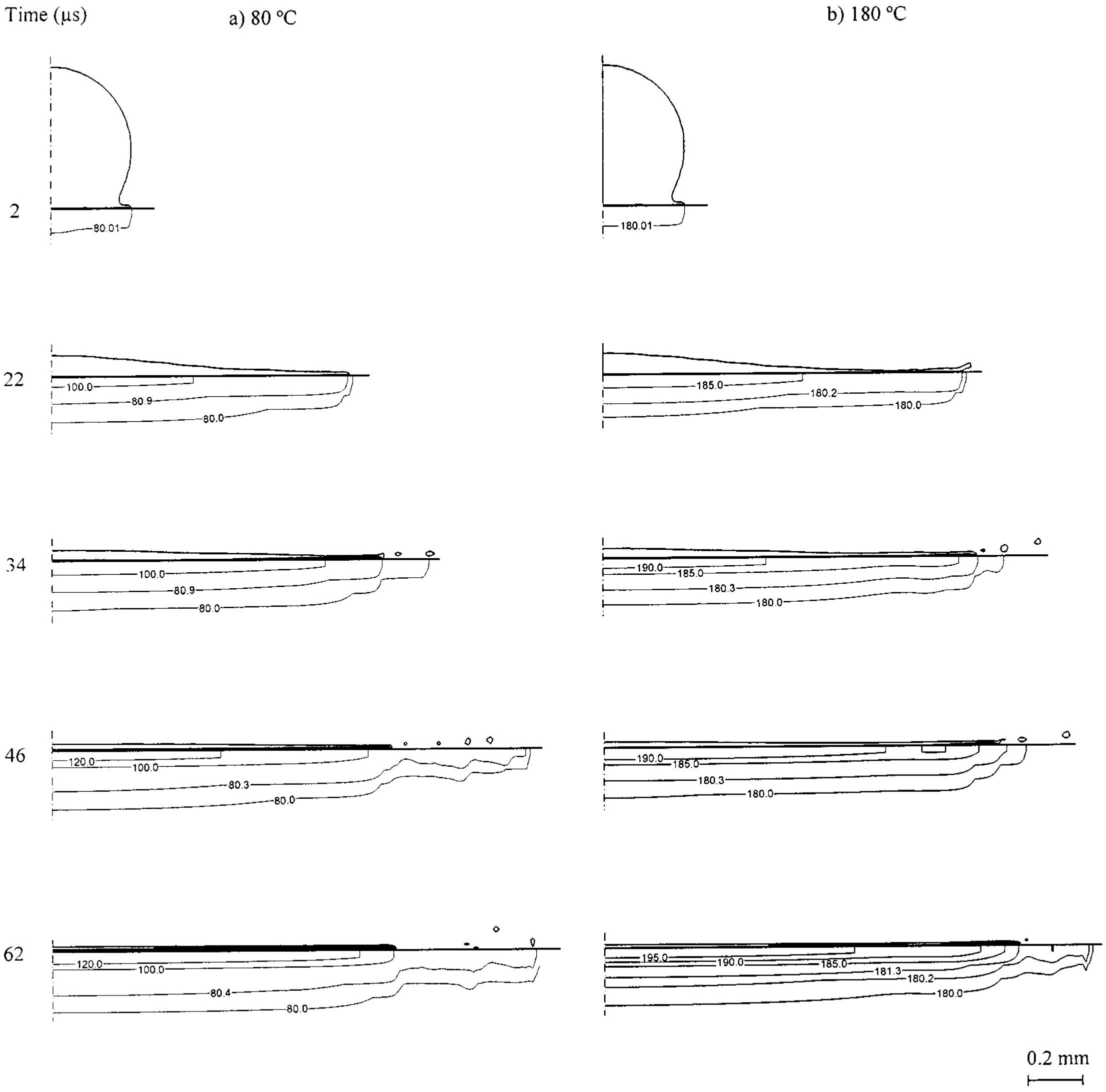

Fig. 9 Calculated temperature distribution under 0.6 mm diameter molten tin droplets at 233°C impacting with a velocity of 40 m/s onto stainless steel substrates initially at temperatures of (a) 80°C and (b) 180°C

Previous researchers [6–9] examining thermal spray splats have identified a "transition temperature," at which droplets stop splashing and form circular splats. There is a certain subjectivity in identifying this temperature, since the transition to circular splats is gradual: we identified a transition temperature range of approximately 160–180°C, above which splashing greatly diminished.

4 Summary and Conclusions

We designed and built an experimental apparatus to photograph high-speed impact of small molten tin droplets on surfaces of varying temperature. We held droplet diameter and surface roughness (0.6 mm, 0.05 μm) constant while varying surface temperature and impact velocity (120–260°C, 10–40 m/s).

On a cold surface (20°C) fragments from the periphery of the droplet broke off and flew off the surface during impact. At a high surface temperature (240°C) there was much less splashing and the droplet formed a roughly circular splat. The transition from splashing to circular splats took place over a range of temperature between 160–180°C.

A three-dimensional model of droplet impact and solidification was used to simulate droplet splashing. Numerical results agreed qualitatively with photographs of droplet splashing. Simulations showed that freezing around the edges of droplets creates instability and triggers splashing.

Nomenclature

D_0 = droplet diameter
R_f = radius of flywheel
V_0 = droplet impact velocity

Greek Symbols

σ = droplet surface tension
ρ = droplet density
μ = droplet viscosity
ν = droplet kinematic viscosity

Dimensionless Numbers

Re = Reynolds number $(=\rho V_0 D_0/\mu)$
We = Weber number $(=\rho V_0^2 D_0/\sigma)$
Ca = Capillary number $(=\mu V_0/\sigma)$

a) T_s=80ºC

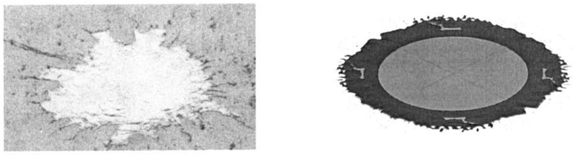

b) T_s=150ºC

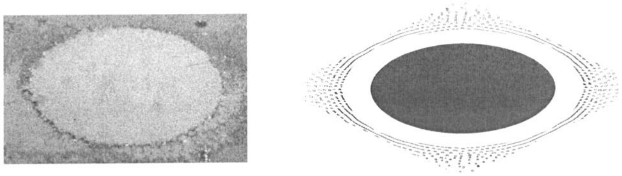

c) T_s=260ºC

Fig. 10 Comparison between simulation and photographs of 0.6 mm molten tin droplets at their maximum diameter impacting with a velocity of 40 m/s onto a stainless steel surface at a temperature of (a) 80°C, (b) 150°C, and (c) 260°C

References

[1] Abedini, A., 2003, ''Splat and Coating Formation in Wire Arc Sprayed Aluminum,'' MASc. thesis, University of Toronto, Toronto, Ontario, Canada.

[2] Sakakibara, N., Tsukuda, H., and Notomi, A., 2000, ''The Splat Morphology of Plasma Sprayed Particle and the Relation to Coating Property,'' *Thermal Spray Surface Engineering via Applied Research*, C. Berndt, ed., ASM International, Materials Park, OH, pp. 753–758.

[3] Prinz, F. B., 1996, ''Numerical and Experimental Invetigation of Interface Bonding via Substrate Remelting of an Impinging Molten Metal Droplet,'' ASME J. Heat Transfer, **118**, pp. 164–172.

[4] Zarzalejo, L. J., Schmaltz, K. S., and Amon, C. H., 1999, ''Molten Droplet Solidification and Substrate Remelting in Microcasting: Part 1—Numerical Modeling and Experimental Verification,'' Heat Mass Transfer, **34**, pp. 477–485.

[5] Schmaltz, K. S., Zarzalejo, L. J., and Amon, C. H., 1999, ''Molten Dropelt Solidification and Substrate Remelting in Microcasting: Part 2—Parametric Study and Effect of Dissimilar Materials,'' Heat Mass Transfer, **35**, pp. 17–23.

[6] Bianchi, L., Blein, F., Lucchese, P., Vardelle, M., Vardelle, A., and Fuchais, P., 1994, ''Effect of Particle Velocity and Substrate Temperature on Alumina and Zirconia Splat Formation,'' *Thermal Spray Industrial Applications*, C. Berndt and S. Sampath, eds., ASM International, Materials Park, OH, pp. 569–574.

[7] Li, C. J., Li, J. L., Wang, W. B., Ohmori, A., and Tani, K., 1998, ''Effect of Particle Substrate Materials Combinations on Morphology of Plasma Sprayed Splats,'' *Thermal Spray Meeting the Challenges of the 21st Century*, C. Coddet, ed., ASM International, Materials Park, OH, pp. 481–487.

[8] Pech, J., Hannoyer, B., Denoirjean, A., and Fauchais, P., 2000, ''Influence of Substrate Preheating Monitoring on Alumina Splat Formation in DC Plasma Process,'' *Thermal Spray Surface Engineering via Applied Research*, C. Berndt, ed., ASM International, Materials Park, OH, pp. 759–765.

[9] Fukomoto, M., Huang, Y., and Ohwatari, M., 1998, ''Flattening Mechanism in Thermal Sprayed Particle Impinging on Flat Substrate,'' *Thermal Spray Meeting the Challenges of the 21st Century*, C. Coddet, ed., ASM International, Materials Park, OH, pp. 410–406.

[10] Li, C. J., Li, J. L., and Wang, W. B., 1998, ''The Effect of Substrate Preheating and Surface Organic Covering on Splat Formation,'' *Thermal Spray Meeting the Challenges of the 21st Century*, C. Coddet, ed., ASM International, Materials Park, OH, pp. 473–480.

[11] Jiang, X., Wan, Y., Hermann, H., and Sampath, S., 2001, ''Role of Condensates and Adsorbates on Substrate Surface on Fragmentation of Impinging Molten Droplets During Thermal Spray,'' Thin Solid Films, **385**, pp. 132–141.

[12] Rein, M., 1993, ''Phenomena of Liquid Drop Impact on Solid and Liquid Surfaces,'' Fluid Dyn. Res., **12**, pp. 61–93.

[13] Thoroddsen, S. T., and Sakakibara, J., 1998, ''Evolution of the Fingering Pattern of an Impacting Drop,'' Phys. Fluids, **10**, pp. 1359–1374.

[14] Range, K., and Feuillebois, F., 1998, ''Influence of Surface Roughness on Liquid Drop Impact,'' J. Colloid Interface Sci., **203**, pp. 16–30.

[15] Pasandideh-Fard, M., Bhola, R., Chandra, S., and Mostaghimi, J., 1998, ''Deposition of tin Droplets on a Steel Plate: Simulations and Experiments,'' Int. J. Heat Mass Transfer, **41**, pp. 2929–2945.

[16] Aziz, S. D., and Chandra, S., 2000, ''Impact, Recoil, and Splashing of Molten Metal Droplets,'' Int. J. Heat Mass Transfer, **43**, pp. 2841–2857.

[17] Pasandideh-Fard, M., Pershin, V., Chandra, S., and Mostaghimi, J., 2002, ''Splat Shapes in a Thermal Spray Coating Process: Simulations and Experiments,'' Journal of Thermal Spray Technology, **11**, pp. 206–217.

[18] Pasandideh-Fard, M., Chandra, S., and Mostaghimi, J., 2002, ''A Three-Dimensional Model of Droplet Impact and Solidification,'' Int. J. Heat Mass Transfer, **45**, pp. 2229–2242.

[19] Bussmann, M., Mostaghimi, J., and Chandra, S., 1999, ''On a Three-Dimensional Volume Tracking Model of Droplet Impact,'' Phys. Fluids, **11**, pp. 1406–1417.

[20] Chandra, S., and Jivraj, R., 2002, ''Apparatus and Method for Generating Uniform Sized Droplets,'' U.S. Patent No. 6,446,878.

[21] Mehdizadeh, N., 2002, Ph.D. thesis, ''Droplet Impact Dynamics: Effect of Varying Substrate Temperature, Roughness, and Droplet Velocity,'' University of Toronto, Toronto, Ontario, Canada.

[22] Allen, R. F., 1975, ''The Role of Surface Tension in Splashing,'' J. Colloid Interface Sci., **51**, pp. 350–351.

[23] Kim, H. Y., Feng, Z. C., and Chun, J. H., 2000, ''Instability of a Liquid Jet Emerging From a Droplet Upon Collision With a Solid Surface,'' Phys. Fluids, **12**, pp. 531–541.

[24] Bussmann, M., Chandra, S., and Mostaghimi, J., 2000, ''Modeling the Splash of a Droplet Impacting a Solid Surface,'' Phys. Fluids, **12**, pp. 3121–3132.

[25] Brackbill, J. U., Kothe, D. B., and Zemach, C., 1992, ''A Continuum Method for Modelling Surface Tension,'' J. Comput. Phys., **100**, pp. 335–354.

[26] Boyer, H. E., and Gall, T. L., 1995, *Metals Handbook, (Desk ed.)*, American Society of Metals, Metals Park, OH.

R. H. Nilson

S. K. Griffiths

S. W. Tchikanda

Fluid and Thermal Modeling Department,
Sandia National Laboratories,
Livermore, California 94551-0969

M. J. Martinez

Multiphase Transport Processes Department,
Sandia National Laboratories,
Albuquerque, New Mexico 87185-5800

Axially Tapered Microchannels of High Aspect Ratio for Evaporative Cooling Devices

Analytical solutions are derived for evaporating flow in open rectangular microchannels having a uniform depth and a width that decreases along the channel axis. The flow generally consists of two sequential domains, an entry domain where the meniscus is attached to the top corners of the channel followed by a recession domain where the meniscus retreats along the sidewalls toward the channel bottom. Analytical solutions applicable within each domain are matched at their interface. Results demonstrate that tapered channels provide substantially better cooling capacity than straight channels of rectangular or triangular cross section, particularly under opposing gravitational forces. A multiplicity of arbitrarily tapered channels can be microfabricated in metals using LIGA, a process involving electrodeposition into a lithographically patterned mold. [DOI: 10.1115/1.1735744]

Keywords: *Channel Flow, Evaporation, Heat Transfer, Heat Pipes, Microscale*

Introduction

Evaporative cooling devices such as heat pipes and capillary pumped loops utilize capillary suction to draw liquid into the evaporation region. This capillary suction results from the pressure differential across the phase interface between a liquid and vapor. According to the Laplace-Young relation, the interfacial pressure difference is proportional to the surface tension and is inversely proportional to the radius of curvature of the interface. Further, since the pressure within the liquid is generally less than that in the adjacent gas, the liquid pressure decreases as the radius of curvature becomes smaller. Thus, liquid is drawn toward regions where the radius of curvature is small and the liquid pressure is low.

In traditional evaporative cooling devices the wick is constructed of a porous material such as a sintered metal, a felt metal, or a layered screen [1]. Metals are used because high thermal conductivity is needed to transfer heat through the wick to the liquid/vapor interface where evaporation is intended to occur, thus avoiding bubble formation within the wick. The performance of a wick material is strongly dependent upon its microstructure. It is generally beneficial to have relatively small pores or interstices within the material since this reduces the minimum radius of curvature of the phase interface, increasing the capillary pressure difference available to draw liquid into the wick. However, smaller pores result in greater frictional resistance and, hence, slower rates of liquid transport through the wick. Thus, the optimum pore size must strike a balance between these opposing requirements.

Engineered wick structures are now being produced by modern microfabrication techniques. Electrical discharge machining (EDM) of metals and chemical etching of silicon have been used to create microgrooves having triangular, trapezoidal, sinusoidal, and nearly rectangular cross sections [2–4]. Of these alternative shapes, triangular grooves have received by far the most attention as illustrated by references in [5–8]. The focus on this geometry may be largely because it provides a monotonic decrease in meniscus radius and capillary pressure as the meniscus recedes into the wedge shaped channel, as illustrated on the left side of Fig. 1. However, the triangular shape provides only half the cross sectional area of a rectangular channel, the viscous friction is greater and, in addition, deep triangular cross sections can not be readily produced using lithographic processes that have been so successful in mass production of semiconductor devices.

Lithographic processes are very well suited to the fabrication of devices having a great multiplicity of highly detailed microscale features. In particular, the LIGA process can be used to produce a multiplicity of metal channels having widths down to a few microns and depths as large as a millimeter or more [9,10]. In LIGA, a high-energy x-ray source is used to expose a thick photoresist, typically PMMA, through a patterned absorber mask. The exposed material is then removed by chemical dissolution in a development bath. This development process yields a nonconducting mold having a conducting substrate beneath deep cavities that are subsequently filled by electrodeposition. The resulting metal parts may be the final product or may be used as injection or embossing molds for mass production. However, since the exposure beam is generally aligned perpendicular to the patterned mask, LIGA and other lithographic processes are best suited for fabrication of channels having vertical sidewalls and hence a rectangular cross section. Multiple x-ray exposures at different angles to the mask could be used to produce triangular channels, but not without added complexity and loss of precision.

Although amenable to LIGA fabrication, straight rectangular microchannels have one notable disadvantage. As illustrated on the right side of Fig. 1, the capillary pressure varies with the liquid height in the channel only so long as the meniscus remains at-

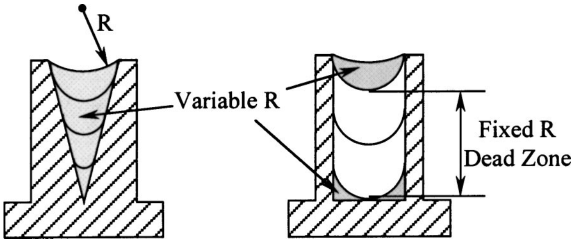

Fig. 1 Liquid configuration within straight microchannels of triangular and rectangular cross section. Straight rectangular channels have a dead zone where capillary pressure does not vary with fluid depth.

Contributed by the Heat Transfer Division for publication in the JOURNAL OF HEAT TRANSFER. Manuscript received by the Heat Transfer Division June 6, 2003; revision received February 17, 2004. Associate Editor: K. D. Kihm.

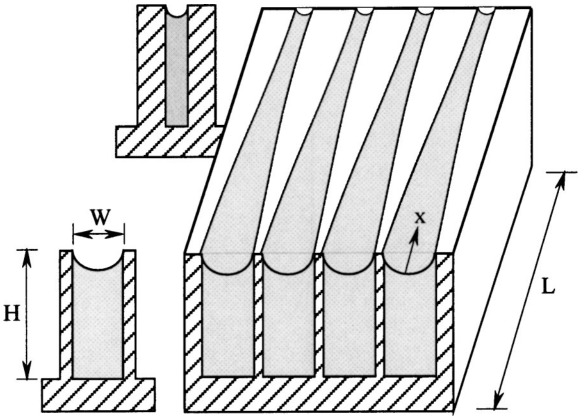

Fig. 2 Axially tapered channels increase the available capillary pressure gradient and eliminate the dead zone normally associated with rectangular channels

tached to the top corners of the channel. The radius of curvature of the interface may then range anywhere between infinity for a flat meniscus to a minimum radius that corresponds to a minimum wetting angle determined by fluid/solid interfacial energies. However, once the meniscus recedes into the channel and leaves the singular corner point, the wetting angle is fixed at its minimum value. Thus, there is a broad range of liquid levels in the channel for which the radius of curvature and the corresponding capillary pressure are invariant. Within this ''dead zone'' [3] there will be no capillary pressure variation to draw fluid toward the drier end of the channel. It is only when the meniscus reaches the channel bottom and begins to recede into the corners that a capillary pressure gradient can again be established. But in this regime the fluid depth can be no greater than half the channel width.

In the present paper we analyze the flow along an axially tapered microchannel having a rectangular cross section that narrows in width along the intended flow path toward the heat source, as illustrated in Fig. 2. Such channels have no dead zone, they can be fabricated by lithographic processes, and they are shown here to generally perform better than triangular grooves or straight rectangular channels. This comparison will be based on the computed ''capillary limit'' [1] describing the heat flux limitations imposed by axial transport of a viscous fluid in response to capillary pressure variations. To address this issue we restrict our modeling to the bulk axial flow. We do not perform detailed modeling of the transverse thin-film flow into the contact line where the meniscus meets the channel wall [5,11] because the influence of these submicron scale processes on the axial flow can be incorporated through an apparent contact angle [12] which should be relatively insensitive to the channel geometry. Although we utilize familiar models of the process physics [1,5–8,12], this is to our knowledge the first analysis of flow in axially tapered microchannels. To facilitate analytical solutions we focus on the case where the channel depth is much greater than the channel width. This limit of high aspect ratio also provides the greatest fluid flow and hence the greatest capillary limit for any given channel width. In addition to these benefits, high aspect ratio metallic structures like these are a primary target of the LIGA microfabrication technology.

Governing Equations

The one dimensional continuity equation describing steady evaporating flow along the tapered microchannels of Fig. 2 may be written as

$$h_{fg}\frac{d}{dx}(s\rho u A_{cc}) = -q'' W_b \tag{1}$$

Here, h_{fg} is the heat of evaporation, x is the axial position, ρ is the liquid density, u is the mean axial speed, $A_{cc}=HW$ is the cross sectional area of a channel of width W and height H, and s is the liquid saturation describing the fraction of the channel cross section containing liquid. It is assumed here that all of the heat flux q'' applied to the channel bottom is carried away by local fluid evaporation. This flux is applied to a base width, W_b, somewhat greater than the corresponding channel width, W, owing to the presence of webs between neighboring channels.

The fluid speed, u, is determined by the balance between viscous friction, the gravity force along the channel, ρg_x, and the gradient of the liquid pressure, P_ℓ,

$$u = -\frac{W^2}{12\mu}\left(\frac{dP_\ell}{dx} + \rho g_x\right) \tag{2}$$

The factor of twelve appearing in the denominator strictly applies only in the limit of deep channels where the flow resembles that between closely spaced parallel plates, but this constant can be adjusted to better approximate the friction in shallower channels [1,13,14]. The viscosity μ is presumed uniform and the sign of the gravitational term implies that a positive gravity force opposes the pressure driven flow.

The Young-Laplace equation relates the pressure difference across the vapor/liquid interface, ΔP, to the surface tension, σ, and the interfacial radius of curvature, R.

$$\Delta P = P_v - P_\ell = \frac{\sigma}{R} \tag{3}$$

The radius of curvature will be based on only the component in the cross sectional plane of the channel since the axial radius of curvature is usually much greater. Moreover, since the Bond Number $\mathrm{Bo} = \rho g W^2/\sigma$ is small in channels of submillimeter width, the radius of curvature may be taken as constant at any cross section. This approximation is made with the understanding that a change in curvature may occur as the circular meniscus merges into a submicron thin film that often covers portions of the wall and sometimes extends onto the webs between channels [2]. Although the presence of a thin film obscures the meaning of a contact angle, it can be defined in the macroscopic sense as the angle between the sidewall and a circular meniscus that is extended to meet the wall. An apparent contact line can be defined in the same manner. Since the axial flow is only sensitive to the macroscopic radius, R, the thin film physics are conveniently incorporated through their influence on the apparent contact angle α, relating the channel width to the bulk radius of curvature, $W/R = 2\cos\alpha$. Finally, for simplicity, we will assume that the external vapor pressure is uniform, so that the pressure gradients in the liquid result only from variations in the capillary pressure differential, $\Delta P = P_v - P_\ell$.

Combination of Eqs. (1) and (2) yields a single ordinary differential equation describing axial variations of the normalized liquid pressure and saturation.

$$\frac{d}{d\xi}\left(s w^3\left(\frac{dp}{d\xi} + G^*\right)\right) = Q^* \tag{4}$$

The lower case variables appearing here have been normalized in the following manner:

$$\xi = \frac{x}{L} \quad w = \frac{W}{W_o} \quad p = \frac{P_\ell - P_v}{\Delta P_o} \tag{5}$$

Here, L is the channel length, and W_o is the channel width at the entrance. The characteristic pressure differential, ΔP_o, represents the maximum attainable capillary pressure in a channel of width W_o associated with a radius of curvature $R_o = W_o/(2\cos\alpha_o)$ corresponding to a prescribed minimum wetting angle, α_o.

$$\Delta P_o = \frac{\sigma}{R_o} = 2\cos\alpha_o \frac{\sigma}{W_o} \tag{6}$$

The two dimensionless parameters appearing in Eq. (4) are the normalized heat flux and normalized gravitational force.

$$Q^* = \frac{q''}{H\rho h_{fg}}\left(\frac{12\mu}{\Delta P_o}\right)\frac{W_b L^2}{W_o^3} \qquad G^* = \frac{\rho g_x L}{\Delta P_o} \tag{7}$$

The channel width is for the moment assumed to vary linearly along the channel from W_o to W_e such that

$$w = \frac{W}{W_o} = 1 - \Delta w \xi \quad \text{where} \quad \Delta w = \frac{W_o - W_e}{W_o} \tag{8}$$

After presenting comprehensive results for this simplest case, we will later briefly consider other power-law variations of the channel width and the reasons why they do not generally perform as well.

Analytical Solutions

The governing differential equation, Eq. (4), can be readily integrated once for any prescription of the axial heat flux variation, here taken as uniform, to obtain

$$s w^3 \left(\frac{dp}{d\xi} + G^*\right) = -Q^*(1-\xi) \tag{9}$$

This expression incorporates the boundary condition that there be no flow at the end of the channel (ξ=1) as appropriate either at a dead-end or at the end of the wetted portion of a longer channel. The two unknown functions, p and s, appearing in Eq. (9) are generally constrained by the following relationship between the liquid pressure and the radius of curvature, R, which is an implicit function of the fluid saturation.

$$p \equiv \frac{P_\ell - P_v}{\Delta P_o} = -\frac{R_o}{R(s)} = -\frac{W_o}{2\cos\alpha_o R(s)} \tag{10}$$

Equations (9–10) must generally be numerically integrated in a coupled manner over two sequential flow domains, an entry domain or ‘‘accommodation'' region [6] wherein the meniscus remains attached or ‘‘pinned'' to the top corners of the channel (see Fig. 1(b)), followed by a recession region in which the meniscus recedes to the channel floor. However, for channels of high aspect ratio it is possible to simplify and to partially decouple the governing equations within each subdomain.

In the entry or pinned-meniscus region, the meniscus curvature increases and the liquid pressure decreases with distance owing to the decreasing volume of fluid within the channel. In this region a thin film of liquid is likely to extend onto the top surface of the webs between channels, as observed in [2], and the apparent contact angle is determined not by fluid/solid interfacial energy considerations but rather by the local fluid volume within the channel and the requirement that the meniscus (excluding the thin film region) have a constant curvature. Although the reduction in fluid depth is required to produce an axial pressure gradient, there is very little reduction in the fractional saturation of a channel having a high aspect ratio. Even for a contact angle of zero, the maximum possible reduction in saturation is readily found to be only π/8A or about 4 percent for an aspect ratio $A = H/W$ of ten. Thus, in the limit of large A it is permissible set $s=1$ in Eq. (9) and to perform the integration, yielding

$$p(\xi) = p(0) - G^*\xi - Q^*F(\xi) \tag{11a}$$

where

$$F(\xi) = \int_o^\xi \frac{1-\xi}{(1-\Delta w\xi)^3}\, d\xi = \frac{\xi}{2}\left(\frac{2-\xi-\Delta w\xi}{(1-\Delta w\xi)^2}\right) \tag{11b}$$

In neglecting the variation in s we accept an error of order $u\Delta s/s\Delta u \sim \Delta s/s < 1/A$ and even this small error is offset by assuming that $s=1$ rather than $(1-\Delta s)$ at the entry to the recession domain.

In the meniscus recession domain, the apparent meniscus contact line recedes below the top corners of the channel and the apparent contact angle is fixed at a minimum value, α_o, that is mainly dependent on solid/fluid interfacial energies. A thin film may still be present above the meniscus contact line, and the value of the minimum contact angle may be altered by local fluid evaporation, as explained later in the discussion of example calculations. However, since the value of the apparent contact angle is constant, or nearly so, the capillary pressure in this domain is controlled primarily by variations in the channel width in accordance with Eq. (10).

$$p = -\frac{R_o}{R} = -\frac{W_o}{W} = -\frac{1}{w} = -\frac{1}{1-\Delta w\xi} \tag{12a}$$

and, hence,

$$\frac{dp}{d\xi} = -\frac{\Delta w}{w^2} \tag{12b}$$

These relationships hold for any value of the minimum wetting angle since the corresponding radius of curvature is always proportional to the channel width. The resulting liquid pressure gradient can be substituted into Eq. (9) to obtain an explicit representation of s in terms of the prescribed variation in w.

$$s = \frac{Q^*(1-\xi)}{w(\Delta w - G^* w^2)} \tag{13}$$

This equation applies either to the recession region of a flow having a fully wetted entry region or to a flow that enters the channel with a saturation less than unity.

The saturation profile given by Eq. (13) must approach zero at the channel end (ξ=1) in order to meet the requirement of zero mass flow. A vanishing saturation is necessary because the pressure gradient in the liquid is determined by the given channel convergence and by the fixed wetting angle on the channel walls. Thus, in the limit of high aspect ratio a finite saturation at the end wall implies a finite flux through the wall unless the meniscus is attached to either the top corners or the channel floor, the gray zones highlighted on the right side of Fig. 1. A vanishing pressure gradient at the end wall can thus be accommodated for all finite aspect ratios by taking into account the flow in the bottom corners of the channel. However, these refinements are unimportant at high aspect ratios and will not alter predictions of maximum sustainable heat fluxes, our main interest, since the saturation certainly goes to zero in that instance.

Matching conditions must be satisfied at the interface between the entry region and the recession region. Continuity of the liquid pressure requires equality of the expressions given in Eqs. (11) and (12a).

$$p(\xi) = -\frac{1}{w} = p(0) - G^*\xi - Q^*F(\xi) \tag{14}$$

Continuity of the mass flux is enforced by equating alternative expressions for Q^* derived form Eqs. (11) and (13).

$$\frac{p(0) - p(\xi) - G^*\xi}{F(\xi)} = \frac{s w(\Delta w - G^* w^2)}{(1-\xi)} \tag{15}$$

Equations (14) and (15) are conveniently combined by substituting $-1/w$ for p(ξ) in Eq. (15). Since a discontinuity in saturation is generally allowable, the value of s on the forward side of the matching interface may be less than unity. For chosen values of this saturation and the parameters G^* and Δw, the two sides of Eq. (15) are simply functions of ξ. Thus, widely available root finding routines can be used to find the value of ξ where the matching conditions are satisfied. We utilized a routine called

FZERO [15] to meet relative and absolute error tolerances of 10^{-10}. The corresponding value of Q^* is then readily computed from either side of Eq. (15).

Pressure and Saturation Profiles

Figure 3 illustrates pressure profiles computed from Eq. (11) that applies when the meniscus is attached to the top corners of the channel. The normalized inlet pressure is taken as zero as appropriate for the flat interface of a fully flooded channel. For the chosen value of $\Delta w = 0.5$, the width of the channel at its end ($\xi = 1$) is half that at the inlet and so the minimum attainable value of the normalized liquid pressure is -2.0. Evaporation within the channel causes depression of the downward bowing meniscus, reducing the local pressure and drawing fluid into the channel. For a given heat flux, the meniscus (and liquid pressure) at the channel end are drawn down to an equilibrium level sufficient to maintain the flow rate needed to offset evaporative losses. With increasing Q^*, the pressure at the end of the channel decreases and the radius of curvature becomes progressively smaller. Note that the pressure gradient at the channel end is always zero, consistent with the requirement that there be no flow through the end wall.

For a dimensionless heat flux of $Q^* = 2$, the exit pressure reaches its minimum value of $p = -2.0$, corresponding to the minimum contact angle. An upper bound on the heat flux associated with this condition can be readily derived by evaluating Eqs. (11) at $\xi = 1$ and substituting the maximum and minimum possible value of the inlet and outlet pressures, $p(0)_{\max} = 0$ and $p(1)_{\min} = -W_o/W_e = -1/(1-\Delta w)$, leading to

$$Q^*_{\max} \leq \frac{1}{F(1)}[p(0)_{\max} - p(1)_{\min}] = 2(1 - G^*(1 - \Delta w)) \tag{16}$$

Remarkably, it is seen that in the absence of a gravitational force along the channel ($G^* = 0$) the corresponding flux, a provisional estimate of the maximum sustainable flux, $Q^*_{\max}$, is the same for all tapers. It might also appear from Eq. (16) that a very strong taper ($\Delta w = 1$) could entirely negate the influence of an adverse gravitational force. However, as explained below, this provisional estimate of the maximum sustainable flux is too optimistic.

The dotted line in Fig. 3 corresponds to a normalized pressure of $p = -1/w$. In accordance with Eq. (12a) this line indicates the minimum attainable liquid pressure at any location along the channel, corresponding to the minimum wetting angle and the width at that location. Since the actual liquid pressure must always be greater, the solution shown for $Q^* = 2$ must be rejected. At a somewhat smaller value of Q^* the end of the channel will begin to dry out causing backward recession of the meniscus. It follows that the liquid saturation at the end of the channel will be zero when the maximum sustainable heat flux is applied. Larger heat fluxes would result in a dry section at the channel end. Thus, we will refer to this limiting dryout heat flux as the maximum sustainable heat flux, or simply the maximum flux. The normalized value of this maximum flux will be denoted $Q^*_{\max}$.

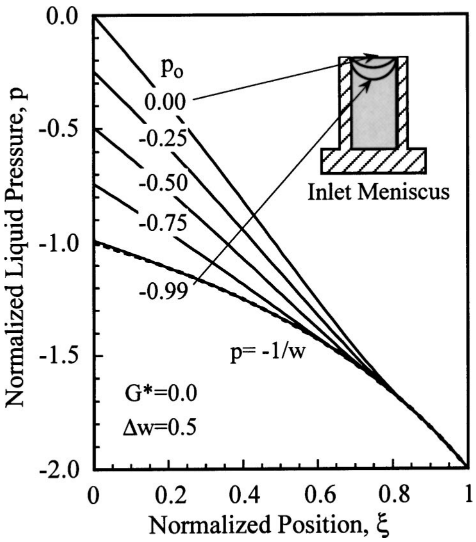

Fig. 4 Pressure distributions under conditions of maximum heat flux for various choices of inlet pressure

Figures 4 and 5 illustrate pressure and saturation profiles corresponding to the maximum sustainable heat flux for $\Delta w = 0.5$ and for various values of the inlet pressure, $p_o = p(0)$. The uppermost curves for $p_o = 0$ describe the end member solution of the family just shown in Fig. 3; the corresponding maximum heat flux is $Q^*_{\max} = 1.87$. The smaller values of the inlet pressure, p_o, correspond to a greater meniscus curvature at the inlet. With decreasing inlet pressure, the transition point from a pinned meniscus to a

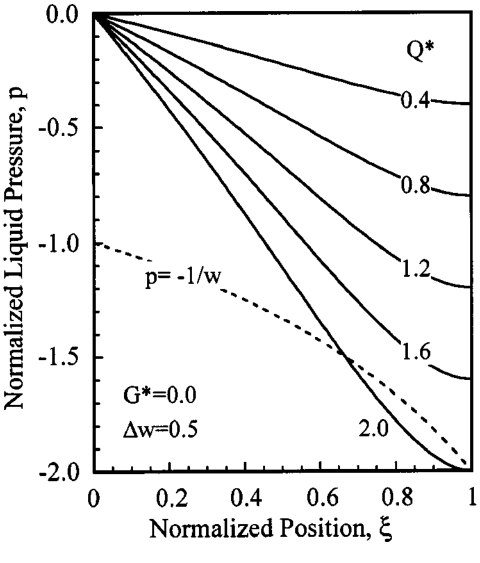

Fig. 3 Pressure distribution along channel having a 50 percent taper for various heat fluxes. Pressure cannot fall below dotted line indicating minimum pressure based on local width.

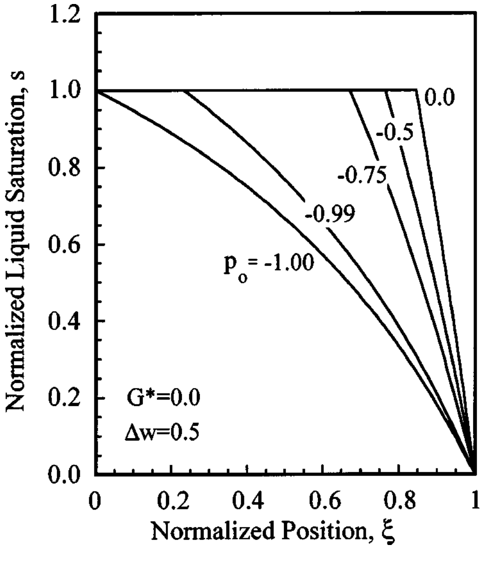

Fig. 5 Saturation profiles under conditions of maximum heat flux for various choices of inlet pressure

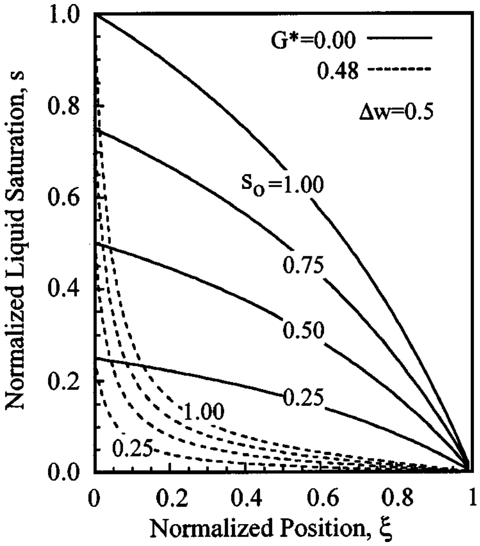

Fig. 6 Saturation profiles under conditions of maximum flux for various choices of the inlet saturation

receding meniscus moves backward, reaching the entrance just as p_o goes to zero. The associated maximum heat fluxes also decrease with p_o, since the available driving pressure differential between the inlet and exit is smaller. Comprehensive calculations of the maximum sustainable heat fluxes for various channel tapers and shapes are presented in the next section.

The saturation profiles in Fig. 5 all begin with $s=1$ at the transition point between the pinned and receding meniscus domains. We sought solutions having an abrupt jump in saturation from unity in the entry region to a smaller value ahead of the transition, but we found no such solutions even for cases where the channel taper was not linear with distance. Given that observation, it can be seen from Eq. (9) that $dp/d\xi$ must be continuous at the transition when s and w are both continuous. This condition is seen to be properly satisfied by the pressure profiles in Fig. 4. The saturation profile for $p_o=-1$ has a saturation of unity at the channel inlet. This is an end-member both for this set of solutions and for those shown in the next figure.

Figure 6 presents saturation profiles for values of the inlet saturation, s_o, ranging from 0.25 to 1.0. Since $s=0$ at the leading edge of each, these represent dryout profiles for increasingly large values of $Q^*_{\max}$, each corresponding to a particular inlet saturation. The relationship between $Q^*_{\max}$, s_o, and G^* is obtained by evaluating Eq. (13) at the inlet location where $w=1$, $\xi=0$ and $s=s_o$.

$$Q^*_{\max}=s_o(\Delta w-G^*) \tag{17}$$

Thus, $Q^*_{\max}$ is simply proportional to s_o. Two sets of profiles are shown in Fig. 6. The upper set for $G^*=0$ has no opposing gravitational force, while the lower set is for a gravitational force of $G^*=0.48$, very close to the limiting value of $G^*=0.50$ for which any heat flux is sufficient to dry out the channel. Equation (17) correctly describes the maximum sustainable heat flux for a channel that is not fully saturated at the inlet. Note that the maximum sustainable heat flux for this domain is proportional to Δw and is therefore zero for a straight channel. There can be no heat flux for $\Delta w=0$ because there can be no pressure gradient along a straight channel with a receding meniscus (see dead zone in Fig. 1) except in the bottom corners where the flow volume and speed become insignificant in the limit of high aspect ratio. The sustainable heat flux for these corner flows can be readily estimated from previous studies of flow in triangular grooves [1,5–8,12,16] or by minor modification of our later analysis of flow in triangular grooves of high aspect ratio.

Maximum Sustainable Heat Fluxes

For a given choice of the parameters, G^*, p_o, and Δw, the maximum sustainable heat flux can be computed by first solving Eq. (15) to identify the normalized position, ξ, of the transition between the entry region and the meniscus recession region. This value of ξ and the corresponding value of w are then substituted into either Eq. (11) or Eq. (13) to obtain $Q^*_{\max}$. Since these equations describe interfacial conditions, the appropriate values of s and $p(\xi)$ are unity and $-1/w$, respectively.

The variation of the maximum sustainable or dryout heat flux with the normalized inlet pressure is illustrated in Fig. 7 for $G^*=0$ and for several values of the normalized taper, Δw. For $\Delta w=0$, the maximum flux is found to increase linearly with p_o, in accordance with the equality of the following relation derived from Eq. (11) by substitution of the limiting minimum value of the outlet pressure, $p(1)_{\min}=-W_o/W_e=-1/(1-\Delta w)$.

$$Q^*_{\max}\leqslant\frac{1}{F(1)}[p(0)-p(1)_{\min}]=2+2(1-\Delta w)p(0) \tag{18}$$

However, as seen in Fig. 7 this relationship clearly does not hold as an equality in the opposite extreme of a very strong taper, $\Delta w=1$. In this instance the maximum flux is simply unity, $Q^*=1$, regardless of the inlet pressure. This behavior for large Δw is very robust in the sense that the maximum flux is not sensitive to inlet conditions that are sometimes influenced by other components within the system such as the pressure drops in the connector tubes of a capillary pumped loop.

For intermediate values of Δw the maximum flux profiles illustrated in Fig. 7 transition between these limiting straight lines that apply in the limits of $\Delta w=0$ and 1. Note that as $p_0\rightarrow-1$, the maximum flux is accurately given by $Q^*_{\max}=\Delta w$, in accordance with Eq. (17). This is expected because the transition point between pinned and receding meniscus domains approaches the channel entrance as $p_0\rightarrow-1$, leaving only the receding meniscus domain described by Eq. (17). Note that in this same limit, the equality of Eq. (18) would have incorrectly predicted that $Q^*_{\max}=2\Delta w$. This inaccuracy is not surprising because Eq. (18) is only strictly applicable to the entry or pinned meniscus region of an untapered channel. The entry region becomes increasing important in the limit as $p_0\rightarrow 0$. In this limit, it is seen in Fig. 7 that the maximum sustainable heat flux decreases with Δw, but the reduction from the global maximum of $Q^*=2.0$ is only about 15 per-

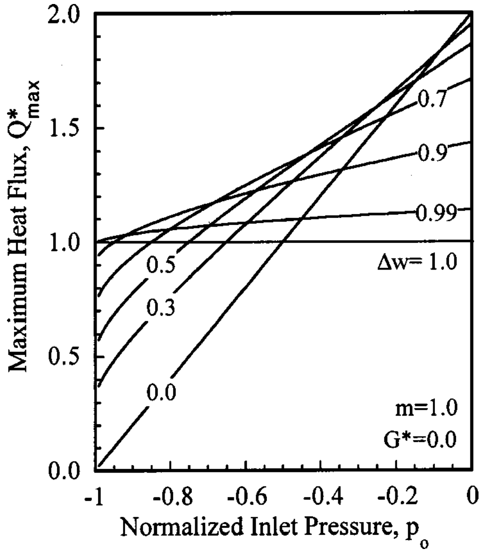

Fig. 7 Variation of maximum heat flux with inlet pressure for various linear tapers

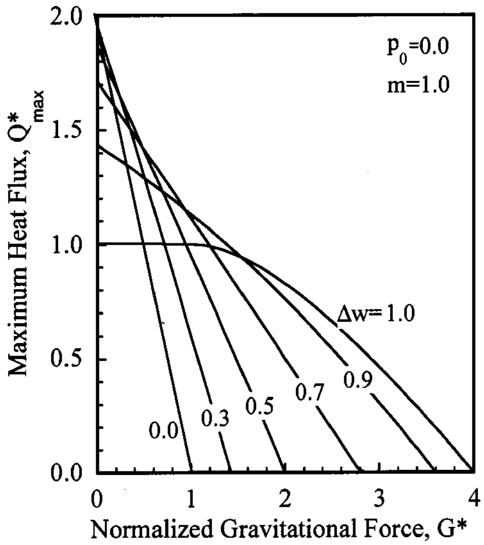

Fig. 8 Variation of maximum heat flux with opposing gravitational force for various linear tapers

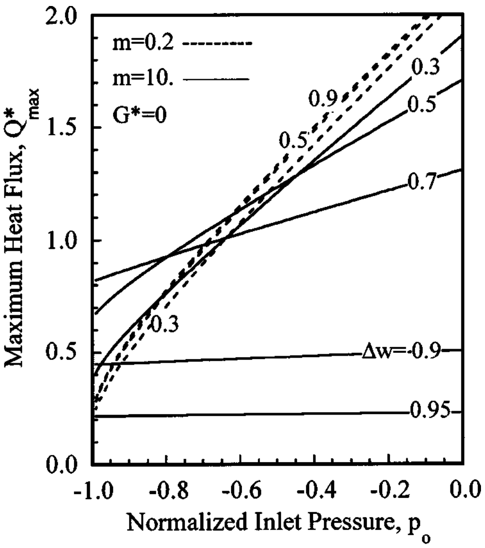

Fig. 9 Variation of maximum heat flux with inlet pressure for various nonlinear tapers

cent for $\Delta w = 0.7$, increasing to a maximum possible reduction of 50 percent for $\Delta w = 1$. So on the whole, it appears that taper is desirable in dealing with inlet conditions that are less than ideal (i.e., $p_o < 0$) but that tapers greater than 70 percent are probably unwise.

The benefit of channel taper is greatest when an opposing gravitational force is present. This is because the stronger taper produces a smaller channel width at the exit, reducing the minimum liquid pressure available to draw fluid upward against gravity. As seen in Fig. 8, a stronger taper extends the operating range of an evaporative cooling device to larger values of G^*. In the absence of taper, the maximum heat flux, Q^*, decreases linearly with G^*, falling to $Q^* = 0$ at $G^* = 1$. A 50 percent taper ($\Delta w = 0.5$) doubles the operating range to $G^* = 2.0$ while only slightly reducing the maximum sustainable heat flux for $G^* = 0$. With increasing taper, the maximum flux for $G^* = 0$ gradually decreases to $Q^* = 1.0$ while the operating range extends to $G^* = 4.0$ in the limit as $\Delta w \rightarrow 1$. However, a 70 percent taper can provide nearly a factor-of-three increase in the operating range while only reducing the maximum attainable flux at $G^* = 0$ by 15 percent. This amount of taper also provided well balanced performance under variations in the channel inlet pressure, as seen earlier in Fig. 7.

Concave and Convex Tapers

The influence of a nonlinear channel taper is now explored for power-law profiles of the form

$$w = \frac{W}{W_o} = (1 - \Delta\omega\xi)^m \tag{19}$$

where the parameter $\Delta\omega$ is chosen as follows to provide a normalized width variation of Δw.

$$\Delta\omega = 1 - (1 - \Delta w)^{1/m} \tag{20}$$

These power-law shapes permit analytic integration of Eq. (9) yielding a pressure profile given by Eq. (11*a*) except that the function F now takes the following form in which $M = 3m$ and M may not have the values of 1 or 2.

$$F(\xi) = \frac{1-\Delta\omega}{(M-1)\Delta\omega^2}\left[1-(1-\Delta\omega\xi)^{-(M-1)}\right] - \frac{1}{(M-2)\Delta\omega^2} \times \left[1-(1-\Delta\omega\xi)^{-(M-2)}\right] \tag{21}$$

Saturation profiles for the receding meniscus domain are given by an expression analogous to Eq. (13) except that the pressure gradient is evaluated as $dp/d\xi = w^{-2}(dw/d\xi)$ based on the above profile shape. The matching conditions between the entry region and the receding meniscus region are analogous to Eqs. (14) and (15).

Figure 9 illustrates the variation of the maximum heat flux with p_o for $m = 0.2$ (dotted lines) and for $m = 10$ (solid lines). As seen in the inset of Fig. 10, the interior of the channel is convex (blunt nosed) for $m > 1$, linear for $m = 1$, and becomes concave (cusp shaped) for $m > 1$. By comparing the results in Figs. 7 and 9 it is clear that convex shapes reduce the influence of taper while convex shapes accentuate it. However, for stronger tapers (e.g., $\Delta w = 0.9$ and 0.95) the concave channel shapes clearly do not perform as well as their linear counterparts. Thus, these results for varying inlet pressures suggest that convex and concave shapes are no better than a linear taper.

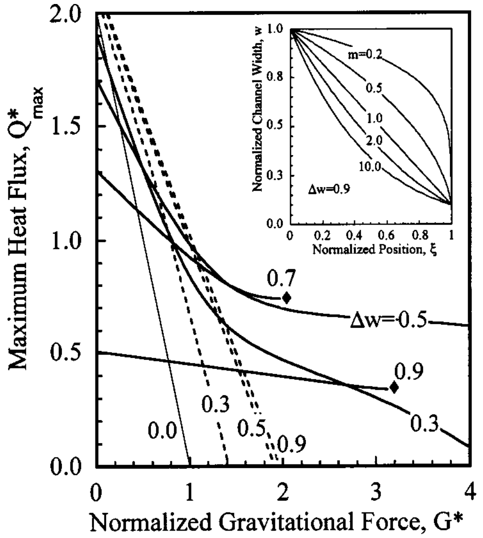

Fig. 10 Variation of maximum heat flux with opposing gravitational force for various nonlinear tapers: $m = 0.2$ (dotted lines); and $m = 10$ (solid lines). Inset illustrates nonlinear taper shapes.

The performance of convex and concave channels under varying gravity forces is illustrated in Fig. 10. Here again, the convex and concave channels generally underperform their linear counterparts. Moreover, the convex channels with strong tapers ($\Delta w = 0.7$ and 0.9) suffer from an abrupt reduction in maximum sustainable heat flux at the points marked by diamond shaped symbols in Fig. 10. At these points, the character of the solutions change in that the sign of $ds/d\xi$ becomes positive on the downstream side of the transition from pinned to receding meniscus, with the unphysical implication that the saturation exceeds unity. We believe that steady solutions for greater G^* enter the channel with unit saturation and have heat fluxes considerably less than those indicated by diamond symbols. Thus, it appears that on the whole, linear tapers are preferred over convex and concave shapes, particularly when robust operation is important.

Cascade of Progressively Bisected Channels

The benefit of channel taper can be realized in a discrete, step-like manner by serial connection of a sequence of successively narrower straight channel segments. As an example, we consider a sequence constructed by insertion of partitions that progressively bisect each of the channels over a portion of their length, as illustrated in the inset of Fig. 11. The resulting flow path consists of N axial stages, with 1 channel in the first stage, 2 identical parallel channels in the second stage, 4 channels in the third stage, and so on. This configuration makes full use of the available plan-form area and is relatively easy to analyze. Application of Eq. (9) to the ith stage yields

$$n_i w_i^3\left(\frac{dp}{d\xi}+G^*\right)=-Q^*(1-\xi)=-Q^*[(1-\xi_{i-1})-(\xi-\xi_{i-1})] \tag{22}$$

where n_i is the number of parallel channel segments of width w_i, ξ_{i-1}, and ξ_i are the normalized coordinate values at the entrance and exit of the ith segment, and $\Delta\xi_i=\xi_i-\xi_{i-1}$ is the segment length. Here, the saturation levels s_i have been taken as unity because all of the channel segments are untapered and so will dry out as soon as the meniscus recedes below the top corners. Integration of this expression over the segment provides a relationship between the geometric parameters, the pressure drop over each segment, $\Delta p_i=p_{i-1}-p_i>0$, and the normalized heat flux applied to each segment, Q_i^*.

$$Q_i^*=\frac{n_i w_i^3(\Delta p_i-G^*\Delta\xi_i)}{\Delta\xi_i\left(1-\xi_{i-1}+\dfrac{\Delta\xi_i}{2}\right)} \tag{23}$$

To optimize the device performance, we determine the lengths of the dividing partitions by requiring that all the available pressure drop be utilized in each successive stage. The meniscus curvature at the outlet of each segment must then be equal to the minimum possible value, and so $p_i=-1/w_i$. Since the pressure must be continuous, the inlet pressure of the ith segment must be the same as the outlet pressure of the $(i-1)$th, $p_{i-1}=-1/w_i$. This requires that the radius of curvature be the same on both sides of the transition between stages, as illustrated in the cross sectional view of Fig. 11. The adjustment between the two meniscus profiles shown in Fig. 11 will take place over about one channel width on each side, a distance far smaller than typical axial dimensions. In the examples presented below the prescribed inlet pressure of the first stage, p_o, is taken as zero, corresponding to a flat inlet meniscus.

$$\Delta p_i=\left(\frac{1}{w_i}\right) \quad \text{for } i=1; \quad \Delta p_i=\left(\frac{1}{w_i}-\frac{1}{w_{i-1}}\right) \quad \text{for } i>1 \tag{24}$$

Since the ith stage consists of n_i identical parallel segments, the width of each segment is computed by subtracting out the total width of (n_i-1) dividers each having a normalized thickness, t, and dividing the remainder by n_i.

$$w_i=\left(\frac{1-t(n_i-1)}{n_i}\right) \quad \text{where } n_i=2^{i-1} \tag{25}$$

The only remaining unknowns are the $N-2$ values of ξ_i for $i=2, N-1$ and the unknown Q_i^*. However, since all Q_i^* must be identical for a spatially uniform heat flux, there are a total of only $N-1$ unknowns (Q^* and $N-2$ ξ's). The corresponding $N-1$ equations are obtained by simply requiring that $Q_i^*=Q_{i-1}^*$ for $i=2, N$. These nonlinear equations are solved to error tolerances of 10^{-10} by a general-purpose iterative routine, DNSQE, developed at Sandia National Laboratories [15].

Figure 11 illustrates the maximum sustainable heat flux as a function of the opposing gravitational force, G^*, for various numbers, N, of stages. For $G^*=0$, the maximum flux increases from $Q^*=2.0$ to 2.5 when a single partition is added, that is, when N increases from 0 to 1. The single partition of optimum length begins at $\xi=0.552$ and extends to $\xi=1$. Introduction of additional optimally sized partitions increases the maximum flux for $G^*=0$ in accordance with the sequence

$$Q_{\max}^*=2+\sum_{i=1}^{N}\left(\frac{1}{2}\right)^{i-1} \tag{26}$$

toward a limit of $Q^*=3$ for an infinite number of stages. Fortunately, most of the benefit is gained with only two or three stages, since it is often impractical to introduce more than a few stages owing to the space occupied by the dividers themselves.

Our example calculations are for an idealized situation where the partition thickness is negligible compared to the inlet channel width. A divider thickness that is 10 percent of the inlet width ($t=0.1$) will only permit a maximum of nine channels, so two or three stages is all that can be used for that case. Thus, a fabrication technology capable of producing very narrow partitions would certainly be beneficial. Although the divider thickness must be large enough to effectively conduct heat from the substrate to the evaporation interface, the width of the dividers can be cut in half at each stage while still maintaining the same total cross sectional area for heat conduction, because the number of dividers doubles at each stage.

The benefit of split channels is greatest when the opposing gravity force is large, as clearly seen in Fig. 11. In the absence of

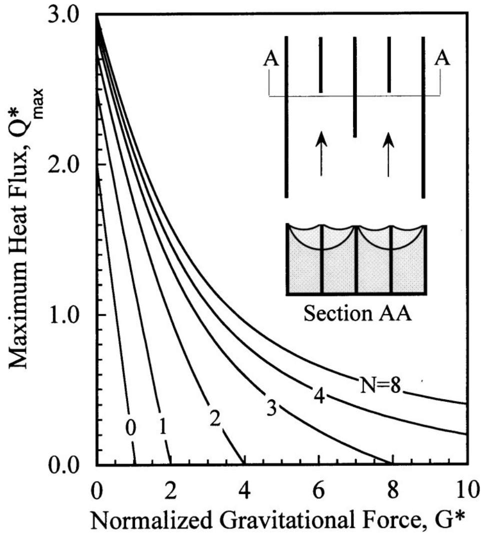

Fig. 11 **Variation of maximum heat flux with gravitational force for channels bisected *N* times by narrow splitter plates ($t^*=0$). Inset schematically illustrates channel geometry for *N* =3.**

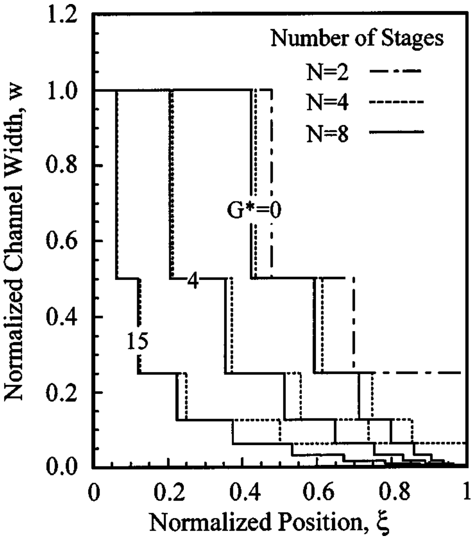

Fig. 12 Stepwise variation of width along channels optimized for various gravitational forces, *G. Lengths of first stages are not very sensitive to number of stages, *N*.**

any dividers $(N=0)$, the maximum heat flux is zero for normalized gravitational forces greater than $G^*=1$. In contrast, the use of two stages extends the range of operation to $G^*=4$, while also increasing the maximum flux to $Q^*=2.75$, for $G^*=0$. To obtain the same gravitational lift using continuous straight channels would necessitate a factor of four reduction in channel width, reducing the sustainable heat fluxes by that same factor as apparent from the scaling relations given by Eqs. (4–7). However, it is important to point out that the results presented in Fig. 11 indicate maximum possible fluxes for configurations that are optimized for the indicated gravitational force. Thus, if we desire a system that operates well in a range from $G^*=0$ to 4, we might choose to optimize the geometry based on a gravitational force of $G^*=2$. Note that the maximum permissible G^* (where Q^* goes to zero) depends only on the number of stages.

The channel width profiles of the optimized multistage channel configurations are illustrated in Fig. 12. The stairstep plots indicate the channel width as a function of axial position for the case of very narrow partitions. Channel shapes optimized for $G^*=0$ are shown for $N=2$, 4, and 8 stages. It is interesting to note that for $G^*=0$ the taper of the channel might be judged as nearly linear based on a construction of lines connecting the centers of the channel segments. It is also seen that the lengths of the first partitions are not greatly altered by insertion of additional partitions, since the locations of the first steps are relatively insensitive to the number of stages, *N*. This observation also holds true for shapes that are optimized for $G^*=4$ and 15. In these latter cases the results for $N=2$ are omitted to reduce the confusion of additional overlapping lines. It is seen that the optimum shapes for large G^* have a convex profile, in agreement with previous results for smoothly tapered channels.

Comparison With Triangular Grooves

Because of the popularity of evaporative cooling channels having a triangular cross section [1–8], we now compare their performance with that of tapered channels. We again consider the case of high aspect ratios partly for simplicity and partly because the maximum heat flux increases linearly with the channel depth, as explained earlier. In this limit, the axial fluid speed at any elevation may be taken as proportional to the width at that depth. Area weighted integration of this speed over the height of the groove indicates that the mean axial speed in the channel is given by Eq. (2) with the divisor in the denominator increased from 12 to 24, in good agreement with numerical results ranging from 24.25 to 27.6 for apex angles from 5 to 60 deg in [16]. This factor of two is combined with an additional factor of two reduction in the cross sectional area of the channel to provide a reduction in heat fluxes by a factor of four. If we leave our scaling of Q^* unchanged, this factor of four can be inserted as a divisor on the left sides of Eqs. (4) and (9).

Assuming that the triangular groove is not tapered along its axis, it follows from our analysis of straight rectangular channels that a heat flux of $Q^*=2./4.=0.5$ can be carried without any recession of the pinned meniscus into a triangular groove. Recall from Figs. 3 and 7 that a tapered channel with a 50 percent reduction in width can carry a flux of about $Q^*=1.8$ without recession of the meniscus. A 70 percent taper can carry a flux of about $Q^*=1.5$ without recession. So by this measure of performance the tapered channel is better by about a factor of three.

An important benefit of triangular grooves is that they continue to draw fluid by capillarity even when the meniscus falls below the pinning points at the top corners. This benefit is shared by axially tapered channels. To assess the relative performance under these conditions, suppose that the saturation at the channel inlet is near unity and that the entry meniscus is at its maximum curvature, so that any evaporation will cause recession of the meniscus into the channel. The governing equation for the triangular groove is obtained by inserting a factor of 4 into Eq. (9).

$$s w_o \frac{w^2}{4}\left(\frac{dp}{d\xi}+G^*\right)=-Q^*(1-\xi) \tag{27}$$

Here, one of the *w*'s is subscripted with a zero to indicate that it should be taken as unity; this factor of w arose from the cross sectional area of the channel which is constant. The remaining factor of w^2 accounts for frictional resistance and is correctly taken as the width of the groove at the top of the meniscus which decreases along the channel. The fractional saturation, *s*, is simply the product of the normalized fluid depth and width, again based on the local meniscus location. Further, since the normalized fluid depth $(h=H/H_0=W/W_0=w)$ and the radius of meniscus curvature are both proportional to the meniscus width,

$$s=hw=w^2 \quad \text{and} \quad \frac{dp}{d\xi}=\frac{1}{w^2}\frac{dw}{d\xi} \tag{28}$$

Inserting these results into Eq. (27) and performing the integration yields a maximum heat flux of $Q^*=1/6$ for $G^*=0$.

$$\frac{w^2}{4}\frac{dw}{d\xi}=-Q^*(1-\xi) \quad \text{and} \quad Q^*_{\max}=\frac{1}{6} \tag{29}$$

The corresponding maximum heat flux for a tapered channel is $Q^*=\Delta w$ as noted earlier in discussing Fig. 6 and Eq. (17). Thus, a channel taper of 20 percent $(\Delta w=0.2)$ provides similar performance while a strongly tapered channel $(\Delta w=1.0)$ can sustain a heat flux that is 6 times greater. Thus, even if the inlet meniscus should recede below the channel top, a tapered channel can easily outperform a triangular groove. In addition, the tapered channel can be readily produced lithographically while a triangular groove cannot.

Example Calculations

A series of example calculations are now presented to illustrate practical application of the foregoing dimensionless results. We consider the case of an open channel system operating in the vicinity of standard temperature and pressure. The vertical channels are of length $L=5$ cm and have one end submerged in a methanol reservoir. The fluid properties are $\rho_1=755\,\text{kg/m}^3$, $h_{fg}=1130\,\text{kJ/kg}$, $\mu_1=0.00035$ pa-s, and $\sigma=19$ mN/m [1]. It is assumed that the channels and the webs between them each account for half of the overall device width at the inlet end such that

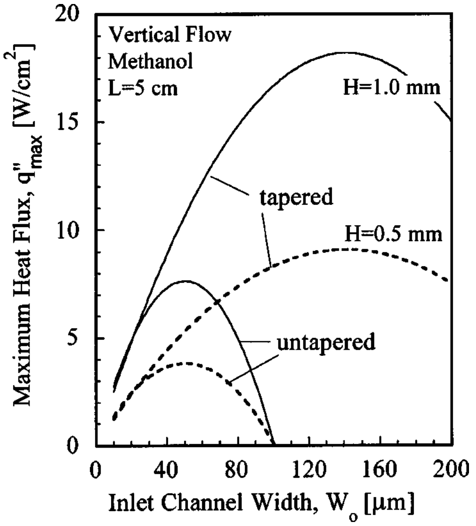

Fig. 13 Comparison of maximum sustainable heat fluxes for tapered ($\Delta w=0.7$) and untapered ($\Delta w=0.0$) channels having various inlet widths, W_o, and two depths, $H=1.0$ mm (solid lines) and 0.5 mm (dotted lines)

$W_b/W_o=0.5$. The quantity of primary interest is the maximum sustainable heat flux, $q''_{\max}$, as limited by the viscous flow considerations modeled here. It is computed from the following inverted form of the defining equation for the dimensionless heat flux in Eq. (7).

$$q''_{\max}=Q^*_{\max}H\rho h_{fg}\frac{W_o}{W_b}\left(\frac{W_o}{L}\right)^2\left(\frac{\Delta P_o}{12\mu}\right) \tag{30}$$

One can alternatively compute the maximum wetted length, $L_{\max}$, of a channel subjected to a prescribed heat flux, q'', using the following rearrangement of the same equation.

$$L_{\max}=W_o\left[Q^*_{\max}\left(\frac{H\rho h_{fg}}{q''}\right)\frac{W_o}{W_b}\left(\frac{\Delta P_o}{12\mu}\right)\right]^{1/2} \tag{31}$$

The dimensionless quantity $Q^*_{\max}$ appearing here depends upon three dimensionless parameters, G^*, p_o and, the normalized taper, Δw. Given that the channel inlets are assumed to be fully submerged, the entry meniscus should be essentially flat corresponding to $p_o=0$. To illustrate the benefit of taper, maximum sustainable heat fluxes, $q''_{\max}$, computed from Eq. (30) are compared for two types of channels, straight channels having $\Delta w=0$ and linearly tapered channels having a 70 percent reduction in width, $\Delta w=0.7$. Inlet channel widths are varied from 10 to 200 microns. For each width, the maximum capillary pressure, ΔP_o and the gravitational parameter G^* are computed from their definitions in Eqs. (6) and (7) assuming a minimum contact angle of zero degrees. The variation of $Q^*_{\max}$ with G^* can be well approximated by straight line fits to the dimensionless results presented in Fig. 8.

Figure 13 displays the maximum sustainable heat flux as a function of the inlet channel width for two choices of the channel height, $H=0.5$ mm and 1.0 mm. Each of the curves passes through a maximum at an optimal value of the channel width. At small channel widths, viscous friction is excessive. Conversely, at large widths the available capillary pressure differential becomes progressively weaker relative the opposing gravitational head (larger G^*), eventually reducing the maximum flux to zero. The tapered channels produce an optimal maximum flux about twice that of a straight channel.

A doubling of the channel height, H, doubles the maximum sustainable heat flux as apparent in Eq. (30) and in Fig. 13. The greater fluid depth simply increases the fluid flow available for evaporation. However, greater channel depth also increases the temperature difference between the base of the channel where heat is applied and the meniscus contact region where evaporation is intended to occur. This temperature difference can be readily estimated from Fourier's law of heat conduction

$$\Delta T=q''\frac{H}{k}\left(\frac{W_b}{W_b-W_o}\right) \tag{32}$$

Here, k is the thermal conductivity, taken as 90 W/m/K for nickel, and the term in brackets accounts for the fact that the flux applied to a base of width W_b must be conducted through webs of width W_b-W_o. Note that for tapered channels ΔT will decrease along the flow path because the web thickness increases as the channels narrow. For the example calculations of Fig. 13, the maximum values of ΔT at the two highest peaks are about 2 and 4 °K for $H=0.5$ and 1.0 mm, respectively. If these values should become excessive, boiling will occur at the channel base instead of the contact line, hindering performance. However, moderate temperature differences are acceptable since the increased gas pressure inside small bubbles at the channel base helps to elevate the vaporization temperature [1,11]. In addition, some channel designs circumvent this limitation by supplying heat from the meniscus side of the channels rather than the base.

The minimum contact angle has been taken as zero in these examples, thus yielding maximum estimates of sustainable heat fluxes. The equilibrium value of this angle is dependent upon the relative interfacial energies of the liquid and the vapor with the adjacent solid as well as the liquid/vapor interfacial energy [1,11]. Typical values are available in the literature [1]. In addition, the apparent contact angle of an evaporating meniscus is generally increased somewhat from its equilibrium value owing to the pressure gradients that result from lateral liquid flow into the evaporation region. This adjustment in the meniscus angle occurs over a distance of about 100 to 200 nanometers along the meniscus wherein the film thickness increases from molecular dimensions to about 50 nm [11,12,16,17]. Since the scale of this zone is usually much smaller than lateral channel dimensions, its primary influence on the flow field is to alter the apparent meniscus contact angle. This alteration of the contact angle increases with the evaporation rate (per unit of meniscus contact length) and is on the order of 10 to 15 deg for the maximum heat fluxes shown in Fig. 13 [17,18]. Thus, one can approach the overall problem in a coupled or iterative manner using the contact angle as the primary link between the axial fluid flow and the thin surface film [12,16–18]. Moreover, when the applied flux is relatively uniform along the channel, so is the apparent contact angle. It is noted that these same models of the thin film physics have been successfully used to predict temperature differences across evaporative films not only for heat pipe applications but also for nucleate boiling phenomena [11].

The example calculations also provide an opportunity to estimate the error introduced by some of the approximations made in our modeling of viscous friction. As noted earlier, the numerical value of $\beta=12$ appearing in Eq. (2) is strictly valid only for channels of high aspect ratio. The error in this approximation is less than 3 percent for aspect ratios of ten or more. However, for the range of conditions shown in Fig. 13, the aspect ratio at the channel inlet is as small as 2.5 for a depth of 500 μm and a width of 200 μm; the corresponding value of β is 13.98 for a contact angle of zero deg [14]. This error of roughly 20 percent will be reduced by channel taper but increased by the meniscus recession that is localized near the exit when p_o is small. The error can be reduced by introducing average values of β or it can be eliminated by integrating the governing equations numerically.

Similarly, we have neglected the excess viscous drag that is required to transform the velocity profile from uniform to nearly parabolic near the channel inlet. The added pressure drop at the entrance of tubes and rectangular channels is on the order of

$\Delta P_i = \rho u^2/2$ for a broad range of Reynolds numbers [19]. Expressed as a fraction of the available capillary pressure this pressure drop may be written as $\Delta P_i/\Delta P_o \cong \mathrm{Re}(w/L)/24$ where $\mathrm{Re} = \rho u w/\mu$ is the Reynolds number based on the inlet fluid speed. For the conditions shown in Fig. 13, Re is less than 15 and the fractional pressure drop is less than 1 percent. So these entrance effects should be unimportant even for a cascade of progressively bisected channels.

Any of the model improvements described above can be readily incorporated into a relatively simple numerical model. Our purpose here has been to demonstrate fundamental concepts based on a simplified mathematical model that captures the essential physics while still admitting analytical solutions.

Summary and Conclusions

Analytical modeling has been used to investigate the evaporative cooling performance of rectangular microchannels having a fixed depth and a width that decreases along the flow path. Attention has been restricted to cases where the channel depth greatly exceeds the channel width; this geometry generally provides improved performance and also permits analytical integration of the governing equations.

Maximum heat fluxes were presented for channels having linear, convex, and concave tapers for a broad range of the relevant dimensionless parameters including: fractional channel taper, Δw, inlet pressure relative to maximum capillary pressure, p_o, and the normalized strength of an opposing gravitational force, G^*. It was found that a straight taper with a width reduction of about 70 percent ($\Delta w = 0.7$) generally provides the most robust performance over a broad range of operating conditions.

Tapered channels expand the operating range of cooling devices by permitting operation under opposing gravitation forces of greater strength. As an example, a linear taper of 70 percent provides a 300 percent increase in the maximum allowable gravity force while only reducing the maximum flux under zero gravity (horizontal operation) by 15 percent. To obtain the same lifting capability in a straight channel would necessitate a factor of three reduction in channel width and, hence, a 300 percent reduction in the maximum heat flux for horizontal operation.

Another benefit of channel taper is improved performance under variations in the inlet liquid pressure. This is important in capillary pumped loops where a portion of the available capillary pressure must be used to overcome liquid and vapor friction in the tubes that connect the evaporator and condenser. This external pressure drop is manifested by a lowering of the liquid pressure (increased meniscus curvature) at the inlet to the evaporation channels. In a straight channel of high aspect ratio, the maximum sustainable heat flux becomes negligible as the inlet curvature approaches its maximum value corresponding to the minimum wetting angle. However, under this same inlet condition a channel with a 70 percent taper can still sustain a heat flux that is 40 percent of the maximum attainable for a flat meniscus at the inlet of a straight channel (Fig. 7). In addition, tapered channels continue to provide strong cooling performance even when the inlet meniscus falls below the top corners of channel, a condition that leads to dryout in straight rectangular channels.

Channels of triangular cross section are frequently used in evaporative cooling applications partly because they offer many of the robust performance features discussed above. However, a comparable tapered channel can sustain a heat flux that is 3 to 6 times greater for the same inlet width and the same high aspect ratio.

Unlike triangular channels, a multiplicity of tapered channels can be fabricated together with peripheral manifolds and reservoirs using lithography-based technologies. In particular, the LIGA fabrication technique is specifically aimed at producing detailed metals parts of high aspect ratio having depth dimensions ranging up to millimeters and lateral dimensions ranging down to a few microns.

Acknowledgment

This work was supported by the Sandia Engineering Sciences Research Foundation. Sandia is a multiprogram laboratory operated by Sandia Corporation, a Lockheed Martin Company, for the United States Department of Energy under contract DE-AC04-94AL85000.

References

[1] Faghri, A, 1995, *Heat Pipe Science and Technology*, Taylor and Francis Publishers, New York, NY.

[2] Stroes, G. R., Rohloff, T. J., and Catton, I., 1992, ''An Experimental Study of the Capillary Forces in Rectangular Versus Triangular Channels,'' *Proceedings of the 28th National Heat Transfer Conference*, HTD-Vol. 200, ASME, New York, pp. 1–7.

[3] Stroes, G. R., and Catton, I., 1997, ''An Experimental Study of the Capillary Performance of Triangular Versus Sinusoidal Channels,'' ASME J. Heat Transfer, **119**, pp. 851–853.

[4] Sivaraman, A., De, S., and Dasgupta, S., 2002, ''Experimental and Theoretical Study of Axial Dryout Point for Evaporation From V-Shaped Microgrooves,'' Int. J. Heat Mass Transfer, **45**, pp. 1535–1543.

[5] Xu, X., and Carey, V. P., 1990, ''Film Evaporation From a Micro-Grooved Surface—An Approximate Heat Transfer Model and Its Comparison With Experimental Data,'' J. Thermophysics, **4**(4), pp. 512–520.

[6] Catton, I., and Stroes, G. R., 2002, ''A Semi-Analytical Model to Predict the Capillary Limit of Heated Inclined Triangular Capillary Grooves,'' ASME J. Heat Transfer, **124**, pp. 162–168.

[7] Ha, J. M., and Peterson, G. P., 1996, ''The Interline Heat Transfer of Evaporating Thin Films Along a Micro Grooved Surface,'' ASME J. Heat Transfer, **118**, pp. 747–755.

[8] Peles, Y. P., and Haber, S., 2000, ''A Steady One Dimensional Model for Boiling Two Phase Flow in a Triangular Microchannel,'' Int. J. Multiphase Flow, **26**, pp. 1095–1115.

[9] Becker, E. W., Ehrfeld, W., Hagmann, P., Maner, A., and Munchmeyer, D., 1986, ''Fabrication of Microstructures With High Aspect Ratios and Great Structural Heights by Synchrotron Radiation Lithography, Galvanoforming and Plastic Moulding (LIGA Process),'' Microelectron. Eng., **4**, pp. 35–56.

[10] Ehrfeld, W., and Schmidt, A., 1998, ''Recent Developments in Deep X-Ray Lithography,'' J. Vac. Sci. Technol. B, **16**(6), pp. 3526–3534.

[11] Wayner, P. C., 1999, ''Intermolecular Forces in Phase-Change Heat Transfer: 1998 Kern Award Review,'' AIChE J., **45**(10), pp. 2055–2068.

[12] Stephan, P. C., and Busse, C. A., 1992, ''Analysis of Heat Transfer Coefficient of Grooved Heat Pipe Evaporator Walls,'' Int. J. Heat Mass Transfer, **35**(2), pp. 383–391.

[13] Schneider, G. E., and DeVos, R., 1980, ''Nondimensional Analysis for the Heat Transport Capability of Axially Grooved Heat Pipes Including Liquid/Vapor Interaction,'' AIAA Paper No. 80-0214.

[14] Tchikanda, S. W., Nilson, R. H., and Griffiths, S. K., 2003, ''Modeling of Pressure and Shear Driven Flows in Open Rectangular Microchannels,'' Int. J. Heat Mass Transfer, **47**, pp. 527–538.

[15] Haskell, K. H., Vandevender, W. H., and Walton, E. L., 1980, ''The SLATEC Mathematical Subroutine Library: SNL Implementation,'' SAND80-2992, Sandia National Laboratories, Albuquerque, NM.

[16] Ayyaswamy, P. S., Catton, I., and Edwards, D. K., 1974, ''Capillary Flow in Triangular Grooves,'' ASME J. Appl. Mech., **41**, pp. 332–336.

[17] Lin, L., and Faghri, A., 1999, ''Heat Transfer in Micro Region of a Rotating Miniature Heat Pipe,'' Int. J. Heat Mass Transfer, **42**, pp. 1363–1369.

[18] Satre, V., Zaghdoudi, M. C., and Lallemand, M., 2002, ''Effect of Interfacial Phenomena on Evaporative Heat Transfer in Micro Heat Pipes,'' Int. J. Therm. Sci., **39**, pp. 498–504.

[19] White, F. M., 1974, *Viscous Fluid Flow*, McGraw Hill, New York, NY.

Forced Convection Heat Transfer From a Low-Profile Block Simulating a Package of Electronic Equipment

Hajime Nakamura
e-mail: nhajime@nda.ac.jp

Tamotsu Igarashi

Department of Mechanical Engineering,
National Defense Academy,
1-10-20 Hashirimizu, Yokosuka, Kanagawa
239-8686,
Japan

Forced convection heat transfer from a low-profile block placed in a rectangular duct, simulating heat transfer in a compact packaged electronic device, is investigated experimentally. Local heat transfer from the block is measured by an infrared camera. A general correlation of the Nusselt number for the block is derived using a modified Reynolds number, $Re_L^* = (U_m/\beta^2)L/\nu$, where U_m is mean duct velocity, β is the opening ratio of the duct, and L is the block length. The correlation is shown to be applicable regardless of the configuration of the block and duct, under the conditions of laminar flow, a low-profile block (height/length$<$0.5), and a low blockage effect ($\beta \geqslant 0.5$).

[DOI: 10.1115/1.1737776]

Keywords: Channel Flow, Convection, Experimental, Heat Transfer, Laminar

1 Introduction

Many studies have been carried out to investigate forced convection heat transfer from rectangular blocks to examine heat transfer in compact electronic equipment, as comprehensively reviewed by Peterson and Ortega [1]. A number of these studies has been presented correlations for the Nusselt number of the blocks as a function of the Reynolds number to provide a practical means of evaluating the thermal design of electronic equipment. However, a general correlation has been difficult to obtain because the heat transfer from the blocks depends on many factors, such as block shape, duct shape, and block arrangement. Moreover, the heat transfer depends heavily on flow conditions, whether the flow is laminar or turbulent, the boundary layer thickness, and the effect of natural convection. Even if the condition for the general correlation is specified only for a single rectangular block in a rectangular duct, there still exist many parameters. Therefore, conventional correlations have been presented with respect to specific conditions.

Roeller et al. [2] investigated the average heat transfer from a rectangular block for various block widths W and duct heights H_D. In that study, the ratio of the height to the side length of the block, H/L, was fixed to 1. The overall Nusselt number correlation obtained for the block was $\mathrm{Nu}_m = 0.256\,\mathrm{Re}_{Dh}^{0.555}\beta_{3D}^{-0.474}(H_D/L)^{-0.603}$ for the range $\mathrm{Re}_{Dh} = 2000-20{,}000$. Here, β_{3D} is the opening ratio of the duct, defined as $\beta_{3D} = 1-(HW/H_DW_D)$. However, this correlation is not applicable for laminar flow, which is the general case for flow in compact electronic equipment, which typically has a low duct Reynolds number ($\mathrm{Re}_{Dh}<2000$). Takasaki [3] investigated local heat transfer from a two-dimensional rectangular block for various block heights H and duct heights H_D. A simple correlation of $\mathrm{Nu}_m = 0.00567\,(\mathrm{Re}_L')^{1.0}$ was obtained by introducing a modified Reynolds number, $\mathrm{Re}_L' = (U_m/\beta)L/\nu$, where β is the opening ratio of $\beta = 1-H/H_D$. However, this correlation is also not applicable for laminar flow. Nakayama and Park [4] investigated the overall heat transfer from a square block with height of $H/L = 7/31$, and obtained a correlation of $\mathrm{Nu}_m = 1.78\,\mathrm{Re}_{Dh}^{0.43}$ in the range $\mathrm{Re}_{Dh} = 2200-16{,}000$. However, this correlation was obtained for specific configurations of the duct and block. Young and Vafai [5] carried out two-dimensional numerical simulations for the region around a rectangular block under the condition of laminar flow, and presented a correlation of $\mathrm{Nu}_m = a\,\mathrm{Re}_{H_D}^{b}[(\lambda_b/\lambda_f)/(c+\lambda_b/\lambda_f)]$, where λ_b and λ_f are the thermal conductivities of the block and the fluid, respectively. However, the coefficients a, b, and c were uniquely given for each block shape.

The review of previous research reveals that the correlations for the Nusselt number of a block have various forms. In addition, the exponent of the Reynolds number varies widely, from 0.31 to 1.0. One reason for this scatter is considered to be the difference in the flow conditions examined, whether laminar, turbulent, or a transition regime. The effect of flow conditions on heat transfer can be clarified by investigating the distribution of local heat transfer, which reflects the characteristics of the flow near the block surface. However, the local heat transfer from a three-dimensional block has not been investigated experimentally for the flow conditions typical of compact electronic equipment, that is, low block height ($H/L<0.5$), and low Reynolds number based on the block height ($\mathrm{Re}_H \leqslant 300$).

In the present study, local heat transfer from a low-profile block placed in a rectangular duct is investigated experimentally to examine the heat transfer conditions in compact electronic equipment packaging and develop a general correlation for the Nusselt number of a low-profile block.

2 Experimental Apparatus and Procedure

Figure 1(a) shows a schematic diagram of the duct equipment, which is equivalent to the benchmark kit designed by the RC181 Research Project of the Computational Mechanics Division, Japan Society of Mechanical Engineers (JSME) [6]. This equipment consisted of a rectangular duct, a low-profile square block, and three small fans. The rectangular duct was fabricated from acrylic resin plates, and had an internal space of 235 mm in length, 200 mm in width (W_D) and 10 mm in height (H_D). The low-profile square block, which was the test model for heat transfer measurement, was 45 mm long (L), 45 mm wide (W), and 2 mm high (H). The leading edge of the block was placed 77.5 mm downstream from the leading edge of the rectangular duct and positioned at the width center of the duct. Three small fans were placed at the downstream end of the rectangular duct. The air velocity in the duct was measured using a hot-wire anemometer having an

---

Contributed by the Heat Transfer Division for publication in the JOURNAL OF HEAT TRANSFER. Manuscript received by the Heat Transfer Division May 16, 2003; revision received February 25, 2004. Associate Editor: C. Amon.

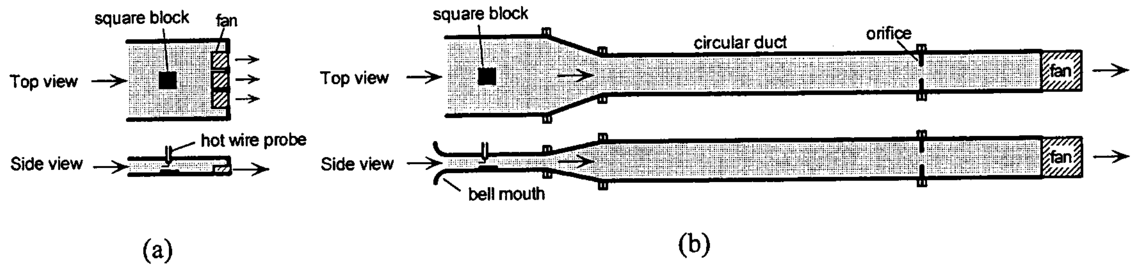

Fig. 1 Schematic diagram of duct equipment for (a) U_m=0.24–0.72 m/s, H_D=10 mm, and (b) U_m=1–4 m/s, H_D=3.8–10 mm

L-shaped probe (55P14, DANTEC), which was inserted from the ceiling of the duct through a hole 2 mm in diameter. The probe was moved vertically to obtain the velocity distribution. The mean velocity upstream of the block ranged from $U_m = 0.24$ to 0.72 m/s depending on the number of working fans. In order to investigate the three-dimensional effect caused by the small fans relatively close to the test block, both the smoke visualization and the measurement of velocity distribution were carried out in the absence of the test block. The results indicated that the three-dimensional flow region was localized 50 mm upstream from the fans, and thus the flow at the position of the test block was substantially two-dimensional, in which the velocity difference along span was within ±1%. The data obtained in this equipment concerning the flow and heat transfer was collected as accurate experimental benchmark data for the RC181 Research Project

In order to investigate heat transfer at higher air velocity, the rectangular duct in Fig. 1(a) was connected to a wind tunnel with a larger fan, as shown in Fig. 1(b). In this case, the mean velocity in the rectangular duct ranged from $U_m = 1.0$ to 4.0 m/s. The height of the rectangular duct was varied from $H_D = 3.8$ to 10 mm. In order to suppress flow turbulence, a pair of curved plates, imitating a bell-mouth, was set at the inlet of the duct.

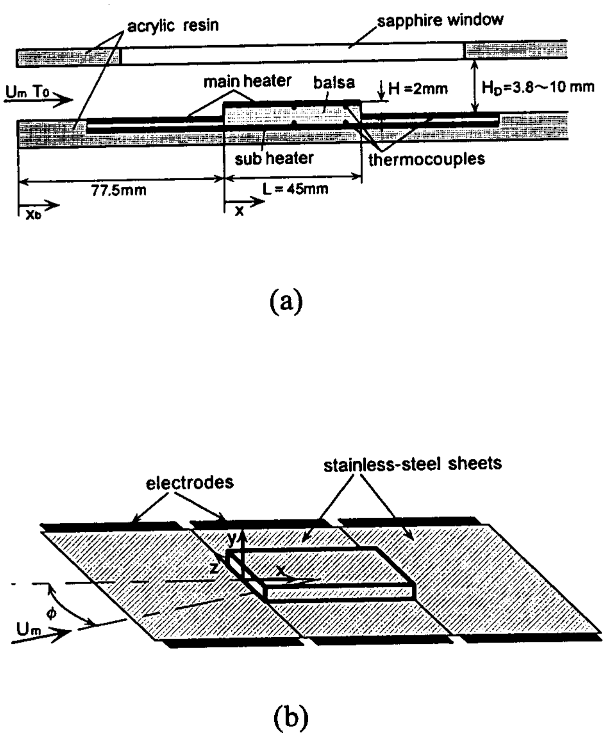

Fig. 2 Test model for heat transfer measurement under conditions of constant heat flux: (a) cross-sectional view of rectangular duct, (b) schematic of test model

Figure 2(a) shows a cross-sectional view of the rectangular duct for the measurement of heat transfer under constant heat flux (CHF). A schematic diagram of the test model, which consisted of a square block and a base wall, is shown in Fig. 2(b). The square block and base wall were fabricated from balsa plates of 2 mm and 1 mm in thickness, respectively. Three stainless-steel sheets of 0.02 mm thickness and 45 mm width were installed to cover the surfaces of the block and the base wall. The middle sheet was set to cover the top and side faces of the block and a part of the base wall by folding it along the edges. The stainless-steel sheets were connected in series electrically, and heated as a main-heater by applying a direct current under the condition of constant heat flux. The temperature difference between the heated surface and the air at duct inlet, $T_w - T_0$, was about 10–15°C. The surface of the main-heater was coated with black paint in order to enhance the infrared emissivity. The temperature distribution on the main-heater was measured by an infrared camera (TVS-8502, Avio) from above the duct through a sapphire window. The infrared camera was calibrated taking into account the infrared absorption and reflection of the sapphire window. Copper-constantan thermocouples of 0.1 mm in diameter were also used to measure the temperature on the heated wall in order to verify the temperature measured by the infrared camera. Heat loss to the balsa plates and the thermocouple leads was suppressed by laying a sub-heater under the balsa plates. The temperature difference between the main-heater and the sub-heater was controlled to be 0°C at the center of the square block. The test model could be rotated around the vertical axis at the center of the block. In the present experiments, the block was aligned parallel to the flow (ϕ=0 deg) for most cases, and some additional experiments were carried out at ϕ=180 deg in order to verify the symmetry of the test model.

The effect of the thermal boundary condition of the heated block was investigated using another test model, heated under the condition of constant wall temperature (CWT). Figure 3 shows a cross-sectional view of the rectangular duct for the CWT model. A square block of 45 mm×45 mm×2 mm was fabricated from copper and fitted with a main-heater. The temperature on the heated wall was measured by both infrared camera and 0.1 mm-diameter copper-constantan thermocouples. The surface of the block and the base wall was coated with black paint in order to fix the total emissivity. The temperature difference between the heated wall

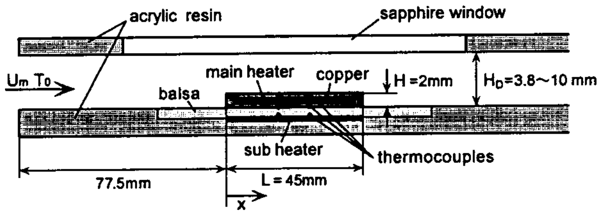

Fig. 3 Cross-sectional view of rectangular duct for heat transfer measurement under conditions of constant wall temperature

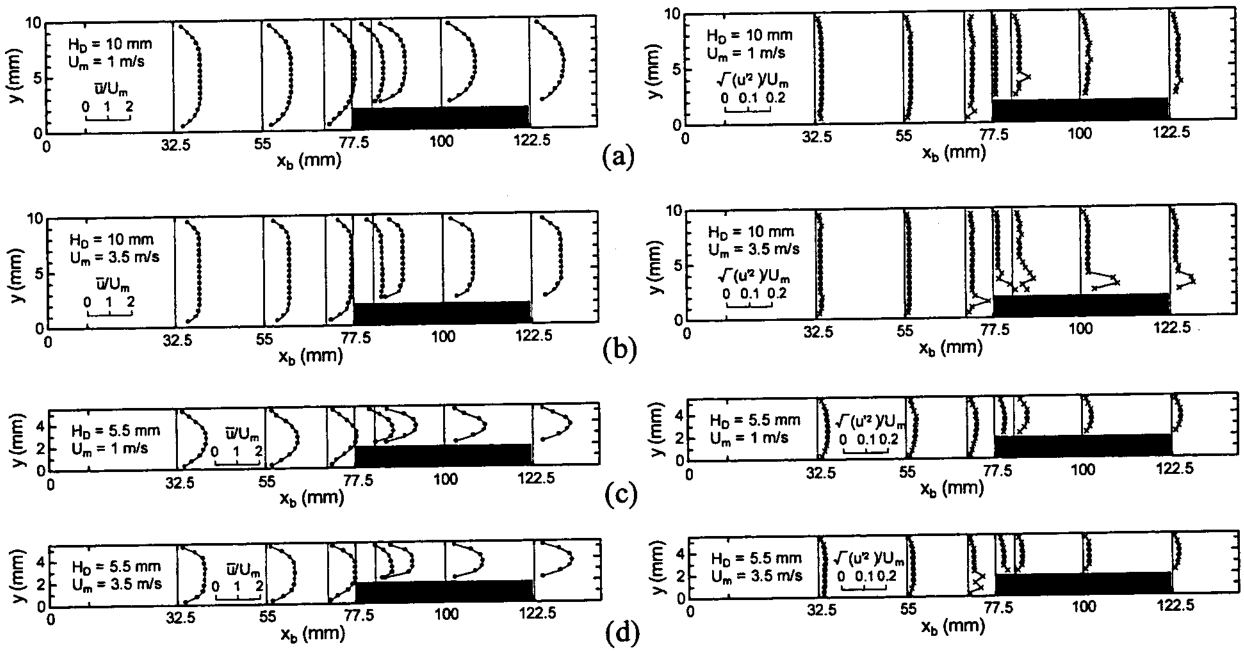

Fig. 4 Distribution of mean and fluctuating velocities in the rectangular duct at $z=0$: (left) Mean velocity $\bar{u}/U_m$, (right) fluctuating velocity $\sqrt{\overline{u'^2}}/U_m$. (a) $H_D=10$ mm, $U_m=1.0$ m/s, $\mathrm{Re}_{Dh}=1220$, (b) $H_D=10$ mm, $U_m=3.5$ m/s, $\mathrm{Re}_{Dh}=4270$, (c) $H_D=5.5$ mm, $U_m=1.0$ m/s, $\mathrm{Re}_{Dh}=690$, and (d) $H_D=5.5$ mm, $U_m=3.5$ m/s, $\mathrm{Re}_{Dh}=2400$.

and the air at the duct inlet was about 12°C. Heat loss to the base wall and the thermocouple leads was suppressed by laying a 1 mm-thick balsa wood sheet below the block and a sub-heater under the balsa sheet.

3 Flow in the Duct

Velocity Distribution. Figure 4 shows typical distributions of mean and fluctuating velocities in the rectangular duct at the width center of the block $(z=0)$. The duct Reynolds number, $\mathrm{Re}_{Dh}=U_m D_h/\nu$, ranged from 290 to 4270. The distribution of mean velocity $\overline{u}/U_m$ approaches a parabolic curve, which is a characteristic of fully developed laminar flow. This is particularly apparent for the lower duct height $(H_D \leqslant 5.5\,\mathrm{mm})$. A transition from laminar to turbulent flow did not occur in the present experimental conditions, even for the higher duct Reynolds numbers $(\mathrm{Re}_{Dh} > 2000-3000)$. This is attributed to the shorter length of the duct, simulating a compact packaged electronic device. However, the turbulence level around the block was fairly high at the higher duct Reynolds numbers.

Temperature Distribution. Figure 5 shows contours of the temperature distribution for the constant heat-flux model, as measured by infrared camera. Three stainless-steel sheets were heated simultaneously, as shown in Fig. 5(a). The values noted in Figs. 5(b–f) are the temperature differences between the heated wall and the inlet air, T_w-T_0. For the low velocities $(U_m \leqslant 1\ \mathrm{m/s})$, the temperature distribution on the top face was almost two-dimensional, as shown in Figs. 5(b), (c), and (e). However, for the high velocity of $U_m=3.5\,\mathrm{m/s}$, shown in Figs. 5(d) and (f), the temperature decreases around both side edges due to the blockage effect. This effect was pronounced for the higher velocity experiments and for the smaller opening ratio of $\beta=1-H/H_D$. The temperature increased in the flow recirculation regions formed both in front and behind the block. Heat transfer in front of the block has been shown in previous research to be greatly enhanced by the formation of horseshoe vortices (e.g., for a square block in a duct by Nakayama and Park [4] and for a wall-mounted cube by Nakamura et al. [7]). However, in the present experiment, the horseshoe vortices were considered to be steady because of the low Reynolds numbers based on the block height $(\mathrm{Re}_H \leqslant 500)$, thereby reducing the enhancement of heat transfer in front of the block.

4 Evaluation of the Heat Transfer Coefficient

Data Reduction. The heat transfer coefficient was defined for the present experiments as

$$h=\frac{\dot{q}}{T_w-T_0}=\frac{\dot{q}_{in}-\dot{q}_{\mathrm{rad}}-\dot{q}_c}{T_w-T_0}, \tag{1}$$

where $\dot{q}$ is the convective heat flux from the heated wall to air, and $\dot{q}_{\mathrm{in}}$ is the input heat flux to the block surface calculated from the input heat quantity to the main-heater. The radiative heat flux $\dot{q}_{\mathrm{rad}}$ was calculated in consideration of the transmissivity τ_{sap} and reflectance ρ_{sap} of the sapphire window as follows:

$$\dot{q}_{\mathrm{rad}}=\frac{\sigma(T_w^4-T_0^4)}{1/\varepsilon_w+2/(1+\tau_{\mathrm{sap}}-\rho_{\mathrm{sap}})-1} \tag{2}$$

where σ is the Stefan-Boltzmann coefficient. The total emissivity of the heated wall was $\varepsilon_w=0.97$. The radiative heat flux was considerably high in the present experimental conditions; the ratio of radiative heat flux to the input heat flux, $\dot{q}_{\mathrm{rad}}/\dot{q}_{\mathrm{in}}$, was about 40% for $U_m=0.24\,\mathrm{m/s}$ and about 10% for $U_m=4.0\,\mathrm{m/s}$. The heat conduction from the main-heater to the base wall, $\dot{q}_c$, was estimated by heat conduction analysis based on the temperature distribution on the base wall.

Experimental Uncertainty. The experimental uncertainties for the constant heat-flux model were attributed mainly to uncertainty of measured temperature, possible inaccuracies in the estimation of radiative heat flux or heat conduction loss, and heat conduction through the stainless-steel sheet. The uncertainty of the temperature measured by the infrared camera is considered to be within ±0.2°C from a comparison with the temperature obtained by the thermocouples. This results in an uncertainty of ±2% for the heat transfer coefficient. The uncertainty of the radiative heat flux is considered to be within ±10%, resulting in an uncertainty of ±4.0% for the heat transfer coefficient at U_m

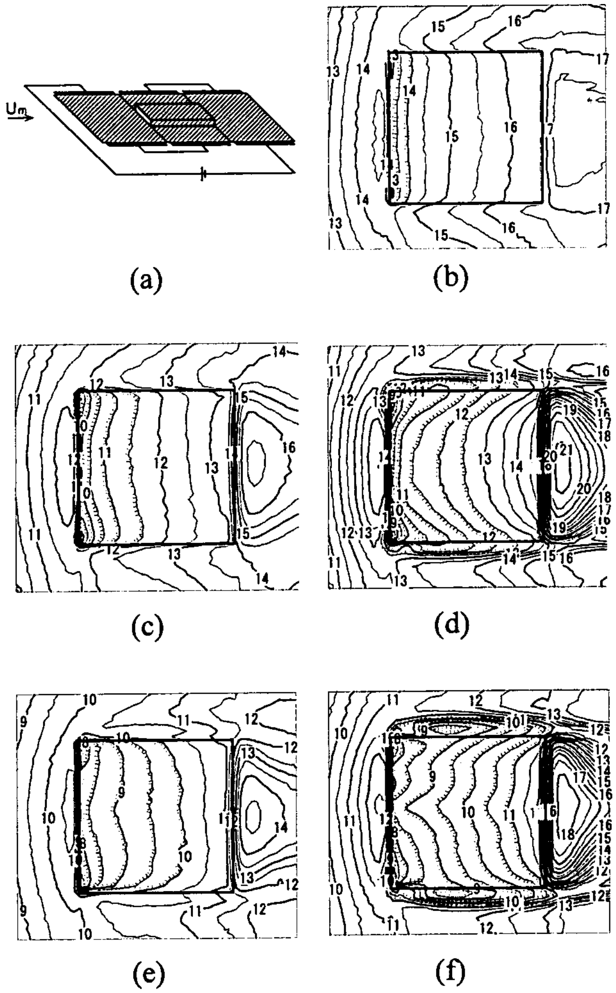

Fig. 5 Contours of temperature difference $T_w - T_0$ for the constant heat-flux model measured by infrared camera: (a) heated surface, (b) $H_D = 10$ mm, $U_m = 0.24$ m/s, $\dot{q}_{in} = 187$ W/m^2, (c) $H_D = 10$ mm, $U_m = 1.0$ m/s, $\dot{q}_{in} = 239$ W/m^2, (d) $H_D = 10$ mm, $U_m = 3.5$ m/s, $\dot{q}_{in} = 412$ W/m^2, (e) $H_D = 5.5$ mm, $U_m = 1.0$ m/s, $\dot{q}_{in} = 239$ W/m^2, and (f) $H_D = 5.5$ mm, $U_m = 3.5$ m/s, $\dot{q}_{in} = 411$ W/m^2

$= 0.24$ m/s, and ±1.0% at $U_m = 4.0$ m/s. Heat conduction to the base wall was suppressed by laying the sub-heater at the bottom of the balsa plates, considerably reducing the uncertainty in the estimation of the heat conduction loss. However, heat conduction analysis of the balsa plates indicated that the uncertainty for the heat transfer coefficient due to heat conduction to the base wall is ±5% at $U_m = 0.24$ m/s and ±1.1% at $U_m = 4.0$ m/s. Heat conduction through the stainless-steel sheet causes a heat flux normal to the sheet, which can be expressed as

$$\dot{q}_{\mathrm{sus}} = -\lambda_{\mathrm{sus}} \frac{d^2 T_w}{dx^2} t_{\mathrm{sus}} \tag{3}$$

where λ_{sus} and t_{sus} are thermal conductivity and thickness of the stainless-steel sheet, and x is the direction of heat conduction through the sheet. This heat conduction gives rise to an uncertainty of ±4.5% for the heat transfer coefficient at $U_m = 0.24$ m/s and ±0.9% at $U_m = 4.0$ m/s. The total uncertainty for the local heat transfer coefficient was calculated from the r.m.s. sum of the above uncertainties as follows; ±8.1% for $U_m = 0.24$ m/s, and ±2.6% for $U_m = 4.0$ m/s.

The experimental uncertainties for the constant wall temperature model were mainly due to inaccuracies in the estimation of the radiative heat flux and heat conduction loss to the base wall. The uncertainty for the overall heat transfer coefficient was estimated to be within ±8% for $U_m = 0.24$ m/s, and ±3% for $U_m = 4.0$ m/s.

Effect of Natural Convection. In general, the Rayleigh number for an enclosed space consisting of horizontal parallel plates and heated from below is defined by

$$\mathrm{Ra} = \mathrm{Gr}\mathrm{Pr} = \frac{g\beta_f (T_w - T_c) H_c^3}{\nu^2} \mathrm{Pr} \tag{4}$$

where H_c is the height of the enclosed space, and T_w and T_c are the temperatures on the bottom and ceiling plates, respectively. According to Pellow and Southwell [8], no fluid motion occurs in the enclosed space for $\mathrm{Ra} < 1708$. Equation (4) may be applicable for the rectangular duct used in the present study. The Rayleigh number for the present experimental condition based on the height $H_D - H$ was estimated to be $\mathrm{Ra} < 700$, which indicates that natural convection did not occur in the rectangular duct. The temperature in practical packages for electronic equipment, such as a microprocessor enclosure, can be expected to be higher than that in the present experiment. If the temperatures T_w and T_c are assumed to be 80°C and 30°C, respectively, the Rayleigh number is estimated to be $\mathrm{Ra} < 1708$ for $H_D - H < 8$ mm and $\mathrm{Ra} > 1708$ for $H_D - H > 9$ mm. For a narrow space of $H_D - H < 8$ mm, natural convection is unlikely to occur.

5 Heat Transfer on the Top Face

Distribution of Heat Transfer at Width Center. Figure 6 shows the distribution of the heat transfer coefficient on the top face of the block for the constant heat-flux model at width center of the block $(z = 0)$. Only one stainless-steel sheet in the middle portion was heated, as shown in Fig. 6(a), in order to prevent an increase in the air temperature upstream of the block. Figure 6(b) shows the effect of duct velocity U_m at a fixed duct height $(H_D = 10\,\mathrm{mm})$. The heat transfer coefficient decreases along the flow direction with the development of a thermal boundary layer on the block, and the heat transfer increases with increasing duct velocity. The heat transfer coefficient for the block orientated $\phi = 0$ deg is very similar to that for the block orientated at $\phi = 180$ deg, demonstrating the excellent symmetry of the test model and the negligible scatter of the experimental data. Figure 6(c) shows the effect of duct height H_D for fixed duct velocity $(U_m = 2.0\,\mathrm{m/s})$. The heat transfer coefficient increases with decreasing duct height due to the blockage effect. As can be seen in Figs. 6(b) and (c), all distributions of the heat transfer coefficient have a similar profile regardless of the duct velocity or duct height. This makes it possible to generalize the heat transfer on the top face of the block.

If the value of the heat transfer coefficient is divided by $U_m^{0.5}$, as shown in Fig. 7(a), the distributions concentrate into a single curve. This means that the heat transfer on the block is proportional to $U_m^{0.5}$. The exponent of 0.5 is higher than that for the theoretical analysis of laminar forced convection heat transfer between parallel plates [9], which is 1/3 for fully developed laminar flow. The higher value for the present experiment is probably due to the higher turbulence level around the block, particularly at the higher velocity, as shown in Fig. 4.

If the flow in the low-profile duct is assumed to be laminar and fully developed, the vertical velocity distribution in the duct without the blockage effect, $u_0(y)$, is expressed as

$$u_0(y) = \frac{6(H_D - y)y}{H_D^2} U_m \tag{5}$$

If a block, with height H, is placed in the duct, the velocity distribution in the upper part of the block, $u(y)$, assuming fully developed flow, is expressed as follows:

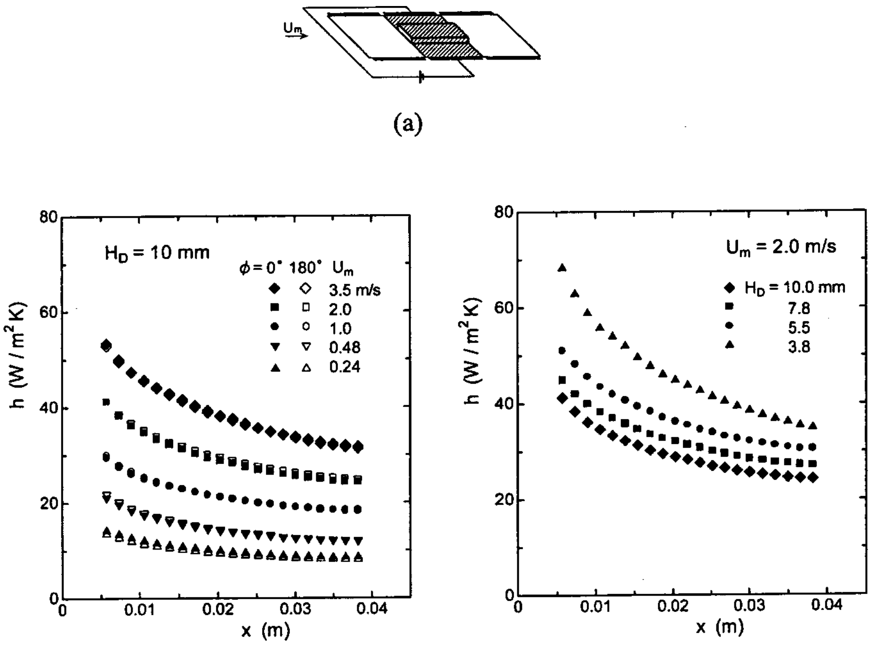

(a)

(b)

(c)

Fig. 6 Distribution of heat transfer coefficient on the top face of the block for the constant heat flux model at $z=0$: (a) heated surface, (b) effect of duct velocity U_m, and (c) effect of duct height H_D

$$u(y)=\frac{6(H_D-y)(y-H)}{(H_D-H)^2}U'_m \tag{6}$$

where U'_m is the mean velocity in the upper part of the block. Using Reynolds's analogy, the heat transfer coefficient on the block can be expressed as

$$h=\frac{C_p\tau_w}{U_{\max}}F(\mathrm{Pr}) \tag{7}$$

where C_p is the heat capacity at constant pressure and $F(\mathrm{Pr})$ is a function of the Prandtl number. The maximum velocity in the upper part of the block, $U_{\max}$, is equal to $1.5U'_m$ for fully developed laminar flow. The shearing stress τ_w is defined by

$$\tau_w=\mu\left(\frac{du}{dy}\right)_w \tag{8}$$

The heat transfer coefficient on the block, h, can be calculated from Eqs. (5)–(8) as

$$\frac{h}{h_0}=\frac{\mu(du(y)/dy)_{(y=H)}/(1.5U'_m)}{\mu(du_0(y)/dy)_{(y=0)}/(1.5U_m)}=\frac{H_D}{H_D-H} \tag{9}$$

where h_0 is the heat transfer coefficient without the blockage effect. By defining the opening ratio as $\beta=1-H/H_D$, the heat transfer coefficient on the block can be expressed in proportion to $1/\beta$. Figure 7(b) shows the heat transfer coefficient for the present experiment, divided by $1/\beta$. The distributions concentrate quite well into a single curve, indicating the appropriateness of the

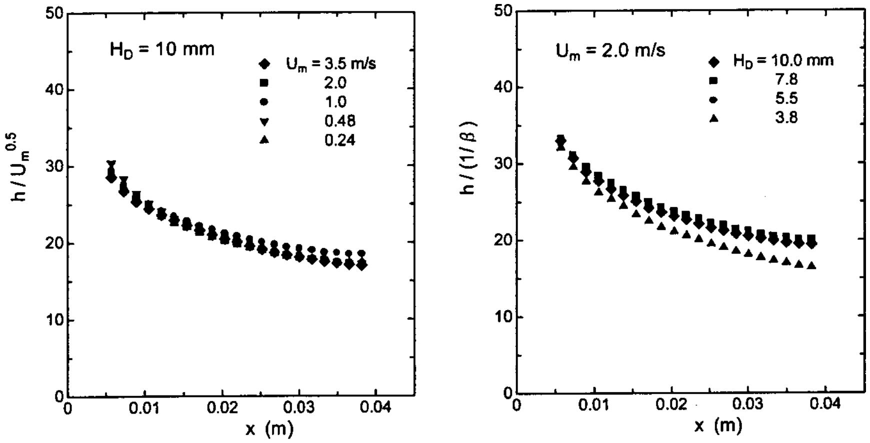

(a)

(b)

Fig. 7 Generalization of the heat transfer distribution: (a) effect of duct velocity U_m, and (b) effect of duct height H_D

Table 1 Existing data

Author	exp/cal 2D/3D	Array /Single	Fluid	H/L	Re_H	β	Boundary condition	Area for Nu_m
Present	exp 3D	Single	Air	0.044	30–500	0.474–0.8	CHF	Top face
Igarashi and Takasaki [11]	exp 2D	Single	Air	0.1	290–390	1	CHF	Top face
Takasaki [3]	exp 2D	Single	Air	0.1	290–390	0.8	CHF	Top face
McEntire and Webb [12]	exp 2D	Array	Air	0.5	175, 256	0.5, 0.67	CHF	Top face
Kang et al. [13]	exp 2D	Single	Air	0.28	122, 232	1	CHF	Top face
Lehmann and Pembroke [10]	exp 3D	Array	Air	0.058	272	0.92	CWT	Overall
Young and Vafai [14]	exp 2D	Single	Air	0.44	70–141	0.857	CWT	Overall
Mahaney et al. [15]	exp 3D	Array	Water	0	0	1	CWT	Top face
Garimella and Eibeck [16]	exp 3D	Array	Water	0.46	47, 373	0.64, 0.72	CWT	Overall
Davalath and Bayazitoglu [17]	cal 2D	Array	$Pr=0.1-2$	0.5	25–375	0.75	CHG	Top face
Young and Vafai [5]	cal 2D	Single	$Pr=0.72$	0.25	12.5–125	0.875	CHFB	Top face

CWT: constant temperature on block surface
CHF: constant heat flux on block surface
CHFB: constant heat flux on bottom face of block ($\lambda_b/\lambda_f=1000$)
CHG: constant heat generation in block ($\lambda_b/\lambda_f=10$)

above theoretical approach. The value for the lowest duct height ($H_D=3.8$ mm) is somewhat lower, probably due to the higher three-dimensional effect of flow around the block.

Based on this analysis, the heat transfer on the top face of the block is considered to be proportional to a function of $U_m^{0.5}/\beta$, regardless of the opening ratio of the duct. Here, a modified Reynolds number, using the square of this function as a reference velocity, is introduced as follows.

$$\mathrm{Re}_l^*=\frac{(U_m/\beta^2)l}{\nu} \tag{10}$$

where l is a reference length. It is expected that the Nusselt number on the top face of the block will be correlated with the modified Reynolds number regardless of the opening ratio.

Average Heat Transfer. Figures 8(a) and (b) show the relationships between the average Nusselt number on the top face, Nu_m, and the modified Reynolds numbers. The experimental data obtained from the constant wall temperature model is also plotted in Fig. 8(b). The Nusselt number for the CWT model is the averaged value for all faces of the block including side faces. However, the contribution of the side faces is insignificant due to the much smaller area compared to the top face. The reference length of the Reynolds number is defined as the hydraulic diameter of the duct, D_h, in Fig. 8(a), and the block length, L, in Fig. 8(b). If the hydraulic diameter is used as the reference length, the relationship becomes heavily dependent on the duct height. In contrast, as shown in Fig. 8(b), the block length for the reference length reduces the effect of the duct height, resulting in the concentration of the Nusselt numbers into a single correlation regardless of the opening ratio. The investigation by Lehmann and Pembroke [10] supports this model; they showed that the heat transfer from low-profile blocks can be well correlated using the Reynolds number based on the block length. The reason for this is considered to be that if the heat in the duct diffuses throughout the entire cross-sectional area of the duct, the hydraulic diameter will determine the performance of heat transfer. However, for the conditions of general electronic equipment, the heat is able to diffuse only in the region of the thermal boundary layer developed in the vicinity of the heat sources, which are placed discretely in the duct, resulting in the existence of unheated fluid in the duct. Therefore, the block

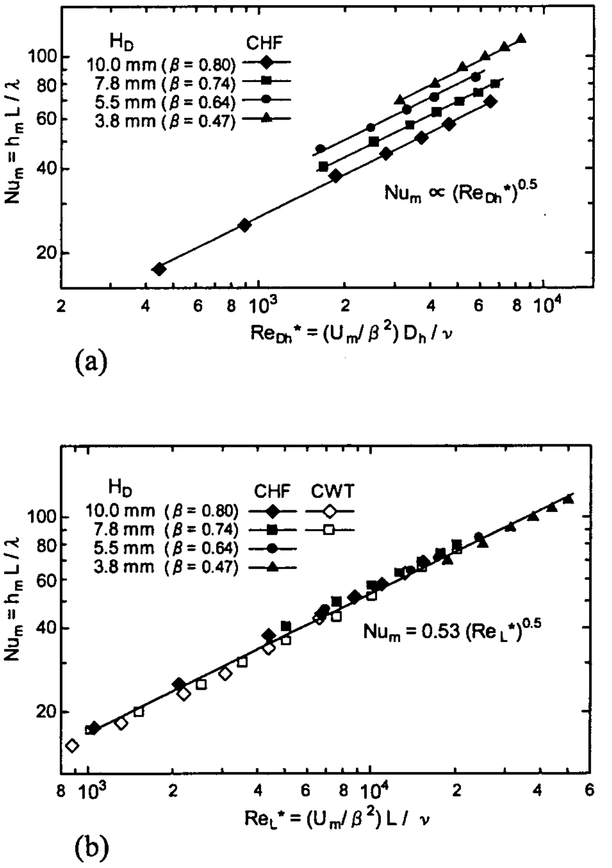

Fig. 8 Relationships between the average Nusselt number Nu_m and the modified Reynolds number: (a) based on hydraulic diameter of duct, Re_{Dh}^*, and (b) based on the side length of block, Re_L^*

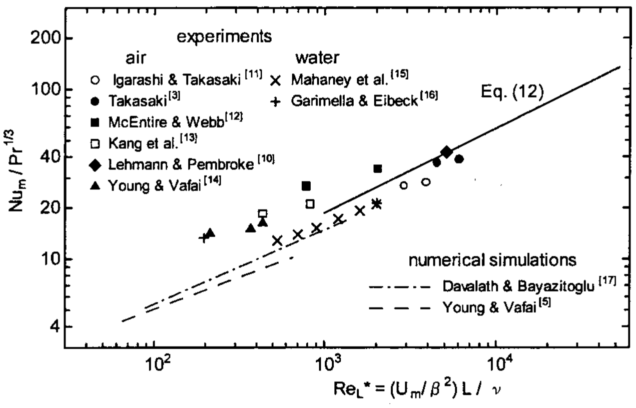

Fig. 9 Comparison of the present correlation Eq. (12) with previous research

length, which is closely related to the heated region of fluid, is preferable for the reference length of the Reynolds number.

According to an analysis of fully developed laminar flow between parallel plates [9], the Nusselt number for constant heat flux is about 1.2 times higher than that for constant wall temperature. However, the present experimental data indicates a smaller difference (~10%) between the CWT and CHF models, as shown in Fig. 8(b), probably due to the presence of turbulence around the block. This allows for the introduction of an approximate correlation that holds regardless of the thermal boundary condition, expressed within ±7%, as follows:

$$\mathrm{Nu}_m = 0.53(\mathrm{Re}_L^*)^{0.5} \quad (\mathrm{Re}_L^* = 1000-50{,}000, \beta \geqslant 0.5) \tag{11}$$

The generality of this correlation was investigated by comparison with existing data obtained under similar flow conditions (i.e., laminar flow, low-profile block of $H/L < 0.5$, and low blockage effect of $\beta \geqslant 0.5$). The correlation given by Eq. (11) can be rewritten using the Prandtl number as

$$\mathrm{Nu}_m = 0.59Pr^{1/3}(\mathrm{Re}_L^*)^{0.5} \quad (\mathrm{Re}_L^* = 1000-50{,}000, \beta \geqslant 0.5) \tag{12}$$

The exponent of the Prandtl number is assumed to be 1/3 based on the theoretical analysis for fully developed laminar flow between parallel plates [9], [3,5,10–17]. Figure 9 shows a comparison of Eq. (12) with previous data (listed in Table 1), including experiments using air and water, and numerical simulations. For the case of an array of blocks, the Nusselt number of the leading block is plotted. The average Nusselt number from Davalath and Bayazitoglu [17] was reproduced from the distribution of the local Nusselt number.

As shown in Fig. 9, the Nusselt number is scattered remarkably, particularly for the experimental data. The main reasons for this scatter are considered to be the difference in the turbulence level of the flow and the effect of natural convection. The experimental values for McEntire and Webb [12] are considerably higher than those given by Eq. (12), probably due to overestimation of the average Nusselt number (the local Nusselt number downstream of the leading block could not be measured). For the lower Reynolds numbers ($\mathrm{Re}_L^* \leqslant 1000$), the experimental values are higher than those by numerical simulation. This difference is mainly due to the effect of natural convection in the experiments. For the experimental data obtained by Young and Vafai [14] and Garimella and Eibeck [16] ($\mathrm{Re}_L^* = 200$), the Rayleigh numbers defined by Eq. (4) were greater than 10^6, leading to an increase in the heat transfer. Experimental uncertainties are considered to be one of the main reasons for the scatter, because the measurement of pure forced convection at low air velocity is very difficult due to the significant effect of heat conduction losses.

The present correlation therefore is in good agreement with existing data if compact electronic equipment without natural convection is supposed. Thus, Eq. (12) can be used to estimate the average Nusselt number of a low-profile block simulating an enclosed electronic device, regardless of the configuration of the block and duct, under the conditions of laminar flow, a low-profile block ($H/L < 0.5$), and a low blockage effect ($\beta \geqslant 0.5$).

6 Conclusion

Forced convection heat transfer from a low-profile block placed in a rectangular duct, simulating a compact packaged electronic device, was investigated experimentally. The square block examined had dimensions of 45 mm×45 mm×2 mm, and the rectangular duct enclosure had dimensions 235 mm×200 mm×3.8–10 mm high. The mean duct velocity upstream of the block ranged from 0.24 to 4 m/s. The thermal boundary conditions of constant heat flux and constant wall temperature systems were examined. A general correlation for the Nusselt number of a low-profile block was derived using a modified Reynolds number, $\mathrm{Re}_L^* = (U_m/\beta^2)L/\nu$. The reference velocity was defined as a function of U_m/β^2, derived theoretically from an assumption of fully developed laminar flow, and the reference length was defined as the block length L. The final general correlation presented in this study, $\mathrm{Nu}_m = 0.59\mathrm{Pr}^{1/3}(\mathrm{Re}_L^*)^{0.5}$, was shown to be applicable regardless of the configuration of the block and duct, under the conditions of laminar flow, a low-profile block ($H/L < 0.5$), and a low blockage effect ($\beta \geqslant 0.5$).

Acknowledgment

This study was performed as a part of the RC181 Research Project of the Computational Mechanics Division, Japan Society of Mechanical Engineers (JSME). The authors wish to express their gratitude to Professor Wataru Nakayama, leader of the Working Group of the Research Project, and all the members of the Working Group for their helpful discussions.

Nomenclature

D_h = hydraulic diameter of duct $= 2H_DW_D/(H_D+W_D)$
Gr = Grashof number
g = acceleration due to gravity
H, L, W = height, side length, and width of block
H_D, W_D = height and width of duct
h = local heat transfer coefficient $= \dot{q}/(T_w - T_0)$
h_m = average heat transfer $= \int_S h dS/S$
Nu = local Nusselt number $= hL/\lambda_f$
Nu_m = average Nusselt number $= h_m L/\lambda_f$
Pr = Prandtl number
$\dot{q}$ = heat flux
Ra = Rayleigh number = GrPr
Re = Reynolds number, $\mathrm{Re}_L = U_m L/\nu$, $\mathrm{Re}_{Dh} = U_m D_h/\nu$
Re* = modified Reynolds number, $\mathrm{Re}_L^* = (U_m/\beta^2)L/\nu$, $\mathrm{Re}_{Dh}^* = (U_m/\beta^2)D_h/\nu$
S = contributing area to the heat transfer
T_0 = air temperature at duct inlet
T_w = temperature on heated wall
U_m = mean duct velocity upstream of the block
$\overline{u}$, u' = mean and fluctuating velocities
x, y, z = streamwise, vertical, and cross-stream coordinates
β = opening ratio $= 1 - H/H_D$
β_f = volumetric thermal expansion coefficient
ε_w = total emissivity of heated wall
ϕ = inclination angle of block
λ_b = thermal conductivity of block
λ_f = thermal conductivity of fluid
μ, ν, ρ = viscosity, kinematic viscosity, and density of fluid
σ = Stefan-Boltzmann coefficient
τ_w = shearing stress

References

[1] Peterson, G. P., and Ortega, A., 1990, *Advances in Heat Transfer*, Academic Press, pp. 181–314.
[2] Roeller, P. T., Stevens, J., and Webb, B. W., 1991, ‘‘Heat Transfer and Turbulent Flow Characteristics of Isolated Three-Dimensional Protrusions in Channels,’’ ASME J. Heat Transfer, **113**, pp. 597–603.
[3] Takasaki, H., 1992, ‘‘Fluid Flow and Heat Transfer Around Rectangular Protrusions,’’ Ph.D. thesis (in Japanese), Tokyo Institute of Technology, Japan.
[4] Nakayama, W., and Park, S. H., 1996, ‘‘Conjugate Heat Transfer From a Single Surface-Mounted Block to Forced Convective Air Flow in a Channel,’’ ASME J. Heat Transfer, **118**, pp. 301–309.
[5] Young, T. J., and Vafai, K., 1998, ‘‘Convective Cooling of a Heated Obstacle in a Channel,’’ Int. J. Heat Mass Transfer, **41**, pp. 3131–3148.
[6] Nakayama, W., 2001, ‘‘An Approach to Fast Thermal Design of Compact Electronic Systems: A JSME Project,’’ *Proc. InterPACK*, Kauai, Hawaii, Paper No. IPACK2001-15532, ASME, NY.
[7] Nakamura, H., Igarashi, T., and Tsutsui, T., 2001, ‘‘Local Heat Transfer Around a Wall-Mounted Cube in the Turbulent Boundary Layer,’’ Int. J. Heat Mass Transfer, **44**, pp. 3385–3395.
[8] Pellow, A., and Southwell, R. V., 1940, ‘‘On Maintained Convective Motion in a Fluid Heated From Below,’’ Proc. R. Soc. London, Ser. A, **176**, pp. 312–343.
[9] Shah, R. K., and London, A. L., 1978, *Laminar Flow Forced Convection in Ducts*, New York Academic Press, pp. 153–195.
[10] Lehmann, G. L., and Pembroke, J., 1991, ‘‘Forced Convection Air Cooling of

Simulated Low Profile Electronic Components: Part 1—Base Case,'' ASME J. Electron. Packag., **113**, pp. 21–26.

[11] Igarashi, T., and Takasaki, H., 1995, ''Fluid Flow and Heat Transfer Around a Rectangular Block Fixed on a Flat Plate Laminar Boundary Layer,'' Proc. 4th ASME/JSME Thermal Engineering Joint Conf., ASME/JSME, NY/Tokyo, Japan, **1**, pp. 295–302.

[12] McEntire, A. B., and Webb, B. W., 1990, ''Local Forced Convective Heat Transfer From Protruding and Flush-Mounted Two-Dimensional Discrete Heat Sources,'' Int. J. Heat Mass Transfer, **33**(7), pp. 1521–1533.

[13] Kang, B. H., Jaluria, Y., and Tewari, S. S., 1990, ''Mixed Convection Transport From an Isolated Heat Source Module on a Horizontal Plate,'' ASME J. Heat Transfer, **112**, pp. 653–661.

[14] Young, T. J., and Vafai, K., 1999, ''Experimental and Numerical Investigation of Forced Convective Characteristics of Arrays of Channel Mounted Obstacles,'' ASME J. Heat Transfer, **121**, pp. 34–42.

[15] Mahaney, H. V., Incropera, F. P., and Ramadhyani, S., 1990, ''Comparison of Predicted and Measured Mixed Convection Heat Transfer From an Array of Discrete Sources in a Horizontal Rectangular Channel,'' Int. J. Heat Mass Transfer, **33**(6), pp. 1233–1245.

[16] Garimella, S. V., and Eibeck, P. A., 1990, ''Heat Transfer Characteristics of an Array of Protruding Elements in Single Phase Forced Convection,'' Int. J. Heat Mass Transfer, **33**(12), pp. 2659–2669.

[17] Davalath, J., and Bayazitoglu, Y., 1987, ''Forced Convection Cooling Across Rectangular Blocks,'' ASME J. Heat Transfer, **109**, pp. 321–328.

Journal of
Heat Transfer

Technical Notes

This section contains shorter technical papers. These shorter papers will be subjected to the same review process as that for full papers.

Analytical Solution of Coupled Diffusion Equations in Semi-Infinite Media

O. Fudym
Laboratoire de Génie des Procédés des Solides Divisés,
UMR 2392 CNRS, Ecole des Mines d'Albi,
81013 Albi, France

J.-C. Batsale
Laboratoire inter-établissements TREFLE-Site ENSAM,
33405 Talence, France

R. Santander

V. Bubnovich

Departamento de Ing. Mecánica, Universidad de Santiago
de Chile, Santiago, Chile

Some analytical solutions of the one dimensional transient coupled heat and mass transfer linear equations in a semi-infinite medium are proposed, based on an extension of the thermal quadrupole formalism, in both axial and radial coordinate systems. A direct relationship is proposed between the local temperature and moisture content, both at wall and inner locations. For a previous characterized medium, these relationships seem to be relevant in order to deduce the moisture content from temperature measurements. Another application would be the transport parameters estimation. [DOI: 10.1115/1.1731317]

Keywords: Analytical, Conduction, Modeling, Moisture, Porous Media

1 Introduction

The modeling of coupled heat and mass transfer problems, such as drying in capillary porous media, is usually based on the Luikov equations [1,2]. Various analytical solutions of these equations exist for finite geometry. For the linear case, that is when the properties are assumed to be constant, the coupled partial equations can be reduced to a uncoupled diffusive system, by substituting the potential variables by some apropriate linear combinations, as proposed by Smirnov [3]. The resulting system is only coupled by the boundary conditions. Mikhailov et al. proposed a general solution of the diffusion equations in a finite region of arbitrary geometry, with coupled boundary conditions, for the study of the temperature-moisture distribution [4]. This two-region Sturm-Liouville problem is solved through a specific integral transform approach, since a common set of eigenvalues is to be found for different eigenfunctions. This methodology was applied to a thin layer contact drying problem [5], but the eigenvalues had to be computed numerically. A general formulation of this integral transform method is available in [6]. An hybrid numerical-analytical approach, based on the integral transforms method coupled with a numerical resolution was proposed by Cotta [7], allowing the implementation of semi-analytical solutions for nonlinear problems [8]. More recently, an analytical approach to the solution of multidimensional drying problems was proposed by Thum et al. [9], based on an integral transform technique associated with the Laplace transform applied on time.

Previous analytical or semi-analytical solutions are difficult to compute for semi-infinite domains, since the corresponding eigenvalues become continuous. In the present work, an analytical solution is proposed for semi-infinite media, in the linear case, in both axial and radial coordinate systems. Discussion of the domain of validity of the constant properties assumption is not within the scope of this paper. This aspect has been investigated by many authors, see for instance Prata [10]. The constant properties model was found to be suitable for low temperature gradients and for moisture contents either below or above the critical moisture content, that is the value for which the liquid phase becomes continuous. Moreover, the transient methods for properties measurement can be implemented with very low temperature and moisture gradients, and consequently the parametric model approaches asymptotically the general non linear model.

2 Constant Properties Model

The porous medium is assumed to be isotropic and homogeneous, treated as a continuum, the solid matrix is rigid, and one-dimensional heat and mass transfer is considered. The mass of vapor is supposed to be small compared to the mass of liquid. Gravity is neglected, the gas phase pressure is assumed to be constant, so only vapor diffusion is present. The convective terms in the energy equation are neglected, and thermal local equilibrium is assumed. The effect of the moisture content gradient in the energy equation is commonly neglected, except in the hygroscopic domain, because it is assumed that the water vapor in the pores is saturated vapor. Hence, the governing equations for both the volumetric moisture content $\theta(x,t)$ and temperature $T(x,t)$ are

$$\frac{\partial \theta}{\partial t}=\frac{D_\theta}{x^p}\frac{\partial}{\partial x}\left(x^p\frac{\partial \theta}{\partial x}\right)+\frac{D_T}{x^p}\frac{\partial}{\partial x}\left(x^p\frac{\partial T}{\partial x}\right) \tag{1a}$$

$$C\frac{\partial T}{\partial t}=\frac{k^*}{x^p}\frac{\partial}{\partial x}\left(x^p\frac{\partial T}{\partial x}\right) \tag{1b}$$

where

Contributed by the Heat Transfer Division for publication in the JOURNAL OF HEAT TRANSFER. Manuscript received by the Heat Transfer Division September 11, 2003; revision received January 23, 2004. Associate Editor: J. N. Chung.

$$p=\begin{cases}0 & \text{slab}\\ 1 & \text{cylinder}\end{cases}$$

The apparent thermal conductivity k^* includes a contribution from transport of latent heat. D_θ and D_T are the isothermal moisture diffusivity and thermal moisture diffusivity respectively, while C is the volumetric specific heat.

The initial and boundary conditions in consideration are given by

$$t=0 \quad T(x,0)=T_i \quad \theta(x,0)=\theta_i \tag{1c}$$

$$x=x_1 \text{ known } T(x_1,t) \text{ or } q(x_1,t) \text{ and } \theta(x_1,t) \text{ or } j(x_1,t) \tag{1d}$$

$$x\to\infty \quad \text{finite temperature and moisture content} \tag{1e}$$

where the total mass flux density is given as

$$j=-S(p)\left(D_\theta\frac{\partial\theta}{\partial x}+D_T\frac{\partial T}{\partial x}\right) \tag{2a}$$

and the heat flux density is

$$q=-k^*S(p)\frac{\partial T}{\partial x} \tag{2b}$$

with $S(p)=(2\pi x)^p$.

For the slab case, j and q are given as a flux density $-\mathrm{kg}\cdot\mathrm{m}^{-2}\cdot\mathrm{s}^{-1}$ and $\mathrm{W}\cdot\mathrm{m}^{-2}$, respectively, while for the cylindrical case, there are expressed as a lineal flux density ($\mathrm{kg}\cdot\mathrm{m}^{-1}\cdot\mathrm{s}^{-1}$ and $\mathrm{W}\cdot\mathrm{m}^{-1}$, respectively).

In next section, an analytical solution of the problem given by Eqs. (1*a*–*e*) is proposed, based on a thermal quadrupole approach.

3 General Analytical Solution in a Semi-Infinite Medium

The basic thermal quadupole formalism is a very efficient method for linear diffusion modeling, when involved in multilayered systems. For homogeneous media, a linear intrinsic transfer matrix relates the input and output temperature and heat flux after a Laplace transformation and some convenient integral space transforms [11]. In a previous work, a general extension of this approach was implemented for heterogeneous media [12], and a semi-numerical general solution was proposed for transient heat transfer in finite or semi-infinite media based on a semi gridding approach. The same methodology applies here in order to solve the system of Eqs. (1*a*–*e*).

The new variables $T'=T-T_i$ and $\theta'=\theta-\theta_i$ are now introduced, but the superscript ⟨′⟩ is omitted for the sake of clarity. Both initial values are then set to zero. Applying a Laplace transformation on time to Eqs. (1*a*–*b*),

$$\overline{\theta}(x,s)=\int_0^\infty \exp(-st)\,\theta(x,t)\cdot dt \tag{3a}$$

$$\overline{T}(x,s)=\int_0^\infty \exp(-st)\,T(x,t)\cdot dt \tag{3b}$$

and arranging the resulting equations in a matricial form yields the following system:

$$\begin{bmatrix}s & 0\\ 0 & s\end{bmatrix}\begin{bmatrix}\overline{\theta}\\ \overline{T}\end{bmatrix}-\frac{1}{x^p}\begin{bmatrix}D_\theta & D_T\\ 0 & a^*\end{bmatrix}\frac{d}{dx}\left(x^p\frac{d}{dx}\left(\begin{bmatrix}\overline{\theta}\\ \overline{T}\end{bmatrix}\right)\right)=\mathbf{0} \qquad a^*=\frac{k^*}{C} \tag{4a}$$

where a^* is the apparent thermal diffusivity. Equation (4*a*) is then written as

$$\mathbf{GW}-\frac{1}{x^p}\frac{d}{dx}\left(x^p\frac{d\mathbf{W}}{dx}\right)=\mathbf{0} \tag{4b}$$

where $\mathbf{W}=[\overline{\theta\,T}]^t$ is the Laplace state variables vector, and

$$\mathbf{G}=\begin{bmatrix}\dfrac{s}{D_\theta} & -\dfrac{D_T s}{a^* D_\theta}\\ 0 & \dfrac{s}{a^*}\end{bmatrix}$$

The direct coupling effect between the heat and mass transfer equations is given by the nondiagonal term in the matrix **G**. Equation (4*b*) is solved by diagonalization of the matrix **G**, such as

$$\mathbf{G}=\mathbf{PDP}^{-1} \tag{5a}$$

where the eigenvalues and eigenvectors matrices are, respectively,

$$\mathbf{D}=\begin{bmatrix}\dfrac{s}{D_\theta} & 0\\ 0 & \dfrac{s}{a^*}\end{bmatrix} \tag{5b}$$

$$\mathbf{P}=\begin{bmatrix}1 & 1\\ 0 & \dfrac{1-Lu}{\delta Lu}\end{bmatrix} \text{ where } Lu=\frac{D_\theta}{a^*} \quad \text{and} \quad \delta=\frac{D_T}{D_\theta} \tag{5c}$$

The dimensionless term Lu introduced in Eq. (5*c*) is known as the Luikov number, while δ is the thermogradient coefficient. The Luikov number is the ratio between the macroscopic isothermal diffusion coefficient and the apparent thermal diffusivity. This number is related to the characteristic times and penetration depths of the temperature and moisture variables: for low values of Lu, the temperature profile is established faster than the moisture field, and the heat and mass transfer are weakly coupled.

The particular case corresponding to $Lu=1$ yields a double eigenvalue, and the eigenvectors matrix is singular. Then the problem becomes ill-posed, but this specific case is not considered in this paper, due to the fact that practically, for physical applications, the Luikov number is smaller than one. The state variables vector is introduced in the eigenvectors basis as

$$\mathbf{V}=\mathbf{P}^{-1}\mathbf{W} \tag{6a}$$

Substituting Eqs. (5*a*) and (6*a*) into Eq. (4*b*) yields

$$\mathbf{DV}-\frac{1}{x^p}\frac{d}{dx}\left(x^p\frac{d\mathbf{V}}{dx}\right)=\mathbf{0} \tag{6b}$$

The solutions of Eq. (6*b*) must be finite when the boundary of the medium is located toward infinite in the *x*-direction. Thus, the general solution can be written as

$$\mathbf{V}(x)=\mathbf{H}^p(\sqrt{\mathbf{D}}\cdot x)\cdot\frac{\mathbf{V}(x_1)}{\mathbf{H}^p(\sqrt{\mathbf{D}}x_1)} \tag{7}$$

where $\mathbf{H}^\mathrm{p}$ is the exponential function exp( ) if $p=0$ (slab) or the modified Bessel function of order zero of second kind K_0 if $p=1$ (cylinder), and x_1 is any particular point in the semi-infinite medium, for instance the input wall.

The boundary conditions are unkown in the eigenvectors basis, thus of practical interest is the Laplace flux vector

$$\mathbf{J}=\begin{bmatrix}\overline{j}\\ \overline{q}\end{bmatrix}=-S(p)\begin{bmatrix}D_\theta & D_T\\ 0 & k^*\end{bmatrix}\frac{d\mathbf{W}}{dx}=-S(p)\mathbf{K}\frac{d\mathbf{W}}{dx} \tag{8}$$

where the matrix **K**, defined in Eq. (8), appear to be a nondiagonal conductivity matrix. Substituting Eqs. (6*a*) and deriving Eq. (7) into Eq. (8) yields a direct relationship between the Laplace state variable vector $\mathbf{W}_1$ and the Laplace flux vector $\mathbf{J}_1$ at location x_1 such as

$$\mathbf{W}_1 = -\frac{1}{S(p)}\mathbf{P}\frac{\mathbf{H}^p(\sqrt{\mathbf{D}}x_1)}{\left(\dfrac{d\mathbf{H}^p(\sqrt{\mathbf{D}}\cdot x)}{dx}\right)_{x=x_1}}\quad(\mathbf{KP})^{-1}\mathbf{J}_1 = \mathbf{Z}_\infty \mathbf{J}_1 \tag{9a}$$

Substituting the particular boundary conditions given by Eq. (1*d*) in Eq. (9*a*) yields the determination of the remaining variables at the input wall.

The transfer matrix $\mathbf{Z}_\infty$ describing the semi-infinite medium, and defined by Eq. (9*a*), yields a generalized impedance between the input state variable and flux vectors. Depending on the geometry, $\mathbf{Z}_\infty$ can be expressed as a function of matrices such as

- p=0 slab

$$\mathbf{Z}_\mathbf{x} = \mathbf{P}\frac{1}{\sqrt{\mathbf{D}}}\mathbf{P}^{-1}\mathbf{K}^{-1} \tag{9b}$$

- p=1 cylinder of internal radius *r*

$$\mathbf{Z}_\mathbf{r} = \frac{1}{2\pi r}\mathbf{P}\frac{K_0(\sqrt{\mathbf{D}}r)}{\sqrt{\mathbf{D}}K_1(\sqrt{\mathbf{D}}r)}\mathbf{P}^{-1}\mathbf{K}^{-1} \tag{9c}$$

where K_0 and K_1 are the modified Bessel function of second kind of order zero and one, respectively. Equation (9*a*) can be used with Eqs. (6*a*) and (7) to determine $\mathbf{W}$ at any inner location *x* as

$$\mathbf{W}(x) = -\frac{1}{S(p)}\mathbf{P}\frac{\mathbf{H}^p(\sqrt{\mathbf{D}}x)}{\left(\dfrac{d\mathbf{H}^p(\sqrt{\mathbf{D}}\cdot x)}{dx}\right)_{x=x_1}}(\mathbf{KP})^{-1}\mathbf{J}_1 \tag{10}$$

The eigenvector and eigenvalue matrices are known analitically—see Eqs. (5*b*–*c*). Moreover, in the next section, some Laplace analytical inversions are to be used. If necessary, a numerical Laplace inversion is performed, using for instance a Gavert-Stehfest algorithm [13].

4 Moisture Content and Temperature Ratio Analysis

4.1 Axial Case. In this section, we consider a semi-infinite medium subjected to a time varying wall heat flux density. Such assumption is used for instance in the hot film experiment, when a heating plane probe is stuck to the medium, and the wall temperature response is measured and analyzed in order to deduce the apparent thermal effusivity of the medium. The heat input must be low enough that significant property variation does not occur. When an input heat flux density $q_0(t)$ applies on the input wall $x_1=0$, Eqs. (9*a*–*b*) are turned into

$$\begin{bmatrix}\overline{\theta_0}\\ \overline{T_0}\end{bmatrix} = \mathbf{P}\frac{1}{\sqrt{\mathbf{D}}}(\mathbf{KP})^{-1}\begin{bmatrix}\overline{j_0}\\ \overline{q_0}\end{bmatrix} \tag{11}$$

If the wall is impermeable, then j_0 is zero. Substituting Eqs. (5*b*–*c*) into Eq. (11) yield

$$\overline{\theta_0} = -\frac{\delta\sqrt{Lu}}{1+\sqrt{Lu}}\frac{1}{bs^{1/2}}\overline{q_0} \tag{12a}$$

$$\overline{T_0} = \frac{1}{bs^{1/2}}\overline{q_0} \tag{12b}$$

where $b=\sqrt{k^*C}$ is the apparent thermal effusivity. As expected, the temperature response analysis is suitable for the estimation of *b* only, while the wall moisture content expression contains information about coupled heat and mass transport properties. The negative sign in Eq. (12*a*) means that the moisture content decreases from the initial value when a positive heat flux is applied. It is interesting to observe the direct relationship between both variables, obtained from Eqs. (12*a*–*b*) such as

$$\overline{\theta_0} = \frac{\delta\sqrt{Lu}}{1+\sqrt{Lu}}\overline{T_0} \tag{12c}$$

and notice that the ratio of these variables is constant, depending only on the thermogradient coefficient and the Luikov number. This result implies that, for a given medium, when those parameters are known, in the domain where the parametric model is valid, the wall moisture content can be directly deduced from wall temperature measurements. This result could be quite suitable for the calibration of a moisture sensor, thus temperature measurements are often more simple and have a better confidence limit that those obtained from moisture measurements.

For a constant input heat flux density *q*, Eqs. (12*a*–*b*) are inverted as

$$\theta_0 = -\frac{\delta\sqrt{Lu}}{1+\sqrt{Lu}}\frac{2q}{b\sqrt{\pi}}\sqrt{t} \tag{13a}$$

$$T_0 = \frac{2q}{b\sqrt{\pi}}\sqrt{t} \tag{13b}$$

This result is well known for the temperature. The wall moisture content is found here to exhibit the same kind of evolution, that is, for a constant input heat flux *q*, a linear dependance on the square root of time. Equation (12*c*) is difficult to use directly, because wall measurements are often a complicated matter. For a point located inside the medium, Eq. (10) yields

$$\overline{\theta_x} = \frac{\delta Lu}{1-Lu}\left(\exp(-K_a x) - \frac{1}{\sqrt{Lu}}\exp(-K_\theta x)\right)\frac{1}{bs^{1/2}}\overline{q_0} \tag{14a}$$

$$\overline{T_x} = \frac{\exp(-K_a x)}{bs^{1/2}}\overline{q_0} \tag{14b}$$

where

$$K_a = \sqrt{\frac{s}{a^*}} \quad \text{and} \quad K_\theta = \sqrt{\frac{s}{D_\theta}}.$$

Equations (14*a*–*b*) are inverted as a convolution product as follows:

$$\theta(x,t) = \int_0^t h_\theta(x,t-\tau)q_0(x,\tau)\,d\tau \tag{15a}$$

where

$$h_\theta(x,t) = \frac{\delta Lu}{(1-Lu)b\sqrt{\pi t}}\left(\exp(-x^2/4a^*t) - \frac{1}{\sqrt{Lu}}\exp(-x^2/4D_\theta t)\right)$$

$$T(x,t) = \int_0^t h_T(x,t-\tau)q_0(x,\tau)\,d\tau \tag{15b}$$

where

$$h_T(x,t) = \frac{\exp(-x^2/4a^*t)}{b\sqrt{\pi t}}$$

The ratio of the moisture content and the temperature in Laplace space is no longer constant, as in Eq. (12*c*) for the wall state variables, but is given as

$$\overline{\theta_x} = F(s,x)\overline{T_x} \tag{16a}$$

with

$$F(s,x) = \frac{\delta Lu}{1-Lu}\left(1 - \frac{\exp(-(K_\theta - K_a)x)}{\sqrt{Lu}}\right)$$

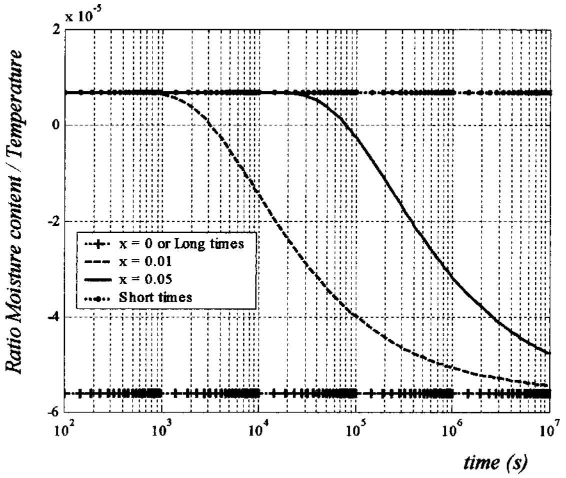

Fig. 1 Moisture content/temperature ratio at the impermeable wall of a semi-infinite slab as a function of time for various locations: $Lu=0.0122$; $\delta=5.64\,10^{-4}$; $a^*=6.49\,10^{-7}\ \mathrm{m^2\cdot s^{-1}}$

For a given inner location, the relationship between the moisture content and the temperature is obtained in the real time space as a convolution product such as

$$\theta(x,t)=\int_0^t h_{\theta T}(x,t-\tau)T(x,\tau)d\tau \qquad (16b)$$

with

$$h_{\theta T}(x,t)=\frac{\delta Lu}{1-Lu}\left(\delta(t)-\frac{\alpha x}{2\sqrt{Lu}\sqrt{\pi t^3}}\exp\left(-\frac{\alpha^2x^2}{4t}\right)\right)$$

where $\alpha=D_\theta^{-1/2}-a^{*-1/2}$ and $\delta(t)$ is the Dirac distribution.

The Dirac term in Eq. $(16b)$ corresponds to the previous constant ratio part, when $x=0$. Nevertheless, the behavior of the transfer function $F(s,x)$ for short times and long times is of interest. According to the final value theorem relative to Laplace transformation, short times (respectively, long times) correspond to the limit when the Laplace variable s tend to infinity (respectively, zero). The conditions relative to the corresponding Fourier number are given assuming that, for practical cases, the Luikov number is less than unity.

Asymptotic Expansion for Short Times $(t \ll x^2/a^*)$.

$$h_{\theta T,st}=\frac{\delta Lu}{1-Lu} \qquad (17a)$$

The latter expression is not valid when x tend to zero.

Asymptotic Expansion for Long Times $(t \gg x^2/D_\theta)$

$$h_{\theta T,lt}=-\frac{\delta\sqrt{Lu}}{1+\sqrt{Lu}} \qquad (17b)$$

In Eqs. $(17a–b)$, $h_{\theta T,st}$ and $h_{\theta T,lt}$ are the Laplace inverse of $F(s,x)$ obtained for short and long times respectively. Both functions are constant, and do not depend on x. The long time asymtotic expansion is consistent with the constant ratio given by Eq. $(12c)$ for $x=0$. On Fig. 1 the ratio between the moisture content and the temperature at a given location is ploted as a function of time. As expected, the short times asymptotic expansion is valid during a longer time for a deeper location, while the long time value is reached after a greater delay.

4.2 Moisture Content and Temperature Ratio in the Semi-Infinite Cylinder.

In this section, we consider the case of a constant input heat flux Q applied at the entrance r_0 of a semi-infinite cylinder of length L. This problem is strongly linked to the hot wire method used for thermal conductivity measurements [14]. Previous Eqs. $(9a)$ and $(9c)$ are turned into

$$\overline{\theta}_0=\frac{\delta Lu}{1-Lu}\frac{1}{2\pi r_0 L}\left(\frac{K_0(K_a r_0)}{K_1(K_a r_0)}-\frac{K_0(K_\theta r_0)}{\sqrt{Lu}K_1(K_\theta r_0)}\right)\frac{Q}{bs^{3/2}} \qquad (18a)$$

$$\overline{T}_0=\frac{1}{2\pi r_0 L}\frac{K_0(K_a r_0)}{K_1(K_a r_0)}\frac{Q}{bs^{3/2}} \qquad (18b)$$

It is apparent that, in this case, the ratio between the moisture content and temperature at the wall is no longer constant. The short times asymptotic expansions are found to be consistent with the previous axial results as given by Eqs. $(13a–b)$ for the corresponding heat flux density. The long times asymptotic expansion is of great interest, since it is usually implemented for the temperature response analysis in the hot wire method.

When $t \gg r_0^2/D_\theta$, Eqs. $(18a–b)$ can be approximated and inverted as

$$\theta_{0,\infty}=-\frac{Q\delta}{4\pi k^*L}\ln(t)+Cste \qquad (19a)$$

$$T_{0,\infty}=\frac{Q}{4\pi k^*L}\ln(t)+Cste \qquad (19b)$$

Equation $(19b)$ is the quite well known hot wire result: the long time temperature response is a function of the natural logarithm of time, and the slope coefficient yields the apparent thermal conductivity. The meaning of Eq. $(19a)$ is that, if the thermogradient coefficient is known, the hot probe temperature response could be used to measure indirectly the moisture content for long times.

5 Conclusion

The solution of the coupled linear heat and mass transfer equations in semi-infinite media, as proposed by Eq. (10) is quite general, and would be also valid if the direct moisture gradient effect in the energy equation, Eq. $(1b)$, would not be neglected. However, the present study is of interest since in the case of Eqs. $(1a–e)$, the solution is fully analytical. The resulting analytical relationships between the local temperature and moisture content could be used in order to implement some measurement methods for the properties estimation or for moisture indirect measurements.

Acknowledgment

This work was partially funded by the FONDECYT program (Awards # 1020349 and 7010354). The authors gratefully acknowledge this support.

References

[1] Luikov, A. V., 1966, *Heat and Mass Transfer in Capillary—Porous Bodies*, Pergamon Press, Oxford.
[2] De Vries, D. A., 1958, "Simultaneous Transfer of Heat and Moisture in Porous Media," Trans., Am. Geophys. Union, **39**(5), pp. 909–916.
[3] Smirnov, M. S., 1962, "On a System of Differential Equations for Highly Intensive Heat and Mass Transfer," Int. J. Heat Mass Transfer, **5**, pp. 521–524.
[4] Mikhailov, M. D., 1973, "General Solutions of the Diffusion Equations Coupled at Boundary Conditions," Int. J. Heat Mass Transfer, **16**, pp. 2155–2164.
[5] Mikhailov, M. D., and Shishedjiev, B. K., 1975, "Temperature and Moisture Distributions During Contact Drying of a Moist Porous Sheet," Int. J. Heat Mass Transfer, **18**, pp. 15–24.
[6] Mikhailov, M. D., and Ozisik, M. N., 1984, *Unified Analysis and Solutions of Heat and Mass Diffusion*, John Wiley, New York.
[7] Cotta, R. M., 1994, "The Integral Transform Method in Computational Heat and Fluid Flow," *Proceedings of the Tenth Int. Heat Transfer Conf.*, T. and F. Ichem Brighton, ed., UK, **1**, pp. 43–60.
[8] Cotta, R. M., 1990, "Hybrid Numerical Analytical Approach to Non-Linear Diffusion Problems," Numer. Heat Trans., Pt. B **17**, pp. 217–226.
[9] Thum, R. L., Barichello, L. B., Vilhena, M. T., and Cotta, R. M., 2001, "An Analytical Approach to the Solution of Multidimensional Drying Problems,"

Proceedings of the 2nd Int. Conf. On Comp. Heat and Mass Transfer, COPPE/EE/UFRJ, Rio de Janeiro, Brazil.
[10] Prata, A. T., and Damanesco-Ferreira, L. S., 1990, "Evaluation of a Parametric Model for Heat and Mass Transfert in Unsaturated Porous Media," in *Multiphase Transport and Particulate Phenomena*, Neyat Veziroglu Hemisphere Publishing Corp., **1**, pp. 201–220.
[11] Maillet, D., André, S., Batsale, J. C., Degiovanni, A., and Moyne, C., 2000, *Thermal Quadrupoles: Solving the Heat Equation Through Integral Transforms*, John Wiley.
[12] Fudym, O., Ladevie, B., and Batsale, J. C., 2002, "A Semi-Numerical Approach for Heat Conduction in Heterogeneous Media: One Extension of the Analytical Quadrupole Method," Numer. Heat Transfer, Part B, **42**(4), pp. 325–348.
[13] Stehfest, H., 1970, "Algorithm 368. Numerical Inversion of Laplace Transform," Commun. A.C.M., **53**, pp. 47–49.
[14] De Vries, D. A., and Peck, A. J., 1958, "On Cylindrical Probe Method of Measuring Thermal Conductivity With Special Reference to Soils," Aust. J. Phys., **11**, pp. 225–271.

Comparison of Two Procedures for the Estimation of Surface Temperature History Using Function Specification Method

Alfonso Corz
e-mail: alfonso.corz@uca.es
Mem. ASME, Senior Professor, Departamento de Ingeniería Industrial e Ingeniería Civil

José M. Gutiérrez
e-mail: josemaria.gutierrez@uca.es
Assistant Professor, Departamento de Física Aplicada

Juan A. Martín
e-mail: juanandres.martin@uca.es
Assistant Professor, Departamento de Ingeniería Eléctrica,
Universidad de Cádiz, Avda. Ramón Pujol, s/n,
11202 Algeciras, (Cádiz), Spain

This work presents a comparative study of two alternative procedures for the estimation of surface temperature of a heated body from transient interior temperature measurements. This Inverse Heat Conduction Problem (IHCP) is solved (in both procedures) by using the Function Specification Method. A numerical test was used in order to compare the best estimation achieved in each procedure. The influences of the time step size, the total number of measurements and the noise level in the measurement have been considered in the estimation. Two criteria (minimization of total error and residual principle [3]) are used to choose the best hyper-parameter (r). The comparisons confirm that the procedures and criteria used provide similar results, nevertheless this study reveals slight differences with respect to the accurate and the CPU time. [DOI: 10.1115/1.1738420]

Keywords: Conduction, Heat Transfer, Inverse, Numerical Methods

Introduction

As it is well known, the main difficulty of the Inverse Heat Conduction Problem (IHCP) is the great amplification of the measurement errors. The influence of the more important factors in this problem can be discussed considering the exact solution of Burggraf [1]. Many methods have been reported to solve IHCPs, among the more versatile (applicable to solve multidimensional and non-linear IHCP) the following can be mentioned: Tikonov regularization [2], iterative regularization [3], mollification [4] and function specification method [1]. Several types of the unknown boundary conditions are considered in the IHCPs. In many problems, the unknown boundary condition is stated as type 2 (or Newman's condition). This one can be considered the most usual procedure because, once the heat flux has been estimated, the temperature field (including the surface temperature) and heat transfer coefficient can be calculated in a "post-processor" [5,6]. Nevertheless, depending on the methodology and the application considered, the procedures can be different. For example, in reference [7] surface temperature and heat flux are estimated simultaneously in steady-state, and in [8] temperature field and heat transfer coefficient are estimated simultaneously in a transitory and nonlinear problem. In other cases, the sequence of calculations is the following: first, the surface temperature (or Dirichlet's condition) is estimated, and then heat flux and heat transfer coefficient are calculated [9,10].

The purpose of this technical note is to present a comparative study of two alternative procedures in order to estimate surface temperature: Procedure I—First, the surface heat flux history is estimated by solving the IHCP, and then the discrete form of Duhamel's integral is used to calculate the surface temperature. Procedure II—The surface temperature is estimated through a direct formulation of the corresponding IHCP. In both procedures, the classic Function Specification Method (FSM) proposed by Beck [1] has been used. It is expected that different procedures provide similar results. Nevertheless, in an IHCP problem, it is suitable to carry out a comparative study. This is due to the ill-posed nature of the IHCP and the different sensitivity coefficients used. The comparison is made by taking into account the best estimation achieved in each procedure using a numerical test. In order to obtain the best estimation, it is necessary to consider a criterion that permits an adequate choice of the hyperparameter. In the FSM, the hyperparameter is the number of future temperature used (r), and the criteria considered are (1) the minimization of total error, and (2) the residual principle [3]. The two criteria have been applied in both procedures.

Analysis

In order to validate the inverse algorithm, the previous formulation of the direct problem will be necessary. The following one-dimensional problem of heat conduction will be considered: a flat plate exposed to a heat flow that varies in time in a triangular fashion (Fig. 1(a)). The opposite face is insulated. The mathematical formulation will be used in dimensionless form in order to simplify the notation. A more detailed description of this linear problem can be found in reference [1]. The problem is governed by the differential equation Eq. (1). The boundary conditions are indicated in Fig. 1(a). It is noted that τ represents the dimensionless duration of the triangular heating (in this case $\tau=1.2$). Finally, the initial condition is: $T(x,0)=0$.

$$\frac{\partial^2 T(x,t)}{\partial x^2}=\frac{\partial T(x,t)}{\partial t} \quad 0\leqslant x\leqslant 1 \tag{1}$$

The solution to this problem is based on the superposition of the fundamental function $\theta(x,t)$, and it can be expressed as

$$\begin{aligned} &0<t<\tau/2 \quad T(x,t)=\theta(x,t)\\ &\tau/2<t<\tau \quad T(x,t)=\theta(x,t)-2\,\theta(x,t-\tau/2)\\ &t>\tau \quad T(x,t)=\theta(x,t)-2\,\theta(x,t-\tau/2)+\theta(x,t-\tau)\end{aligned} \tag{2}$$

where $\theta(x,t)$ represents the analytical solution [11] of the problem when $q(t)=t$ for $t>0$:

Contributed by the Heat Transfer Division for publication in the JOURNAL OF HEAT TRANSFER. Manuscript received by the Heat Transfer Division February 26, 2002; revision received November 19, 2003. Associate Editor: G. S. Dulikravich.

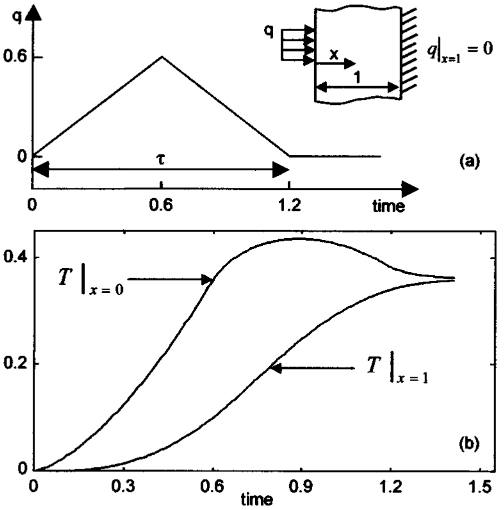

Fig. 1 (*a*) One-dimensional problem and heat flow considered; and (*b*) analytical solution of the problem at $x=0$ and at $x=1$

$$\theta(x,t)=8t^{3/2}\sum_{n=0}^{\infty}\left\{i^3\,\mathrm{erfc}\,\frac{2n+x}{2t^{1/2}}+i^3\,\mathrm{erfc}\,\frac{2(n+1)-x}{2t^{1/2}}\right\} \quad (3)$$

For subsequent discussion, the solution, Eq. (2), will be evaluated at two points of special interest: at $x=1$, where a sensor will be placed, and at $x=0$, which corresponds to the surface temperature that will be estimated. Both functions are represented in Fig. 1(*b*).

The previous direct problem will be used as a test for the validation of the inverse problem. In the IHCP, the unknown boundary condition at $x=0$ is stated as type-I (or Dirichlet's condition), and the objective is to estimate the surface temperature using the discrete reading of temperature provided by a sensor located at $x=1$. As the measured temperatures Y_i are affected by errors, they are simulated using the discrete values of the analytical (or exact) temperature $T_i=T(1,t_i)$ (from Eq. (2)) at times $t_i=i\Delta t$ (the time intervals of the measurements). Then, random errors ε_i are added according to: $T_i+\varepsilon_i$, where $\varepsilon_i=Cu_i$. The random numbers u_i have been obtained using a random generator according to a normal (or Gaussian) distribution with zero mean, uncorrelated, and unit standard deviation. The constant C is chosen, so that $C=\sigma_Y$, where σ_Y is the standard deviation of measured temperatures. FSM method is based on the specification of the functional form corresponding to an unknown input Ψ. To avoid unnecessary repetitions, the input denoted as Ψ, can be used in this problem for the surface heat flux q (in procedure I) or the surface temperature T_S (in procedure II). The specification of this method includes only r future steps from the last estimated component (component $M-1$). Then, the future components $\Psi_M, \Psi_{M+1}, \ldots, \Psi_{M+r-1}$, can be written in terms of Ψ_M, and only this component is estimated in each step. The temporary assumption can be made by several ways. In this note the simplest form is used, that being a piecewise constant form, and the r future components being assumed temporarily constant. With this assumption, a particular sequential inverse algorithm is derived from the minimization of the difference (in the least squares sense) between the measured (Y) and calculated (T) temperatures within the interval of future times. Details of this algorithm can be seen in reference [1]. The estimated component, noted as $\hat{\Psi}_M$ can be expressed as

$$\hat{\Psi}_M=\frac{\sum_{i=1}^{r}(Y_{M+i-1}-\hat{T}_{M+i-1}|_{\Psi fut.=0})Z_i}{\sum_{i=1}^{r}Z_i^2} \quad (4)$$

where subscript i denotes the future times. $\hat{T}_{M+i-1}|_{\Psi fut.=0}$ represents the calculated temperatures assuming that the future components $\Psi_M, \Psi_{M+1}, \ldots, \Psi_{M+r-1}$ are equal to zero. Z is the first derivative of calculated temperature with respect to Ψ_M. This derivative, represents the sensitivity coefficient to a unit step change in the input, and can be obtained by analytical [11] or numerical methods. In Eq. (4), Z_i is evaluated at $x=1$ (sensor location) and for the times $t_i=i\Delta t$, $i=1,2,\ldots,r$.

Depending on the procedure used, different inputs and different sensitivity coefficients are used. Details of the two procedures are described below.

Procedure I. With this procedure, the previous estimation of surface heat flux history $\hat{q}$ is necessary. Then, the surface temperature $\hat{T}_S$ is calculated from $\hat{q}$. Accordingly, the input Ψ in the inverse algorithm, Eq. (4), represents the surface flux history q, and Z represents the respective sensitivity coefficients. Once the estimation of $\hat{q}$ has been completed, we can recover the field temperature using the discrete form of Duhamel's integral, according to

$$\hat{T}(x,t_M)=T_0+\sum_{i=1}^{M}\hat{q}_i(t_{i+1/2})X_i(x,t_{M-i}) \quad (5)$$

where the initial temperature, noted as T_0, will be $T_0=0$ in accordance with the mathematical formulation of the problem. In agreement with the temporal assumption considered in the inverse algorithm, Duhamel's integral is approximated by a constant piecewise function centered at the middle of the time step ($t_{i+1/2}$). Consequently the sensitivity coefficients X_i represent the temperature response to a unit pulse in the input, and hence it is evident that $X_i=Z_{i+1}-Z_i$. The surface temperature is obtained from Eq. (5) by setting $x=0$.

Procedure II. With this procedure, the surface temperature history $\hat{T}_S$ is directly estimated from Eq. (4). Now, Ψ and Z represent the surface temperature and the respective sensitivity coefficients. The estimation of surface temperature in this form has been described by Woodbury [9]. Nevertheless, the purpose of Woodbury's study was the surface flux estimation, whereas this study is focused on the surface temperature.

In order to compare the best estimation of surface temperature by the two procedures (I and II), it is necessary to select the optimal value of r for a given time step. In this comparison, the following criteria are considered:

Criterion A. In an IHCP there are two sources of error in the estimation. The first source is the unavoidable bias deviation (or deterministic error) when $r>1$. The second source of error is the variance due to the amplification of measurement errors (stochastic error), which can be very important, especially when the time steps are small. The global effect of deterministic and stochastic errors is considered in the mean squared error or total error. Details of these types of error and the corresponding estimates can be found in reference [1]. The estimates used in this study for the bias (D), the variance (σ_Ψ) and the total error ($\mathcal{S}$) are defined by Eqs. (6), (7), and (8), respectively.

$$D=\left[\frac{1}{N-1}\sum_{i=1}^{N}(\hat{\Psi}_i|_{\sigma_Y=0}-\Psi_i)^2\right]^{1/2} \quad (6)$$

$$\sigma_\Psi=\left[\frac{1}{N-1}\sum_{i=1}^{N}(\hat{\Psi}_i-\hat{\Psi}_i|_{\sigma_Y=0})^2\right]^{1/2} \quad (7)$$

$$\mathcal{S}=\left[\frac{1}{N-1}\sum_{i=1}^{N}(\hat{\Psi}_i-\Psi_i)^2\right]^{1/2} \quad (8)$$

where $\hat{\Psi}_i|_{\sigma_Y=0}$ are the "virtual" estimations using errorless measurements, and Ψ_i are the true values of input. The optimality criterion is based on the minimization of $\mathcal{S}$, which allows determination of the necessary balance between the two error sources. As it is evident, the interest of this criterion is mainly theoretical, and it can only be useful in comparative studies.

Criterion B. This criterion is based on the residual principle [3]. Once the vector of input $(\hat{\Psi}_1, \cdots \hat{\Psi}_N)$ has been estimated, the evaluation of the residual obtained from the comparison between the measured temperatures Y_i and the recovered temperatures $\hat{T}_i(r)$ is possible. The residual R is defined as

$$R(r) = \left[\frac{1}{N-1} \sum_{i=1}^{N} (Y_i - \hat{T}_i(r))^2 \right]^{1/2} \tag{9}$$

For the procedure-I, $\hat{T}_i(r)$ can be obtained from Eq. (5) by setting $x=1$ (sensor location). As $T_0=0$, the Eq. (5) can be used in same form to obtain $\hat{T}_i(r)$ in procedure II, nevertheless the $\hat{q}_i$ components must be replaced by $\hat{T}_{Si}$, and the sensitivity coefficients X_i represent the temperature response to a unit pulse of imposed surface temperature. In the function specification method, the residual principle is satisfied when r is such that the residual R assumes the closest (and superior) value to the standard deviation of measurement [12]. This condition can be expressed as follows: $\min_r \{R(r) \geqslant \sigma_Y\}$.

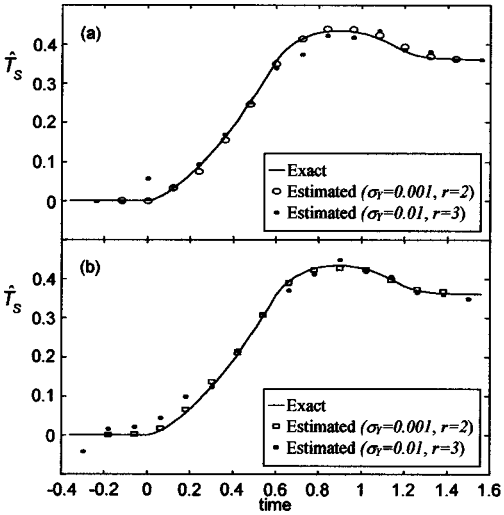

Fig. 2 Case-1: (*a*) Procedure-I; and (*b*) Procedure II

Numerical Results

A numerical test was carried out for three cases and 24 subcases. The results are presented in tabular and graphical forms, and they correspond to the optimum r-value obtained by each procedure (I and II), criterion (A and B) and level of noise, respectively, as can be seen in Table 1. Each case corresponds to a particular value of the total number of measurements (N) during the time interval τ and a size of time step (Δt). The parameters Δt and N are modified using the condition: $\Delta t\, N = \tau = 1.2$, so that, N is increased gradually and the time step is reduced. Two levels of noise measurements σ_Y (0.001 and 0.01) are considered in each case. Taking as reference the maximum increase of dimensionless temperature at location sensor (0.3581), which corresponds to the maximum of lower curve of Fig. 1(*b*), and considering (around the exact temperatures) an error range between $\pm 2.576\sigma_Y$ (or 99 percent confidence interval), these noise levels correspond to percentages error of 0.72 percent and 7.2 percent respectively. Finally it is noted that estimates σ_{TS}, S and R are random variables. Therefore, the choice of optimum value of r needs the application of Monte Carlo method. A total of 30 sets random errors have been generated in each sub-case, and the results presented in Table 1 are the arithmetic mean of the corresponding estimates.

Table 1 Summary of numerical results for optimum estimations

P.	σ_Y	$C.$	r	σ_{TS}	D	$\mathcal{S}$	R
			CASE-1, Δt=0.12, N=10				
I	0.001	A/B	2	0.0049	0.0090	0.0100	0.0015
	0.01	A/B	3	0.0187	0.0107	0.0209	0.0108
II	0.001	A/B	2	0.0033	0.0060	0.0068	0.0039
	0.01	A/B	3	0.0161	0.0211	0.0267	0.0156
			CASE-2, Δt=0.03, N=40				
	0.001	A	7*(6*)	0.0023	0.0034	0.0041	0.0018
I		B	6	0.0035	0.0021	0.0040	0.0012
	0.01	A	10*(9*)	0.0098	0.0101	0.0141	0.0107
		B	10	0.0098	0.0101	0.0141	0.0107
	0.001	A	6	0.0035	0.0043	0.0056	0.0024
II		B	5	0.0058	0.0023	0.0063	0.0014
	0.01	A	9*(8*)	0.0140	0.0132	0.0193	0.0121
		B	8	0.0179	0.0098	0.0204	0.0108
			CASE-3, Δt=0.01, N=120				
	0.001	A	16*(17*)	0.0023	0.0017	0.0029	0.0011
I		B	16	0.0023	0.0017	0.0029	0.0011
	0.01	A	25*(27*)	0.0077	0.0066	0.0101	$<\sigma_Y$
		B	28	0.0064	0.0091	0.0111	0.0106
	0.001	A	15*(16*)	0.0035	0.0027	0.0043	0.0016
II		B	12	0.0067	0.0012	0.0068	0.0011
	0.01	A	22	0.0126	0.0082	0.0126	0.0147
		B	21	0.0141	0.0072	0.0159	0.0105

The first case (case-1 in Table 1) considers a relatively large time step $\Delta t = 0.12$. Due to their size, only ten measurements ($N=10$) are included in the interval τ. For all subcases considered, the optimal r-value has been $r=2$ (for $\sigma_Y=0.001$) and $r=3$ (for $\sigma_Y=0.01$), with independence of criterion (A or B). Graphical representations of $\hat{T}_S$ versus time are plotted in Fig. 2. Considering a visual inspection, the estimations obtained by both procedures are similar. Nevertheless, taking into account the values of $\mathcal{S}$ in Table 1, for low noise, procedure II is slightly better than procedure-I, and for high noise, the opposite occurs.

In the second case (case-2 in Table 1), the time step is $\Delta t = 0.03$. This value implies $N=40$, according to the previous considerations. As it is expected, shorter time step requires larger r-value in order to assure the stability. Comparing the tabulated results to the corresponding to previous case, the estimations are now slightly more accurate. In this case, the estimation of $\hat{T}_S$ by procedure I is slightly better than the one obtained by procedure II. For sub-case procedure I and $\sigma_Y = 0.001$, the best estimation corresponds to $r=7$ (criterion A) and $r=6$ (criterion B). Never-

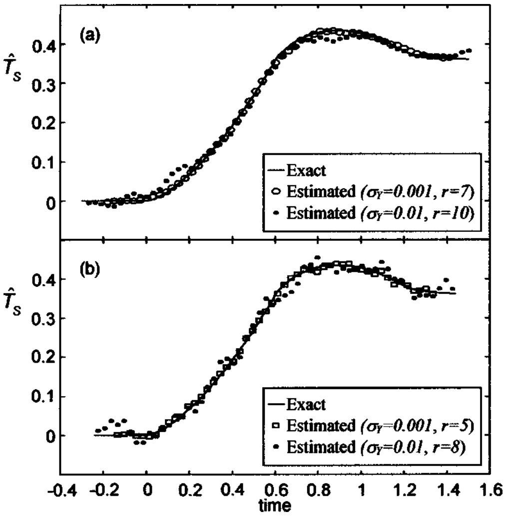

Fig. 3 Case-2: (*a*) Procedure-I; and (*b*) Procedure II

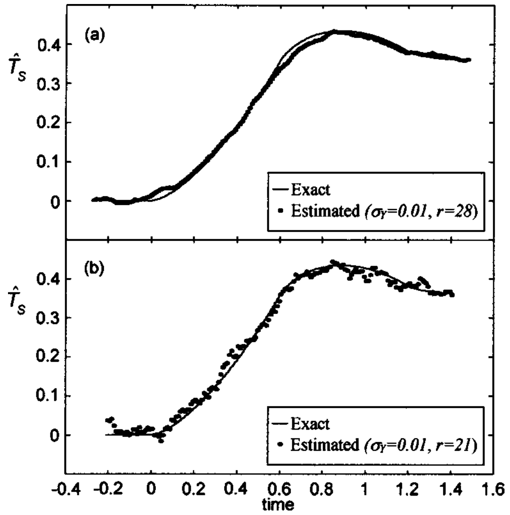

Fig. 4 Case-3: (*a*) Procedure-I; and (*b*) Procedure II

theless, a new statistical analysis reveals that the choice based on criterion A is affected by uncertainty. If the arithmetic mean value of $\mathcal{S}$ is recalculated a set of 30 times, according to the central limit theorem, these mean values are nearly normally distributed. This particular point has been corroborated using the Kolmogorov-Smirnov test. This fact permits to establish confidence intervals. The 95 percent confidence interval for $\mathcal{S}$ with $r=6$ is: (0.0038, 0.0042) and the corresponding interval with $r=7$ is: (0.0039, 0.0041). There is obviously an overlapping, and any of the two values can be considered as the optimum. The cases affected by this type of uncertainty are noted in Table 1 with (*). Similar overlapping exists in the sub-case: procedure I, $\sigma_Y=0.01$. On the other hand, and considering the criterion B corresponding to procedure I and $\sigma_Y=0.01$, the 95 percent confidence interval for R with $r=9$ is as follows: (0.0097, 0.0105). As $0.0097<\sigma_Y$, this implies that in some samples the residual principle is not statistically satisfied, consequently the minimum r-value that satisfies (with 95 percent confidence) the residual principle is $r=10$ (see Table 1). When procedure II is applied, only the estimations corresponding to a high noise level ($\sigma_Y=0.01$) are affected by uncertainty. The estimations obtained by procedure I and II are plotted in Fig. 3. In each case two noise levels are considered. The criteria selected have been: criterion A, in Fig. 3(*a*), and criterion B, in Fig. 3(*b*).

In the third case (case-3 in Table 1) $\hat{T}_S$ is estimated with a very high temporal resolution. The estimations corresponding to sub-cases of low noise level are the most accurate results, and for the sake of clarity are not plotted. Considering the high noise level and the residual principle (criterion B), the best estimations obtained by procedure I and II are plotted in Fig. 4.

Finally, the computational time has also been evaluated. It is evident that procedure I needs more computation time than the used by procedure II. Moreover, the r-value used by procedure I (in the best estimation) is higher that the one used by procedure II, especially in cases of high temporal resolution. For example, comparing the estimation of surface temperature corresponding to Fig. 4, the CPU time required by procedure I and procedure II has been 11.43 s. and 7.08 s, respectively. This advantage of procedure II can be attractive in an on-line process. All numerical calculations were performed on a personal computer with a Pentium III 700 MHz processor.

Conclusions

Two procedures in conjunction with two possible criteria have been considered in this comparative study in order to estimate the surface temperature. The results obtained in this numerical simulation reveal that, the accuracy of both procedures is similar, nevertheless procedure I provides results slightly more accurate than procedure II. On the other hand, procedure II requires less computational time and needs a smaller number of future temperatures. This fact suggests that procedure II can be more adequate in those applications where the surface temperature must be estimated in an on-line process of long duration.

A comparison has also been made between the criterion of minimum mean squared error and the residual principle. Taking into account the uncertainty in the determination of the optimum r-value, this simulation confirms that both criteria provide equal or similar values in all the cases considered.

Acknowledgment

This work is supported in part by a grant from the Andalusian Government through P.A.I. (Group TEP-157). The authors are very grateful for the helpful comments and suggestions offered by reviewers.

Nomenclature

C = constant chosen
D = estimate of bias
q = dimensionless heat flux
M = present time step
N = number of measurement during τ
n = integer
T = dimensionless temperature
T_0 = initial temperature
r = number of future time steps
t = dimensionless time
R = estimate of residual
$\mathcal{S}$ = estimate of total error
u = Gaussian random numbers (normalized)
x = dimensionless coordinate
X = sensitivity coefficient, Eq. (5)
Y = measured temperature
Z = sensitivity coefficient, Eq. (4)

Greek Symbols

Δt = dimensionless time step size
ε = random error
θ = analytical solution, Eq. (3)
σ = standard deviation
τ = dimensionless temporal interval
Ψ = input unknown

Subscripts

i = at time t_i
fut. = future components
S = surface location

Superscripts

$\hat{}$ = estimated
$*$ = uncertainty

References

[1] Beck, J. V., Blackwell, B., and St. Clair, C. R., 1985, *Inverse Heat Conduction, Ill-Posed Problems*, Wiley-Interscience, New York.
[2] Tikhonov, A. N., and Arsenin, V. Y., 1977, *Solution of Ill-Posed Problems*, V. H. Winston & Sons, Washington, DC.
[3] Alifanov, O. M., 1994, *Inverse Heat Transfer Problems*, Springer, New York.
[4] Murio, D. A., 1993, The Mollification Method and the Numerical Solution of Ill-Posed Problems, Wiley-Interscience, New York.
[5] Beck, J. V., Litkouhi, B., and St. Clair, Jr., C. R., 1982, "Efficient Sequential Solution of the Nonlinear Heat Conduction Problem," Numer. Heat Transfer, **5**, pp. 275–286.
[6] Blanc, G., Raynaud, M., and Chau, T. C., 1998, "A Guide for the Use of the Function Specification Method for 2D Inverse Heat Conduction Problems," Rev. Gén. Therm. Elsevier., **37**, pp. 17–30.
[7] Martin, T. J., and Dulikravich, G. S., 1996, "Inverse Determination of Boundary Conditions and Sources in Steady Heat Conduction With Heat Generation," ASME J. Heat Transfer, **118**, pp. 546–554.
[8] Matsevityi, Yu. M., Maliarenko, V. A., and Multanovskii, A. V., 1979, "Iden-

tification of Time-Variable Coefficients of Heat Transfer by Solving a Nonlinear Inverse Problem of Heat Conduction,'' J. Eng. Phys., **35(3)**, pp. 1094–1098.
[9] Woodbury, K. A., and Jin X., 1995, ''A Temperature-Based Sequential Specification Algorithm for the IHCP,'' *National Heat Transfer Conference*, HTD Vol. 312, pp. 141–150.
[10] Flach, G. P., and Özişik, M. N., 1988, ''Inverse Heat Conduction Problem of Periodically Contacting Surfaces,'' ASME J. Heat Transfer, **110**, pp. 821–829.
[11] Carslaw, H. S., and Jaeger, J. C., 1959, *Conduction of Heat in Solids*, Oxford University Press, London.
[12] Blanc, G., Beck, J. V., and Raynaud, M., 1997, ''Solution of the Inverse Heat Conduction Problem With a Time-Variable Numbers of Future Temperatures,'' Numer. Heat Transfer, Part B, **32**, pp. 437–451.

Critical Values of Gr/Re for Mixed Convection in Vertical Eccentric Annuli With Isothermal/Adiabatic Walls

Esmail M. A. Mokheimer[1]
Associate Professor

Maged A. I. El-Shaarawi
Professor

Mechanical Engineering Department, King Fahd
University of Petroleum and Minerals, Dhahran 31261,
Saudi Arabia

[DOI: 10.1115/1.1725116]

Keywords: Analytical, Annular Flow, Convection, Heat Transfer, Mixed Convection

1 Introduction

Mixed (forced-free) convection heat transfer in vertical eccentric annuli can be found in the drilling and cementing operations of oil wells [1], double-pipe heat-exchangers, and cooling of vertical electric motors and generators [2]. Most articles dealing with eccentric annuli treated the fully developed forced flow and the fully developed forced convection [3–9]. Sathymurthy et al. [10] investigated the problem of fully developed mixed (combined forced and free) convection for a Newtonian fluid in an eccentric annulus.

The main objective of this paper is to present an analytical solution for the problem of fully developed laminar mixed convection in vertical eccentric annuli under the thermal boundary conditions of one isothermally heated cylinder while the other cylinder is insulated. This analytical solution is used to obtain the critical values of Gr/Re that create buoyancy effects that balance the friction in the annulus. Flows having Gr/Re above these critical values would make the channel, which has a constant cross-sectional area perpendicular to the flow direction, acts as a diffuser with possible incipient flow separation.

2 Problem Description

The geometry under consideration is shown in Fig. 1(*a*). This eccentric geometry can easily be described by the bipolar coordinate system (η, ξ and z) shown in Fig. 1(*b*).

A Newtonian fluid at ambient temperature T_o is forced to flow through this vertical annulus from its bottom. Free convection exists inside this vertical channel as a result of heating one of its walls at a uniform temperature (T_w) different from that of the ambient while keeping the other wall insulated. The fluid is assumed to have constant physical properties but obeys the Boussinesq approximation (its density is allowed to vary with temperature in only the gravitational body force (buoyancy) term of the vertical (axial) momentum equation). Body forces in other than the vertical direction, viscous dissipation, internal heat generation, and radiation heat transfer are absent. Using the appropriate coordinate scale factors [11], the governing equations in bipolar coordinates under the above-mentioned assumptions can be obtained.

3 Fully Developed Mixed-Convection Flow

3.1 The Fully Developed Velocity Profile. At large values of the dimensionless axial distance Z the flow becomes fully developed with $v=w=0$ and $\partial u/\partial z=0$. Hence the continuity equation and the inertia terms of the axial momentum equation vanish while the ξ and η-momentum equations reduce to $\partial p/\partial\xi=0$ and $\partial p/\partial\eta=0$, respectively. In the axial momentum equation, the gravitational body force per unit volume $F_z=-\rho g$ and according to the Boussinesq approximation: $\rho=\rho_o(1-\beta|T-T_o|)$. Hence, $F_z=-\rho_o g+\rho_o g\beta|T-T_o|$. Using the dimensionless parameters given in the nomenclature, one can write: $F_z=-\rho_o g+(\rho_o \mathrm{Gr}\gamma^2/D_h^3)\theta$. Accordingly, for a hydrodynamic fully developed mixed/forced flow $\partial p/\partial z=[(dp/dz)_{fd}]=\text{constant}$ and the resulting axial momentum equation reduces to

$$\mu\left(\frac{\partial^2 u_{fd}}{\partial\xi^2}+\frac{\partial^2 u_{fd}}{\partial\eta^2}\right)=h^2\left(\left(\frac{dp'}{dz}\right)_{fd}-\frac{\rho_o \mathrm{Gr}\gamma^2}{D_h^3}\theta_{fd}\right) \tag{1}$$

For values of $\mathrm{Pr}<1$, thermal full-development occurs before the hydrodynamic full development and since the boundary conditions under consideration have one wall isothermal, $\theta_{fd}=1$. With $\theta_{fd}=1$ and using the dimensionless parameters given in the nomenclature the above equation reduces to

$$\frac{\partial^2 U_{fd}}{\partial\xi^2}+\frac{\partial^2 U_{fd}}{\partial\eta^2}=H^2\left(\left(\frac{dP}{dZ}\right)_{fd}-\frac{\mathrm{Gr}}{\mathrm{Re}}\right)=\frac{C^*\left(\left(\frac{dP}{dZ}\right)_{fd}-\frac{\mathrm{Gr}}{\mathrm{Re}}\right)}{(\cosh\eta-\cos\xi)^2} \tag{2}$$

where C^* is a dimensionless constant that depends on the geometry and is given by

$$C^*=(\sinh^2\eta_o)/[4(1-\mathrm{N})^2]. \tag{3}$$

It is worth mentioning that Re and Gr cannot, in strict sense, be independently varied for mixed-convection problems in vertical channels. This is because the entrance velocity u_o (which equals to $\bar{u}$, under the steady-state steady-flow conditions) is physically influenced by the value of Gr, in vertical duct flows. However, forced and free convection effects can be comparable when an external flow is superimposed on a buoyancy-driven flow. In such a case, ''there exists a well-defined forced convection velocity'' [12]. Nonetheless, in the case under investigation, the governing Eq. (2) will be handled for given values of the parameter Gr/Re, rather than independent values of each.

Let $C^{**}=-\{(dP/dZ)_{fd}-\mathrm{Gr}/\mathrm{Re}\}$, which is a dimensionless quantity, and dividing both sides of (2) by C^{**}

$$\frac{\partial^2(U_{fd}/C^{**})}{\partial\xi^2}+\frac{\partial^2(U_{fd}/C^{**})}{\partial\eta^2}=\frac{-C^*}{(\cosh\eta-\cos\xi)^2} \tag{4}$$

Define the variable U_{fd}/C^{**} as the modified velocity profile (U_{fdm}) then the above equation becomes

$$\frac{\partial^2 U_{\mathrm{fdm}}}{\partial\xi^2}+\frac{\partial^2 U_{\mathrm{fdm}}}{\partial\eta^2}=\frac{-C^*}{(\cosh\eta-\cos\xi)^2} \tag{5}$$

---

[1] On leave from Ain Shams University, Cairo, Egypt.

Contributed by the Heat Transfer Division for publication in the JOURNAL OF HEAT TRANSFER. Manuscript received by the Heat Transfer Division January 16, 2003; revision received January 21, 2004. Associate Editor: B. Farouk.

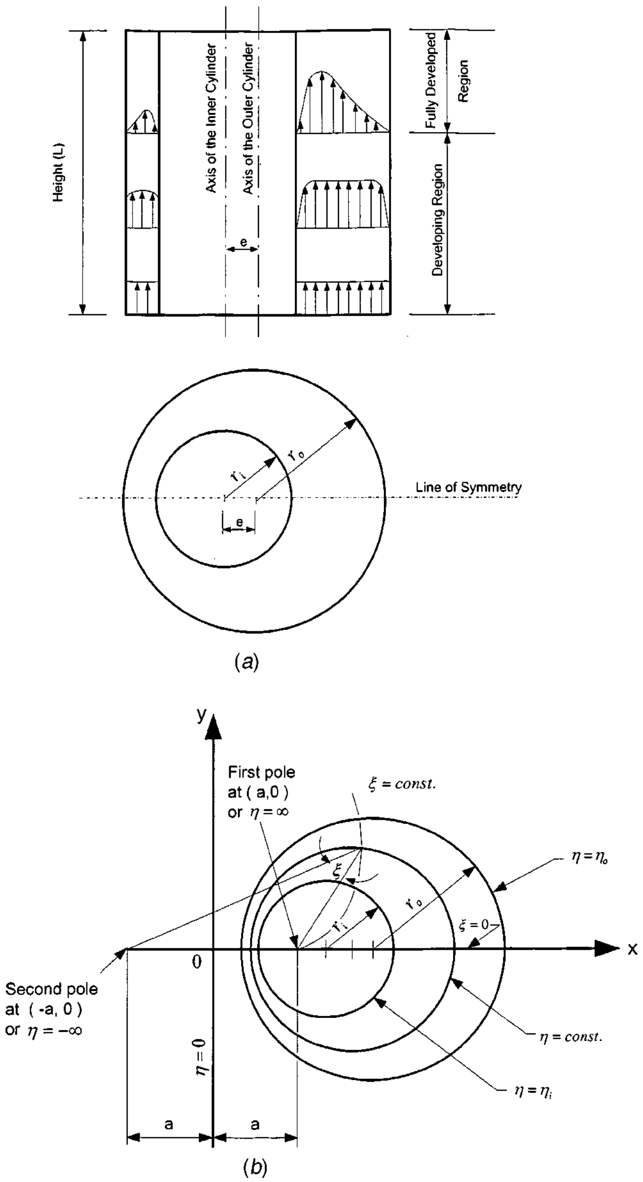

(*a*)

(*b*)

Fig. 1 (*a*) Two-dimensional elevation and plan for the geometry under consideration; and (*b*) Bipolar coordinate system

This equation is identical to the steady-state heat conduction equation with internal heat generation solved by El-Saden [13] and it has the following solution

$$U_{\rm fdm}=A\eta+B-\frac{C^*}{2}\coth\eta+\sum_{n=1}^{\infty}\cos\eta\xi[Ce^{n\eta}+(D-C^*\coth\eta)e^{-n\eta}] \qquad (6)$$

Applying the nonslip boundary conditions at the walls, the constants of integration *A*, *B*, *C*, and *D* are obtained as given hereinafter

$$A=C^*(\coth\eta_i-\coth\eta_o)/[2(\eta_i-\eta_o)] \qquad (7)$$

$$B=C^*(\eta_i\coth\eta_o-\eta_o\coth\eta_i)/[2(\eta_i-\eta_o)] \qquad (8)$$

$$C=C^*(\coth\eta_i-\coth\eta_o)/(e^{2n\eta_i}-e^{2n\eta_o}) \qquad (9)$$

$$D=C^*(e^{2n\eta_i}\coth\eta_o-e^{2n\eta_o}\coth\eta_i)/(e^{2n\eta_i}-e^{2n\eta_o}) \qquad (10)$$

As the constants C^*, *A*, *B*, *C*, and *D* are independent of the value of Gr/Re, the above solution (6) shows, accordingly, that the modified dimensionless velocity profile ($U_{\rm fdm}$) is independent of Gr/Re. Thus, $U_{\rm fdm}$ is the same for both the forced convection (Gr/Re=0) and the mixed convection (Gr/Re≠0). Now, since $U_{fd}=U_{\rm fdm}C^{**}$, then taking the average for both sides gives

$$\overline{U_{fd}}=\overline{U_{\rm fdm}}C^{**} \qquad (11)$$

and since the dimensionless average axial velocity $\overline{U_{fd}}=1$, hence,

$$C^{**}=\frac{1}{\overline{U_{\rm fdm}}} \qquad (12)$$

As the solution (6) proves that $\overline{U_{\rm fdm}}$ is independent of the value of Gr/Re, then Eq. (12) means that C^{**} is also independent of Gr/Re, i.e., it is constant. Hence, C^{**} for mixed convection (Gr/Re ≠0) has the same value as that for forced convection (Gr/Re =0).

3.2 Critical Values of Gr/Re.

As per the definition of C^{**},

$$C^{**}=-\{(dP/dZ)_{fd}-\mathrm{Gr/Re}\} \qquad (13)$$

Notice that for the case of pure forced convection Gr/Re=0, $C^{**}=-(dP/dZ)_{fd,\rm forced}$. Since C^{**} is a constant that is independent of the value of Gr/Re, consequently, it has the same value for both forced and mixed convection flows. Thus, one can rewrite (13) as

$$(dP/dZ)_{fd,\rm mixed}=(dP/dZ)_{fd,\rm forced}+\mathrm{Gr/Re}. \qquad (14)$$

In this equation $(dP/dZ)_{fd,\rm forced}$ is always negative. Hence, in fully developed mixed-convection flows, the pressure gradient $(dP/dZ)_{fd,\rm mixed}$ can have a value of zero or positive values if the free convection is aiding the forced flow. When $(dP/dZ)_{fd,\rm mixed}$ equals zero the buoyancy forces offset the viscous forces and the fluid flows in the vertical channel with a constant value of pressure. On the other hand, when $(dP/dZ)_{fd,\rm mixed}$ is >0, the vertical channel acts as a diffuser; the pressure increases in the vertical flow direction. The value of Gr/Re at which the buoyancy force offsets the pressure drop due to friction (i.e., at which $(dP/dZ)_{fd,\rm mixed}=0$) will be named the critical value of Gr/Re or $(\mathrm{Gr/Re})_{cr}$. This critical value can be found by equating $(dP/dZ)_{fd,\rm mixed}$ to zero, i.e.,

$$(\mathrm{Gr/Re})_{cr}=-(dP/dZ)_{fd,\rm forced}=C^{**} \qquad (15)$$

Values of $(dP/dZ)_{fd,\rm forced}$ in eccentric annuli are already available in the literature [5,6,10,14,16,17].

4 Results and Discussion

A FORTRAN computer program has been written to compute the values of the fully developed laminar mixed convection modified dimensionless velocity profile of a fluid of Pr<1 in vertical eccentric annuli from the analytical series solution given by Eq. (6). Then the average of this modified velocity profile has been computed and the reciprocal of this average velocity gives the value of the constant C^{**}, as per equation (12). Values of C^{**} (i.e., $(dP/dZ)_{fd,\rm forced}$, which equals $(\mathrm{Gr/Re})_{cr}$) have been computed over wide ranges of the governing geometrical parameters, namely, the dimensionless eccentricity ($E=0.1-0.9$) and the annulus radius ratio ($N=0.1-0.9$). The obtained results are given in Table 1. This table shows that for small values of the eccentricity *E*, in the range $E=0.1-0.3$, the critical values $(\mathrm{Gr/Re})_{cr}$ increases with the radius ratio. However, for the larger range of eccentricity ($E=0.4-0.9$), these values decrease with the radius ratio.

This table is of practical importance to the designers of heat transfer equipment. The values of $(\mathrm{Gr/Re})_{cr}$ presented in this table provide the designers with information that can be used to set the thermal boundary conditions for a specific eccentric vertical annulus (of given eccentricity and radius ratio) to achieve the buoyancy effect that counterbalances the pressure drop due to friction and thus reduces the pumping power through the annulus. Moreover, the designer can set the thermal boundary conditions (T_w

Table 1 Critical values of Gr/Re for mixed convection in vertical eccentric annuli for different values of dimensionless eccentricity and radius ratio along with validation of present results and comparisons with other works for $(dP/dZ)_{fd,\mathrm{forced}}$

Radius Ratio ▼	Eccentricity ▶	0.1	0.2	0.3	0.4	0.5	0.6	0.7	0.8	0.9
		$(\mathrm{Gr/Re})_{\mathrm{cr}}$								
0.1	Present	44.64	43.52	41.81	39.73	37.50	35.30	33.31	31.69	30.65
	Tiedt	44.28	43.12	41.36	39.20	36.85	34.49	32.26	30.26	28.56
	Others					36.71*			$30.26^{\times}$	28.17*
0.2	Present	45.88	44.42	42.22	39.56	36.71	33.87	31.22	28.84	26.79
	Tiedt	45.66	44.19	41.97	39.28	36.39	33.52	30.81	28.36	26.21
	Others								$28.36^{\times}$	
0.3	Present	46.49	44.83	42.34	39.34	36.14	32.97	29.99	27.29	24.90
	Tiedt	46.34	44.67	42.17	39.16	35.95	32.77	29.77	27.06	24.65
	Others							29.72*		
0.4	Present	46.85	45.05	42.37	39.16	35.73	32.34	29.17	26.28	23.72
	Tiedt	46.72	44.93	42.25	39.03	35.60	32.21	29.03	26.15	23.58
0.5	Present	47.14	45.24	42.44	39.07	35.49	31.96	28.60	25.60	22.93
	Tiedt	46.96	45.08	42.28	38.92	35.34	31.82	28.51	25.51	22.84
	Others		44.93^{+}			35.33* 35.39**	31.75^{+}			22.82*
0.6	Present	47.20	45.26	42.37	38.91	35.24	31.61	28.22	25.14	22.40
	Tiedt	47.11	45.17	42.29	38.83	35.16	31.54	28.15	25.07	22.34
0.7	Present	47.29	45.31	42.37	38.84	35.10	31.42	27.97	24.84	22.06
	Tiedt	47.20	45.23	42.29	38.77	35.04	31.36	27.91	24.78	22.01
0.8	Present	47.35	45.34	42.36	38.80	35.02	31.30	27.81	24.65	21.85
	Tiedt	47.25	45.26	42.29	38.73	34.96	31.24	27.76	24.61	21.81
0.9	Present	47.35	45.35	42.36	38.77	34.98	31.24	27.73	24.56	21.74
	Tiedt	47.82	45.28	42.29	38.72	34.92	31.19	27.69	24.52	21.70

*Feldman et al. [16].

**Sathymurthy et al. [10].

$^{\times}$Trombeta [6].

$^{+}$Dipanker Choudhury and Kailash Karki [17].

$-T_o$) and/or the geometric parameters (N and E) such that she/he obtains values of $\mathrm{Gr/Re} > (\mathrm{Gr/Re})_{cr}$. Consequently, the eccentric annulus of constant cross-section flow area would act in this case as a diffuser that builds up the pressure along the channel height by means of the aiding free convection effects.

To validate the obtained results, comparisons with the available values in the literature for $(dP/dZ)_{fd,\mathrm{forced}}$ have been made. Table 1 also presents these comparisons, taking into consideration that the present definition of $(dP/dZ)_{fd,\mathrm{forced}}$ corresponds to double the values of f Re of Tiedt [5]. As can be seen from this table, a maximum difference of 7.31% occurs at the lowest radius ratio ($N=0.1$) with the highest eccentricity ($E=0.9$). For radius ratios $\geqslant 0.2$, the maximum deviation is 2.2%. Moreover, for the typical practical range of radius ratio around 0.5 ($N=0.4$–0.6), the maximum deviation is 0.58%.

The above-tabulated results have been further processed using a standard regression technique [15] to reach at an equation that correlates the critical values of Gr/Re with the geometric parameters of the eccentric annulus (namely, the radius ratio N and the dimensionless eccentricity E). The following equation has been obtained:

$$(\mathrm{Gr/Re})_{cr} = b_o + b_1 N + b_2 E + b_3 N^2 + b_4 E^2 + b_5 NE + b_6 \mathrm{Ln}(N) + b_7 \mathrm{Ln}(E) + b_8 N \mathrm{Ln}(E) + b_9 E \mathrm{Ln}(N)$$

where the values of the ten constants are

b_o	71.6438	b_4	16.9926	b_8	1.1425
b_1	−4.0220	b_5	8.2770	b_9	−10.8790
b_2	−75.3630	b_6	4.0868		
b_3	1.2168	b_7	5.4223		

This correlation has a coefficient of multiple determination, $R^2 = 0.9997$ with a maximum deviation between the tabulated values and that calculated using the correlation of 1.5163%.

Conclusions

An analytical expression for the fully developed velocity profile of laminar mixed convection has been derived for a fluid of $\mathrm{Pr} < 1$ in a vertical eccentric annulus under thermal boundary conditions of having one wall isothermal while the other wall is thermally insulated. This analytical expression has been utilized, over wide ranges of the governing geometrical parameters (namely the dimensionless eccentricity ($E=0.1$–0.9) and the annulus radius ratio ($N=0.1$–0.9)), to obtain the critical values of Gr/Re that would make the free convection effects offset the friction inside a vertical eccentric annulus. Moreover, an equation that correlates the critical values of Gr/Re with the geometric parameters of the eccentric annulus (namely, the radius ratio N and the dimensionless eccentricity E) has been obtained.

Acknowledgment

The authors gratefully acknowledge the support of King Fahd University of Petroleum and Minerals to carry out this investigation as a part of projects FT-20-2000 and FT 2002/10.

Nomenclature

a = location of the positive pole of the bipolar coordinate system on the x-axis, equal $r \sinh \eta_i$ or $r_o \sinh \eta_o$

β = thermal expansion coefficient

c_p = specific heat of fluid at constant pressure

D_h = equivalent (hydraulic) diameter of annulus, $2(r_o - r_i) = 2a(1-N)\mathrm{csch}\, \eta_o$

e = eccentricity (distance between the two centers of the two cylinders forming the eccentric annulus), $a(\coth \eta_o - \coth \eta_i)$

E = dimensionless eccentricity (dimensionless center-to-center distance), $e/(r_o - r_i) = \sinh(\eta_i - \eta_o)/(\sinh \eta_i - \sinh \eta_o)$

F_z = body force in the axial (vertical) direction per unit volume, $-\rho g$

g = gravitational body force per unit mass (acceleration)
Gr = Grashof number, $g\beta(T_w-T_o)D_h^3/\gamma^2$
h = coordinate transformation scale factor, $a(\cosh\eta-\cos\xi)$
H = dimensionless coordinate transformation factor, $h/D_h=0.5\sinh(\eta_o)/(1-N)(\cosh(\eta)-\cos(\xi))$
k = thermal conductivity of fluid
n = infinite-series summation parameter in analytical solution
N = annulus radius ratio, $\mathrm{r_i}/\mathrm{r_o}=\sinh\eta_\mathrm{o}/\sinh\eta_\mathrm{i}$
p = pressure of fluid inside the channel at any cross-section
p' = difference between the pressure of the fluid inside the channel at any cross-section and the corresponding hydrostatic pressure, $\mathrm{p}-\rho_\mathrm{o}\mathrm{gz}$
p_o = pressure of fluid at annulus entrance
P = dimensionless pressure defect at any point, $(p'-p_o)/(\rho_o\overline{u}^2)$
Pr = Prandtl number, $\mu\mathrm{c_p}/\mathrm{k}$
r_i = inner radius of annulus
r_o = outer radius of annulus
Re = Reynolds number, $\overline{u}D_h/\gamma$
T = temperature at any point
u = axial (streamwise) velocity component at any point
u_o = entrance axial velocity, $\overline{u}$
$\overline{u}$ = average axial velocity over the annulus cross section at any vertical location
U = dimensionless axial velocity at any point, $u/\overline{u}$
$\overline{U}$ = dimensionless average axial velocity, 1
v = velocity component in η-direction
y = the second transverse direction in the Cartesian coordinate system
w = velocity component in ξ-direction
z = axial coordinate in both the Cartesian and bipolar coordinate systems
Z = dimensionless axial coordinate, $z/(D_h\,\mathrm{Re})$

Greek Letters

β = volumetric coefficient of thermal expansion
η = the first transverse bipolar coordinate
η_i = value of η on the inner surface of the annulus, $\eta_i=\cosh^{-1}((N(1+E^2)+(1-E^2))/2\,NE)$
η_o = value of η on the outer surface of the annulus, $\eta_o=\cosh^{-1}((N(1-E^2)+(1+-E^2))/2\,E)$
θ = dimensionless temperature, $(T-T_o)/(T_w-T_o)$
μ = dynamic viscosity of fluid
γ = kinematic viscosity of fluid, μ/ρ
ξ = the second transverse bipolar coordinate
ρ_o = fluid density at ambient (entrance) temperature

References

[1] Yonggang, Z., and Junfang, H., 1995, "Study of the Displacement Mechanics for Non-Newtonian Fluid and its Application in Well Cementing Techniques," J. Hydrodynam., **7**(3), pp. 107–110.
[2] El-Shaarawi, M. A. I., and Sarhan, A., 1981, "Developing Laminar Free Convection in an Open Ended Vertical Annulus with a Rotating Inner Cylinder," ASME J. Heat Transfer, **103**, pp. 552–558.
[3] Snyder, W. T., and Goldstein, G. A., 1965, "An Analysis of a Fully Developed Laminar Flow in an Eccentric Annulus," AIChE J., **11**(3), pp. 462–469.
[4] Cheng, K. C., and Hwang, G. J., 1968, "Laminar Forced Convection in Eccentric Annuli," AIChE J., **14**(3), pp. 510–512.
[5] Tiedt, W., 1971, English translation-Transl. Bur. No. 0151, P. 248, Transp. Dev. Agency Libr., Montereal.
[6] Trombeta, M. L., 1972, "Laminar Forced Convection in Eccentric Annuli," Int. J. Heat Mass Transfer, **14**, pp. 1161–1172.
[7] Guckes, T. L., 1975, "Laminar Flow of Non-Newtonian Fluids in an Eccentric Annulus," ASME J. Eng. Ind., **97**, pp. 498–506.
[8] Özgen, C., and Tuson, I., 1987, "Application of Geometric Inversion to the Eccentric Annulus System," AIChE J., **33**(11), pp. 1903–1907.
[9] Suzuki, K., Szmyd, J. S., and Ohtsuka, H., 1990, "Laminar Forced Convection Heat Transfer in Eccentric Annuli," Heat Transfer-Jpn. Res., **20**, pp. 169–183.
[10] Sathymurthy, P., Karki, K. C., and Patankar, S. V., 1992, "Laminar Fully Developed Mixed Convection in a Vertical Eccentric Annulus," Numer. Heat Transfer, Part A, **22**, pp. 71–85.
[11] Hughes, W. F., and Gaylord, E. W., 1964, *Basic Equations of Engineering Science*, Schaum Outline Ser., McGraw Hill, pp. 12–13.
[12] Incropera, F. P., and Dewitt, D. P., 1996, *Introduction of Heat Transfer*, 3rd ed, Wiley, p. 451.
[13] El-Saden, M. R., 1961, "Heat Conduction in an Eccentrically Hollow, Infinitely Long Cylinder With Internal Heat Generation," ASME J. Heat Transfer, **83**(4), pp. 510–511.
[14] El-Shaarawi, M. A. I., Abualhamayel, H. I., and Mokheimer, E. M. A., 1997, "Laminar Flow in Eccentric Annuli," ASME J. Fluids Eng., **119**, pp. 724–728.
[15] Montgomery, D. C., 1997, *Design and Analysis of Experiments*, Wiley.
[16] Feldman, E. F., Hornbeck, R. W., and Osterle, J. F., 1982, "A Numerical Solution of Laminar Developing Flow in Eccentric Annular Ducts," Int. J. Heat Mass Transfer, **25**(2), pp. 231–241.
[17] Choudhury, D., and Karki, K., 1992, "Laminar Mixed Convection in a Horizontal Eccentric Annulus," Numer. Heat Transfer, Part A, **22**, pp. 87–108.

Critical Heat Flux of Multi-Nozzle Spray Cooling

Lanchao Lin
Universal Energy Systems, Inc.,
4401 Dayton-Xenia Road Dayton, OH 45432-1894

Rengasamy Ponnappan
Propulsion Directorate,
Air Force Research Laboratory,
Wright-Patterson AFB, OH 45433-7251

Tiny nozzles are developed that are capable of creating the swirling flow necessary to generate a full cone spray. Eight miniature nozzles are embedded in a multi-nozzle plate used to generate a spray array for the cooling of high heat flux laser diodes. The target spray cooling area is a 1×2 cm^2 flat surface of a copper heater plate. A closed loop spray cooling test setup is established. FC-87, FC-72 and methanol are used as the working fluids. Critical heat flux (CHF) is experimentally investigated at various spray saturation temperatures and nozzle pressure drops (from 0.690 bar to 3.10 bar). It is demonstrated that the spray cooler can reach the CHF levels up to 91.5 W/cm^2 with FC-87 and 490 W/cm^2 with methanol. [DOI: 10.1115/1.1738418]

Keywords: Boiling, Cooling, Heat Transfer, Sprays, Two-Phase, Vaporization

Introduction

Evaporative spray cooling has been exhibited to be an effective method of removing high heat fluxes from surfaces with low superheat. For water as the working fluid, a spray cooling heat flux of 1000 W/cm^2 was reached [1]. The heat flux enhancement due to spray cooling is attributed to the dynamic behavior of the droplets impinging on the hot surface and interacting with the bubbles and the thin liquid film.

Recent applications of spray cooling involved the cooling of different kinds of electronics. In this application, a major portion of heat transfer results from nucleate boiling heat transfer. Other emerging applications include the cooling of high heat flux laser diodes, x-ray medical devices, avionics and so on. The heat transfer mechanism of spray cooling deals with three phenomena, namely nucleate boiling due to both surface and secondary nucleation, convection heat transfer and direct evaporation from the surface of the liquid film [2]. The concept of secondary nucleation is helpful for understanding the heat transfer enhancement of spray cooling. It has been concluded that increasing the droplet

---

Contributed by the Heat Transfer Division for publication in the JOURNAL OF HEAT TRANSFER. Manuscript received by the Heat Transfer Division December 11, 2002; revision received October 17, 2003. Associate Editor: D. B. R. Kenning.

flux increases the number of secondary nuclei, increases heat transfer of nucleate boiling and convection, and helps to lower surface temperature for a given heat flux [2]. Several experiments were performed to understand nucleate boiling heat transfer and critical heat flux (CHF) for full cone sprays using single nozzles [1–6]. The effects of spray nozzle, volumetric flux, Sauter mean diameter of spray, subcooling and working fluid were investigated. Estes and Mudawar [3] presented a CHF correlation with suitable dimensionless parameters that accurately predicted data for FC-72, FC-87, and water. The correlation by Estes and Mudawar had a strong dependence of CHF on volumetric flux and Sauter mean diameter. Sehmbey et al. [4] developed a semiempirical correlation for CHF that was based on a macrolayer dryout model and correlated with data for water and LN2.

Lin and Ponnappan reported the multi-nozzle spray cooling in a closed system with and without air involved and discussed the effect of air on the thermal performance of the spray cooling [7]. The closed loop multi-nozzle spray cooling system was developed for the cooling of high power laser diode arrays. The spray cooling occurred in the confined and closed system [7]. Existing CHF data were applicable mainly for free spray cooling of small surfaces using a single nozzle at relatively higher pressure drops across the spray nozzle [3–5], most of the applied pressure drops being greater than 2.0 bar. In this paper, CHF is experimentally investigated under the spray pressure drops ranging from 0.69 bar to 3.1 bar.

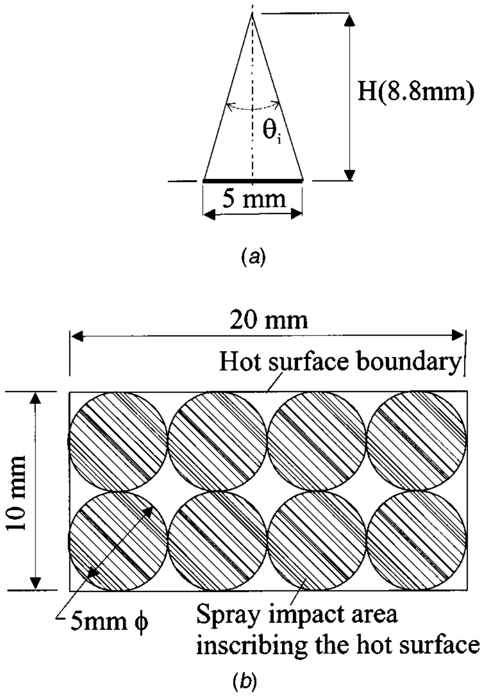

Fig. 1 Spray array: (*a*) individual spray cone; and (*b*) inscription area of spray

Test Setup and Procedure

A miniature nozzle array is designed to generate the full cone sprays that impinge on a hot surface with an area of 1×2 cm^2. Eight miniature nozzles are made in a multi-nozzle plate [7]. The distance between two nozzles is 5.0 mm. The nozzle discharge orifice diameter is 0.25 mm. As the pressurized liquid passes through the nozzle, a swirling liquid jet is generated at the discharge orifice and this intensifies liquid breakup into the fine droplets forming a full cone spray. Multi-nozzle spray performance tests in the atmospheric environment are conducted with FC-72, FC-87 and methanol as the working fluid. It is observed that at the pressure drop of 1.72 bar, sufficiently fine droplets have developed at a spray distance greater than 6.0 mm (measured from the nozzle exit). Figure 1 describes a spray array pattern that just inscribes a rectangular cooling surface. The spray pressure drop is around 1.72 bar for the fluorocarbon fluids and 2.41 bar for methanol in order for the spray array to inscribe the target area at a spray distance of 8.8 mm. The higher the pressure drop, the greater is the spray cone angle and the shorter is the spray distance necessitated for developing the sufficiently fine droplets.

The schematic of test setup for the thermal performance test is shown in Fig. 2. The system consists of the multi-nozzle plate, a heater assembly, a liquid chamber, a spray chamber, a helical coil condenser, flow channels (for two-phase flow and liquid flow), a magnetic gear pump, a preheater, a bypass loop, and a filter. A cold bath is used to supply cooling water to and from the condenser. The spray chamber is sealed to the copper heater plate which is on the top of the heater block (heat focusing block). The hot surface of the heater plate is polished with 14 μm grit SiC paper before testing. The distance between the nozzle exit and the hot surface is 8.8 mm which is sufficiently high for breaking up the liquid into fine droplets. The spray chamber space dimensions are 8.8 mm (high), 28.5 mm (long), and 17.0 mm (wide). For visualization experiments, the frame of the spray chamber is replaced with a transparent one (acrylic material) with the same dimensions as the metallic frame used for the thermal performance test. Working fluids include FC-87, FC-72, and methanol. The system of the closed loop is evacuated to a pressure below 5×10^{-6} Torr before filling with the working fluid. The liquid fill amount is 190 ml which is about 38 percent of the internal volume of the loop. The pressure difference generated by the micro-pump maintains the circulation flow. The multiple sprays interfere with adjacent ones in the near surface region. The pressurized liquid is fed to a plenum chamber before ejecting through the nozzles. In the spray chamber, the slightly subcooled droplets impinge onto the hot surface. A large part of the droplets turn into a thin film on the hot surface and a small part of them vaporize, removing the heat through phase change. The vapor flows along with the liquid out of the spray chamber into the two-phase channel which guides the two-phase flow to the condenser where it condenses. The subcooled liquid from the condenser is pumped back to the liquid chamber. The spray cooling capability is limited by CHF from the hot surface.

The liquid flow rate of the spray cooling system is measured using a turbine flow meter. The spray chamber pressure (p_3), the pressure at the inlet of the liquid chamber (p_2) and the pressure at the outlet of the condenser (p_1) are measured using three pressure

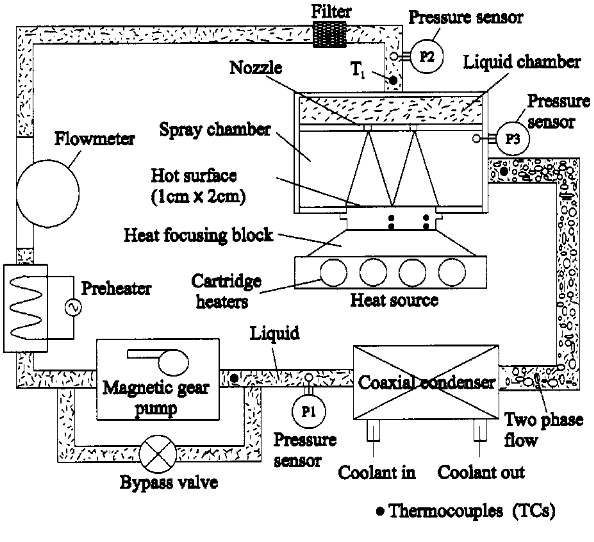

Fig. 2 Schematic of experimental setup

sensors. The spray chamber pressure corresponds to the fluid saturation temperature, T_{sat}, in the spray chamber. The spray pressure drop, $\Delta p = p_2 - p_3$, is controlled by the pump and bypass valve. The rotational speed of the magnetic pump is adjustable through a variable DC power supply. The working fluid temperatures in the spray cooling loop are measured using T-type probe thermocouples. The supply liquid temperature (at the inlet of liquid chamber), T_1, is regulated by adjusting the cold bath temperature and input power to the preheater. It is desired that T_1 is set to be as close to T_{sat} as possible to minimize the subcooling effect.

A copper heater block with four cartridge heaters inserted is used as the heat source. Eight thermocouples are embedded in 0.58 mm holes drilled along two planes in the heater plate, forming four pairs of thermocouples. Four thermocouple locations in the front of the heater plate are shown in Fig. 2. The distance between two thermocouple location planes, t_2, is 2.54 mm. The distance between the hot surface and the upper plane of the thermocouple locations, t_1, is 2.16 mm. The thermocouple bead diameter is 0.3 mm. The heater plate with the hot surface towards the spray chamber is embraced by an insulation plate made of silicone and glass and is tightly attached to the heater block by a compression assembly. Thermal grease is used to minimize the contact thermal resistance between the heater plate and heater block. The heater assembly is well insulated with fiberfrax. The hot surface heat flux or the heat rate per unit hot surface area is calculated by

$$q'' = \frac{c_w k_h}{t_2}(T_{2,m} - T_{1,m}), \tag{1}$$

where $T_{1,m}$ and $T_{2,m}$ are the arithmetic means of the temperatures indicated by the four thermocouples at the upper plane and those at the lower plane, k_h is the thermal conductivity of heater plate, and the constant c_w is obtained through calibration. The average temperature on the hot surface, T_w, is extrapolated in terms of $T_{1,m}$ and q'' [7]. AC power is applied to the cartridge heaters. The input power is monitored by a power analyzer.

All signals of the measured parameters are transferred to a PC for recording. During the test, the input power is varied up to the amount relating with CHF. The spray pressure drop is adjusted at the levels of 0.69 bar, 1.03 bar, 1.72 bar, 2.41 bar, and 3.1 bar. The spray chamber pressure is changed according to the working fluid being used. All data are acquired 50 times in an interval of 1 minute and the average values are recorded after a steady state is reached. The measurement uncertainties for the relevant test parameters have been analyzed [7].

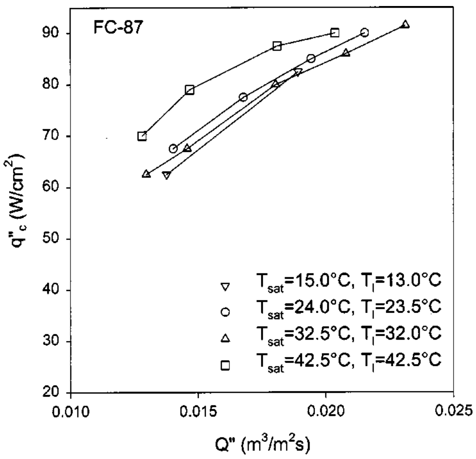

Fig. 3 CHF versus Q″ at different saturation temperature levels for FC-87

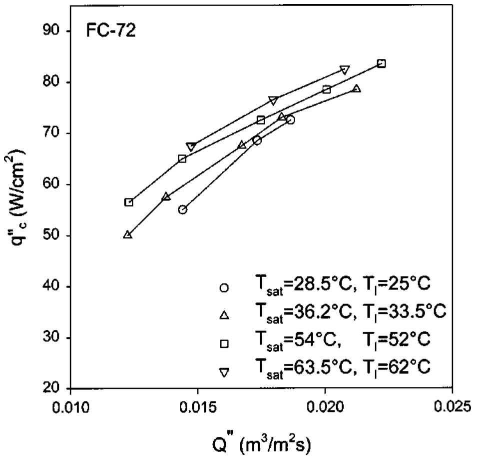

Fig. 4 CHF versus Q″ at different saturation temperature levels for FC-72

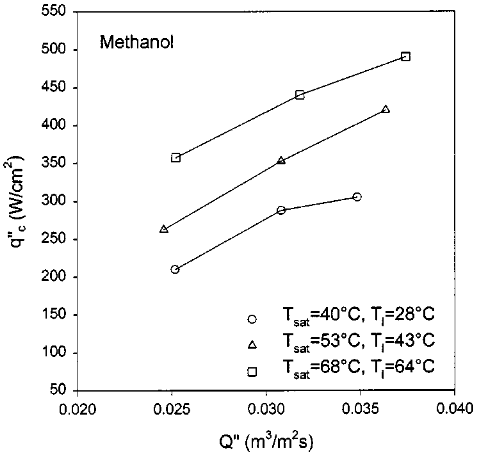

Fig. 5 CHF versus *Q″* at different saturation temperature levels for methanol

Results and Discussion

It is observed in the visualization experiment that nucleate boiling heat transfer occurs in all tested cases. The spray cones are surrounded by the agitated two-phase fluid. The droplets impinge onto the hot surface and splash to the circumference of the spray. The splashing liquid is restricted by the wall and is forced to rebound to the space surrounding the sprays. The interaction between the spray cone and surrounding fluid is stronger in the case of multi-nozzle spray cooling than in the case of single nozzle spray cooling and this could lower CHF.

Experimental data of CHF, q_c'', for FC-87, FC-72, and methanol are plotted in Figs. 3–5, as functions of volumetric flow rate per unit cooling area, Q''. Also presented in these figures are the different saturation temperatures, T_{sat}, in the spray chamber and the supply liquid temperatures, T_1. For FC-87 and FC-72, the values of subcooling, $T_{\text{sat}} - T_1$, are very small (less than 3.5°C). For methanol, the subcooling is relatively higher (between 4°C and 12°C) but still considered as being small since CHF for methanol is much higher. Generally, CHF increases with an increase of the volumetric flux and saturation temperature under the present condition. In these figures, the highest CHF value is 91.5 W/cm^2 for FC-87, 83.5 W/cm^2 for FC-72 and 490 W/cm^2 for methanol. The surface superheat, $T_w - T_{\text{sat}}$, at the heat flux close

Table 1 Spray parameters

Working Fluid	T_{sat} (°C)	Δp (bar)	Q'' (m^3/m^2s)	d_{32} (μm)	η_c (−)
FC-87	42.5	0.69	0.0128	50.0	0.378
		1.03	0.0147	45.3	0.374
		1.72	0.0181	39.6	0.336
		2.41	0.0204	36.5	0.306
FC-72	54	0.69	0.0123	57.8	0.330
		1.03	0.0144	52.1	0.324
		1.72	0.0175	45.2	0.300
		2.41	0.0201	41.4	0.282
		3.10	0.0222	38.7	0.271
Methanol	53	1.03	0.0246	79.6	0.122
		1.72	0.0308	68.6	0.131
		2.41	0.0363	62.3	0.133

to CHF ranges approximately from 42°C to 50°C for FC-87, from 37°C to 40°C for FC-72 and from 50°C to 60°C for methanol. For each fluorocarbon fluid, CHF values at various T_{sat} levels tend to merge with each other as Q'' increases.

To obtain more spray cooling information, the effectiveness of spray cooling at CHF, $\eta_c(q_c''/h_{fg}Q''\rho_1$ where h_{fg} and ρ_1 are the latent heat of vaporization and liquid density), and Sauter mean diameter (SMD), d_{32}, are calculated. The present values of SMD are estimated using the correlation of Estes and Mudawar [4]. The values of η_c and d_{32} as well as other three parameters are listed in Table 1. It is shown that η_c is much smaller and d_{32} is greater for methanol than for FC-87 and FC-72 at the same Δp. Increasing Δp decreases d_{32}.

Conclusions

A closed loop spray cooling test setup employing the multi-nozzle array is established that can be operated for a pure working fluid test without air in the system. CHF of the spray cooling is experimentally investigated. Dryout occurs if the droplets are unable to touch the surface. CHF of methanol is much higher than that of the fluorocarbon fluids. CHF increases with an increase of the volumetric flux or pressure drop.

Acknowledgment

This research was supported by the Propulsion Directorate of the Air Force Research Laboratory (AFRL), Wright-Patterson Air Force Base, Ohio, and performed at the Power Division's Thermal Laboratory. The authors would like to thank Richard J. Harris, University of Dayton Research Institute, for his efforts in making the nozzle array and establishing the data acquisition system and John E. Tennant and Roger P. Carr (UES, Inc.) for their support in building the spray cooling system.

References

[1] Yang, J., Chow, L. C., and Pais, M. R., 1996, ''Nucleate Boiling Heat Transfer in Spray Cooling,'' ASME J. Heat Transfer, **118**, pp. 668–671.

[2] Rini, D. P., Chen, R. H., and Chow, L. C., 2002, ''Bubble Behavior and Nucleate Boiling Heat Transfer in Saturated FC-72 Spray Cooling,'' ASME J. Heat Transfer, **124**, pp. 63–72.

[3] Estes, K. A., and Mudawar, I., 1995, ''Correlations of Sauter Mean Diameter and Critical Heat Flux for Spray Cooling of Small Surfaces,'' Int. J. Heat Mass Transfer, **38**(16), pp. 2985–2996.

[4] Sehmbey, M. S., Chow, L. C., Hahn, O. J., and Pais, M. R., 1995, ''Effect of Spray Characteristics on Spray Cooling With Liquid Nitrogen,'' J. Thermophys. Heat Transfer, **9**(4), pp. 757–765.

[5] Mudawar, I., and Estes, K. A., 1996, ''Optimizing and Predicting CHF in Spray Cooling of a Square Surface,'' ASME J. Heat Transfer, **118**, pp. 672–679.

[6] Mudawar, I., and Valentine, W. S., 1989, ''Determination of the Local Quench Curve for Spray-Cooled Metallic Surfaces,'' J. Heat Treating, **7**(2), pp. 107–121.

[7] Lin, L., and Ponnappan, R., 2003, ''Heat Transfer Characteristics of Spray Cooling in a Closed Loop,'' Int. J. Heat Mass Transfer, **46**(20), pp. 3737–3746.

Analysis of Madejski Splat-Quench Solidification Model With Modified Initial Conditions

D. Sivakumar
e-mail: siva@paris.ifs.tohoku.ac.jp
Research Fellow Electromagnetic Intelligent Fluids Laboratory, Institute of Fluid Science, Tohoku University, 2-1-1 Katahira, Aoba-ku, Sendai 980-8577, Japan

H. Nishiyama
e-mail: nishiyama@ifs.tohoku.ac.jp
Professor Electromagnetic Intelligent Fluids Laboratory, Institute of Fluid Science, Tohoku University, 2-1-1 Katahira, Aoba-ku, Sendai 980-8577, Japan

The initial conditions of Madejski's splat-quench solidification model for the impact of molten droplets on a solid substrate surface are modified by eliminating the adjustable parameter "ε" used in the estimation of initial spreading droplet radius. In the present model, the initial conditions are estimated after a definite time interval from the start of impact. Numerical predictions obtained from an improved Madejski model with different ε and the corresponding experimental measurements published in the literature are used for the comparison of the present model predictions. The improvements noted from the model predictions are reported.
[DOI: 10.1115/1.1738421]

Keywords: Droplet, Solidification, Impingement

Introduction

Metallic surface coatings produced by thermal spraying process are shown to be efficient and cost effective for several technological applications [1]. Several experimental and theoretical investigations have been carried out under this topic to elucidate the physical processes involved in the droplet impact process, and also to enhance the coating quality [1,2]. The quality of coating depends on two major mechanisms: the spreading behavior of the impinging molten metallic droplets, and the solidification process of the spreading molten liquid layer. The fluid dynamic processes associated with the impact of liquid droplets on solid surfaces without solidification have been studied well in the literature [3–7]. For the impact of a molten metal droplet involving solidification, the coupling effects between fluid dynamics, heat transfer, and phase transition processes made the metal droplet impact process more challenging for the numerical modelers working in this topic [8–12]. Madejski [13] proposed a simple mathematical model to predict the diameter and thickness of splats formed during the impact of molten metal droplets. The author had assumed that the spherical droplet initially takes the shape of cylinder with radius, R_o, equivalent to a fraction of the impinging droplet diameter, D, i.e., $R_o = \varepsilon D$, just after the instant at which the droplet touches the impact surface and obtained numerical predictions by selecting an arbitrary value for ε as 0.5. Several researchers have modified the original model of Madejski by better predicting the viscous dissipation losses and wetting effects [14–18]. Note that the droplet impact model proposed by Madejski [13] has not considered the physical processes in detail for the flow analysis. These processes may include the effect of compressibility devel-

---

Contributed by the Heat Transfer Division for publication in the JOURNAL OF HEAT TRANSFER. Manuscript received by the Heat Transfer Division July 16, 2003; revision received November 20, 2003. Associate Editor: C. Amon.

oped during the impact of a high speed droplet [19–21], freezing of the contact line observed during the impact of molten metal droplets with low We [22], and the effect of thermal contact resistance [23].

In the present work, the improved model of droplet impact and solidification processes proposed by Delplanque and Rangel [15] has been modified by following a more realistic approach for the initial estimation of R_o. Until now, the theoretical studies [15–18] based on Madejski's approach [13] are developed with the assumption that $R_o = \varepsilon D$. Note that no specific details may be available in the literature to indicate the cylindrical disc shape assumed in Madejski model [13] just after the first instant of droplet impact. The value of ε is chosen arbitrarily in many of these investigations mainly by comparing the model predictions with the experimental results or advanced numerical simulations [16,17]. The main objective of this technical note is to eliminate the assumed parameter, ε employed in Madejski's approach [13]. With the present work, R_o can be estimated directly from the impinging droplet parameters like the droplet diameter, D and velocity, W. However, the modified model can be used for numerical predictions only after a definite initial time period, $t_o = D/W$ from the instant at which the droplet touches the surface.

Model Details

The model described in this study is based on the splat-quench solidification model proposed by Madejski [13] and its improved version proposed by Delplanque and Rangel [15]. Hereafter the model proposed by Delplanque and Rangel [15] is referred in this paper as DR model. The major modification considered in the present model lies in the initial conditions used to describe the droplet deformation and solidification processes. Consider a molten metal droplet of diameter, D impinges on a flat surface with velocity, W along the normal to the flat surface. The Weber number, We and Reynolds number, Re are defined, respectively, as $\mathrm{We} = \rho_l W^2 D/\sigma$ and $\mathrm{Re} = \rho_l W D/\mu$, where ρ_l is the density, μ, the viscosity, and σ, the surface tension of molten metal liquid. As mentioned in the previous section, earlier models based on Madejski's approach have assumed that the impinging droplet takes the shape of cylindrical disc as it touches the surface. However, under practical circumstances, this assumption may be justified only after a definite period of time, t_o from the start of impact. By assuming that the entire droplet liquid is moving with the velocity W during the initial stage of impact, t_o may be of the order D/W.

The solidification starts as the droplet touches the surface and the thickness of solidified layer, y is expressed as $y = U\sqrt{\alpha(t-\tau)}$ [13], where α is the thermal diffusivity of the solidified layer and τ, the time at which solidification begins at a given radial location, r (refer to Fig. 1). The solidification constant, U is a function of the Stefan number, St and expressed as

$$\mathrm{St} = \sqrt{\pi}\left(\frac{U}{2}\right)\mathrm{erf}\left(\frac{U}{2}\right)\exp\left(\frac{U^2}{4}\right), \tag{1}$$

where

$$\mathrm{St} = \frac{C_p(T_m - T_o)}{h_s}. \tag{2}$$

C_p and h_s are the specific heat and latent heat of the droplet material, respectively, T_m is the melting point of the droplet material, and T_o, the impact surface temperature. Note that the dependence of U with t [24] is not considered in Eq. (1), and, hence, U is assumed to be constant during the entire solidification process as in the classical Stefan problem. For $r < R_o$ and $\tau = 0$, the solidified layer thickness is expressed only as a function of time, $y_o = U\sqrt{\alpha t}$. The volume of solidified layer, V_s is estimated as

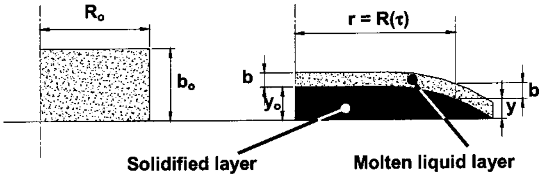

Fig. 1 Schematic sketch showing the parameters used in Madejski [13] model

$$V_s = \pi R_o^2 y_o + \int_{\tau=0}^{\tau=t} 2\pi R(\tau) y \, dR(\tau). \tag{3}$$

By using the principle of mass conservation, the thickness of liquid layer, b shown in Fig. 1 is expressed as

$$b = \frac{(\pi/6) D^3 \rho_l - \rho V_s}{\pi R^2 \rho_l}, \tag{4}$$

where ρ is the density of the solidified metal layer.

As shown by Madejski [13], the equation for the droplet deformation is derived from the conservation of mechanical energy expressed as

$$\frac{d}{dt}(E_k + E_p + E_d) = 0, \tag{5}$$

where E_k is the kinetic energy, E_p, the potential energy, and E_d, the viscous dissipation energy. In order to obtain negative integral rate of viscous energy over the spreading droplet, Markworth and Saunders [14] employed a higher order velocity field to describe the droplet deformation process. By following their work, Delplanque and Rangel [15] modified the inaccurate viscous dissipation, proposed earlier by Madejski [13], and expressed E_k and E_d as

$$E_k = \frac{3}{10}\pi\rho_l\left(\frac{dR}{dt}\right)^2\left(R^2 b + \frac{11}{7}b^3\right), \tag{6}$$

$$\frac{dE_d}{dt} = \frac{\pi\mu R^2}{b}\left(\frac{dR}{dt}\right)^2\left(\frac{3}{2} + \frac{72}{5}\frac{b^2}{R^2}\right). \tag{7}$$

The potential energy is expressed by including the effect of wetting as

$$E_p = \sigma\pi R^2(1 - \cos\theta) + \sigma 2\pi R b, \tag{8}$$

where θ is the contact angle made by the spreading droplet with the solid surface. By using Eqs. (6)–(8), Eq. (5) is modified as

$$\frac{d}{dt}\left[\frac{3}{10}\rho_l\left(\frac{dR}{dt}\right)^2\left(R^2 b + \frac{11}{7}b^3\right) + \sigma(R^2(1-\cos\theta) + 2Rb)\right] + \frac{\mu R^2}{b}\left(\frac{dR}{dt}\right)^2\left[\frac{3}{2} + \frac{72}{5}\frac{b^2}{R^2}\right] = 0. \tag{9}$$

Initial Conditions Used in DR Model. The initial conditions needed to solve Eq. (9) at $t_o = 0$ are expressed in DR model as

$$R(t_o) = R_o = \varepsilon D, \tag{10}$$

$$b(t_o) = b_o = \frac{D}{6\varepsilon^2}, \tag{11}$$

and

$$\frac{dR}{dt}(t_o)=\left(\frac{dR}{dt}\right)_o=W\left[\frac{\frac{5}{3}}{\left(1+\frac{11}{252\varepsilon^6}\right)}\right]^{1/2} \tag{12}$$

Modified Initial Conditions. Consider that the impinging droplet spreads out radially and attains a cylindrical disc of radius, R_0 at time, $t_o=D/W$ estimated from the instant at which the droplet touches the impact surface. An explicit relation to determine the thickness of liquid layer, b_o at $t_o=D/W$, proposed recently by Roisman et al. [7], from the impinging droplet parameters is expressed as

$$3We+5(1-\cos\theta)\mathrm{Re}\,\overline{b}_o=10\,\mathrm{Re}\,We\overline{b}_o^3, \tag{13}$$

where $\overline{b}_o$ is the thickness of liquid layer nondimensionalized with D. For a given impinging droplet, Eq. (13) provides the thickness of liquid layer, b_0 of the deformed droplet at $t_o=D/W$. The corresponding radius of droplet spread at $t_o=D/W$, R_0 is determined by using the mass conservation. Thus, the modified initial condition for R_o is expressed as

$$R(t_o)=R_o=\sqrt{\frac{D^3}{6b_o}}, \tag{14}$$

where $b_o=b(t_o)=\overline{b}_oD$. The expression for $(dR/dt)_o$ is obtained by comparing the kinetic energy of the spreading droplet liquid layer at the instant $t_o=D/W$ with the kinetic energy of the droplet before impact. The kinetic energy of spreading droplet at the instant $t_o=D/W$ is estimated by considering the energy losses as

$$E_{ko}=\Lambda(\overline{b}_o,\mathrm{Re},\mathrm{We},\theta)\left(\frac{\pi\rho_lD^3W^2}{12}\right), \tag{15}$$

where the factor Λ is expressed as [7]

$$\Lambda=1+\frac{12}{\mathrm{We}}-\frac{3}{5\,\mathrm{Re}}\left(\frac{1}{\overline{b}_o^3}+\frac{12}{\overline{b}_o}\right)-\frac{2(1-\cos\theta)}{\mathrm{We}\overline{b}_o}-\frac{\sqrt{96\overline{b}_o}}{\mathrm{We}}. \tag{16}$$

By comparing Eqs. (6) and (15), the initial condition for (dR/dt) is obtained as

$$\frac{dR}{dt}(t_o)=\left(\frac{dR}{dt}\right)_o=W\left[\frac{\frac{5}{3}\Lambda}{\left(1+\frac{66}{7}\overline{b}_o^3\right)}\right]^{1/2} \tag{17}$$

Nondimensionalization. The energy conservation equation and initial conditions are nondimensionalized by using the variables $\xi=R/R_o$, $\phi=b/R_o$, and $\tilde{t}=Wt/R_o$. After simplification, Eq. (9) becomes

$$\frac{d}{d\tilde{t}}\left[\frac{3}{10}\left(\frac{d\xi}{d\tilde{t}}\right)^2\phi\left(\xi^2+\frac{11}{7}\phi^2\right)+\frac{\sqrt{6b_o}}{\mathrm{We}}\xi(\xi(1-\cos\theta)+2\phi)\right]+\frac{\sqrt{b_o}}{\mathrm{Re}}\frac{\xi^2}{\phi}\left(\frac{d\xi}{d\tilde{t}}\right)^2\left(\sqrt{\frac{27}{2}}+\frac{72\sqrt{6}}{5}\frac{\phi^2}{\xi^2}\right)=0, \tag{18}$$

where

$$\phi=\frac{\sqrt{6}(\overline{b}_o)^{3/2}}{\xi^2}\left[1-K\left(\sqrt{\tilde{t}}+2\int_0^{\tilde{t}}\xi(t)\frac{d\xi(t)}{dt}\sqrt{(\tilde{t}-t)}dt\right)\right] \tag{19}$$

is obtained from Eqs. (3) and (4), and

$$K=\frac{\rho}{\rho_l}U\sqrt{\frac{1}{6^{1/2}\mathrm{Pe}(\overline{b}_o)^{5/2}}}. \tag{20}$$

Here K is the solidification parameter and Pe, the Peclet number defined by $\mathrm{Pe}=WD/\alpha$ with α as the thermal diffusivity of the droplet material. The nondimensionalized initial conditions are expressed as

$$\tilde{t}(t_o)=\tilde{t}_o=\sqrt{6\overline{b}_o}, \tag{21}$$

$$\xi(\tilde{t}_o)=1.0, \tag{22}$$

$$\phi(\tilde{t}_o)=\sqrt{6}(\overline{b}_o)^{3/2}, \tag{23}$$

and

$$\frac{d\xi}{d\tilde{t}}(\tilde{t}_o)=\left[\frac{\frac{5}{3}\Lambda}{\left(1+\frac{66}{7}\overline{b}_o^3\right)}\right]^{1/2}. \tag{24}$$

Results and Discussion

Numerical calculations are carried out for different droplet impact conditions to obtain the time evolution of the spreading droplet radius by solving Eqs. (18) to (24) without considering the effect of wetting. A predictor-corrector numerical scheme is used for the numerical calculation. Note that the effect of wetting is ignored in the calculations just to show the improvement of the present modified model through the comparison between the present model predictions with that of DR model. The calculations of the droplet spreading by previous models employing Madejski's approach [13,15–18] rely on the arbitrary choice of ε. For instance, Madejski [13] and Zhang [17] chosen ε arbitrarily as 0.5 for the estimation of R_0. In this context, Delplanque and Rangel [15] suggested that $\varepsilon=0.74$ as the only physically possible value, however their continued investigation considered a different value for ε as 0.39 [16]. In this study, the predictions of the spreading droplet radius from DR model are obtained with $\varepsilon=0.39$ and 0.74.

Without Solidification ($K=0$). At first, the comparisons are made without considering the solidification process, i.e., $K=0$. Figure 2 shows the variation of R with time for an ink droplet of $D=2.96$ mm impinging with velocity $W=1.36$ m/s. The experimental data for this specific case is taken from [16] and [20]. The present model calculation requires the value of θ for the calculation of R_0 and Λ. The value θ can be estimated from the static contact angle, θ_s as

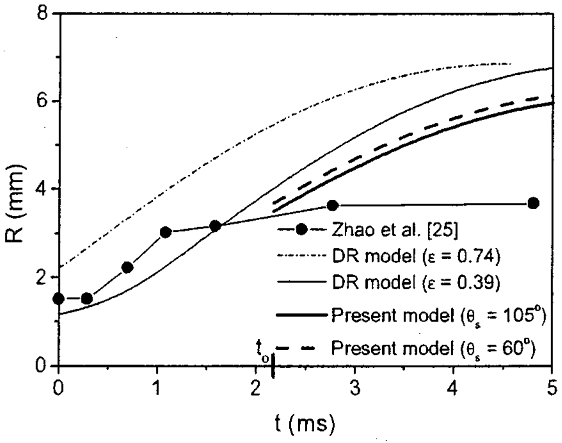

Fig. 2 Comparison of the model predictions on the evolution of the spreading droplet radius (R) for the impact of an ink droplet with D=2.96 mm and W=1.36 m/s (Re=4000 and We =72)

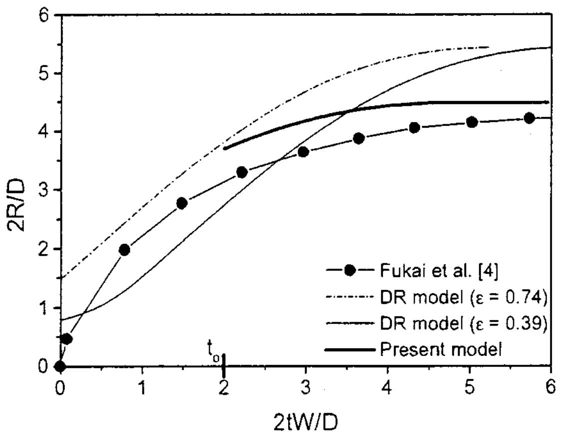

Fig. 3 Comparison of the model predictions on the evolution of the spreading droplet radius (R) for the impact of a water droplet with $D=3.7$ mm and $W=1.48$ m/s (Re=6980 and We =114). The experimentally measured value of the dynamic contact angle, $\theta=49°$ is used for the present calculations.

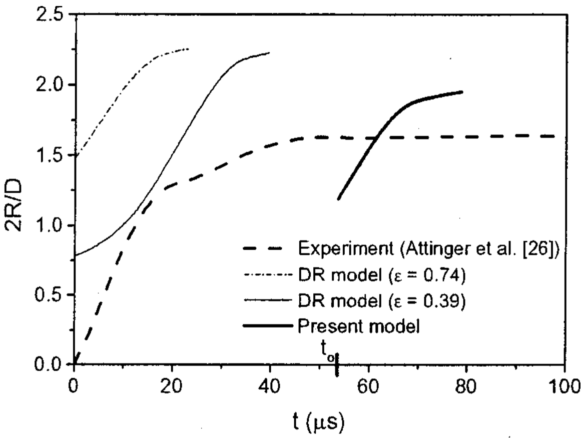

Fig. 4 Comparison of the model predictions on the evolution of the droplet spreading radius (R) with solidification for a molten solder droplet of $D=81.4\,\mu$m and $W=1.52$ m/s impinging on a substrate with $T_o=135°$C

$$\theta=\cos^{-1}\left\{1-2\tanh\left[5.16\left(\frac{Ca}{1+1.31Ca^{0.99}}\right)^{0.706}\right]\right\}+\theta_s \tag{25}$$

where $\mathrm{Ca}=\mu W_c/\sigma$ is the capillary number based on the liquid contact line velocity, W_c which is approximated during the initial stages of impact as W. For this particular calculation, the value of θ_s is taken arbitrarily as 105 deg from the previous experiments of the droplet impact obtained by using water as the experimental liquid [7]. Note that the value of θ_s chosen for the present calculation is showing a minor change in the variation of R as seen from the comparison of the present model results obtained for $\theta_s=105$ deg and 60 deg. Since the present model predictions start only after t_o, the variation of R at the beginning of drop impact is not shown in Fig. 2. In general, the variation trend of the present model results is same as the DR model results with $\varepsilon=0.39$; however, as seen in Fig. 2, the present predictions are found to be closer to the experimental measurements than the results of DR model.

Fukai et al. [4] reported the experimental measurements of θ for their droplet impact experiments in addition to the instantaneous variation of the droplet spreading radius. Figure 3 shows the variation of the spreading droplet radius with the nondimensional time parameter, tW/D for an experimental case reported by Fukai et al. [4]. The details of the impinging water droplet are given in the figure caption and the value of θ is taken as 49 deg, as reported by Fukai et al. [4], for the present model calculations. As observed in the previous case, the present model results are much closer to the experimental results than that of DR model.

With Solidification ($K>0$). The droplet spreading characteristics for the solidification case are shown in Figs. 4 and 5 for the impinging molten solder droplets with $D=81.4\,\mu$m and $W=1.52$ m/s (We=4.4 and Re=381) at different substrate temperature, T_o. The variation in T_o provides the droplet impact cases with varying solidification parameter, K. The corresponding experimental data on the instantaneous variation of R are taken from the study reported by Attinger et al. [26]. For every T_o, the Stefan number (St) is calculated by using Eq. (2) and the corresponding value of U is obtained by solving Eq. (1). The value of θ_s is taken as 105 deg for the calculation of b_o. Figure 4 shows the numerical predictions obtained from the present model and DR model on the variation of R with t for St=0.027 along with the experimental trace taken from Attinger et al. [26]. As seen in Fig. 4, the predictions of R made by using the present model agree with experimental results in qualitative comparisons. Nevertheless a better prediction of the maximum spreading droplet radius is seen from the present model results compared to the results obtained from DR model. The variation of the maximum spreading droplet radius, $(2R/D)_{\max}$, at which the radial velocity of the spreading molten liquid layer is zero, with St is shown in Fig. 5. It is clearly seen from Fig. 5 that the present model is improved the quantitative predictions of $R_{\max}$ significantly.

The above results clearly indicate that the present modified model shows better predictions for the droplet spreading process without solidification. In the case of the droplet spreading with solidification, an improved quantitative agreement for the maximum spreading droplet radius is obtained. It is also emphasized here that the present model with modified initial conditions is eliminated the adjustable parameter ε used in previous models [13,15–18] without losing the salient features of the original model. Although the present predictions for the droplet spreading with solidification agree only on the qualitative terms, it may be possible to improve the predictions further by including the effect of wettability, energy losses due to solidification, and thermal contact resistance [23] in the governing equation and initial conditions.

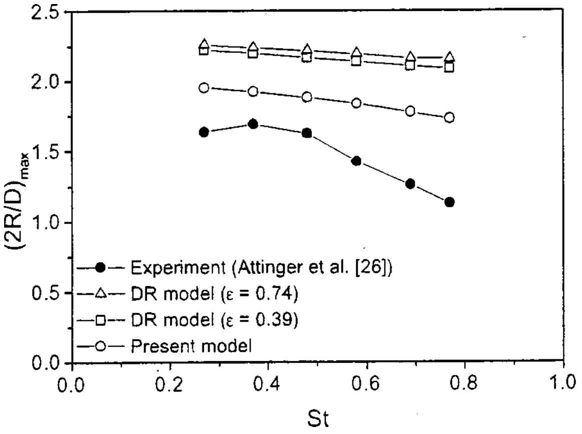

Fig. 5 Present model predictions on the variation of the maximum spreading droplet radius with St for the impact of molten solder droplets with $D=81.4\,\mu$m and $W=1.52$ m/s

Conclusion

The initial conditions employed in Madejski's splat quench solidification model are modified by considering a more realistic approach in which the initial conditions are estimated at a definite time after the start of impact. With the current approach, the arbitrary parameter involved in the previous models employing Madejski's approach for the estimation of initial conditions can be removed. The results obtained from the present model are compared with the previous model results and experimental results reported in the literature. It is observed that the present modified model shows better agreements with the experimental results.

Acknowledgment

The authors thank Japan Society for the Promotion of Science (JSPS) for the financial support during the academic year 2003–2004.

References

[1] Pawlowski, L., 1995, *The Science and Engineering of Thermal Spray Coatings*, Wiley, New York.

[2] Mostaghimi, J., Pasandideh-Fard, M., and Chandra, S., 2002, ''Dynamics of Splat Formation in Plasma Spray Coating Process,'' Plasma Chem. Plasma Process., **22**, pp. 59–84.

[3] Chandra, S., and Avedisian, C. T., 1991, ''On the Collision of a Droplet With a Solid Surface,'' Proc. R. Soc. London, Ser. A, **432**, pp. 13–41.

[4] Fukai, J., Shiiba, Y., Yamomoto, T., Poulikakos, D., Megaridis, C. M., and Zhao, Z., 1995, ''Wetting Effects on the Spreading of a Liquid Droplet Colliding With a Flat Surface: Experiment and Modeling,'' Phys. Fluids, **7**, pp. 236–247.

[5] Bussmann, M., Mostaghimi, J., and Chandra, S., 1999, ''On a Three-Dimensional Volume Tracking Model of Droplet Impact,'' Phys. Fluids, **11**, pp. 1406–1417.

[6] Rioboo, R., Marengo, M., and Tropea, C., 2002, ''Time Evolution of Liquid Drop Impact Onto Solid, Dry Surfaces,'' Exp. Fluids, **33**, pp. 112–124.

[7] Roisman, I. V., Romain, R., and Tropea, C., 2002, ''Normal Impact of a Liquid Drop on a Dry Surface: Model for Spreading and Receding,'' Proc. R. Soc. London, Ser. A, **458**, pp. 1411–1430.

[8] Pasandideh-Fard, M., Chandra, S., Bhola, R., and Mostaghimi, J., 1998, ''Deposition of Tin Droplets on a Steel Plate: Simulations and Experiments,'' Int. J. Heat Mass Transfer, **41**, pp. 2929–2945.

[9] Amon, C. H., Schmaltz, K. S., Merz, R., and Prinz, F. B., 1996, ''Numerical and Experimental Investigation of Interface Bonding Via Substrate Remelting of an Impinging Molten Metal Droplet,'' ASME J. Heat Transfer, **118**, pp. 164–172.

[10] Zarzalejo, L. J., Schmaltz, K. S., and Amon, C. H., 1999, ''Molten Droplet Solidification and Substrate Remelting in Microcasting Part I: Numerical Modeling and Experimental Verification,'' Heat Mass Transfer, **34**, pp. 477–485.

[11] Schmaltz, K. S., Zarzalejo, L. J., and Amon, C. H., 1999, ''Molten Droplet Solidification and Substrate Remelting in Microcasting Part II: Parametric Study and Effect of Dissimilar Materials,'' Heat Mass Transfer, **35**, pp. 17–23.

[12] Pasandideh-Fard, M., Chandra, S., and Mostaghimi, J., 2002, ''A Three-Dimensional Model of Droplet Impact and Solidification,'' Int. J. Heat Mass Transfer, **45**, pp. 2229–2242.

[13] Madejski, J., 1976, ''Solidification of Droplets on a Cold Surface,'' Int. J. Heat Mass Transfer, **19**, pp. 1009–1013.

[14] Markworth, A. J., and Saunders, J. H., 1992, ''An Improved Velocity Field for the Madejski Splat-Quench Solidification Model,'' Int. J. Heat Mass Transfer, **35**, pp. 1836–1837.

[15] Delplanque, J. P., and Rangel, R. H., 1997, ''An Improved Model for Droplet Solidification on a Flat Surface,'' J. Mater. Sci., **32**, pp. 1519–1530.

[16] Delplanque, J. P., and Rangel, R. H., 1998, ''A Comparison of Models, Numerical Simulation, and Experimental Results in Droplet Deposition Processes,'' Acta Mater., **46**, pp. 4925–4933.

[17] Zhang, H., 1999, ''Theoretical Analysis of Spreading and Solidification of Molten Droplet During Thermal Spray Deposition,'' Int. J. Heat Mass Transfer, **42**, pp. 2499–2508.

[18] Wan, Y. P., Zhang, H., Jiang, X. Y., Sampath, S., and Prasad, V., 2001, ''Role of Solidification, Substrate Temperature and Reynolds Number on Droplet Spreading in Thermal Spray Deposition: Measurements and Modeling,'' ASME J. Heat Transfer, **123**, pp. 382–389.

[19] Haller, K. K., Ventikos, Y., Poulikakos, D., and Monkewitz, P., 2002, ''A Computational Study High Speed Liquid Droplet Impact,'' J. Appl. Phys., **92**, pp. 2821–2828.

[20] Haller, K. K., Ventikos, Y., and Poulikakos, D., 2003, ''Wave Structure in the Contact Line Region During High Speed Droplet Impact on a Surface: Solution of the Riemann Problem for the Stiffened Gas Equation of State,'' J. Appl. Phys., **93**, pp. 3090–3097.

[21] Haller, K. K., Ventikos, Y., Poulikakos, D., and Monkewitz, P., 2003, ''Shock Wave Formation in Droplet Impact on a Rigid Surface: Lateral Liquid Motion and Multiple Wave Structure in the Contact Line Region,'' J. Fluid Mech., **490**, pp. 1–14.

[22] Schiaffino, S., and Sonin, A. A., 1997, ''Motion and Arrest of a Molten Contact Line on a Cold Surface: An Experimental Study,'' Phys. Fluids, **9**, pp. 2217–2226.

[23] Aziz, S. D., and Chandra, S., 2000, ''Impact, Recoil and Splashing of Molten Metal Droplets,'' Int. J. Heat Mass Transfer, **43**, pp. 2841–2857.

[24] Rangel, R. H., and Bian, X., 1996, ''The Inviscid Stagnation-Flow Solidification Problem,'' Int. J. Heat Mass Transfer, **39**, pp. 1591–1602.

[25] Zhao, Z., Poulikakos, D., and Fukai, J., 1996, ''Heat Transfer and Fluid Dynamics During the Collision of a Droplet on a Substrate: II—Experiments,'' Int. J. Heat Mass Transfer, **39**, pp. 2791–2802.

[26] Attinger, D., Zhao, Z., and Poulikakos, D., 2000, ''An Experimental Study of Molten Microdroplet Surface Deposition and Solidification: Transient Behavior and Wetting Angle Dynamics,'' ASME J. Heat Transfer, **122**, pp. 544–556.

Journal of Heat Transfer

Erratum

Erratum: "Radiative Heating of Semi-Transparent Diesel Fuel Droplets" [Journal of Heat Transfer, 2004, 126(1), pp. 105–109]

S. S. Sazhin, W. A. Abdelghaffar, E. M. Sazhina, S. V. Mikhalovsky, S. T. Meikle, and C. Bai

[DOI: 10.1115/1.1738419]

The number of digits presented for some values of coefficients in Tables 1 and 2 are not sufficient for accurate calculation of the parameter Λ_0 at high temperatures. More accurate values of these coefficients are presented below in the revised versions of these tables. Authors are grateful to Dr. B. Abramzon for drawing their attention to this inconsistency of the paper.

Table 1

Type of fuel	$R_{\min}/\mu m$	$R_{\max}/\mu m$	a_0	a_1 (K^{-1})	a_2 (K^{-2})	b_0	b_1 (K^{-1})	b_2 (K^{-2})
Yellow unboiled	5	50	0.10400	−0.054320	0.008000	0.49162	0.098369	−0.007857
Yellow unboiled	5	100	0.12358	−0.066360	0.010000	0.42402	0.115583	−0.009886
Yellow unboiled	5	200	0.01689	−0.094840	0.014800	0.31518	0.146189	−0.014057
Yellow unboiled	2	50	0.10350	−0.053210	0.007980	0.49590	0.096781	−0.007632
Yellow unboiled	2	200	0.15412	−0.085400	0.013200	0.33988	0.138394	−0.013029
Pink unboiled	5	50	0.08876	−0.046280	0.006800	0.44544	0.131457	−0.013714
Pink unboiled	5	100	0.09654	−0.050609	0.007457	0.41346	0.136374	−0.014029
Pink unboiled	5	200	0.11596	−0.061626	0.009171	0.35694	0.141951	−0.014143
Pink unboiled	2	50	0.09040	−0.046110	0.006724	0.44300	0.129870	−0.012980
Pink unboiled	2	200	0.11116	−0.058757	0.008714	0.36804	0.138994	−0.013829
Yellow boiled	5	50	0.10930	−0.056446	0.008171	0.50826	0.079017	−0.007314
Yellow boiled	5	100	0.13188	−0.069380	0.010200	0.44010	0.087643	−0.007686
Yellow boiled	5	200	0.18430	−0.100843	0.015286	0.33048	0.109137	−0.009714
Yellow boiled	2	50	0.10800	−0.054320	0.008014	0.51330	0.078932	−0.007312
Yellow boiled	2	200	0.16624	−0.090011	0.013543	0.35550	0.104551	−0.009343
Pink boiled	5	50	0.07160	−0.031469	0.004057	0.44202	0.177531	−0.022343
Pink boiled	5	100	0.07786	−0.033474	0.004229	0.41654	0.169563	−0.021686
Pink boiled	5	200	0.09168	−0.035854	0.004029	0.38168	0.139197	−0.016714
Pink boiled	2	50	0.07250	−0.030875	0.004032	0.44220	0.017540	−0.022120
Pink boiled	2	200	0.08784	−0.034866	0.003971	0.38976	0.141946	−0.016771

Table 2

Type of fuel	$R_{\mathrm{min}}/\mu\mathrm{m}$	$R_{\mathrm{max}}/\mu\mathrm{m}$	a_0	a_1 (K^1)	a_2 (K^{-2})	a_3 (K^{-3})	a_4 (K^{-4})	b_0	b_1 (K^{-1})	b_2 (K^{-2})	b_3 (K^{-3})	b_4 (K^{-4})
Yellow unboiled	5	50	−0.0417	0.28362	−0.26836	0.09526	−0.011767	0.9671	−0.9761	0.84533	−0.28534	0.034233
Yellow unboiled	5	100	−0.0442	0.32398	−0.31034	0.11081	−0.013733	0.8819	−0.9163	0.80674	−0.27215	0.032533
Yellow unboiled	5	200	−0.0463	0.40945	−0.40219	0.14532	−0.018133	0.7496	−0.8308	0.75706	−0.25621	0.030533
Yellow unboiled	2	50	−0.0440	0.27981	−0.25981	0.09478	−0.011520	0.9798	−0.9698	0.85673	−0.27982	0.033134
Yellow unboiled	2	200	−0.0474	0.38577	−0.37553	0.13517	−0.016833	0.7824	−0.8579	0.77432	−0.26198	0.031267
Pink unboiled	5	50	−0.0565	0.29014	−0.26793	0.09457	−0.011667	0.9862	−1.1016	0.97560	−0.33451	0.040567
Pink unboiled	5	100	−0.0621	0.31707	−0.29294	0.10345	−0.012767	0.9636	−1.1152	0.98742	−0.33765	0.040833
Pink unboiled	5	200	−0.0720	0.37382	−0.34642	0.12240	−0.015100	0.8995	−1.0880	0.96582	−0.32892	0.039600
Pink unboiled	2	50	−0.0570	0.29030	−0.26583	0.09352	−0.011392	0.9681	−1.1009	0.96537	−0.27613	0.042184
Pink unboiled	2	200	−0.0689	0.35806	−0.33151	0.11706	−0.014433	0.9063	−1.0819	0.95965	−0.32700	0.039400
Yellow boiled	5	50	−0.0395	0.28796	−0.27275	0.09658	−0.011900	0.9388	−0.9035	0.78188	−0.26714	0.032433
Yellow boiled	5	100	−0.0409	0.33132	−0.31734	0.11285	−0.013933	0.8375	−0.8168	0.71621	−0.24414	0.029533
Yellow boiled	5	200	−0.0410	0.42355	−0.41523	0.14897	−0.018467	0.6954	−0.7176	0.64863	−0.22082	0.026567
Yellow boiled	2	50	−0.0420	0.27893	−0.26731	0.09367	−0.016721	0.9596	−0.9007	0.76258	−0.25817	0.031425
Yellow boiled	2	200	−0.0432	0.39663	−0.38514	0.13767	−0.017033	0.7331	−0.7515	0.67277	−0.22896	0.027567
Pink boiled	5	50	−0.0850	0.32863	−0.28769	0.09964	−0.012200	1.4481	−2.1310	1.84306	−0.63536	0.077600
Pink boiled	5	100	−0.0848	0.34028	−0.29836	0.10326	−0.012633	1.2870	−1.8292	1.59459	−0.55092	0.067333
Pink boiled	5	200	−0.0906	0.38067	−0.33095	0.11353	−0.013800	1.1103	−1.5294	1.32851	−0.45711	0.055700
Pink boiled	2	50	−0.0970	0.31872	−0.27829	0.09872	−0.021091	1.6235	−2.5023	0.18522	−0.63022	0.085020
Pink boiled	2	200	−0.0973	0.38854	−0.33685	0.11562	−0.014067	1.2056	−1.7258	1.48863	−0.51140	0.062300